frontiers | Research Topics

Structural aspects of peroxisome biogenesis and functions

Edited by
Marek Skoneczny, Ralf Erdmann, Tânia Francisco and Christos Gatsogiannis

Published in
Frontiers in Cell and Developmental Biology

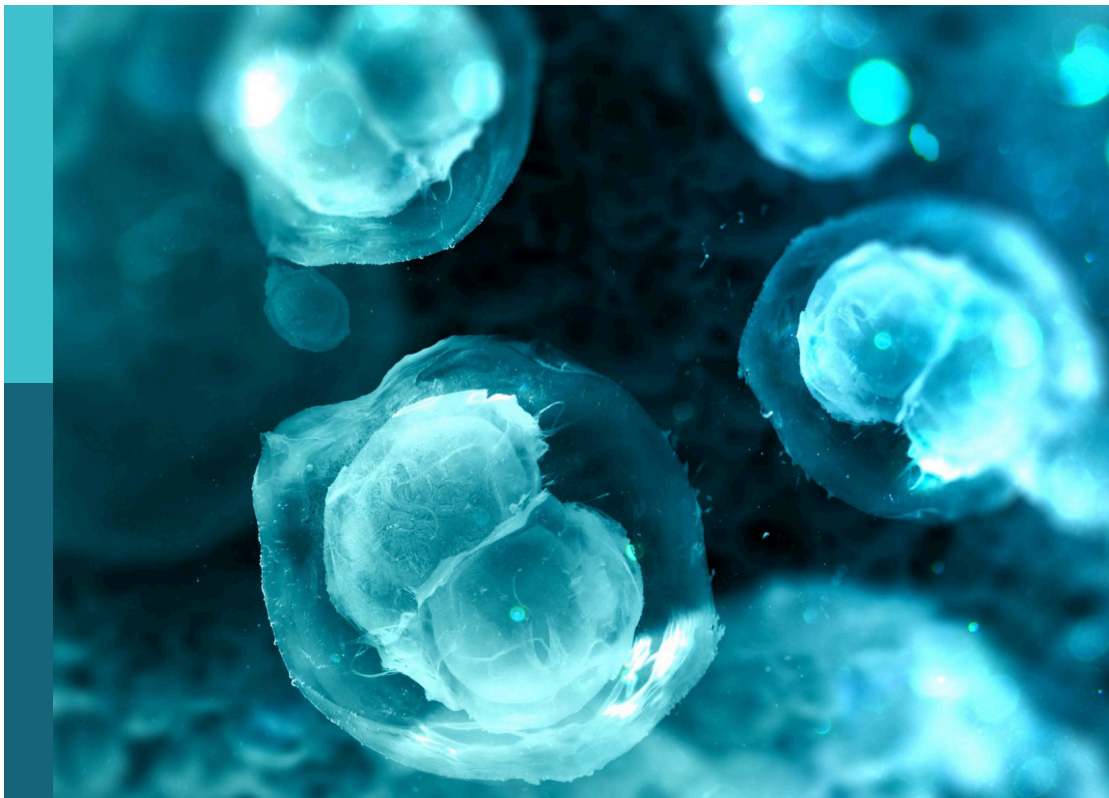

ISSN 1664-8714
ISBN 978-2-83251-177-0
DOI 10.3389/978-2-83251-177-0

About Frontiers

Frontiers is more than just an open access publisher of scholarly articles: it is a pioneering approach to the world of academia, radically improving the way scholarly research is managed. The grand vision of Frontiers is a world where all people have an equal opportunity to seek, share and generate knowledge. Frontiers provides immediate and permanent online open access to all its publications, but this alone is not enough to realize our grand goals.

Frontiers journal series

The Frontiers journal series is a multi-tier and interdisciplinary set of open-access, online journals, promising a paradigm shift from the current review, selection and dissemination processes in academic publishing. All Frontiers journals are driven by researchers for researchers; therefore, they constitute a service to the scholarly community. At the same time, the *Frontiers journal series* operates on a revolutionary invention, the tiered publishing system, initially addressing specific communities of scholars, and gradually climbing up to broader public understanding, thus serving the interests of the lay society, too.

Dedication to quality

Each Frontiers article is a landmark of the highest quality, thanks to genuinely collaborative interactions between authors and review editors, who include some of the world's best academicians. Research must be certified by peers before entering a stream of knowledge that may eventually reach the public - and shape society; therefore, Frontiers only applies the most rigorous and unbiased reviews. Frontiers revolutionizes research publishing by freely delivering the most outstanding research, evaluated with no bias from both the academic and social point of view. By applying the most advanced information technologies, Frontiers is catapulting scholarly publishing into a new generation.

What are Frontiers Research Topics?

Frontiers Research Topics are very popular trademarks of the *Frontiers journals series*: they are collections of at least ten articles, all centered on a particular subject. With their unique mix of varied contributions from Original Research to Review Articles, Frontiers Research Topics unify the most influential researchers, the latest key findings and historical advances in a hot research area.

Find out more on how to host your own Frontiers Research Topic or contribute to one as an author by contacting the Frontiers editorial office: frontiersin.org/about/contact

Structural aspects of peroxisome biogenesis and functions

Topic editors

Marek Skoneczny — Institute of Biochemistry and Biophysics, Polish Academy of Sciences, Poland

Ralf Erdmann — Ruhr University Bochum, Germany

Tânia Francisco — Universidade do Porto, Portugal

Christos Gatsogiannis — University of Münster, Germany

Citation

Skoneczny, M., Erdmann, R., Francisco, T., Gatsogiannis, C., eds. (2023). *Structural aspects of peroxisome biogenesis and functions*. Lausanne: Frontiers Media SA. doi: 10.3389/978-2-83251-177-0

Table of contents

frontiers | Frontiers in Cell and Developmental Biology

TYPE Editorial
PUBLISHED 15 December 2022
DOI 10.3389/fcell.2022.1114759

OPEN ACCESS

EDITED BY
Vladimir Lupashin,
University of Arkansas for Medical Sciences, United States

REVIEWED BY
Richard Rachubinski,
University of Alberta, Canada

*CORRESPONDENCE
Marek Skoneczny,
kicia@ibb.waw.pl

SPECIALTY SECTION
This article was submitted to Membrane Traffic, a section of the journal Frontiers in Cell and Developmental Biology

RECEIVED 02 December 2022
ACCEPTED 07 December 2022
PUBLISHED 15 December 2022

CITATION
Skoneczny M, Francisco T, Erdmann R and Gatsogiannis C (2022), Editorial: Structural aspects of peroxisome biogenesis and functions.
Front. Cell Dev. Biol. 10:1114759.
doi: 10.3389/fcell.2022.1114759

Editorial: Structural aspects of peroxisome biogenesis and functions

Marek Skoneczny[1]*, Tânia Francisco[2,3], Ralf Erdmann[4] and Christos Gatsogiannis[5]

[1]Institute of Biochemistry and Biophysics, Polish Academy of Sciences, Warsaw, Poland, [2]Instituto de Investigação e Inovação em Saúde (i3S), Universidade do Porto, Porto, Portugal, [3]Instituto de Biologia Molecular e Celular (IBMC), Universidade do Porto, Porto, Portugal, [4]Institut für Biochemie und Pathobiochemie, Abteilung für Systembiochemie, Ruhr-Universität Bochum, Bochum, Germany, [5]Center for Soft Nanoscience, Institute of Medical Physics and Biophysics, Münster, Germany

KEYWORDS

eukaryotic cells, glycosomes, import mechanisms, human health, signaling

Editorial on the Research Topic
Structural aspects of peroxisome biogenesis and functions

Peroxisomes and their cognate organelles glyoxysomes and glycosomes comprise vital compartments of eukaryotic cells. Despite the wealth of knowledge about this subcellular compartment accumulated over recent decades, peroxisomes are always ready to surprise us with novelty. Many aspects of peroxisome function and biogenesis are still not fully explored and the structural complexities of peroxisomal constituents are also not explained in full detail. Some functions of these organelles are common to the cells of all eukaryotic kingdoms, whereas others can be found only in cells of specific organisms. Even though the articles encompassing this Research Topic represent but a small sample of what is currently happening in peroxisomal studies, they document the structural and functional diversity of this ubiquitous organelle.

The import mechanisms of peroxisomal proteins constitute a considerable portion of peroxisomal research. In this Research Topic, three articles are devoted to this subject, reporting studies in yeast, plant, and mammalian cells. In Traver et al., the authors determined the crystal structure of the PEX4-PEX22 complex that ubiquitinates peroxisomal membrane proteins and thereby participates in peroxisome biogenesis. In Hochreiter et al., the authors employed a modification of the FRET technique to study the interaction between peroxisomal import receptor PEX5 and several peroxisomal targeting signal 1 (PTS1)-containing cargoes. In Ast et al., the authors reported a Research Topic on the theme of Pex5 cargo recognition found in *Ustilago maydis*.

Another aspect of peroxisome function well known to peroxisome researchers but mostly unknown to other life scientists is the presence of specialized peroxisomes called glycosomes in the parasitic protozoa, such as the Trypanosoma. The uniqueness of the functions of this peroxisome variant is fodder for evolutionary considerations. In the Hypothesis and Theory paper (Andrade-Alviárez et al.), the authors explored the

evolution of glycosomes by analyzing genomic, transcriptomic, and proteomic data available for these protozoa. Studying glycosomes is not just purely of scientific interest but is also crucial for human health. The evolutionary distance between Trypanosoma and humans spawned the search for drugs that could inhibit the growth of this parasite by poisoning its glycosomal function without affecting the peroxisomal functions of the human host. Two articles in this Research Topic (Li et al., Banerjee et al.) presented the results of such searches where the authors employed the collection of chemical compounds (DIVERSet-CL and LOPAC 1280, respectively) and obtained promising candidate drugs. Those compounds may be the starting point for developing safe and effective anti-trypanosomal therapies.

Studying human peroxisomes has important medical implications as well. Mutations inactivating genes encoding proteins involved in peroxisome biogenesis often lead to death in early infancy. However, the severity of symptoms of these peroxisome biogenesis disorders (PBDs) is variable; some mutations cause milder, non-lethal variants of these diseases. In the article by Liu et al., the authors found a compound from the LOPAC 1280 drug library that improved the functions of peroxisomes in fibroblasts bearing such non-lethal mutation. These findings may ultimately lead to the development of novel therapies that would improve the quality of life of patients suffering from compromised peroxisomal functions.

Recently, peroxisomes have been widely recognized as signaling hubs and protective organelles with central regulatory roles in immunity. Peroxisomes provide a platform for cellular anti-viral signaling, and they play a role in the control of bacterial infections and as regulators of inflammatory processes. The authors of two papers investigated such functions of peroxisomes in mammals. Ferreira et al. explored the specifics of peroxisome involvement in anti-viral signaling, while Meghnem et al. demonstrated that peroxisome functions, especially in fatty acid homeostasis, are crucial for activating mast cells, a component of the mammalian immune system.

Author contributions

MS wrote the first draft of the manuscript. All authors contributed to manuscript revision, read, and approved the submitted version.

Conflict of interest

The authors declare that the research was conducted in the absence of any commercial or financial relationships that could be construed as a potential conflict of interest.

Publisher's note

frontiers in Cell and Developmental Biology

ORIGINAL RESEARCH
published: 19 July 2021
doi: 10.3389/fcell.2021.703603

A Small Molecule Inhibitor of Pex3–Pex19 Interaction Disrupts Glycosome Biogenesis and Causes Lethality in *Trypanosoma brucei*

*Hiren Banerjee, Paul LaPointe, Gary Eitzen and Richard A. Rachubinski**

Department of Cell Biology, University of Alberta, Edmonton, AB, Canada

OPEN ACCESS

Edited by:
Marek Skoneczny, Institute of Biochemistry and Biophysics, Polish Academy of Sciences (PAN), Poland

Reviewed by:
Paul Michels, University of Edinburgh, United Kingdom
Tsuneo Imanaka, Hiroshima International University, Japan

***Correspondence:**
Richard A. Rachubinski
rick.rachubinski@ualberta.ca

Specialty section:
This article was submitted to Membrane Traffic, a section of the journal Frontiers in Cell and Developmental Biology

Received: *30 April 2021*
Accepted: *22 June 2021*
Published: *19 July 2021*

Citation:
Banerjee H, LaPointe P, Eitzen G and Rachubinski RA (2021) A Small Molecule Inhibitor of Pex3–Pex19 Interaction Disrupts Glycosome Biogenesis and Causes Lethality in Trypanosoma brucei. Front. Cell Dev. Biol. 9:703603. doi: 10.3389/fcell.2021.703603

Trypanosomatid parasites, including *Trypanosoma* and *Leishmania*, are infectious zoonotic agents for a number of severe diseases such as African sleeping sickness and American trypanosomiasis (Chagas disease) that affect millions of people, mostly in the emergent world. The glycosome is a specialized member of the peroxisome family of organelles found in trypanosomatids. These organelles compartmentalize essential enzymes of the glycolytic pathway, making them a prime target for drugs that can kill these organisms by interfering with either their biochemical functions or their formation. Glycosome biogenesis, like peroxisome biogenesis, is controlled by a group of proteins called peroxins (Pex). Pex3 is an early acting peroxin that docks Pex19, the receptor for peroxisomal membrane proteins, to initiate biogenesis of peroxisomes from the endoplasmic reticulum. Identification of Pex3 as the essential master regulator of glycosome biogenesis has implications in developing small molecule inhibitors that can impede Pex3–Pex19 interaction. Low amino acid sequence conservation between trypanosomatid Pex3 and human Pex3 (HsPex3) would aid in the identification of small molecule inhibitors that selectively interfere with the trypanosomatid Pex3–Pex19 interaction. We tested a library of pharmacologically active compounds in a modified yeast two-hybrid assay and identified a compound that preferentially inhibited the interaction of *Trypanosoma brucei* Pex3 and Pex19 versus HsPex3 and Pex19. Addition of this compound to either the insect or bloodstream form of *T. brucei* disrupted glycosome biogenesis, leading to mislocalization of glycosomal enzymes to the cytosol and lethality for the parasite. Our results show that preferential disruption of trypanosomal Pex3 function by small molecule inhibitors could help in the accelerated development of drugs for the treatment of trypanosomiases.

Keywords: neglected tropical disease, trypanosome, glycosome, organelle biogenesis, protein–protein interaction, yeast two-hybrid, drug screening, small molecule inhibitor

Abbreviations: BSF, bloodstream form; DMNQ, 2,3-dimethoxy-1,4-naphthoquinone; EC_{50}, half-maximal effective concentration; ER, endoplasmic reticulum; NTD, neglected tropical disease; PCF, procyclic form; *PEX*, gene required for peroxisome (glycosome) assembly; Pex, protein encoded by *PEX* gene; PMP, peroxisomal membrane protein.

INTRODUCTION

Neglected tropical diseases (NTDs) are a group of infectious parasitic diseases that threaten the populations of many emerging nations (Stuart et al., 2008; Mitra and Mawson, 2017; World Health Organization, 2017). Sleeping sickness is a NTD of sub-Saharan Africa whose infectious agent is the protozoan parasite, *T. brucei*. Left untreated, sleeping sickness is fatal. Current drugs such as melarsoprol, suramin, pentamidine, eflornithine, fexinidazole, and nifurtimox have shown efficacy in treating sleeping sickness, but their utility can be restricted because of toxicity, severe side effects, and complicated administration (Nwaka and Hudson, 2006; Giordani et al., 2016; de Rycker et al., 2018; De Koning, 2020). Moreover, NTDs impact mostly those countries that lack the financial or infrastructural resources needed to develop or deliver new therapies. Therefore, the identification of novel drug targets and the development of new drugs for these targets remain ongoing pursuits.

Trypanosomatid parasites contain a specialized peroxisome called the glycosome. Glycosomes compartmentalize enzymes of the glycolytic pathway, which are located in the cytosol of cells of other organisms (Guerra-Giraldez et al., 2002; Haanstra et al., 2008, 2016). Because glycosomes are both unique to trypanosomatids and house essential metabolic enzymes (Haanstra et al., 2016; Crowe and Morris, 2021), they are an ideal target for drug development. The biogenesis of glycosomes is controlled by *PEX* genes that encode proteins called peroxins (Pex). Pex3 docks Pex19, the receptor for peroxisomal membrane proteins (PMPs), which results in the biogenesis of peroxisome precursors from the endoplasmic reticulum (ER) (Ghaedi et al., 2000; Fang et al., 2004; Smith and Aitchison, 2013). We identified the long sought trypanosomal Pex3 (TbPex3) by an analysis of human Pex3 (HsPex3) through the HHpred bioinformatics platform, which looks for similarities in protein secondary structure rather than for similarities in protein primary structure (Banerjee et al., 2019). TbPex3 was also identified independently using biochemical means (Kalel et al., 2019). Reduction in the amounts of TbPex3 led to reduced numbers of enlarged glycosomes and to the mislocalization of glycosomal matrix enzymes to the cytosol in both procyclic form (PCF) cells and bloodstream form (BSF) cells of *T. brucei*. Notably, reductions in the amount of TbPex3 led to death of all PCF and BSF cells.

Trypanosomal Pex3 exhibits only 7% amino acid identity with HsPex3 but does maintain a relatively conserved Pex19 interaction domain (Banerjee et al., 2019; Kalel et al., 2019). This limited primary sequence similarity between TbPex3 and mammalian Pex3 proteins makes TbPex3 and its interactions with protein partners attractive therapeutic targets. We used the yeast two-hybrid assay to reconstitute the trypanosomal and HsPex3–Pex19 interaction in *Saccharomyces cerevisiae*. We then screened a library of pharmacologically active compounds (LOPAC 1280) to search for compounds that preferentially inhibit the trypanosomal versus the HsPex3–Pex19 interaction. The screen identified six potential candidate molecules meeting this criterion. Further analyses identified one compound more effective at blocking the interaction between TbPex3 and TbPex19 compared to HsPex3 and HsPex19. Administration of this compound led to compromised glycosome biogenesis in *T. brucei* and was lethal for both PCF and BSF cells of *T. brucei* at concentrations that have limited effect on the viability of human cells.

MATERIALS AND METHODS

Yeast Two-Hybrid Assay

PCR products encoding full-length TbPex3 and full-length HsPex3 were cloned in-frame and downstream of the DNA-binding domain (BD) of the *GAL4* transcriptional activator in pGBT9 (Clontech). Full-length TbPex19 and full-length HsPex19 were cloned in-frame and downstream of the activation domain (AD) of the *GAL4* transcriptional activator in pGAD424 (Clontech). The *S. cerevisiae* strain HF7c deleted for the *PDR5* gene (HF7c *pdr5*Δ) encoding the major drug efflux pump of yeast (Golin and Ambudkar, 2015) was transformed with plasmids, and transformed cells were grown on synthetic dropout medium agar lacking leucine and tryptophan (-Leu -Trp) to determine total cell growth and on synthetic dropout medium agar lacking histidine, leucine, and tryptophan (-His -Leu -Trp) to determine growth of cells exhibiting protein–protein interaction between the AD-fusion and BD-fusion constructs.

Yeast Two-Hybrid Screening of a Library of Small Molecules for Inhibitors of TbPex3/TbPex19 Interaction

Yeast strain H7Fc *pdr5*Δ expressing BD-TbPex3/AD-TbPex19 or BD-HsPex3/AD-HsPex19 was cultured in complete synthetic medium lacking histidine to an OD_{600} of 0.1. The 10 mM 3-aminotriazole (3AT) was added to the strain expressing BD-HsPex3/AD-HsPex19 to inhibit basal expression of the *HIS3* gene in this strain and to achieve yeast strains expressing trypanosome or human yeast two-hybrid constructs that would be equally sensitive to exogenously added compounds. 0.1 mL of cultures was dispensed into 384-well Matrix WellMate Microplates (Thermo Fisher Scientific), and 1 μL of compound from the LOPAC 1280 was added to each well to give a compound concentration of 100 μM. One microliter of DMSO was added to each well of the second row of each plate as a negative control (no inhibition), while 100 mM 3AT (final concentration) was added to wells of the 23rd row as a positive control (100% inhibition). The wells of the first and last rows contained water. Plates were incubated at 30°C, and after 24 h growth was determined by measuring the OD_{600} of each well using a Synergy HTX Multi-Mode Microplate Reader (BioTek). For each well, percent growth inhibition was calculated as $100 - 100 \times$ (growth with compound/growth no compound). Wells exhibiting >65% growth inhibition of the BD-TbPex3/AD-TbPex19 strain and <65% growth inhibition of the BD-HsPex3/AD-HsPex19 strain defined compounds were considered as preferentially inhibiting the TbPex3/TbPex19 interaction. To identify compounds that non-selectively inhibited yeast growth, the BD-TbPex3/AD-TbPex19 strain was cultured in complete synthetic medium containing histidine but lacking

tryptophan and leucine. Compounds from the LOPAC 1280 library that showed growth inhibition under these conditions were considered as general growth inhibitors.

Assay for Protein Binding

Binding between TbPex3 and TbPex19 and between HsPex3 and HsPex19 was examined essentially as described (Banerjee et al., 2019). MBP fusions to TbPex3 and HsPex3 were constructed in pMAL-c2 (New England Biolabs). 6 × His fusion to TbPex19 and HsPex19 was constructed in pET-30a (Novagen). Recombinant proteins were expressed in *Escherichia coli* strain BL21 (Invitrogen). His-TbPex19 or His-HsPex19 was immobilized on Ni-NTA Agarose (Qiagen) and incubated with purified MBP-TbPex3 or MBP-HsPex3 proteins at 4°C for 2.5 h under non-denaturing conditions suggested by the manufacturer (Qiagen). Twofold dilutions of the small molecule 2,3-dimethoxy-1,4-naphthoquinone (DMNQ) from 200 to 6 μM was added to the incubation to determine its inhibitory effect on the TbPex3–TbPex19 and the HsPex3–HsPex19 interactions. Immobilized proteins were eluted in sample buffer (50 mM Tris–HCl, pH 6.8, 2% SDS, 5% (vol/vol) glycerol, 0.002% bromophenol blue, 100 mM 2-mercaptoethanol) and subjected to immunoblotting with anti-MBP antibody (New England Biolabs) and anti-His-Tag antibody (Sigma-Aldrich).

Microscale Thermophoresis Determination of Pex3–Pex19 Binding Affinity

The binding affinity between TbPex3 and TbPex19 and between HsPex3 and HsPex19 was determined by microscale thermophoresis (MST) analysis using a Monolith NT.115 instrument under conditions suggested by the manufacturer (NanoTemper Technologies). His-TbPex19 and His-HsPex19 were labeled with NT-647 fluorescent dye (NanoTemper Technologies). Binding affinity of Pex3–Pex19 pairs was determined by combining increasing concentrations of MBP-Pex3 protein (0–2.5 μM) with 100 nM of NT-647-labeled His-Pex19 in MST buffer (50 mM Tris–HCl, pH 7.4, 150 mM NaCl, 10 mM $MgCl_2$, 0.05% Tween-20). To analyze the effect of the presence of DMNQ on the binding affinity between TbPex3 and TbPex19 and between HsPex3 and HsPex19, measurements were made using 100 nM each of NT-647-labeled His-Pex19 and MBP-Pex3 and different concentrations of DMNQ from 3 nM to 100 μM. Data analysis was done using Monolith software (NanoTemper Technologies).

Trypanocidal Activity of the Small Molecule Compound DMNQ

Bloodstream form cells of *T. brucei* Lister 427 were maintained in HMI-9 medium containing 10% fetal bovine serum (FBS), 10% Serum Plus (Sigma-Aldrich) at 37°C with 5% CO_2. PCF cells of *T. brucei* Lister 427 were maintained in SDM-79 medium (Invitrogen) containing 10% FBS at 25°C with 5% CO_2. HEK293T cells were maintained in DMEM medium containing 10% FBS at 37°C with 5% CO_2.

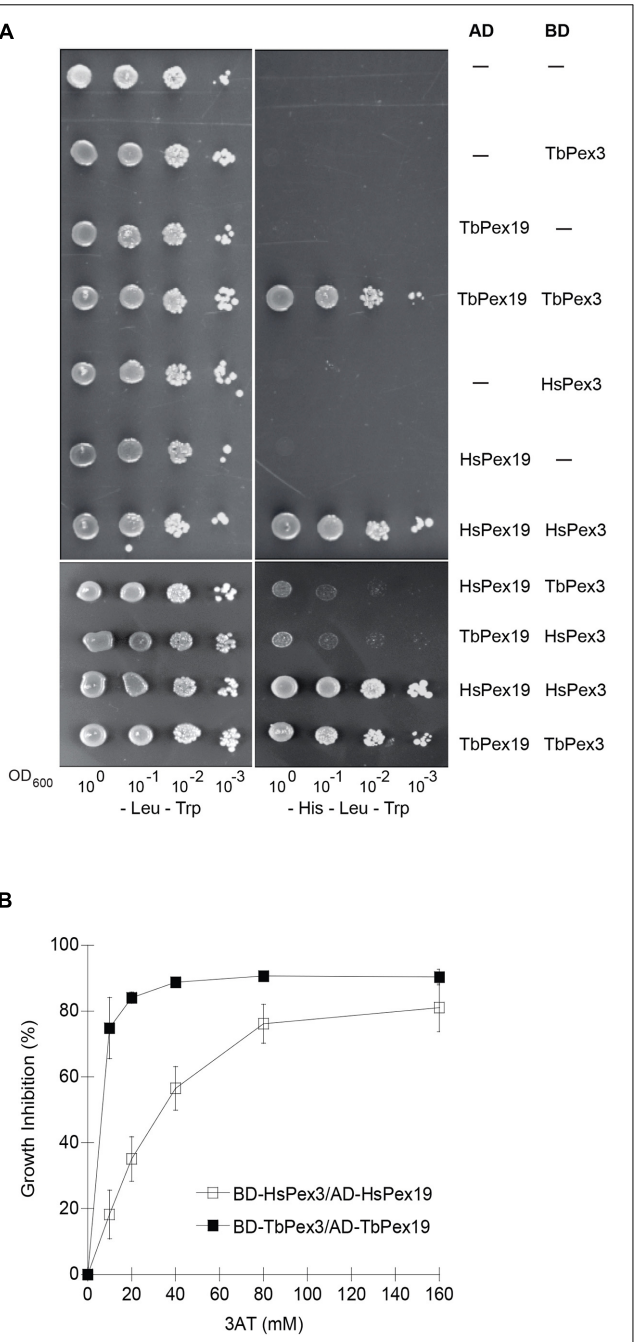

FIGURE 1 | Yeast two-hybrid analysis of protein interactions between TbPex3 and TbPex19, and between HsPex3 and HsPex19. **(A)** *S. cerevisiae* HF7c *pdr5*Δ cells expressing Gal4-AD protein fusions to human (Hs) and *T. brucei* (Tb) Pex19 and Gal4-BD protein fusions to HsPex3 and TbPex3 were grown in liquid synthetic dropout medium and adjusted to an OD_{600} of 1.0. A 10-fold serial dilution series was spotted onto -Leu -Trp (left) and -His -Leu -Trp (right) plates. Growth on -Leu -Trp medium requires cells to have both AD and BD plasmids and is indicative of cell number. Growth on -His -Leu -Trp medium occurs only when there is a protein–protein interaction. **(B)** Sensitivity of HF7c *pdr5*Δ cells expressing *T. brucei* (Tb) or human (Hs) BD-Pex3/AD-Pex19 pairs to 3-aminotriazole (3AT). Basal expression of the *HIS3* gene of yeast is competitively inhibited by 3AT. The BD-TbPex3/AD-TbPex19 interaction showed greater sensitivity than the BD-HsPex3/AD-HsPex19 interaction to the presence of 3AT.

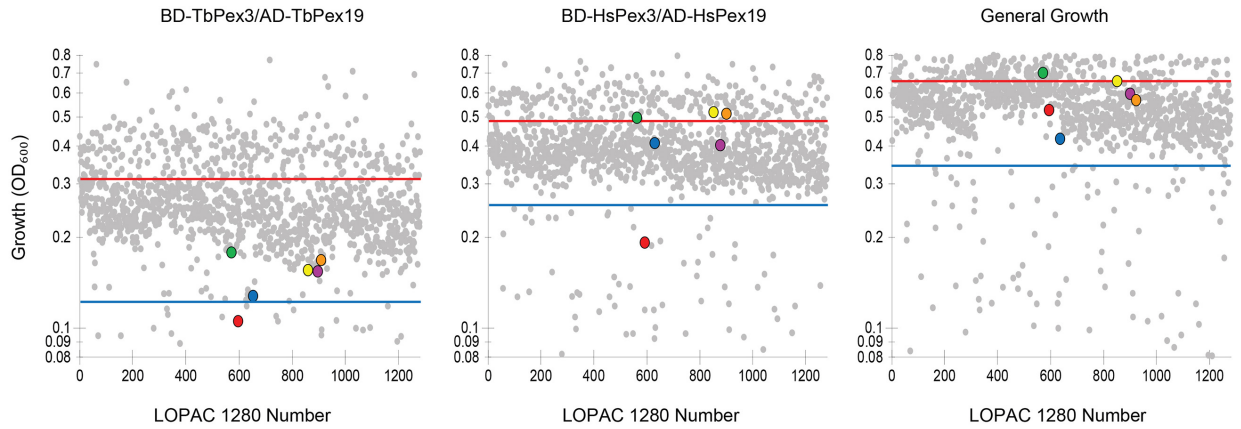

FIGURE 2 | Growth of HF7c *pdr5*Δ cells expressing *T. brucei* (Tb) or human (Hs) BD-Pex3/AD-Pex19 fusion proteins in the presence of compounds from the LOPAC 1280 library. Each compound was at 100 μM final concentration. Each dot represents the level of growth of yeast as measured by OD_{600} in the presence of a particular compound. Cells expressing BD-TbPex3/AD-TbPex19 or BD-HsPex3/AD-HsPex19 were grown in -His -Leu -Trp medium lacking histidine. General growth was measured by growth of HF7c *pdr5*Δ cells containing the parental pGAD424 and pGBT9 two-hybrid vectors in -Leu -Trp medium. The solid red line indicates average level of growth level. The blue line indicates a reduction in the level of growth of 1.5 times the standard deviation. Color legend: ● 5,7-dichlorokynurenic acid monohydrate, ● (±)-α-methyl-(4-carboxyphenyl)glycine, ● 2,3-dimethoxy-1,4-naphthoquinone, ● 7-cyclopentyl-5-(4-phenoxyphenyl)-7H-pyrrolo[2,3-d]pyrimidin-4-ylamine, ● podophyllotoxin, ● Lidocaine hydrochloride. See **Supplementary Tables 1**, **2** for details.

To measure the trypanocidal activity of the small molecule DMNQ, 50 μL of BSF cells (2×10^4 cells mL^{-1}), PCF cells (2×10^5 cells mL^{-1}), or HEK293T cells (5×10^4 mL^{-1}) were seeded into wells of a 96-well Optical-Bottom Plates (Thermo Fisher Scientific). Fifty microliters of DMSO or DMSO containing the small molecule DMNQ were added to wells to achieve a concentration of DMNQ ranging from 0 to 10 μM. Following incubation of cells at their appropriate temperatures for 24 or 48 h in the presence of DMNQ, 100 μL of CellTiter-Glo reagent (Promega) was added to each well, the plate was incubated at room temperature for 30 min, luminescence was measured, and cell viability was determined according to the manufacturer's protocol.

Immunofluorescence Microscopy and Image Analysis

Harvesting, fixation, antibody staining, confocal fluorescence microscopy, image deconvolution and image processing of PCF and BSF cells were performed essentially as described (Banerjee et al., 2019).

RESULTS

Yeast Two-Hybrid Screening Identifies a Small Molecule Inhibitor of Trypanosomal Pex3–Pex19 Interaction

The Pex3–Pex19 protein complex initiates peroxisome formation at the ER in a diversity of organisms, including the trypanosomatids. We (Banerjee et al., 2019) and others (Kalel et al., 2019) recently identified a trypanosomal ortholog of Pex3 that interacts with trypanosomal Pex19 to initiate glycosome biogenesis. Glycosomes are specialized peroxisomes that have been shown to be essential for the viability of *T. brucei* and are probably essential for the viability of all trypanosomatids. TbPex3 shows very limited amino acid sequence identity with mammalian Pex3 proteins, including HsPex3, although TbPex3 does contain a Pex19 interaction domain that is conserved in Pex3 proteins of other organisms (Banerjee et al., 2019; Kalel et al., 2019). Given the essentiality of functional glycosomes and the low amino acid sequence identity between TbPex3 and mammalian Pex3 proteins, makes TbPex3 and its interaction with Pex19 an attractive therapeutic target for the treatment of NTDs like African sleeping sickness and American trypanosomiasis.

Target-directed drug discovery is often complicated by difficulties in purifying targets or producing them in functional recombinant form, particularly if they are components of multi-protein complexes. Yeast cells expressing foreign proteins have been shown to be useful platforms for screens to identify novel drugs, including anti-parasitics (Blangy et al., 2006; Lentze and Auerbach, 2008; Bilsland et al., 2011; Wong et al., 2017). We adapted the yeast Two-hybrid protein–protein interaction reporter system to screen for compounds that preferentially impair the TbPex3–Pex19 interaction over the HsPex3–Pex19 interaction. Protein–protein interaction in the yeast Two-hybrid system leads to expression of the *HIS3* gene and growth on medium lacking histidine (-His). We used the *Saccharomyces cerevisiae* reporter strain HF7c deleted for the *PDR5* gene encoding the major drug efflux pump (HF7c *pdr5*Δ) for yeast Two-hybrid analysis (Bilsland et al., 2011). As expected, *T. brucei* Pex3 (TbPex3) interacted with TbPex19 and HsPex3 interacted with HsPex19 as shown by growth of strains containing these construct pairs on -His medium (**Figure 1A**). The lack of yeast growth on -His medium

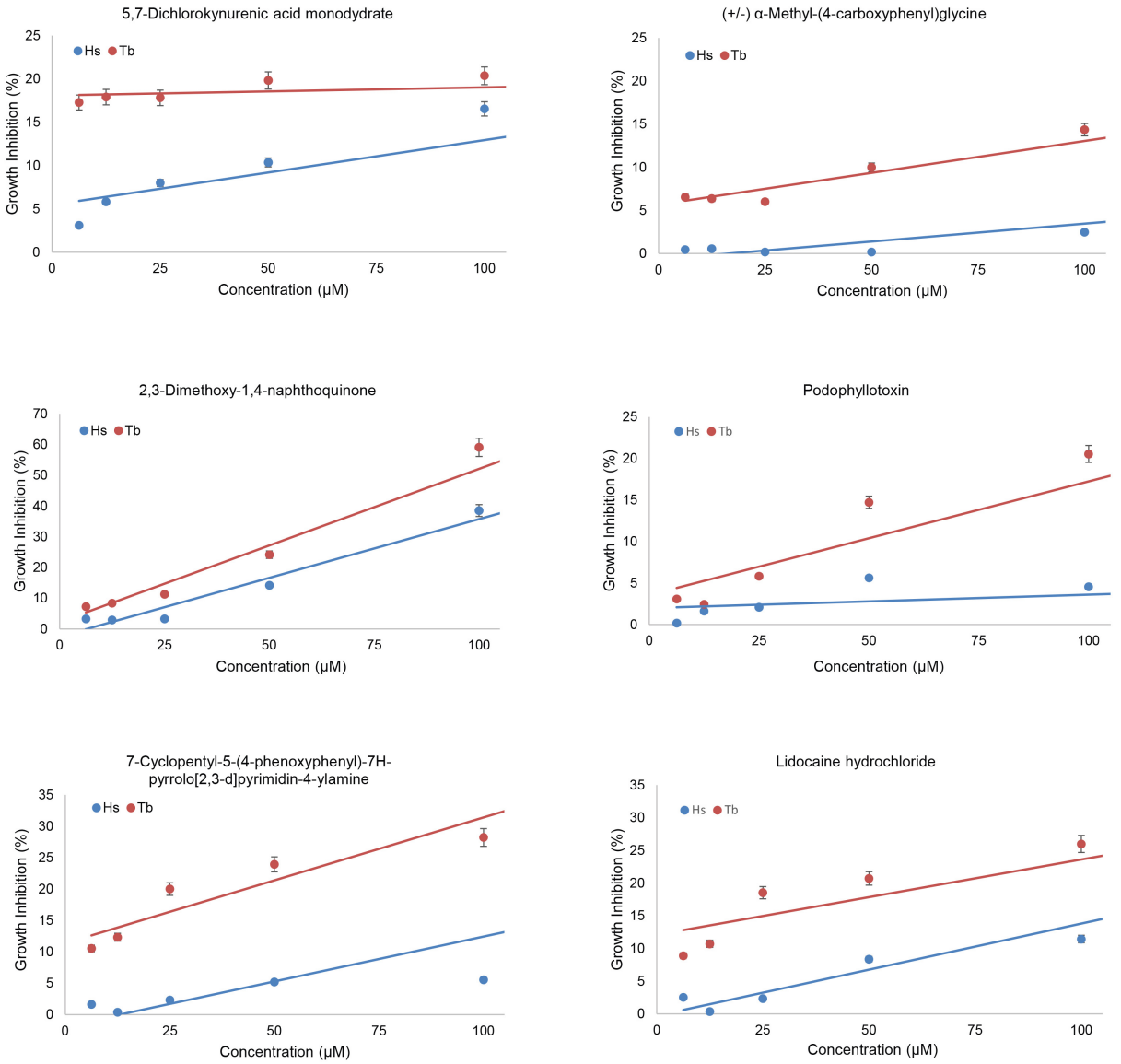

FIGURE 3 | Effects of compounds on growth of yeast two-hybrid strains expressing trypanosomal (Tb) or human (Hs) BD-Pex3/AD-Pex19. The growth of HF7c *pdr5*Δ cells expressing BD-TbPex3/AD-TbPex19 or BD-HsPex3/AD-HsPex19 in the presence of twofold dilutions from 100 to 6.25 μM of the six compounds identified by yeast two-hybrid screening of the LOPAC 1280 library was measured as OD_{600}. Growth Inhibition (%) was calculated as 100 – 100 × (growth with compound/growth no compound). The values reported are averages ± SEM of three independent experiments, each done in duplicate.

showed that there was no auto activation of any construct. There was marginal growth of strains expressing a human and *T. brucei* Pex protein pair, suggesting that there was limited interaction of Pex3 and Pex19 across species (**Figure 1A**). Therefore, compounds that disrupt a species-specific Pex3–Pex19 interaction can be found by identifying those compounds that reduce the growth of yeast strains expressing Pex3 and Pex19 from one species.

Basal expression of the *HIS3* gene of yeast is competitively inhibited by 3AT. Before beginning our compound screen using the yeast Two-hybrid system, we performed a titration to define the optimal amount of 3AT to be added to our assay to produce BD-HsPex3/AD-HsPex19 and BD-TbPex3/AD-TbPex19 expressing strains that would be equally sensitive to the addition of compound. We found that the BD-TbPex3/AD-TbPex19 interaction was more sensitive to 3AT with an IC_{50} of 6.2 mM compared to the IC_{50} of 44 mM for the BD-HsPex3/AD-HsPex19 interaction (**Figure 1B**), suggesting that the strength of interaction between Pex3 and Pex19 in the yeast Two-hybrid system was greater for the human proteins compared to the trypanosomal proteins. Accordingly, 10 mM 3AT was added to the medium for the yeast strain expressing BD-HsPex3/AD-HsPex19 to achieve equal sensitivity with the BD-TbPex3/AD-TbPex19 strain to the addition of compound.

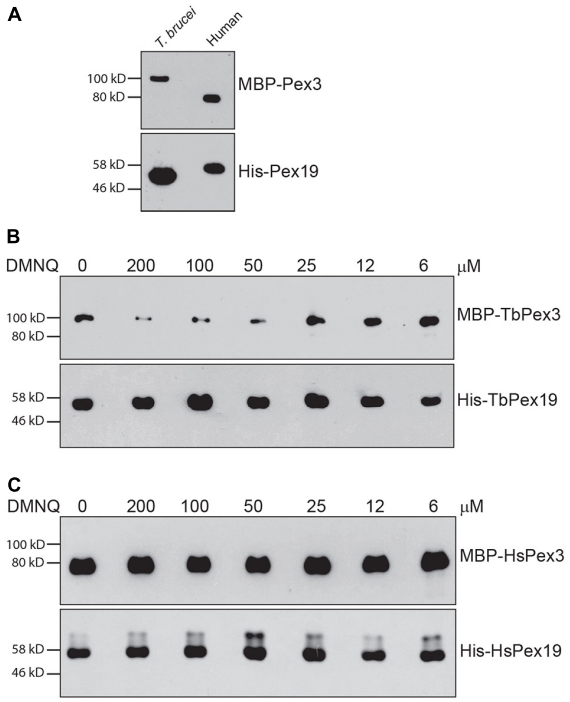

FIGURE 4 | 2,3-Dimethoxy-1,4-naphthoquinone preferentially disrupts the interaction of TbPex3/TbPex19 over HsPex3/HsPex19 in a pull-down assay. **(A)** Relative migrations in SDS-PAGE of MBP-fusions to *T. brucei* and human Pex3 proteins and of 6 × His fusions to *T. brucei* and human Pex19 proteins. Fusion proteins were detected by anti-MBP and anti-His-Tag antibodies. **(B,C)** His-Pex19 fusions were immobilized on Ni-Agarose beads and incubated with purified MBP-Pex3 fusion. Bound MBP-Pex3 protein was detected by immunoblotting with anti-MBP antibody. Total His-Pex19 protein was visualized by immunoblotting with anti-His-Tag antibody. Twofold dilutions of DMNQ from 200 to 6 μM were added during incubations. Numbers at left denote migration of molecular mass markers in kilodaltons (kD). Images are representative of three independent experiments.

We screened the LOPAC 1280 to identify compounds that interfered preferentially with the BD-TbPex3/AD-TbPex19 interaction compared to the BD-HsPex3/AD-HsPex19 interaction as measured by inhibition of growth of the respective yeast expression strains in -His -Leu -Trp medium. Non-specific inhibition of growth by compounds was evaluated in -Leu -Trp medium. Each compound was assayed at a final concentration of 100 μM. The extent of inhibition of both BD-Pex3/AD-Pex19 pairs for all compounds tested is presented in **Figure 2** and **Supplementary Table 1**. The compounds assayed are listed in **Supplementary Table 2**. Six compounds that preferentially inhibited the BD-TbPex3/AD-TbPex19 interaction over its human pairing (**Figure 2** and **Supplementary Figure 1**) were selected for further analysis. Addition of the six compounds at concentrations from 200 to 6.25 μM showed that DMNQ at concentrations up to 200 μM preferentially reduced the survival of yeast harboring the BD-TbPex3/AD-TbPex19 interaction pair over the BD-HsPex3/AD-HsPex19 interaction pair (**Figure 3**). Accordingly, all subsequent experiments were limited to studies that tested the effects of DMNQ.

The Small Molecule DMNQ Preferentially Inhibits the Interaction of TbPex3–TbPex19 Over HsPex3–HsPex19

Trypanosomal Pex3 binds TbPex19 and HsPex3 binds HsPex19 in a pull-down assay (**Figure 4A**), as previously shown (Sato et al., 2008; Banerjee et al., 2019). Addition of the small molecule DMNQ at increasing twofold concentrations from 6 to 200 μM to the pull-down assay showed that DMNQ reduced the interaction between TbPex3 and TbPex19 but not between HsPex3 and HsPex19 at concentrations between 50 and 100 μM of DMNQ (**Figures 4B,C**). Off-site effects occurring outside the site of interaction between Pex3 and Pex19 in the yeast cell may underlie the observed growth inhibition of cells expressing BD-HsPex3/AD-HsPex19 by DMNQ at concentrations from 50 to 100 μM (**Figure 3**). DMNQ and the other five compounds that preferentially inhibited the BD-TbPex3/AD-TbPex19 interaction over its human pairing all showed varying inhibition of yeast general growth (**Supplementary Figure 2**).

Microscale thermophoresis analysis showed that TbPex3 bound TbPex19 with a K_D of 3.80 ± 1.31 nM (SEM), while HsPex3 bound HsPex19 with a K_D of 4.37 ± 2.30 nM, similar to what has been previously reported (Sato et al., 2008). Titration of DMNQ into the assay increased the apparent K_D of the TbPex3 interaction with TbPex19 by more than 10,000-fold (to 39.6 ± 0.86 μM), while only slightly increasing the K_D of the HsPex3 interaction with HsPex19 (to 14.53 ± 1.97 nM). Therefore, DMNQ preferentially inhibits the binding of TbPex3 to TbPex19 versus the binding of HsPex3 to HsPex19.

The Small Molecule DMNQ Is Toxic to *T. brucei* Cells Due to Compromised Glycosome Biogenesis

We tested the toxicity of the small molecule DMNQ for the BSF and PCF of *T. brucei* and for human HEK293T cells (**Figure 5**). Twofold dilutions of DMNQ from 0.07 to 10 μM concentration were added to equal numbers of cells for 24 or 48 h and the percentage of surviving cells was determined. The half-maximal effective concentration (EC_{50}) for BSF cells was 3.75 and 2.0 μM at 24 and 48 h of treatment with DMNQ, respectively. Low toxicity of HEK293T cells were observed at these concentrations of DMNQ at these respective time points. The EC_{50} for PCF cells was 5.6 and 3.5 μM at 24 and 48 h of treatment with DMNQ, respectively.

We performed immunofluorescence analysis on BSF and PCF cells that were untreated or treated with DMNQ for 48 h using antibodies against the glycosomal enzyme aldolase (**Figure 6**). Aldolase is targeted to the glycosomal matrix by a N-terminal peroxisome targeting signal type 2 (PTS2) (Chudzik et al., 2000). Aldolase showed a predominantly punctate pattern of staining characteristic of glycosomes in untreated BSF and PCF cells. In contrast, BSF and PCF cells treated with DMNQ showed reduced numbers of glycosomes and glycosome biogenesis defects that resulted in a diffuse pattern of staining for aldolase characteristic of mislocalization of the enzyme to the cytosol. A total absence of glycosomes and a total mislocalization of aldolase to the

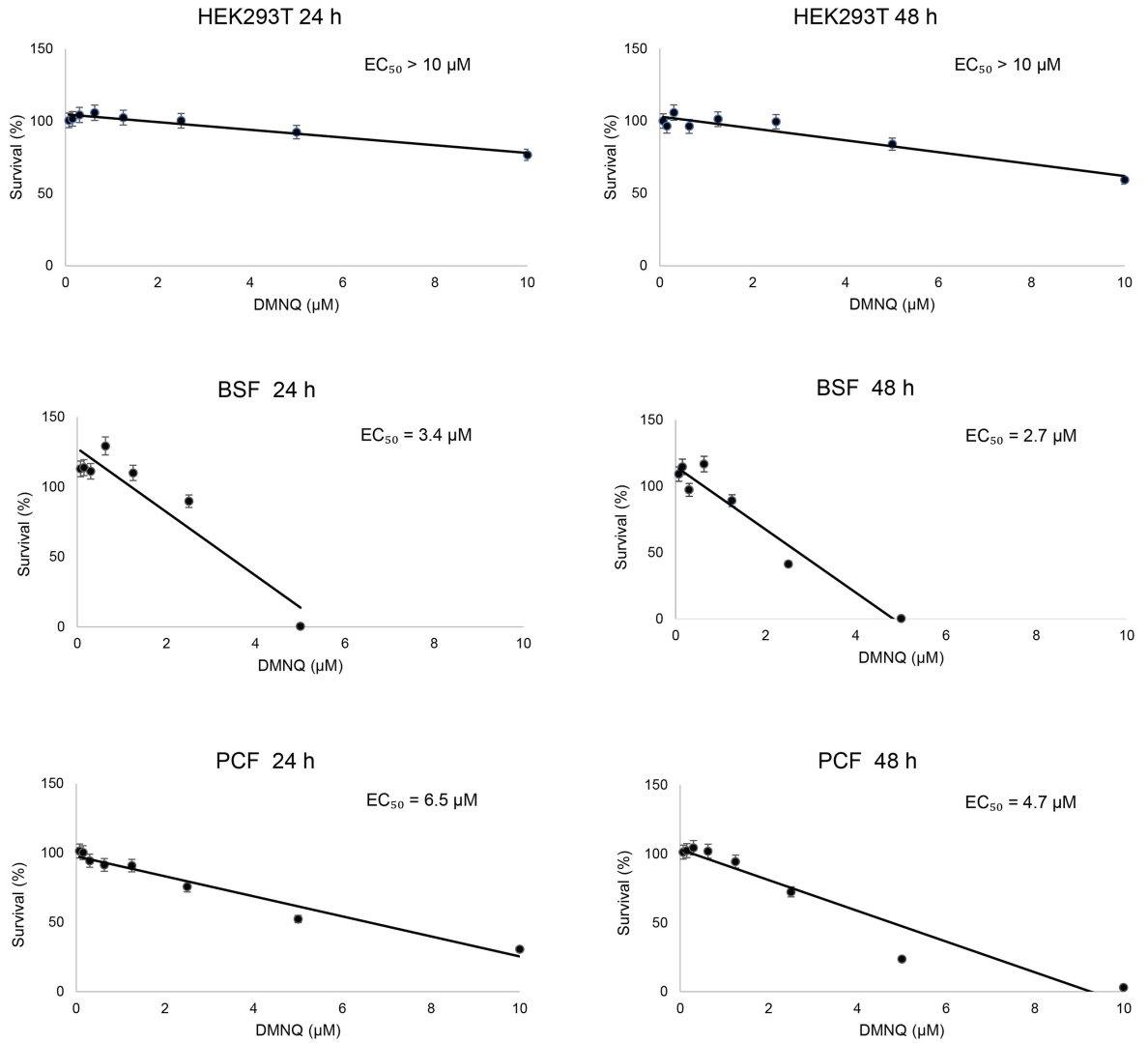

FIGURE 5 | *In vitro* cytotoxicity of DMNQ in HEK293T cells and in *T. brucei* BSF and PCF cells. Cells were incubated with increasing concentrations of DMNQ from 0 to 10 μM for 24 or 48 h. After incubation, cell viability was determined using CellTiter-Glo (CTG). Viability at each concentration of compound is expressed as a percentage of the number of viable cells observed in the absence of DMNQ, which was taken as 100%. A best-fit dose-response curve was generated for each condition and used to determine the half-maximal effective concentration (EC_{50}) for each condition. The values reported are averages ± SEM of three independent experiments, each done in duplicate.

cytosol were not expected, as cells require some fraction of intact functioning glycosomes to remain viable. The compromised glycosome population in DMNQ-treated BSF and PCF cells is consistent with our observations that DMNQ interferes with the interaction between TbPex3 and TbPex19 that is required for the biogenesis of glycosomes (**Figure 4**).

DISCUSSION

African sleeping sickness is caused by the protozoan *T. brucei* and, if left untreated, is fatal. Other trypanosomiases inflict additional financial and societal burdens on the peoples of sub-Saharan Africa. Current drugs used to treat trypanosomiases are often limited in their usefulness because of toxicity, complicated administration, side effects, limited efficacy to different stages of disease, and emergent drug resistance. Therefore, the identification of new drug targets and new drugs, as well as the repurposing of old drugs, remains an important venue of investigation for the continued improvement in treatment for trypanosomiases.

Glycosomes are specialized members of the peroxisome family of membrane-enclosed organelles. Glycosomes present an ideal target for drugs that compromise their function or biogenesis because glycosomes are unique to trypanosomatids and house essential metabolic pathways. Like peroxisomes, the biogenesis of glycosomes is dependent on the coordinated activity of proteins called peroxins, or Pex proteins, encoded by the *PEX* genes

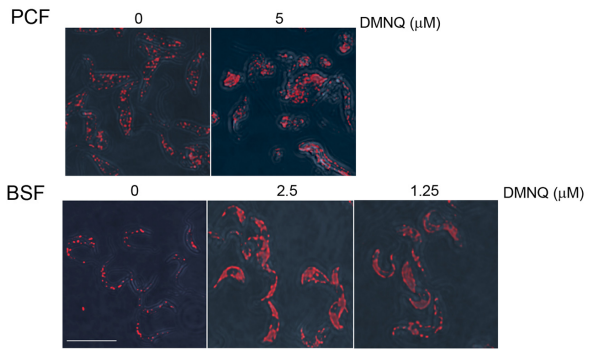

FIGURE 6 | Glycosome biogenesis is disrupted in PCF cells and BSF cells of *T. brucei* by addition of DMNQ. Addition of DMNQ at the concentrations indicated for 48 h led to mislocalization of the glycosomal matrix enzyme aldolase to the cytosol. Aldolase was detected with rabbit anti-aldolase antibodies and Alexa Fluor 568 goat anti-rabbit IgG. Bar, 5 μM.

(Haanstra et al., 2016; Crowe and Morris, 2021). Pex proteins have a diversity of roles in peroxisome biogenesis, including formation of nascent peroxisomes, import of peroxisomal matrix proteins from the cytosol, and control of peroxisomal size and number. The Pex3 protein has been ascribed the role of master regulator of peroxisome biogenesis in all organisms studied. Pex3 functions in making peroxisomes *de novo* from the ER through its interaction with the PMP receptor, Pex19 (Ghaedi et al., 2000; Fang et al., 2004). The identification of a Pex3 protein in trypanosomatids had long remained elusive but was reported independently by two groups in 2019 (Banerjee et al., 2019; Kalel et al., 2019). TbPex3 protein shows limited amino acid sequence identity with Pex3 proteins from other organisms, including human, although TbPex3 like other Pex3 proteins does maintain a Pex19 BD. The essentiality of TbPex3 for glycosome formation and the distinctiveness of its protein primary structure compared to Pex3 proteins from other organisms make TbPex3 an attractive therapeutic target.

Expression of foreign proteins in yeast has been used in the drug discovery process to identify and validate targets and to select affinity reagents for protein targets, such as peptides and small molecules (Blangy et al., 2006; Lentze and Auerbach, 2008; Bilsland et al., 2011; Wong et al., 2017). The yeast two-hybrid system is a widely used genetic assay for the identification and characterization of protein interactions. The yeast two-hybrid system has proved valuable for the screening and characterization of small molecules that inhibit the interactions between medically important proteins (Lentze and Auerbach, 2008; Wong et al., 2017). Given that TbPex3 is distinct in protein primary structure from other Pex3 proteins yet binds its partner protein Pex19 through a domain that is relatively well conserved in all Pex3 proteins makes yeast two-hybrid a system of choice for the screening and identification of small molecules that preferentially inhibit the interaction between TbPex3/Pex19 in comparison to HsPex3/Pex19.

We screened the LOPAC 1280 using the yeast two-hybrid strain HF7c deleted for the *PDR5* gene encoding the major drug efflux pump and identified six small molecules that preferentially inhibited the interaction of TbPex3/TbPex19 over HsPex3/HsPex19. Additional yeast two-hybrid analysis testing the six small molecules individually at different concentrations showed reduced survival of yeast harboring the BD-TbPex3/AD-TbPex19 interaction pair over the BD-HsPex3/AD-HsPex19 interaction pair in the presence of DMNQ. *In vitro* pull-down assays confirmed that DMNQ inhibited the interaction between TbPex3 and TbPex19 while leaving the interaction between HsPex3 and HsPex19 essentially unaffected. The results from the yeast two-hybrid and pull-down assays are consistent with the greatly reduced affinity of TbPex3/TbPex19 (39.6 ± 0.86 μM) compared to HsPex3/HsPex19 (14.53 ± 1.97 nM) for DMNQ, notwithstanding the similar affinities of Pex3 for Pex19 between trypanosomal (K_D = 3.80 ± 1.31 nM) and human (K_D of 4.37 ± 2.30 nM) pairs.

2,3-Dimethoxy-1,4-naphthoquinone was effective at killing both BSF cells and PCF cells, with EC_{50} values ranging from 2.7 to 3.4 μM for BSF cells and 4.7 to 6.5 μM for PCF cells. Small molecule inhibitors of the interaction between trypanosomal Pex5 and Pex14, two components of the glycosomal matrix protein import machinery, showed similar EC_{50} values for *T. brucei* BSF cells (Dawidowski et al., 2017). Human HEK293T cells at these concentrations of DMNQ showed no or limited decrease in viability. Microscopic analysis showed that DMNQ functions in killing both BSF cells and PCF cells of *T. brucei* by interfering with glycosome biogenesis as evidenced by mislocalization of glycosomal matrix enzymes to the cytosol and overall reduced numbers of punctate glycosome profiles, as would be expected by the capacity of DMNQ to interfere with the interaction between TbPex3 and TbPex19. Naphthoquinones have also been reported to cause trypanosomal death by enhanced production of toxic oxygen free radicals (Pieretti et al., 2013) or by targeting parasite enzymes, for example to inhibit specific parasite cysteine proteases (Klein et al., 2020).

2,3-Dimethoxy-1,4-naphthoquinone docking to TbPex3 and TbPex19 is modeled in **Figure 7**. Since DMNQ disrupts the binding between TbPex3 and TbPex19 as shown in pull-down experiments, DMNQ can be envisaged to dock to TbPex3 or TbPex19 either at the site of binding between TbPex3 and TbPex19, or at other sites leading to conformational change in TbPex3 or TbPex19, which in turn disrupts the interaction between TbPex3 and TbPex19. The disrupted interaction between TbPex3 and TbPex19 results in failure to import PMPs, compromised glycosome biogenesis, and death of the *T. brucei* parasite. Whether DMNQ would disrupt the interaction between Pex3 and Pex19 in other *Trypanosoma* spp. or in *Leishmania* spp. remains to be investigated but might be expected given that their Pex3 proteins and TbPex3 exhibit conservation of amino acid sequence of the Pex3 binding interface with Pex19 (**Supplementary Figure 3**) and their Pex3 proteins do not identify HsPex3 by BLAST analysis but do identify HsPex3 by HHpred analysis, as was reported for TbPex3 (Banerjee et al., 2019).

In closing, we have shown the utility of yeast to screen existent small compound libraries to identify compounds that

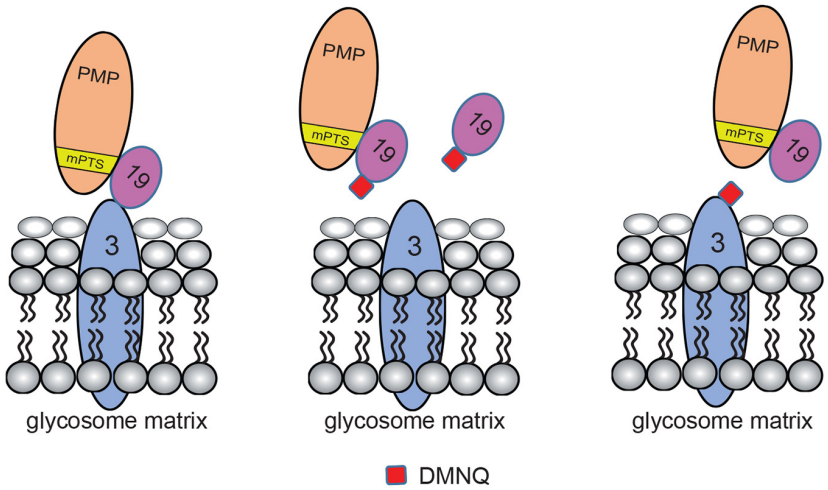

FIGURE 7 | Models for DMNQ docking to TbPex3 and TbPex19. Cartoons showing disruption of the binding between TbPex3 and TbPex19 by DMNQ. The cartoon at extreme left shows TbPex19 with its attached PMP cargo bound to TbPex3. Docking of DMNQ to TbPex19 (middle cartoon) or to TbPex3 (cartoon at extreme right) disrupts the interaction between TbPex3 and TbPex19, leading to failure of import of PMPs and compromised glycosome biogenesis. DMNQ docking to TbPex19 may or may not also impair TbPex19's binding to its PMP cargo. mPTS, PMP targeting signal.

will selectively kill the zoonotic parasite *T. brucei* by interfering with glycosome biogenesis. Our results identify an expedited approach to identifying other compounds that interfere with glycosome biogenesis or function, thereby expanding the pharmacopeia of compounds that can be used to treat the trypanosomiases.

DATA AVAILABILITY STATEMENT

The original contributions presented in the study are included in the article/**Supplementary Material**, further inquiries can be directed to the corresponding author/s.

AUTHOR CONTRIBUTIONS

RR conceived the research, analyzed the data, prepared the figures, and co-wrote the manuscript. HB and GE conducted the experiments, analyzed the data, prepared the figures, and co-wrote the manuscript. PL analyzed the data and co-wrote the manuscript. All authors contributed to the article and approved the submitted version.

FUNDING

This work was supported by foundation grant FDN-143289 from the Canadian Institutes of Health Research to RR.

ACKNOWLEDGMENTS

We thank K. Tedrick for help with yeast two-hybrid analysis and pull-down assays, P. A. M. Michels (University of Edinburgh) for the gift of anti-aldolase antibodies, and M. Michalak and J. Groenendyk for help with microscale thermophoresis. We would also acknowledge the Faculty of Medicine and Dentistry High Content Analysis Core at the University of Alberta for help in screening the LOPAC 1280 library.

SUPPLEMENTARY MATERIAL

The Supplementary Material for this article can be found online at: https://www.frontiersin.org/articles/10.3389/fcell.2021.703603/full#supplementary-material

Supplementary Figure 1 | Structures and yeast two-hybrid growth inhibition efficacies of six small molecules of the LOPAC 1280 library selected for further analysis.

Supplementary Figure 2 | Effects on yeast growth of the six selected LOPAC 1280 compounds. Compounds are identified by their LOPAC 1280 numbers (see **Supplementary Figure 1**). General growth was measured using strain H7Fc *pdr5*Δ. Growth Inhibition (%) was calculated as 100 − 100 × (growth with compound/growth no compound). The values reported are averages ± SEM of three independent experiments, each done in duplicate.

Supplementary Figure 3 | Alignment of the amino acid sequences corresponding to the binding interface between Pex3 and Pex19 proteins of three *Trypanosoma* spp. and three *Leishmania* spp. Pex3 proteins. Pex3 protein sequences are from *T. brucei* (Tb; Accession no. XP_829090.1), *T. cruzi* (Tc; Accession no. XP_810175.1), *T. vivax* (Tv; Accession no. CCC53628.1), *L. major* (Lm; Accession no. XP_001686984.1), *L. donovani* (Ld; Accession no. XP_003865535.1), and *L. braziliensis* (Lb; Accession no. XP_001569044.1). The number at right denotes the position of the last amino acid in the designated Pex3 sequence. Sequences were aligned using Clustal W (https://embnet.vital-it.ch/software/ClustalW.html). An amino acid that is identical to its corresponding amino acid in TbPex3 is highlighted in blue. An amino acid that is similar to its corresponding amino acid in TbPex3 is highlighted in yellow. Similar amino acids are grouped as follows: (G, A, S), (A, V), (V, I, L, M), (I, L, M, F, Y, W), (K, R, H), (D, E, Q, N), and (S, T, Q, N). The hydrophobic amino acid of Pex3 required for interaction with Pex19 is designated by an asterisk.

REFERENCES

Banerjee, H., Knoblach, B., and Rachubinski, R. A. (2019). The early-acting glycosome biogenic protein Pex3 is essential for trypanosome viability. *Life Sci. Alliance* 2:e201900421. doi: 10.26508/lsa.201900421

Bilsland, E., Pir, P., Gutteridge, A., Johns, A., King, R. D., and Oliver, S. G. (2011). Functional expression of parasite drug targets and their human orthologs in yeast. *PLoS Negl. Trop. Dis.* 5:e1320. doi: 10.1371/journal.pntd.0001320

Blangy, A., Bouquier, N., Gauthier-Rouvière, C., Schmidt, S., Debant, A., Leonetti, J.-P., et al. (2006). Identification of TRIO-GEFD1 chemical inhibitors using the yeast exchange assay. *Biol. Cell* 98, 511–522. doi: 10.1042/BC20060023

Chudzik, D. M., Michels, P. A., de Walque, S., and Hol, W. G. J. (2000). Structure of Type 2 peroxisomal targeting signals in two trypanosomatid aldolases. *J. Mol. Biol.* 300, 697–707. doi: 10.1006/jmbi.2000.3910

Crowe, L. P., and Morris, M. T. (2021). Glycosome heterogeneity in kinetoplastids. *Biochem. Soc. Trans.* 49, 29–39. doi: 10.1042/BST20190517

Dawidowski, M., Emmanouilidis, L., Kalel, V. C., Tripsianes, K., Schorpp, K., Hadian, K., et al. (2017). Inhibitors of PEX14 disrupt protein import into glycosomes and kill Trypanosoma parasites. *Science* 355, 1416–1420. doi: 10.1126/science.aal1807

De Koning, H. P. (2020). The drugs of sleeping sickness: Their mechanisms of action and resistance, and a brief history. *Trop. Med. Infect. Dis.* 5:14. doi: 10.3390/tropicalmed5010014

de Rycker, M., Baragaña, B., Duce, S. L., and Gilbert, I. H. (2018). Challenges and recent progress in drug discovery for tropical diseases. *Nature* 559, 498–506. doi: 10.1038/s41586-018-0327-4

Fang, Y., Morell, J. C., Jones, J. M., and Gould, S. J. (2004). PEX3 functions as a PEX19 docking factor in the import of class1 peroxisomal membrane proteins. *J. Cell Biol.* 164, 863–875. doi: 10.1083/jcb.200311131

Ghaedi, K., Tamura, S., Okumoto, K., Matsuzono, Y., and Fujiki, Y. (2000). The peroxin Pex3p initiates membrane assembly in peroxisome biogenesis. *Mol. Biol. Cell* 11, 2085–2102. doi: 10.1091/mbc.11.6.2085

Giordani, F., Morrison, L. J., Rowan, T. G., de Koning, H. P., and Barrett, M. P. (2016). The animal trypanosomiases and their chemotherapy: a review. *Parasitology* 143, 1862–1889. doi: 10.1017/s0031182016001268

Golin, J., and Ambudkar, S. V. (2015). The multidrug transporter Pdr5 on the 25th anniversary of its discovery: an important model for the study of asymmetric ABC transporters. *Biochem. J.* 467, 353–363. doi: 10.1042/BJ20150042

Guerra-Giraldez, C., Quijada, L., and Clayton, C. E. (2002). Compartmentation of enzymes in a microbody, the glycosome, is essential in Trypanosoma brucei. *J. Cell Sci.* 115, 2651–2658. doi: 10.1242/jcs.115.13.2651

Haanstra, J. R., Gonzalez-Marcano, E. B., Gualdron-Lopez, M., and Michels, P. A. M. (2016). Biogenesis, maintenance, and dynamics of glycosomes in trypanosomatid parasites. *Biochim. Biophys. Acta* 1863, 1038–1048. doi: 10.1016/j.bbamcr.2015.09.015

Haanstra, J. R., van Tuijl, A., Kessler, P., Reijnders, W., Michels, P. A. M., Westerhoff, H. V., et al. (2008). Compartmentation prevents a lethal turbo-explosion of glycolysis in trypanosomes. *Proc. Natl. Acad. Sci. U.S.A.* 105, 17718–17723. doi: 10.1073/pnas.0806664105

Kalel, V. C., Li, M., Gaussmann, S., Delhommel, F., Schäfer, A.-B., Tippler, B., et al. (2019). Evolutionarily divergent PEX3 is essential for glycosome biogenesis and survival of trypanosomatid parasites. *Biochim. Biophys Acta* 1866:118520. doi: 10.1016/j.bbamcr.2019.07.015

Klein, P., Barthels, F., Johe, P., Wagner, A., Tenzer, S., Distler, U., et al. (2020). Naphthoquinones as covalent reversible inhibitors of cysteine proteases studies on inhibition mechanism and kinetics. *Molecules* 25:2064. doi: 10.3390/molecules25092064

Lentze, N., and Auerbach, D. (2008). The yeast two-hybrid system and its role in drug discovery. *Expert Opin. Ther. Targets* 12, 505–515. doi: 10.1517/14728222.12.4.505

Mitra, A. K., and Mawson, A. R. (2017). Neglected tropical diseases: epidemiology and global burden. *Trop. Med. Infect. Dis.* 2:36. doi: 10.3390/tropicalmed2030036

Nwaka, S., and Hudson, A. (2006). Innovative lead discovery strategies for tropical diseases. *Nat. Rev. Drug Discov.* 5, 941–955. doi: 10.1038/nrd2144

Pieretti, S., Haanstra, J. R., Mazet, M., Perozzo, R., Bergamini, C., Prati, F., et al. (2013). Naphthoquinone derivatives exert their antitrypanosomal activity via a multi-target mechanism. *PLoS Negl. Trop. Dis.* 7:e2012. doi: 10.1371/journal.pntd.0002012

Sato, Y., Shibata, H., Nakano, H., Kashiwayama, Y., Imanaka, T., and Kato, H. (2008). Characterization of the interaction between recombinant human peroxin Pex3p and Pex19p: identification of Trp-104 in Pex3p as a critical residue for the interaction. *J. Biol. Chem.* 283, 6136–6144. doi: 10.1074/jbc.m706139200

Smith, J. J., and Aitchison, J. D. (2013). Peroxisomes take shape. *Nat. Rev. Mol. Cell Biol.* 14, 803–817. doi: 10.1038/nrm3700

Stuart, K., Brun, R., Croft, S., Fairlamb, A., Gürtler, R. E., McKerrow, J., et al. (2008). Kinetoplastids: related pathogens, different diseases. *J. Clin. Invest.* 118, 1301–1310. doi: 10.1172/jci33945

Wong, J. H., Alfatah, M., Sin, M. F., Sim, H. M., Verma, C. S., Lane, D. P., et al. (2017). A yeast two-hybrid system for screening and characterization of small molecule inhibitors of protein-protein interactions identifies a novel putative Mdm2-binding site p53. *BMC Biol.* 15:108. doi: 10.1186/s12915-017-0446-7

World Health Organization (2017). *Integrating Neglected Tropical Diseases in Global Health and Development*. 4th WHO Report on Neglected Tropical Diseases. Geneva: World Health Organization.

Conflict of Interest: The authors declare that the research was conducted in the absence of any commercial or financial relationships that could be construed as a potential conflict of interest.

frontiers in Cell and Developmental Biology

ORIGINAL RESEARCH
published: 09 August 2021
doi: 10.3389/fcell.2021.714710

The Nitric Oxide Donor, *S*-Nitrosoglutathione, Rescues Peroxisome Number and Activity Defects in *PEX1G843D* Mild Zellweger Syndrome Fibroblasts

Yidi Liu[1†], Ceileigh M. Weaver[2†], Yarina Sen[1], Gary Eitzen[1], Andrew J. Simmonds[1], Lilliana Linchieh[1], Olivier Lurette[3], Etienne Hebert-Chatelain[3], Richard A. Rachubinski[1‡] and Francesca Di Cara[2*‡]*

[1] Department of Cell Biology, University of Alberta, Edmonton, AB, Canada, [2] Department of Microbiology and Immunology, IWK Research Centre, Dalhousie University, Halifax, NS, Canada, [3] Department of Biology, University of Moncton, Moncton, NB, Canada

OPEN ACCESS

Edited by:
Marek Skoneczny, Institute of Biochemistry and Biophysics (PAN), Poland

Reviewed by:
Jose M. Manuel Palma, Consejo Superior de Investigaciones Científicas (CSIC), Spain
Myriam Baes, KU Leuven, Belgium

***Correspondence:**
Richard A. Rachubinski
rick.rachubinski@ualberta.ca
Francesca Di Cara
dicara@dal.ca

[†] These authors have contributed equally to this work and share first authorship

[‡] These authors have contributed equally to this work and share last authorship

Specialty section:
This article was submitted to Membrane Traffic, a section of the journal Frontiers in Cell and Developmental Biology

Received: 25 May 2021
Accepted: 20 July 2021
Published: 09 August 2021

Citation:
Liu Y, Weaver CM, Sen Y, Eitzen G, Simmonds AJ, Linchieh L, Lurette O, Hebert-Chatelain E, Rachubinski RA and Di Cara F (2021) The Nitric Oxide Donor, S-Nitrosoglutathione, Rescues Peroxisome Number and Activity Defects in PEX1G843D Mild Zellweger Syndrome Fibroblasts. Front. Cell Dev. Biol. 9:714710. doi: 10.3389/fcell.2021.714710

Peroxisome biogenesis disorders (PBDs) are a group of metabolic developmental diseases caused by mutations in one or more genes encoding peroxisomal proteins. Zellweger syndrome spectrum (PBD-ZSS) results from metabolic dysfunction caused by damaged or non-functional peroxisomes and manifests as a multi-organ syndrome with significant morbidity and mortality for which there is no current drug therapy. Mild PBD-ZSS patients can exhibit a more progressive disease course and could benefit from the identification of drugs to improve the quality of life and extend the lifespan of affected individuals. Our study used a high-throughput screen of FDA-approved compounds to identify compounds that improve peroxisome function and biogenesis in human fibroblast cells carrying the mild PBD-ZSS variant, *PEX1G843D*. Our screen identified the nitrogen oxide donor, *S*-nitrosoglutathione (GSNO), as a potential therapeutic for this mild form of PBD-ZSS. Further biochemical characterization showed that GSNO enhances both peroxisome number and function in *PEX1G843D* mutant fibroblasts and leads to increased survival and longer lifespan in an *in vivo* humanized *Drosophila* model carrying the *PEX1G843D* mutation. GSNO is therefore a strong candidate to be translated to clinical trials as a potential therapeutic for mild PBD-ZSS.

Keywords: peroxisome, *PEX1G843D* mutation, Zellweger spectrum disorders, *S*-nitrosoglutathione, high-throughput screen, drug library, fatty acids, *Drosophila melanogaster*

INTRODUCTION

Peroxisomes are cellular organelles present in almost every eukaryotic cell and are the site of essential metabolic reactions for organismal development and survival. Matrix enzymes within the peroxisome metabolize reactive oxygen and nitrogen species and catalyze the β-oxidation of very-long chain fatty acids (VLCFAs), synthesis of ether lipids, and processing of other complex

Abbreviations: AAA-ATPase, ATPase associated with diverse cellular activities-ATPase; ER, endoplasmic reticulum; FA, fatty acid; FDA, Food and Drug Administration; GSNO, *S*-nitrosoglutathione; HTS, high-throughput screening; IF, immunofluorescence; LOPAC 1280, library of 1280 pharmacologically active compounds; MiNA, Mitochondrial Network Analysis; *PEX*, gene required for peroxisome assembly; PBD, peroxisome biogenesis disorder; PEX, protein encoded by a *PEX* gene; RNS, reactive nitrogen species; ROS, reactive oxygen species; VLCFA, very long-chain fatty acid.

lipids (Wanders and Waterham, 2006). Peroxisome biogenesis, fission, and maturation through the import of proteins into the peroxisome matrix are dependent on a set of peroxin (PEX) proteins (Smith and Aitchison, 2013). Mutations in the genes encoding PEX proteins impair peroxisome biogenesis and function, and underlie a clinical spectrum of disorders known as the Peroxisome Biogenesis Disorders (PBDs). PBDs are divided into two distinct syndromes: Zellweger syndrome spectrum (PBD-ZSS) and Rhizomelic Chondrodysplasia Punctata spectrum (PBD-RCDP). With the exception of the *PEX7* mutation underlying most cases of PBD-RCDP, most other *PEX* gene mutations result in generalized peroxisome dysfunction and the PBD-ZSS phenotype (Braverman et al., 2013).

The metabolic dysfunctions that arise in PBD-ZSS often affect the development of multiple organs, including the brain (Braverman et al., 2013). While patients with severe PBD-ZSS can present with refractory epilepsy, neuronal migration disorders, and leukodystrophy, patients with mild cases of PBD-ZSS can exhibit sensorineural hearing loss, retinal abnormalities, leukodystrophy, and developmental and cognitive delays. While severe PBD-ZSS is often detected in the neonate and results in death in the first year of age, patients with mild disease present after the newborn period and can live into adulthood.

The clinical severity of PBDs varies with the genetic basis of the disease. Pathogenic variants in the *PEX1* gene are the most common cause of PBD-ZSS and are found in almost 60% of affected individuals (Yik et al., 2009; Ebberink et al., 2011). The most common mutant *PEX1* allele is *PEX1-p.Gly843Asp* (*PEX1G843D*), a disease-causing allele found mainly in patients of European origin (Reuber et al., 1997; Collins and Gould, 1999; Walter et al., 2001; Preuss et al., 2002), probably due to a founder effect (Collins and Gould, 1999). The *PEX1G843D* mutation accounts for 12–30% of all PBD-ZSS alleles and contributes to a milder PBD phenotype than patients with *PEX1* truncations, insertions, deletions or other pathogenic variations (Preuss et al., 2002; Crane et al., 2005; Ventura et al., 2016). Moreover, patients carrying the *PEX1G843D* mutant allele or other missense mutant alleles linked to mild PBD-ZSS present less severe biochemical deficiencies and have more functional peroxisomes than do other PBD-ZSS patients due to residual peroxin function in the cells of patients with a mild form of PBD-ZSS (Walter et al., 2001; Preuss et al., 2002; Braverman et al., 2013).

PEX1 is an AAA (ATPase associated with diverse cellular activities)-ATPase that oligomerizes with the PEX6 AAA-ATPase. Together PEX1 and PEX6 form a complex with PEX26 to recycle PEX5, the soluble receptor necessary for peroxisomal protein import from the cytosol into the peroxisome matrix (Ito et al., 2007; Platta and Erdmann, 2007; Smith and Aitchison, 2013). The *PEX1G843D* mutation affects PEX1 folding and attenuates the physical interaction between PEX1 and PEX6 necessary for peroxisomal import by 70% (Geisbrecht et al., 1998; Zhang et al., 2010). Although the variability in disease severity of patients homozygous for the *PEX1G843D* mutation (Poll-The et al., 2004) makes it difficult to predict outcomes solely from genotype, the overall milder phenotype of the homozygous *PEX1G843D* mutation (Berendse et al., 2016) makes it amenable to liver or hepatocyte transplantation (Demaret et al., 2018, 2021) and pharmaceutical therapy to improve quality of life and lifespan for patients carrying this mutation (Zhang et al., 2010).

High-throughput screening (HTS) of libraries of Food and Drug Administration (FDA)-approved compounds can be employed to streamline the process of identifying novel drug candidates for clinical trials. HTS has been successfully used to identify candidate compounds for therapeutic benefit in a number of diseases, including cancer, amyotrophic lateral sclerosis, and diabetes (Sexton et al., 2010; Willoughby et al., 2013; Joardar et al., 2015). A previous HTS of *PEX1G843D* human fibroblasts identified drug candidates that appeared to improve peroxisome function by stabilizing the mutated PEX1 protein (Zhang et al., 2010); however, no drug to date has passed clinical validation. Regardless, previous studies have suggested that *PEX1G843D* patient defects are amenable to intervention at the cellular level and implicate peroxin stabilization and peroxisome proliferation as mechanisms that drugs could target.

Model organisms have been useful in providing *in vivo* models for drug discovery and/or validation of drugs, and the fruit fly *Drosophila melanogaster* has been adopted to develop HTS protocols using flies with human disease-causing mutations (Willoughby et al., 2013). Peroxins and peroxisome functions are conserved between human and flies (Mast et al., 2011; Faust et al., 2012; Baron et al., 2016; Di Cara et al., 2017, 2019), and *Drosophila* is a well established model organism with which to study human diseases (Sanchez-Martinez et al., 2006; Sen and Cox, 2017) and for drug discovery (Willoughby et al., 2013).

In our study, we performed a HTS of an FDA-approved small molecule library with 1,280 pharmacologically active compounds (LOPAC 1280) to screen for molecules that increased peroxisome number in *PEX1G843D* human fibroblasts. We then performed a double-blind validation of hit compounds and various biochemical assays to select for molecules that rescued peroxisome functions in *PEX1G843D* human fibroblasts. We confirmed the efficacy of the candidate compounds on animal survival and lifespan improvement by testing it on a humanized *Drosophila* model carrying the *PEX1G843D* human mutation. Our work demonstrated that *S*-nitrosoglutathione (GSNO), a nitric oxide (NO) donor that is regarded as an intracellular NO reservoir and as a vehicle for NO throughout the cell (Corpas et al., 2013), increases peroxisome numbers in *PEX1G843D* mutant fibroblasts, improves the overall biochemical activities associated with peroxisomes in these mutant fibroblasts, and increases the survival and extends the lifespan of humanized flies with the *PEX1G843D* mutation, thereby opening up the possibility of developing GSNO into a clinical therapy for mild PBD-ZSS patients.

MATERIALS AND METHODS

Cell Culture

Human wild-type (WT) fibroblasts and *PEX1G843D* mutant fibroblasts were kind gifts of Dr. Nancy Braverman (McGill University). Informed consent for research was obtained from the Office of Human Research Administration at the

Kennedy Krieger Institute (Baltimore, MD, United States) to the Peroxisome Disease Laboratory, McGill University under Clinical Research Centre grants RR0052 and RR00722. Cells at passages 5–9 were cultured at 37°C in 5% CO_2 in DMEM with 4.5 g D-Glucose/L, 4.5 g L-Glutamate/L, and 110 mg sodium pyruvate/L supplemented with 10% Fetal Bovine Serum (Hyclone, Thermo Fisher), 50 U penicillin/mL, and 50 μg streptomycin sulfate/mL. PCR amplification using the MycoSensor PCR Assay Kit (Agilent) detected no mycoplasma contamination of cultures.

Fly Stocks and Husbandry

Drosophila strains were cultured at 25°C on standard Bloomington Drosophila Stock Center (BDSC) corn meal medium supplemented with soy powder. For compound treatment experiments, food was supplemented with 50, 100, or 500 μM T6. All compound concentrations tested showed an increase in lifespan of *P*{*UAS- PEX1G843D*} flies compared to the same flies raised on food supplemented only with vehicle (DMSO). The ubiquitous driver line *P*{Ubi-GAL4.U}2/CyO (32551) was purchased from BDSC. *P*{*UAS- PEX1G843D*} mutants were allowed to lay eggs on apple juice agar plates for 2 days. Each day mutant embryos were collected every 2 h and transferred to compound-supplemented medium, and control medium embryos were incubated on apple juice agar plates at 25°C. After 24 h, hatched larvae were transferred to standard corn meal medium or corn meal medium supplemented with compound for oral treatment throughout development. Surviving animals were counted at the same time each day.

LOPAC 1280 Library Reformatting

Compounds from the LOPAC 1280 library (Sigma-Aldrich) were used at a final concentration of 25 μM in the screen. To minimize pipetting during the screen, we reformatted the original library from a 96-well format into a 384-well format as outlined below:

- Compounds at 10 mM in DMSO were originally in 16 96-well plates (columns 1 and 12 empty). Compounds were reformatted in four 384-well plates (columns 1, 12, 13, and 24 empty).
- 384-well plates were prepared for compound dilution. Each well (except column 12) was filled with 99 μL of serum-free medium and 1 μL of a compound from the 10 mM stock library. 1 μL of DMSO was added to 99 μL of serum-free medium in columns 1, 13, and 24.
- 100 μL of betaine (400 mM stock solution in serum-free medium) was added to the wells in column 12.

High-Throughput Screening, Immunofluorescence, and Imaging

On day 1, wild-type (WT) and *PEX1G843D* fibroblasts were trypsinized with 2.5% trypsin (Gibco) and seeded onto μClear (Greiner Bio-One) 384-well plates (500 cells per well in 40 μL of medium). On day 2, compounds (13.4 μL of the 1:100 dilution of the stock in DMEM) were added to wells containing *PEX1G843D* fibroblasts, while 13.4 μL of the control drug betaine were added to columns 12 and 13. Four μL of DMSO (vehicle) were added to columns 1, 13, and 24. Untreated WT fibroblasts were used as a positive control for the detection system. Each compound, and positive and negative controls, were tested in duplicate. Cell plates were incubated for 2 days at 37°C and 5% CO_2. On day 5, cells were fixed in 4% formaldehyde in 1× phosphate buffered saline (PBS) for 30 min, washed once with PBT 0.05% (PBS containing 0.05% Triton X-100) for 2 min, permeabilized in PBT 0.1% (PBS containing 0.1% Triton X-100) for 3 min, washed in PBT 0.05% for 2 min and blocked for 40 min in PBT 0.05% containing 3% BSA. Rabbit antibodies to the C-terminal Peroxisome Targeting Signal Type 1 (PTS1), Ser-Lys-Leu (SKL) (Szilard et al., 1995) were added at 1:200 dilution in 0.3% BSA. Plates were incubated overnight at 4°C. On day 6 primary antibody was removed, and cells were washed in PBT 0.05% three times and incubated in Alexa Fluor 488 anti-rabbit secondary antibody (Abcam, 1:1,000 dilution) and DAPI (1 μg/mL) to detect DNA for 30 min at room temperature. Cells were then washed twice in PBT 0.05% (2 min each wash) and once with PBS. Cells were imaged in PBS. The screen was done at the High Content Analysis Core, University of Alberta, Faculty of Medicine and Dentistry. All pipetting was done using the PerkinElmer Janus Standard Deck automated liquid handling system enclosed in a Class II biosafety cabinet. Plates were imaged using the Operetta High Content Imaging System (PerkinElmer).

A primary screen quantifying the number of SKL-positive puncta per cell area was done using automated Harmony Software (PerkinElmer) as follows:

(1) Find nuclei based on intensity of nuclear staining.
(2) Count total number of nuclei.
(3) Identify the cytoplasm of each cell based on the intensity of Alexa Fluor 488 staining surrounding individual nuclei.
(4) Exclude cells on the edges of each image to reduce the chance that a cell is counted multiple times.
(5) Select a region of the cell in which to quantify spots. The set region was 10 pixels in from the border and including the nucleus.
(6) Calculate the area of the cell region for all cells.
(7) Find spots in the selected cell region. This quantifies the spots (spots/μm^2). Each spot is detected as a small region on the image having an intensity greater than the intensity of the surrounding region.
(8) Calculate the morphological properties of the spots to get the spot area.
(9) Create a formula to calculate the number of spots per mean cell area.

We applied *z*-score analysis to normalize the number of spots/cell area across the entire screen. *Z*-scores were calculated by subtracting the number of spots/cell area value for each compound by the plate median value and dividing by the standard deviation of the plate. *Z*-scores assume normal distribution and represent the standard deviation of every value from the plate median for each treatment. *Z*-scores with values above 2 represent the 99% confidence interval. *Z*-scores with values above 1.96 represent the 95% confidence interval.

This initial analysis identified 123 compounds with *z*-scores above 2 (**Supplementary Table 1**). To validate the accuracy of the software, we performed a double-blind screen and confirmed by visual analysis microscopic images of the 11 compounds that produced a greater than 10% increase in the number of SKL-positive puncta per cell area compared to vehicle-treated cells (**Supplementary Table 2**). Only compounds showing an increase of more than 25% SKL-positive puncta per cell area compared to vehicle-treated cells were chosen for further validation.

For secondary screening, WT fibroblasts and *PEX1G843D* fibroblasts were seeded onto round glass coverslips at a density of 100,000 cells per well in a 24-well plate containing growth medium. The following day, the medium was replaced and supplemented with 25 μM of each compound selected in the primary screen (**Supplementary Table 1**), 0.4% DMSO (negative control), or 100 mM betaine (positive control). Medium added to WT fibroblasts contained no compound. Cells were incubated with each compound for 2, 3, or 6 days. For prolonged treatments, medium was changed every 2 days. For compound titration studies, cells were treated with 5, 10, 25, 35, or 50 μM of compound for 2 days.

After each treatment, cells were processed for indirect confocal immunofluorescence (IF) microscopy. In brief, fibroblasts were fixed for 30 min in 4% paraformaldehyde in PBS, rinsed twice in PBST (PBS, 0.1% Triton X-100), and blocked for 1 h in 5% normal goat serum (Sigma-Aldrich) before incubation for 16 h at 4°C with primary antibody. After four washes in PBST, cells were incubated with secondary antibody for 16 h at 4°C, washed four times in PBST, and mounted in Prolong-Gold (Thermo Fisher). Images were captured using a C9100 camera (Hamamatsu) at 130-μm vertical spacing using a 100× oil immersion objective (NA = 1.4) on a Zeiss AxioObserver M1 microscope coupled to an ERS spinning disk confocal microscope (PerkinElmer). Primary antibodies were mouse anti-ABCD3 (Sigma-Aldrich) to stain peroxisomal membranes (Imanaka et al., 2000), rabbit anti-SKL to stain the peroxisomal matrix (Szilard et al., 1995) and mouse anti-KDEL (Santa Cruz Biotechnology) to stain the ER. Secondary antibodies were Alexa Fluor 568 donkey anti-mouse and Alexa Fluor 488 donkey anti-rabbit (Abcam).

Confocal image stacks were processed to remove noise and reassign blur using a classical maximum likelihood estimation confocal algorithm provided by Huygens Professional Software and an experimentally determined point spread function constructed from multiple images of 0.1 μm Tetraspeck beads (Life Technologies). Individual peroxisome volume and average number of peroxisomes per cell were calculated using the Spots function of Imaris 8 software (Bitplane). Each calculation (volume and size) represents a mean of 20 independent cells from each biological sample. Each experiment had at least three biological replicates. For the final validation of the GSNO hit we processed and analyzed images for over 600 biological replicates with Imaris 8 software or with the automated Harmony software. The number was established by G*Power analysis (Faul et al., 2007), a statistical software that indicates the number of biological replicates required to claim robust statistical significance based on the standard deviation in a small sample of the analyzed population.

ER expansion was determined by measuring the corrected total anti-KDEL IF and comparing the fluorescence intensity of KDEL-positive regions between cells of the reported genotype and under the reported condition. Analysis of IF images was done as follows:

(1) Outline desired cell with Freehand ROI tool.
(2) Set desired parameters by going to Analyze > Set Measurements > Select: Area, Integrated Density, and Mean Gray Value.
(3) Go to Analyze > Measure.
(4) Copy data into a spreadsheet.
(5) Then select a small area of the image that has no fluorescence (background).
(6) Analyze > Measure for that region. Copy data into spreadsheet.
(7) Repeat steps 3–6 for 20 cells and background regions.
(8) Calculate the mean fluorescence of background readings.
(9) Calculate corrected total cell fluorescence (CTCF) = Integrated Density − (Area of Selected Cell × Mean Fluorescence of Background Readings).
(10) Calculate CTCF for each cell.

MitoTracker Red and LysoTracker Red Staining

Wild-type and *PEX1G843D* fibroblasts were seeded at a density of 100,000 cells per well onto round glass coverslips in a 24-well plate containing medium. The following day, the medium was replaced with medium containing 25 μM of each compound selected in the primary screen (**Supplementary Table 2**) or 0.4% DMSO (vehicle). Medium without compound was added to WT fibroblasts. On day 2, MitoTracker Red or LysoTracker Red was added to wells at a final concentration of 25 nM or 25 μM, respectively, for 30 min at 37°C. The medium was then removed, and cells were fixed for 30 min in 4% paraformaldehyde in PBS, rinsed twice in PBS and mounted in Prolong-Gold (Thermo Fisher). Images were captured using a C9100 camera at 130-μm vertical spacing using a 100× oil immersion objective (NA = 1.4) on a Zeiss AxioObserver M1 microscope coupled to an ERS spinning disk confocal microscope. Determination of mitochondria shape and quantification of mitochondria networks per cell genotype and under each condition were performed using ImageJ and the macro MiNA-master following a published protocol (Valente et al., 2017). The number of LysoTracker Red-positive puncta per cell genotype and under each condition was determined as described (Di Cara et al., 2018).

Cloning

The coding sequence for the mutant human protein PEX1G843D in the plasmid pcDNA3-PEX1G843D (a gift from Dr. Nancy Braverman, McGill University) was amplified using the primers *PEX1*-Forward 5′-CACCATGTGGGGCAGCGAT and *PEX1*-Reverse 5′-TTATGCTAAAGTTACTTTCT and Phusion High Fidelity DNA polymerase (Thermo Fisher). PCR product was directionally cloned into the pENTR/D entry vector by TOPO cloning (Invitrogen) for the Gateway System (Life Technologies).

Plasmid inserts were verified by sequencing. Inserts were then recombined into pTW destination vectors (Drosophila Gateway Vector Collection) using LR clonase II (Life Technologies). The purified final recombinant DNA construct was provided to BestGene[1] for injection into the *Drosophila* strain y^1 w^{67c23}; *P{CaryP}attP40* strain to establish a transgenic fly line able to express PEX1G843D using the Gal4/UAS system (Brand and Perrimon, 1993).

Lipid Analysis

One million cells of each genotype and under each condition were resuspended in 1 mL of PBS buffer and sonicated for 5 min using a BioRuptor (Diagenode) at low power to produce a cell lysate. The protein content of cell lysates was determined using a Qubit II fluorimeter (Thermo Fisher). One million cells yielded 1 mg total protein. Lipids were extracted using chloroform:methanol (2:1) as described (Folch et al., 1957). Extracts were centrifuged at 3,400 × *g*, and the chloroform phase containing lipids was passed through a sodium sulfate column (GE Healthcare). Five μg of heptadecane (C_{17}) in chloroform was used as an internal control. The eluate was dried under nitrogen gas and resuspended in 100 μL of HPLC-grade hexane. Ten μL of material were injected into an Agilent 6890 gas chromatograph with a flame-ionization detector.

Assay for Peroxisomal β-Oxidation Activity

Fibroblasts were homogenized in 0.25 M STKM buffer (0.25 M sucrose, 25 mM HEPES-KOH, pH 7.4, 25 mM KOAc, 5 mM $MgCl_2$, 0.1 mM EDTA, 1× Roche Complete Protease Inhibitor, 1 mM DTT) and sonicated for 5 min using a BioRuptor (Diagenode) at low power. Lysates were centrifuged at 1,000 × *g* for 10 min at 4°C, and the resultant supernatant was centrifuged at 20,000 × *g* for 20 min at 4°C to yield a pellet enriched for peroxisomes. The protein content of peroxisome-enriched subcellular fractions was determined using a Qubit II fluorimeter. Peroxisomal ß-oxidation enzymatic activity of subcellular fractions was measured essentially as described (Lazarow and de Duve, 1976).

Assay for Catalase Activity

Fibroblasts were homogenized in 0.25 M STKM buffer and sonicated for 5 min using a BioRuptor at low power. Lysates were centrifuged at 1,000 × *g* for 10 min at 4°C, and the resultant supernatant was centrifuged at 20,000 × *g* for 20 min at 4°C to yield a pellet enriched for peroxisomes. Catalase activity of subcellular fractions was determined using the Amplex Red Catalase Assay Kit (Thermo Fisher) and normalized to protein amount. Experiments were done in triplicate.

Protein Analysis and Immunoblotting

Fifty μL of cold Ephrussi-Beadle Ringer's solution supplemented with 10 mM EDTA, 10 mM DTT, 1× complete protease inhibitor, and 1× PhosStop phosphatase inhibitor (Roche) were added to 3×10^6 pelleted cells, and a cell lysate was prepared by sonication for 5 min using a BioRuptor at low power. Protein amounts of lysates were determined using a Qubit II fluorimeter. Twenty-five μL of 3× SDS-PAGE Buffer (Bio-Rad) containing 10 mM DTT at 70°C were added to the lysate and placed in boiling water for 10 min. Samples were resolved by SDS-PAGE on 10% acrylamide gels and transferred to nitrocellulose membranes (Bio-Rad). Membranes were blocked with 5% skimmed milk powder in TBS + Tween 20 (TBSTw) (150 mM NaCl, 20 mM Tris-HCl, pH 7.5, 0.05% Tween 20) for 1 h and incubated for 16 h with primary antibody in TBSTw. After washing three times for 5 min each with TBSTw, membranes were incubated with HRP-conjugated secondary antibody (Bio-Rad) at 1:10,000 dilution for 1 h at 24°C. Membranes were washed as above, and HRP activity was detected by enhanced chemiluminescence (Amersham). Primary antibodies were rabbit anti-3-ketoacyl-CoA thiolase (Bodnar and Rachubinski, 1990) and mouse anti-α-tubulin (Sigma-Aldrich).

RESULTS

Identification of Candidate Compound T6 by High-Throughput Screening of the LOPAC 1280 Library

To identify compounds that improve peroxisome function in patients carrying the *PEX1G843D* mutation, we performed a HTS of the 1280-compound library of pharmacologically active compounds (LOPAC 1280) on *PEX1G843D* mutant human fibroblasts. To do the HTS, *PEX1G843D* fibroblasts and WT fibroblasts were treated either with 25 μM of each compound from the library or with 0.4% vehicle (DMSO). As a positive control, fibroblasts were treated with 100 mM betaine, a compound previously reported to increase peroxisome number in *PEX1G843D* fibroblasts (MacLean et al., 2019). After 3 days, we performed indirect immunofluorescence (IF) microscopy using an antibody against the C-terminal Peroxisome Targeting Sequence Type 1 Ser-Lys-Leu (SKL), the canonical marker for peroxisomal matrix proteins (Szilard et al., 1995). We imaged the fibroblasts using a high-content analysis imager with automated cell counting software to identify compounds that increased the number of SKL-positive puncta in compound-treated *PEX1G843D* fibroblasts compared to untreated *PEX1G843D* fibroblasts.

We quantified the number of SKL-positive puncta per cell area for each experimental and control well using Harmony image analysis software. We calculated the *z*-score of the resulting quantification of SKL-positive puncta for all compounds tested to establish thresholds of significance and to enable plate-to-plate comparisons. The *z*-score analysis separated chemical compounds by efficacy as a deviation from baseline (**Figure 1A**). The threshold *z*-score of 2 was dictated by the 99% confidence interval of the *z*-score. The positive control compound betaine was below the threshold *z*-score of 2 (**Figure 1A**), indicating that all hit compounds identified in this screen pipeline were more efficacious than betaine. Each compound hit from the primary HTS was visually inspected for increased numbers of peroxisome

[1]https://www.thebestgene.com

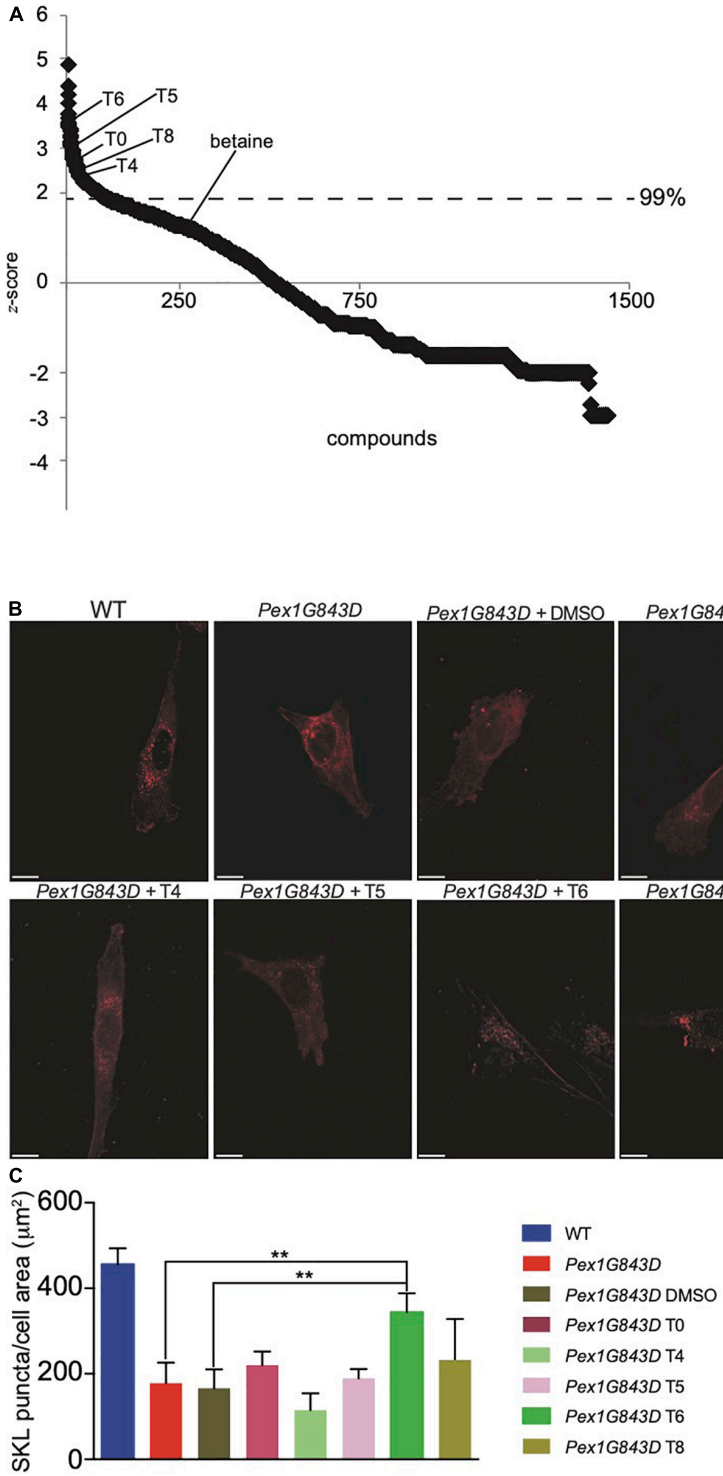

FIGURE 1 | HTS of the LOPAC 1280 library identified candidate compounds to rescue peroxisome number in *PEX1G843D* human fibroblasts. **(A)** Statistical analysis of candidate compounds measured by *z*-score. Significant activity threshold was $z > 2$. Note that betaine, a compound known to increase peroxisome numbers and used as a positive control, was below threshold in this screen. **(B)** Detection of SKL-positive puncta by indirect IF microscopy in fibroblasts of the reported genotypes and under the designated conditions. Images of *PEX1G843D* fibroblasts treated with some candidate compounds are shown and compared to the images of WT fibroblasts, untreated *PEX1G843D* fibroblasts, and *PEX1G843D* fibroblasts treated with vehicle (0.04% DMSO). Note that treatment with DMSO alone does not result in increased numbers of SKL-positive puncta. Scale bars, 10 μm. **(C)** Histogram reporting the quantification of SKL-positive puncta per cell area (μm^2) for cells of each genotype and under each condition observed by indirect IF microscopy. Error bars represent standard deviation. Statistical significance was calculated using 2-way ANOVA. $^{**}p < 0.01$.

puncta in a double-blind analysis. Of the 123 compounds identified (**Supplementary Table 1**), 11 compounds were validated by secondary analysis, and structural and functional information was compiled for each of the compounds, which targeted a wide-range of cellular functions (**Supplementary Table 2**). We assigned arbitrary identifiers, T0-T10, to each compound and performed an indirect IF microscopy screen to confirm an increase in SKL-positive puncta with compound treatment (**Figures 1B,C**). We tested every compound that showed greater than 25% rescue of the number of SKL-positive puncta in our secondary screen. Indirect IF microscopy analyses revealed that only treatment with T6, the nitric oxide donor GSNO (Stolz et al., 2002; Corpas et al., 2013, 2017, 2021), reproducibly increased the number of SKL-positive puncta in *PEX1G843D* fibroblasts almost to numbers observed in WT fibroblasts (**Figures 1B,C** and **Supplementary Figure 1A**). We therefore further characterized the effect of T6 treatment on peroxisome numbers and functions in *PEX1-G843D* fibroblasts.

T6 Treatment of *PEX1G843D* Fibroblasts Leads to Increased Peroxisomal Matrix Protein Import and Increased Peroxisome Biogenesis

We investigated how T6 might increase peroxisomal SKL-positive puncta and therefore increase peroxisomal protein import in *PEX1G843D* fibroblasts. As the *PEX1G843D* mutation only partially impairs peroxisomal protein import, we hypothesized that T6 can aid peroxisomal import of proteins containing a PTS1 either by improving peroxisomal protein import *per se* or by increasing the *de novo* biogenesis of peroxisomes and, as a consequence, the overall activity of peroxisomes in the mutant cells. To confirm that T6 treatment impacts peroxisomal protein import, we performed indirect IF microscopy of peroxisomal puncta labeled by anti-SKL antibodies in *PEX1G843D* fibroblasts treated with 25 μM T6, vehicle (0.4% DMSO, negative control), 100 mM betaine (positive control), together with WT fibroblasts that function as reference. To obtain the highest statistical significance on the efficacy of T6, we performed an *a priori* sample size analysis, using G*Power analysis, a statistical software that indicates the number of biological replicates necessary to obtain robust statistical significance based on the standard deviation of the analyzed population (Faul et al., 2007) (**Figure 2A**). Imaris quantification of the number of SKL-positive puncta per cell area showed a statistically significant increase in the number of SKL-positive puncta in T6-treated *PEX1G843D* fibroblasts, similar to the numbers of SKL-positive puncta in WT cells in 646 independent biological replicates (**Figure 2B**), strongly supporting the conclusion that peroxisomal protein import was improved in *PEX1G843D* fibroblasts upon T6 treatment. The number of SKL-positive puncta in T6-treated *PEX1G843D* fibroblasts increased significantly with respect to the number of puncta in untreated *PEX1G843D* fibroblasts at concentrations of T6 25 μM and higher, although concentrations of T6 greater than 25 μM did not lead to correspondingly increased numbers of SKL-positive puncta in *PEX1G843D* fibroblasts treated with 25 μM T6 (**Figure 2C**). Accordingly, we used T6 at 25 μM concentration for all subsequent analyses. To test whether the observed effect on peroxisomal protein import improved with longer treatment of *PEX1G843D* fibroblasts with T6, we increased the period of T6 treatment from 3 to 6 days and measured the number of SKL-positive puncta in treated *PEX1G843D* fibroblasts compared to untreated *PEX1G843D* fibroblasts and to WT fibroblasts (**Figure 2D**). Although the number of SKL-positive puncta in T6-treated *PEX1G843D* fibroblasts increased in number relative to untreated *PEX1G843D* fibroblasts at both 3 and 6 days, increasing the time of treatment with T6 from 3 to 6 days did not produce a statistically significant increase in the number of SKL-positive puncta in *PEX1G843D* fibroblasts compared to WT fibroblasts. Therefore, the effects of T6 treatment did not appear to depend on the length of time of treatment beyond 3 days.

Indirect IF microscopy of cells labeled with antibodies to ATP Binding Cassette Subfamily D Member 3 (ABCD3), a peroxisomal membrane protein, showed that T6-treated *PEX1G843D* fibroblasts exhibited more ABCD3-positive puncta than untreated *PEX1G843D* fibroblasts, and the numbers of ABCD3-positive puncta in T6-treated *PEX1G843D* fibroblasts were similar to the numbers of ABCD3-positive puncta in WT fibroblasts (**Figures 2E,F**), indicating that T6 treatment increases the number of peroxisome structures by increased peroxisome biogenesis or enhanced peroxisome stability. Interestingly, treatment of *PEX1G843D* fibroblasts with betaine did not increase the number of ABCD3-positive puncta (**Figures 2E,F**). However, T6 treatment did increase the number of ABCD3-positive structures also in WT cells (**Supplementary Figure 1A**), suggesting that T6 increases the number of peroxisomes in *PEX1G843D* fibroblasts at least in part by enhanced peroxisome biogenesis or reduced peroxisome degradation.

T6 Treatment Leads to Increased Peroxisomal Biochemical Activities in *PEX1G843D* Fibroblasts

As treatment of *PEX1G843D* fibroblasts with T6 led to increased numbers of peroxisome structures as seen by indirect IF microscopy, we performed a series of biochemical analyses to investigate if treatment with T6 also led to increased peroxisomal function and also increased peroxisomal protein import. One key metabolic function of peroxisomes is the metabolism of very long-chain fatty acids (VLCFAs) (Wanders and Waterham, 2006), which are fatty acids (FAs) equal to or greater than C_{22} in length. As such, improved peroxisomal FA metabolism can be monitored by investigating the FA profiles of cells under various conditions. We performed gas chromatography to analyze and compare the FA profiles of T6-treated *PEX1G843D* fibroblasts, untreated *PEX1G843D* fibroblasts, and WT fibroblasts (**Figure 3A**). FA quantification in cells of each genotype and under each condition was normalized to total protein. Untreated *PEX1G843D* mutant fibroblasts had decreased medium-chain fatty acids (MCFAs, C_{16-22}), decreased C_{22} FAs and slightly increased C_{24} FAs relative to WT fibroblasts (**Figure 3A**). T6 treatment increased C_{22} FAs

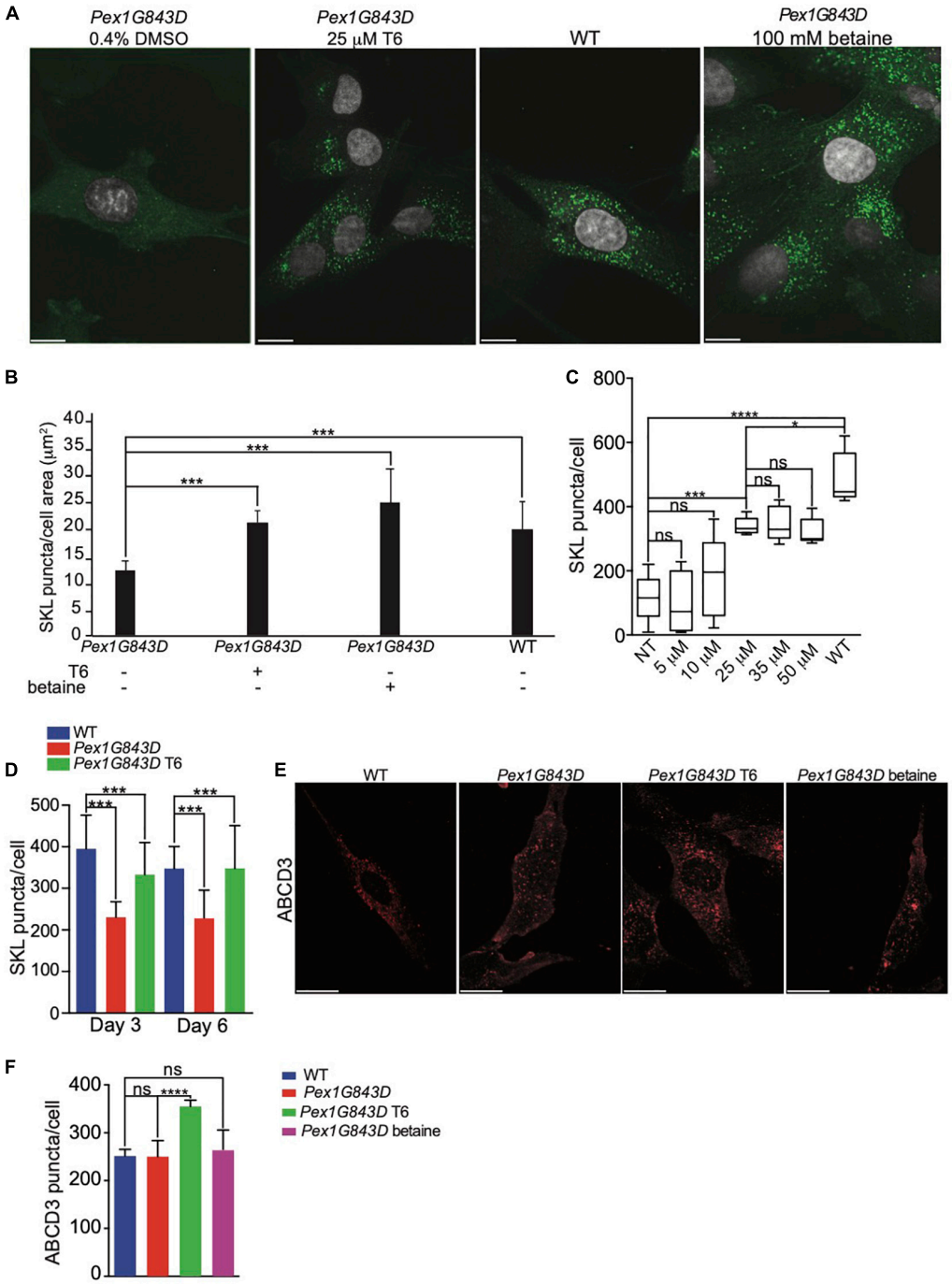

FIGURE 2 | Treatment with compound T6 enhances peroxisomal matrix protein import and increases peroxisome number in *PEX1G843D* fibroblasts. **(A)** Indirect IF microscopy of *PEX1G843D* fibroblasts with anti-SKL antibodies to compare the effects of treatment with T6 to treatment with betaine (positive control) or vehicle (DMSO). Green puncta, anti-SKL. Gray, nuclei. Scale bars, 10 μm. **(B)** Histogram reporting the quantification of SKL-positive puncta per unit of cell area (μm^2) for each genotype and condition. Error bars represent standard deviation ($N = 646$). Statistical significance was calculated using 2-way ANOVA. ***$p < 0.001$. **(C)** Quantification of the number of SKL-positive puncta in *PEX1G843D* fibroblasts in response to increasing concentrations of T6. Error bars report the standard deviation ($N = 25$). Statistical significance was calculated using 1-way ANOVA. ***$p < 0.001$. ns, not significant. NT, not treated. **(D)** T6 treatment beyond 3 days does not lead to correspondingly increased numbers of peroxisomes in *PEX1G843D* fibroblasts. Histogram reports the quantification of SKL-positive puncta per cell for each genotype and condition. Error bars represent standard deviation ($N = 25$). Statistical significance was calculated using 2-way ANOVA. ***$p < 0.001$. **(E)** Indirect IF microscopy of *PEX1G843D* fibroblasts with anti-ABCD3 antibodies comparing treatment with T6 to treatment with betaine. Scale bars, 10 μm. **(F)** Histogram reporting the quantification of ABCD3-positive puncta in cells of each genotype and condition as in **(E)**. Note that treatment with T6 led to increased numbers of ABCD3-positive puncta in *PEX1G843D* fibroblasts relative to numbers in WT cells. Error bars represent standard deviation ($N = 25$). Statistical significance was calculated using 2-way ANOVA. *$p < 0.05$, ***$p < 0.001$, ****$p < 0.0001$. ns, not significant.

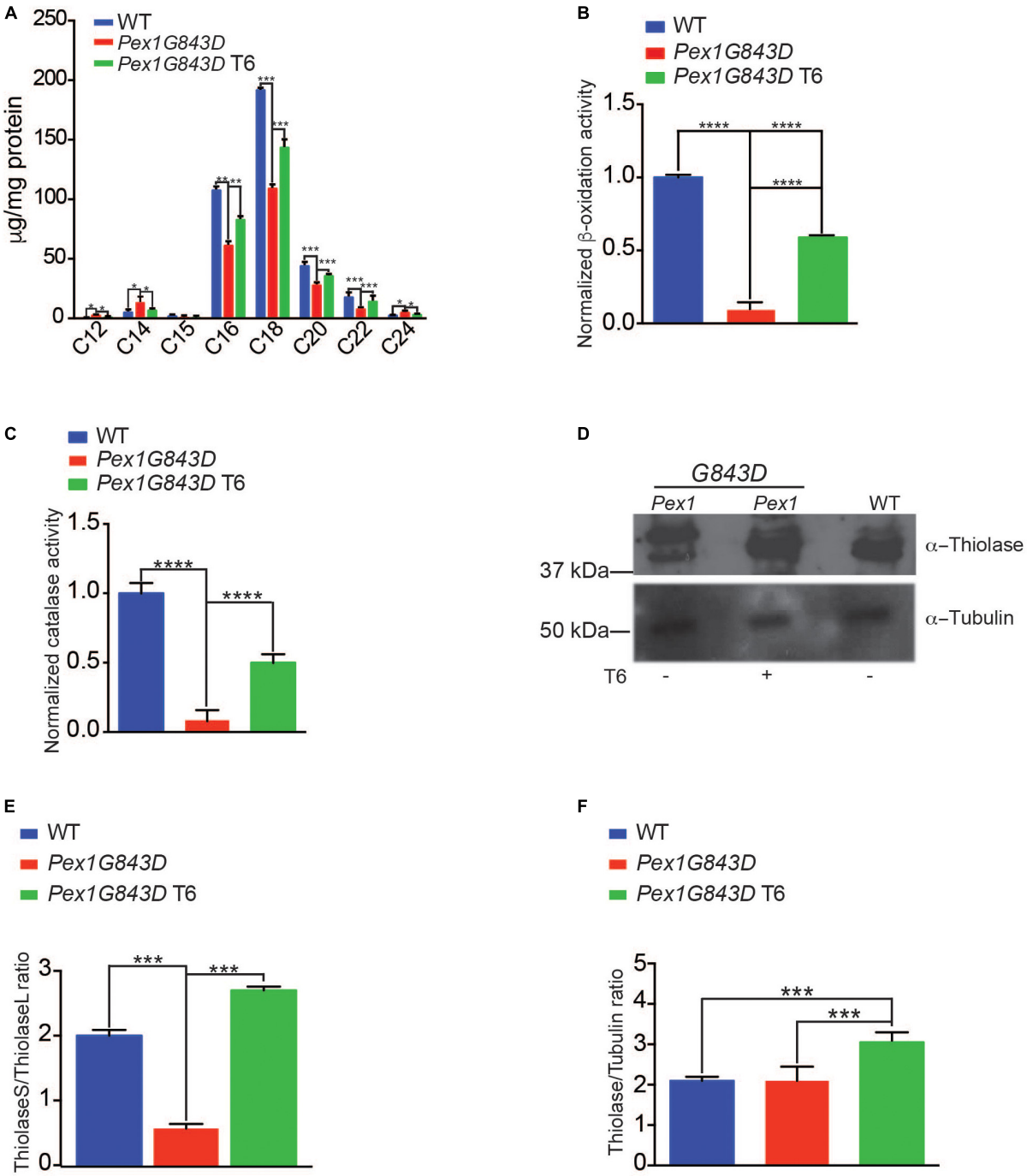

FIGURE 3 | T6 treatment improves peroxisomal function of *PEX1G843D* fibroblasts. **(A)** Fatty acid (FA) profiles in cells of the reported genotypes and under the reported conditions. FA amounts were normalized to mg protein for each sample ($N = 4$). Error bars represent standard deviation. Statistical significance was calculated using 2-way ANOVA. $^{***}p < 0.001$, $^{**}p < 0.01$, $^{*}p < 0.05$. **(B)** Treatment of *PEX1G843D* fibroblasts with T6 leads to increased peroxisomal β-oxidation activity in a peroxisome-enriched subcellular fraction compared to the same fraction from untreated *PEX1G843D* fibroblasts. Error bars represent standard deviation ($N = 4$). Statistical significance was calculated using 2-way ANOVA. $^{***}p < 0.001$. **(C)** Treatment of *PEX1G843D* fibroblasts with T6 leads to increased catalase activity in a peroxisome-enriched subcellular fraction compared to the same fractions from untreated *PEX1G843D* fibroblasts. Error bars represent standard deviation ($N = 4$). Statistical significance was calculated using 2-way ANOVA. $^{***}p < 0.001$. **(D)** Representative immunoblot showing increased amounts of mature imported ThiolaseS (42 kDa) in T6-treated *PEX1G843D* fibroblasts versus untreated *PEX1G843D* fibroblasts. Tubulin served as a control for protein loading. Immunoblotting was repeated three times. Equal amounts of protein (500 µg) were loaded in each lane. **(E)** Histogram reporting quantification of immunoblot results of the ratio ThiolaseS/ThiolaseL for each genotype and under each condition. Error bars represent standard deviation ($N = 3$). Statistical significance was calculated using 2-way ANOVA. $^{***}p < 0.001$. **(F)** Histogram reporting increased levels of thiolase in T6-treated *PEX1G843D* fibroblasts versus untreated *PEX1G843D* fibroblasts or WT fibroblasts. Error bars represent standard deviation ($N = 3$). Statistical significance was calculated using 2-way ANOVA. $^{***}p < 0.001$.

and decreased C_{24} FAs in *PEX1G843D* fibroblasts compared to the levels in WT fibroblasts and also rescued the levels of MCFAs to the levels found in WT fibroblasts (**Figure 3A**), altogether indicating improved FA metabolism in T6-treated *PEX1G843D* fibroblasts. T6 treatment of *PEX1G843D* fibroblasts also improves peroxisomal ß-oxidation activity over untreated fibroblasts (**Figure 3B**). leads not only to increased numbers of peroxisomes but also rescues peroxisomal ß-oxidation activity levels in these fibroblasts to levels approaching those observed in WT fibroblasts.

To obtain further support for the overall improvement in peroxisomal function in T6-treated versus untreated *PEX1G843D* fibroblasts, we monitored the relative activities of peroxisomal ß-oxidation (Lazarow and de Duve, 1976) and of peroxisomal catalase, the enzyme responsible for the breakdown of hydrogen peroxide into molecular oxygen and water (Wanders and Waterham, 2006). Treatment of *PEX1G843D* fibroblasts with T6 led to significantly increased peroxisomal ß-oxidation activity (**Figure 3B**) and catalase activity (**Figure 3C**) in a subcellular fraction enriched for peroxisomes compared to the fraction from untreated *PEX1G843D* fibroblasts, providing additional indicators of the recovery of peroxisome function in T6-treated *PEX1G843D* fibroblasts.

To provide additional support for the rescue of peroxisome activity by treatment of *PEX1G843D* fibroblasts with T6, we performed immunoblot analysis to monitor thiolase import into the peroxisomal matrix. Peroxisomal thiolase is an enzyme involved in FA ß-oxidation and catalyzes the reversible thiolytic cleavage of 3-ketoacyl-CoA into acyl-CoA and acetyl-CoA. Thiolase is synthesized as a larger precursor in the cytosol and is cleaved to a shorter active form upon import into peroxisomes (Wanders and Waterham, 2006). Immunoblot assays performed on WT fibroblasts, untreated *PEX1G843D* fibroblasts, and T6-treated *PEX1G843D* fibroblasts showed that immature thiolase (44 kDa, ThiolaseL) was the major form detected in untreated *PEX1G843D* fibroblasts (**Figure 3D**), whereas the amount of mature thiolase (42 kDa, ThiolaseS) increased upon T6 treatment of *PEX1G843D* fibroblasts to levels similar to those observed in WT fibroblasts (**Figure 3D**). To quantify thiolase maturation, we calculated the ratio of ThiolaseS to ThiolaseL measured from immunoblot signals (**Figure 3E**). Treatment with T6 significantly increased the ThiolaseS/ThiolaseL ratio (**Figure 3E**) and overall thiolase amounts (**Figure 3F**) of *PEX1G843D* fibroblasts, consistent with the improvement in peroxisomal ß-oxidation activity of T6-treated *PEX1G843D* fibroblasts (**Figure 3B**). Altogether, our findings indicate that T6 treatment improves peroxisomal function in *PEX1G843D* fibroblasts.

T6 Treatment of *PEX1G843D* Fibroblasts Restores the Size and Structure of the Mitochondrial Compartment Found in WT Fibroblasts

The absence of functional peroxisomes in PBD-ZSS leads to the proliferation of mitochondria and alteration of their structure. These changed mitochondria produce increased amounts of reactive oxygen species (ROS). Increased oxidative stress is posited to contribute significantly to the pathogenesis of PBD-ZSS (Baumgart et al., 2001). We therefore investigated whether there were any changes in mitochondrial morphology in *PEX1G843D* mutant fibroblasts compared to WT fibroblasts and whether these changes could be reversed by treatment of the mutant fibroblasts with T6. We observed mitochondria stained with MitoTracker Red by fluorescence microscopy and used the MiNA (Mitochondrial Network Analysis) platform (Valente et al., 2017) to compare the organization of mitochondria in *PEX1G843D* mutant fibroblasts to that of mitochondria in WT fibroblasts and T6-treated *PEX1G843D* fibroblasts. Mitochondria that were punctate or rod-shaped in appearance were defined as 'Individuals,' while mitochondria that were rods with three or more side branches were defined as a 'Network' (**Figure 4A**). MiNA showed that the number of individual mitochondria did not change between WT fibroblasts, *PEX1G843D* mutant fibroblasts, and T6-treated *PEX1G843D* fibroblasts (**Figures 4B,C**). Mitochondrial networks showed increased complexity in *PEX1G843D* mutant fibroblasts compared to WT fibroblasts, but treatment of *PEX1G843D* fibroblasts with T6 reduced the complexity of their mitochondrial networks to the level of complexity observed in WT fibroblasts (**Figures 4B,D–F**). The mitochondrial footprint was larger in untreated *PEX1G843D* mutant fibroblasts compared to WT fibroblasts (**Figure 4G**), suggesting that mitochondrial metabolism is altered in *PEX1G843D* fibroblasts, as expansion of the mitochondrial compartment has been linked to changes in mitochondrial metabolism (McCarron et al., 2013). Again, treatment of *PEX1G843D* fibroblasts with T6 restored the mitochondrial footprint of the mutant fibroblasts to essentially the area of the mitochondrial footprint in WT fibroblasts (**Figure 4G**). Because NO donors like GSNO (T6) have been associated with remodeling of the endoplasmic reticulum (ER), we also investigated whether there were any differences in ER morphology between WT fibroblasts, *PEX1G843D* mutant fibroblasts, and T6-treated *PEX1G843D* fibroblasts. Indirect IF microscopy using anti-KDEL antibodies that label the ER did not show a change in the size of the ER compartment between cells of the different genotypes and under the different conditions (**Supplementary Figures 1D,E**). Together, our experiments show that T6 treatment of *PEX1G843D* fibroblasts restores peroxisome functions and the structure and extent of the mitochondrial compartment to at or near what is observed in WT fibroblasts.

T6 Treatment Reduces the Amount of Autophagy in *PEX1G843D* Fibroblasts

Increased pexophagy (peroxisome-specific autophagy) has been suggested as an alternative to defective peroxisome biogenesis as a cause of PBD-ZSS (Law et al., 2017). Loss of the PEX1/PEX6 AAA-complex results in increased ubiquitination of PEX5 on peroxisome membranes, which can then signal pexophagy (Law et al., 2017). Given the potential link between increased pexophagy, PEX1 and PBD-ZSS, we monitored the number of lysosomes in WT fibroblasts, *PEX1G843D* mutant fibroblasts, and T6-treated *PEX1G843D* fibroblasts by

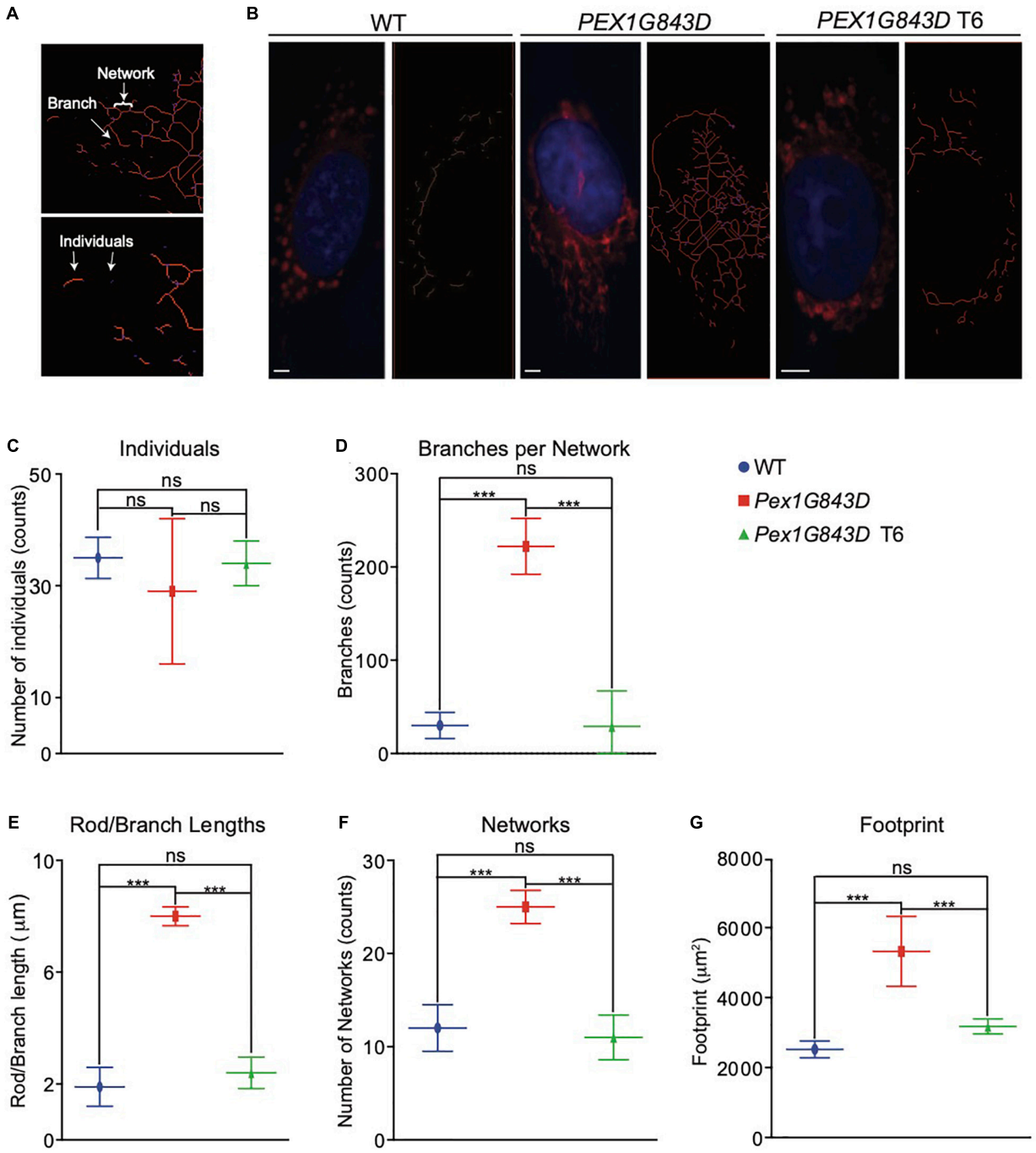

FIGURE 4 | T6 treatment restores the mitochondrial compartment in *PEX1G843D* fibroblasts. **(A)** Mitochondria were stained by MitoTracker Red and observed by fluorescence microscopy. Examples of the two types of mitochondrial features, individuals and networks, recognized by MiNA are shown. Networks can have different numbers of branches. **(B)** Fluorescence images of MitoTracker Red-stained WT fibroblasts, *PEX1G843D* mutant fibroblasts, and T6-treated *PEX1G843D* fibroblasts. The image at right in each pair of images shows skeletonized mitochondria required for analysis by MiNA. DNA was stained with DAPI. Red, mitochondria. Blue, nuclei. Scale bars, 10 μm. Histograms reporting the number of individuals **(C)**, mean branches per network **(D)**, mean rod to branch length **(E)**, number of networks **(F)**, and footprint area per cell **(G)** obtained by MiNA for WT fibroblasts, *PEX1G843D* mutant fibroblasts, and T6-treated *PEX1G843D* fibroblasts. Error bars represent standard deviation ($N = 25$). Statistical significance was calculated using 1-way ANOVA. ***$p < 0.001$. ns, not significant.

fluorescence microscopy of cells stained with LysoTracker Red. *PEX1G843D* mutant fibroblasts have more stained puncta in their cytoplasm compared to WT fibroblasts (**Figures 5A,B**). T6 treatment of *PEX1G843D* fibroblasts reduced the number of stained puncta to essentially WT numbers (**Figures 5A,B**). Our data suggest that T6 treatment might increase the number

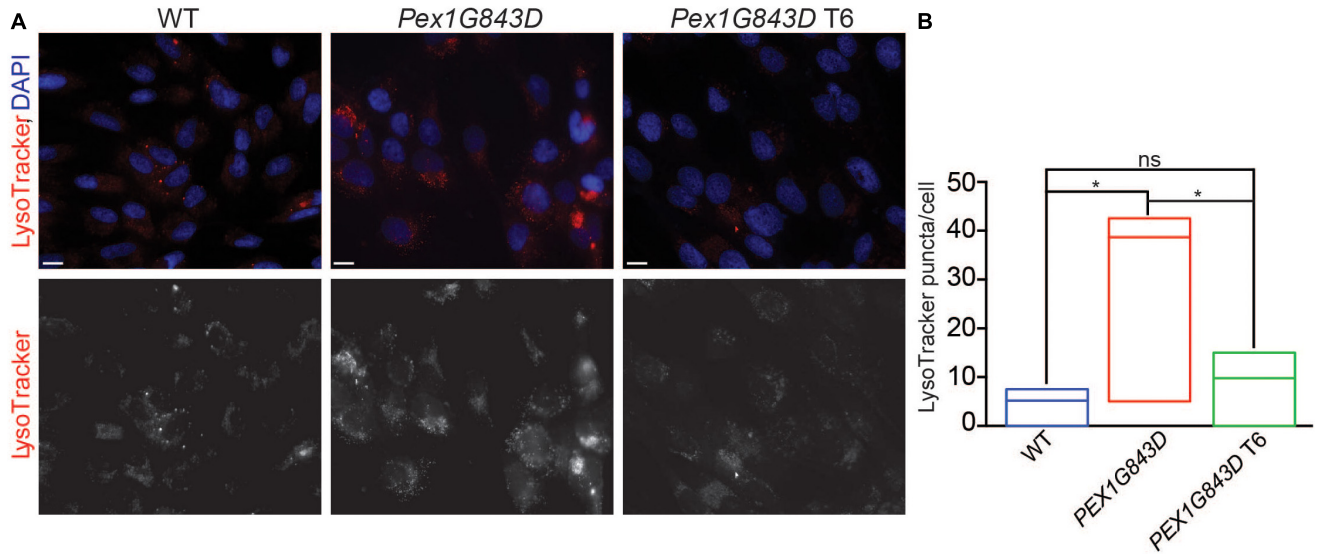

FIGURE 5 | T6 treatment reduces the number of lysosomes in *PEX1G843D* mutant fibroblasts. **(A)** WT fibroblasts, *PEX1G843D* mutant fibroblasts, and T6-treated *PEX1G843D* fibroblasts were stained with LysoTracker Red and observed by fluorescence microscopy. Nuclei were stained with DAPI (blue). Scale bars, 10 μm. **(B)** Histogram reporting the number of LysoTracker Red-stained puncta per cell of each genotype and under each condition. Error bars represent standard deviation ($N = 20$). Statistical significance was calculated using 1-way ANOVA. *$p < 0.05$. ns, not significant.

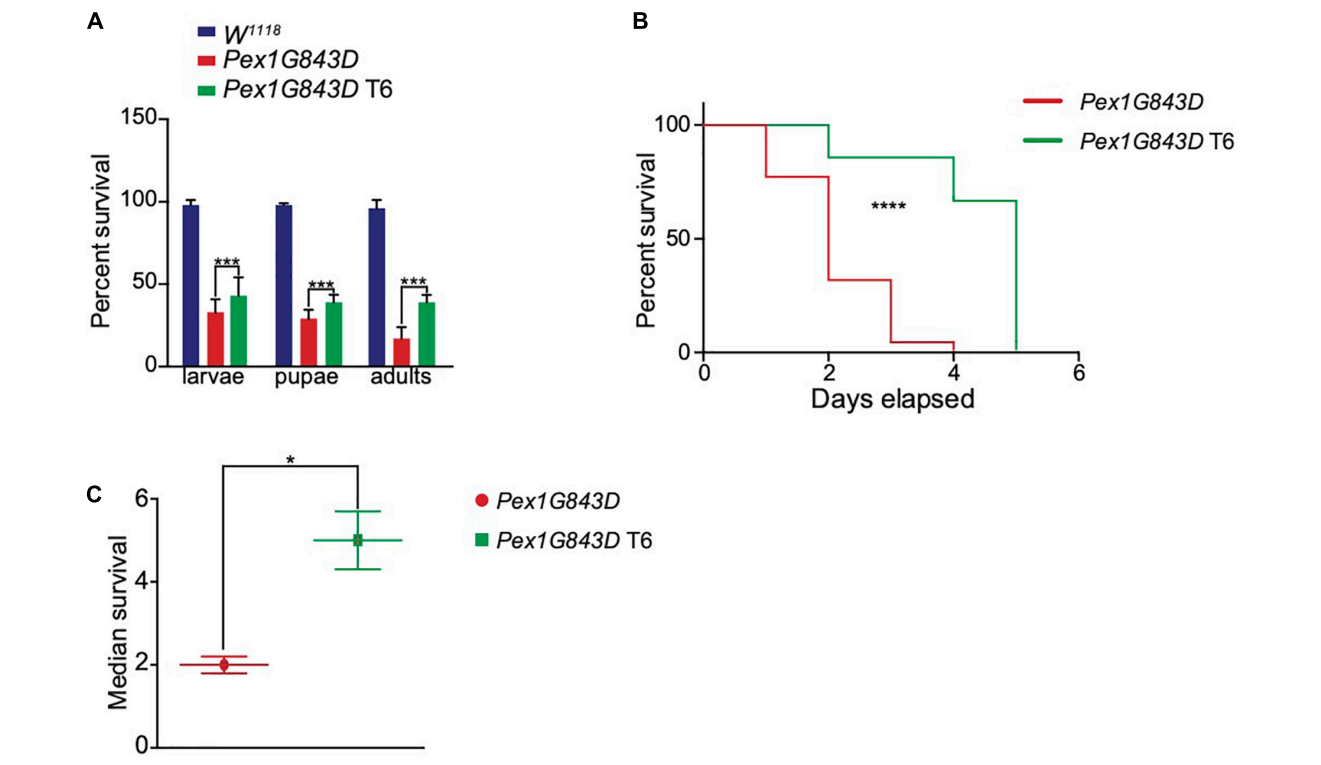

FIGURE 6 | T6 treatment improves survival and extends lifespan in a *Drosophila PEX1G843D* PBD-ZSS model. **(A)** Percent survival of wild-type (W^{1118}), *PEX1G843D* humanized mutant, and T6-treated *PEX1G843D* humanized mutant *Drosophila* at each stage of fly development. 200 eggs per genotype and condition were collected at the start. Note that T6 significantly increased the survival of *PEX1G843D* humanized mutant flies at each stage of development. Statistical significance was calculated using 1-way ANOVA. ***$p < 0.001$. **(B)** Survival curves of age-matched untreated and T6-treated *PEX1G843D* humanized *Drosophila* mutant. Statistical significance was calculated using the Log-rank test and the Gehan–Breslow–Wilcoxon test. ****$p < 0.0001$. **(C)** Median survival of age-matched untreated flies and T6-treated *PEX1G843D* humanized *Drosophila* mutant flies. Statistical significance was calculated using 1-way ANOVA. *$p < 0.05$.

of peroxisomes in *PEX1G843D* mutant fibroblasts by reducing peroxisome damage and/or degradation by pexophagy.

T6 Treatment Contributes to Increased Survival and Longer Lifespan in a *PEX1G843D* Humanized *Drosophila* Model of PBD-ZSS

The *PEX1G843D* mutation only partially impairs PEX1 function, a contributing factor in the relatively mild severity of the PBD-ZSS phenotype observed in patients with this mutation. For this reason, there is significant potential for pharmaceutical intervention to improve the lifespan of patients carrying the *PEX1G843D* mutation. To investigate whether T6 could improve developmental survival and lifespan *in vivo*, we generated a humanized *Drosophila* PBD-ZSS disease model carrying the human *PEX1G843D* mutation. To follow the effects of T6 administration on *PEX1G843D* mutant fly development and survival, we collected *PEX1G843D*-mutant eggs and WT eggs and allowed them to develop on normal corn meal medium or T6-supplemented corn meal medium. The percent survival of larvae, pupae, and adult *PEX1G843D* flies significantly increased with T6 supplementation (**Figures 6A,C**), although not to WT levels, indicating T6 treatment improved survival at each stage of the fly life cycle. Mutant flies raised on T6-supplemented corn meal medium showed a modest but significant improvement in lifespan compared to mutant flies raised on unsupplemented corn meal medium with an increase in median survival of 3 days (**Figures 6B,C**). Therefore, T6 treatment caused significant but modest improvements on the survival and lifespan of flies with the humanized *PEX1G843D* mutation.

DISCUSSION

Our study aimed to identify FDA-approved compounds that improve peroxisomal function of *PEX1G843D* PBD-ZSS mutant fibroblasts via HTS. Our HTS led to the identification of the compound GSNO, a NO donor, as a candidate therapeutic for the restoration of peroxisome number and function affected by the *PEX1G843D* mutation.

The HTS reported here initially identified 123 compounds out of the 1280-compound LOPAC library that increased the number of SKL-positive puncta in *PEX1G843D* fibroblasts above the *z*-score threshold specified by the 99% confidence interval. However, we were only able to confirm 11 compounds that increased the number of peroxisome puncta upon visual inspection, and only one compound that could reproduce this result upon repeated IF microscopy experiments using antibodies to peroxisomal matrix proteins (SKL) and to the peroxisomal membrane protein, ATP Binding Cassette Subfamily D Member 3 (ABCD3). The number of false positive hits is not unexpected, as *PEX1G843D* fibroblasts have been reported to exhibit a high degree of mosaicism in regards to their numbers of peroxisomes (Preuss et al., 2002; Zhang et al., 2010). Therefore, the identification of compounds able to rescue the *PEX1G843D* mutation through this HTS approach may be affected by peroxisomal mosaicism and the presence of a partially functional PEX1 protein in the *PEX1G843D* mutant fibroblasts.

We reported that GSNO treatment increases peroxisome number, enhances peroxisomal protein import, and improves peroxisome function in *PEX1G843D* fibroblasts, although how GSNO accomplishes these changes remains unknown. GSNO is a peroxisomal source of NO (Corpas et al., 2017), a reactive nitrogen specie (RNS) with important roles in physiological (Desikan et al., 2004; Rosales et al., 2014; Mata-Perez et al., 2016) and pathological (Foley and O'Farrell, 2003; Tripathi et al., 2007; Fransen et al., 2012; Agurla et al., 2014; Di Cara et al., 2017) signaling pathways. NO is also produced at peroxisomes through the activity of the enzyme nitric oxide synthase (Barroso et al., 1999; Stolz et al., 2002; Loughran et al., 2005). NO has been implicated in the stress response and developmental signaling in plants (Barroso et al., 2006; Bright et al., 2009; Chaki et al., 2011; Corpas et al., 2013), while in mammals NO has been implicated in neurotransmission, immune regulation, vascular smooth muscle relaxation, and inhibition of platelet aggregation (Liu et al., 2004; Moore et al., 2009; Corti et al., 2014).

S-nitrosoglutathione can regulate the activities of signaling pathways by promoting the post-translational modification of key proteins in specific signaling cascades. In particular, GSNO can promote the *S*-nitrosation of proteins (Wolhuter and Eaton, 2017; Palma et al., 2020). *S*-nitrosation is a reversible post-translational modification by which NO is bound to cysteinyl residues of proteins, which can lead to either reduced or enhanced activity of a protein (Hess and Stamler, 2012; Wolhuter and Eaton, 2017). GSNO has been shown to promote the *S*-nitrosation of catalase, which modulates its activity in processes like growth, development and response to stress in plants (Corpas et al., 2019) and animals (Tyther et al., 2007), and GSNO-directed inhibition of catalase by *S*-nitrosation has been linked to obesity in humans (Palma et al., 2020). Moreover, *S*-nitrosothiols such as GSNO have been used for many years as cardiovascular therapeutics and are currently under investigation as treatments for other diseases, including Crohn's disease (Shah et al., 2016). There, the ability of GSNO to regulate and modulate the actions of signaling cascades by post-translational modifications like *S*-nitrosation could account for its efficacy as a therapeutic for a variety of conditions.

Modulation of NO signaling has been associated with remodeling and increased biogenesis of mitochondria, Golgi, and ER in human pulmonary epithelium cells (Lee et al., 2013). Thus, GSNO could potentially increase peroxisome numbers by acting on ER or mitochondrial expansion. In our experiments, we did not observe an expansion of the ER in cells of any genotype and under any condition. However, we did observe that treatment with GSNO altered the structure of the mitochondrial network in *PEX1G843D* fibroblasts. Changes in mitochondrial shape and volume have been linked to changes in cell metabolism and signaling (McCarron et al., 2013). Interestingly, previous studies have reported that absence of functional peroxisomes in PBD-ZSS cells leads to proliferation of pleomorphic mitochondria with severely altered activity of the mitochondrial respiratory chain complexes,

which is accompanied by increased production of ROS. This increased oxidative stress combined with accumulation of lipid intermediates produced by the peroxisomal ß-oxidation system was proposed to contribute significantly to the pathogenesis of PBD-ZSS (Baumgart et al., 2001). GSNO treatment of *PEX1G843D* fibroblasts rescued the mitochondrial morphology in these cells to the extent of WT fibroblasts, suggesting that GSNO improves peroxisome activity and rescues the mitochondrial morphological defects caused by alteration in peroxisome functions in *PEX1G843D* fibroblasts. Additionally, GSNO could mitigate the damage that dysfunctional peroxisomes cause to other organelles by enhancing the activity of catalase that reduces the oxidative status of peroxisome mutant cells (Fransen et al., 2012). Interestingly, *Saccharomyces cerevisiae* cells treated with GSNO exhibit enhanced catalase activity, reduced cellular oxidative stress (Lushchak and Lushchak, 2008), and less damage to organelles such as mitochondria (Fransen et al., 2017). Finally, peroxisomal NO has a defined role in the post-translational modification of proteins by *S*-nitrosation and/or nitration by which NO could modulate the activity of peroxisomal enzymes involved in ROS metabolism and affect processes like pexophagy (von Knethen and Brüne, 2002; Di Cara et al., 2017; Corpas et al., 2021). Of note, a previous study demonstrated that the observed reduction in peroxisomal protein import in *PEX1G843D* fibroblasts is not caused by defects in peroxisomal import machinery but rather by increased degradation of peroxisomes by increased autophagy (pexophagy) (Law et al., 2017). We found that compared to WT fibroblasts, *PEX1G843D* fibroblasts have a greater number of vesicles stained with LysoTracker, which stains lysosomes and late autophagosomes. Thus, GSNO could cause the increase in peroxisome number observed in our study by controlling peroxisome turnover through the regulation of pexophagy. Although a recent study showed that inhibition of pexophagy in *PEX1G843D* fibroblasts did not correlate with a reduction in cellular VLCFAs (Klouwer et al., 2021), the identification of GSNO as a pharmaceutical with the ability to improve peroxisomal function may point to yet unknown interrelationships between peroxisomal protein networks, peroxisome biogenesis, and pexophagy.

The fly *D. melanogaster* is a proven model organism for evaluating the effects of a particular drug on a human mutation (Su, 2019). Studies have shown that drugs that act on a diversity of cellular targets like the cytoskeleton, kinases, phosphatases, ion channels, cell surface receptors, chaperones, and proteases often have the same target, or act through the same mechanism, in *Drosophila* as in humans (Fernandez-Hernandez et al., 2016). Our study using a humanized *Drosophila* model for PBD-ZSS highlights the validity of a pipeline in which potential therapeutics identified by a HTS of primary cell lines are validated by administration to humanized *Drosophila*, thereby shortening the time frame for moving a therapeutic to clinical evaluation. Taken altogether our findings show that GSNO is a promising drug candidate for clinical trials in patients with mild PBD-ZSS and serves as a starting molecule for the development of other compounds optimized for the treatment of these disorders.

DATA AVAILABILITY STATEMENT

The original contributions generated for this study are included in the article/**Supplementary Material**, further inquiries can be directed to the corresponding authors.

ETHICS STATEMENT

The studies involving human participants were reviewed and approved by the Office of Human Research Administration at the Kennedy Krieger Institute (Baltimore, MD, United States) to the Peroxisome Disease Laboratory, McGill University under Clinical Research Centre grants RR0052 and RR00722. Written informed consent to participate in this study was provided by the participants' legal guardian/next of kin.

AUTHOR CONTRIBUTIONS

CMW performed some of the *in vivo* analyses and wrote the first draft of the manuscript. YL performed the secondary screen and analyses and the biochemical assays. YS performed the secondary screen with YL. LL performed the first trial of *in vivo* analyses. GE and AS advised on the design of the primary screen. OL and EH-C contributed to mitochondria analysis. FD designed and performed the primary and secondary screens, analyzed data from the screens, selected positive hits, and conceived and designed the experiments to characterize the hits. RR conceived the project together with AS and FD. RR and FD edited the final copy of the manuscript. All authors contributed to the article and approved the submitted version.

FUNDING

This work was funded by a Collaborative Research Innovation Opportunities grant from Alberta Innovates Health Solutions to RR and AS; a Foundation Grant from the Canadian Institutes of Health Research (CIHR) to RR; a Discovery Grant from the Natural Sciences and Engineering Research Council of Canada to FD (RGPIN/04083-2019); and an Operating Grant from the CIHR (PJT-169179) to FD. We thank the Dalhousie Medical Research Foundation and the Beatrice Hunter Cancer Institute for supporting CMW.

ACKNOWLEDGMENTS

We thank Nancy Braverman (McGill University) for advice and for providing wild-type human fibroblasts and *PEX1G843D* mutant human fibroblasts. Lipid profiling was done at the Lipidomics Core Facility at the University of Alberta, which is supported by funding from the Faculty of Medicine & Dentistry and the Women and Children's Health Research Institute, University of Alberta. The compound screen was performed at the High Content Analysis Core, University of Alberta, Faculty of Medicine & Dentistry.

SUPPLEMENTARY MATERIAL

The Supplementary Material for this article can be found online at: https://www.frontiersin.org/articles/10.3389/fcell.2021.714710/full#supplementary-material

Supplementary Figure 1 | T6 treatment increases peroxisome number in *PEX1G843D* fibroblasts. **(A)** Detection of ABCD3-positive puncta by indirect IF microscopy in untreated and T6-treated WT fibroblasts. Scale bars, 10 μm. **(B)** Histogram reporting the quantification of ABCD3-positive puncta per cell in untreated and T6-treated WT fibroblasts. Error bars represent standard deviation ($N = 20$). Statistical significance was calculated using 2-way ANOVA. $^{**}p < 0.01$. **(C)** Fluorescence images of WT fibroblasts and of *PEX1G843D* mutant fibroblasts treated with vehicle (DMSO) or T6. Green, anti-KDEL antibody staining ER. Blue, DAPI-stained nuclei. Red, phalloidin-stained cytoskeleton. Scale bars, 10 μm. **(D)** Histogram reporting the quantification of the total ER-associated fluorescence per cell in each genotype and under each condition. Error bars represent standard deviation ($N = 20$). Statistical significance was calculated using 1-way ANOVA. ns, not significant.

REFERENCES

Agurla, S., Gayatri, G., and Raghavendra, A. S. (2014). Nitric oxide as a secondary messenger during stomatal closure as a part of plant immunity response against pathogens. *Nitric Oxide* 43, 89–96. doi: 10.1016/j.niox.2014.07.004

Baron, M. N., Klinger, C. M., Rachubinski, R. A., and Simmonds, A. J. (2016). A systematic cell-based analysis of localization of predicted *Drosophila* peroxisomal proteins. *Traffic* 17, 536–553. doi: 10.1111/tra.12384

Barroso, J. B., Corpas, F. J., Carreras, A., Rodriguez-Serrano, M., Esteban, F. J., Fernandez-Ocana, A., et al. (2006). Localization of S-nitrosoglutathione and expression of S-nitrosoglutathione reductase in pea plants under cadmium stress. *J. Exp. Bot.* 57, 1785–1793. doi: 10.1093/jxb/erj175

Barroso, J. B., Corpas, F. J., Carreras, A., Sandalio, L. M., Valderrama, R., Palma, J. M., et al. (1999). Localization of nitric-oxide synthase in plant peroxisomes. *J. Biol. Chem.* 274, 36729–36733.

Baumgart, E., Vanhorebeek, I., Grabenbauer, M., Borgers, M., Declercq, P. E., Fahimi, H. D., et al. (2001). Mitochondrial alterations caused by defective peroxisomal biogenesis in a mouse model for Zellweger syndrome (*PEX5* knockout mouse). *Am. J. Pathol.* 159, 1477–1494. doi: 10.1016/s0002-9440(10)62534-5

Berendse, K., Engelen, M., Ferdinandusse, S., Majoie, C. B. L. M., Waterham, H. R., Vaz, F. M., et al. (2016). Zellweger spectrum disorders: clinical manifestations in patients surviving into adulthood. *J. Inheritdemaret. Metab. Dis.* 39, 93–106. doi: 10.1007/s10545-015-9880-2

Bodnar, A. G., and Rachubinski, R. A. (1990). Cloning and sequence determination of cDNA encoding a second rat liver peroxisomal 3-ketoacyl-CoA thiolase. *Gene* 91, 193–199. doi: 10.1016/0378-1119(90)90088-9

Brand, A. H., and Perrimon, N. (1993). Targeted gene expression as a means of altering cell fates and generating dominant phenotypes. *Development* 118, 401–415. doi: 10.1242/dev.118.2.401

Braverman, N. E., D'Agostino, M. D., and MacLean, G. E. (2013). Peroxisome biogenesis disorders: biological, clinical and pathophysiological perspectives. *Dev. Disabil. Res. Rev.* 17, 187–196. doi: 10.1002/ddrr.1113

Bright, J., Hiscock, S. J., James, P. E., and Hancock, J. T. (2009). Pollen generates nitric oxide and nitrite: a possible link to pollen-induced allergic responses. *Plant Physiol. Biochem.* 47, 49–55. doi: 10.1016/j.plaphy.2008.09.005

Chaki, M., Valderrama, R., Fernandez-Ocana, A. M., Carreras, A., Gomez-Rodriguez, M. V., Lopez-Jaramillo, J., et al. (2011). High temperature triggers the metabolism of S-nitrosothiols in sunflower mediating a process of nitrosative stress which provokes the inhibition of ferredoxin-NADP reductase by tyrosine nitration. *Plant Cell Environ.* 34, 1803–1818. doi: 10.1111/j.1365-3040.2011.02376.x

Collins, C. S., and Gould, S. J. (1999). Identification of a common PEX1 mutation in Zellweger syndrome. *Hum. Mutat.* 14, 45–53. doi: 10.1002/(sici)1098-1004(1999)14:1<45::aid-humu6>3.0.co;2-j

Corpas, F. J., Alche, J. D., and Barroso, J. B. (2013). Current overview of S-nitrosoglutathione (GSNO) in higher plants. *Front. Plant Sci.* 4:126. doi: 10.3389/fpls.2013.00126

Corpas, F. J., Barroso, J. B., Gonzalez-Gordo, S., Munoz-Vargas, M. A., and Palma, J. M. (2019). Hydrogen sulfide: a novel component in *Arabidopsis* peroxisomes which triggers catalase inhibition. *J. Integr. Plant Biol.* 61, 871–883.

Corpas, F. J., Barroso, J. B., Palma, J. M., and Rodriguez-Ruiz, M. (2017). Plant peroxisomes: a nitro-oxidative cocktail. *Redox Biol.* 11, 535–542. doi: 10.1016/j.redox.2016.12.033

Corpas, F. J., González-Gordo, S., and Palma, J. M. (2021). Nitric oxide (NO) scaffolds the peroxisomal protein–protein interaction network in higher plants. *Intl. J. Mol. Sci.* 22:2444. doi: 10.3390/ijms22052444

Corti, A., Franzini, M., Scataglini, I., and Pompella, A. (2014). Mechanisms and targets of the modulatory action of S-nitrosoglutathione (GSNO) on inflammatory cytokines expression. *Arch. Biochem. Biophys.* 562, 80–91. doi: 10.1016/j.abb.2014.08.002

Crane, D. I., Maxwell, M. A., and Paton, B. C. (2005). *PEX1* mutations in the Zellweger spectrum of the peroxisome biogenesis disorders. *Hum. Mutat.* 26, 167–175. doi: 10.1002/humu.20211

Demaret, T., Evraerts, J., Ravau, J., Roumain, M., Muccioli, G. G., Najimi, M., et al. (2021). High dose versus low dose syngeneic hepatocyte transplantation in *Pex1*G844D NMRI mouse model is safe but does not achieve long term engraftment. *Cells* 10:40. doi: 10.3390/cells10010040

Demaret, T., Varma, S., Stephenne, X., Smets, F., Scheers, I., Wanders, R., et al. (2018). Living-donor liver transplantation for mild Zellweger spectrum disorder: up to 17 years follow-up. *Pediatr. Transplant.* 22:e13112. doi: 10.1111/petr.13112

Desikan, R., Cheung, M. K., Bright, J., Henson, D., Hancock, J. T., and Neill, S. J. (2004). ABA, hydrogen peroxide and nitric oxide signalling in stomatal guard cells. *J. Exp. Bot.* 55, 205–212. doi: 10.1093/jxb/erh033

Di Cara, F., Bülow, M. H., Simmonds, A. J., and Rachubinski, R. A. (2018). Dysfunctional peroxisomes compromise gut structure and host defense by increased cell death and Tor-dependent autophogy. *Mol. Biol. Cell* 29, 2766–2783. doi: 10.1091/mbc.e18-07-0434

Di Cara, F., Rachubinski, R. A., and Simmonds, A. J. (2019). Distinct roles for peroxisomal targeting signal receptors Pex5 and Pex7 in *Drosophila*. *Genetics* 211, 141–149. doi: 10.1534/genetics.118.301628

Di Cara, F., Sheshachalam, A., Braverman, N. E., Rachubinski, R. A., and Simmonds, A. J. (2017). Peroxisomes are required for the immune response to microbial infection. *Immunity* 47, 93–106. doi: 10.1016/j.immuni.2017.06.016

Ebberink, M. S., Mooijer, P. A. W., Gootjes, J., Koster, J., Wanders, R. J. A., and Waterham, H. R. (2011). Genetic classification and mutational spectrum of more than 600 patients with a Zellweger syndrome spectrum disorder. *Hum. Mutat.* 32, 59–69. doi: 10.1002/humu.21388

Faul, F., Erdfelder, E., Lang, A. G., and Buchner, A. (2007). G*Power 3: a flexible statistical power analysis program for the social, behavioral, and biomedical sciences. *Behav. Res. Methods* 39, 175–191. doi: 10.3758/bf03193146

Faust, J. E., Verma, A., Peng, C., and McNew, J. A. (2012). An inventory of peroxisomal proteins and pathways in *Drosophila melanogaster*. *Traffic* 13, 1378–1392. doi: 10.1111/j.1600-0854.2012.01393.x

Fernandez-Hernandez, I., Scheenaard, E., Pollarolo, G., and Gonzalez, C. (2016). The translational relevance of *Drosophila* in drug discovery. *EMBO Rep.* 17, 471–472. doi: 10.15252/embr.201642080

Folch, J., Lees, M., and Sloane Stanley, G. H. (1957). A simple method for the isolation and purification of total lipides from animal tissues. *J. Biol. Chem.* 226, 497–509. doi: 10.1016/s0021-9258(18)64849-5

Foley, E., and O'Farrell, P. H. (2003). Nitric oxide contributes to induction of innate immune responses to gram-negative bacteria in *Drosophila*. *Genes Dev.* 17, 115–125. doi: 10.1101/gad.1018503

Fransen, M., Lismont, C., and Walton, P. (2017). The peroxisome-mitochondria connection: how and why? *Int. J. Mol. Sci.* 18:1126. doi: 10.3390/ijms18061126

Fransen, M., Nordgren, M., Wang, B., and Apanasets, O. (2012). Role of peroxisomes in ROS/RNS-metabolism: implications for human disease. *Biochim. Biophys. Acta* 1822, 1363–1373. doi: 10.1016/j.bbadis.2011.12.001

Geisbrecht, B. V., Collins, C. S., Reuber, B. E., and Gould, S. J. (1998). Disruption of a PEX1–PEX6 interaction is the most common cause of the neurologic disorders Zellweger syndrome, neonatal adrenoleukodystrophy, and infantile Refsum disease. *Proc. Natl. Acad. Sci. U.S.A.* 95, 8630–8635. doi: 10.1073/pnas.95.15.8630

Hess, D. T., and Stamler, J. S. (2012). Regulation by S-nitrosylation of protein post-translational modification. *J. Biol. Chem.* 287, 4411–4418. doi: 10.1074/jbc.r111.285742

Imanaka, T., Aihara, K., Suzuki, Y., Yokota, S., and Osumi, T. (2000). The 70-kDa peroxisomal membrane protein (PMP70), an ATP-binding cassette transporter. *Cell Biochem. Biophys.* 32, 131–138. doi: 10.1385/cbb:32:1-3:131

Ito, T., Fujimura, S., Matsufuji, Y., Miyaji, T., Nakagawa, T., and Tomizuka, N. (2007). Molecular characterization of the *PEX5* gene encoding peroxisomal targeting signal 1 receptor from the methylotrophic yeast *Pichia methanolica*. *Yeast* 24, 589–597. doi: 10.1002/yea.1484

Joardar, A., Menzl, J., Podolsky, T. C., Manzo, E., Estes, P. S., Ashford, S., et al. (2015). PPARγ activation is neuroprotective in a *Drosophila* model of ALS based on TDP-43. *Hum. Mol. Genet.* 24, 1741–1754. doi: 10.1093/hmg/ddu587

Klouwer, F. C. C., Falkenberg, K. D., Ofman, R., Koster, J., van Gent, D., Ferdinandusse, S., et al. (2021). Autophagy inhibitors do not restore peroxisomal functions in cells with the most common peroxisome biogenesis defect. *Front. Cell Dev. Biol.* 9:661298. doi: 10.3389/fcell.2021.661298

Law, K. B., Bronte-Tinkew, D., Di Pietro, E., Snowden, A., Jones, R. O., Moser, A., et al. (2017). The peroxisomal AAA ATPase complex prevents pexophagy and development of peroxisome biogenesis disorders. *Autophagy* 13, 868–884. doi: 10.1080/15548627.2017.1291470

Lazarow, P. B., and de Duve, C. (1976). A fatty acyl-CoA oxidizing system in rat liver peroxisomes; enhancement by clofibrate, a hypolipidemic drug. *Proc. Natl. Acad. Sci. U.S.A.* 73, 2043–2046. doi: 10.1073/pnas.73.6.2043

Lee, J. E., Yuan, H., Liang, F.-X., and Sehgal, P. B. (2013). Nitric oxide scavenging causes remodeling of the endoplasmic reticulum, Golgi apparatus and mitochondria in pulmonary arterial endothelial cells. *Nitric Oxide* 33, 64–73. doi: 10.1016/j.niox.2013.06.005

Liu, L., Yan, Y., Zeng, M., Zhang, J., Hanes, M. A., Ahearn, G., et al. (2004). Essential roles of S-nitrosothiols in vascular homeostasis and endotoxic shock. *Cell* 116, 617–628. doi: 10.1016/s0092-8674(04)00131-x

Loughran, P. A., Stolz, D. B., Vodovotz, Y., Watkins, S. C., Simmons, R. L., and Billiar, T. R. (2005). Monomeric inducible nitric oxide synthase localizes to peroxisomes in hepatocytes. *Proc. Natl. Acad. Sci. U.S.A.* 102, 13837–13842. doi: 10.1073/pnas.0503926102

Lushchak, O. V., and Lushchak, V. I. (2008). Catalase modifies yeast *Saccharomyces cerevisiae* response towards S-nitrosoglutathione-induced stress. *Redox Rep.* 13, 283–291. doi: 10.1179/135100008x309037

MacLean, G. E., Argyriou, C., Di Pietro, E., Sun, X., Birjandian, S., Saberian, P., et al. (2019). Zellweger spectrum disorder patient-derived fibroblasts with the PEX1-Gly843Asp allele recover peroxisome functions in response to flavonoids. *J. Cell. Biochem.* 120, 3243–3258. doi: 10.1002/jcb.27591

Mast, F. D., Li, J., Virk, M. K., Hughes, S. C., Simmonds, A. J., and Rachubinski, R. A. (2011). A *Drosophila* model for the Zellweger spectrum of peroxisome biogenesis disorders. *Dis. Model Mech.* 4, 659–672. doi: 10.1242/dmm.007419

Mata-Perez, C., Sanchez-Calvo, B., Begara-Morales, J. C., Carreras, A., Padilla, M. N., Melguizo, M., et al. (2016). Nitro-linolenic acid is a nitric oxide donor. *Nitric Oxide* 57, 57–63. doi: 10.1016/j.niox.2016.05.003

McCarron, J. G., Wilson, C., Sandison, M. E., Olson, M. L., Girkin, J. M., Saunter, C., et al. (2013). From structure to function: mitochondrial morphology, motion and shaping in vascular smooth muscle. *J. Vasc. Res.* 50, 357–371. doi: 10.1159/000353883

Moore, P. E., Ryckman, K. K., Williams, S. M., Patel, N., Summar, M. L., and Sheller, J. R. (2009). Genetic variants of GSNOR and ADRB2 influence response to albuterol in African-American children with severe asthma. *Pediatr. Pulmonol.* 44, 649–654. doi: 10.1002/ppul.21033

Palma, J. M., Mateos, R. M., Lopez-Jaramillo, J., Rodriguez-Ruiz, M., Gonzalez-Gordo, S., Lechuga-Sancho, A. M., et al. (2020). Plant catalases as NO and H_2S targets. *Redox Biol.* 34:101525. doi: 10.1016/j.redox.2020.101525

Platta, H. W., and Erdmann, R. (2007). Peroxisomal dynamics. *Trends Cell Biol.* 17, 474–484. doi: 10.1016/j.tcb.2007.06.009

Poll-The, B. T., Gootjes, J., Duran, M., de Klerk, J. B. C., Maillette de Buy Wenniger-Prick, L. J., Admiraal, R. J. C., et al. (2004). Peroxisome biogenesis disorders with prolonged survival: phenotypic expression in a cohort of 31 patients. *Am. J. Med. Genet.* 126A, 333–338. doi: 10.1002/ajmg.a.20664

Preuss, N., Brosius, U., Biermanns, M., Muntau, A. C., Conzelmann, E., and Gartner, J. (2002). PEX1 mutations in complementation group 1 of Zellweger spectrum patients correlate with severity of disease. *Pediatr. Res.* 51, 706–714. doi: 10.1203/00006450-200206000-00008

Reuber, B. E., Germain-Lee, E., Collins, C. S., Morrell, J. C., Ameritunga, R., Moser, H. W., et al. (1997). Mutations in *PEX1* are the most common cause of peroxisome biogenesis disorders. *Nat. Genet.* 17, 445–448. doi: 10.1038/ng1297-445

Rosales, M. A., Silva, K. C., Duarte, D. A., de Oliveira, M. G., de Souza, G. F., Catharino, R. R., et al. (2014). S-nitrosoglutathione inhibits inducible nitric oxide synthase upregulation by redox posttranslational modification in experimental diabetic retinopathy. *Invest. Ophthalmol. Vis. Sci.* 55, 2921–2932. doi: 10.1167/iovs.13-13762

Sanchez-Martinez, A., Luo, N., Clemente, P., Adan, C., Hernandez-Sierra, R., Ochoa, P., et al. (2006). Modeling human mitochondrial diseases in flies. *Biochim. Biophys. Acta* 1757, 1190–1198. doi: 10.1016/j.bbabio.2006.05.008

Sen, A., and Cox, R. T. (2017). Fly models of human diseases: *Drosophila* as a model for understanding human mitochondrial mutations and disease. *Curr. Top. Dev. Biol.* 121, 1–27. doi: 10.1016/bs.ctdb.2016.07.001

Sexton, J. Z., He, Q., Forsberg, L. J., and Brenman, J. E. (2010). High content screening for nonclassical peroxisome proliferators. *Int. J. High Throughput Screen.* 1, 127–140. doi: 10.2147/ijhts.s10547

Shah, S. U., Socha, M., Fries, I., and Gibaud, S. (2016). Synthesis of S-nitrosoglutathione-alginate for prolonged delivery of nitric oxide in intestines. *Drug Deliv.* 23, 2927–2935. doi: 10.3109/10717544.2015.1122676

Smith, J. J., and Aitchison, J. D. (2013). Peroxisomes take shape. *Nat. Rev. Mol. Cell Biol.* 14, 803–817. doi: 10.1038/nrm3700

Stolz, D. B., Zamora, R., Vodovotz, Y., Loughran, P. A., Billiar, T. R., Kim, Y. M., et al. (2002). Peroxisomal localization of inducible nitric oxide synthase in hepatocytes. *Hepatology* 36, 81–93. doi: 10.1053/jhep.2002.33716

Su, T. T. (2019). Drug screening in *Drosophila*; why, when, and when not? *Wiley Interdiscip. Rev. Dev. Biol.* 8, e346.

Szilard, R. K., Titorenko, V. I., Veenhuis, M., and Rachubinski, R. A. (1995). Pay32p of the yeast *Yarrowia lipolytica* is an intraperoxisomal component of the matrix protein translocation machinery. *J. Cell Biol.* 131, 1453–1469. doi: 10.1083/jcb.131.6.1453

Tripathi, P., Tripathi, P., Kashyap, L., and Singh, V. (2007). The role of nitric oxide in inflammatory reactions. *FEMS Immunol. Med. Microbiol.* 51, 443–452. doi: 10.1111/j.1574-695x.2007.00329.x

Tyther, R., Ahmeda, A., Johns, E., and Sheehan, D. (2007). Proteomic identification of tyrosine nitration targets in kidney of spontaneously hypertensive rats. *Proteomics* 7, 4555–4564. doi: 10.1002/pmic.200700503

Valente, A. J., Maddalena, L. A., Robb, E. L., Moradi, F., and Stuart, J. A. (2017). A simple ImageJ macro tool for analyzing mitochondrial network morphology in mammalian cell culture. *Acta Histochem.* 119, 315–326. doi: 10.1016/j.acthis.2017.03.001

Ventura, M. J., Wheaton, D., Xu, M., Birch, D., Bowne, S. J., Sullivan, L. S., et al. (2016). Diagnosis of a mild peroxisomal phenotype with next-generation sequencing. *Mol. Genet. Metab. Rep.* 9, 75–78. doi: 10.1016/j.ymgmr.2016.10.006

von Knethen, A., and Brüne, B. (2002). Activation of peroxisome proliferator-activated receptor γ by nitric oxide in monocytes/macrophages down-regulates $p47^{phox}$ and attenuates the respiratory burst. *J. Immunol.* 169, 2619–2626. doi: 10.4049/jimmunol.169.5.2619

Walter, C., Gootjes, J., Mooijer, P. A., Portsteffen, H., Klein, C., Waterham, H. R., et al. (2001). Disorders of peroxisome biogenesis due to mutations in *PEX1*: phenotypes and PEX1 protein levels. *Am. J. Hum. Genet.* 69, 35–48. doi: 10.1086/321265

Wanders, R. J., and Waterham, H. R. (2006). Biochemistry of mammalian peroxisomes revisited. *Annu. Rev. Biochem.* 75, 295–332. doi: 10.1146/annurev.biochem.74.082803.133329

Willoughby, L. F., Schlosser, T., Manning, S. A., Parisot, J. P., Street, I. P., Richardson, H. E., et al. (2013). An *in vivo* large-scale chemical screening platform using *Drosophila* for anti-cancer drug discovery. *Dis. Model. Mech.* 6, 521–529.

Wolhuter, K., and Eaton, P. (2017). How widespread is stable protein S-nitrosylation as an end-effector of protein regulation? *Free Radic. Biol. Med.* 109, 156–166. doi: 10.1016/j.freeradbiomed.2017.02.013

Yik, W. Y., Steinberg, S. J., Moser, A. B., Moser, H. W., and Hacia, J. G. (2009). Identification of novel mutations and sequence variation in the Zellweger syndrome spectrum of peroxisome biogenesis disorders. *Hum. Mutat.* 30, E467–E480.

Zhang, R., Chen, L., Jiralerspong, S., Snowden, A., Steinberg, S., and Braverman, N. (2010). Recovery of PEX1-Gly843Asp peroxisome dysfunction by small-molecule compounds. *Proc. Natl. Acad. Sci. U.S.A.* 107, 5569–5574. doi: 10.1073/pnas.0914960107

Conflict of Interest: The authors declare that the research was conducted in the absence of any commercial or financial relationships that could be construed as a potential conflict of interest.

frontiers in Cell and Developmental Biology

ORIGINAL RESEARCH
published: 20 December 2021
doi: 10.3389/fcell.2021.737159

Novel Trypanocidal Inhibitors that Block Glycosome Biogenesis by Targeting PEX3–PEX19 Interaction

Mengqiao Li[1], Stefan Gaussmann[2,3], Bettina Tippler[1], Julia Ott[1], Grzegorz M Popowicz[2,3], Wolfgang Schliebs[1], Michael Sattler[2,3], Ralf Erdmann[1] and Vishal C Kalel[1]**

[1]Department of Systems Biochemistry, Faculty of Medicine, Institute of Biochemistry and Pathobiochemistry, Ruhr University Bochum, Bochum, Germany, [2]Institute of Structural Biology, Helmholtz Zentrum München, Neuherberg, Germany, [3]Department of Chemistry, Bavarian NMR Center, Technical University of Munich, Garching, Germany

Human pathogenic trypanosomatid parasites harbor a unique form of peroxisomes termed glycosomes that are essential for parasite viability. We and others previously identified and characterized the essential *Trypanosoma brucei* ortholog TbPEX3, which is the membrane-docking factor for the cytosolic receptor PEX19 bound to the glycosomal membrane proteins. Knockdown of TbPEX3 expression leads to mislocalization of glycosomal membrane and matrix proteins, and subsequent cell death. As an early step in glycosome biogenesis, the PEX3–PEX19 interaction is an attractive drug target. We established a high-throughput assay for TbPEX3–TbPEX19 interaction and screened a compound library for small-molecule inhibitors. Hits from the screen were further validated using an *in vitro* ELISA assay. We identified three compounds, which exhibit significant trypanocidal activity but show no apparent toxicity to human cells. Furthermore, we show that these compounds lead to mislocalization of glycosomal proteins, which is toxic to the trypanosomes. Moreover, NMR-based experiments indicate that the inhibitors bind to PEX3. The inhibitors interfering with glycosomal biogenesis by targeting the TbPEX3–TbPEX19 interaction serve as starting points for further optimization and anti-trypanosomal drug development.

Keywords: neglected tropical diseases, trypanosoma, glycosome biogenesis, protein–protein interaction, PPI inhibitors, alphascreen, small-molecule inhibitor screen, PEX3-PEX19 inhibitor

OPEN ACCESS

Edited by:
Jorge E. Azevedo, Universidade do Porto, Portugal

Reviewed by:
Armando Jardim, McGill University, Canada
J. Fraser Glickman, The Rockefeller University, United States
Paul Michels, University of Edinburgh, United Kingdom

****Correspondence:***
Ralf Erdmann
ralf.erdmann@rub.de
Vishal C. Kalel
vishal.kalel@rub.de

Specialty section:
This article was submitted to Membrane Traffic, a section of the journal Frontiers in Cell and Developmental Biology

Received: *06 July 2021*
Accepted: *15 November 2021*
Published: *20 December 2021*

Citation:
Li M, Gaussmann S, Tippler B, Ott J, Popowicz GM, Schliebs W, Sattler M, Erdmann R and Kalel VC (2021) Novel Trypanocidal Inhibitors that Block Glycosome Biogenesis by Targeting PEX3–PEX19 Interaction. Front. Cell Dev. Biol. 9:737159. doi: 10.3389/fcell.2021.737159

INTRODUCTION

Trypanosomatids are vector-borne protozoan parasites responsible for highly divergent range of eukaryotic infections in humans and animals. Particularly in the tropical and sub-tropical regions of the world, *Trypanosoma brucei* (*T. brucei*), *T. cruzi*, and various *Leishmania* species cause African and American trypanosomiases and leishmaniasis, respectively. *T. brucei* sub-species cause human infections termed African sleeping sickness (human African trypanosomiasis, HAT), and its close related species *T. congolense* and *T. vivax* cause animal infections termed nagana disease in sub-Saharan regions. The human infections are fatal without treatment and affect across 36 countries in sub-Sahara African area, and majority of the reported cases (>95%) were caused by the sub-species *T. brucei gambiense* (Kennedy, 2019; WHO). In addition, nagana has been a burden for economic development by affecting domestic animals (Richards et al., 2021). More than 20 million people are currently infected with *T. cruzi* or *Leishmania*, leading to over 30 thousand deaths each year. With the fact that there is no effective vaccine against HAT due to the antigenic variation, chemotherapies

have been the only major approach for treating the diseases. The well-known frontline drugs, suramin, pentamidine, melarsoprol, and eflornithine have various limitations, i.e., they are constrained by stage and causative-strain of the disease, toxicity, logistical issues, and the emergence of drug resistance. Furthermore, the fifth drug nifurtimox has been used off-label in the combination therapy with eflornithine (NECT) to treat second-stage *T. b. gambiense* infections. Melarsoprol remains the only treatment for stage 2 infection caused by *T. b. rhodesiense* (Pépin and Milord, 1994; Wang, 1995; Babokhov et al., 2013; Büscher et al., 2017).

Despite a long history for treatments with these compounds, the cellular targets were not clear for a long time. Except for eflornithine, which is an irreversible inhibitor of ornithine decarboxylase that functions in the spermidine biosynthesis. Extensive studies have been performed to identify the mode of actions of these drugs. To be specific, it has been reported that melarsoprol and suramin target mitosis and cytokinesis, respectively. In addition, nifurtimox and pentamidine interfere with the parasite mitochondria by disrupting its membrane potential and inducing loss of kinetoplast DNA (Alsford et al., 2012; Thomas et al., 2018). Inhibitors of known targets in rational drug development have been reported in the past decades, including phenothiazine that blocks trypanothione reductase (Chan et al., 1998; Khan et al., 2000; Persch et al., 2014); other targets are purine metabolism of parasites (El Kouni, 2003), *T. brucei* topoisomerase IB (Bakshi and Shapiro, 2004), glycosomal enzymes glycerol kinase (Balogun et al., 2019), and phosphofructokinase (McNae et al., 2021), as well as proteins involved in the glycosome biogenesis (Dawidowski et al., 2017; Banerjee et al., 2019; Kalel et al., 2019).

Fexinidazole has been the first oral treatment for HAT, and its treatment for both stages of *T. b. gambiense* HAT was approved by the European Medicines Agency's (EMA) Committee in 2018. In 2019, the compound was added to the WHO Essential Medicines List and very recently was approved by the United States Food and Drug Administration (FDA) (Mullard, 2021). Using of the compound with rhodesiense HAT is still undergoing clinical trial (DNDi). Fexinidazole is a prodrug activated by NADH-specific nitroreductase (NTR1), and the resulting highly reactive nitro-reduced products kill parasites by hitting multiple targets. Fexinidazole is also interested for potentially targeting *T. cruzi*, which is the causative agent for the Chagas disease; *T. cruzi* harbors an orthologous nitroreductase enzyme (Dickie et al., 2020). The cellular target of acoziborole and the related benzoxaborole AN7973 is RNA cleavage and polyadenylation specificity factor subunit (CPSF3) (Begolo et al., 2018). To be specific, clinical trials with acoziborole, as another oral treatment, have been completed in 2020. The drug is now undergoing approval by EMA and FDA (DNDi). Because of decades of efforts in research and control of the HAT, a number of recorded new cases were decreased to 992 in 2019 (WHO). *T. brucei*, however, remains as the very important model organism for studies in resolving potential cellular targets for the closely related parasites. It is experimentally more amenable model system compared to *T. cruzi* and *Leishmania* species, responsible for the infections of higher impacts, which demand updating in therapeutic strategies. Moreover, *T. brucei* has been verified as a valid model system for *T. cruzi*, for compounds targeting the PEX14 and PEX5 interaction (Dawidowski et al., 2017). Last but not the least, animal infections of livestock (nagana) caused by *T. congolense*, *T. vivax*, and *T. brucei* species, leading to the annual loss of over 4 billion United States dollars are remaining great challenges (Shereni et al., 2021). This demonstrates the importance of using *T. brucei* as the model organism for drug development.

Trypanosomatid parasites harbor a unique form of peroxisome termed glycosome, which compartmentalizes the first seven enzymes of the glycolytic pathway (Opperdoes and Borst, 1977). Unlike peroxisomes, glycosomes are essential for the survival of bloodstream form (BSF) parasites as glycolysis is the sole source of ATP in this stage. Defects in the glycosome biogenesis lead to mislocalization of glycolytic enzymes to the cytosol, where their unregulated enzyme activities deplete cellular ATP levels and accumulate glucose metabolites to the toxic levels that kills the BSF parasites (Bakker et al., 1999; Furuya et al., 2002; Haanstra et al., 2016). Glycosomal matrix and membrane protein import involves distinct sets of Peroxin (PEX) proteins. Small-molecule inhibitors of the TbPEX14–TbPEX5 interaction that block the glycosomal matrix protein import are lethal to the *Trypanosoma* parasites (Dawidowski et al., 2017) and have recently established the import machinery and glycosome biogenesis as novel therapeutic targets for the development of trypanocidal drugs. Peroxisomal membrane protein (PMP) import is mediated by PEX19, PEX3, and PEX16 (Giannopoulou et al., 2016). PEX19 is the cytosolic receptor and chaperone for newly synthesized PMPs, which targets the cargo PMPs to the peroxisomal membrane by docking at PEX3 (Fang et al., 2004; Jones et al., 2004). Mammalian PEX16 and its functional homolog Pex36 in yeast are involved in ER-to-peroxisome trafficking of PMPs (Honsho et al., 2002; Farré et al., 2017). TbPEX19 and TbPEX16 have been identified and characterized previously (Banerjee et al., 2005; Kalel et al., 2015). We and others recently identified a highly divergent *Trypanosoma* ortholog of PEX3 with very low sequence identity with the known PEX3 proteins from other organisms (Banerjee et al., 2019; Kalel et al., 2019). TbPEX3 was shown to be essential for the parasite survival, because RNA interference (RNAi) knockdown of TbPEX3 expression is lethal to the trypanosomes.

The TbPEX3–TbPEX19 interaction is expected to be an attractive candidate drug target because 1) TbPEX3 acts in the early stages of glycosome biogenesis, particularly in the recruitment of PMPs to the glycosome, which subsequently affects matrix protein import. 2) Sequence similarity of TbPEX3 to its human homolog is low. Here, we report the development of a high-throughput assay to screen small-molecule inhibitors of the TbPEX3–TbPEX19 interaction. We have identified compounds that act on-target in trypanosomes to disrupt glycosome biogenesis and kill *Trypanosoma* parasites but with no apparent toxicity to mammalian cells. The establishment of the high-throughput assay and novel TbPEX3–TbPEX19 inhibitors serve as the starting points for further optimization to develop novel therapies against trypanosomatid parasite infections.

TABLE 1 | Primer list.

Primer name	Sequence (5′-3′)
RE6944	CGGGATCCCCCGTGCAAAACAGCATTGTTG
RE6945	ACGCGTCGACTTATAAATCGCGGCATGTAACTCTAATCGTCTC
RE7033	CCGCTCGAGCACTGATGGTTGCACATCGGCAAGTC
RE7130	CATGCCATGGATGTCTCATCCCGACAATGACGCCG
RE7131	GAATTCTCATGCACTCTTCTCGAATTGTGGGTGAGACCACAC TGATGGTTGCACATCGGCAAGTC
RE7148	CATGCCATGGGCATGTCTCATCCCGACAATGACGCCG
RE8070	AAGAATTCGAAATGTCTGAGTTCCAAAGGTTTGTT
RE8071	AAGACGGATCCGATTTGATCTTGTTCCAGTTCAA
TbPEX19F	ATGTCTCATCCCGACAATGACG
TbPEX19R	TTACACTGATGGTTGCACATCGGC
pCDF11F	GAATCTTTATTTTCAGGGCATGTCTCATCCCGACAATGACG
pCDF11R	CGCCTTGTGACGTGTCTTACACTGATGGTTGCACATCGGC

METHODS

Molecular Cloning

The *TbPEX3* gene (Tb427tmp.01.2020) was amplified from genomic DNA, to tag the soluble fraction of TbPEX3 (residues 45–476) with N-terminal GST tag, the *TbPEX3* gene was amplified with primers RE6944 and RE6945 spanned by *Bam*HI and *Sal*I sites and cloned into vector pGEX-4T2. The full-length *TbPEX19* gene (Tb427tmp.211.3300) was amplified using primers RE7130 and RE7033 containing *Nco*I and *Xho*I sites, by cloning of the gene into vector pET24d; the expressed protein was tagged C-terminally by six Histidine residues. *TbPEX19* was cloned downstream of a His_6 tag and a TEV cleavage site, into the vector pCDF using the method of SLIM (site directed, ligase-independent mutagenesis), with primers: TbPEX19F, TbPEX19R, pCDF11F, and pCDF11R. *TbPEX19* was cloned into pCOLA with C-terminal tagging of StrepII (RE7146 and RE7148). The *TbPEX11* gene (Tb427tmp.01.3370) was cloned into vector pGN1 using *Bst*BI and *Bam*HI sites (primers RE8070 and RE8071) with GFP tag at its C-terminus. Primers are shown in **Table 1**.

Recombinant Protein Overexpression and Purification

E. coli BL21(DE3) cells were transformed with corresponding plasmids, and protein expression was induced when OD_{600} reached ~0.6. Protein expression of either GST-TbPEX3d44 alone or dual expression with TbPEX19-His was initiated by addition of 0.4 mM IPTG, followed by growth for 16 h at 18°C. The expression of TbPEX19-His and GST-His (pET42b) was induced with 1 mM IPTG, and cells were cultured for 3 h to allow overexpression. The *E. coli* BL21(DE3) cultures were harvested, and clarified supernatant was prepared as described in Kalel et al. (2019). GST-TbPEX3d44 and the co-expressed complex were captured with affinity chromatography using glutathione agarose beads (Protino®, Macherey-Nagel). TbPEX19-His was purified by Nickel-NTA resin (Protino®, Macherey-Nagel) using gravity-flow columns (30-μm pore size, Pierce®). Protein-bound beads were washed with 5× volume of phosphate-buffered saline (PBS) (pH 7.4), and proteins were eluted with either 10 mM reduced glutathione or 200-mM imidazole supplemented with PBS buffer. To produce tag-free TbPEX19, His-TbPEX19 was purified similarly and incubated with His-tagged TEV protease, and the cleaved-off His tag and TEV protease were removed by Ni^+-NTA resin. TbPEX19-Strep was purified using StrepTactin Sepharose resin according to the user manual (IBA). Purified proteins were loaded into size-exclusion chromatography column (Superdex® 200 10/300 GL), and the predicted size of the co-migrated complex (GST-TbPEX3d44 and TbPEX19-His) was around 117 kDa by comparing with the calibration curve using the same column (data not shown). Protein aliquots were snap-frozen with liquid nitrogen and stored at −80°C.

High-Throughput Compound Screening

Co-expressed TbPEX3–TbPEX19 (5 nM) and GST-His (54 nM) were used for the primary and counter screens, and these protein concentrations provided strong and very similar range of signal window to allow reliable statistical analysis (data not shown). Screening of 4,480 diversity-oriented compounds (DIVERSet-CL, collection No. 1511-1, ChemBridge) was performed in the format of 384-well plates (AlphaScreen-384 plates, PerkinElmer®). The 25-μl reactions consist of 10 μl of protein solution (5 nM for PEX3/PEX19 complex and 54 nM for GST-His; all concentrations for the Alpha assays were final concentrations unless otherwise stated), 5 μl of compound solution (10 μM), and 5 μl of solution for each of the donor and acceptor beads (1:1,250, v/v). The above solutions were prepared in the reaction buffer [0.5% BSA v/v, 0.05% Tween 80 v/v, 0.2 mM DTT, PBS (pH7.4)] on the day of assay, diluting the compounds from 1 mM stocks in DMSO. Compounds were incubated with the proteins for 30 min at room temperature (RT). Five microliters of AlphaScreen Nickel-chelate acceptor beads (cat. no. 6760619C, PerkinElmer®) and AlphaScreen Glutathione donor beads (cat. no. 6765300, PerkinElmer®) were distributed to the mixture consecutively, with a 15-min interval. The complete 25-μl reaction solutions were incubated for 45 min at RT in the dark, and Alpha signals were captured with Cytation 5 plate reader (BioTek®) with the gain value set at 180. Schematic representation of the experiment setup of the high-throughput screening assays was prepared with BioRender.com.

Estimation of the Binding Affinity of the TbPEX3–PEX19 Interaction Using AlphaScreen Approach

Binding affinity of TbPEX3 and TbPEX19 was estimated in the formats of 1) saturation binding assays and 2) competitive binding assays; each of the assays was performed with triplicates, and drug candidates were substituted with buffer. 1) Constant concentrations of TbPEX19-His (0.3, 1, and 10 nM) were saturated with serial dilutions of GST-TbPEX3 from 0 to 300 nM. The saturation curves were fitted with the one-site specific binding model with GraphPad Prism 9; the mean of apparent equilibrium dissociation constants (K_D) from the best fits was obtained from three independent assays with varied concentration of TbPEX19-His. 2) TbPEX19-His (10× or 5×)

was used to saturate GST-TbPEX3d44 (0.2, 0.3, 1, and 2 nM). Serial dilutions of either tag-free TbPEX19 (0–5 μM) or TbPEX19-Strep (0–7.2 μM) were used to compete away the TbPEX19-His from its complex with GST-TbPEX3d44. Alpha signals were normalized to % for comparison between assays, and curves were fitted using one-site homologous model in GraphPad, which assume that tag-free TbPEX19 and TbPEX19-Strep binds in identical way as of TbPEX19-His to GST-TbPEX3d44.

Hit Selection From the Screen

Individual assays with the Z' factor above 0.5 (Zhang et al., 1999) indicate good assay capacity in distinguishing between positive and negative controls. Hits were selected by the criteria 1) 50% signal cutoff and 2) robust Z-score ($\leq$ 3) (Malo et al., 2006; Chung et al., 2008; Birmingham et al., 2009). Following initial hit selection, 10 μM of drugs were tested with GST-His (54 nM) and TbPEX19/TbPEX3 (5 nM) in smaller scale, and the level of signal was normalized (in %) and compared. Compounds with specific inhibition activity were prioritized. IC50 of four candidate compounds targeting the interaction of TbPEX3–TbPEX19 (compound **1**, **2**, **3**, and **4**) were tested by incubation of the complex with serial dilutions of compounds from 0 to 100 μM.

ELISA Assays

Dose-dependent responses of the inhibitors were analyzed with TbPEX19–TbPEX3 interaction. One hundred microliters of TbPEX19-His (10 μg/ml) diluted in PBS (pH 7.4) was coated on 96-well plates (Immulon® 2 HB, Thermo Fisher Scientific) at RT for 1 h. Wells were washed twice with 250 μl of PBS to remove unbound protein and blocked with 200 μl of buffer C [3% BSA in PBS (pH 7.4)] for 1 h. The inhibitors were diluted to desired concentrations in PBS, and 100 μl of each of the compounds were added to TbPEX19-coated wells, followed by 1-h incubation. To these wells, 100 μl of GST-TbPEX3d44 was added to reach final concentration of 0.3 nM and incubated for 1 h further. After three washes with PBS, bound GST-TbPEX3d44 was detected by mouse monoclonal anti-GST antibody (Sigma-Aldrich, 1:1,000 v/v in buffer D) [0.05% v/v Tween 20 in PBS (pH 7.4)]; signal was amplified by rabbit anti-mouse horseradish peroxidase (1:1,000 v/v in buffer D, Invitrogen). Substrate 3,3′,5,5′-tetramethylbenzidine (TMB, Thermo Fisher Scientific) was added to initiate the colorimetric reaction, which was terminated after 20 min by adding H_2SO_4, and the absorbance was measured at wavelength of 450 nm.

ELISA with TbPEX14–TbPEX5 was used as an independent assay to confirm compound specificity by examining the compound activity on TbPEX14–TbPEX5 interaction. TbPEX14–TbPEX5 assays were performed similarly with following changes. GST-TbPEX14$_{1\text{-}84}$ was coated, and biotinylated TbPEX5 peptide (Biotin-Aca-Aca-EQWAQEYAQMQAM) was used as analyte to a final concentration of 500 nM. Bound PEX5 was detected using streptavidin-conjugated alkaline phosphatase [1:2,000 v/v in PBS, 0.05% v/v Tween 20 (pH 7.4), buffer D, Promega] and *p*-nitrophenylphosphate (PNPP, Thermo Fisher Scientific) as a substrate, reactions stopped with 3 M NaOH and absorbance read at 405 nm.

Trypanosoma Culture, Transfection and Cell Viability Assays

BSF strain Lister 427 (termed hereafter as BSF427) and cell line 90-13 (stably expressing Tet repressor) were used in this study. BSF cells were grown in HMI-11 medium and maintained in logarithmic phase [below 2×10^6 cells/ml as described in Kalel et al. (2019)]. Genomically integrated stable transfections were performed with *Not*I-linearized plasmid constructs (pGN1-TbPEX11), which integrate into the spacer region of the ribosomal RNA repeat locus in the genome of cell line 90-13, and the clones were selected using blasticidin as described previously (Kalel et al., 2015). Expression of TbPEX11-GFP was confirmed with fluorescence microscopy following induction tests (data not shown) with a serial dilution of tetracycline, and minimal concentration (5 ng/ml) of tetracycline was used to achieve expression of the protein in more than 80% of the cells.

T. brucei BSF427 and compound dilutions were mixed in 1 : 1 (v/v) ratio to total volume of 200 μl, to reach final concentrations of 2×10^3 cells/ml and 0.19–100 μM of inhibitors, in quadruplicates in 96-well plates. Culture medium with no cells was used as negative control and cultures without presence of compounds as positive control representing normal rate of cell growth. Cells were grown at 37°C in an incubator with humidified air containing 5% CO_2 for 3 days. Cell viabilities were measured quantitatively using resazurin dye, by adding 25-μl resazurin (0.1 mg/ml in HBSS) to each well, and the mixture incubated for 6 h in the incubator. Fluorescence emission was detected at 570 and 585 nm after excitation at 530 nm, and fluorescence at 570 nm was subtracted from 585 nm. The inhibition curves were fitted with normalized fluorescence signal (in percentage) against concentration of compounds in Log10 scale using GraphPad Prism, and best fit was used for EC50 estimation. Chemical structures were drawn with ChemDraw 20.0.

Immunofluorescence Microscopy

BSF 90-13 cells with genomically integrated PEX11-GFP were induced with 5 ng/ml of tetracycline and cultured overnight to initiate stable expression of PEX11-GFP. BSF427- and PEX11-GFP–expressing cells were treated for 24 h with 100 μM, 50 and 25 μM of each of the inhibitor, and DMSO was used as control. Compound-treated cultures with growth rates of about 50% compared to the DMSO control were harvested and stained for immunofluorescence and statistical analysis. Cells were fixed with 4% paraformaldehyde in PBS containing 250 mM sucrose for 20 min. Fixed cells were immobilized on adhesive slide (StarFrost®) pre-coated with 10% (v/v) of poly-L-lysine (Sigma-Aldrich®) in water after 1-h incubation at RT. Cells were permeabilized with 0.1% (v/v) Triton X-100 in PBS (pH7.4) for 15 min and blocked in buffer D [PBS supplemented with 1% (w/v) BSA and 0.25% (v/v) Tween 20] for 1 h. Anti-TbAldolase primary antibody was used at 1:500

dilution in buffer D for 1.5 h incubation. After five washes in PBS for 30 min, samples were treated with Goat anti-rabbit secondary antibody (1:200, v/v, Alexa Fluor™ 594). Samples were washed, dried, and mounted with Mowiol containing 4′,6-diamidino-2-phenylindole (DAPI). Immuno-stained cells were visualized with Zeiss Elyra microscopy. Pictures of stack 3 (of 5), rotation 1 (of 3), and phase 5 (of 5) were chosen for all control and compound-treated samples.

Digitonin Fractionation

BSF427 cells were treated with compound **2**, compound **3**, or equivalent volume of DMSO for 24 h, and 2.4×10^6 cells (16.5 μg protein) were harvested for each condition by centrifugation and washed once with homogenization buffer, containing 25 mM Tris-HCl (pH 7.4), 1 mM EDTA, 0.3 M sucrose, 1 mM DTT, and leupeptin (2 μg/ml). Pellets were resuspended in 420 μl of homogenization buffer and distributed evenly into four tubes each with 100 μl (4 μg protein). Digitonin (5% w/v stock in water) was diluted to corresponding concentrations, and 25 μl of which was added to the cell suspension to reach final concentration of 0.025×, 0.05×, 0.1×, or 2× (digitonin/protein, μg/μg). The mixture was incubated for 2 min at 37°C, vortexed for 10 s, and centrifuged (16,000 g) at 4°C for 15 min. 100 μl from the supernatant (solubilized fractions) was taken for Western blot analysis. Remaining pellet fractions were washed by adding homogenization buffer up to 125 μl and centrifuged again, supernatants were discarded, and pellets were resuspended in 100 μl for Western blotting.

NMR Hit Validation Using Saturation Transfer Difference Experiments

NMR saturation transfer difference (STD) experiments (Mayer and Meyer, 1999) were carried out on a Bruker AVIII 600-MHz spectrometer equipped with a cryoprobe and a SampleJet auto sampler. One-dimensional (1D) and STD spectra were acquired at 298 K. Compounds were dissolved in DMSO-d6 to a final concentration of 50 mM. STD experiments with GST-TbPEX3, TbPEX19-His, and GST-His were performed in PBS (pH 7.4), 10% D_2O at a protein concentration of 10 μM, and a ligand concentration of 300 μM. Saturation time and interscan delay within STD experiments were set to 2 and 2.5 s, respectively.

RESULTS

Establishment of an AlphaScreen Assay for High-Throughput Screening of PEX3–PEX19 Interaction Inhibitors

PEX19, the cytosolic receptor for PMPs, recognizes its cargo proteins through its C-terminal PMP binding domain. The N-terminal region of PEX19 mediates docking of the receptor cargo complex to the peroxisomal membrane via binding to PEX3. Thus, the PEX3–PEX19 interaction is the key step for the peroxisomal targeting and insertion of PMPs. Blocking this interaction will disrupt membrane biogenesis and, subsequently, matrix protein import, thus exerting lethal effect on trypanosomes. We previously showed that the recombinantly expressed GST-TbPEX3 lacking N-terminal 44 amino acids, which form the single-pass transmembrane domain (referred to as GST-TbPEX3d44 from here onward), interacts with the N-terminal 50 amino acid fragment of His-tagged TbPEX19 ($TbPEX19_{1\text{-}50aa}$-His) in a pull-down assay (Kalel et al., 2019). To establish the high-throughput screening procedure for PEX3–PEX19 inhibitors, we utilized the AlphaScreen (PerkinElmer, Yasgar et al., 2016) technology, which we have previously used to identify PEX14–PEX5 inhibitors (Dawidowski et al., 2017). The AlphaScreen assay was established with purified GST-TbPEX3d44 and His-tagged full-length TbPEX19 (TbPEX19FL-His) (**Figure 1A**, **Supplementary Figure S1A**). Co-expressed and co-purified GST-TbPEX3d44 and TbPEX19-His was used for the compound screening assays. The complex co-migrated in size exclusion column with equimolar amounts of the components (**Supplementary Figure S1B,C**). These results indicate that the complexes are stable and that the tags do not interfere with the interaction. A saturation assay and two competitive assays were performed to confirm the stability and interaction between the purified proteins. The analysis of the interaction revealed apparent dissociation constants of K_D = 32.83 ± 7.04 nM (saturation assay) and K_D = 9.7 ± 1.9 nM (competitive assay using tag-free TbPEX19) (**Figure 1B**). An additional competitive assay was performed with TbPEX19-Strep, with apparent K_D of 3.7 ± 0.2 nM (**Supplementary Figure S2**). For the compound screening, the co-expressed and co-isolated complex of GST-TbPEX3d44 and TbPEX19FL-His was applied.

The assay was established in 384-well format with in-plate controls, including negative controls (no protein complex present) and positive controls (protein complex in the absence of chemical compounds). The two controls are indicative for the background noise and the signal without compound interference. As an additional negative control, dissociation of the PEX3–PEX19 interaction was achieved by incubation with 1 M NaCl (Ihrig and Obermann, 2017). We screened more than 4,000 compounds from the ChemBridge diversity library at a fixed concentration of 10 μM to test their capacity for inhibiting the TbPEX3–PEX19 interaction. An example of an individual assay, including the three controls and 320 compounds tested per 384-well plate is shown in **Figure 1C** (upper panel). The Z' factor calculation considered positive (proteins present) and negative (no-proteins present) controls, as well as the corresponding dynamic range (Zhang et al., 1999). Therefore, it is regarded as a general approach for the evaluation and comparison for individual assays and an overview for all assays in our screenings, with a cutoff value of 0.5 (**Figure 1C**, middle panel). Robust Z-score was initially developed for RNAi screens. It is preferable for incorporating the variation among individual samples and, meanwhile, insensitive to the outliers (Chung et al., 2008; Birmingham et al., 2009). It utilizes median and median absolute deviation, and compounds with robust Z-score smaller than −3 were considered as causing significantly decreased signals from the majority (**Figure 1C**, lower panel).

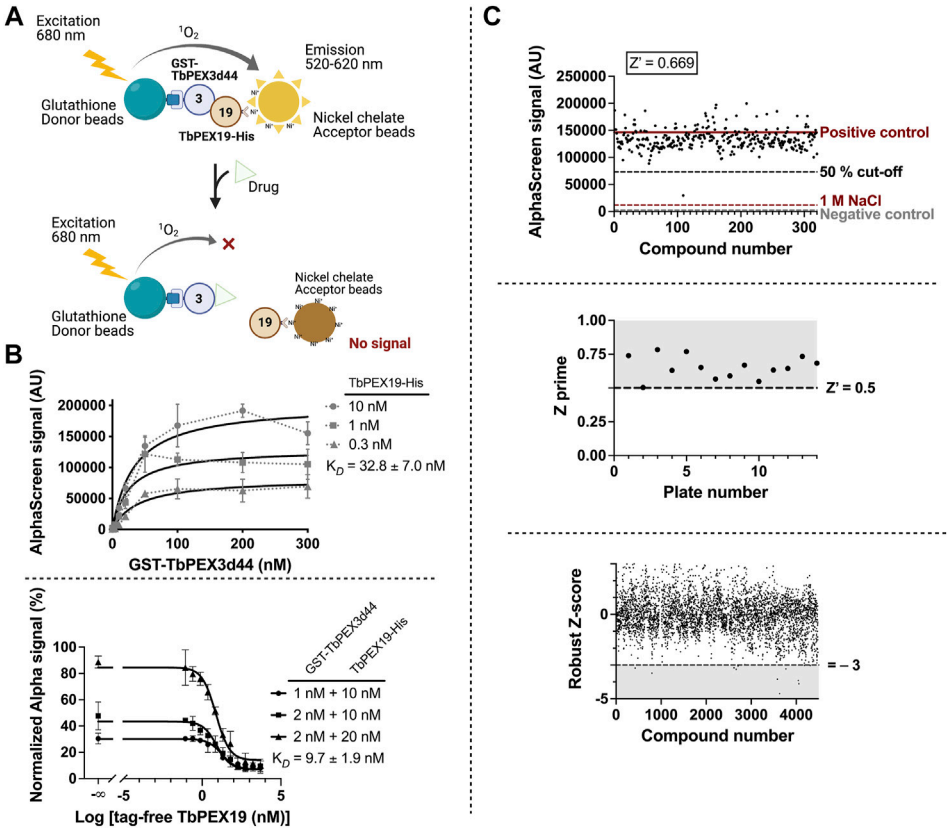

FIGURE 1 | High-throughput TbPEX3–PEX19 inhibitor screening using AlphaScreen. **(A)** The screening assay with GST-TbPEX3d44 and TbPEX19FL-His. Interaction of the two proteins leads to different levels of light emission in the absence and presence of inhibitors, which can be quantitatively measured. **(B)** Binding of GST-TbPEX3d44 and TbPEX19FL-His was analyzed in a saturation assay **(upper panel)**; curves were fitted using one-site specific binding model with GraphPad. TbPEX19 was tested at three concentrations in independent saturation assays with serial dilution of TbPEX3, each of the data points represent the average of triplicates, and standard deviation is shown as vertical bars. An apparent K_D of 32.83 ± 7.04 nM was obtained from the three assays. **Lower panel** shows the binding affinity between GST-TbPEX19 and TbPEX19-His analyzed by competitive binding assay using tag-free TbPEX19. Curves were fitted using one-site homologous model which assumes tag-free TbPEX19 binds in the identical way as of TbPEX19-His to GST-TbPEX3d44. An apparent K_D of 9.7 ± 1.9 nM was estimated. **(C)** Compound screening assays were performed in 384-well plate format and individual plates contained following controls: negative control in the absence of protein complex showing background signal; positive control representing normal protein interaction, 1 M NaCl was used to completely dissociate the complex **(upper panel)**. Raw readings from an example plate with original AlphaScreen signal are shown in the upper panel using a 50% signal cutoff. Z prime value of each plate was calculated to ensure the assay reliability, with $0.5 \leq Z' \leq 1$ **(middle panel)**. Hits were selected using robust Z score; compounds giving robust Z score ≤ –3 were prioritized **(lower panel)**.

On the basis of the above criteria, six compounds were prioritized for further analysis. A counter-screen assay using GST-His was performed to elucidate whether these compounds interfere with the Alpha signal systematically, for example, by intrinsic fluorescence or unspecific binding to the affinity tags or the beads (**Figure 2A**). Ten micromolars of each compound in DMSO or DMSO alone were incubated with either TbPEX3–TbPEX19 complex or GST-His in parallel, and $signal_{compound}$ was normalized to $signal_{DMSO}$ in percentage for each assay condition. $Signal_{compound}$ from GST-His was adjusted to 100% to allow comparison with the percent signal of TbPEX3–TbPEX19 (**Figure 2B**). Binding of two hits did not yield reproducible results, whereas the remaining compounds **1**, **2**, **3**, and **4** showed varied levels of specific inhibition of TbPEX3–TbPEX19 in comparison with GST-His. The four drug candidates showed a dose-dependent response in the TbPEX3–TbPEX19 interaction. The IC50 values (50% inhibitory concentration) of compounds **4**, **1**, **3**, and **2** were determined to be 0.5, 1.0, 14.3, and 37.5 μM, respectively (**Figure 2C**).

Validation of the Hits Using an Independent *in vitro* Assay

To confirm the inhibition of TbPEX3–TbPEX19 interaction by an independent assay, an ELISA assay was established. To determine the binding affinity, TbPEX19FL-His was coated to the wells of a microtiter plate, and different concentrations of GST-TbPEX3d44 were titrated. This saturation assay showed strong binding of TbPEX3 to TbPEX19, with an apparent K_D of 0.16 ± 0.015 nM (**Figure 3A**). The lower K_D value, when compared with AlphaScreen assay, is probably due to the dimerization of GST that causes amplification of signal via detection with anti-GST antibody. The presence of the dimerizing GST in the complex, detection via anti-GST antibody and secondary enzyme-coupled antibodies, which are

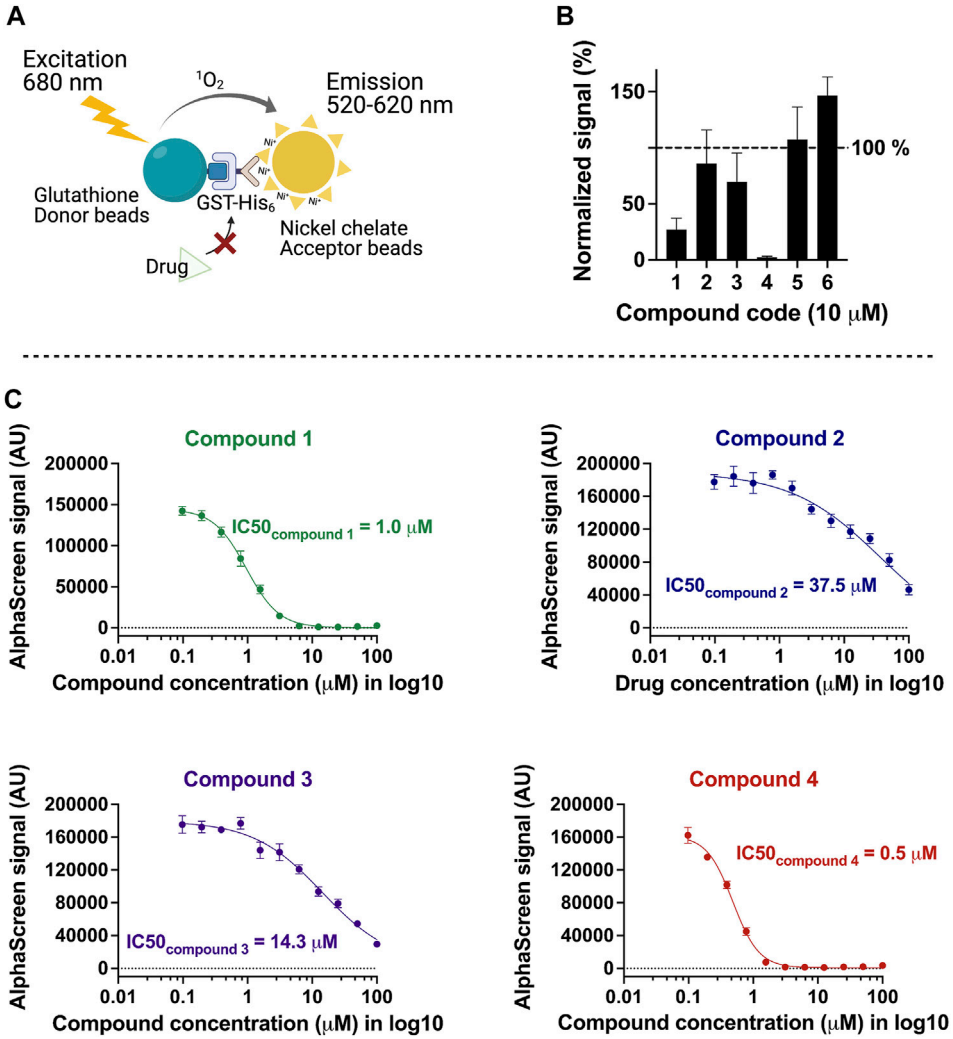

FIGURE 2 | Characterization of inhibitors with the counter screen assay and dose-dependent response analysis. **(A)** Recombinant GST-His was used as a control to identify compounds that non-specifically reduce the AlphaScreen signal. **(B)** Normalized levels of compound-response using test (signal$_{TbPEX19\text{-}TbPEX3}$) against control (signal$_{GST\text{-}His}$), 10 μM of each compound was tested with TbPEX19–TbPEX3 complex or GST-His, four of six candidates (compounds **1**, **2**, **3**, and **4**) were selected for future analyses. **(C)** Dose-dependent response of the four compounds against TbPEX19–TbPEX3 interaction. IC50 values of the four compounds are 0.5, 1.0, 14.3, and 37.5 μM for compounds **4**, **1**, **3**, and **2**, respectively.

used to detect ELISA signal, can lead to a considerable level of signal amplification independent of PEX19-binding and might be the cause for the lower K_D value. Therefore, the calculated binding constant can only be considered as apparent K_D value.

Next, we measured the dose-dependent response for the four identified compounds on the PEX3–PEX19 interaction using the ELISA. NaCl (1 M), which blocks protein–protein interactions (PPIs) (Ihrig and Obermann, 2017) and the TbPEX14–TbPEX5 inhibitor MAB-NH_2 (Dawidowski et al., 2017) that should not block the PEX3–PEX19 interaction served as negative controls. Dose-dependent inhibition of the interaction was observed for all four compounds, whereas MAB-NH_2 did not affect the interaction, thus demonstrating the specificity of the PEX3–PEX19 inhibitors (**Figure 3B**). About 50 μM of the compounds was required to achieve 50% of reduction in the normalized absorbance. Furthermore, these compounds were also tested on other protein complexes to investigate the possibility of unspecific inhibition. To this end, binding of TbPEX14-His and biotinylated TbPEX5 peptide was analyzed. None of the compounds affected the interaction up to 10 μM tested conditions, indicating that they do not block protein interactions in the ELISA assay unspecifically (**Supplementary Figure S3**).

Hit Validation and Target Identification by NMR

We performed two independent NMR STD experiments to validate the hits (compounds **1**–**6**) and to identify which protein is directly targeted by the inhibitors. STD experiments were performed with GST-TbPEX3d44,

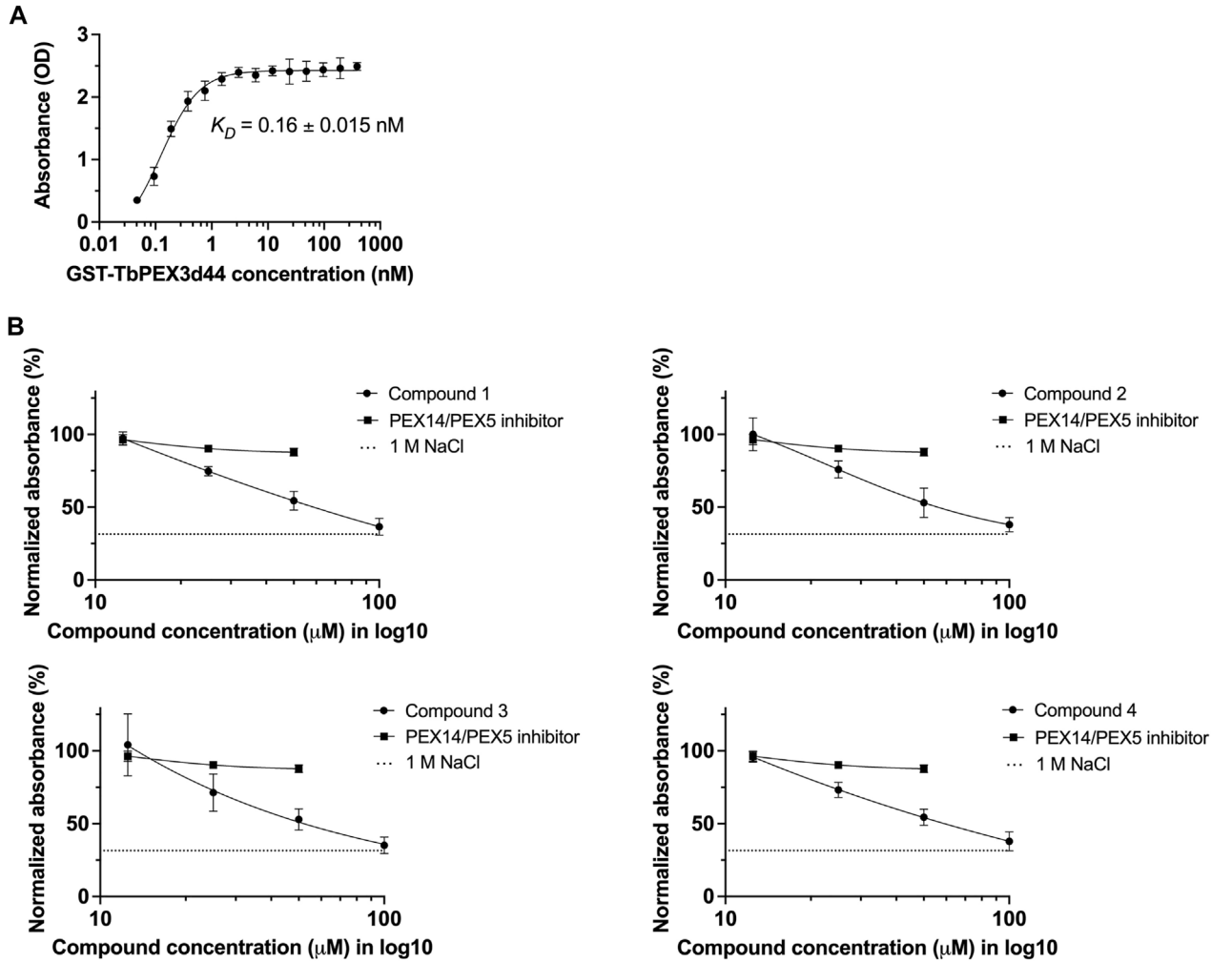

FIGURE 3 | Validation of TbPEX3–TbPEX19 interaction inhibition using ELISA assays. **(A)** 1 μg of PEX19-His was coated to the wells of ELISA plate, blocked with BSA followed by incubation with different concentrations of GST-TbPEX3d44. Unbound PEX3 was removed, and bound PEX3 was detected using anti-GST primary antibody, horseradish peroxidase (HRP)–coupled secondary antibody, TMB as colorimetric substrate, and detection of absorbance at 450 nm. The binding curve of GST-TbPEX3d44 and TbPEX19FL-His was fitted using a simple 1 to 1 binding model and an apparent K_D value of 0.16 ± 0.015 nM was estimated (n = 2). **(B)** Dose-dependent inhibition of PEX3–PEX19 interaction by all four selected compounds was confirmed with ELISA assays. A TbPEX14–TbPEX5 inhibitor was used as a negative control. Incubation with 1 M NaCl abolished the interaction.

TbPEX19-His, and GST-His alone. The level of confidence of binding is generally indicated by signal intensities in the STD difference spectra (**Figure 4**, red). In both analyses, compounds **1**, **2**, and **4** showed significant STD effects upon binding to TbPEX3 (**Figure 4** and **Supplementary Figure S5A**, **GST-TbPEX3/left panels**) and not to GST-His, indicating that they directly bound to TbPEX3d44. In addition, compounds **5** and **6** also showed consistent STD effects for binding to TbPEX3 (**Supplementary Figure S5B**). In the initial NMR experiments, compound **3** showed notable STD signal with TbPEX19 and line-broadening with GST-TbPEX3d44 (**Supplementary Figure S5A**, row **3**). In the NMR analysis with optimized relaxation filter, compound **3** experienced line-broadening effect with GST-TbPEX3d44 and, to a much less extent, with GST-His (**Figure 4**, **TbPEX3/left panel**; **GST-His/right panel**). The higher level of line-broadening seen with compound **3** with GST-TbPEX3d44 may be explained by binding of compound **3** to both GST and TbPEX3d44.

Anti-trypanosomal Activity and Cytotoxicity Analysis

We tested the activity of the PEX3–PEX19 inhibitors against cultured BSF *T. brucei* parasites. Parasites were treated with increasing concentrations of the compounds, and cell viability was estimated using resazurin-based assay after 3 days of incubation (**Figure 5**). The potent inhibitor suramin was used as a positive control, resulting in a half-maximal effective concentration of 37 nM (concentration leading to 50% reduction in cell survival,

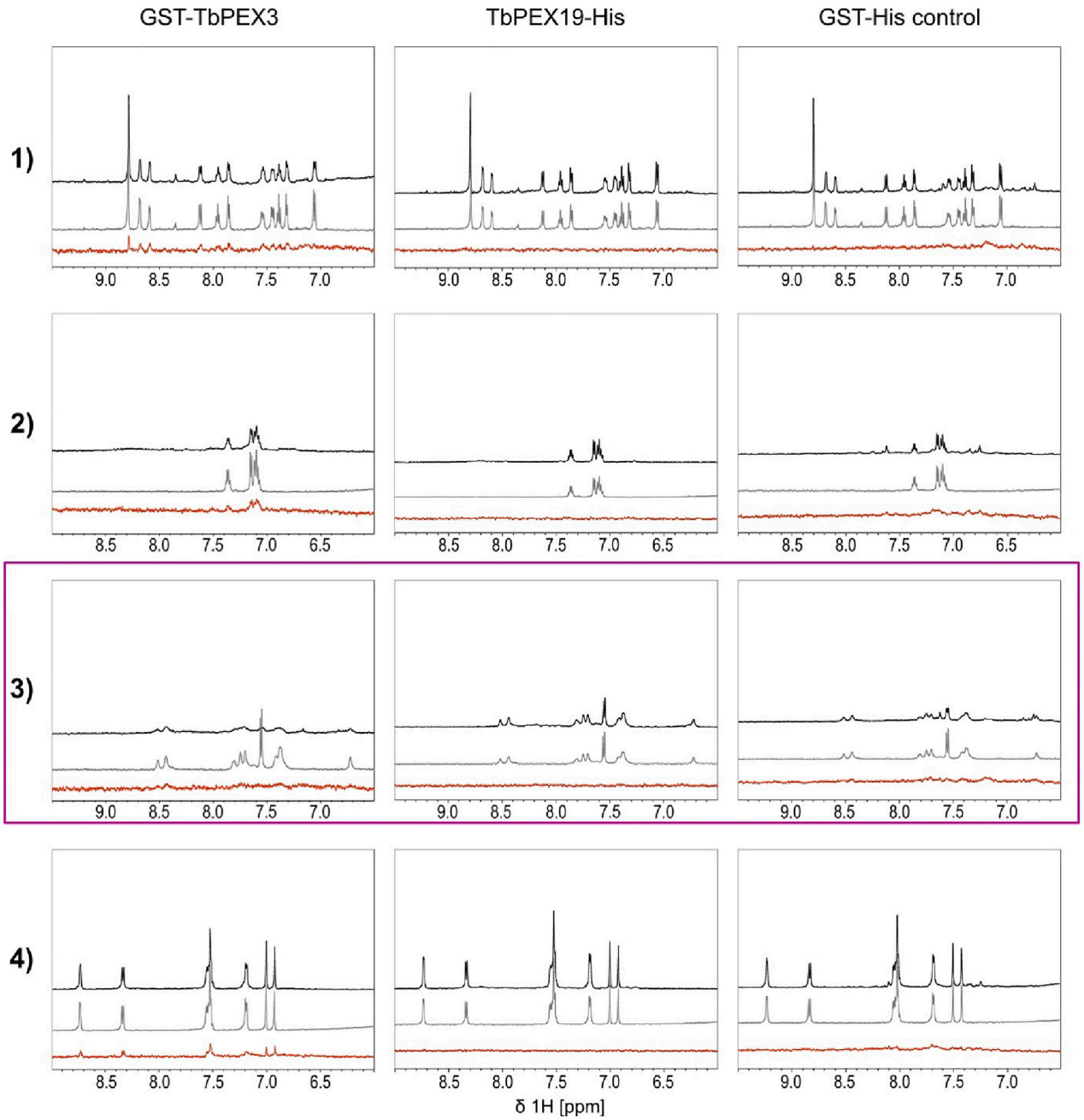

FIGURE 4 | Saturation transfer difference (STD) NMR experiments**.** STD experiments were carried out with the compounds **1** to **4** and the targets GST-TbPEX3 **(left panels)**, TbPEX19-His **(middle panels)**, and as a GST-His control **(right panels)**. 1D spectra of compound in the presence and absence of protein are shown on black and gray, respectively. STD difference spectra of the compound in the presence of protein are shown in red. Compounds **1**, **2**, and **4** show strong STD signal with GST-TbPEX3 but not with TbPEX19 or GST representing good binding toward TbPEX3. Compound **3** shows strong line-broadening with GST-TbPEX3, and weak line-broadening when measured with the GST-His control.

EC50). The identified compounds **2** (navy blue) and **1** (green, which exhibited one of the lowest IC50 values in the AlphaScreen assays) showed EC50 values of 27 and 33 μM, respectively. Compound **3** (purple) showed an EC50 of 38 μM, and compound **4** (red) exhibited an EC50 of 71 μM.

The compounds were also tested against human cells using a similar assay to estimate cytotoxicity of the compounds. HepG2 cells were treated with the four selected compounds with serial dilutions of up to 200 μM. No dose-dependent response curve could be fitted with cells incubated with compound **1**, **2**, and **4** but

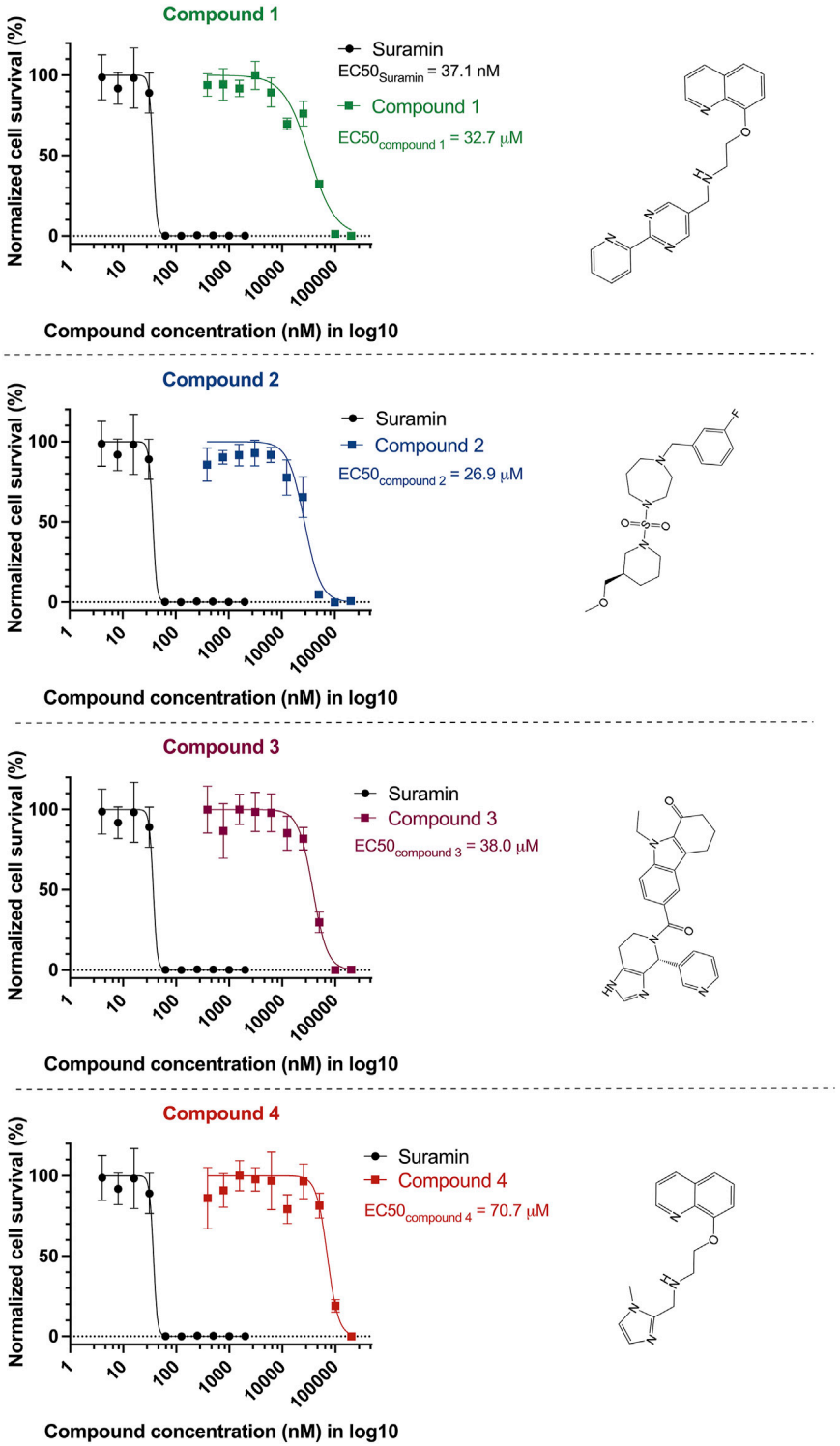

FIGURE 5 | Anti-trypanosomal activity of the inhibitors. Bloodstream form of wild-type *T. brucei* parasites (BSF427) was treated with serial dilutions of PEX3–PEX19 inhibitors or suramin as a positive control. After 3 days of incubation, cell viability was estimated using resazurin-based assay. Cell survival levels for all compound-treated conditions were normalized and shown in percentage plotted against compound concentration in Log_{10} scale, EC50 of suramin is 37 nM (black curve). Survival percentage for other compounds is drawn in curves of corresponding colors; the EC50 values of the four compounds are as follows: 33 μM (compound **1**, green), 27 μM (compound **2**, navy blue), 38 μM (compound **3**, purple), and 71 μM (compound **4**, orange). The corresponding structure of the compounds is shown on the right.

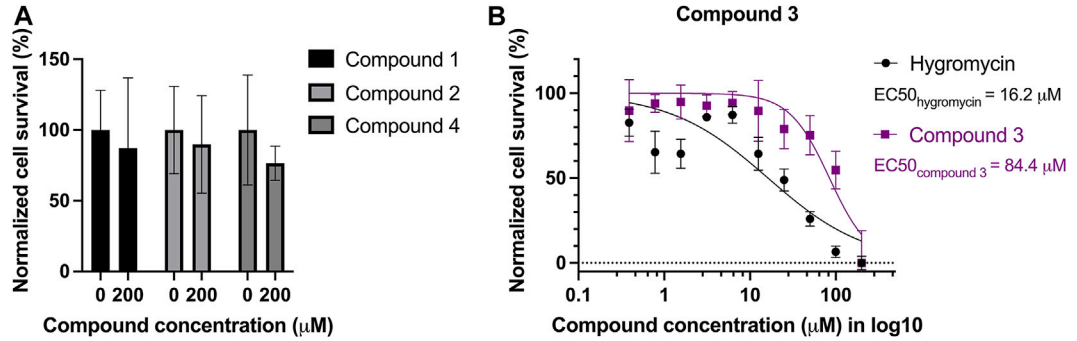

FIGURE 6 | Cytotoxicity test of the four compounds on HepG2 cells. Mammalian cell line HepG2 was treated with serial dilutions of the four compounds: **(A)** compound **1**, **2**, and **4** led to minor reduction of the survival rate, ranging from 75% to 90% at 200 μM, in comparison to the survival rate without treatment. **(B)** Compound **3** is toxic to HepG2 with an EC50 of 84.4 μM. Hygromycin was used as a control for an active drug, and it has an EC50 of 16.2 μM.

treated cells showed 75%–90% of survival at 200 μM (**Figure 6A**), whereas compound **3** seems to be toxic to the cells at high concentrations, with an EC50 of 84.4 μM. Hygromycin served as an active drug control (**Figure 6B**).

Trypanosomal On-Target Activity of the Compounds

We performed immunofluorescence microscopy analysis to evaluate the effects of PEX3–PEX19 inhibitors on glycosomes. Cells were treated with the compounds or with DMSO alone as control. Treated cells were fixed, permeabilized, and immunolabeled using antibodies against glycosomal marker enzyme aldolase. Fluorescence microscopy revealed different levels of mislocalization of the glycosomal matrix marker enzyme aldolase when comparing to the DMSO-treated cells (**Figure 7A**). Cells marked with white boxes are zoomed in for better illustration (**Figure 7C**). In DMSO-treated sample, aldolase labeling indicates a typical punctate pattern in vast majority of the cells. In contrast, the compound-treated cells exhibited a diffuse cytosolic staining of aldolase. In particular, compound 1 caused the well-recognized diffused pattern of aldolase labeling (**Figure 7A**). Compound **2** caused large numbers of cells that showed an aberrant morphology, and cells with normal shape exhibited mislocalization of aldolase to the cytosol. Compound **3**–treated cells mostly retained their cell morphology, and partial mislocalization of aldolase to the cytosol is observed. Compound **4** caused patches of stained aldolase, suggesting clustering of the glycosomes. The slight difference in the compound-treated phenotypes could be due to the low solubility and hydrophobicity of the compounds, which lead to a distinctive diffusion of the compounds after being taken up by the cells and, hence, a localized or varied level of exposure to the glycosomes. For statistical analysis, numbers of cells analyzed for each compound treated condition are shown in **Figure 7B**. Although the DMSO control showed no mislocalization, about 23% (compound 1), 21% (compound 2), 27% (compound 3), and 14% (compound 4) of cells treated with corresponding compounds were showing a diffuse labeling pattern of aldolase, indicative of mislocalization of glycosomal enzyme to the cytosol.

Moreover, when treating PEX11-GFP–expressing BSF cells with compound 2 (**Supplementary Figure S4**), it was observed in some cells that not only matrix proteins but also PEX11 were partly mislocalized to cytosol, whereas PEX11 was partly still glycosomal. When cells were treated with compound **3** (**Supplementary Figure S4**), mislocalization of both PEX11 and matrix proteins (aldolase and hexokinase) was even more pronounced with no obvious glycosomal localization of PEX11.

Digitonin fractionation experiments (**Figure 8**) were performed as an independent method to investigate the mislocalization of the glycosomal matrix proteins. Compound **2**– and compound **3**–treated BSF cells were harvested and solubilized at different concentrations of digitonin varied from 0.025× to 2× (digitonin/protein, v/v). When compound-treated cells were incubated with the lowest concentration of digitonin (0.025 μg of digitonin/μg of total protein), higher level of hexokinase (HK) and glycosomal GAPDH were released into the supernatant fractions in comparison to the corresponding DMSO control. HK behaved similarly to the cytosolic marker enolase, indicating that the treatment with compounds **2** and **3** results in mislocalization of the matrix protein into cytosol.

DISCUSSION

Existing trypanocidal drugs have been extensively studied but novel compounds with potential in treating these infections are urgently required. Inhibition of glycosomal compartmentation affects several essential metabolic pathways and thus provides an attractive drug target. We previously developed small-molecule inhibitors of PEX14–PEX5 PPI that block glycosomal matrix protein import and kill *T. brucei* parasites (Dawidowski et al., 2017, 2020). These inhibitors also showed therapeutic efficacy upon oral delivery in animal models of infection (Dawidowski et al., 2017). Recently, we and others identified *Trypanosoma* PEX3, a long-sought docking factor for the membrane protein import receptor PEX19 (Banerjee et al., 2019; Kalel et al., 2019). This discovery enabled the exploration of a therapeutic approach targeting the PEX3–PEX19 interaction as a candidate for drug

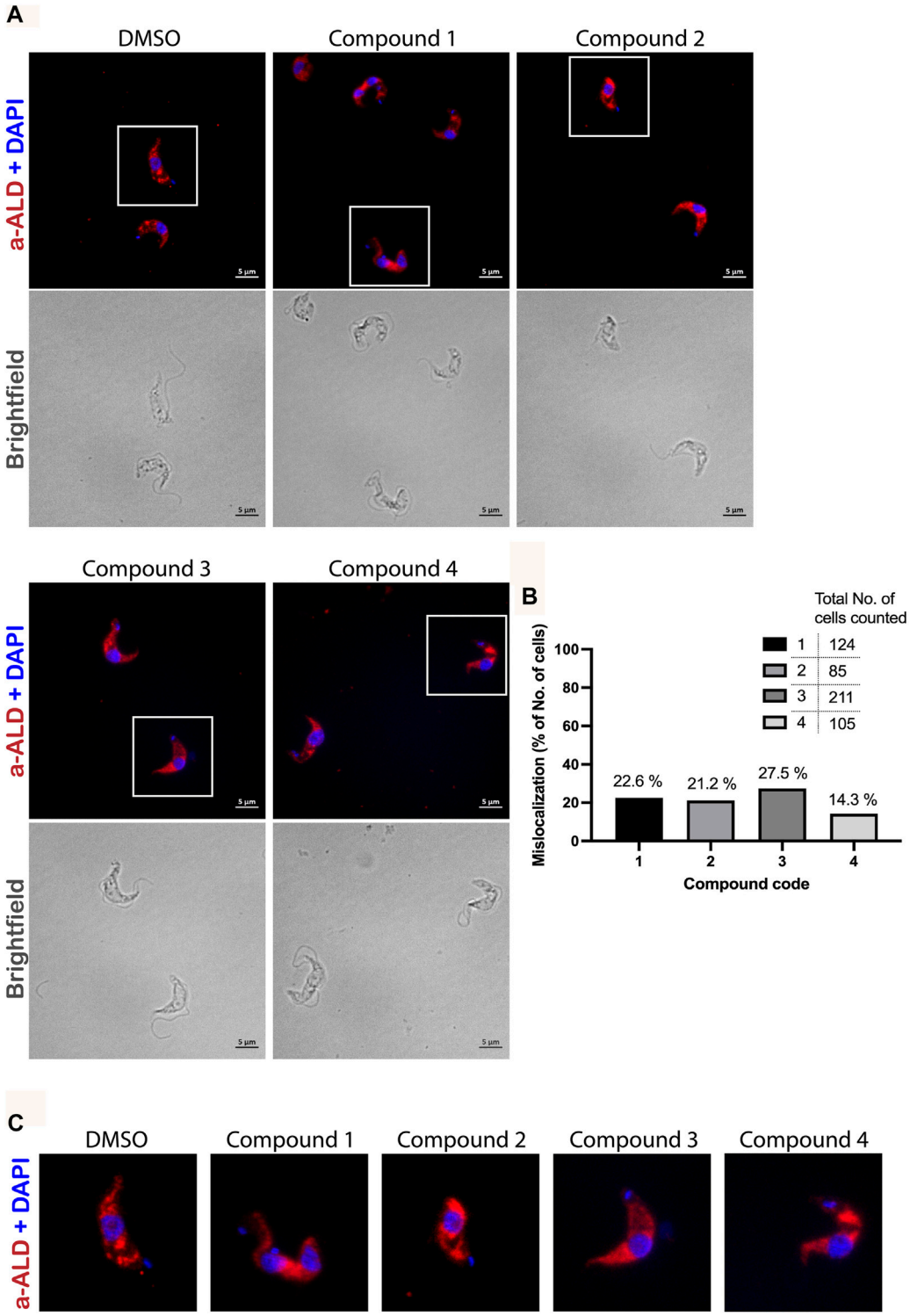

FIGURE 7 | Immunofluorescence microscopy analysis of the effect of PEX3–PEX19 inhibitors on glycosomes. **(A)** Wild-type *T. brucei* bloodstream form parasites were treated with DMSO or inhibitors for 24 h. Compound-treated cultures with 50% of the growth rate compared to the DMSO control were fixed followed by staining with anti-TbAldolase primary antibody and Alexa Fluor 594–labeled secondary antibody. (a-ALD, red; DAPI-labeled nucleus and kinetoplast, blue). Corresponding bright-field images are shown in the lower panels. A punctate pattern indicated the localization of aldolase in glycosomes (DMSO). Different levels of mislocalization of aldolase to the cytosol were noticed in each of the compound-treated samples. **(B)** Numbers of cells showing aldolase mislocalization were counted. About 20%–30% of cells treated with compounds **1**, **2**, and **3** and 15% of compound **4** treated cells showed aldolase mislocalized to the cytosol. **(C)** Images of individual cells, which are marked by white boxes in **(A)**, were 2X magnified for better illustration.

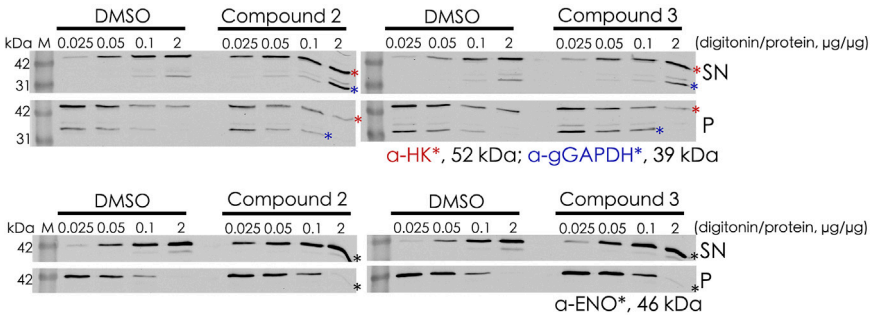

FIGURE 8 | Digitonin fractionation of compound 2– and compound 3–treated BSF cells. Digitonin-solubilized fractions are indicated as supernatant (SN), and the non-solubilized fractions are indicated as pellet (P). Four concentrations of digitonin treatment were used to investigate the mislocalization of matrix proteins, and hexokinase (HK) and glyceraldehyde 3-phosphate dehydrogenase (gGAPDH) are labeled with red and blue asterisks, respectively **(upper panel)**. Enolase (ENO) as the cytosolic marker is indicated by a black asterik **(lower panel)**. At the lowest level of digitonin treatment (0.025 μg of digitonin/μg of total protein), HK and gGAPDH were released from compound-treated cells to a greater extent than from the corresponding DMSO control cells, indicating mislocalization of these proteins to the cytosol upon treatment.

target to identify small molecules that disrupt glycosome biogenesis and kill parasites.

In this study, we report on a high-throughput, 384 well-plate compatible, AlphaScreen-based screening method to identify inhibitors of the TbPEX3–PEX19 interaction. For discovering PPI modulators, use of chemically diverse compound libraries are preferable to maximize the chances of matching the PPI target (Lu et al., 2020). We screened 4,480 compounds (**Supplementary File S1**) from the ChemBridge Diversity library, which led to the identification of six initial hits after applying statistical quality control and hit selection criteria. Interference of the compounds with assay reagents or readout can lead to false positives, and these can be distinguished using counter-screening (Schorpp et al., 2014). Our counter-screen using GST-His identified four compounds that displayed higher specificity targeting the TbPEX3–TbPEX19 interaction. Independent ELISA-based biochemical assays further validated that the shortlisted compounds specifically blocked TbPEX3–PEX19 interaction *in vitro*.

Cellular assays showed that all four compounds exhibit trypanocidal activity against BSF *Trypanosoma* parasites. Compound **2** showed the highest trypanocidal activity with EC50 of 27 μM (concentration leading to 50% cell death). The compounds identified in this study represent chemical starting points like the first TbPEX14–PEX5 inhibitor compound **1** with EC50 of 21 μM (Dawidowski et al., 2017). As the specific target and structure were known, this PEX14–PEX5 inhibitor was successfully optimized to potent trypanocidal compounds with nanomolar EC50, using a structure-guided approach. Similar optimization of the PEX3–PEX19 inhibitors could enhance their trypanocidal efficacy in future.

The compounds showed no apparent toxicity to human cells, except compound **3**, which showed cytotoxicity with EC50 of 84 μM. However, patient-derived PEX3 defective human fibroblast cells (Ghaedi et al., 2000; Muntau et al., 2000) are viable in cell culture. This suggests that cytotoxicity of compound **3** could be non-specific and not PEX3–PEX19 related.

We also performed hit validation and target confirmation using NMR. The STD effects observed for compounds **1**, **2**, and **4** with TbPEX3 or TbPEX19 are in good agreement with the trypanocidal activity and the performance of the compounds in inhibiting the PEX19-PEX3 interaction. It is less conclusive to which proteins compound **3** binds; based on the second NMR analysis with optimized settings, it is possible that the compound binds to TbPEX3 and to a less extent to GST. Although compounds **5** and **6** did not inhibit TbPEX3–PEX19 interaction, they show STD effect with TbPEX3. It is possible that compounds **5** and **6** bind to TbPEX3 distant from the binding interface with TbPEX19 and that this has no significant effect on the interaction between these proteins. Activities of the compounds in various assays in this study are summarized in **Table 2**.

Finally, immunofluorescence analysis and digitonin fractionation showed that these compounds disrupt glycosome

TABLE 2 | Comparison of drug properties from *in vitro* and *in vivo* analyses.

Compound	TbPEX3-19 affinity (IC50, μM)	*T. brucei* toxicity (EC50, μM)	Target protein (NMR analysis)	Human cell cytotoxicity (EC50, μM)
1	1.0	33	TbPEX3	>> 200
2	37.5	27	TbPEX3	>> 200
3	14.3	38	TbPEX19	84
4	0.5	71	TbPEX3	>> 200

biogenesis, leading to mislocalization of glycosomal enzyme and parasite death. Inhibition of the PEX3–PEX19 interaction would disrupt import of PMPs, including those involved in matrix protein import. Even partial mislocalization of glycosomal enzymes is toxic for trypanosomes, and thus, parasites would be killed before mislocalization of PMPs is evident. Clustering of glycosomes was also seen in some cells, which could be due to imbalance of membrane protein targeting. Clustering of glycosomes was also seen in trypanosomes overexpressing GFP-tagged TbPEX16, but it is also frequently seen in normal cells (Kalel et al., 2015; Hughes et al., 2017). Considering the cytotoxicity of compound **3** and the NMR analysis suggesting a potential GST binding, this compound could be less specific in comparison to compound **2**. To this extent, compound **2** is in higher priority for future structural-based optimization. Structural studies have shown that PEX3 provides the binding surface/pocket for the binding of the N-terminal helix in PEX19 (Sato et al., 2010; Schmidt et al., 2010). Therefore, it is more likely that the inhibitors of the PEX3–PEX19 interaction identified in this study bind to PEX3, block the binding pocket, and thereby prevent docking of PEX19.

The physicochemical properties of the four compounds are in consistence with Lipinski's rule of 5 (**Supplementary Figure S6**). These parameters describe the permeability and solubility of the compounds and suggest that these compounds exhibit promising drug-like properties. The quinoline and triazolopyrimidine scaffolds have been reported as drug-like in the *in vitro* assays and a wide range of *in vivo* anti-microbial activities. To be specific, three chloroquinoline derivatives, which were previously evaluated as anti-malarial compounds have been identified as sub-micromolar inhibitors of intracellular *T. cruzi* (Magdaleno et al., 2009; Fonseca-Berzal et al., 2014). It has also been reported that triazolopyrimidine derivatives lead to nanomolar range of EC50 in *T. brucei* and *T. cruzi*, and three triazolopyrimidines are showing better suppression of the disease in *T. cruzi* mouse infection model than the front-line drug benznidazole (Nagendar et al., 2019).

Our study demonstrates that PEX3–PEX19 interaction is a druggable target in *Trypanosoma* and provides a high-throughput compatible screening platform for further screening of the inhibitors of this PPI. Structural investigations such as co-crystallization of the protein-compound complex would certainly aid in the future structural-guided optimization of these compounds to develop new therapies against trypanosomiasis and leishmaniasis.

DATA AVAILABILITY STATEMENT

The original contributions presented in the study are included in the article/**Supplementary Material**, further inquiries can be directed to the corresponding authors.

AUTHOR CONTRIBUTIONS

ML, VK, and RE conceived and planned the experiments. ML, SG, and BT carried out the experiments. JO handled the super-resolution fluorescence microscope. ML and VK wrote the manuscript with support from WS, RE, MS, and GP. VK and RE supervised the project.

FUNDING

This work was supported by DFG grant FOR1905 to RE. and MS. SR-SIM microscopy was funded by the German Research Foundation and the State Government of North Rhine-Westphalia (INST 213/840-1 FUGG).

ACKNOWLEDGMENTS

We acknowledge support by the Open Access Publication Funds of the Ruhr-Universität Bochum.

SUPPLEMENTARY MATERIAL

The Supplementary Material for this article can be found online at: https://www.frontiersin.org/articles/10.3389/fcell.2021.737159/full#supplementary-material

REFERENCES

Alsford, S., Eckert, S., Baker, N., Glover, L., Sanchez-Flores, A., Leung, K. F., et al. (2012). High-throughput Decoding of Antitrypanosomal Drug Efficacy and Resistance. *Nature* 482, 232–236. doi:10.1038/nature10771

Babokhov, P., Sanyaolu, A. O., Oyibo, W. A., Fagbenro-Beyioku, A. F., and Iriemenam, N. C. (2013). A Current Analysis of Chemotherapy Strategies for the Treatment of Human African Trypanosomiasis. *Pathog. Glob. Health* 107, 242–252. doi:10.1179/2047773213y.0000000105

Bakker, B. M., Michels, P. A. M., Opperdoes, F. R., and Westerhoff, H. V. (1999). What Controls Glycolysis in Bloodstream Form Trypanosoma Brucei? *J. Biol. Chem.* 274, 14551–14559. doi:10.1074/jbc.274.21.14551

Bakshi, R. P., and Shapiro, T. A. (2004). RNA Interference of Trypanosoma Brucei Topoisomerase IB: Both Subunits Are Essential. *Mol. Biochem. Parasitol.* 136, 249–255. doi:10.1016/j.molbiopara.2004.04.006

Balogun, E. O., Inaoka, D. K., Shiba, T., Tsuge, C., May, B., Sato, T., et al. (2019). Discovery of Trypanocidal Coumarins with Dual Inhibition of Both the Glycerol Kinase and Alternative Oxidase of Trypanosoma Brucei Brucei. *FASEB j.* 33, 13002–13013. doi:10.1096/fj.201901342r

Banerjee, S. K., Kessler, P. S., Saveria, T., and Parsons, M. (2005). Identification of Trypanosomatid PEX19: Functional Characterization Reveals Impact on Cell Growth and Glycosome Size and Number. *Mol. Biochem. Parasitol.* 142, 47–55. doi:10.1016/j.molbiopara.2005.03.008

Banerjee, H., Knoblach, B., and Rachubinski, R. A. (2019). The Early-Acting Glycosome Biogenic Protein Pex3 Is Essential for Trypanosome Viability. *Life Sci. Alliance* 2, 1–9. doi:10.26508/lsa.201900421

Begolo, D., Vincent, I. M., Giordani, F., Pöhner, I., Witty, M. J., Rowan, T. G., et al. (2018). The Trypanocidal Benzoxaborole AN7973 Inhibits Trypanosome mRNA Processing. *PLoS Pathog.* 14, e1007315. doi:10.1371/journal.ppat.1007315

Birmingham, A., Selfors, L. M., Forster, T., Wrobel, D., Kennedy, C. J., Shanks, E., et al. (2009). Statistical Methods for Analysis of High-Throughput RNA Interference Screens. *Nat. Methods* 6, 569–575. doi:10.1038/nmeth.1351

Büscher, P., Cecchi, G., Jamonneau, V., and Priotto, G. (2017). Human African Trypanosomiasis. *Lancet* 390, 2397–2409. doi:10.1016/s0140-6736(17)31510-6

Chan, C., Yin, H., Garforth, J., McKie, J. H., Jaouhari, R., Speers, P., et al. (1998). Phenothiazine Inhibitors of Trypanothione Reductase as Potential Antitrypanosomal and Antileishmanial Drugs. *J. Med. Chem.* 41, 148–156. doi:10.1021/jm960814j

Chung, N., Zhang, X. D., Kreamer, A., Locco, L., Kuan, P.-F., Bartz, S., et al. (2008). Median Absolute Deviation to Improve Hit Selection for Genome-Scale RNAi Screens. *J. Biomol. Screen.* 13, 149–158. doi:10.1177/1087057107312035

Dawidowski, M., Emmanouilidis, L., Kalel, V. C., Tripsianes, K., Schorpp, K., Hadian, K., et al. (2017). Inhibitors of PEX14 Disrupt Protein Import into Glycosomes and Kill Trypanosoma Parasites. *Science* 355, 1416–1420. doi:10.1126/science.aal1807

Dawidowski, M., Kalel, V. C., Napolitano, V., Fino, R., Schorpp, K., Emmanouilidis, L., et al. (2020). Structure-Activity Relationship in Pyrazolo[4,3-C]pyridines, First Inhibitors of PEX14-PEX5 Protein-Protein Interaction with Trypanocidal Activity. *J. Med. Chem.* 63, 847–879. doi:10.1021/acs.jmedchem.9b01876

Dickie, E. A., Giordani, F., Gould, M. K., Mäser, P., Burri, C., Mottram, J. C., et al. (2020). New Drugs for Human African Trypanosomiasis: A Twenty First Century Success Story. *TropicalMed* 5, 29. doi:10.3390/tropicalmed5010029

El Kouni, M. H. (2003). Potential Chemotherapeutic Targets in the Purine Metabolism of Parasites. *Pharmacol. Ther.* 99, 283–309. doi:10.1016/s0163-7258(03)00071-8

Fang, Y., Morrell, J. C., Jones, J. M., and Gould, S. J. (2004). PEX3 Functions as a PEX19 Docking Factor in the Import of Class I Peroxisomal Membrane Proteins. *J. Cel Biol.* 164, 863–875. doi:10.1083/jcb.200311131

Farré, J.-C., Carolino, K., Stasyk, O. V., Stasyk, O. G., Hodzic, Z., Agrawal, G., et al. (2017). A New Yeast Peroxin, Pex36, a Functional Homolog of Mammalian PEX16, Functions in the ER-To-Peroxisome Traffic of Peroxisomal Membrane Proteins. *J. Mol. Biol.* 429, 3743–3762. doi:10.1016/j.jmb.2017.10.009

Fonseca-Berzal, C., Rojas Ruiz, F. A., Escario, J. A., Kouznetsov, V. V., and Gómez-Barrio, A. (2014). *In Vitro* phenotypic Screening of 7-Chloro-4-Amino(oxy) quinoline Derivatives as Putative Anti- Trypanosoma Cruzi Agents. *Bioorg. Med. Chem. Lett.* 24, 1209–1213. doi:10.1016/j.bmcl.2013.12.071

Furuya, T., Kessler, P., Jardim, A., Schnaufer, A., Crudder, C., and Parsons, M. (2002). Glucose Is Toxic to Glycosome-Deficient Trypanosomes. *Proc. Natl. Acad. Sci.* 99, 14177–14182. doi:10.1073/pnas.222454899

Ghaedi, K., Honsho, M., Shimozawa, N., Suzuki, Y., Kondo, N., and Fujiki, Y. (2000). PEX3 Is the Causal Gene Responsible for Peroxisome Membrane Assembly-Defective Zellweger Syndrome of Complementation Group G. *Am. J. Hum. Genet.* 67, 976–981. doi:10.1086/303086

Giannopoulou, E.-A., Emmanouilidis, L., Sattler, M., Dodt, G., and Wilmanns, M. (2016). Towards the Molecular Mechanism of the Integration of Peroxisomal Membrane Proteins. *Biochim. Biophys. Acta (Bba) - Mol. Cel Res.* 1863, 863–869. doi:10.1016/j.bbamcr.2015.09.031

Haanstra, J. R., González-Marcano, E. B., Gualdrón-López, M., and Michels, P. A. M. (2016). Biogenesis, Maintenance and Dynamics of Glycosomes in Trypanosomatid Parasites. *Biochim. Biophys. Acta (Bba) - Mol. Cel Res.* 1863, 1038–1048. doi:10.1016/j.bbamcr.2015.09.015

Honsho, M., Hiroshige, T., and Fujiki, Y. (2002). The Membrane Biogenesis Peroxin Pex16p. *J. Biol. Chem.* 277, 44513–44524. doi:10.1074/jbc.m206139200

Hughes, L., Borrett, S., Towers, K., Starborg, T., and Vaughan, S. (2017). Patterns of Organelle Ontogeny through a Cell Cycle Revealed by Whole-Cell Reconstructions Using 3D Electron Microscopy. *J. Cel Sci.* 130, 637–647. doi:10.1242/jcs.198887

Ihrig, V., and Obermann, W. M. J. (2017). Identifying Inhibitors of the Hsp90-Aha1 Protein Complex, a Potential Target to Drug Cystic Fibrosis, by Alpha Technology. *SLAS DISCOVERY: Adv. Sci. Drug Discov.* 22, 923–928. doi:10.1177/2472555216688312

Jones, J. M., Morrell, J. C., and Gould, S. J. (2004). PEX19 Is a Predominantly Cytosolic Chaperone and Import Receptor for Class 1 Peroxisomal Membrane Proteins. *J. Cel Biol.* 164, 57–67. doi:10.1083/jcb.200304111

Kalel, V. C., Schliebs, W., and Erdmann, R. (2015). Identification and Functional Characterization of Trypanosoma Brucei Peroxin 16. *Biochim. Biophys. Acta (Bba) - Mol. Cel Res.* 1853, 2326–2337. doi:10.1016/j.bbamcr.2015.05.024

Kalel, V. C., Li, M., Gaussmann, S., Delhommel, F., Schäfer, A.-B., Tippler, B., et al. (2019). Evolutionary Divergent PEX3 Is Essential for Glycosome Biogenesis and Survival of Trypanosomatid Parasites. *Biochim. Biophys. Acta (Bba) - Mol. Cel Res.* 1866, 118520. doi:10.1016/j.bbamcr.2019.07.015

Kennedy, P. G. E. (2019). Update on Human African Trypanosomiasis (Sleeping Sickness). *J. Neurol.* 266, 2334–2337. doi:10.1007/s00415-019-09425-7

Khan, M. O. F., Austin, S. E., Chan, C., Yin, H., Marks, D., Vaghjiani, S. N., et al. (2000). Use of an Additional Hydrophobic Binding Site, the Z Site, in the Rational Drug Design of a New Class of Stronger Trypanothione Reductase Inhibitor, Quaternary Alkylammonium Phenothiazines§. *J. Med. Chem.* 43, 3148–3156. doi:10.1021/jm000156+

Lu, H., Zhou, Q., He, J., Jiang, Z., Peng, C., Tong, R., et al. (2020). Recent Advances in the Development of Protein-Protein Interactions Modulators: Mechanisms and Clinical Trials. *Signal. Transduct. Target. Ther.* 5, 213. doi:10.1038/s41392-020-00315-3

Magdaleno, A., Ahn, I. Y., Paes, L. S., and Silber, A. M. (2009). Actions of a Proline Analogue, L-Thiazolidine-4-Carboxylic Acid (T4C), on Trypanosoma Cruzi. *PLoS One* 4, e4534. doi:10.1371/journal.pone.0004534

Malo, N., Hanley, J. A., Cerquozzi, S., Pelletier, J., and Nadon, R. (2006). Statistical Practice in High-Throughput Screening Data Analysis. *Nat. Biotechnol.* 24, 167–175. doi:10.1038/nbt1186

Mayer, M., and Meyer, B. (1999). Characterization of Ligand Binding by Saturation Transfer Difference NMR Spectroscopy. *Angew. Chem. Int. Ed.* 38, 1784–1788. doi:10.1002/(sici)1521-3773(19990614)38:12<1784:aid-anie1784>3.0.co;2-q

McNae, I. W., Kinkead, J., Malik, D., Yen, L. H., Walker, M. K., Swain, C., et al. (2021). Fast Acting Allosteric Phosphofructokinase Inhibitors Block Trypanosome Glycolysis and Cure Acute African Trypanosomiasis in Mice. *Nat. Commun.* 12, 1052. doi:10.1038/s41467-021-21273-6

Mullard, A. (2021). FDA Approves First All-Oral Sleeping Sickness Drug. *Nat. Rev. Drug Discov.* 20, 652. doi:10.1038/d41573-021-00140-5

Muntau, A. C., Mayerhofer, P. U., Paton, B. C., Kammerer, S., and Roscher, A. A. (2000). Defective Peroxisome Membrane Synthesis Due to Mutations in Human PEX3 Causes Zellweger Syndrome, Complementation Group G. *Am. J. Hum. Genet.* 67, 967–975. doi:10.1086/303071

Nagendar, P., Gillespie, J. R., Herbst, Z. M., Ranade, R. M., Molasky, N. M. R., Faghih, O., et al. (2019). Triazolopyrimidines and Imidazopyridines: Structure-Activity Relationships and *In Vivo* Efficacy for Trypanosomiasis. *ACS Med. Chem. Lett.* 10, 105–110. doi:10.1021/acsmedchemlett.8b00498

Opperdoes, F. R., and Borst, P. (1977). Localization of Nine Glycolytic Enzymes in a Microbody-like Organelle in Trypanosoma Brucei : The Glycosome. *FEBS Lett.* 80, 360–364. doi:10.1016/0014-5793(77)80476-6

Pépin, J., and Milord, F. (1994). The Treatment of Human African Trypanosomiasis. *Adv. Parasitol.* 33, 1–47. doi:10.1016/s0065-308x(08)60410-8

Persch, E., Bryson, S., Todoroff, N. K., Eberle, C., Thelemann, J., Dirdjaja, N., et al. (2014). Binding to Large Enzyme Pockets: Small-Molecule Inhibitors of Trypanothione Reductase. *ChemMedChem* 9, 1880–1891. doi:10.1002/cmdc.201402032

Richards, S., Morrison, L. J., Torr, S. J., Barrett, M. P., Manangwa, O., Mramba, F., et al. (2021). Pharma to Farmer: Field Challenges of Optimizing Trypanocide Use in African Animal Trypanosomiasis. *Trends Parasitol.* xx, 1–13. doi:10.1016/j.pt.2021.04.007

Sato, Y., Shibata, H., Nakatsu, T., Nakano, H., Kashiwayama, Y., Imanaka, T., et al. (2010). Structural Basis for Docking of Peroxisomal Membrane Protein Carrier Pex19p onto its Receptor Pex3p. *EMBO J.* 29, 4083–4093. doi:10.1038/emboj.2010.293

Schmidt, F., Treiber, N., Zocher, G., Bjelic, S., Steinmetz, M. O., Kalbacher, H., et al. (2010). Insights into Peroxisome Function from the Structure of PEX3 in Complex with a Soluble Fragment of PEX19. *J. Biol. Chem.* 285, 25410–25417. doi:10.1074/jbc.m110.138503

Schorpp, K., Rothenaigner, I., Salmina, E., Reinshagen, J., Low, T., Brenke, J. K., et al. (2014). Identification of Small-Molecule Frequent Hitters from Alphascreen High-Throughput Screens. *J. Biomol. Screen.* 19, 715–726. doi:10.1177/1087057113516861

Shereni, W., Neves, L., Argilés, R., Nyakupinda, L., and Cecchi, G. (2021). An Atlas of Tsetse and Animal African Trypanosomiasis in Zimbabwe. *Parasit Vectors* 14, 50–10. doi:10.1186/s13071-020-04555-8

Thomas, J. A., Baker, N., Hutchinson, S., Dominicus, C., Trenaman, A., Glover, L., et al. (2018). Insights into Antitrypanosomal Drug Mode-Of-Action from Cytology-Based Profiling. *Plos Negl. Trop. Dis.* 12, e0006980–19. doi:10.1371/journal.pntd.0006980

Wang, C. C. (1995). Molecular Mechanisms and Therapeutic Approaches to the Treatment of African Trypanosomiasis. *Annu. Rev. Pharmacol. Toxicol.* 35, 93–127. doi:10.1146/annurev.pa.35.040195.000521

Yasgar, A., Jadhav, A., Simeonov, A., and Coussens, N. P. (2016). AlphaScreen-Based Assays: Ultra-high-throughput Screening for Small-Molecule Inhibitors of Challenging Enzymes and Protein-Protein Interactions. *Methods Mol. Biol.* 1439, 77–98. doi:10.1007/978-1-4939-3673-1_5

Zhang, J.-H., Chung, T. D. Y., and Oldenburg, K. R. (1999). A Simple Statistical Parameter for Use in Evaluation and Validation of High Throughput Screening Assays. *J. Biomol. Screen.* 4, 67–73. doi:10.1177/108705719900400206

Conflict of Interest: The authors declare that the research was conducted in the absence of any commercial or financial relationships that could be construed as a potential conflict of interest.

Publisher's Note: All claims expressed in this article are solely those of the authors and do not necessarily represent those of their affiliated organizations or those of the publisher, the editors, and the reviewers. Any product that may be evaluated in this article, or claim that may be made by its manufacturer, is not guaranteed or endorsed by the publisher.

frontiers in Cell and Developmental Biology

ORIGINAL RESEARCH
published: 18 February 2022
doi: 10.3389/fcell.2022.838923

The Structure of the *Arabidopsis* PEX4-PEX22 Peroxin Complex—Insights Into Ubiquitination at the Peroxisomal Membrane

Melissa S. Traver[1†], *Sarah E. Bradford*[1†], *Jose Luis Olmos Jr*[1], *Zachary J. Wright*[1], *Mitchell D. Miller*[1], *Weijun Xu*[1], *George N. Phillips Jr*[1,2] *and Bonnie Bartel*[1*]

[1]*Department of Biosciences, Rice University, Houston, TX, United States,* [2]*Department of Chemistry, Rice University, Houston, TX, United States*

Peroxisomes are eukaryotic organelles that sequester critical oxidative reactions and process the resulting reactive oxygen species into less toxic byproducts. Peroxisome function and formation are coordinated by peroxins (PEX proteins) that guide peroxisome biogenesis and division and shuttle proteins into the lumen and membrane of the organelle. Despite the importance of peroxins in plant metabolism and development, no plant peroxin structures have been reported. Here we report the X-ray crystal structure of the PEX4-PEX22 peroxin complex from the reference plant *Arabidopsis thaliana*. PEX4 is a ubiquitin-conjugating enzyme (UBC) that ubiquitinates proteins associated with the peroxisomal membrane, and PEX22 is a peroxisomal membrane protein that anchors PEX4 to the peroxisome and facilitates PEX4 activity. We co-expressed *Arabidopsis* PEX4 as a translational fusion with the soluble PEX4-interacting domain of PEX22 in *E. coli*. The fusion was linked *via* a protease recognition site, allowing us to separate PEX4 and PEX22 following purification and solve the structure of the complex. We compared the structure of the PEX4-PEX22 complex to the previously published structures of yeast orthologs. *Arabidopsis* PEX4 displays the typical UBC structure expected from its sequence. Although *Arabidopsis* PEX22 lacks notable sequence identity to yeast PEX22, it maintains a similar Rossmann fold-like structure. Several salt bridges are positioned to contribute to the specificity of PEX22 for PEX4 versus other *Arabidopsis* UBCs, and the long unstructured PEX22 tether would allow PEX4-mediated ubiquitination of distant peroxisomal membrane targets without dissociation from PEX22. The *Arabidopsis* PEX4-PEX22 structure also revealed that the residue altered in *pex4-1* (P123L), a mutant previously isolated *via* a forward-genetic screen for peroxisomal dysfunction, is near the active site cysteine of PEX4. We demonstrated *in vitro* UBC activity for the PEX4-

OPEN ACCESS

Edited by:
Ralf Erdmann,
Ruhr University Bochum, Germany

Reviewed by:
Santosh Panjikar,
Australian Synchrotron, Australia
Shuh-ichi Nishikawa,
Niigata University, Japan
Sigrun Reumann,
University of Hamburg, Germany

***Correspondence:**
Bonnie Bartel
bartel@rice.edu

[†]*These authors contributed equally to this work*

Specialty section:
This article was submitted to Membrane Traffic, a section of the journal Frontiers in Cell and Developmental Biology

Received: *18 December 2021*
Accepted: *28 January 2022*
Published: *18 February 2022*

Citation:
Traver MS, Bradford SE, Olmos JL, Wright ZJ, Miller MD, Xu W, Phillips GN and Bartel B (2022) The Structure of the Arabidopsis PEX4-PEX22 Peroxin Complex—Insights Into Ubiquitination at the Peroxisomal Membrane. Front. Cell Dev. Biol. 10:838923. doi: 10.3389/fcell.2022.838923

Abbreviations: aa, amino acid residues; At, *Arabidopsis thaliana;* BSA, buried surface area; DTT, dithiothreitol; ER, endoplasmic reticulum; ICL, isocitrate lyase; LB, Luria broth; mito, mitochondrial; Oa, *Ogataea angusta;* PDB, Protein Data Bank; PEX, peroxin; PN, plant nutrient; PTS, peroxisome targeting signal; RING, really interesting new gene; RMSD, root-mean-square deviation; RT, room temperature; RWD, domain found in RING fingers, WD-domain-containing-proteins, and DEAD-like helicases; Sc, *Saccharomyces cerevisiae;* SCE, SUMO conjugating enzyme; TB, terrific broth; TCEP, Tris(2-carboxyethyl)phosphine hydrochloride; TMD, transmembrane domain; Ub, ubiquitin; UBC, ubiquitin conjugating enzyme; UEV, ubiquitin E2 variant; IPTG, β-D-1-thiogalactopyranoside.

PEX22 complex and found that the pex4-1 enzyme has reduced *in vitro* ubiquitin-conjugating activity and altered specificity compared to PEX4. Our findings illuminate the role of PEX4 and PEX22 in peroxisome structure and function and provide tools for future exploration of ubiquitination at the peroxisome surface.

Keywords: *Arabidopis thaliana*, peroxin, ubiquitin conjugating enzyme (E2), organelle tether, X-ray crystal analysis, peroxisome, ubiquitination

INTRODUCTION

Peroxisomes are membrane-bound organelles that are essential for life in almost all multicellular eukaryotes because they house critical metabolism, including the β-oxidation of fatty acids and the breakdown of hydrogen peroxide and other reactive oxygen species. In plants, peroxisomes are the sole site of fatty acid β-oxidation and also participate in photorespiration, biosynthesis of several phytohormones, co-factor biosynthesis, and diverse secondary metabolic pathways (reviewed in Reumann and Bartel, 2016).

Peroxisomes import fully-folded and even oligomeric proteins (McNew and Goodman, 1994; Lee et al., 1997) *via* the coordinated action of a group of peroxins (PEX proteins). This import is mediated by shuttling cargo receptors that accompany proteins containing a peroxisome-targeting signal (PTS) to the organelle. For example, PEX5 binds to cytosolic cargo proteins that have a C-terminal PTS1 and guides them to a docking complex at the peroxisomal membrane, where PEX5 inserts into the membrane to deliver the cargo into the organelle (reviewed in Kao et al., 2018). Returning PEX5 to the cytosol for additional rounds of import requires ubiquitination of a cysteine residue near the PEX5 N-terminus mediated by a complex of RING-type ubiquitin-protein ligases: PEX2, PEX10, and PEX12 (Kragt et al., 2005; Carvalho et al., 2007; Grou et al., 2008; Platta et al., 2009). In metazoans, these RING peroxins recruit a cytosolic ubiquitin-conjugating enzyme (UBC) (Grou et al., 2008). In contrast, yeast RING peroxins collaborate with a dedicated UBC, Pex4, or a cytosolic UBC, Ubc4, to ubiquitinate Pex5 for recycling or degradation, respectively (Kragt et al., 2005; Platta et al., 2007; Williams et al., 2008). Yeast Pex4 is anchored to the outside of the peroxisomal membrane by binding to Pex22 (Koller et al., 1999), a rapidly-evolving protein with an N-terminal transmembrane domain inserted in the peroxisomal membrane and a C-terminal cytosolic Pex4-binding domain. Pex22 is required for Pex4 function beyond its role as a membrane anchor (Williams et al., 2012; El Magraoui et al., 2014). For example, in the presence of Pex22, *Ogataea angusta* (previously known as *Hansenula polymorpha*) Pex4 adopts an active conformation and is able to build polyubiquitin chains *in vitro* (Groves et al., 2018).

Like yeast, plants have a dedicated peroxisomal UBC, PEX4, that is tethered to peroxisomes *via* a membrane-bound peroxin, PEX22 (Zolman et al., 2005). Although no validated null alleles of either PEX4 or PEX22 are present in publicly available T-DNA collections (Alonso et al., 2003), two *Arabidopsis thaliana pex4* mutants have emerged from forward-genetic screens for peroxisome dysfunction (Zolman et al., 2000, 2005; Kao and Bartel, 2015). The *pex4-1* P123L missense allele confers peroxisome-defective phenotypes that are exacerbated in combination with the *pex22-1* mutant, a T-DNA insertion in the 5′-UTR of *PEX22* (Zolman et al., 2005). The *pex4-2* mutant carries an intronic mutation that reduces accumulation of PEX4 protein and displays similar but less severe defects than *pex4-1* (Kao and Bartel, 2015). Thus, both *pex4-1* and *pex4-2* are partial-loss-of-function alleles. Several peroxin mutations confer embryo lethality in *A. thaliana*, including null alleles of any of the three RING peroxins that guide PEX4 to ubiquitinate PEX5 (Schumann et al., 2003; Sparkes et al., 2003; Fan et al., 2005; Prestele et al., 2010), but it is unknown whether PEX4 or PEX22 are essential for embryogenesis. Additionally, whereas many of the 37 potential UBCs in *A. thaliana* have been experimentally validated (Bachmair et al., 2001; Kraft et al., 2005), ubiquitination by PEX4 has not been directly demonstrated. In contrast to many UBCs, which are encoded by closely related genes in Arabidopsis, phylogenetic analysis places PEX4 as the sole member of a UBC subfamily (Kraft et al., 2005). This observation, along with the characteristic peroxisome-defective phenotypes of *pex4* mutants (Zolman et al., 2005; Kao and Bartel, 2015), implies that PEX4 acts non-redundantly and that PEX22 binds specifically to PEX4 among all UBCs. The structural basis for this specificity is unknown.

The three RING peroxins function in a complex (El Magraoui et al., 2012). Partial loss-of-function alleles of any of the *A. thaliana* RING peroxins, PEX2, PEX10, and PEX12, can destabilize other members of the complex (Burkhart et al., 2014; Kao et al., 2016). Unexpectedly, reducing PEX4 function *via* the *pex4-1* or *pex4-2* mutations partially restores RING complex stability and peroxisome function in the *A. thaliana pex12-1* mutant (Kao et al., 2016). These data suggest that the lysine residue provided by the pex12-1 E171K mutation serves as an ectopic PEX4 ubiquitination site, leading to pex12-1 degradation and destabilization of the RING complex when PEX4 is functional (Kao et al., 2016). Moreover, certain lumenal proteins are stabilized in a *pex4-1 pex22-1* double mutant (Lingard et al., 2009). Thus, it is possible that PEX4 participates in ubiquitination of peroxisomal proteins beyond its established substrate, PEX5.

Structural information is available for two yeast (*S. cerevisiae* and *O. angusta*) Pex4-Pex22 complexes (Williams et al., 2012; Groves et al., 2018). These studies reveal that yeast Pex4 binds to Pex22 *via* a binding site at the C-terminus of Pex4 that does not overlap with other known UBC-interaction surfaces (Williams et al., 2012; Groves et al., 2018). Whereas *A. thaliana* PEX4 is 38–42% identical to its

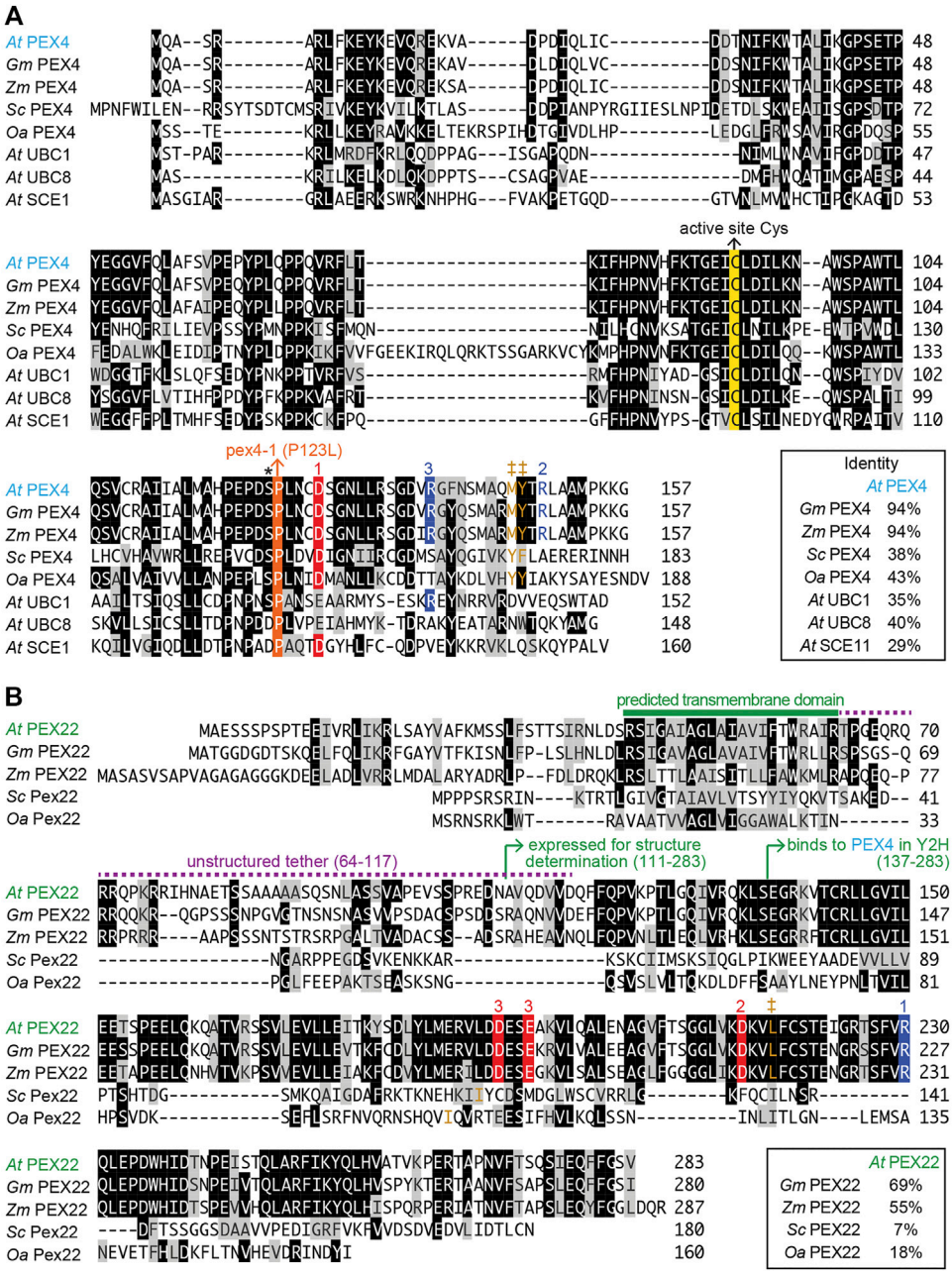

FIGURE 1 | Alignment of *Arabidopsis* PEX4 and PEX22 with homologs from *Arabidopsis* and other organisms. Ar*abidopsis thaliana* (*At*) PEX4 is highly conserved in plants [*Glycine max* (*Gm*), XP_003522698.1; *Zea mays* (*Zm*), NP_001130714.1] and similar to yeast Pex4 [*Saccharomyces cerevisiae* (*Sc*), P29340.1; *Ogataea angusta* (*Oa*), O60015.1] and other *A. thaliana* conjugating enzymes (*At* UBC1, OAP18713.1; *At* UBC8, NP_001190447.1; *At* SCE1, Q42551.1) **(A)**, whereas *A. thaliana* PEX22 (*At* PEX22) is somewhat conserved in plants (*Gm*, XP_003543380.1; Zm, NP_001358459.1) but is highly diverged from yeast Pex22 (*Sc*; KZV13408.1; *Oa*, ABD37672.1) **(B)**. Proteins were aligned using the Clustal W method of the Megalign program (DNAStar). Identical residues in at least four **(A)** or three **(B)** sequences are in black or colored boxes; chemically similar residues are in gray. The active site cysteine (yellow), the pex4-1 missense mutation (orange), and the "gateway" residue (asterisk; reviewed in Stewart et al., 2016) are highlighted in panel **A**. Numbers above sequences indicate acidic (red) or basic (blue) residues involved in three *At* PEX4-PEX22 salt bridges deduced from the crystal structure. Hydrophobic residues in analogous positions as Y172 in *Sc* Pex4, which is essential for *Sc* Pex4-Pex22 interaction (Williams et al., 2012), and interacting hydrophobic residues in PEX22 are shown in brown and marked with ‡.

yeast orthologs (**Figure 1A**) and was originally identified by homology to yeast Pex4 (Mullen et al., 2001), *A. thaliana* PEX22 lacks notable amino acid sequence similarity to the yeast proteins (**Figure 1B**), and was originally identified by its ability to bind to *A. thaliana* PEX4 in yeast two-hybrid experiments (Zolman et al., 2005).

To elucidate the basis of PEX4-PEX22 specificity, to better understand the nature of *pex4* mutations, and to begin to address

the lack of plant peroxin structural information, we solved the crystal structure of *A. thaliana* PEX4 complexed with the C-terminal domain of PEX22. We analyzed this structure to illuminate the details of PEX4-PEX22 binding. Additionally, we demonstrated *in vitro* PEX4-PEX22 ubiquitin-conjugating activity and found that the protein encoded by the *pex4-1* missense allele displays altered ubiquitination specificity without markedly impacting PEX22 binding.

MATERIALS AND METHODS

Plant Materials and Growth Conditions

Plants in the Col-0 accession of *Arabidopsis thaliana* and the *pex4-1* missense allele (Zolman et al., 2005) were grown at 22°C under constant light. Seeds were surface sterilized and sown on plant nutrient (PN) medium (Haughn and Somerville, 1986) solidified with 0.6% (w/v) agar and supplemented with 0.5% (w/v) sucrose. Seedlings were collected for immunoblotting or transferred to soil after 1–2 weeks for seed production.

Construction of PEX4-PEX22 Expression Plasmids

We constructed a plasmid for expressing full-length *A. thaliana* PEX4 (At5g25760; also named UBC21) without a stop codon and fused to truncated PEX22 (At3g21865; residues 111-283) *via* a linker consisting of a PreScission protease (Genscript Z03092) cleavage site (LEVLFQ|GP, where "|" designates the cleavage site). The PEX4-PEX22 fusion was expressed in *E. coli* with an N-terminal His_6-maltose-binding protein (MBP) tag that was connected *via* a linker consisting of a TEV protease cleavage site (ENLYFQ|S). *PEX4* and *PEX22* cDNA fragments were cloned into the pET-His6-MBP-TEV-LIC cloning vector (a gift from Scott Gradia; Addgene plasmid 29656). PCR amplification was performed on the pET vector using primers pET-F and pET-R (**Supplementary Table S1**). Primers PEX4-F and PEX4-R (**Supplementary Table S1**) were used to PCR amplify a *PEX4* cDNA (Zolman et al., 2005), and primers PEX22-F and PEX22-R (**Supplementary Table S1**) were used to PCR amplify a *PEX22* cDNA (Zolman et al., 2005). The PEX4, PEX22, and pET vector amplicons were combined using Gibson assembly (Gibson et al., 2009) with Gibson Assembly Master Mix (New England Biolabs E2611) to give plasmid His6-MBP-PEX4-PEX22, which was verified by sequencing.

To construct His6-MBP-pex4^{P123L}-PEX22, Gibson assembly was used to combine the pET vector (amplified with pET-F and pET-R) with PCR products amplified from the His6-MBP-PEX4-PEX22 plasmid with primers PEX4-F paired with pex4-1-R and pex4-1-PEX22-F paired with PEX22-R (**Supplementary Table S1**).

PEX4-PEX22 Protein Expression and Purification

Chemically competent BL21 Star (DE3) *E. coli* cells (Invitrogen C601003) were transformed with either the His_6-MBP-PEX4-PEX22 or His_6-MBP-pex4^{P123L}-PEX22 expression plasmids. Transformed *E. coli* were selected on LB (Fisher BP1426) agar plates supplemented with kanamycin (50 μg/mL). Single colonies were used to inoculate 50 mL cultures of LB supplemented with kanamycin (50 μg/mL), and cultures were incubated overnight at 37°C with shaking. 3 mL of each overnight culture was used to inoculate 500 mL of Terrific Broth (Invitrogen 22711022) supplemented with kanamycin (50 μg/mL) and cultures were incubated at 37°C with shaking to an OD_{600} of 0.6–0.8. Cultures were then supplemented to 0.75 mM isopropyl β-D-1-thiogalactopyranoside (IPTG) and incubated 30°C overnight with shaking. Cells were harvested by centrifugation and stored at −80°C until lysis.

Partially thawed cell pellets were resuspended in 5 mL lysis buffer (25 mM HEPES pH 8, 300 mM NaCl, 5% glycerol, 10 mM imidazole, 1 mM Tris(2-carboxyethyl)phosphine hydrochloride (TCEP)) per gram of cell pellet and lysed by sonication on ice for 5 min (cycling 15 s on, 15 s off) or 10 min (cycling 1 s on, 1 s off). The lysate was then clarified by centrifugation (39,000 x *g*) and incubated for at least 1 h with 10 mL Ni-NTA Superflow resin (Qiagen 30410) equilibrated with lysis buffer at 4°C with rocking. After incubation, the resin was loaded onto a gravity-flow column and washed with 50 mL buffer A (25 mM HEPES pH 8, 300 mM NaCl, 5% glycerol, 1 mM TCEP) and then washed sequentially with 12.5 mL aliquots of a step gradient from 20 to 500 mM imidazole, using combinations of buffer A and buffer B (25 mM HEPES pH 8, 300 mM NaCl, 5% glycerol, 1 mM TCEP, 500 mM imidazole). The presence of eluted protein was assessed using SDS-PAGE and Coomassie staining (SimplyBlue SafeStain, Fisher LC6060). Fractions containing the target protein were concentrated to 2 mL using centrifugal concentrators (3,000 Da cutoff, Amicon Ultra-15, Millipore Sigma UFC900324) and subjected to cleavage with His-tagged PreScission protease (Genscript Z03092) alone or with His-tagged TEV protease, produced as described (Tropea et al., 2009). Using a ratio of 1 mg TEV protease and 500 units PreScission protease for every 50 mg of fusion protein, the reaction mixture was allowed to incubate overnight at 4°C on a rotary mixer then clarified by centrifugation (39,000 × *g*). TEV protease, PreScission protease, and N-terminal cleavage products containing His_6 tags were removed by an additional purification with Ni-NTA Superflow resin equilibrated with buffer A. PEX4 or pex4-1 and PEX22$^{111-283}$ were present in the flowthrough and in the first two to three washes with buffer A as confirmed by SDS-PAGE and Coomassie staining. Fractions containing PEX4 or pex4-1 and PEX22$^{111-283}$ were concentrated, and PEX4-PEX22$^{111-283}$ fractions selected for crystallization were further purified using anion-exchange resin HiTrap DEAE Sepharose FF (Cytiva 17515401) equilibrated with buffer 1 (25 mM HEPES pH 8, 5% glycerol, 1 mM TCEP). PEX4 and PEX22$^{111-283}$ were present in the flowthrough as confirmed by SDS-PAGE and Coomassie staining.

PEX4-PEX22 Protein Crystallization

Purified PEX4-PEX22$^{111-283}$ was concentrated using centrifugal concentrators (10,000 Da cutoff, Amicon Ultra-0.5, Millipore Sigma) to 20 mg/mL in 20 mM Tris pH 7.5, 200 mM NaCl,

TABLE 1 | Data collection and refinement statistics for *Arabidopsis* PEX4-PEX22 structure.

PDB ID	6XOD
Space group	C 2 2 2_1
Unit cell lengths (Å)	a = 57.39 b = 100.48 c = 112.10
Temperature (K)	100
Wavelength (Å)	1.033
Data collection statistics	
Resolution range (Å)	56.0–2.01 (2.04–2.01)[a]
Number of observations	144,846 (6499)
Number of unique reflections	22014 (1079)
Completeness (%)	99.9 (100.0)
R_{merge}[b]	0.096 (1.56)
R_{meas}[c]	0.104 (1.71)
Redundancy	6.6 (6.0)
Mean I/σ	10.5 (1.1)
$CC_{1/2}$[d]	0.998 (0.464)
Wilson B-factor	43.6
Refinement statistics	
Resolution range (Å)	49.8–2.01 (2.10–2.01)
R_{cryst}[e]	0.194 (0.278)
R_{free}[f]	0.237 (0.320)
RMSD bonds (Å)	0.004
RMSD angles (°)	1.0
Average B factors (Å^2)	
Protein	56.5
Water	55.1
Number of protein non-H atoms	2562
Number of water molecules	131
Ramachandran favored (%)	97.2
Ramachandran allowed (%)	2.5
Ramachandran outliers (%)	0.3
Clashscore	1.8

[a]*Values in parentheses are for the highest-resolution shell.*
[b]$R_{merge} = \Sigma_h\Sigma_i|I_i(h) - <I(h)>|/\Sigma_h\Sigma_i I_i(h)$, *where* $I_i(h)$ *is the intensity of an individual measurement of the reflection and* $<I(h)>$ *is the mean intensity of the reflection.*
[c]$R_{meas} = \Sigma_h(n_h/(n_h\text{-}1)\ \Sigma_i|I_i(h) - <I(h)>|/\Sigma_h\Sigma_i I_i(h)$, *where* n_h *denotes the redundancy.*
[d]$CC_{1/2} = \sum (x-<x>)(y-<x>)/[\sum(x-<x>)^2\Sigma(y-<y>)^2]^{1/2}$
[e]$R_{cryst} = \Sigma_h||F_{obs}|-|F_{calc}||/\Sigma_h|F_{obs}|$, *where* F_{obs} *and* F_{calc} *are the observed and calculated structure factor amplitudes, respectively.*
[f]R_{free} *was calculated as* R_{cryst} *using 5% of the randomly selected unique reflections that were omitted from structure refinement.*

1 mM DTT for crystallization trials. A 1:1 ratio was assumed and a calculated extinction coefficient of 0.850 M^{-1} cm^{-1} for PEX4 and PEX22 (https://www.expasy.org) was used to estimate concentration. PEX4-PEX22$^{111-283}$ crystallization conditions were established using a sitting drop vapor diffusion setup with a Mosquito LCP automated high-throughput nanoliter pipettor (SPT Labtech) and several commercial crystallization screening kits, including PEG Rx HT, Index HT (Hampton Research), Wizard Classic 1 and 2, 3 and 4 (Rigaku Reagents), Midas, and Morpheus (Molecular Dimensions). Crystal hits were identified *via* UV-excitation of aromatic amino acids using a JANSi UVEX instrument (SWISSCI). Crystals suitable for X-ray diffraction were grown at 20°C after mixing 200 nL of recombinant protein (20 mg/mL) with 200 nL of precipitant (100 mM NaCl, 100 mM Bis-Tris Propane pH 9.0, 25% (w/v) PEG 1,500) from the reservoir. Crystals were transferred to a cryobuffer consisting of reservoir buffer supplemented with 10% (v/v) glycerol, flash cooled in liquid nitrogen, and shipped using a dry shipping dewar (Taylor-Wharton) to Argonne National Laboratory's Advanced Photon Source (Lemont, IL, United States) for diffraction data collection.

Data Collection, Structural Determination, Refinement, and Analysis

PEX4-PEX22$^{111-283}$ crystals diffracted to a resolution of 2.01 Å, and X-ray data were collected on the 23-ID-B beamline at Argonne National Laboratory's Advanced Photon Source (Lemont, IL, United States) at a wavelength of 1.033 Å with an EIGER X 16M detector (DECTRIS Ltd.). Data were processed using the *autoPROC* toolbox (Vonrhein et al., 2011), which indexed and integrated the data with *XDS* (Kabsch, 2010) and scaled the data with *aimless* (Winn et al., 2011; Evans and Murshudov, 2013). Crystals belonged to the C-centered orthorhombic space group $C222_1$, with unit cell lengths of 57.39, 100.48, and 112.10 Å. Initial phases were obtained by molecular replacement with Phaser-MR (McCoy et al., 2007; Liebschner et al., 2019) using the *O. angusta* Pex4-Pex22 complex structure (PDB ID: 5NKZ; PEX4: 43% identity) as a search model for PEX4, and an FFAS/SCRWL built poly-Ser model for PEX22 (Jaroszewski et al., 2005). This initial MR phasing solution was subjected to iterative density modification and poly-alanine autotracing with *shelxe* (Sheldrick, 2008; Thorn and Sheldrick, 2013), which improved the phases and built an initial poly-Ala model of PEX22. The *shelxe* poly-Ala model was rebuilt and side-chains docked using *ARP/wARP* (Langer et al., 2008). Autotracing with *shelxe* and *ARP/wARP* failed to build the PEX22 C-terminal helix. However, MR runs using *ab initio* models generated with AWSEM-Suite (Jin et al., 2020) correctly placed the PEX22 C-terminal helix, which was merged with the ARP/wARP model. Subsequent model building and refinement were performed with Coot (Emsley et al., 2010) and phenix.refine (Liebschner et al., 2019). Data processing and refinement software were compiled and supported by the SBGrid Consortium (Morin et al., 2013). Structures were viewed and analyzed using a collaborative 3-D visualization system (Yennamalli et al., 2014), and structural figures were prepared using ChimeraX (Goddard et al., 2018; Pettersen et al., 2021; https://www.rbvi.ucsf.edu/chimerax). Data processing and refinement statistics are shown in **Table 1**. PDB-wide structure comparisons were performed with Dali (Holm, 2020) using the PDB90 reference dataset and a Z-value cutoff of >6.0. Root-mean-square deviation (RMSD) values were calculated with Dali (over the alignment length for whole subunits) or the MatchMaker function in ChimeraX (for the interfacing residue regions).

In vitro Ubiquitination Assays

In vitro ubiquitination reactions were performed at 30°C in 1X ubiquitination reaction buffer (Boston Biochem SK-10) at a total volume of 50 µL and contained: 33 µM ubiquitin (either Boston Biochem *A. thaliana* wild-type ubiquitin, U-100At; R&D Systems human K48R ubiquitin, UM-K48R-01M; or R&D Systems human K48-only ubiquitin, UM-K480-01M), 0.1 µM human E1 (His_6-UBE1; Boston Biochem E-304), and 5 µM purified *A.*

thaliana PEX4- or pex4^{P123L}-PEX22$^{111-283}$. Reactions were initiated by the addition of Mg-ATP to 1 mM (Boston Biochem, SK-10) and quenched with 1X E1 Stop Buffer (Boston Biochem, SK-10). Proteins were visualized using SDS-PAGE and SimplyBlue SafeStain or immunoblotting.

Immunoblot Analysis

Two volumes of sample buffer (500 mM Tris pH 8.0, 4% (w/v) lithium dodecyl sulfate, 1 mM EDTA, 20% (w/v) glycerol, 22 μM Coomassie blue G250, 16.6 μM mM phenol red, 50 μM dithiothreitol (DTT)) were added to *in vitro* ubiquitination samples, which were then heated at 100°C for 5 min. Equal volumes of sample (3 μL for immunoblots; 20 μL for Coomassie-stained gels) and pre-stained markers (New England Biolabs, P7712 or P7719) were loaded on Bolt 10% (w/v) Bis-Tris gels (Invitrogen). Gels were electrophoresed in 50 mM MES-SDS running buffer (50 mM MES hydrate, 50 mM Tris base, 3.5 mM SDS, 1.27 mM EDTA). Proteins were transferred from the gel to Hybond-ECL nitrocellulose membranes (Amersham, Protran Premium 0.45 μm NC 10600003) using the standard setting on a GenScript eBlot L1 transfer system (GenScript, L00686). Following transfer, membranes were air-dried at room temperature (RT) for 1 h followed by 1 h blocking with Intercept Blocking Buffer (LI-COR, 927-60001) at RT with rocking. After blocking, membranes were incubated overnight with rocking at 4°C with various primary antibodies diluted in 8% (w/v) Carnation instant non-fat dry milk in TBST (20 mM Tris pH 7.5, 150 mM NaCl, 0.1% (v/v) Tween-20). Membranes were then incubated 1–2 h with secondary antibody with rocking at RT. Primary antibodies used were rabbit anti-PEX4 (1:100; Kao and Bartel, 2015) and mouse anti-ubiquitin (P4D1, 1:300; Santa Cruz sc-8017). Secondary antibodies used were horseradish peroxidase (HRP)-linked goat anti-rabbit antibody (1:5,000; GenScript A00098) and IRDye 800CW-linked goat anti-mouse secondary antibodies (1:10,000, LI-COR 926-32210). Following secondary antibody incubation, membranes were imaged with (HRP-linked secondary antibodies) or without (IRDye secondary antibodies) WesternSure Premium Chemiluminescent substrate (Fisher, 50-489–552) using an Odyssey Fc imaging system (LI-COR, 2801-02). Quantification was performed using Image Studio software (LI-COR, version 5.2). Ubiquitination activity rates were separately calculated for three replicates using the slope value of a linear trendline. Statistical comparison of rates between wild type and mutant purified proteins was performed using Graphpad Prism (version 9.3.0).

Fractionation of extracts from 6-day-old dark-grown seedlings was conducted as previously described (Kao and Bartel, 2015). Proteins were separated on Bolt 10% (w/v) Bis-Tris gels and transferred to membranes as described above. Membranes were probed sequentially (without stripping) with rabbit anti-PEX4 (1:100), rabbit anti-PEX5 (1:100; Zolman and Bartel, 2004), mouse anti-HSC70 (1:50,000), rabbit anti-PEX14 (1:10,000, Agrisera AS08 372), mouse anti-mitochondrial ATP synthase α subunit (1:2,000; Mito-Science MS507), and rabbit anti-isocitrate lyase (1:1,000; Maeshima et al., 1988) and processed as described above.

In vitro PEX4-PEX22 Interaction Assay

Purified His$_6$-MBP-PEX4-PEX22 and His$_6$-MBP-pex4^{P123L}-PEX22 were cut with PreScission protease as described above. The reaction was incubated for 1 h with Ni-NTA Superflow resin equilibrated with buffer A with rocking at 4°C, washed four times with buffer A, then washed four times with buffer B. Resin was separated from wash fractions *via* low-speed centrifugation. Samples from each fraction were analyzed *via* SDS-PAGE and Coomassie staining.

RESULTS

PEX4-PEX22 Expression and Purification

To understand the specificity of plant PEX4-PEX22 interactions and to gain mechanistic insight into the defects conferred by the *pex4-1* missense allele, we determined the structure of the *A. thaliana* PEX4-PEX22 complex. *S. cerevisiae* Pex4 is inactive without Pex22 (Williams et al., 2012), and prior efforts to heterologously express *A. thaliana* PEX4 in *E. coli* or insect cells yielded insoluble enzyme (Kraft et al., 2005). Therefore, we co-expressed PEX4 and PEX22$^{111-283}$ in *E. coli* as a translational fusion linked by a synthetic PreScission protease cleavage site (**Figure 2A**). The N-terminal region of *A. thaliana* PEX22 includes a predicted transmembrane domain (**Figure 1B**) and is dispensable for PEX4 binding in yeast two-hybrid assays (Zolman et al., 2005), thus we did not include the N-terminal 110 amino acids of PEX22 in the construct. We expressed PEX4 at the N-terminus of this PEX22 region because the C-terminus of Pex4 is only ~21 Å from the N-terminus of Pex22 (lacking the transmembrane domain) in the yeast co-crystal structures (Williams et al., 2012, PDB ID 2Y9M; Groves et al., 2018, PDB ID 5NKZ). We expressed this *A. thaliana* PEX4-PEX22$^{111-283}$ fusion with N-terminal His$_6$ and maltose-binding protein (MBP) tags to facilitate purification and solubility, respectively. His$_6$-MBP-PEX4-PEX22$^{111-283}$ was soluble following expression in *E. coli*, and we purified the fusion protein using nickel chromatography, cleaved the fusion with TEV and PreScission proteases to separate His$_6$-MBP, PEX4, and PEX22$^{111-283}$, and removed the His$_6$-MBP and His-tagged-proteases by collecting PEX4-PEX22$^{111-283}$ from the flow-through of second round of nickel chromatography (**Figure 2B**). Ion-exchange chromatography of the PEX4-PEX22$^{111-283}$ complex yielded protein suitable for crystallization.

Crystal Structure of the *Arabidopsis* PEX4-PEX22 Complex

We crystallized and solved the structure of the *A. thaliana* PEX4-PEX22$^{111-283}$ complex at 2.01 Å resolution (PDB ID 6XOD; **Table 1**, **Figure 3**). The final model included residues 1-154 of PEX4, residues 118-283 of PEX22$^{111-283}$, and 131 water molecules. One residue following the TEV protease cleavage site (0 at the N-terminus), three PEX4 C-terminal residues (155-157), and six C-terminal PreScission cleavage site residues (158-163) were disordered and were not modeled (**Supplementary Figure S1**). Similarly, two N-terminal PreScission cleavage site residues and seven N-terminal residues

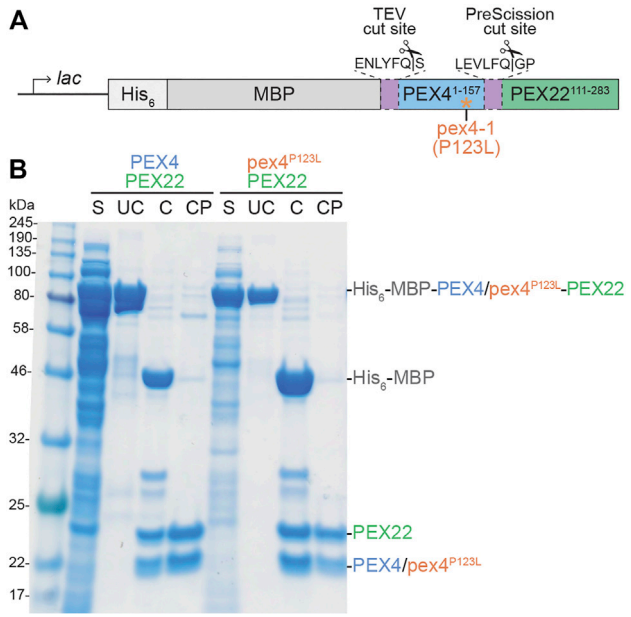

FIGURE 2 | Expression and purification of *Arabidopsis* PEX4/pex4^{P123L}-PEX22$^{111-283}$ complexes. **(A)**. Schematic of constructs used to express full-length PEX4 and pex4-1 (pex4^{P123L}) with PEX22 (amino acids 111-283). His$_6$-MBP-PEX4/pex4^{P123L}-PEX22$^{111-283}$ fusions were expressed in *E. coli* following IPTG induction of the *lac* promoter. His$_6$ was included as a purification tag, maltose binding protein (MBP) was included as a solubility tag, and unique protease sites separated MBP and PEX4/pex4^{P123L} (TEV cut site) and PEX4/pex4^{P123L} and PEX22$^{111-283}$ (PreScission cut site). **(B)**. PEX4/pex4^{P123L} and PEX22$^{111-283}$ purification. After expression in *E. coli*, cells were lysed and the full-length uncleaved (UC) protein (81 kDa) was purified from the soluble fraction (S). Purified protein was cleaved with TEV and PreScission proteases (C) and separated from His$_6$-MBP (43 kDa) and proteases to give cleaved and purified (CP) PEX4/pex4^{P123L} (18 kDa) and PEX22$^{111-283}$ (20 kDa).

(111-117) of PEX22$^{111-283}$ were disordered and were not modeled. The model includes a single Ramachandran outlier (PEX22 Pro^{122}) that is part of the N-terminal linker region and can be explained by poor density.

PEX4 adopts a canonical UBC fold (reviewed in Stewart et al., 2016), with four α-helices, four β-strands, and the active site cysteine between β-strand 4 and α-helix 2 (**Figure 3**; **Supplementary Figure S1**). The active site cysteine (C90) is in a cleft bordered by the PEX4 3_{10} helix (η1) and the loop region between α-helices 2 and 3. α-helix 2 is the "crossover" helix that extends across the antiparallel β-sheet formed by the four β-strands (**Figure 3**). The PEX4 structure, including the active site region, aligns closely (1.0–1.8 Å RMSD) with structures of ubiquitin- and SUMO-conjugating enzymes from *A. thaliana* (**Figure 4A**). Similarly, aligning the *A. thaliana* PEX4 structure with Pex4 structures from *S. cerevisiae* and *O. angusta* revealed close similarity (1.3–1.4 Å RMSD), apart from the insertion found on the backside (relative to the active site cysteine) of the *O. angusta* enzyme (**Figure 4B**). A Dali (Holm, 2020) structural similarity search of PEX4 to the PDB90 dataset (the subset of the PDB with ≤90% identity) revealed numerous similar structures. As expected, most of the close matches (Z-values greater than 6.0; 80 structures) were UBC enzymes from a variety of eukaryotes, which displayed 22–44% sequence identity with *At* PEX4. The closest match was *Oa* Pex4 (44% identity, Z = 19.4), and *Sc* Pex4 was also detected (38% identity, Z = 22). Most proteins displaying between 10 and 20% identity with PEX4 were annotated as having a UBC-related domain. For example, PEX4-related proteins also included Ubiquitin E2 variant (UEV)-domains (a ubiquitin-binding domain that lacks the two C-terminal α-helices of the UBC domain; Sundquist et al., 2004) or RWD-domains (a domain found in RING fingers, WD-domain-containing-proteins, and DEAD-like helicases; Doerks et al., 2002).

We found that *A. thaliana* PEX22$^{111-283}$ folds as a single domain consisting of a parallel six-stranded β-sheet flanked by α-helices on both sides (**Figure 3**). Comparing PEX22 to the PDB90 dataset using Dali (Holm, 2020) revealed 344 structures with Z-values greater than 6.0. The sequence identities for PEX22 matches were lower than for PEX4, ranging from 3 to 16%. Although not among the top matches, this list did include both *Sc* Pex22 (15% identity, Z = 8) and *Oa* Pex22 (13% identity, Z = 6.9) along with a variety of eukaryotic and bacterial enzymes. A topology plot for PEX22 (**Supplementary Figure S2**; Laskowski et al., 2018) revealed a pattern of alternating β-strands and α-helices similar to the Rossmann tertiary fold motif, with the exception of a loop rather than an α-helix joining β-strands 5 and 6 in PEX22 (**Figure 3**; **Supplementary Figure S2**). A Rossmann fold is found in about 20% of structures in the PDB,

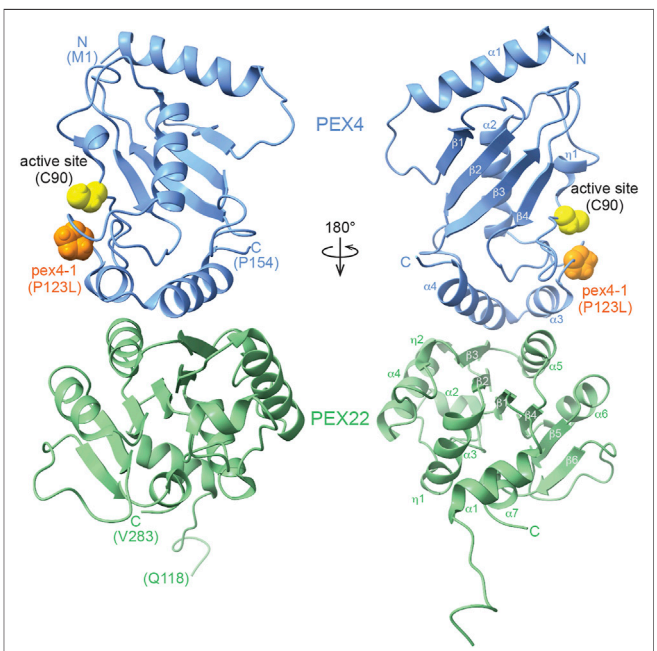

FIGURE 3 | X-ray crystal structure of the *Arabidopsis thaliana* PEX4-PEX22$^{111-283}$ complex. The ribbon diagram illustrates that PEX4 (blue) α-helices 3 and 4 interact with a surface of PEX22 (green) formed by a PEX22 3_{10} helix (η2), β-strand 3, and α-helix 5. The PEX4 active site cysteine (C90) is highlighted in yellow and is positioned between the PEX4 3_{10} helix (η1) and the loop connecting PEX4 α-helix 2 (the "crossover" helix) and α-helix 3. The proline residue mutated in *pex4-1* (P123L) is situated in this loop and is highlighted in orange.

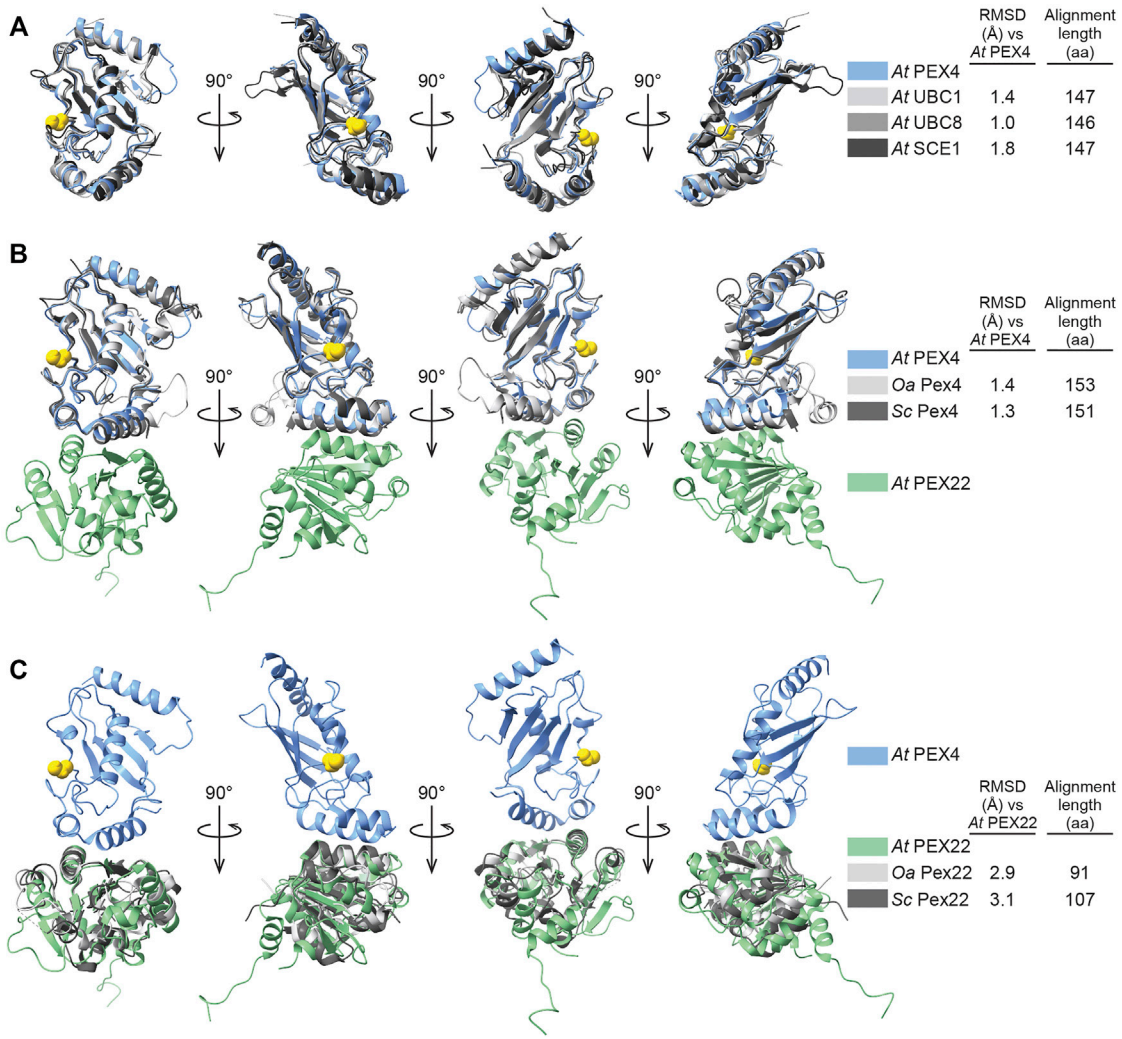

FIGURE 4 | Comparison of *Arabidopsis* PEX4 and PEX22 with similar proteins in *Arabidopsis* and yeast. **(A)**. Aligned X-ray crystal structures of *Arabidopsis thaliana* (*At*) PEX4 with paralogs: ubiquitin-conjugating enzymes *At* UBC1 (PDB 2AAK) and *At* UBC8 (PDB 4X57), and the SUMO-conjugating enzyme *At* SCE1 (PDB 6GV3). The PEX4 active-site cysteine is highlighted in yellow. Root mean square deviation (RMSD) values and alignment lengths were computed by using pairwise Dali alignments (Holm, 2020). **(B,C)**. X-ray crystal structures of the *Arabidopsis thaliana* (*At*) PEX4-PEX22 complex aligned with orthologs from *Saccharomyces cerevisiae* (*Sc*, PDB 2Y9M) and *Ogataea angusta* (*Oa*, previously known as *Hansenula polymorpha*; PDB 5NKZ). Structures were aligned to PEX4 **(B)** or PEX22 **(C)**. The PEX4 active-site cysteine is highlighted in yellow. RMSD values and alignment lengths were computed by using pairwise Dali alignments (Holm, 2020).

often as a nucleotide binding domain (reviewed in Shin and Kihara, 2019). This fold is the likely origin of the broad homology matches to PEX22. Indeed, a Rossmann fold resemblance was previously noted for yeast Pex22 (Williams et al., 2012).

We aligned the *A. thaliana* PEX22$^{111-283}$ structure with the two yeast Pex22 structures (**Figure 4C**). In parallel with reduced amino acid sequence similarity (**Figure 1B**), the PEX22$^{111-283}$ structure aligns less precisely to those of its homologs (~3 Å RMSD over a 91-107 aa alignment) than PEX4. We observed considerable differences at both the N- and C-terminus of the structures. For example, α-helix 1 of *At* PEX22 is not found in the yeast Pex22 proteins, which both have a β-strand as the first secondary structural element (**Supplementary Figure S2**). Moreover, the *At* PEX22 β-sheet is comprised of six β-strands (**Figure 3**), whereas the yeast proteins have five β-strands (**Supplementary Figure S2**). Notably, the region of highest similarity appeared to be the interface between PEX4 and PEX22 (**Figure 4C**). Indeed, the Pex4-interacting-regions of *Sc* Pex22 (aa 111-132) and *Oa* Pex22 (aa 99-120) aligned considerably more closely with the PEX4-interacting-residues of *At* PEX22 (aa 212-233) (~0.8 Å RMSD over 22 Cα pairs) than the overall structures.

The PEX4-PEX22 interface is formed by interactions of the two C-terminal α-helices of PEX4 (α-helix 3 and 4) with β-strand 3 and α-helix 5 in the middle region of PEX22$^{111-283}$

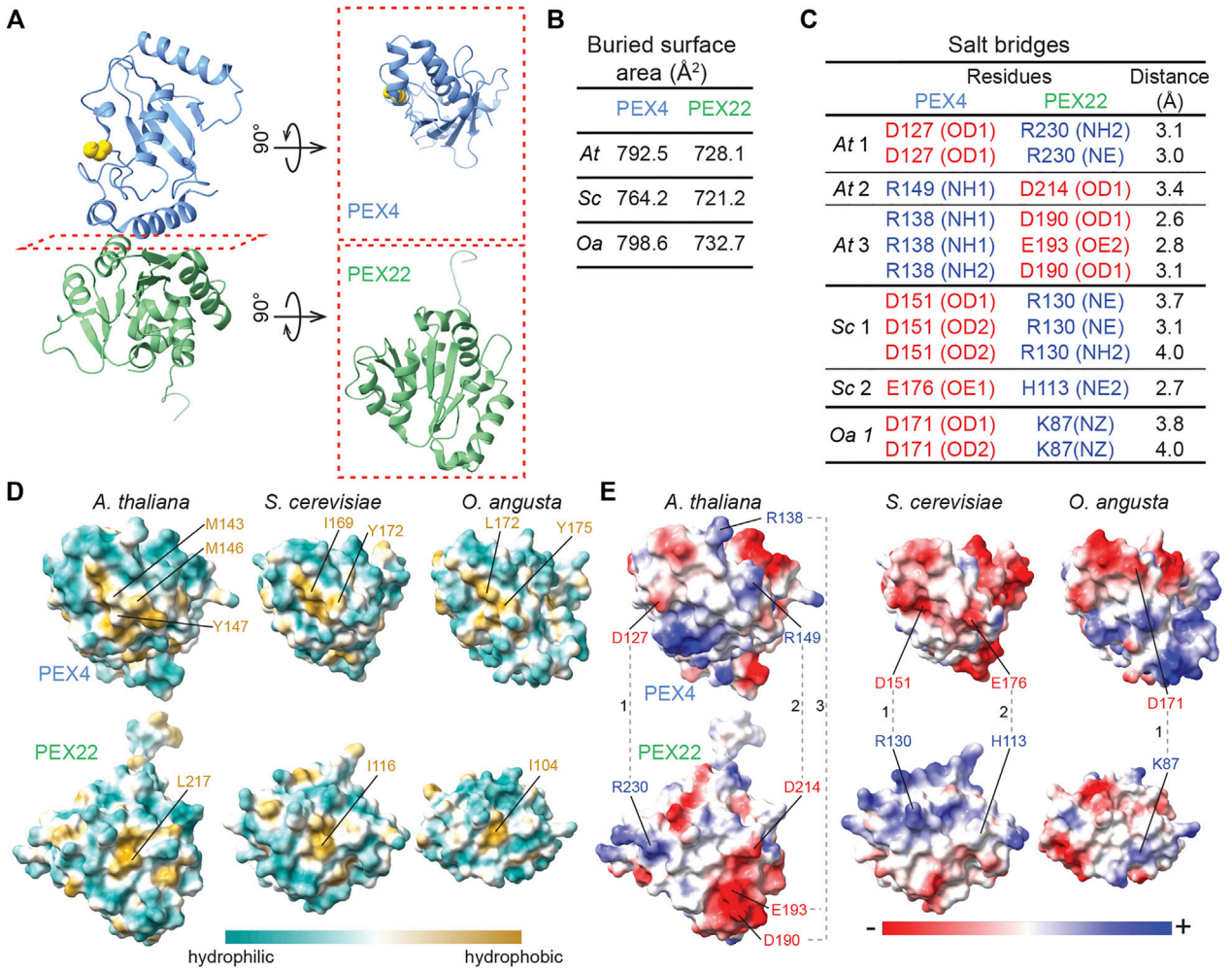

FIGURE 5 | A central hydrophobic patch and complementary electrostatic surfaces mediate *Arabidopsis* PEX4-PEX22 interactions. **(A)**. Ribbon diagram of *A. thaliana* (*At*) PEX4-PEX22 (left) with subunits rotated 90° to allow a top view of the "bottom" of PEX4 and the "top" of PEX22 that form the interaction surface (right). **(B)**. Buried surface area at the interface between PEX4 and PEX22 deduced from the crystal structures using PDBePISA (Krissinel and Henrick, 2007; www.ebi.ac.uk/pdbe/prot_int/pistart.html). **(C)**. Salt bridges linking PEX4 and PEX22 predicted from the crystal structures using PDBePISA (Krissinel and Henrick, 2007; www.ebi.ac.uk/pdbe/prot_int/pistart.html). Positively charged residues are blue and negatively charged residues are red. Salt bridges are numbered as shown in panel **E** for the structures from each organism: *At, A. thaliana*; *Sc*, *S. cerevisiae*; and *Oa*, *O. angusta* Specific atoms involved in salt bridges are listed in parentheses (NE, epsilon nitrogen of arginine or histidine; NH, eta nitrogen of arginine; NZ, zeta nitrogen of lysine; OD, delta oxygen of aspartate; OE, epsilon oxygen of glutamate). **(D)**. Visualization of surface hydrophobicity of the interaction surfaces of PEX4 (top row) and PEX22 (bottom row) from *A. thaliana*, *S. cerevisiae*, and *O. angusta*. Structures are rotated as shown in the panel **A** right column. Residues in the central hydrophobic patches (gold) are labeled. **(E)**. Visualization of surface electrostatic potential of the interaction surfaces of PEX4 (top row) and PEX22 (bottom row) from *A. thaliana*, *S. cerevisiae*, and *O. angusta*. Structures are rotated as shown in the panel **A** right column. Residues involved in salt bridges **(B)** are labeled and connected with dashed lines. Complementary charge patterns are evident in each PEX4-PEX22 pair, despite the differences across species.

(**Figures 3**, **5A**; **Supplementary Figure S1**). Using PDBePISA, we quantified the buried surface area (BSA) at the interface of the PEX4-PEX22 complex (**Figure 5B**). PEX4 has a buried surface area of 793 Å^2 and PEX22 has a buried surface area of 728 Å^2. The interface comprises 8–9% of the surface area of each structure. We also used PDBePISA to identify three likely salt bridges at the interface of the PEX4-PEX22$^{111-283}$ complex (**Figures 5C,E**) that are positioned to contribute to PEX4-PEX22 binding. We found that the residues forming these salt bridges are conserved in plant PEX4 and PEX22 orthologs from *Glycine max* and *Zea mays* (**Figure 1A**), suggesting that the mode of interaction may be conserved in higher plants.

Electrostatic Interactions at the PEX4-PEX22 Interface Appear to Contribute to Binding Specificity

Despite the structural similarity of *A. thaliana* PEX4 and *S. cerevisiae* Pex4 (**Figure 4B**), genetic complementation experiments reveal that *At* PEX4 selectively binds *At* PEX22 and not *Sc* Pex22 and vice versa (Zolman et al., 2005). To

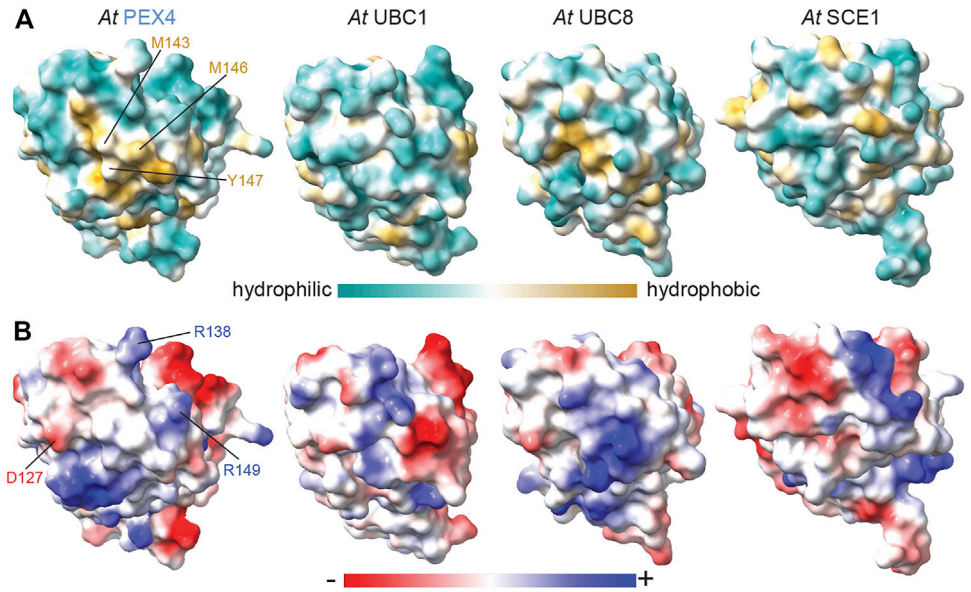

FIGURE 6 | Hydrophobic and electrostatic properties of *Arabidopsis* ubiquitin- and sumo-conjugating enzyme surfaces provide insight into PEX4-PEX22 binding specificity. Surface hydrophobicity **(A)** and electrostatic **(B)** projections of *A. thaliana* (*At*) PEX4, UBC1 (PDB 2AAK), UBC8 (PDB 4X57), and SCE1 (PDB 6GV3). Structures were aligned to *At* PEX4 and are oriented as in **Figure 5** to show the PEX22-interacting and analogous surfaces. PEX4 residues in the conserved hydrophobic patch implicated in PEX22 binding are labeled in panel **A**, and residues involved in salt bridges with PEX22 are labeled in panel **B**. The surfaces are quite distinct, consistent with the expected inability of PEX4 paralogs to bind PEX22.

examine PEX4-PEX22 binding specificity, we compared the hydrophobic (**Figure 5D**) and electrostatic (**Figure 5E**) characteristics of the interacting surfaces of PEX4 and PEX22 from *A. thaliana, S. cerevisiae*, and *O. angusta*. The backbones of the PEX4 proteins align at the PEX22 binding interface (**Figure 4B**), and all protein pairs have similarly sized interaction surfaces (720-800 Å^2; **Figure 5B**). Moreover, the central hydrophobic pocket important for *S. cerevisiae* Pex4-Pex22 interaction (Williams et al., 2012) appears to be conserved among the three PEX4 proteins (**Figures 1A**, **5D**). In contrast, the electrostatic properties of the surfaces are not well conserved (**Figure 5E**). For example, the positions of the salt bridges in the *A. thaliana* complex are not conserved in *S. cerevisiae* or *O. angusta* Pex4-Pex22 (**Figures 5C,E**), and residues corresponding to *A. thaliana* PEX4 R138 and R149, which are involved in salt bridges with PEX22, are uncharged in the yeast Pex4 proteins (**Figures 1A**, **5E**).

Despite the overall similarity of PEX4 to other UBCs (**Figures 1A**, **4A**), the peroxisome-defective phenotypes of *pex4* mutants (Zolman et al., 2005; Kao et al., 2016) imply that other *A. thaliana* UBCs do not substitute for PEX4 in binding to PEX22. To understand the basis for this selectivity, we compared the PEX22-interacting surface of PEX4 with the corresponding surfaces of similar *A. thaliana* enzymes with available structural information: UBC1, UBC8, and SCE1. This comparison revealed substantially different hydrophobicity patterns (**Figure 6A**) and a lack of charge conservation of at least one of the three PEX4 residues involved in salt bridges with PEX22 (**Figures 1A**, **6B**) that are likely to preclude interaction with PEX22.

PEX4 Builds K48-Linked Ubiquitin Chains and pex4-1 Displays Altered Ubiquitination Substrate Specificity

Examining the PEX4 residue altered in the *pex4-1* missense allele revealed that the mutated P123 residue was positioned on the protein surface ~6 Å from the PEX4 active site C90 residue (**Figure 3**); this proximity suggests that pex4-1 enzymatic activity might be impaired or modified. To directly examine the impacts of the pex4-1 mutation (P123L) on enzymatic function, we generated a construct to express His$_6$-MBP-pex4^{P123L}-PEX22$^{111-283}$ in *E. coli*. Like the wild-type construct, the mutant fusion protein was soluble, and we purified pex4^{P123L}-PEX22$^{111-283}$ (**Figure 2B**) and compared *in vitro* self-ubiquitination activity of the two complexes. After incubating PEX4-PEX22$^{111-283}$ or pex4^{P123L}-PEX22$^{111-283}$ with ubiquitin, ubiquitin-activating enzyme (E1), and ATP, we monitored self-ubiquitination using SDS-PAGE and Coomassie staining (**Figure 7A**) and immunoblotting with antibodies recognizing ubiquitin (**Figure 7B**) or PEX4 (**Figure 7C**).

We found that reactions using wild-type PEX4-PEX22$^{111-283}$ accumulated a protein the size of diubiquitin and a ladder of ubiquitinated proteins of increasing molecular

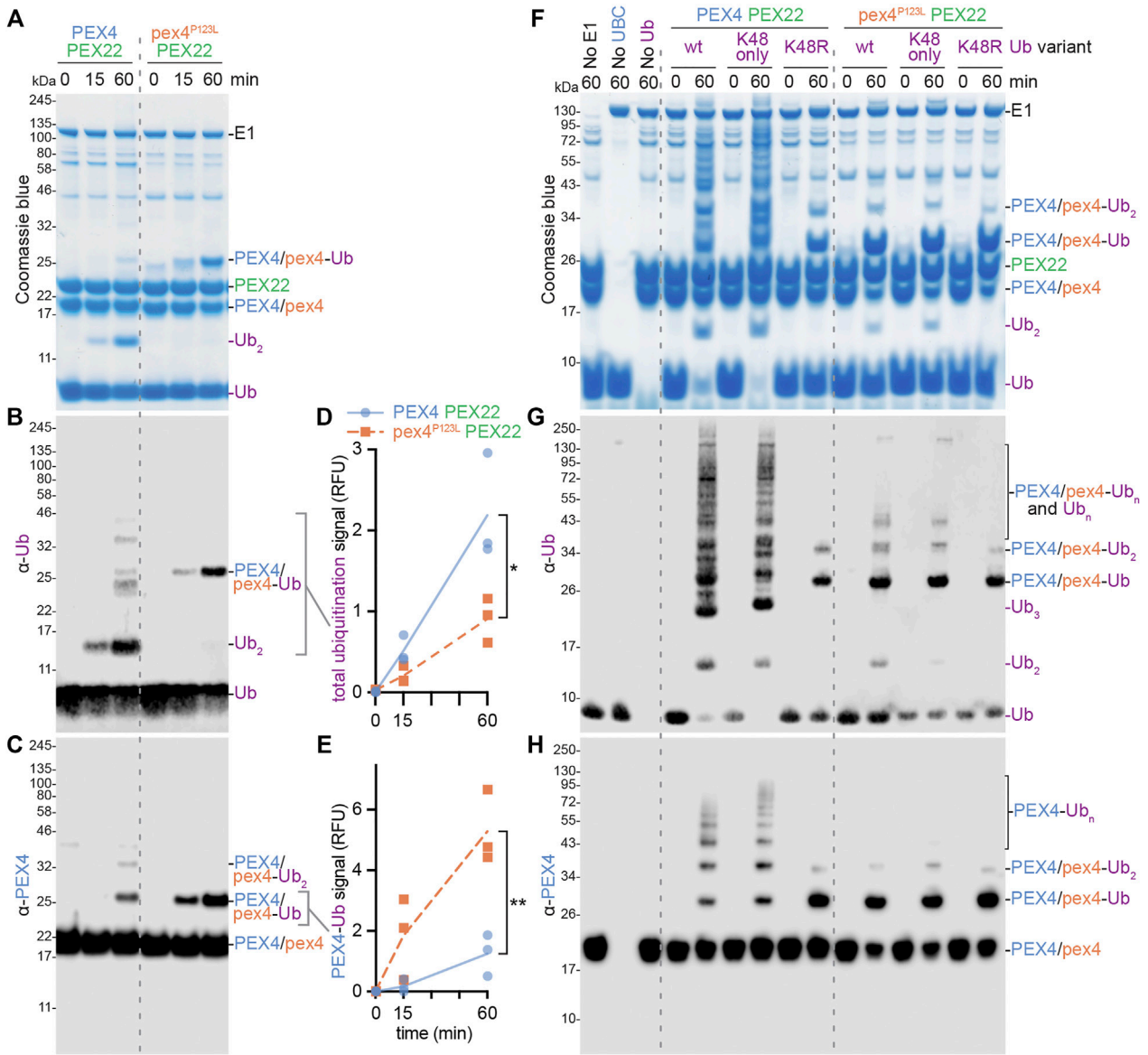

FIGURE 7 | PEX4 builds K48-linked ubiquitin chains and pex4-1 (pex4^{P123L}) displays altered ubiquitination activity *in vitro*. **(A–C)**. Ubiquitination assays containing recombinant human ubiquitin-activating enzyme (E1), *A. thaliana* UBC (either PEX4-PEX22$^{111–283}$ or pex4^{P123L}-PEX22$^{111–283}$), and *A. thaliana* ubiquitin (Ub) were initiated by ATP addition and stopped at the indicated timepoints. The resulting samples were analyzed by SDS-PAGE followed by Coomassie staining **(A)** or immunoblotting with α-Ub **(B)** or α-PEX4 **(C)** antibodies. This experiment was conducted three times and representative results are shown. Ub, ubiquitin; Ub_2, diubiquitin. **(D–E)**. Accumulation of various ubiquitinated proteins. Graphs display quantification of signals detected by the α-Ub **(D)** or α-PEX4 **(E)** antibodies in the indicated regions of the immunoblots **(B,C)**. Each point represents the quantification from a technical replicate at the indicated timepoint. The accumulation rate was calculated for each replicate, and the average rate is plotted. Significance was determined by two-tailed t-tests comparing the accumulation rates from pex4^{P123L}-PEX22$^{111–283}$ to PEX4-PEX22$^{111–283}$. Brackets indicate significant differences between PEX4-PEX22$^{111–283}$ and pex4^{P123L}-PEX22$^{111–283}$ rates (*$p < 0.05$; **$p < 0.005$). **(F–H)**. Ubiquitination assays as in panels **A–C** except that various ubiquitin variants were used: *A. thaliana* Ub (wt), human Ub with all lysine residues substituted with arginine except K48 (K48 only), or human Ub with K48 substituted with arginine (K48R). Samples were analyzed by SDS-PAGE followed by Coomassie staining **(F)** or immunoblotting with α-Ub **(G)** or α-PEX4 **(H)** antibodies.

mass over time (**Figures 7A,B,F,G**), indicating that our assay successfully facilitated and detected *in vitro* ubiquitination. Immunoblotting revealed that one of the ubiquitinated proteins detected was PEX4 itself (**Figures 7C,H**), indicating that the wild-type complex was able to ubiquitinate not only ubiquitin but also PEX4. We found that pex4^{P123L}-PEX22$^{111–283}$ displayed somewhat reduced total ubiquitination activity (**Figures 7B,D**). Interestingly, pex4^{P123L}-PEX22$^{111–283}$ accumulated less diubiquitin (**Figures 7A,B,F,G**) and polyubiquitin ladder (**Figure 7B**) but instead accumulated increased levels of monoubiquitinated PEX4 (**Figures 7A–C,E,F,H**). Taken

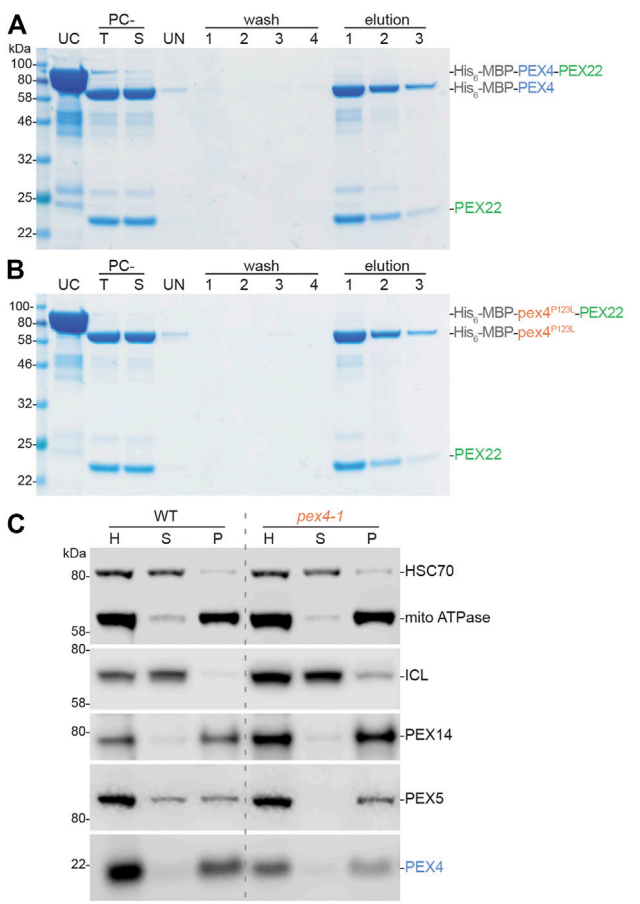

FIGURE 8 | *Arabidopsis* PEX4 and pex4-1 proteins remain associated with PEX22. **A, B.** PEX4 and pex4-1 (pex4^{P123L}) bind PEX22$^{111-283}$ *in vitro*. Purified His$_6$-MBP-PEX4-PEX22$^{111-283}$ **(A)** or His$_6$-MBP-pex4^{P123L}-PEX22$^{111-283}$ **(B)** fusion proteins (UC) were cleaved with PreScission protease, the PreScission-cleaved total (PC-T) reaction was centrifuged to remove insoluble protein, and the supernatant (PC-S) was incubated with Ni-NTA resin. After removing the unbound material (UN), the resin was washed four times in buffer without imidazole to remove unbound proteins (wash 1-4), then washed three times with imidazole to elute His-tagged proteins from the resin (elution 1-3). Equal portions of each fraction were analyzed *via* SDS-PAGE and Coomassie staining. PEX22$^{111-283}$ co-purified similarly with wild-type MBP-PEX4 **(A)** and mutant MBP-pex4^{P123L} **(B)**. **(C)**. PEX4 and pex4-1 are membrane-associated (presumably via PEX22) in plants. Homogenates (H) from 6-day-old dark-grown seedlings were separated by centrifugation to yield soluble (supernatant, S) and insoluble (pellet, P) fractions. Samples were processed for immunoblotting and serially probed with antibodies recognizing HSC70 (soluble protein control), mitochondrial (mito) ATPase (membrane protein control), the peroxisome lumenal protein isocitrate lyase (ICL), and three peroxins (the membrane protein PEX14, the PEX5 receptor for lumenal proteins, and PEX4).

together, these data revealed that the pex4-1 mutation altered PEX4 substrate specificity without abolishing ubiquitination ability.

Ubiquitin contains seven lysine residues (and an N-terminus) that can be sites of ubiquitination; the resultant patterns of mono-, multi-, and poly-ubiquitination can target substrates for various fates (Yau and Rape, 2016). Because yeast Pex4-Pex22 builds K48-linked polyubiquitin chains on Pex4 (Groves et al., 2018), we also assessed PEX4-PEX22$^{111-283}$ and pex4^{P123L}-PEX22$^{111-283}$ activity in the presence of ubiquitin (Ub) in which lysine 48 was replaced with arginine (Ub^{K48R}) and ubiquitin in which all lysines other than K48 were replaced with arginine residues (Ub^{K48only}). We found that ubiquitination patterns and levels were similar when wild-type PEX4-PEX22$^{111-283}$ was provided with Ub or Ub^{K48only} (**Figures 7F–H**). In contrast, only mono- and di-ubiquitinated PEX4, and no polyubiquitin chains, were detected when PEX4-PEX22$^{111-283}$ was provided with Ub^{K48R} (**Figures 7F–H**). These data indicate that PEX4-PEX22$^{111-283}$ built polyubiquitin chains using K48 linkages. The persistence of di-ubiquitinated PEX4 when PEX4-PEX22$^{111-283}$ was provided with Ub^{K48R} (**Figures 7F–H**) indicates that this di-ubiquitin is joined *via* a linkage other than K48, or that PEX4 is monoubiquitinated at two sites.

As with wild-type PEX4-PEX22$^{111-283}$, the small amount of di-ubiquitin detected when pex4^{P123L}-PEX22$^{111-283}$ was incubated with Ub or Ub^{K48only} was abolished when pex4^{P123L}-PEX22$^{111-283}$ was incubated with Ub^{K48R}. Interestingly, the ubiquitination pattern that resulted when PEX4-PEX22$^{111-283}$ was provided with Ub^{K48R} resembled pex4^{P123L}-PEX22$^{111-283}$ provided with any of the ubiquitin variants (**Figures 7G–I**), reinforcing the conclusion that the pex4-1 mutation reduced the ability of PEX4 to build polyubiquitin chains.

PEX4-PEX22 Binding Is Not Notably Impacted by the pex4-1 Mutation

The Pex4-Pex22 complex is tightly bound in fungi, with dissociation constants of 1.9 nM in *O. angusta* (Ali et al., 2018) and 2.0 nM in *S. cerevisiae* (Williams et al., 2012). This tight association is likely explained by the extensive interactions revealed in the Pex4-Pex22 crystal structures (**Figure 5**; Williams et al., 2012; Ali et al., 2018). To assess binding of our recombinant PEX22$^{111-283}$ to PEX4, we purified His$_6$-MBP-PEX4-PEX22$^{111-283}$, used the PreScission protease to release PEX22$^{111-283}$, and then re-purified His$_6$-MBP-PEX4 *via* nickel chromatography. SDS-PAGE (**Figure 8A**) revealed that PEX22$^{111-283}$ remained bound to PEX4 throughout purification following cleavage, consistent with tight binding. We similarly tested pex4-1 in this assay and found that PEX22$^{111-283}$ also co-purified with pex4-1 (**Figure 8B**).

To examine PEX4-PEX22 interactions in an endogenous context, we separated soluble and membrane-bound proteins from seedling extracts *via* centrifugation and examined peroxin localization by immunoblotting (**Figure 8C**). As expected, we found soluble (HSC70) and membrane (mitochondrial ATPase) proteins in the supernatant and pellet, respectively. The peroxisomal membrane peroxin PEX14 was in the pellet fraction, confirming that we had pelleted peroxisomal membranes. In contrast, the peroxisome lumenal protein isocitrate lyase was largely in the supernatant, indicating that the fractionation was not pelleting intact peroxisomes. PEX5 is recycled between the cytosol and the peroxisomal membrane and is found in both soluble and insoluble fractions (Ratzel et al., 2011). As previously reported (Ratzel et al., 2011; Kao and Bartel, 2015), PEX5 was more membrane-associated in *pex4-1* than in wild type (**Figure 8C**),

presumably because PEX5 retrotranslocation from the peroxisomal membrane is reduced in *pex4-1*. Like PEX14, we found PEX4 largely in the pellet fraction in wild type (**Figure 8C**). This localization was unaltered in the *pex4-1* mutant (**Figure 8C**), implying that membrane association, presumably mediated by PEX22 interaction, is not dramatically impacted by the pex4-1 alteration.

DISCUSSION

To deepen our understanding of PEX4 function, PEX4-PEX22 interactions, and the potential molecular consequences of PEX4 mutations, we solved the structure of the *A. thaliana* PEX4-PEX22$^{111-283}$ complex. To promote PEX4 folding, solubility, and enzymatic activity, we co-expressed PEX4 and PEX22 (without the N-terminal transmembrane domain) for structural and biochemical analyses (**Figure 2**). The *A. thaliana* PEX4 sequence is relatively conserved, with over 90% identity with other plant PEX4 orthologs, about 40% identity with yeast Pex4, and 35–40% identity with other *A. thaliana* UBCs (**Figure 1A**). As expected from this sequence conservation, the PEX4-PEX22$^{111-283}$ crystal structure (PDB ID: 6XOD) revealed that PEX4 closely resembles other UBCs, including yeast Pex4 (**Figures 4A,B**). In contrast, PEX22 is much less conserved, and *A. thaliana* PEX22 shares only 55–69% amino acid sequence identity with PEX22 from other angiosperms, and no substantial identity with yeast Pex22 (**Figure 1B**). Despite this notable divergence, *A. thaliana* PEX22 and yeast Pex22 do share similar secondary structural elements that resemble a Rossmann fold (**Figure 4C**; **Supplementary Figure S2**).

When determining the PEX4 structure we were able to use *O. angusta* Pex4 for our initial molecular replacement model, but the PEX22 structure was completed using additional information from *ab initio* modeling. The use of modern modeling methods such as AlphaFold (Jumper et al., 2021) is expected to help in future structure determinations. In fact, the PEX22 structure was submitted as part of the CASP14 (Critical Assessment of Structure Prediction) competition (Ozden et al., 2021), and retrospective analysis showed that the best predicted models of PEX22 alone provided better initial molecular replacement solutions than did our PEX4 homology model.

PEX22 is more than a simple tether anchoring PEX4 to the peroxisomal membrane. For example, *O. angusta* Pex22 appears to activate Pex4 *via* allosteric active site remodeling (Groves et al., 2018). Upon binding to Pex22, an α-helix adjacent to the active-site cysteine in Pex4 relaxes to form a 3_{10} helix (Groves et al., 2018), a motif common in many UBCs (Streich and Lima, 2014). The 3_{10} helix is absent in *O. angusta* Pex4 crystallized without Pex22, and Pex4 without Pex22 is able to ubiquitinate Pex4 but unable to create polyubiquitin chains, hinting that this 3_{10} helix is necessary for full Pex4 activity (Groves et al., 2018). *A. thaliana* PEX4 in our PEX4-PEX22 structure forms the analogous 3_{10} helix near the active site (**Figures 3–5**), suggesting an active conformation. Like the yeast Pex4-Pex22 complex (Groves et al., 2018), the *A. thaliana* PEX4-PEX22 complex can build K48-linked polyubiquitin chains *in vitro* (**Figure 7**). We detected K48-linked polyubiquitin chains both on PEX4 (**Figure 7H**) and on ubiquitin (**Figure 7G**). Free ubiquitin chains were not detected in the yeast studies (Groves et al., 2018), and we did not exclude the possibility that these chains were built on ubiquitin linked *via* a thioester bond to the PEX4 active-site cysteine residue and released upon DTT treatment of the samples prior to electrophoresis.

Interestingly, we found that the *A. thaliana* pex4-1 enzyme is able to ubiquitinate pex4-1 but forms ubiquitin chains inefficiently even in the presence of PEX22 (**Figure 7**), reminiscent of yeast Pex4 in the absence of Pex22 (Groves et al., 2018). However, *A. thaliana* pex4-1 still binds tightly to PEX22 (**Figure 8**). Perhaps the pex4-1 P123L mutation causes a structural perturbation similar to that seen in yeast Pex4 in the absence of Pex22, but without preventing PEX22 binding.

Alternatively, the pex4-1 P123L mutation could alter catalysis more directly. P123 is positioned on a loop near the active site cleft (**Figures 3**, **9A**), and pex4-1 alters the residue immediately following the "gateway residue" implicated in modulating active site access (reviewed in Stewart et al., 2016). This residue is often an aspartate or a serine (e.g., PEX4 S122 in **Figure 1A**), and phosphorylation of a serine at this position may modulate the activity of some human UBCs (reviewed in Stewart et al., 2016). Although S122 adjacent to the pex4-1 mutation is conserved in various PEX4 enzymes (**Figure 1A**), phosphorylation of *A. thaliana* PEX4 has not been reported in phosphoproteomic studies compiled in the PhosPhAt database (Heazlewood et al., 2008). Moreover, the altered *in vitro* pex4-1 activity that we observed with protein purified from *E. coli* indicates that the pex4-1 mutation changes enzymatic activity even in the absence of phosphorylation. The proximity of P123 to the active site cysteine (**Figures 3**, **9A**), along with the modified *in vitro* activity of the pex4-1 enzyme (**Figure 7**), highlights the importance of this loop for UBC activity.

Our crystal structure also provides insight into the expected specificity of the PEX4-PEX22 interaction. Of the 37 predicted or confirmed UBCs in *A. thaliana* (Bachmair et al., 2001; Kraft et al., 2005), only PEX22 is expected to bind PEX4. Comparing the PEX22-binding surface of PEX4 to several other UBCs revealed differences in both hydrophobicity and electrostatics that could contribute to specificity (**Figure 6**). However, we did not directly examine PEX22 interactions with other *A. thaliana* UBCs, and isolation and characterization of a *pex4* null allele will be necessary to definitively determine whether any *A. thaliana* UBCs can substitute for PEX4 *in vivo*. Like yeast and plants, *Trypanosoma brucei* utilizes a PEX4-PEX22 system to ubiquitinate PEX5 (Gualdrón-López et al., 2013). Interestingly, residual lumenal protein import and ubiquitinated PEX5 are observed in a *T. brucei pex4* null mutant, implying that another UBC can partially substitute in the absence of PEX4 in this protozoan (Gualdrón-López et al., 2013). Whether this residual function requires *T. brucei* PEX22 has not been reported.

Although the PEX4 and PEX22 residues involved in salt bridges are conserved in plants (**Figure 1**), the details of the interaction have diverged during evolution. The *S. cerevisiae* and *O. angusta* Pex4-Pex22 interaction surfaces show substantially different electrostatic patterns (**Figures 1**, **5E**), including differently positioned salt bridges (**Figures 5C,E**). Indeed,

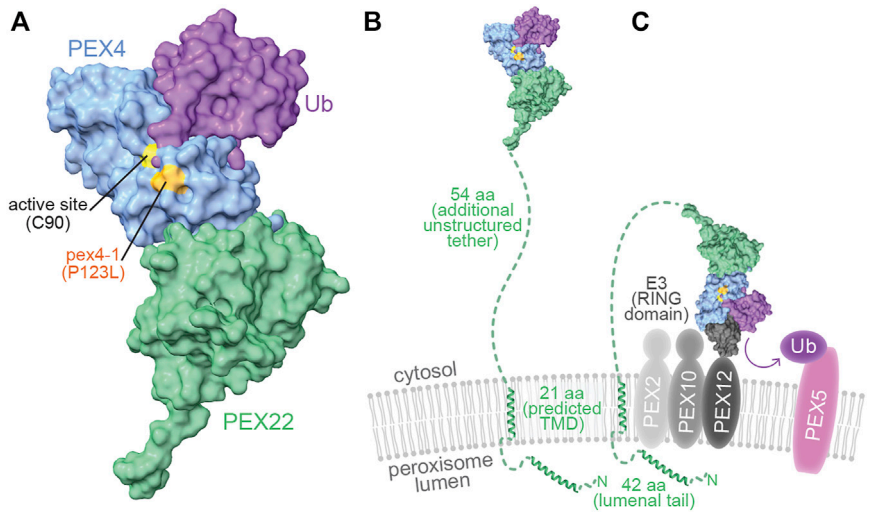

FIGURE 9 | pex4-1 alters a residue near the PEX4 active site and PEX4 may reach distant peroxisomal membrane targets through an unstructured PEX22 tether. **(A)**. When charged, ubiquitin (purple) is predicted to dock onto PEX4 (blue) with the ubiquitin C-terminus nestled within the active site cleft, which is flanked by the residue mutated in pex4-1 (P123). A human UBC-Ub-RING domain co-structure (PDB ID 5FER) was aligned to the PEX4 chain of *At* PEX4-PEX22$^{111-283}$ to show how PEX4 might interact with ubiquitin. **(B)**. The model of PEX4-PEX22-Ub from panel **A** displayed to approximate scale with the peroxisomal membrane. The N-terminal 117 amino acid residues (aa) of PEX22 (dashed green line and ribbon diagrams) were not part of the solved structure and include a peroxisomal lumenal tail predicted to include an alpha helix, a predicted α-helical transmembrane domain (TMD) that anchors PEX22 in the peroxisomal membrane, and an unstructured tether that links the TMD to the PEX4-binding domain of PEX22. The TMD and lumenal ribbon structures were predicted using AlphaFold Monomer v2.0 (Jumper et al., 2021; Varadi et al., 2022). **(C)**. PEX4-PEX22-Ub is predicted to bind the RING domain of the E3 ubiquitin-protein ligases PEX2, PEX10, or PEX12 (charcoal) in the peroxisomal membrane to ubiquitinate substrates including PEX5 (pink). The UBC of a human UBC-Ub-RING domain co-structure (PDB ID 5FER) was aligned to the PEX4 chain of *At* PEX4-PEX22$^{111-283}$ to show how PEX4 (blue) might interact with ubiquitin (purple) and a RING domain (charcoal) to promote substrate (e.g., PEX5) ubiquitination.

although expression of *A. thaliana PEX4* is unable to rescue a *S. cerevisiae pex4* mutant, and *At PEX22* is unable to rescue a *Sc pex22* mutant, expressing *At PEX4* and *At PEX22* together rescue either *Sc pex4* or *pex22* mutants (Zolman et al., 2005). These experiments reveal that *At* PEX4 is active in yeast when bound to *At* PEX22 and imply that *At* PEX4 does not bind to *Sc* Pex22 and that *Sc* Pex4 does not bind to *At* PEX22.

The PEX4-PEX22 interface covers about 800 Å^2, which is smaller than many heterodimer interfaces with nM dissociation constants (Chen et al., 2013). The strong affinity (~2 nM dissociation constants) of the yeast Pex4-Pex22 complexes (Williams et al., 2012; Groves et al., 2018) is likely shared by the *A. thaliana* PEX4-PEX22 complex; we did not find non-denaturing conditions that dissociated PEX4 and PEX22 (**Figure 8** and data not shown). It is likely that multiple features contribute to this tight binding. The hydrophobic residue Y172 at the Pex22-interacting surface of *Sc* Pex4 is necessary for *Sc* Pex4-Pex22 binding (Williams et al., 2012). The central hydrophobic patches on the interacting surfaces of Pex4 and Pex22 appear to be conserved across *A. thaliana*, *S. cerevisiae*, and *O. angusta* (**Figure 5D**), suggesting that the central hydrophobic region is important for PEX4-PEX22 binding. Taken together, these data imply that the tight binding of PEX4-PEX22 is dominated by conserved hydrophobic interactions at the center of the interaction surface, while binding specificity is controlled by flanking non-conserved salt bridges.

As a UBC, PEX4 is expected to have multiple interacting partners beyond PEX22, including ubiquitin, the ubiquitin-activating enzyme, and the RING-type ubiquitin-protein ligases, PEX2, PEX10, and PEX12. Structural studies of other UBCs have revealed that the ubiquitin-activating enzyme and the RING domains of ubiquitin protein ligases bind to overlapping surfaces on the active-site face and top of the UBC (Olsen and Lima, 2013; Koliopoulos et al., 2016). Thus, PEX4 presumably alternates between binding the ubiquitin-activating enzyme to receive ubiquitin and binding the RING peroxins to ubiquitinate substrates. The position of the PEX22-binding surface on the bottom of PEX4 (**Figures 3**, **9**) is distinct from the predicted ubiquitin-activating enzyme (not shown) and RING interaction surfaces (**Figure 9C**). This use of non-overlapping interaction surfaces, along with the tight binding of PEX4 to PEX22 (**Figure 8**) implies that PEX4 can cycle through ubiquitin loading and delivery without releasing PEX22.

In addition to interactions with the other enzymes in the ubiquitination cascade, several UBCs non-covalently bind ubiquitin, ubiquitin chains, or ubiquitin-like proteins on the "backside" of the enzyme (reviewed in Stewart et al., 2016). This binding can provide allosteric regulation to increase chain-building processivity. Moreover, Ubc7, which acts in ER-associated protein degradation, binds the Cue1 ER tether *via* the backside (reviewed in Stewart et al., 2016). Cue1 binding of the Ubc7 backside both tethers Ubc7 to the ER and increases Ubc7-RING domain binding affinity (Metzger et al., 2013). Similarly, membrane-anchored ubiquitin fold (MUB) proteins tether UBCs to the plasma membrane *via* backside binding (Lu et al., 2016). Unlike these other tethered UBCs, the backside of

PEX4 appears to remain free for additional interactions even when PEX4 is tethered to the peroxisomal membrane *via* PEX22 binding (**Figure 3**), providing additional opportunities for allosteric regulation.

The PEX4-PEX22 structure illuminates potential molecular consequences of the *pex4-1* missense mutation. The mutated P123 residue is positioned on the protein surface ~6 Å from the PEX4 active site C90 residue (**Figures 3**, **9A**). To visualize this pex4-1 alteration and the PEX4-PEX22 interaction surface in relation to other expected PEX4 binding partners, we modeled possible PEX4 interactions with ubiquitin (**Figure 9A**) and the RING domain of a ubiquitin-protein ligase (**Figure 9C**). This modeling took advantage of the similarity of the PEX4 structure to other UBCs, including a human UBC that has been co-crystalized with ubiquitin and a RING domain (Koliopoulos et al., 2016; PDB 5FER). Our model predicts that the residue altered by the pex4-1 mutation (P123) borders the active site cleft that holds the C-terminal tail of ubiquitin (**Figure 9A**) and is consistent with the altered *in vitro* ubiquitination selectivity of pex4^{P123L}-PEX22$^{111-283}$ (**Figure 7**).

The availability of enzymatically active *A. thaliana* PEX4 and pex4-1 (**Figure 7**) will enable future biochemical and structural studies with PEX4, the RING peroxins, and their various substrates. The three RING peroxins form a complex (El Magraoui et al., 2012) and act non-redundantly to maintain peroxisome function. In yeast, Pex12 works with Pex4 to monoubiquitinate Pex5 for recycling, Pex2 works with the cytosolic Ubc4 to polyubiquitinate Pex5 for degradation (Kragt et al., 2005; Williams et al., 2008; Platta et al., 2009), and Pex10 enhances both activities (El Magraoui et al., 2012). Interestingly, *Sc* Ubc4 targets Pex5 lysine residues, whereas *Sc* Pex4 ubiquitinates Pex5 on a conserved cysteine residue *in vivo* (Williams et al., 2007); the analogous PEX5 cysteine residue is also ubiquitinated in mammalian cells (Carvalho et al., 2007). Although PEX5 ubiquitination has not been directly demonstrated in plants, the relevant cysteine residue is conserved, and accumulating indirect evidence supports the hypothesis that PEX5 ubiquitination is necessary for PEX5 recycling in *A. thaliana*. *At* PEX5 is more membrane associated in *pex4* mutants than in wild type (**Figure 8C**; Ratzel et al., 2011; Kao and Bartel, 2015), suggesting that PEX4 is involved in the ubiquitination needed to remove PEX5 from the peroxisomal membrane. Moreover, *At* PEX5 levels are decreased in most *pex6* mutants (Zolman and Bartel, 2004; Gonzalez et al., 2017, 2018), which are defective in an ATPase implicated in retrotranslocating ubiquitinated PEX5 from the membrane. In addition, PEX5 levels are restored in *pex6-1* double mutants with *pex4-1* (Ratzel et al., 2011) or *pex2-1* (Burkhart et al., 2014). These data implicate *At* PEX4 in the PEX5 degradation that ensues when PEX5 recycling is slowed. Together, these studies suggest that PEX4 ubiquitinates PEX5 for both recycling and degradation in plants, and it will be interesting to learn if this ubiquitination can be reconstituted *in vitro*. The RING peroxins are also implicated in ubiquitination and degradation of other proteins in the peroxisomal membrane (Williams and van der Klei, 2013; Chen et al., 2018). The *A. thaliana* RING peroxins are essential for embryogenesis (Schumann et al., 2003; Sparkes et al., 2003; Fan et al., 2005; Prestele et al., 2010) and RING domains of *At* PEX2, PEX10, and PEX12 display *in vitro* monoubiquitination activity when paired with human UBCH5b/c (Kaur et al., 2012). Future studies may reveal how RING peroxin activity is impacted by *A. thaliana* PEX4 versus cytosolic UBCs.

Although not part of our crystal structure, a 62-amino acid tether links the N-terminus of α-helix 1 of the structured region of PEX22 to the C-terminal end of the *At* PEX22 predicted transmembrane domain (**Figure 9B**). This tether is poorly conserved (**Figure 1B**) and lacks confidently predicted secondary structure (Jumper et al., 2021). The corresponding regions separating the N-termini of the first yeast Pex22 structural elements (β-strand 1; **Supplementary Figure S2**) from the C-termini of the predicted transmembrane domains also lack predicted secondary structure but are considerably shorter (21-25 aa; **Figure 1B**). An extended conformation and lack of secondary structure in this linker region would allow *At* PEX4 to reach relatively distant targets (~200 Å) on the peroxisomal membrane (**Figure 9C**). It will be interesting to learn the full repertoire of PEX4 substrates, and whether the lengthening of this tether in plants (**Figure 1B**) has functional significance.

DATA AVAILABILITY STATEMENT

The original contributions presented in the study are included in the article/**Supplementary Material**, further inquiries can be directed to the corresponding author.

AUTHOR CONTRIBUTIONS

MST, SEB, JLO, ZJW, GNP, and BB conceived the study and designed the research. MST, SEB, JLO, and WX performed the research. MST, SEB, JLO, MDM, GNP, and BB analyzed the data. MST, SEB, and BB wrote the manuscript with input from all authors.

FUNDING

This research was supported by the National Institutes of Health (NIH; R35GM130338 to BB), the Robert A. Welch Foundation (C-1309 to BB), and the National Science Foundation (NSF) Science and Technology Center 'BioXFEL' award STC-1231306 (to GNP). SEB was supported in part by a supplement to STC-1231306. JLO was supported in part by the NSF (Graduate Research Fellowship Program grant no. 1450681). The content is solely the responsibility of the authors and does not necessarily represent the official views of the NIH or the NSF.

ACKNOWLEDGMENTS

We thank Yun-Ting Kao for piloting the fractionation experiment, Scott Gradia for the pET vector, and Gabrielle Buck, Yun-Ting Kao, Roxanna Llinas, DurreShahwar Muhammad, Kathryn Smith, and Nathan Tharp for critical comments on the manuscript. This research used resources of

the Advanced Photon Source, a U.S. Department of Energy (DOE) Office of Science User Facility operated for the DOE Office of Science by Argonne National Laboratory under Contract No. DE-AC02-06CH11357. GM/CA-CAT at APS has been funded by the National Cancer Institute (ACB-12002) and the National Institute of General Medical Sciences (AGM-12006, P30GM138396). The Eiger 16M detector at GM/CA-XSD was funded by NIH grant S10 OD012289. Molecular graphics and analyses were performed with UCSF ChimeraX, developed by the Resource for Biocomputing, Visualization, and Informatics at the University of California, San Francisco, with support from NIH R01-GM129325 and the Office of Cyber Infrastructure and Computational Biology, National Institute of Allergy and Infectious Diseases.

SUPPLEMENTARY MATERIAL

The Supplementary Material for this article can be found online at: https://www.frontiersin.org/articles/10.3389/fcell.2022.838923/full#supplementary-material

REFERENCES

Ali, A. M., Atmaj, J., Adawy, A., Lunev, S., Van Oosterwijk, N., Yan, S. R., et al. (2018). The Pex4p-Pex22p Complex from *Hansenula polymorpha*: Biophysical Analysis, Crystallization and X-ray Diffraction Characterization. *Acta Cryst. Sect F* 74, 76–81. doi:10.1107/s2053230x17018428

Alonso, J. M., Stepanova, A. N., Leisse, T. J., Kim, C. J., Chen, H., Shinn, P., et al. (2003). Genome-Wide Insertional Mutagenesis of *Arabidopsis thaliana*. *Science* 301, 653–657. doi:10.1126/science.1086391

Bachmair, A., Novatchkova, M., Potuschak, T., and Eisenhaber, F. (2001). Ubiquitylation in Plants: a Post-genomic Look at a Post-translational Modification. *Trends Plant Sci.* 6, 463–470. doi:10.1016/s1360-1385(01)02080-5

Berman, H., Henrick, K., and Nakamura, H. (2003). Announcing the Worldwide Protein Data Bank. *Nat. Struct. Mol. Biol.* 10, 980. doi:10.1038/nsb1203-980

Burkhart, S. E., Kao, Y.-T., and Bartel, B. (2014). Peroxisomal Ubiquitin-Protein Ligases Peroxin2 and Peroxin10 Have Distinct but Synergistic Roles in Matrix Protein Import and Peroxin5 Retrotranslocation in *Arabidopsis*. *Plant Physiol.* 166, 1329–1344. doi:10.1104/pp.114.247148

Carvalho, A. F., Pinto, M. P., Grou, C. P., Alencastre, I. S., Fransen, M., Sá-Miranda, C., et al. (2007). Ubiquitination of Mammalian Pex5p, the Peroxisomal Import Receptor. *J. Biol. Chem.* 282, 31267–31272. doi:10.1074/jbc.m706325200

Chen, J., Sawyer, N., and Regan, L. (2013). Protein-protein Interactions: General Trends in the Relationship between Binding Affinity and Interfacial Buried Surface Area. *Protein Sci.* 22, 510–515. doi:10.1002/pro.2230

Chen, X., Devarajan, S., Danda, N., and Williams, C. (2018). Insights into the Role of the Peroxisomal Ubiquitination Machinery in Pex13p Degradation in the Yeast *Hansenula polymorpha*. *J. Mol. Biol.* 430, 1545–1558. doi:10.1016/j.jmb.2018.03.033

Doerks, T., Copley, R. R., Schultz, J., Ponting, C. P., and Bork, P. (2002). Systematic Identification of Novel Protein Domain Families Associated with Nuclear Functions. *Genome Res.* 12, 47–56. doi:10.1101/gr.203201

El Magraoui, F., Bäumer, B. E., Platta, H. W., Baumann, J. S., Girzalsky, W., and Erdmann, R. (2012). The RING-type Ubiquitin Ligases Pex2p, Pex10p and Pex12p Form a Heteromeric Complex that Displays Enhanced Activity in an Ubiquitin Conjugating Enzyme-Selective Manner. *FEBS J.* 279, 2060–2070. doi:10.1111/j.1742-4658.2012.08591.x

El Magraoui, F., Schrötter, A., Brinkmeier, R., Kunst, L., Mastalski, T., Müller, T., et al. (2014). The Cytosolic Domain of Pex22p Stimulates the Pex4p-dependent Ubiquitination of the PTS1-Receptor. *PloS One* 9, e105894. doi:10.1371/journal.pone.0105894

Emsley, P., Lohkamp, B., Scott, W. G., and Cowtan, K. (2010). Features and Development of *Coot*. *Acta Crystallogr. D Biol. Cryst.* 66, 486–501. doi:10.1107/s0907444910007493

Evans, P. R., and Murshudov, G. N. (2013). How Good Are My Data and What Is the Resolution? *Acta Crystallogr. D Biol. Cryst.* 69, 1204–1214. doi:10.1107/s0907444913000061

Fan, J., Quan, S., Orth, T., Awai, C., Chory, J., and Hu, J. (2005). The *Arabidopsis PEX12* Gene Is Required for Peroxisome Biogenesis and Is Essential for Development. *Plant Physiol.* 139, 231–239. doi:10.1104/pp.105.066811

Gibson, D. G., Young, L., Chuang, R.-Y., Venter, J. C., Hutchison, C. A., and Smith, H. O. (2009). Enzymatic Assembly of DNA Molecules up to Several Hundred Kilobases. *Nat. Methods* 6, 343–345. doi:10.1038/nmeth.1318

Goddard, T. D., Huang, C. C., Meng, E. C., Pettersen, E. F., Couch, G. S., Morris, J. H., et al. (2018). UCSF ChimeraX: Meeting Modern Challenges in Visualization and Analysis. *Protein Sci.* 27, 14–25. doi:10.1002/pro.3235

Gonzalez, K. L., Ratzel, S. E., Burks, K. H., Danan, C. H., Wages, J. M., Zolman, B. K., et al. (2018). A *pex1* Missense Mutation Improves Peroxisome Function in a Subset of *Arabidopsis pex6* Mutants without Restoring PEX5 Recycling. *Proc. Natl. Acad. Sci. U S A.* 115, E3163–E3172. doi:10.1073/pnas.1721279115

Gonzalez, K. L., Fleming, W. A., Kao, Y. T., Wright, Z. J., Venkova, S. V., Ventura, M. J., et al. (2017). Disparate Peroxisome-related Defects in Arabidopsis *pex6* and *pex26* Mutants Link Peroxisomal Retrotranslocation and Oil Body Utilization. *Plant J.* 92, 110–128. doi:10.1111/tpj.13641

Grou, C. P., Carvalho, A. F., Pinto, M. P., Wiese, S., Piechura, H., Meyer, H. E., et al. (2008). Members of the E2D (UbcH5) Family Mediate the Ubiquitination of the Conserved Cysteine of Pex5p, the Peroxisomal Import Receptor. *J. Biol. Chem.* 283, 14190–14197. doi:10.1074/jbc.m800402200

Groves, M. R., Schroer, C. F. E., Middleton, A. J., Lunev, S., Danda, N., Ali, A. M., et al. (2018). Structural Insights into K48-Linked Ubiquitin Chain Formation by the Pex4p-Pex22p Complex. *Biochem. Biophysical Res. Commun.* 496, 562–567. doi:10.1016/j.bbrc.2017.12.150

Gualdrón-López, M., Chevalier, N., Van Der Smissen, P., Courtoy, P. J., Rigden, D. J., and Michels, P. A. M. (2013). Ubiquitination of the Glycosomal Matrix Protein Receptor PEX5 in *Trypanosoma Brucei* by PEX4 Displays Novel Features. *Biochim. Biophys. Acta (Bba) - Mol. Cel Res.* 1833, 3076–3092. doi:10.1016/j.bbamcr.2013.08.008

Haughn, G. W., and Somerville, C. (1986). Sulfonylurea-resistant Mutants of *Arabidopsis thaliana*. *Mol. Gen Genet* 204, 430–434. doi:10.1007/bf00331020

Heazlewood, J. L., Durek, P., Hummel, J., Selbig, J., Weckwerth, W., Walther, D., et al. (2008). PhosPhAt: a Database of Phosphorylation Sites in *Arabidopsis thaliana* and a Plant-specific Phosphorylation Site Predictor. *Nucleic Acids Res.* 36, D1015–D1021. doi:10.1093/nar/gkm812

Holm, L. (2020). "Using Dali for Protein Structure Comparison," in *Structural Bioinformatics. Methods in Molecular Biology*. Editor Z. Gáspári (New York, NY: Humana Press) 2212, 29–42. doi:10.1007/978-1-0716-0270-6_3

Jaroszewski, L., Rychlewski, L., Li, Z., Li, W., and Godzik, A. (2005). FFAS03: a Server for Profile-Pprofile Sequence Alignments. *Nucleic Acids Res.* 33, W284–W288. doi:10.1093/nar/gki418

Jin, S., Miller, M. D., Chen, M., Schafer, N. P., Lin, X., Chen, X., et al. (2020). Molecular-replacement Phasing Using Predicted Protein Structures from AWSEM-Suite. *Int. Union Crystallogr. J.* 7, 1168–1178. doi:10.1107/s2052252520013494

Jumper, J., Evans, R., Pritzel, A., Green, T., Figurnov, M., Ronneberger, O., et al. (2021). Highly Accurate Protein Structure Prediction with AlphaFold. *Nature* 596, 583–589. doi:10.1038/s41586-021-03819-2

Kabsch, W. (2010) *XDS*. *Acta Crystallogr. D Biol. Cryst.* 66, 125–132. doi:10.1107/s0907444909047337

Kao, Y.-T., Fleming, W. A., Ventura, M. J., and Bartel, B. (2016). Genetic Interactions between *PEROXIN12* and Other Peroxisome-Associated Ubiquitination Components. *Plant Physiol.* 172, 1643–1656. doi:10.1104/pp.16.01211

Kao, Y.-T., Gonzalez, K. L., and Bartel, B. (2018). Peroxisome Function, Biogenesis, and Dynamics in Plants. *Plant Physiol.* 176, 162–177. doi:10.1104/pp.17.01050

Kao, Y. T., and Bartel, B. (2015). Elevated Growth Temperature Decreases Levels of the PEX5 Peroxisome-Targeting Signal Receptor and Ameliorates Defects of

Arabidopsis Mutants with an Impaired PEX4 Ubiquitin-Conjugating Enzyme. *BMC Plant Biol.* 15, 224. doi:10.1186/s12870-015-0605-3

Kaur, N., Zhao, Q., Xie, Q., and Hu, J. (2012). Arabidopsis RING Peroxins Are E3 Ubiquitin Ligases that Interact with Two Homologous Ubiquitin Receptor Proteins. *J. Integr. Plant Biol.* 55, 108–120. doi:10.1111/jipb.12014

Koliopoulos, M. G., Esposito, D., Christodoulou, E., Taylor, I. A., and Rittinger, K. (2016). Functional Role of TRIM E3 Ligase Oligomerization and Regulation of Catalytic Activity. *EMBO J.* 35, 1204–1218. doi:10.15252/embj.201593741

Koller, A., Snyder, W. B., Faber, K. N., Wenzel, T. J., Rangell, L., Keller, G. A., et al. (1999). Pex22p of *Pichia pastoris*, Essential for Peroxisomal Matrix Protein Import, Anchors the Ubiquitin-Conjugating Enzyme, Pex4p, on the Peroxisomal Membrane. *J. Cel Biol* 146, 99–112. doi:10.1083/jcb.146.1.99

Kraft, E., Stone, S. L., Ma, L., Su, N., Gao, Y., Lau, O.-S., et al. (2005). Genome Analysis and Functional Characterization of the E2 and RING-type E3 Ligase Ubiquitination Enzymes of *Arabidopsis*. *Plant Physiol.* 139, 1597–1611. doi:10.1104/pp.105.067983

Kragt, A., Voorn-Brouwer, T., van den Berg, M., and Distel, B. (2005). The *Saccharomyces cerevisiae* Peroxisomal Import Receptor Pex5p Is Monoubiquitinated in Wild Type Cells. *J. Biol. Chem.* 280, 7867–7874. doi:10.1074/jbc.m413553200

Krissinel, E., and Henrick, K. (2007). Inference of Macromolecular Assemblies from Crystalline State. *J. Mol. Biol.* 372, 774–797. doi:10.1016/j.jmb.2007.05.022

Langer, G., Cohen, S. X., Lamzin, V. S., and Perrakis, A. (2008). Automated Macromolecular Model Building for X-ray Crystallography Using ARP/wARP Version 7. *Nat. Protoc.* 3, 1171–1179. doi:10.1038/nprot.2008.91

Laskowski, R. A., Jabłońska, J., Pravda, L., Vařeková, R. S., and Thornton, J. M. (2018). PDBsum: Structural Summaries of PDB Entries. *Protein Sci.* 27, 129–134. doi:10.1002/pro.3289

Lee, M. S., Mullen, R. T., and Trelease, R. N. (1997). Oilseed Isocitrate Lyases Lacking Their Essential Type 1 Peroxisomal Targeting Signal Are Piggybacked to Glyoxysomes. *Plant Cell* 9, 185–197. doi:10.1105/tpc.9.2.185

Liebschner, D., Afonine, P. V., Baker, M. L., Bunkóczi, G., Chen, V. B., Croll, T. I., et al. (2019). Macromolecular Structure Determination Using X-Rays, Neutrons and Electrons: Recent Developments in Phenix. *Acta Cryst. Sect D Struct. Biol.* 75, 861–877. doi:10.1107/s2059798319011471

Lingard, M. J., Monroe-Augustus, M., and Bartel, B. (2009). Peroxisome-associated Matrix Protein Degradation in *Arabidopsis*. *Proc. Natl. Acad. Sci.* 106, 4561–4566. doi:10.1073/pnas.0811329106

Lu, X., Malley, K. R., Brenner, C. C., Koroleva, O., Korolev, S., and Downes, B. P. (2016). A MUB E2 Structure Reveals E1 Selectivity between Cognate Ubiquitin E2s in Eukaryotes. *Nat. Commun.* 7, 12580. doi:10.1038/ncomms12580

Maeshima, M., Yokoi, H., and Asahi, T. (1988). Evidence for No Proteolytic Processing during Transport of Isocitrate Lyase into Glyoxysomes in Castor Bean Endosperm. *Plant Cel Physiol.* 29, 381–384.

McCoy, A. J., Grosse-Kunstleve, R. W., Adams, P. D., Winn, M. D., Storoni, L. C., and Read, R. J. (2007). *Phaser* Crystallographic Software. *J. Appl. Cryst.* 40, 658–674. doi:10.1107/s0021889807021206

McNew, J. A., and Goodman, J. M. (1994). An Oligomeric Protein Is Imported into Peroxisomes *In Vivo*. *J. Cel Biol* 127, 1245–1257. doi:10.1083/jcb.127.5.1245

Metzger, M. B., Liang, Y.-H., Das, R., Mariano, J., Li, S., Li, J., et al. (2013). A Structurally Unique E2-Binding Domain Activates Ubiquitination by the ERAD E2, Ubc7p, through Multiple Mechanisms. *Mol. Cel* 50, 516–527. doi:10.1016/j.molcel.2013.04.004

Morin, A., Eisenbraun, B., Key, J., Sanschagrin, P. C., Timony, M. A., Ottaviano, M., et al. (2013). Collaboration Gets the Most Out of Software. *ELife* 2, e01456. doi:10.7554/eLife.01456

Mullen, R. T., Flynn, C. R., and Trelease, R. N. (2001). How Are Peroxisomes Formed? The Role of the Endoplasmic Reticulum and Peroxins. *Trends Plant Sci.* 6, 256–261. doi:10.1016/s1360-1385(01)01951-3

Olsen, S. K., and Lima, C. D. (2013). Structure of a Ubiquitin E1-E2 Complex: Insights to E1-E2 Thioester Transfer. *Mol. Cel* 49, 884–896. doi:10.1016/j.molcel.2013.01.013

Ozden, B., Kryshtafovych, A., and Karaca, E. (2021). Assessment of the CASP14 Assembly Predictions. *Proteins* 89, 1787–1799. doi:10.1002/prot.26199

Pettersen, E. F., Goddard, T. D., Huang, C. C., Meng, E. C., Couch, G. S., Croll, T. I., et al. (2021). UCSF ChimeraX: Structure Visualization for Researchers, Educators, and Developers. *Protein Sci.* 30, 70–82. doi:10.1002/pro.3943

Platta, H. W., El Magraoui, F., Bäumer, B. E., Schlee, D., Girzalsky, W., and Erdmann, R. (2009). Pex2 and Pex12 Function as Protein-Ubiquitin Ligases in Peroxisomal Protein Import. *Mol. Cel Biol* 29, 5505–5516. doi:10.1128/mcb.00388-09

Platta, H. W., Magraoui, F. E., Schlee, D., Grunau, S., Girzalsky, W., and Erdmann, R. (2007). Ubiquitination of the Peroxisomal Import Receptor Pex5p Is Required for its Recycling. *J. Cel Biol* 177, 197–204. doi:10.1083/jcb.200611012

Prestele, J., Hierl, G., Scherling, C., Hetkamp, S., Schwechheimer, C., Isono, E., et al. (2010). Different Functions of the C3HC4 Zinc RING finger Peroxins PEX10, PEX2, and PEX12 in Peroxisome Formation and Matrix Protein Import. *Proc. Natl. Acad. Sci.* 107, 14915–14920. doi:10.1073/pnas.1009174107

Ratzel, S. E., Lingard, M. J., Woodward, A. W., and Bartel, B. (2011). Reducing *PEX13* Expression Ameliorates Physiological Defects of Late-Acting Peroxin Mutants. *Traffic* 12, 121–134. doi:10.1111/j.1600-0854.2010.01136.x

Reumann, S., and Bartel, B. (2016). Plant Peroxisomes: Recent Discoveries in Functional Complexity, Organelle Homeostasis, and Morphological Dynamics. *Curr. Opin. Plant Biol.* 34, 17–26. doi:10.1016/j.pbi.2016.07.008

Robert, X., and Gouet, P. (2014). Deciphering Key Features in Protein Structures with the New ENDscript Server. *Nucleic Acids Res.* 42, W320–W324. doi:10.1093/nar/gku316

Schumann, U., Wanner, G., Veenhuis, M., Schmid, M., and Gietl, C. (2003). *AthPEX10*, a Nuclear Gene Essential for Peroxisome and Storage Organelle Formation during *Arabidopsis* Embryogenesis. *Proc. Natl. Acad. Sci.* 100, 9626–9631. doi:10.1073/pnas.1633697100

Sheldrick, G. M. (2008). A Short History of *SHELX*. *Acta Cryst. Sect A.* 64, 112–122. doi:10.1107/s0108767307043930

Shin, W.-H., and Kihara, D. (2019). "55 Years of the Rossmann Fold," in *Protein Supersecondary Structures. Methods in Molecular Biology*. Editor A. Kister (New York, NY: Humana Press) 1958, 1–13. doi:10.1007/978-1-4939-9161-7_1

Sparkes, I. A., Brandizzi, F., Slocombe, S. P., El-Shami, M., Hawes, C., and Baker, A. (2003). An *Arabidopsis pex10* Null Mutant Is Embryo Lethal, Implicating Peroxisomes in an Essential Role during Plant Embryogenesis. *Plant Physiol.* 133, 1809–1819. doi:10.1104/pp.103.031252

Stewart, M. D., Ritterhoff, T., Klevit, R. E., and Brzovic, P. S. (2016). E2 Enzymes: More Than Just Middle Men. *Cell Res* 26, 423–440. doi:10.1038/cr.2016.35

Streich, F. C., and Lima, C. D. (2014). Structural and Functional Insights to Ubiquitin-like Protein Conjugation. *Annu. Rev. Biophys.* 43, 357–379. doi:10.1146/annurev-biophys-051013-022958

Sundquist, W. I., Schubert, H. L., Kelly, B. N., Hill, G. C., Holton, J. M., and Hill, C. P. (2004). Ubiquitin Recognition by the Human TSG101 Protein. *Mol. Cel* 13, 783–789. doi:10.1016/s1097-2765(04)00129-7

Thorn, A., and Sheldrick, G. M. (2013). Extending Molecular-Replacement Solutions with *SHELXE*. *Acta Crystallogr. D Biol. Cryst.* 69, 2251–2256. doi:10.1107/s0907444913027534

Tropea, J. E., Cherry, S., and Waugh, D. S. (2009). "Expression and Purification of Soluble His6-Tagged TEV Protease," in *High Throughput Protein Expression and Purification: Methods and Protocols*. Editor S. A. Doyle (New York, NY: Humana Press), 297–307. doi:10.1007/978-1-59745-196-3_19

Varadi, M., Anyango, S., Deshpande, M., Nair, S., Natassia, C., Yordanova, G., et al. (2022). AlphaFold Protein Structure Database: Massively Expanding the Structural Coverage of Protein-Sequence Space with High-Accuracy Models. *Nucleic Acids Res.* 50, D439–D444. doi:10.1093/nar/gkab1061

Vonrhein, C., Flensburg, C., Keller, P., Sharff, A., Smart, O., Paciorek, W., et al. (2011). Data Processing and Analysis with the *autoPROC* toolbox. *Acta Crystallogr. D Biol. Cryst.* 67, 293–302. doi:10.1107/s0907444911007773

Williams, C., van den Berg, M., Geers, E., and Distel, B. (2008). Pex10p Functions as an E3 Ligase for the Ubc4p-dependent Ubiquitination of Pex5p. *Biochem. Biophysical Res. Commun.* 374, 620–624. doi:10.1016/j.bbrc.2008.07.054

Williams, C., van den Berg, M., Panjikar, S., Stanley, W. A., Distel, B., and Wilmanns, M. (2012). Insights into Ubiquitin-Conjugating Enzyme/Co-activator Interactions from the Structure of the Pex4p:Pex22p Complex. *EMBO J.* 31, 391–402. doi:10.1038/emboj.2011.411

Williams, C., van den Berg, M., Sprenger, R. R., and Distel, B. (2007). A Conserved Cysteine Is Essential for Pex4p-dependent Ubiquitination of the Peroxisomal Import Receptor Pex5p. *J. Biol. Chem.* 282, 22534–22543. doi:10.1074/jbc.m702038200

Williams, C., and van der Klei, I. J. (2013). Pexophagy-linked Degradation of the Peroxisomal Membrane Protein Pex3p Involves the Ubiquitin-Proteasome System. *Biochem. Biophysical Res. Commun.* 438, 395–401. doi:10.1016/j.bbrc.2013.07.086

Winn, M. D., Ballard, C. C., Cowtan, K. D., Dodson, E. J., Emsley, P., Evans, P. R., et al. (2011). Overview of the *CCP4* Suite and Current Developments. *Acta Crystallogr. D Biol. Cryst.* 67, 235–242. doi:10.1107/s0907444910045749

Yau, R., and Rape, M. (2016). The Increasing Complexity of the Ubiquitin Code. *Nat. Cel Biol* 18, 579–586. doi:10.1038/ncb3358

Yennamalli, R., Arangarasan, R., Bryden, A., Gleicher, M., and Phillips, G. N., Jr. (2014). Using a Commodity High-Definition Television for Collaborative Structural Biology. *J. Appl. Cryst.* 47, 1153–1157. doi:10.1107/s160057671400939x

Zolman, B. K., and Bartel, B. (2004). An *Arabidopsis* Indole-3-Butyric Acid-Response Mutant Defective in PEROXIN6, an Apparent ATPase Implicated in Peroxisomal Function. *Proc. Natl. Acad. Sci.* 101, 1786–1791. doi:10.1073/pnas.0304368101

Zolman, B. K., Monroe-Augustus, M., Silva, I. D., and Bartel, B. (2005). Identification and Functional Characterization of *Arabidopsis* PEROXIN4 and the Interacting Protein PEROXIN22. *The Plant Cell* 17, 3422–3435. doi:10.1105/tpc.105.035691

Zolman, B. K., Yoder, A., and Bartel, B. (2000). Genetic Analysis of Indole-3-Butyric Acid Responses in *Arabidopsis thaliana* Reveals Four Mutant Classes. *Genetics* 156, 1323–1337. doi:10.1093/genetics/156.3.1323

Conflict of Interest: The authors declare that the research was conducted in the absence of any commercial or financial relationships that could be construed as a potential conflict of interest.

frontiers | Frontiers in Cell and Developmental Biology

ORIGINAL RESEARCH
published: 04 April 2022
doi: 10.3389/fcell.2022.871977

Human Cytomegalovirus vMIA Inhibits MAVS Oligomerization at Peroxisomes in an MFF-Dependent Manner

Ana Rita Ferreira[1,2†], *Ana Gouveia*[1†], *Ana Cristina Magalhães*[1], *Isabel Valença*[1], *Mariana Marques*[1], *Jonathan C. Kagan*[2] *and Daniela Ribeiro*[1*]

[1]*Institute of Biomedicine (iBiMED), Department of Medical Sciences, University of Aveiro, Aveiro, Portugal,* [2]*Division of Gastroenterology, Hepatology and Nutrition, Boston Children's Hospital and Harvard Medical School, Boston, MA, United States*

Upon intracellular recognition of viral RNA, RIG-I-like proteins interact with MAVS at peroxisomes and mitochondria, inducing its oligomerization and the downstream production of direct antiviral effectors. The human cytomegalovirus (HCMV) is able to specifically evade this antiviral response, *via* its antiapoptotic protein vMIA. Besides suppressing the programmed cell death of infected cells, vMIA inhibits the antiviral signalling at mitochondria by inducing the organelle's fragmentation, consequently hindering the interaction between MAVS and the endoplasmic reticulum protein STING. Here we demonstrate that vMIA interferes with the peroxisomal antiviral signalling *via* a distinct mechanism that is independent of the organelle's morphology and does not affect STING. vMIA interacts with MAVS at peroxisomes and inhibits its oligomerization, restraining downstream signalling, in an MFF-dependent manner. This study also demonstrates that vMIA is totally dependent on the organelle's fission machinery to induce peroxisomal fragmentation, while this dependency is not observed at mitochondria. Furthermore, although we demonstrate that vMIA is also able to inhibit MAVS oligomerization at mitochondria, our results indicate that this process, such as the whole vMIA-mediated inhibition of the mitochondrial antiviral response, is independent of MFF. These observed differences in the mechanisms of action of vMIA towards both organelles, likely reflect their intrinsic differences and roles throughout the viral infection. This study uncovers specific molecular mechanisms that may be further explored as targets for antiviral therapy and highlights the relevance of peroxisomes as platforms for antiviral signalling against HCMV.

Keywords: peroxisomes, human cytomegalovirus, vMIA, antiviral signalling, MAVS

OPEN ACCESS

Edited by:
Marek Skoneczny, Institute of Biochemistry and Biophysics (PAN), Poland

Reviewed by:
Damien Arnoult, INSERM U1197 Unité Mixte de Recherche Interactions Cellules Souches-Niches, France
Mitsutoshi Yoneyama, Chiba University, Japan

***Correspondence:**
Daniela Ribeiro
daniela.ribeiro@ua.pt

[†]These authors have contributed equally to this work and share first authorship

Specialty section:
This article was submitted to Membrane Traffic, a section of the journal Frontiers in Cell and Developmental Biology

Received: *09 February 2022*
Accepted: *04 March 2022*
Published: *04 April 2022*

Citation:
Ferreira AR, Gouveia A, Magalhães AC, Valença I, Marques M, Kagan JC and Ribeiro D (2022) Human Cytomegalovirus vMIA Inhibits MAVS Oligomerization at Peroxisomes in an MFF-Dependent Manner. Front. Cell Dev. Biol. 10:871977. doi: 10.3389/fcell.2022.871977

INTRODUCTION

Upon viral infection, the intracellular retinoic acid-inducible gene-I (RIG-I)-like receptors (RLRs), such as RIG-I and melanoma differentiation-associated gene-5 (MDA-5), interact with viral RNA (Saito and Gale, 2008) and subsequently activate the adaptor protein mitochondrial antiviral signalling (MAVS) at mitochondria (Kawai et al., 2005; Meylan et al., 2005; Seth et al., 2005; Xu et al., 2005), peroxisomes (Dixit et al., 2010) and mitochondrial-associated membranes (MAMs)

(Horner et al., 2011). Interaction between the caspase activation and recruitment domains (CARDs) of both RLR and MAVS, induces MAVS oligomerization and amplifies antiviral signalling (Seth et al., 2005; Hou et al., 2011), culminating with the production of interferons (IFNs) and IFN-stimulated genes (ISGs) (Dixit and Kagan, 2013; Kell and Gale, 2015). Together, peroxisomes and mitochondria orchestrate the antiviral immune response mediated by MAVS: peroxisomal MAVS leads to a rapid expression of ISGs, which is then complemented by the mitochondrial counterpart, prompting a long-term, more stable and amplified response (Dixit et al., 2010).

The importance of peroxisomes for the cellular antiviral response is highlighted by recent studies demonstrating that distinct viruses, such as the human cytomegalovirus (HCMV) (Magalhães et al., 2016; Marques et al., 2018), dengue and West Nile viruses (You et al., 2015), hepatitis C virus (Bender et al., 2015; Ferreira et al., 2016, Ferreira et al., 2020) and herpes simplex virus 1 (Zheng and Su, 2017) have developed unique strategies to specifically target and evade the peroxisomal antiviral signalling (Ferreira et al., 2019, Ferreira et al., 2022).

Peroxisomes and mitochondria are membrane-bound and highly dynamic organelles. Besides cooperating as important antiviral platforms, they also collaborate in, among others, reactive oxygen species (ROS) metabolism and fatty acids β-oxidation (Ribeiro et al., 2012; Fransen et al., 2017; Farmer et al., 2018; Islinger et al., 2018; Tilokani et al., 2018; Schrader et al., 2020; Wanders et al., 2020). Additionally, peroxisomes and mitochondria share key components of their morphology-control machinery, such as dynamin-1-like protein (DLP1) (Koch et al., 2003; Li and Gould, 2003), mitochondrial fission factor (MFF) (Gandre-Babbe and van der Bliek, 2008; Itoyama et al., 2013) and mitochondrial fission 1 protein (FIS1) (Kobayashi et al., 2007). Mitochondrial morphology plays an important role on the MAVS-mediated antiviral response originating from this organelle (Castanier et al., 2010): upon infection, mitochondrial MAVS activation allows the induction of the mitochondrial fusion protein mitofusin-1 (MFN1), leading to the organelle's fusion (Castanier et al., 2010; Onoguchi et al., 2010). Mitochondrial elongation/fusion is also required to enhance the interaction between MAVS and the cytosolic DNA sensing adaptor stimulator of interferon genes (STING) at the endoplasmic reticulum (ER) membranes (Castanier et al., 2010). In contrast, the relevance of peroxisome morphology for the establishment of the cellular antiviral response has not yet been established.

HCMV is a large, enveloped DNA virus belonging to the *Herpesviridae* family. HCMV infections represent one of the major causes of birth defects and opportunistic diseases in immuno-compromised patients. With a slow replication cycle, HCMV has evolved several mechanisms to evade the cellular antiviral response and cell death (Goldmacher, 2005; Jackson et al., 2011; Fliss and Brune, 2012; Marques et al., 2018). This virus encodes several immediate early proteins, such as the viral mitochondrial-localized inhibitor of apoptosis (vMIA; also known as predominant UL37 exon 1 protein (pUL37 × 1) (Goldmacher et al., 1999; Ma et al., 2012). vMIA has been initially reported to localize at mitochondria and to abolish apoptosis, either by disrupting the mitochondrial transition pore formation or by blocking the permeabilization of the mitochondrial outer membrane (Goldmacher et al., 1999; McCormick et al., 2003). At mitochondria, vMIA recruits the pro-apoptotic Bcl-2 family member BAX and neutralizes it by inducing its oligomerization and membrane sequestering (Arnoult et al., 2004; Poncet et al., 2004). Through the suppression of the programmed cell death of infected cells, vMIA plays a crucial role in HCMV propagation (Goldmacher et al., 1999; Arnoult et al., 2004; Poncet et al., 2004; Sharon-Friling et al., 2006; Ma et al., 2012; Zhang et al., 2013). vMIA has also been reported to impact the modulation of the mitochondrial fission/fusion process and thus, lead to the organelle network disruption. While some authors have associated the perturbation of the mitochondrial network to vMIA's anti-apoptotic function (Goldmacher, 2005), others defend that it also plays a role on the modulation of the RLR/MAVS signalling at this organelle: by inducing mitochondrial fragmentation, the contacts with the ER would be reduced, hindering the interactions between MAVS and STING (Castanier et al., 2010).

vMIA also localizes at peroxisomes, where it interacts with MAVS and inhibits the peroxisomal MAVS-dependent antiviral signalling (Magalhães et al., 2016). Peroxisomal fragmentation is also induced by vMIA but, contrarily to mitochondria, this alteration of organelle morphology does not impact the antiviral signalling inhibition (Magalhães et al., 2016).

The mechanisms by which vMIA acts towards peroxisomes, either by inhibiting antiviral signalling or disturbing organelle morphology, are still unknown. In this work, we further unravel these processes and propose a model in which vMIA inhibits antiviral signalling at peroxisomes by hindering MAVS oligomerization in an MFF-dependent manner.

Our work further demonstrates that HCMV has developed distinct mechanisms to interfere with peroxisomes and mitochondria, which may result from intrinsic differences between these two organelles and their role throughout the viral infection.

MATERIALS AND METHODS

Antibodies and Plasmids

Rabbit antibodies against MFF (17090-1-AP, ProteinTech, Manchester, UK) 30, Myc-tag (71D10, 2,278, Cell Signalling Technology, Beverly, MA, United States), FLAG epitope (F7425, Sigma-Aldrich, St. Louis, MO, United States), β-Actin (4,967, Cell Signalling, Danvers, MA, United States), PEX14 (GTX129230, GeneTex, CA,United States) and MAVS (A300-782A, Bethyl Laboratories, TX, United States), and mouse antibodies against MAVS (E-3, SC-166583, Santa Cruz Biotechnology, Dallas, TX, United States), p-STAT1 (Y701, BD Biosciences, San Jose, CA, United States), DLP1 (611,113, BD Bioscience, San Jose, CA, United States), PMP70 (SAB4200181, Sigma-Aldrich, St. Louis, MO, United States), COXIV (4,850, Cell Signalling Technology, Beverly, MA, United States) and α-Tubulin (T9026, Sigma-Aldrich, St. Louis, MO, United States) were used for immunoblotting. Mouse antibodies against PMP70

(SAB4200181, Sigma-Aldrich, St. Louis, MO, United States), Myc epitope (9E10, SC-40, Santa Cruz Biotechnology, Dallas, TX, United States) were used for immunofluorescence analyses. Additionally, mouse antibodies against Myc epitope (9E10, SC-40, Santa Cruz Biotechnology, Dallas, TX, United States) and MAVS (E-3, SC-166583, Santa Cruz Biotechnology, Dallas, TX, United States) were also used for the immunoprecipitation experiments. Species-specific anti-IgG antibodies conjugated to HRP (Bio-Rad, Richmond, CA, United States) or IRDye 800 CW and IRDye 680RD secondary antibodies (LI-COR Biotechonology, Cambridge, UK) were used for immunoblotting and the fluorophores TRITC (Jackson ImmunoResearch, Cambridge, UK) and Alexa 488 (Invitrogen, Waltham, MA, United States) were used for immunofluorescence.

The plasmids STING-FLAG and GFP-RIG-I-CARD (kindly provided by Dr F. Weber, Justus-Liebig Universität Giessen, Germany) and vMIA-Myc (kindly provided by Dr V. Goldmacher, ImmunoGen Inc., Cambridge, MA, United States) were used for mammalian expression.

Cell Culture, Transfections and RNA Interference Experiments

Mouse embryonic fibroblasts (MEFs) MAVS-PEX cells and MEFs MAVS-KO cells (described in (Dixit et al., 2010), MEFs MAVS-MITO (described below) and human embryonic kidney (HEK) 293T cells (kindly provided by Dr M. J. Amorim, Instituto Gulbenkian para a Ciência, Portugal) were cultured in Dulbecco's modified Eagle's medium supplemented with 100 U/ml penicillin, 100 mg/ml streptomycin and 10% fetal bovine serum (all from GIBCO, Thermo Scientific, Waltham, MA, United States) at 37°C in a humidified atmosphere of 5% CO2. MEFs MAVS-PEX cells, MEFs MAVS-MITO and MEFs MAVS-KO cells were transfected with Lipofectamine 3,000 (Invitrogen, Waltham, MA, United States) or microporated with Neon® Transfection System (Invitrogen, Waltham, MA, United States) (1700 V, width: 20, 1 pulse), following manufacturer's instructions. HEK293T cells were transfected using 1 mg/ml of Polyethylenimine (PEI, Linear, MW 25000, Polysciences, PA, United States) at a ratio of 1:6 (DNA:PEI). Cells were fixed for organelle morphology or harvested for western blot or co-immunoprecipitation assays, 24–72 h after transfection.

To knock-down the expression of MFF and DLP1 by RNA interference, 21-nucleotide small interfering RNA (siRNA) duplexes were transfected into MEFs MAVS-PEX and MEFs MAVS-MITO cells using Lipofectamine RNAiMAX (Invitrogen, Waltham, MA, United States) according to the manufacturer's instructions. Control cells were treated with transfection mix without siRNAs complexes. Cells were assayed for silencing and organelle morphology 72 h after seeding. siRNA oligonucleotides were obtained as pre-designed siRNAs as follows: MFF–sense strand: 5′-CGCUGACCUGGAACAAGGAdTdT-3′ for exon 2 30 (Ambion, Austin, TX, United States); DLP1–sense strand: 5′-UCCGUGAUGAGUAUGCUUUdTdT-3′ 31 (Ambion, Austin, TX, United States).

Generation of Stable Cell Lines

To generate a MEFs MAVS-MITO stable cell line, MEFs MAVS-KO were transduced with retroviruses, which were first produced by transfecting HEK293T cells with pCL-Ampho and pVSV-G (provided by Dr B. Jesus, University of Aveiro, Portugal), and MSCV2.2 IRES-GFP MAVS-MITO. Twenty-four hours upon transfection, cell media was renewed and 24 h later cell media was collected, filtered and added to MEFs MAVS KO cells, plated 24 h before. Transduced cells were left to grow until full confluence before being split and sorted for low GFP expression level using BD FACSARIA II.

Viral Infections

HEK293T cells were infected with SeV (Cantell strain, Charles River Laboratories, Wilmington, MA, United States) with a final concentration of 100 HA units/ml, diluted in serum- and antibiotic- free media. Cells were incubated for 1 h at 37°C and, afterwards growth media containing 20% of FBS was added to cells. Infection continued for 14 h before cells collection.

Immunofluorescence and Microscopy

Cells grown on glass coverslips were fixed with 4% paraformaldehyde in PBS, pH 7.4, for 20 min, permeabilized with 0.2% Triton X-100, for 10 min, blocked with 1% BSA solution, for 10 min, and incubated with the indicated primary and secondary antibodies, for 1 h at room temperature in a humid environment. Cells were then stained with Hoechst (1:2000) for 3 min, before mounting the slide. Confocal images were acquired using a Zeiss LSM 880 confocal microscope (Carl Zeiss, Oberkochen, Germany) using a Plan- Apochromat 63× and 100×/1.4 NA oil objectives, a 561 nm DPSS laser and the argon laser line 488 nm (BP 505–550 and 595–750 nm filters). Images were processed using ZEN Black and ZEN Blue software (Carl Zeiss, Oberkochen, Germany). Digital images were optimized for contrast and brightness using Adobe Photoshop (Adobe Systems, San Jose, CA, United States).

Organelle Morphology Quantification

For the evaluation of organelles morphology, around six hundred cells from three independent experiments were counted for each condition, considering the size/shape and number of their peroxisomes or mitochondria. For these analyses, cells were considered as containing "fragmented organelles" when organelles were significantly smaller and in higher number than the ones from the control cells. We considered cells containing "elongated organelles" as those whose organelles had a tubular shape and were significantly longer when compared to the control cells.

Immunoprecipitation Analyses

To study the interaction between STING and vMIA, MEFs MAVS-PEX cells were co-transfected with vMIA-Myc and STING-FLAG by Lipofectamine 3,000 (Invitrogen, Waltham, MA, United States). Lysates were incubated with anti-MAVS antibody for 2 h at 4°C on a rotary mixer. Then, 50 µL of beads were added to the mixture and rotated for 10 min at room temperature. The complex was washed 3 times with PBS

containing 0.1% Tween20 and then resuspended in 3x SDS-sample buffer and boiled for 10 min to elute bound proteins. Untransfected MEFs MAVS-PEX cells were used as negative control for each immunoprecipitation. In all immunoprecipitations, 50 µg of total cell lysate was used as input, and for the output the same volume of input was saved from the cell lysate extracted after incubation with the antibody and beads.

Immunoblotting

Cells lysates were obtained by using a specific lysis buffer (25 mM Tris-HCl pH 7.5, pH 8.0, 50 mM sodium chloride, 0.5% sodium deoxycholate, 0.5% Triton X-100 and supplemented with a protease-inhibitor mix) and by passing them 20 times through a 26-gauge syringe needle. Then, samples were incubated on a rotary mixer for 30 min at 4°C, before being cleared by centrifugation (17,000 x g, 15 min, 4°C). Protein concentration was determined using the Bradford assay (Bio-Rad Protein Assay, Bio-Rad, Hercules, CA, United States). Protein samples were separated by SDS-PAGE on 10% or 12.5% polyacrylamide gels, transferred to nitrocellulose (PROTAN®, Whatman®, Dassel, Germany) using a semidry apparatus or wet transfer system (Bio-Rad, Hercules, CA, United States), and analysed by immunoblotting.

Immunoblots were processed after blocking membranes with 5% milk (Molico Skimmed dry milk powder, Nestlé, Vevey, Switzerland) in TBS-T (10 mM Tris pH 8, 150 mM, 0.005% Tween20) and using specific primary antibodies and secondary antibodies diluted in TBS-T. Between incubations, membranes were washed 3 times for 5 min in TBS-T. Immunoblots were scanned with a Bio-Rad GS-800 calibrated imaging densitometer or ChemiDoc™ Touch Gel Imaging System (Bio-Rad, Hercules, CA, United States) for chemiluminescence detection, while Li-COR Odyssey imaging system for fluorescence detection (LI-COR Biotechonology, Cambridge, UK). Images were processed using Quantity One software (Bio-Rad, Hercules, CA, United States) or Image Studio Lite 5.2 (LI-COR Biotechonology, Cambridge, UK). Bands' quantification was done using the volume tools from Quantity One software (Bio-Rad, Hercules, CA, United States), where the background intensity was calculated using the local background subtraction method.

RNA Extraction, cDNA Synthesis and Quantitative Real-Time Polymerase Chain Reaction

Twenty-four hours after cells transfection, total RNA was isolated using Nzyol (NZYTech, Lisbon, PT), following manufacturer's protocol. After quantifying RNA with DS-11 spectrophotometer (DeNovix Inc., Wilmington, DE, United States), 1 µg of total RNA was treated with 1 µL DNase I (Thermo Scientific, Waltham, MA, United States). cDNA was produced from treated RNA using Revert Aid Reverse Transcriptase (Thermo Scientific, Waltham, MA, United States) and Oligo-dT15 primer (Eurofins Genomics, Ebersberg, Germany) following manufacturer's protocol. For quantitative real-time polymerase chain reaction, 2 µL of 1:10 diluted cDNA was added to 10 µL of 2x SYBR Green qPCR Master Mix (Low Rox) (Bimake, Houston, TX, United States). The final concentration of each primer was 250 nM in 20 µL of total master mix volume. Duplicates of each sample were done, and reactions were run on 7,500 Real-Time PCR System (Applied Biosystems, Waltham, MA, United States). Primer sequences were designed using Beacon Designer 7 (Premier Biosoft, Palo Alto, CA, United States) for IRF1, RSAD2 and GAPDH mouse genes. The oligonucleotides used for mouse IRF1 were 5′-GGTCAGGACTTGGATATGGAA-3′ and 5′-AGTGGTGCTATCTGGTATAATGT-3'; for mouse RSAD2 were 5′-TGTGAGCATAGTGAGCAATGG-3′ and 5′-TGTCGCAGGAGATAGCAAGA-3'; for mouse GAPDH were 5′-AGTATGTCGTGGAGTCTA-3′ and 5′-CAATCTTGAGTG AGTTGTC-3' (Eurofins Genomics, Ebersberg, Germany) GAPDH was used as a reference gene. The thermocycling reaction was done by heating at 95°C for 3 min, followed by 40 cycles of a 12 s denaturation step at 95°C and a 30 s annealing/elongation step at 60°C. The fluorescence was measured after the extension step using the Applied Biosystems software (Applied Biosystems, Waltham, MA, United States). After the thermocycling reaction, the melting step was performed with slow heating, starting at 60°C and with a rate of 1%, up to 95°C, with continuous measurement of fluorescence. Data analysis was performed using the $2^{-\Delta\Delta CT}$ method.

Organelle-Enriched Fractions and Sucrose Gradient

HEK 293T cellular fractionation was performed by homogenizing cells in Buffer A (10 mM Tris-HCl pH 7.5, 10 mM KCl, 1.5 mM MgCl2, 0.25 M D-mannitol, supplemented with cOmplete™, EDTA-free Protease Inhibitor Cocktail (Roche, Basel, Switzerland) and passing samples gently through a 26-gauge syringe needle. The homogenate was cleared of nuclei and membranes by centrifugation at 1,000 g for 5 min at 4°C. Mitochondria-enriched fraction pellet was obtained by centrifugation at 2000 g for 10 min at 4°C. The supernatant was then centrifuged again at 25,000 g for 25 min at 4°C to obtain the peroxisome-enriched fraction pellet. Both pellets were gently resuspended in homogenization buffer supplemented with 2% n-Dodecyl β-D-maltoside, to disrupt the organelle membrane without affecting protein's quaternary structure.

Organelle's fractions were then processed for the separation of MAVS oligomers by sucrose gradient (as described in (Seth et al., 2005) with minor adaptations). The organelle's-enriched fractions were loaded in 30–60% sucrose gradients and centrifuged at 170 000 g for 2 h at 4°C. Starting from the top, 7 equal fractions were collected and processed for SDS-PAGE and analysed by immunoblotting.

Statistical Analysis

Statistical analysis was performed in Graph Pad Prism 9 (GraphPad Software, Inc., La Jolla, CA, United States). Data are presented as mean ± standard error mean (SEM). Differences among groups were analysed by one-way ANOVA,

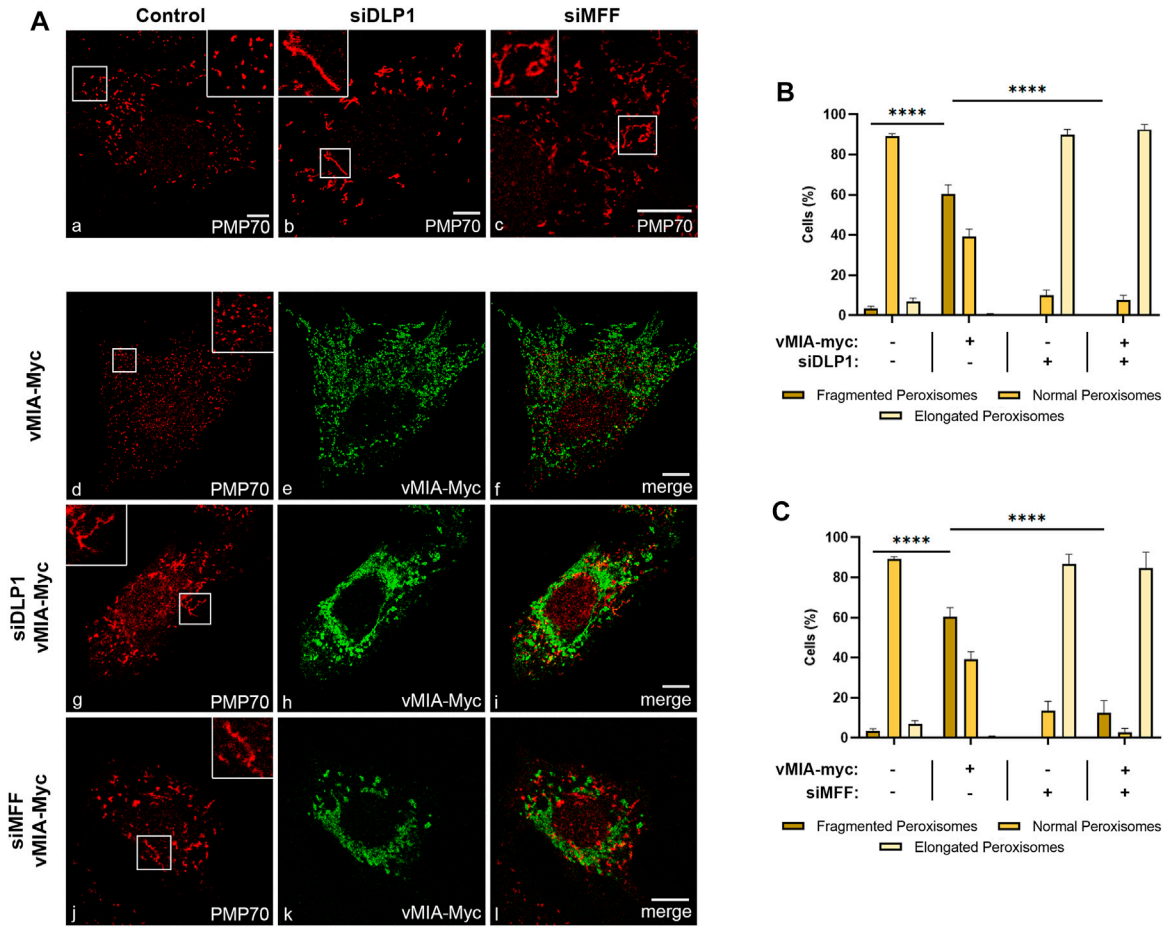

FIGURE 1 | vMIA-mediated peroxisomal fragmentation is dependent on the fission machinery proteins DLP1 and MFF. **(A)** Immunofluorescence analyses of MEFs MAVS-PEX cells: (a) control cells, (b) DLP1 silenced cells, (c) MFF silenced cells: (a–c) anti-PMP70; (d–f) overexpression of vMIA-Myc: (d) anti-PMP70, (e) anti-Myc, (f) merge image of d and e; (g–i) overexpression of vMIA-Myc in DLP1 silenced cells: (g) anti-PM70, (h) anti-Myc, (i) merge image of g and h; (j–l) overexpression of vMIA-Myc in MFF silenced cells: (j) anti-PMP70, (k) anti-Myc, (l) merge image of j and k. Bars represent 10 μm. **(B,C)** Statistical analysis of peroxisomal morphology upon overexpression of vMIA-Myc in MEFs MAVS-PEX cells in the absence of DLP1 or MFF, respectively. Approximately 600 cells were analysed per condition. Data represents the means ± SEM of three independent experiments analysed using two-way ANOVA with Bonferroni's multi comparations test (ns = non-significant, ****–$p <$ 0.0001). Error bars represent SEM.

followed by Bonferroni's multiple comparison test; comparisons between two groups were made using unpaired T test, and p-values of <0.05 were considered as significant (****–$p <$ 0.0001, ***–$p <$ 0.001, **–$p <$ 0.01, *–$p <$ 0.05 and ns–non-significant).

RESULTS

Contrarily to Mitochondria, vMIA Depends on the Organelle Fission Machinery to Induce Peroxisome Fragmentation

Although the contribution of peroxisomes, in concert with mitochondria, to the cellular antiviral response has been established (Dixit et al., 2010), the key differences between the signalling pathways, originating from these two organelles, with distinct kinetics and end products, remains unknown. HCMV vMIA has been shown to inhibit both pathways and, in parallel, induce the fragmentation of both organelles (Castanier et al., 2010; Magalhães et al., 2016). This morphology change has been pinpointed as the main trigger for the vMIA-dependent antiviral signalling inhibition at mitochondria, as it would consequently reduce its association with the ER, hindering the interaction between MAVS and STING (Castanier et al., 2010). At peroxisomes, however, the antiviral signalling inhibition induced by vMIA was shown to be independent of the organelle fragmentation (Magalhães et al., 2016).

These observed differences led us to further investigate the mechanism by which vMIA induces the morphology changes at peroxisomes, in comparison with mitochondria. To that end, we evaluated its dependence on the organelles' fission machinery, more specifically on the cytoplasmic protein DLP1, the main responsible for the final membrane fission. vMIA's ability to

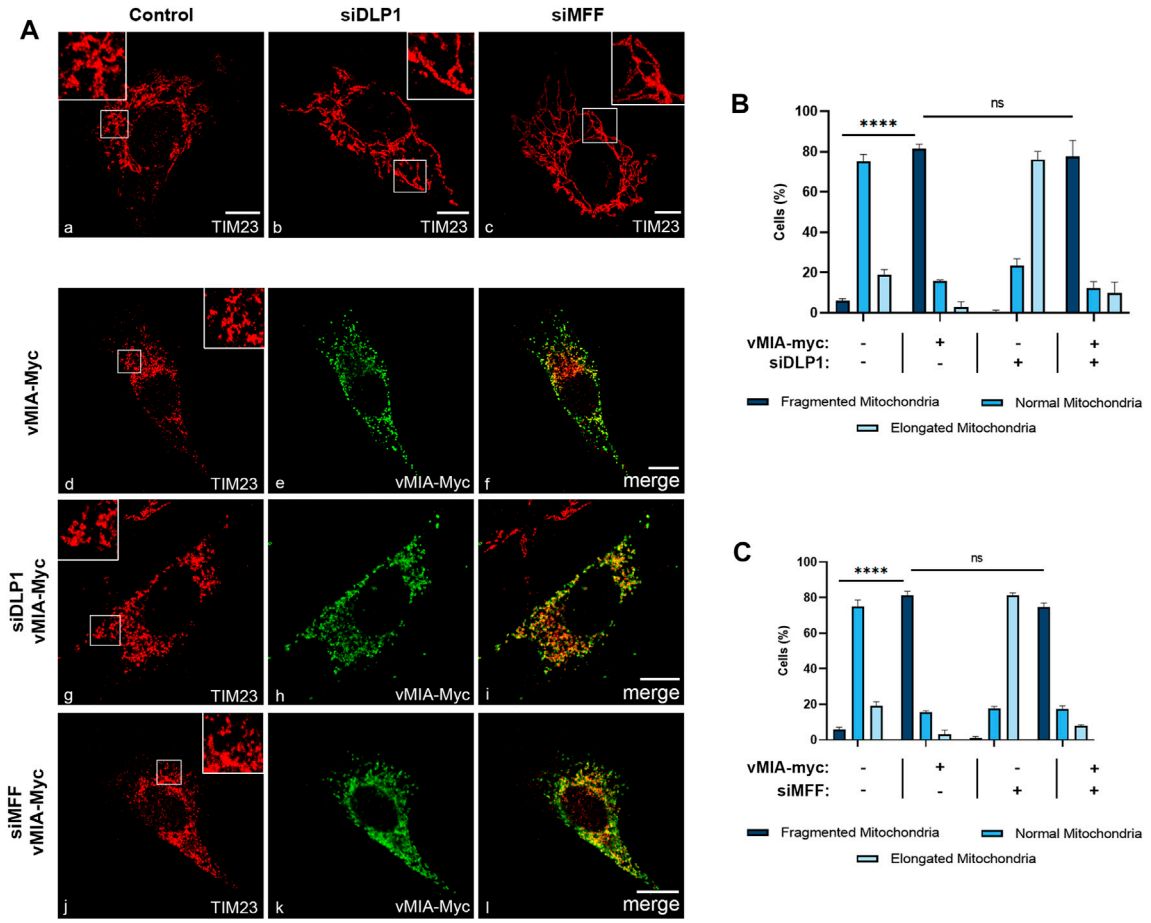

FIGURE 2 | vMIA-mediated mitochondrial fragmentation is independent on the fission machinery proteins DLP1 and MFF. **(A)** Immunofluorescence analyses of MEFs MAVS-MITO cells: (a) control cells, (b) DLP1 silenced cells, (c) MFF silenced cells: (a–c) anti-TIM23; (d–f) overexpression of vMIA-Myc: (d) anti-TIM23, (e) anti-Myc, (f) merge image of d and e; (g–i) overexpression of vMIA-Myc in DLP1 silenced cells: (g) anti-TIM23, (h) anti-Myc, (i) merge image of g and h; (j–l) overexpression of vMIA-Myc in MFF silenced cells: (j) anti-TIM23, (k) anti-Myc, (l) merge image of j and k. Bars represent 10 μm. **(B,C)** Statistical analysis of mitochondrial morphologies upon overexpression of vMIA-Myc in MEFs MAVS-MITO cells in the absence of DLP1 or MFF, respectively. Approximately 600 cells were analysed per condition. Data represents the means ± SEM of three independent experiments analysed using two-way ANOVA with Bonferroni's multi comparations test (ns = non-significant, ****– $p <$ 0.0001). Error bars represent SEM.

induce peroxisome fragmentation was analysed upon overexpression of Myc-tagged vMIA (vMIA-Myc) and silencing of DLP1 (*via* small interference RNA (siRNAs) against DLP1, (siDLP1)) in mouse embryonic fibroblasts (MEFs) that contain MAVS solely at peroxisomes (MEFs MAVS-PEX (Dixit et al., 2010)) (**Figure 1**) Upon immunolocalization with antibodies against the Myc-tag and the peroxisomal marker PMP70, the cells were examined by confocal microscopy (**Figure 1A**) and the organelles' morphological alterations were quantified (**Figure 1B,C**). As expected, silencing of DLP1 induced peroxisomal elongation when compared with control cells (**Figure 1Aa,b** and **Supplementary Figure S1A**). Interestingly, vMIA was no longer able to induce peroxisome fragmentation in the absence of DLP1, as no significant differences in morphology were observed in the presence of the viral protein (**Figures 1Ag–i,B**). We have also analysed the ability of vMIA to induce peroxisome fragmentation in the absence of MFF, another major player on peroxisomal fission and one of the main anchors of DLP1 at the organelle's membrane. Upon analysis of MEFs MAVS PEX cells containing siMFF and vMIA-Myc (**Figures 1Aj–l,C** and **Supplementary Figure S1A**), no significant changes in peroxisome morphology were detected, when compared to the elongated peroxisomes observed upon silencing of MFF (**Figures 1Ac,C**). These results clearly show that vMIA depends on a fully functional peroxisome fission machinery to be able to induce the organelle's fragmentation.

In order to analyse whether an analogous dependence occurs at mitochondria, we performed similar analyses in MEFs MAVS-MITO cells (where MAVS is present solely at mitochondria). Mitochondria morphology was analysed by confocal microscopy upon immunolocalization with antibodies against Myc and the mitochondrial marker TIM23, in cells expressing vMIA-Myc in the presence or

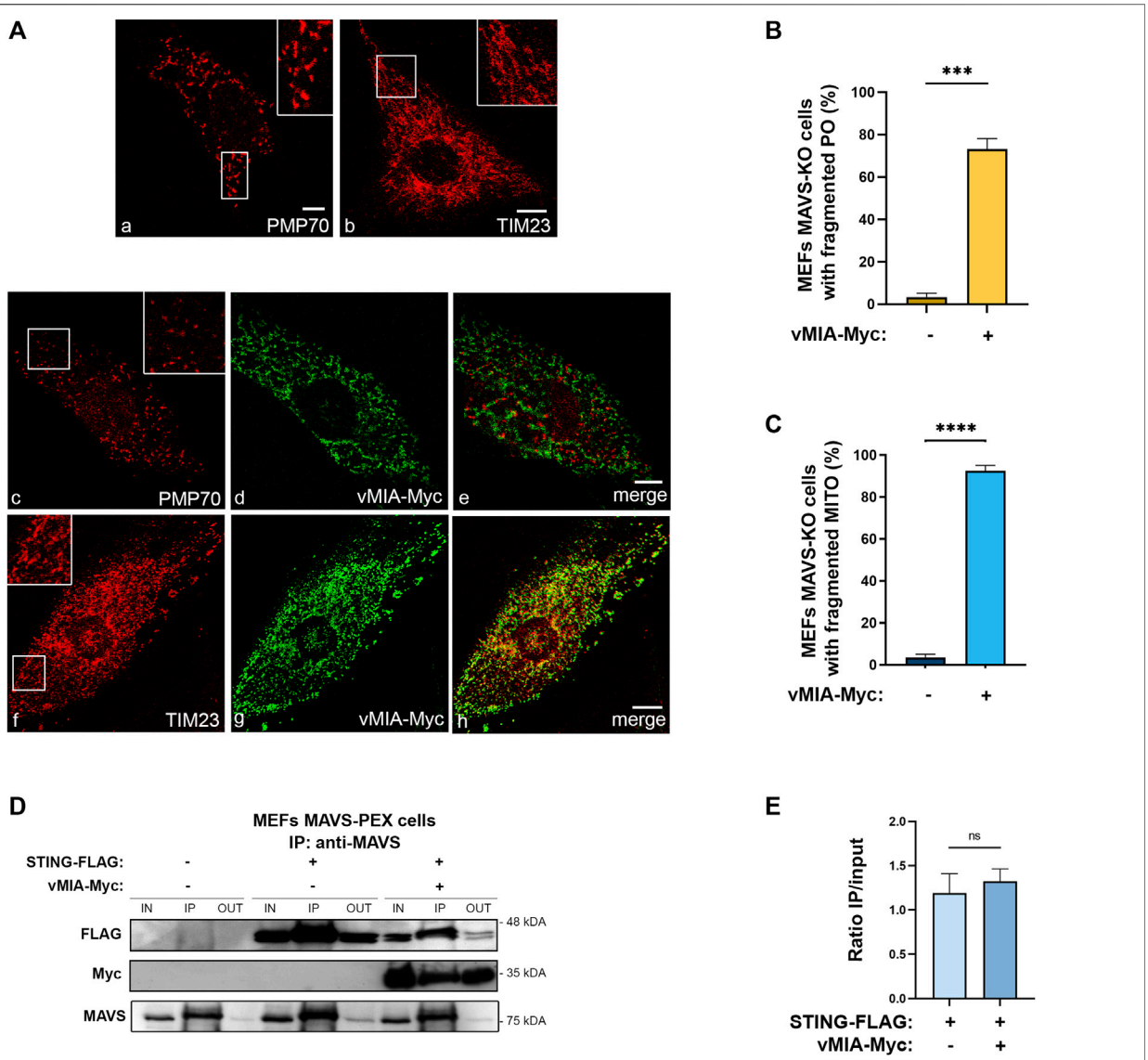

FIGURE 3 | vMIA-induced peroxisomal and mitochondrial fragmentation is independent of MAVS. vMIA does not disrupt STING-MAVS interaction at peroxisomes. **(A)** Immunofluorescence analyses of MEFs MAVS KO cells: (a, b) peroxisomal and mitochondrial morphologies in control cells: (a) anti-PMP70, (b) anti-TIM23; (c–e) peroxisomal morphology upon overexpression of vMIA-Myc: (c) anti-PMP70, (d) anti-Myc, (e) merge image of c and d; (f, h) mitochondrial morphology upon overexpression of vMIA-Myc: (f) anti-TIM23, (g) anti-Myc, (h) merge image of f and g. Bars represent 10 μm. **(B,C)** Statistical analysis of peroxisomal or mitochondrial morphologies upon overexpression of vMIA-Myc in MEFs MAVS KO cells, respectively. Approximately 600 cells were analysed per condition. **(D)** Co-immunoprecipitation analysis of the interaction between overexpressed STING-FLAG and vMIA-Myc in MEFs MAVS-PEX cells. The pull-down was performed using an antibody against MAVS. Western blot was performed with antibodies against FLAG and Myc. IN represents total cell lysate (input), IP represents immunoprecipitation and OUT represents the cell lysate extracted after incubation with the antibody (output). **(E)** Quantification of the ratio between IP and IN, in the presence or absence of vMIA. Data represents the means ± SEM of three independent experiments, analysed using unpaired T test (ns - non-significant; ***–$p < 0.001$, ****–$p < 0.0001$).

absence of DLP1 or MFF (siDLP1 or siMFF) (**Figure 2**). Surprisingly, vMIA was still able to induce mitochondria fragmentation in the absence of either DLP1 or MFF, totally reverting the organelle elongation observed upon silencing of any of these proteins (**Figures 2Ag–l,B,C**, **Supplementary Figure S1B**). These results were also observed upon analysis of mitochondria morphology in MEFs MAVS PEX cells, in the absence of DLP1 or MFF (**Supplementary Figure S1C Figures 3Ag–l,D,E**). This data indicates that, contrarily to peroxisomes, vMIA is able to interfere with mitochondria morphology in a fission machinery-independent manner.

vMIA-Induced Peroxisome and Mitochondria Fragmentation is Independent of MAVS Signalling

The independence on the organelle morphology for the vMIA-induced antiviral signalling inhibition at peroxisomes (Magalhães

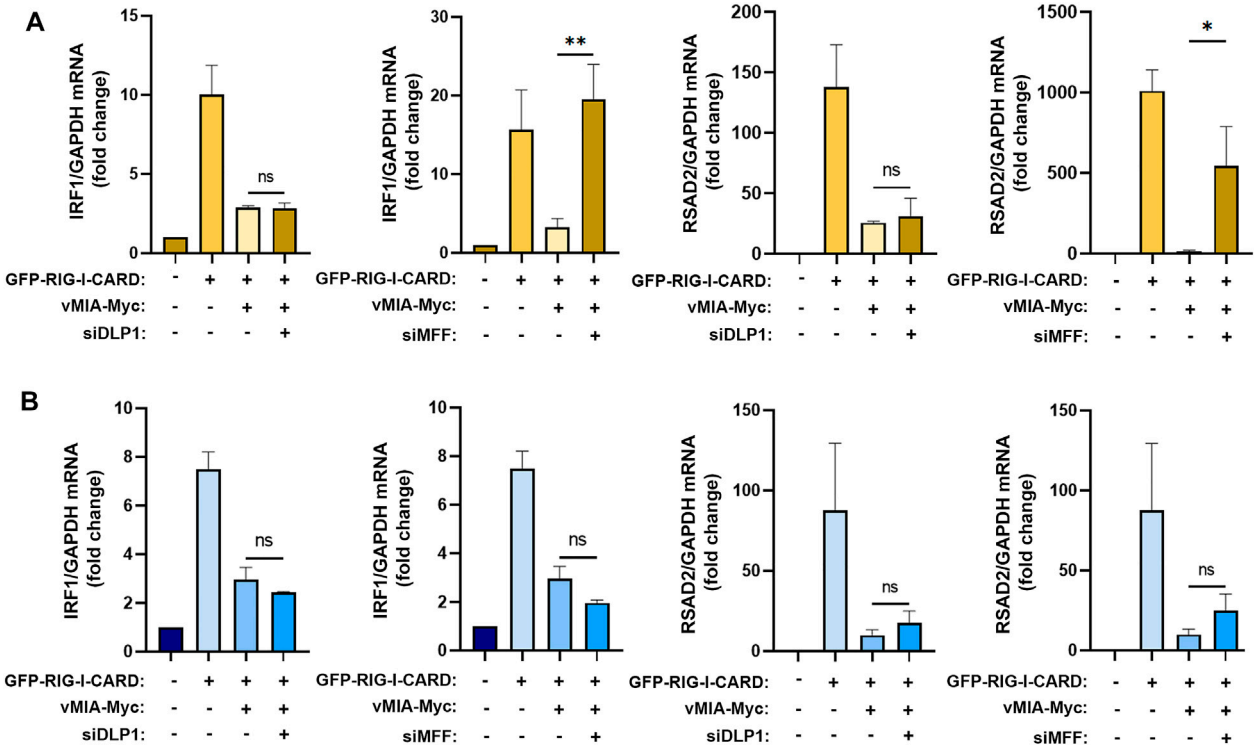

FIGURE 4 | MFF is required for vMIA-mediated inhibition of the MAVS signalling at peroxisomes but not at mitochondria. **(A,B)** RT-qPCR analysis of IRF1 and RSAD2 (viperin) mRNA expression in **(A)** MEFs MAVS-PEX cells or **(B)** MEFs MAVS-MITO cells stimulated with GFP-RIG-I-CARD, upon vMIA-Myc overexpression in the absence of DLP1 or MFF. GAPDH was used as normalizer gene and graphs depict fold change in comparation to untreated samples. Data represents the means ± SEM of at least three independent experiments analysed using one-way ANOVA with Bonferroni's multi comparations test (ns - non-significant; *–$p < 0.005$; **–$p < 0.01$).

et al., 2016), contrarily to what was observed at mitochondria (Castanier et al., 2010), suggests that these two processes may be less correlated than initially anticipated. In order to conclude on whether the peroxisomal and mitochondrial fragmentation prompted by vMIA is in any way dependent on MAVS signalling, we analysed the organelles' morphology in cells lacking MAVS and in the presence of the viral protein. To that end, MEFs MAVS-KO cells were transfected with vMIA-Myc, and confocal microscopy analyses were performed upon immunolocalization with antibodies against PMP70 or TIM23. As shown in **Figure 3A**, even in the absence of MAVS, vMIA was able to induce a strong fragmentation of both peroxisomes (**Figure 3B**) and mitochondria (**Figure 3C**). These results demonstrate that the organelles morphology and the mechanism of vMIA-mediated inhibition of the MAVS signalling are less related than anticipated.

Nevertheless, as the mitochondria fragmentation induced by vMIA has been associated to a decrease in MAVS-STING interaction and the consequent inhibition of the immune response (Castanier et al., 2010), we analysed whether the same would be observed upon peroxisomal fragmentation. We started by analysing the occurrence of an interaction between the peroxisomal MAVS and STING, as this had not yet been demonstrated. To that end, we transfected MEFs MAVS-PEX with a FLAG-tagged STING (STING-FLAG) and, 24 h after, performed co-immunoprecipitation analyses with a pull-down against MAVS. As shown in **Figure 3D**, STING interacts with the peroxisomal MAVS. In order to investigate whether this interaction is eventually compromised by vMIA, these experiments were also performed upon co-transfection with vMIA-Myc. As shown in **Figures 3D,E**, the presence of the viral protein does not inhibit the interaction between STING and peroxisomal MAVS, contrarily to what had been observed at mitochondria. These results, together with the distinct dependencies on organelle morphology, point out major differences between the mechanisms involved in the modulation of the peroxisomal and mitochondrial antiviral signalling by vMIA.

MFF is Essential for the vMIA-Mediated Inhibition of the Peroxisome-Dependent Antiviral Signalling

To further unravel the mechanism by which vMIA inhibits the MAVS signalling at peroxisomes, we once more evaluated the importance of the fission machinery proteins DLP1 and MFF. Upon silencing of any of these proteins in MEFs MAVS-PEX cells, vMIA-Myc was transfected and, 24 h after, the MAVS-dependent antiviral signalling was stimulated by overexpressing a constitutively active form of RIG-I (GFP-RIG-I-CARD, as in (Yoneyama et al., 2004; Magalhães et al., 2016). In correlation with our previous results, the absence of DLP1 did not hinder the

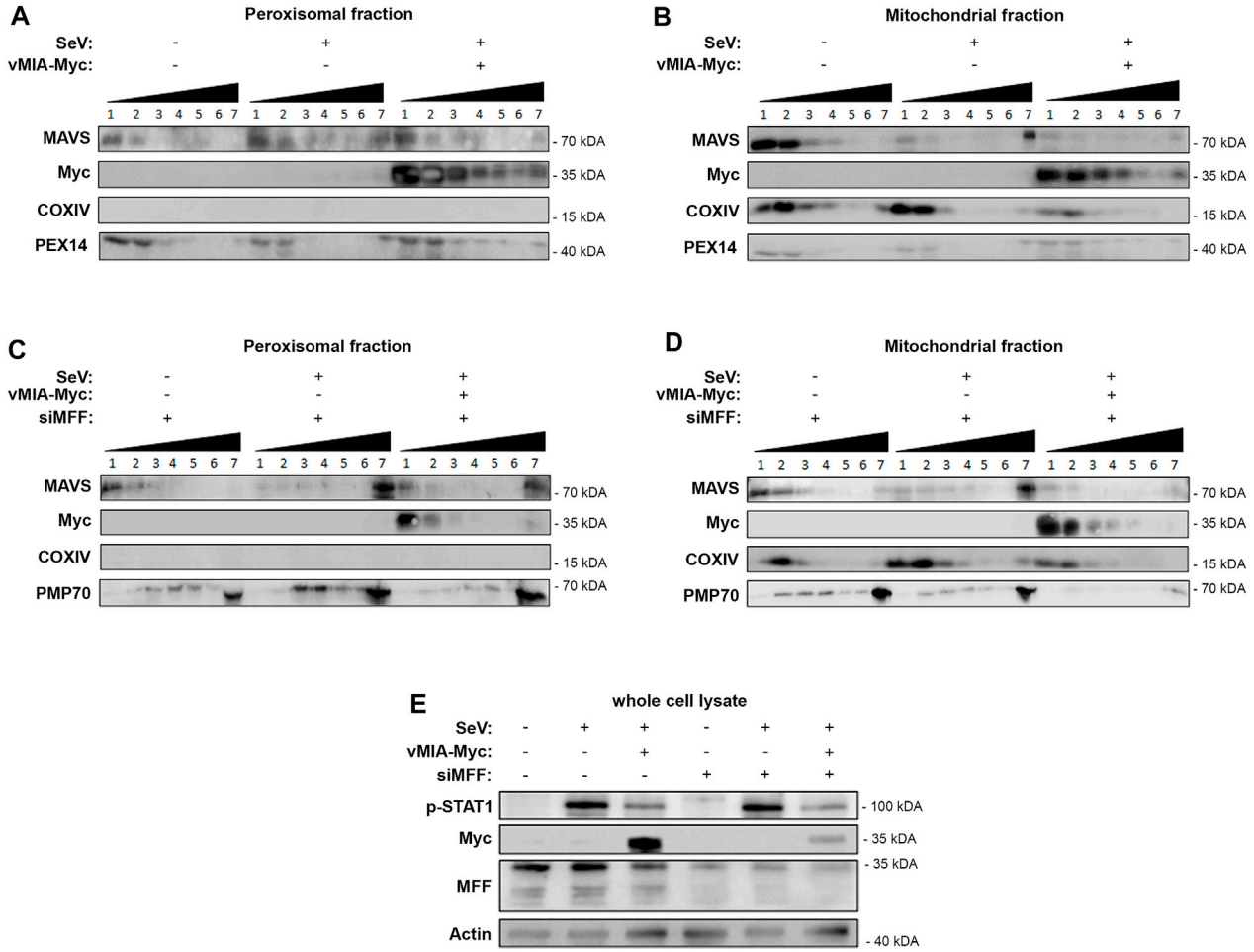

FIGURE 5 | vMIA inhibits MAVS oligomerization at peroxisomes and mitochondria. MFF is essential for the vMIA-mediated inhibition of MAVS oligomerization at peroxisomes but not at mitochondria. **(A,B)** HEK293T cells infected with SeV in the presence or absence of vMIA. Density gradient assay was performed to demonstrate the separation of endogenous MAVS based on its density. 1—7 represent the fractions isolated from the gradient assay, where 1 represents the fraction with lowest density and 7 represents the fraction with highest density. **(A)** Peroxisome-enriched fraction, **(B)** Mitochondria-enriched fraction. **(C,D)** HEK293T cells infected with SeV in the presence or absence of vMIA and in the absence of MFF. Density gradient assay was performed to demonstrate the separation of endogenous MAVS based on its density. 1—7 represent the fractions isolated from the gradient assay, where 1 represents the fraction with lowest density and 7 represents the fraction with highest density. **(C)** Peroxisome-enriched fraction, **(D)** Mitochondria-enriched fraction. **(A–D)** Immunoblots were performed with antibodies against MAVS, Myc-tag, COXIV, PEX14 and PMP70. **(E)** Whole cell lysates were resolved by SDS-PAGE. SeV infection, and consequential activation of MAVS downstream signalling, was confirmed using anti-p-STAT1. vMIA-Myc overexpression and MFF silencing were also confirmed using anti-Myc and anti-MFF, respectively. Antibody against Actin was used as loading control.

peroxisomal antiviral response, leading to similar expression levels of ISGs (IRF1 and RSAD2) when comparing with the ones obtained in the stimulated control cells (**Figure 4A**). However, our results clearly show that, at peroxisomes, MFF's absence strongly impairs the vMIA-mediated inhibition of IRF1 and RSAD2 mRNA expression (**Figure 4A**). MFF, hence, rises as the first identified peroxisomal protein to play an important role on the mechanism of vMIA-mediated inhibition of the peroxisome-dependent antiviral response.

In order to determine whether the same dependency is observed at mitochondria, similar experiments were performed in MEFs MAVS-MITO cells. Surprisingly, in these cells, neither the lack of DLP1 nor MFF had significant effects on ISGs expression (**Figure 4B**).

The importance of MFF for the antiviral signalling inhibition mediated by vMIA seems to be, hence, exclusive for the peroxisomal response.

vMIA Inhibits MAVS Oligomerization at Peroxisomes and Mitochondria

One of the crucial steps of the cellular RIG-I/MAVS antiviral signalling, is the oligomerization of MAVS at the peroxisomal and mitochondrial membranes upon interaction with RIG-I, forming functional high molecular weight prion-like aggregates, essential for the activation of the downstream proteins (Seth et al., 2005; Hou et al., 2011). To further unravel the mechanism of action of vMIA towards the peroxisomal MAVS signalling, and as we had

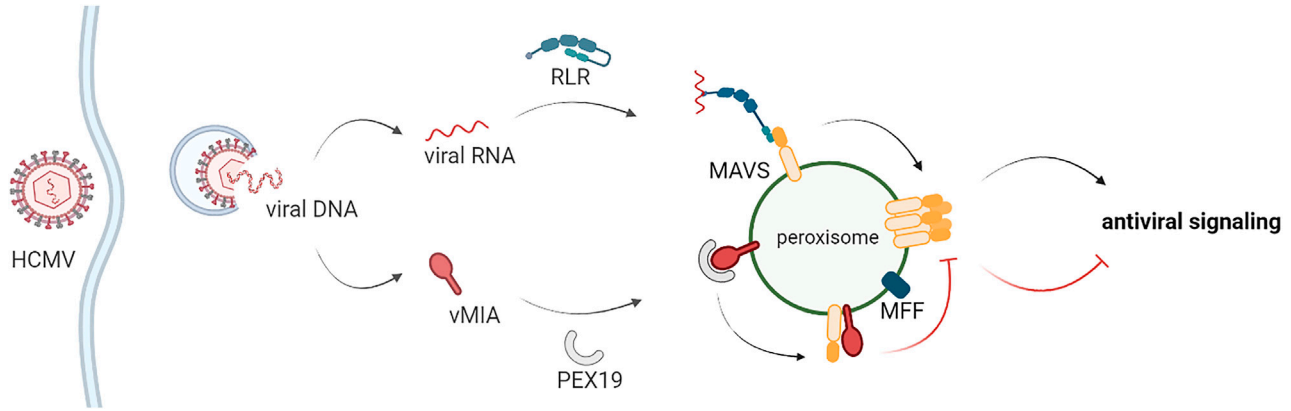

FIGURE 6 | Schematic representation of the proposed model for the vMIA-dependent inhibition of the peroxisomal antiviral signalling. Upon stimulation, RIG-I-like proteins interact with MAVS at peroxisomes, inducing its oligomerization and the downstream production of direct antiviral effectors. HCMV vMIA is able to specifically evade this peroxisomal antiviral signalling. vMIA interacts with PEX19 at the cytoplasm and travels to peroxisomes, where it interacts with MAVS. This interaction interferes, in an MFF-dependent manner, with the formation of MAVS oligomers and inhibits the consequent activation of the downstream antiviral signalling.

previously observed that this viral protein interacts with MAVS, we analysed its effect on MAVS oligomerization upon infection with Sendai virus (SeV) in HEK293T cells. As these cells contain MAVS at both peroxisomes and mitochondria, we used differential centrifugation to prepare peroxisome-enriched fractions and analyse solely the oligomerization of peroxisomal MAVS. Gradient assay experiments were then implemented to separate peroxisomal MAVS in different density fractions, depending on its oligomerization degree. As shown in **Figure 5A**, upon infection with SeV, confirmed by the increase in p-STAT1 (**Figure 5E**), peroxisomal MAVS oligomers appear at the higher density fraction. Interestingly, this is no longer observed in the presence of vMIA (**Figure 5A**). These results suggest that this viral protein, likely through direct interaction (previously reported in (Magalhães et al., 2016)), prevents the formation of MAVS oligomers, inhibiting the downstream antiviral signalling (**Figures 5A,E**).

In order to unravel whether this oligomerization inhibition also occurs at the mitochondrial membranes, we have performed similar analysis on mitochondria-enriched fractions isolated by differential centrifugation. As shown in **Figure 5B**, the results were in all similar to the ones obtained in peroxisomes, demonstrating that, vMIA is also able to inhibit mitochondrial MAVS oligomerization and, consequently, the downstream antiviral signalling (**Figures 5B,E**).

vMIA-Mediated Inhibition of MAVS Oligomerization at Peroxisomes, but not at Mitochondria, is Dependent on MFF

The dependency on MFF for the vMIA influence towards the peroxisomal antiviral response, led us to investigate whether this protein would be involved in the observed inhibition of MAVS oligomerization. Similar gradient separation analysis of peroxisome-enriched fractions was performed in MFF silenced (*via* siMFF transfection) HEK293T cells infected with SeV. Interestingly, our results show that, in the absence of MFF, vMIA is no longer capable of inhibiting the formation of peroxisomal MAVS oligomers, and hence the downstream antiviral signalling (**Figures 5C,E**).

On the other hand, similar experiments performed in mitochondrial-enriched fractions of HEK293T cells infected with SeV, indicate that vMIA is still able to inhibit MAVS oligomerization in the absence of MFF and, hence, hinder the downstream antiviral signalling (**Figures 5D,E**). These results correlate to our previous observation that MFF is not essential for the vMIA-mediated inhibition of the antiviral signalling at mitochondria.

Altogether our results demonstrate that vMIA inhibits MAVS oligomerization at peroxisomes in an MFF-dependent manner and highlight important differences between its mechanisms of action towards both organelles.

DISCUSSION

The significance of peroxisomes for the establishment of the cellular immune response has been highlighted by different reports demonstrating that distinct viruses have developed specific strategies to target and evade the peroxisomal antiviral signalling (Cohen et al., 2000; Berg et al., 2012; Han et al., 2014; Jefferson et al., 2014; You et al., 2015; Ferreira et al., 2016, 2019, 2022; Xu et al., 2017; Zheng and Su, 2017). We have also previously demonstrated that HCMV interferes with the peroxisomal antiviral pathway through its protein vMIA (Magalhães et al., 2016). In that study, we show that vMIA interacts with PEX19 to be transported to the peroxisomal membranes, where it interacts with MAVS, induces the organelle's fragmentation, and inhibits the antiviral immune response. Peroxisomal fragmentation has, however, been shown not to influence the vMIA-induced inhibition of the antiviral signalling, suggesting that two vMIA-mediated independent processes are occurring at this organelle (Magalhães et al., 2016). These results have also uncovered dissimilarities between the mechanisms of action of vMIA towards peroxisomes and mitochondria, as, at mitochondria, vMIA inhibition of the antiviral signalling is dependent on the organelle's fission (Castanier et al., 2010).

These observations were not initially anticipated, as these organelles, besides sharing MAVS, are dependent on the same fission machinery, harbouring proteins, such as MFF (Gandre-Babbe and van der Bliek, 2008), which anchors DLP1 at the membranes of both organelles for final fission (Imoto et al., 2020).

The reasoning behind the vMIA-mediated inhibition of the antiviral response at mitochondria has been suggested to be based on the disruption of the MAVS-STING interactions due to the reduction of mitochondria-ER contact sites, as a consequence of the organelle's fragmentation (Castanier et al., 2010). Here, we show, for the first time, that STING and MAVS also interact at the peroxisomal level but, contrarily to mitochondria, this interaction is not disturbed by the presence of vMIA. This result uncovers key differences between the mechanisms of action of vMIA at these two organelles, which may reflect intrinsic, yet unidentified, dissimilarities between the two antiviral signalling pathways.

By evaluating vMIA's dependence on the organelles' fission machineries to fragment peroxisomes and mitochondria, we have unraveled further discrepancies between the two pathways. While at peroxisomes, vMIA is not able to induce fragmentation in the absence of DLP1 and MFF, these proteins are not essential for its action towards mitochondrial fragmentation. It is then tempting to suggest that, at peroxisomes, vMIA somehow stimulates MFF to recruit more DLP1 and induce organelle fragmentation. At mitochondria, however, the organelle fragmentation induced by vMIA may be related to the role of this viral protein on the control of apoptosis, interfering with BAX to prevent mitochondrial outer-membrane permeabilization, and mediating the release of ER Ca^{2+} stores into the cytosol (Poncet et al., 2006; Sharon-Friling et al., 2006; Ma et al., 2012). One could hypothesize that one of vMIA's roles at peroxisomes could also be related with its anti-apoptotic function. Although a direct influence of peroxisomes on apoptosis has not yet been demonstrated, the anti-apoptotic proteins Bcl2 and Bcl-XL, as well as the pro-apoptotic protein BAK (Costello et al., 2017; Fujiki et al., 2017; Hosoi et al., 2017) have also been identified at peroxisomes. It has also been demonstrated that peroxisomal BAK regulates membrane integrity and the release of soluble peroxisomal matrix proteins, such as catalase (Fujiki et al., 2017; Hosoi et al., 2017). The presence of anti-apoptotic proteins, such as vMIA, at the peroxisomal membranes could, hence, protect the organelle from excessive matrix protein release into the cytosol. However, it has been shown that, at least in mitochondria, vMIA does not block BAK-mediated apoptosis and that this inhibition is mediated by another HCMV protein (Arnoult et al., 2004; Cam et al., 2010).

Besides showing that the antiviral signalling inhibition is unrelated to the organelle morphology changes, we have also demonstrated that the vMIA-induced peroxisomal fragmentation is totally independent of the presence of MAVS at the organelle's membranes. It was recently shown that HCMV induces the upregulation of peroxisomal proteins and peroxisome growth and fission, mainly at late times post-infection, increasing peroxisome number and leading to a higher production of plasmalogens, contributing to the enhancement of virus production (Beltran et al., 2018). In a subsequent study, the authors suggest a model by which vMIA activates PEX11β, which in turn induces MFF to upregulate peroxisome fission during infection (Federspiel et al., 2020). These results are in line with our data and together indicate that vMIA induces peroxisome fragmentation to favor viral propagation at late times post-infection, while, earlier in infection, it specifically inhibits the peroxisome-dependent signalling.

Our results clearly also demonstrate that MFF is essential for the vMIA-mediated inhibition of the immune response at peroxisomes, but not at mitochondria, revealing once more important differences between the mechanisms occurring at both organelles. Importantly, we further reveal that vMIA, likely though direct interaction (Magalhães et al., 2016), inhibits MAVS oligomerization at both peroxisomes and mitochondria, further impairing the downstream signalling. Coherently, MFF has been shown to be essential for this oligomerization inhibition at peroxisomes, but not at mitochondria. The involvement of peroxisome specific proteins, such as PEX11 (Visser et al., 2007; Carmichael and Schrader, 2022), and other fission machinery proteins, such as FIS1 (Ihenacho et al., 2021), on the vMIA-dependent evasion of antiviral signalling should be adressed in the future, in order to further unravel de mechanisms involved and explain the observed differences between the processes occuring at peroxisomes and mitochondria. Based on all our results, we suggest a model for vMIA's mechanism of action towards peroxisomes, which is depicted in **Figure 6**: upon infection, vMIA interacts with PEX19 at the cytoplasm and travels to peroxisomes, where it interacts with MAVS. This interaction interferes, in an MFF-dependent manner, with the formation of MAVS oligomers and inhibits the consequent activation of the downstream antiviral signalling. In parallel, vMIA induces peroxisome fragmentation in an MFF- and DLP1- dependent manner, but independently of MAVS, which may be important for the enhancement of lipid metabolism and virus particles formation at late times post-infection.

In conclusion, in this manuscript we not only propose the molecular mechanism by which HCMV evades the peroxisomal antiviral response, but also shed some light on possible molecular processes that may be occurring at mitochondria. Our results once more emphasize the relevance of peroxisomes as platforms for antiviral signalling against HCMV and uncover molecular mechanisms that may be explored as targets for antiviral therapy.

DATA AVAILABILITY STATEMENT

The raw data supporting the conclusions of this article will be made available by the authors, without undue reservation.

AUTHOR CONTRIBUTIONS

AF, AG, JK and DR contributed to conception and design of the study. AF, AG, AM, IV and MM acquired the data; AF, AG, JK, and DR wrote the manuscript; All authors contributed to manuscript revision, read, and approved the submitted version.

FUNDING

This work was financially supported by the Portuguese Foundation for Science and Technology (FCT): PTDC/BIA-CEL/31378/2017

(POCI-01-0145-FEDER-031378), PTDC/IMI-MIC/0828/2012, CEECIND/03747/2017, SFRH/BPD/77619/2011, SFRH/BD/81223/2011, SFRH/BPD/103580/2014, SFRH/BD/121432/2016, SFRH/BD/137851/2018, UID/ BIM/04501/2013 and UIDB/04501/2020, under the scope of the Operational Program "Competitiveness and internationalization", in its FEDER/FNR component. It was also supported by the CCDRC and FEDER: pAGE–CENTRO-01-0145-FEDER-000003. It was furthermore supported by the European Union thought the Horizon 2020 program: H2020-WIDESPREAD-2020-5 ID-952373. This study was supported by NIH grants AI133524, AI093589, AI116550 and P30DK34854 to JCK. This study was also supported by NIH grants AI133524, AI093589, AI116550 and P30DK34854 to JCK.

ACKNOWLEDGMENTS

We thank Dr Victor Goldmacher for kindly providing the vMIA-Myc plasmid, Dr Friedemann Weber for kindly providing the GFP-RIG-I-CARD plasmid, Dr Maria João Amorim for providing the HEK293T cells and Dr Bruno Jesus for providing pCL-Ampho and pVSV-G. The authors thank Dr Michael Schrader, Dr Markus Islinger and Dr Jorge Azevedo for the valuable discussions. The authors also thank all the members of the Virus Host-cell Interactions Laboratory (especially Vanessa Ferreira and Bruno Ramos, who prepared the MEFs MAVS-MITO cell line) and Kagan's Laboratory, for the valuable inputs and discussions. Image acquisition was performed in the LiM facility of iBiMED, a node of PPBI (Portuguese Platform of BioImaging): POCI-01-0145-FEDER-022122.

SUPPLEMENTARY MATERIAL

The Supplementary Material for this article can be found online at: https://www.frontiersin.org/articles/10.3389/fcell.2022.871977/full#supplementary-material

REFERENCES

Arnoult, D., Bartle, L. M., Skaletskaya, A., Poncet, D., Zamzami, N., Park, P. U., et al. (2004). Cytomegalovirus Cell Death Suppressor vMIA Blocks Bax- but Not Bak-Mediated Apoptosis by Binding and Sequestering Bax at Mitochondria. *Proc. Natl. Acad. Sci.* 101, 7988–7993. doi:10.1073/pnas.0401897101

Bender, S., Reuter, A., Eberle, F., Einhorn, E., Binder, M., and Bartenschlager, R. (2015). Activation of Type I and III Interferon Response by Mitochondrial and Peroxisomal MAVS and Inhibition by Hepatitis C Virus. *PLOS Pathog.* 11, e1005264. doi:10.1371/journal.ppat.1005264

Berg, R. K., Melchjorsen, J., Rintahaka, J., Diget, E., Søby, S., Horan, K. A., et al. (2012). Genomic HIV RNA Induces Innate Immune Responses through RIG-I-dependent Sensing of Secondary-Structured RNA. *PLoS One* 7, e29291. doi:10.1371/journal.pone.0029291

Çam, M., Handke, W., Picard-Maureau, M., and Brune, W. (2010). Cytomegaloviruses Inhibit Bak- and Bax-Mediated Apoptosis with Two Separate Viral Proteins. *Cell Death Differ* 17, 655–665. doi:10.1038/cdd.2009.147

Carmichael, R. E., and Schrader, M. (2022). Determinants of Peroxisome Membrane Dynamics. *Front. Physiol.* 13, 834411. doi:10.3389/fphys.2022.834411

Castanier, C., Garcin, D., Vazquez, A., Arnoult, D., Ablasser, A., Bauernfeind, F., et al. (2010). Mitochondrial Dynamics Regulate the RIG-I-like Receptor Antiviral Pathway. *EMBO Rep.* 11, 133–138. doi:10.1038/embor.2009.258

Cohen, G. B., Rangan, V. S., Chen, B. K., Smith, S., and Baltimore, D. (2000). The Human Thioesterase II Protein Binds to a Site on HIV-1 Nef Critical for CD4 Down-Regulation. *J. Biol. Chem.* 275, 23097–23105. doi:10.1074/jbc.M000536200

Costello, J. L., Castro, I. G., Camões, F., Schrader, T. A., McNeall, D., Yang, J., et al. (2017). Predicting the Targeting of Tail-Anchored Proteins to Subcellular Compartments in Mammalian Cells. *J. Cel Sci.* 130, 1675–1687. doi:10.1242/jcs.200204

Dixit, E., Boulant, S., Zhang, Y., Lee, A. S. Y., Odendall, C., Shum, B., et al. (2010). Peroxisomes Are Signaling Platforms for Antiviral Innate Immunity. *Cell* 141, 668–681. doi:10.1016/j.cell.2010.04.018

Dixit, E., and Kagan, J. C. (2013). Intracellular Pathogen Detection by RIG-I-like Receptors. *Adv. Immunol.* 117, 99–125. doi:10.1016/B978-0-12-410524-9.00004-9

Farmer, T., Naslavsky, N., and Caplan, S. (2018). Tying Trafficking to Fusion and Fission at the Mighty Mitochondria. *Traffic* 19, 569–577. doi:10.1111/tra.12573

Federspiel, J. D., Cook, K. C., Kennedy, M. A., Venkatesh, S. S., Otter, C. J., Hofstadter, W. A., et al. (2020). Mitochondria and Peroxisome Remodeling across Cytomegalovirus Infection Time Viewed through the Lens of Inter-ViSTA. *Cel Rep.* 32, 107943. doi:10.1016/j.celrep.2020.107943

Ferreira, A. R., Magalhães, A. C., Camões, F., Gouveia, A., Vieira, M., Kagan, J. C., et al. (2016). Hepatitis C Virus NS 3-4A Inhibits the Peroxisomal MAVS -dependent Antiviral Signalling Response. *J. Cel. Mol. Med.* 20, 750–757. doi:10.1111/jcmm.12801

Ferreira, A. R., Marques, M., Ramos, B., Kagan, J. C., and Ribeiro, D. (2022). Emerging Roles of Peroxisomes in Viral Infections. *Trends Cel Biol.* 32, 124–139. doi:10.1016/J.TCB.2021.09.010

Ferreira, A. R., Marques, M., and Ribeiro, D. (2019). Peroxisomes and Innate Immunity: Antiviral Response and beyond. *Ijms* 20, 3795. doi:10.3390/ijms20153795

Ferreira, A. R., Ramos, B., Nunes, A., and Ribeiro, D. (2020). Hepatitis C Virus: Evading the Intracellular Innate Immunity. *Jcm* 9, 790. doi:10.3390/jcm9030790

Fliss, P. M., and Brune, W. (2012). Prevention of Cellular Suicide by Cytomegaloviruses. *Viruses* 4, 1928–1949. doi:10.3390/v4101928

Fransen, M., Lismont, C., and Walton, P. (2017). The Peroxisome-Mitochondria Connection: How and Why? *Ijms* 18, 1126. doi:10.3390/ijms18061126

Fujiki, Y., Miyata, N., Mukai, S., Okumoto, K., and Cheng, E. H. (2017). BAK Regulates Catalase Release from Peroxisomes. *Mol. Cell Oncol.* 4, e1306610. doi:10.1080/23723556.2017.1306610

Gandre-Babbe, S., and van der Bliek, A. M. (2008). The Novel Tail-Anchored Membrane Protein Mff Controls Mitochondrial and Peroxisomal Fission in Mammalian Cells. *MBoC* 19, 2402–2412. doi:10.1091/mbc.E07-12-1287

Goldmacher, V. S., Bartle, L. M., Skaletskaya, A., Dionne, C. A., Kedersha, N. L., Vater, C. A., et al. (1999). A Cytomegalovirus-Encoded Mitochondria-Localized Inhibitor of Apoptosis Structurally Unrelated to Bcl-2. *Proc. Natl. Acad. Sci.* 96, 12536–12541. doi:10.1073/PNAS.96.22.12536

Goldmacher, V. S. (2005). Cell Death Suppression by Cytomegaloviruses. *Apoptosis* 10, 251–265. doi:10.1007/s10495-005-0800-z

Han, J.-M., Kang, J.-A., Han, M.-H., Chung, K.-H., Lee, C.-R., Song, W.-K., et al. (2014). Peroxisome-localized Hepatitis Bx Protein Increases the Invasion Property of Hepatocellular Carcinoma Cells. *Arch. Virol.* 159, 2549–2557. doi:10.1007/s00705-014-2105-4

Horner, S. M., Liu, H. M., Park, H. S., Briley, J., and Gale, M. (2011). Mitochondrial-associated Endoplasmic Reticulum Membranes (MAM) Form Innate Immune Synapses and Are Targeted by Hepatitis C Virus. *Proc. Natl. Acad. Sci. U.S.A.* 108, 14590–14595. doi:10.1073/pnas.1110133108/

Hosoi, K.-I., Miyata, N., Mukai, S., Furuki, S., Okumoto, K., Cheng, E. H., et al. (2017). The VDAC2-BAK axis Regulates Peroxisomal Membrane Permeability. *J. Cel Biol.* 216, 709–722. doi:10.1083/jcb.201605002

Hou, F., Sun, L., Zheng, H., Skaug, B., Jiang, Q.-X., and Chen, Z. J. (2011). MAVS Forms Functional Prion-like Aggregates to Activate and Propagate Antiviral Innate Immune Response. *Cell* 146, 448–461. doi:10.1016/j.cell.2011.06.041

Ihenacho, U. K., Meacham, K. A., Harwig, M. C., Widlansky, M. E., and Hill, R. B. (2021). Mitochondrial Fission Protein 1: Emerging Roles in Organellar Form and Function in Health and Disease. *Front. Endocrinol.* 12. doi:10.3389/FENDO.2021.660095

Imoto, Y., Itoh, K., and Fujiki, Y. (2020). Molecular Basis of Mitochondrial and Peroxisomal Division Machineries. *Ijms* 21, 5452. doi:10.3390/ijms21155452

Islinger, M., Voelkl, A., Fahimi, H. D., and Schrader, M. (2018). The Peroxisome: an Update on Mysteries 2.0. *Histochem. Cel Biol.* 150, 443–471. doi:10.1007/s00418-018-1722-5

Itoyama, A., Michiyuki, S., Honsho, M., Yamamoto, T., Moser, A., Yoshida, Y., et al. (2013). Mff Functions with Pex11pβ and DLP1 in Peroxisomal Fission. *Biol. Open* 2, 998–1006. doi:10.1242/bio.20135298

Jackson, S. E., Mason, G. M., and Wills, M. R. (2011). Human Cytomegalovirus Immunity and Immune Evasion. *Virus. Res.* 157, 151–160. doi:10.1016/j.virusres.2010.10.031

Jean Beltran, P. M., Cook, K. C., Hashimoto, Y., Galitzine, C., Murray, L. A., Vitek, O., et al. (2018). Infection-Induced Peroxisome Biogenesis Is a Metabolic Strategy for Herpesvirus Replication. *Cell Host & Microbe* 24, 526–541. doi:10.1016/j.chom.2018.09.002

Jefferson, M., Whelband, M., Mohorianu, I., and Powell, P. P. (2014). The Pestivirus N Terminal Protease Npro Redistributes to Mitochondria and Peroxisomes Suggesting New Sites for Regulation of IRF3 by Npro. *PLoS One* 9, e88838. doi:10.1371/journal.pone.0088838

Kawai, T., Takahashi, K., Sato, S., Coban, C., Kumar, H., Kato, H., et al. (2005). IPS-1, an Adaptor Triggering RIG-I- and Mda5-Mediated Type I Interferon Induction. *Nat. Immunol.* 6, 981–988. doi:10.1038/ni1243

Kell, A. M., and Gale, M. (2015). RIG-I in RNA Virus Recognition. *Virology* 479-480, 110–121. doi:10.1016/j.virol.2015.02.017

Kobayashi, S., Tanaka, A., and Fujiki, Y. (2007). Fis1, DLP1, and Pex11p Coordinately Regulate Peroxisome Morphogenesis. *Exp. Cel Res.* 313, 1675–1686. doi:10.1016/j.yexcr.2007.02.028

Koch, A., Thiemann, M., Grabenbauer, M., Yoon, Y., McNiven, M. A., and Schrader, M. (2003). Dynamin-like Protein 1 Is Involved in Peroxisomal Fission. *J. Biol. Chem.* 278, 8597–8605. doi:10.1074/jbc.M211761200

Li, X., and Gould, S. J. (2003). The Dynamin-like GTPase DLP1 Is Essential for Peroxisome Division and Is Recruited to Peroxisomes in Part by PEX11. *J. Biol. Chem.* 278, 17012–17020. doi:10.1074/jbc.M212031200

Ma, J., Edlich, F., Bermejo, G. A., Norris, K. L., Youle, R. J., and Tjandra, N. (2012). Structural Mechanism of Bax Inhibition by Cytomegalovirus Protein vMIA. *Proc. Natl. Acad. Sci. U.S.A.* 109, 20901–20906–6. doi:10.1073/pnas.1217094110

Magalhães, A. C., Ferreira, A. R., Gomes, S., Vieira, M., Gouveia, A., Valença, I., et al. (2016). Peroxisomes Are Platforms for Cytomegalovirus' Evasion from the Cellular Immune Response. *Sci. Rep.* 6, 26028. doi:10.1038/srep26028

Marques, M., Ferreira, A., and Ribeiro, D. (2018). The Interplay between Human Cytomegalovirus and Pathogen Recognition Receptor Signaling. *Viruses* 10, 514. doi:10.3390/v10100514

McCormick, A. L., Smith, V. L., Chow, D., and Mocarski, E. S. (2003). Disruption of Mitochondrial Networks by the Human Cytomegalovirus UL37 Gene Product Viral Mitochondrion-Localized Inhibitor of Apoptosis. *J. Virol.* 77, 631–641. doi:10.1128/JVI.77.1.63110.1128/jvi.77.1.631-641.2003

Meylan, E., Curran, J., Hofmann, K., Moradpour, D., Binder, M., Bartenschlager, R., et al. (2005). Cardif Is an Adaptor Protein in the RIG-I Antiviral Pathway and Is Targeted by Hepatitis C Virus. *Nature* 437, 1167–1172. doi:10.1038/nature04193

Onoguchi, K., Onomoto, K., Takamatsu, S., Jogi, M., Takemura, A., Morimoto, S., et al. (2010). Virus-Infection or 5′ppp-RNA Activates Antiviral Signal through Redistribution of IPS-1 Mediated by MFN1. *Plos Pathog.* 6, e1001012. doi:10.1371/journal.ppat.1001012

Poncet, D., Larochette, N., Pauleau, A.-L., Boya, P., Jalil, A.-A., Cartron, P.-F., et al. (2004). An Anti-apoptotic Viral Protein that Recruits Bax to Mitochondria. *J. Biol. Chem.* 279, 22605–22614. doi:10.1074/jbc.M308408200

Poncet, D., Pauleau, A.-L., Szabadkai, G., Vozza, A., Scholz, S. R., Le Bras, M., et al. (2006). Cytopathic Effects of the Cytomegalovirus-Encoded Apoptosis Inhibitory Protein vMIA. *J. Cel Biol.* 174, 985–996. doi:10.1083/jcb.200604069

Ribeiro, D., Castro, I., Fahimi, H. D., and Schrader, M. (2012). Peroxisome Morphology in Pathology. *Histol. Histopathol.* 27, 661–676. doi:10.14670/HH-27.661

Saito, T., and Gale, M. (2008). Differential Recognition of Double-Stranded RNA by RIG-I-like Receptors in Antiviral Immunity. *J. Exp. Med.* 205, 1523–1527. doi:10.1084/jem.20081210

Schrader, M., Kamoshita, M., and Islinger, M. (2020). Organelle Interplay-Peroxisome Interactions in Health and Disease. *Jrnl Inher Metab. Disea* 43, 71–89. doi:10.1002/jimd.12083

Seth, R. B., Sun, L., Ea, C.-K., and Chen, Z. J. (2005). Identification and Characterization of MAVS, a Mitochondrial Antiviral Signaling Protein that Activates NF-Kb and IRF3. *Cell* 122, 669–682. doi:10.1016/j.cell.2005.08.012

Sharon-Friling, R., Goodhouse, J., Colberg-Poley, A. M., and Shenk, T. (2006). Human Cytomegalovirus pUL37x1 Induces the Release of Endoplasmic Reticulum Calcium Stores. *Proc. Natl. Acad. Sci. U.S.A.* 103, 19117–19122. doi:10.1073/pnas.0609353103

Tilokani, L., Nagashima, S., Paupe, V., and Prudent, J. (2018). Mitochondrial Dynamics: Overview of Molecular Mechanisms. *Essays Biochem.* 62, 341–360. doi:10.1042/EBC20170104

Visser, W. F., van Roermund, C. W. T., Ijlst, L., Waterham, H. R., and Wanders, R. J. A. (2007). Metabolite Transport across the Peroxisomal Membrane. *Biochem. J.* 401, 365–375. doi:10.1042/BJ20061352

Wanders, R. J. A., Vaz, F. M., Waterham, H. R., and Ferdinandusse, S. (2020). Fatty Acid Oxidation in Peroxisomes: Enzymology, Metabolic Crosstalk with Other Organelles and Peroxisomal Disorders. *Adv. Exp. Med. Biol.* 1299, 55–70. doi:10.1007/978-3-030-60204-8_5

Xu, L.-G., Wang, Y.-Y., Han, K.-J., Li, L.-Y., Zhai, Z., and Shu, H.-B. (2005). VISA Is an Adapter Protein Required for Virus-Triggered IFN-β Signaling. *Mol. Cel* 19, 727–740. doi:10.1016/j.molcel.2005.08.014

Xu, Z., Asahchop, E. L., Branton, W. G., Gelman, B. B., Power, C., and Hobman, T. C. (2017). MicroRNAs Upregulated during HIV Infection Target Peroxisome Biogenesis Factors: Implications for Virus Biology, Disease Mechanisms and Neuropathology. *Plos Pathog.* 13, e1006360. doi:10.1371/journal.ppat.1006360

Yoneyama, M., Kikuchi, M., Natsukawa, T., Shinobu, N., Imaizumi, T., Miyagishi, M., et al. (2004). The RNA Helicase RIG-I Has an Essential Function in Double-Stranded RNA-Induced Innate Antiviral Responses. *Nat. Immunol.* 5, 730–737. doi:10.1038/ni1087

You, J., Hou, S., Malik-Soni, N., Xu, Z., Kumar, A., Rachubinski, R. A., et al. (2015). Flavivirus Infection Impairs Peroxisome Biogenesis and Early Antiviral Signaling. *J. Virol.* 89, 12349–12361. doi:10.1128/JVI.01365-15

Zhang, A., Hildreth, R. L., and Colberg-Poley, A. M. (2013). Human Cytomegalovirus Inhibits Apoptosis by Proteasome-Mediated Degradation of Bax at Endoplasmic Reticulum-Mitochondrion Contacts. *J. Virol.* 87, 5657–5668. doi:10.1128/JVI.00145-13

Zheng, C., and Su, C. (2017). Herpes Simplex Virus 1 Infection Dampens the Immediate Early Antiviral Innate Immunity Signaling from Peroxisomes by Tegument Protein VP16. *Virol. J.* 14, 35. doi:10.1186/s12985-017-0709-5

Conflict of Interest: JCK consults for IFM Therapeutics and consults and holds equity in Corner Therapeutics, Larkspur Biosciences and Neumora Therapeutics.

The remaining authors declare that the research was conducted in the absence of any commercial or financial relationships that could be construed as a potential conflict of interest.

Publisher's Note: All claims expressed in this article are solely those of the authors and do not necessarily represent those of their affiliated organizations, or those of the publisher, the editors and the reviewers. Any product that may be evaluated in this article, or claim that may be made by its manufacturer, is not guaranteed or endorsed by the publisher.

frontiers | Frontiers in Cell and Developmental Biology

ORIGINAL RESEARCH
published: 12 May 2022
doi: 10.3389/fcell.2022.858084

Two Pex5 Proteins With Different Cargo Specificity Are Critical for Peroxisome Function in Ustilago maydis

Julia Ast[1,2], *Nils Bäcker*[1], *Elena Bittner*[1], *Domenica Martorana*[1], *Humda Ahmad*[1], *Michael Bölker*[1,3] *and Johannes Freitag*[1]*

[1]Department of Biology, Philipps-University Marburg, Marburg, Germany, [2]Institute of Metabolism and Systems Research (IMSR), and Centre of Membrane Proteins and Receptors (COMPARE), University of Birmingham, Birmingham, United Kingdom, [3]Center for Synthetic Microbiology, Philipps-University Marburg, Marburg, Germany

Peroxisomes are dynamic multipurpose organelles with a major function in fatty acid oxidation and breakdown of hydrogen peroxide. Many proteins destined for the peroxisomal matrix contain a *C*-terminal peroxisomal targeting signal type 1 (PTS1), which is recognized by tetratricopeptide repeat (TPR) proteins of the Pex5 family. Various species express at least two different Pex5 proteins, but how this contributes to protein import and organelle function is not fully understood. Here, we analyzed truncated and chimeric variants of two Pex5 proteins, Pex5a and Pex5b, from the fungus *Ustilago maydis*. Both proteins are required for optimal growth on oleic acid-containing medium. The *N*-terminal domain (NTD) of Pex5b is critical for import of all investigated peroxisomal matrix proteins including PTS2 proteins and at least one protein without a canonical PTS. In contrast, the NTD of Pex5a is not sufficient for translocation of peroxisomal matrix proteins. In the presence of Pex5b, however, specific cargo can be imported *via* this domain of Pex5a. The TPR domains of Pex5a and Pex5b differ in their affinity to variations of the PTS1 motif and thus can mediate import of different subsets of matrix proteins. Together, our data reveal that *U. maydis* employs versatile targeting modules to control peroxisome function. These findings will promote our understanding of peroxisomal protein import also in other biological systems.

Keywords: PEX5, PEX7, beta oxidation, peroxisome, targeting signal, Ustilago maydis, PTS1, PTS2

OPEN ACCESS

Edited by:
Marek Skoneczny, Institute of Biochemistry and Biophysics (PAN), Poland

Reviewed by:
Jorge E. Azevedo, Universidade do Porto, Portugal
Markus Kunze, Medical University of Vienna, Austria

***Correspondence:**
Johannes Freitag
johannes.freitag@biologie.uni-marburg.de

Specialty section:
This article was submitted to Membrane Traffic, a section of the journal Frontiers in Cell and Developmental Biology

Received: *19 January 2022*
Accepted: *31 March 2022*
Published: *12 May 2022*

Citation:
Ast J, Bäcker N, Bittner E, Martorana D, Ahmad H, Bölker M and Freitag J (2022) Two Pex5 Proteins With Different Cargo Specificity Are Critical for Peroxisome Function in Ustilago maydis. Front. Cell Dev. Biol. 10:858084. doi: 10.3389/fcell.2022.858084

INTRODUCTION

In eukaryotic cells specific metabolic pathways are often contained inside of organelles such as mitochondria and peroxisomes (Lodish et al., 2000). Peroxisomes have versatile biological roles including detoxification of hydrogen peroxide, degradation of fatty acids and metabolism of amino acids and are essential for human health (Smith and Aitchison, 2013; Wanders, 2014). Peroxisomal matrix proteins are imported into the organelle lumen from the cytosol *via* an evolutionary conserved set of cytosolic receptors and peroxisomal membrane proteins (Gabaldón, 2010; Kim and Hettema, 2015; Walter and Erdmann, 2019). The majority of known matrix proteins contains one of two conserved targeting signals termed peroxisomal targeting signal type 1 (PTS1) and type 2 (PTS2). PTS1 motifs are located at the *C*-terminus, originally identified as a tripeptide with the

sequence Ser-Lys-Leu (SKL), occurring in many variations of this prototype sequence (Gould et al., 1989; Brocard and Hartig, 2006; Lingner et al., 2011; Nötzel et al., 2016). The amino acid sequence upstream of the *C*-terminal tripeptide contributes to PTS1 recognition (Brocard and Hartig, 2006). PTS2 motifs are located in the *N*-terminal part of a protein and are recognized by the receptor protein Pex7 (Braverman et al., 1997; Lazarow, 2006; Kunze et al., 2011; Kunze, 2020). Several proteins lacking canonical targeting signals have been described (van der Klei and Veenhuis, 2006). These either rely on piggy-back import mediated by their interaction with other PTS-containing proteins (Glover et al., 1994; McNew and Goodman, 1994; Islinger et al., 2009; Schueren et al., 2014; Effelsberg et al., 2015; Saryi et al., 2017; Gabay-Maskit et al., 2020) or on direct interaction with Pex5 (Skoneczny and Lazarow, 1998; Klein et al., 2002; Rymer et al., 2018; Kempiński et al., 2020; Rosenthal et al., 2020; Yifrach et al., 2021).

Pex5 recognizes PTS1 motifs *via* several tetratricopeptide repeats (TPRs) located in its *C*-terminal domain (CTD) (Brocard et al., 1994; Gatto et al., 2000). Subsequently, the receptor-cargo complex interacts with the peroxisomal membrane proteins Pex13 and Pex14 (Gould et al., 1996; Urquhart et al., 2000; Lill et al., 2020), followed by import of cargo proteins into the peroxisomal lumen without the requirement for ATP turnover (for review see: Miyata and Fujiki, 2005; Kim and Hettema, 2015; Francisco et al., 2017). The interaction with Pex14 is mediated *via* a conserved di-aromatic amino acid motif located within the unstructured *N*-terminal domain (NTD) of Pex5 (Saidowsky et al., 2001; Otera et al., 2002; Carvalho et al., 2006; Su et al., 2009). The exact mechanistic functionality of the translocation machinery is still a matter of investigation and so far lacks structural data, but probably has a transient character (Meinecke et al., 2010; Dias et al., 2017; Bürgi et al., 2021). After cargo release, Pex5 proteins are recycled from the peroxisome to the cytosol. Recycling involves ubiquitination, unfolding, energy provided by the AAA-ATPases Pex1 and Pex6, and deubiquitination (Miyata and Fujiki, 2005; Platta et al., 2005; Platta et al., 2007; Gardner et al., 2018; Pedrosa et al., 2018; El Magraoui et al., 2019).

In mammals, two isoforms of Pex5 – Pex5-small and Pex5-large – are generated that derive from alternative splicing (Braverman et al., 1998). The longer isoform contains an additional Pex7 binding domain inside of the NTD. In mammals, another TPR-containing protein with significant homology to Pex5 was identified, which can interact with PTS1 proteins but also with an ion channel (Amery et al., 2001; Santoro et al., 2004, 2011). Many fungi encode two proteins with homology to the PTS1 receptor Pex5 (Kiel et al., 2006; Freitag et al., 2012). In *Saccharomyces cerevisae*, the Pex5 paralog Pex9 is induced in cells grown in oleic acid-containing medium and controls peroxisomal import of the glyoxylate cycle enzyme malate synthase and additional cargo (Effelsberg et al., 2016; Yifrach et al., 2016; Yifrach et al., 2022). Thus, distinct pathways to target PTS1 proteins to peroxisomes are found in diverse eukaryotes and may be crucial for the regulation of peroxisomal protein import and peroxisome function.

In the phytopathogenic fungus *U. maydis,* which causes smut disease on corn (Lanver et al., 2017), we have identified two Pex5-paralogs – termed Pex5a and Pex5b (Freitag et al., 2012). Pex5b is the longer paralog and contains a putative binding domain for the PTS2 receptor Pex7 (**Figure 1A**). Here, we show that the NTDs and the *C*-terminal TPR-domains of Pex5a and Pex5b each can recognize and import specific cargo. Additionally, we found that the NTD of Pex5b is essential for import of all peroxisomal matrix proteins investigated, and thus acts as a critical component in a dynamic network of receptors that target soluble proteins into peroxisomes.

RESULTS

Functional Analysis of Pex5a and Pex5b From *U. maydis*

In a previous study we have described two Pex5-like proteins, Pex5a (Um02528) and Pex5b (Um10172) from *U. maydis* required for optimal growth of the fungus in different nutrient conditions and for pathogenic development (**Figure 1A**; Freitag et al., 2012). To discriminate the specific contributions of both proteins for growth on different carbon sources (Freitag et al., 2012; Camões et al., 2015), we tested *pex5a* and *pex5b* single and double deletion mutants on media containing either glucose or oleic acid as sole carbon source (**Figure 1B**). We found that Δ*pex5a* cells did not exhibit a severe growth defect on glucose plates but on oleic acid-containing medium (**Figure 1B**). Growth of mutants lacking *pex5b* or both genes was reduced on glucose-containing medium indicated by smaller colonies on solid medium and lower growth rates in liquid medium (**Figure 1B** and **Supplementary Figure S1**). On plates containing oleic acid as sole carbon source proliferation of these mutants was almost abolished (**Figure 1B**). This indicates that the presence of both Pex5 proteins is required for peroxisome function in *U. maydis*.

Next, we followed localization of the peroxisomal reporter protein mCherry-SKL in Δ*pex5a* and Δ*pex5b* cells (**Figure 1C**). Peroxisomal localization of mCherry-SKL was observed in Δ*pex5a* mutants but not in Δ*pex5b* mutants suggesting that Pex5b is necessary for peroxisomal import of PTS1 proteins in *U. maydis*. To test whether impaired binding of PTS1 cargo was responsible for the phenotype of Δ*pex5b* cells we deleted the TPR domains of Pex5b. Although the partial deletion of *pex5b* affected growth on oleic acid-containing medium (**Figure 1B**), *pex5bΔTPR* mutants still were able to import mCherry-SKL into peroxisomes (**Figure 1C**). Pex5b can therefore import PTS1 proteins into peroxisomes in the absence of Pex5a, while Pex5a-mediated protein import depends on the Pex5b NTD.

To address whether the observed growth phenotype of Δ*pex5a* cells (**Figure 1B**) results from different specificities of the Pex5a and Pex5b receptors for distinct subsets of peroxisomal matrix proteins or is caused by the reduced overall amount of Pex5 receptors, we overexpressed Pex5 derivatives. Overexpression of Pex5b rescued the growth phenotype of Δ*pex5b* cells but did not restore the growth phenotype of Δ*pex5a* cells (**Supplementary Figures S2A,B**). This indicates that it is not the reduced dosage of

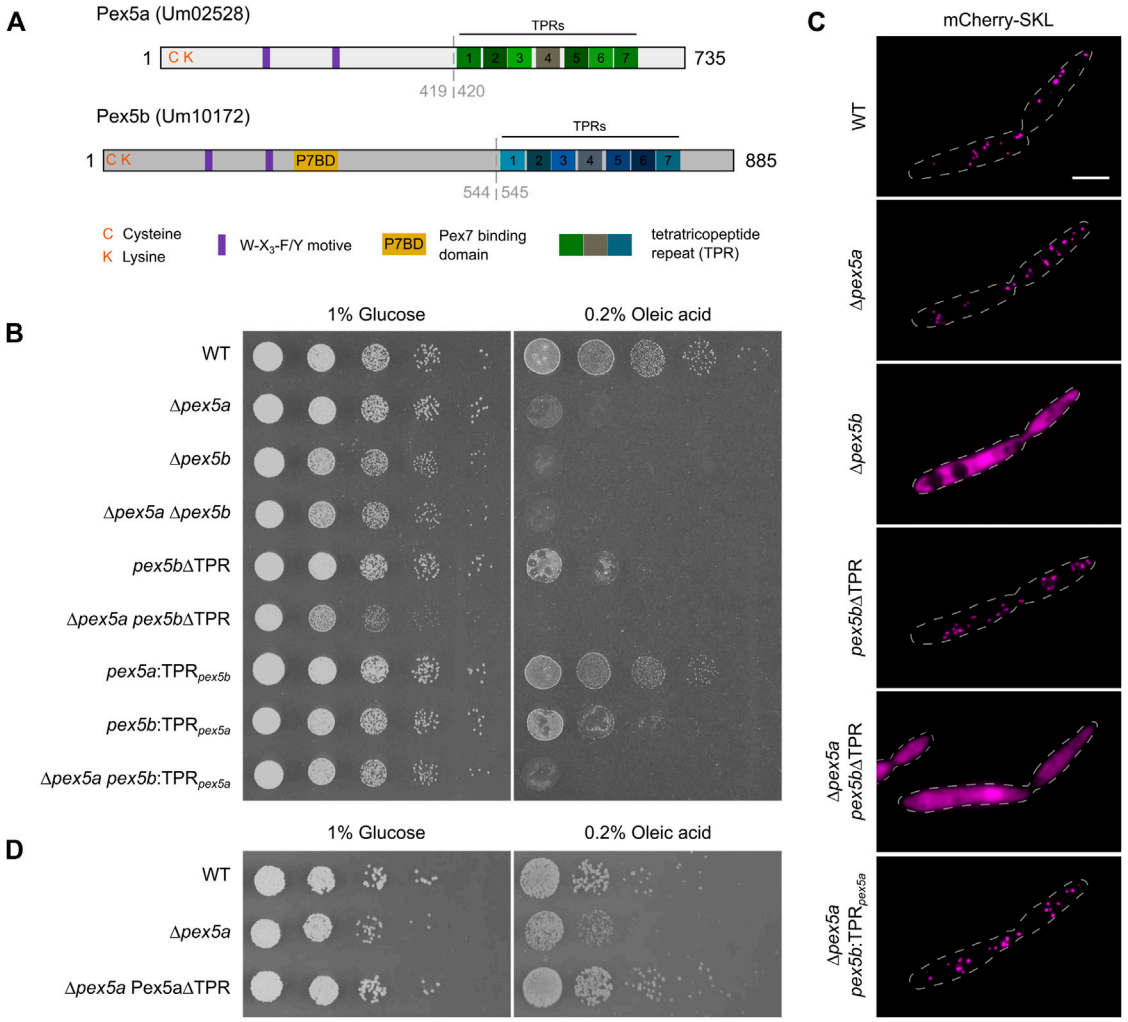

FIGURE 1 | Contribution of the *N*- and *C*-terminal domains of two Pex5 proteins to peroxisome function. **(A)** Scheme illustrating the domain organization of Pex5a and Pex5b from *U. maydis*. C and K refer to a cysteine and a lysine residue possibly involved in ubiquitination. Purple rectangles denote the position of W-X_3-F/Y motifs required for docking complex interaction. A putative Pex7 binding domain (P7BD) of Pex5b is shown in yellow. The position of the TPR domains is highlighted with rectangles. Gray dashed lines indicate the position of domain swaps to generate chimeras (see **Supplementary Figure S3**). **(B)** Serial tenfold dilutions of indicated strains were spotted on minimal media containing either glucose or oleic acid as sole carbon source. Plates were photographed after 2 days of incubation at 23°C. The assays reveal that both the NTD and the CTD of Pex5a and Pex5b contribute to peroxisome function to a different extent. It is yet unclear why growth of mutants only expressing the NTD of Pex5b is heavily affected on glucose media. **(C)** Fluorescence microscopic images of indicated strains expressing the peroxisomal marker protein mCherry-SKL. Scale bar represents 5 µm. Notably, the Δ*pex5a pex5b*:TPR_{pex5a} mutant shows peroxisomal localization of mCherry-SKL but is heavily affected in the growth assays (**Figure 1B**). **(D)** Serial tenfold dilutions of wild type cells, Δ*pex5a* mutants and Δ*pex5a* mutants overexpressing the NTD of Pex5a were spotted on minimal media containing either glucose or oleic acid as sole carbon source. Plates were photographed after 3 days of incubation at 23°C. Accordingly, Pex5aΔTPR is a functional targeting factor.

TPR proteins but rather the specificity of the Pex5a receptor, which explains the phenotype of Δ*pex5a* mutants.

We addressed this hypothesis by construction of strains expressing Pex5a and Pex5b chimeric variants (**Supplementary Figure S3**). A mutant expressing Pex5 proteins containing only the TPR domain of Pex5a (*pex5b:*TPR_{pex5a}) exhibited a much stronger growth defect on oleic acid-containing medium compared to a mutant expressing only the TPR domain of Pex5b (*pex5a:*TPR_{pex5b}), which only showed a slightly reduced colony size (**Figure 1B**). The TPR domain of Pex5b, therefore, recognizes specific PTS1 proteins required for peroxisome function in these conditions. This is further supported by the finding that, although growth was abolished on oleic acid-containing medium (**Figure 1B**), mCherry-SKL is localized to peroxisomes in Δ*pex5a pex5b:*TPR_{pex5a} cells indicating that this chimeric protein is not generally affected in peroxisomal import of PTS1 proteins (**Figure 1C**).

In addition, our experiments reveal that the absence of the NTD of Pex5a is primarily responsible for the growth defect of the Δ*pex5a* strain on oleic acid-containing medium (**Figure 1B**,

TABLE 1 | Candidates tested in the screen for Pex5a cargo.

Functional prediction	*U.MAYDIS* GENE	PTS1
Acyl-CoA oxidases	um01966	PMLKAAAERSNL*
	um02028	GEAVPFTERARL*
	um02208	TDFDSDLPRAKL*
Acyl-CoA dehydrogenases	um06400	ALLAKAGIKSHL*
	um01466	QALRMMPENARL*
	um00122	WTQGSGDVKSHL*
	um10665	QQLKLVGPQSKF*
Enoyl-CoA hydratases	um01747	VANDDVARFAKL*
	um02097	LAPPSSHARSKL*
	um11001	EADRARSRASNL*
	um10825	IRLDGASRLGKL*
Sterol carrier proteins	um11938	LDGVLKSQKAKL*
	um01850	NEVKKMSRVAKL*
Dienoyl-CoA isomerase	um01273	VMQKQTPKFAKL*
3,2-Trans-enoyl-CoA isomerases	um01599	FENIAAGARHKL*
	um03158	ESLRAAAAKSKL*

compare mutant Δ*pex5a* with *pex5a:TPR*$_{pex5b}$). Indeed, overexpression of Pex5aΔTPR was able to rescue the phenotype of a Δ*pex5a* strain (**Figure 1D**). Critical peroxisomal matrix proteins are likely to exist, which specifically require the NTD for import. Moreover, the data suggest that Pex5a can act as a targeting factor even in the absence of its TPR domains.

Identification of Pex5a-Specific Cargo

Several proteins from other fungi are known, which are imported into peroxisomes *via* binding to the NTD of Pex5 although they lack a canonical PTS or the PTS1 has been removed (van der Klei and Veenhuis, 2006). We reasoned that PTS1-containing substrates that require the NTD of Pex5a may as well display specificity for the TPR domain of this cargo receptor. To identify such proteins, we generated a library of GFP proteins with *C*-terminal dodecameric PTS1 motifs derived from *U. maydis* enzymes presumably involved in peroxisomal ß-oxidation (**Table 1**; **Figure 2A** and **Supplementary Figure S4**; Brocard and Hartig, 2006; Camões et al., 2015). Constructs were expressed in WT and in Δ*pex5a* cells (**Supplementary Figure S4**). GFP fused to PTS1 motifs of the candidate proteins Um01966, Um10665 and Um11001 showed peroxisomal localization in WT cells but accumulated in the cytosol in the absence of Pex5a (**Figure 2A** and **Supplementary Figure S4**).

Um01966 is a putative acyl-CoA oxidase with high similarity to yeast Pox1, Um10665 a putative acyl-CoA dehydrogenase

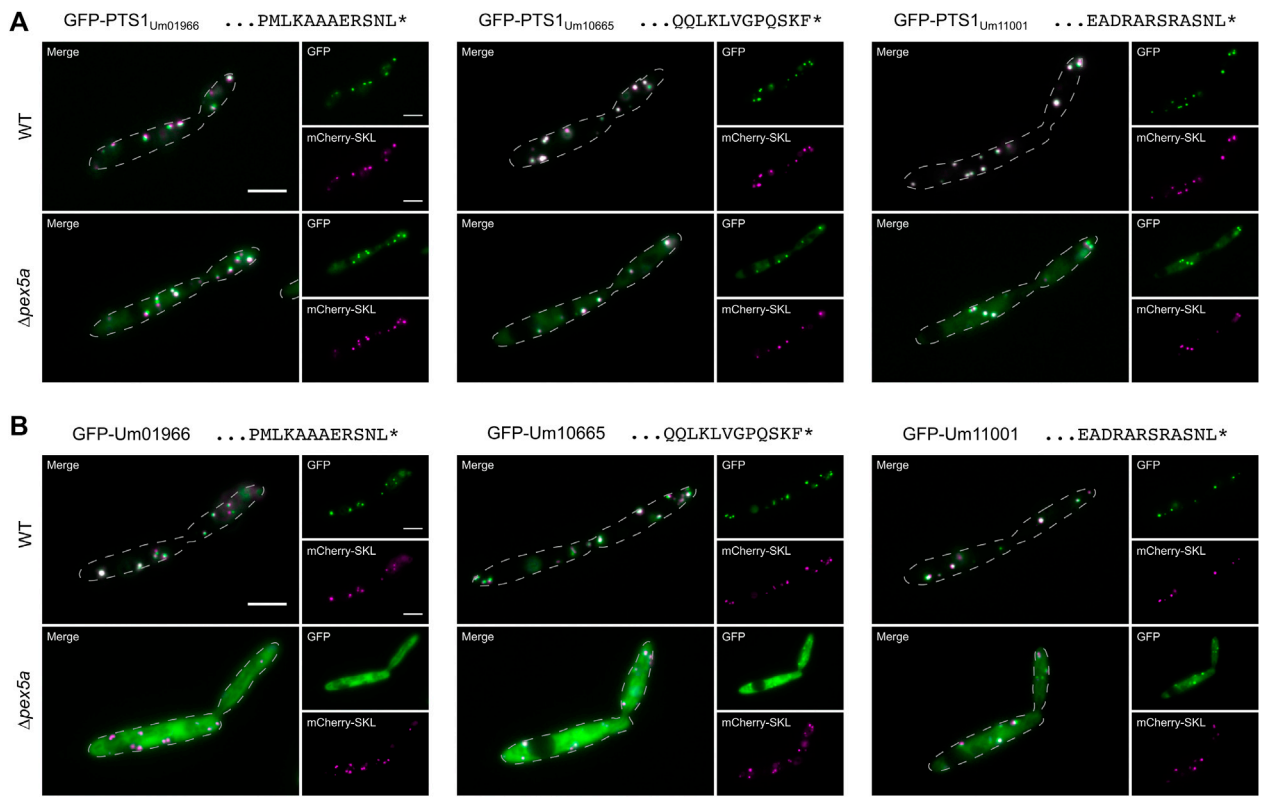

FIGURE 2 | Identification of three cargo proteins of Pex5a. Fluorescence microscopic images of indicated strains expressing the peroxisomal marker protein mCherry-SKL (magenta) together with GFP (green) fused to *C*-terminal dodecamers including the PTS1 motifs of the *U. maydis* proteins Um01966, Um10665 and Um11001 **(A)**, with GFP-tagged full-length version of these proteins **(B)**. Scale bars represent 5 µm. These experiments show that localization of Um01966, Um10665 and Um11001 to peroxisomes is affected upon deletion of *pex5a*.

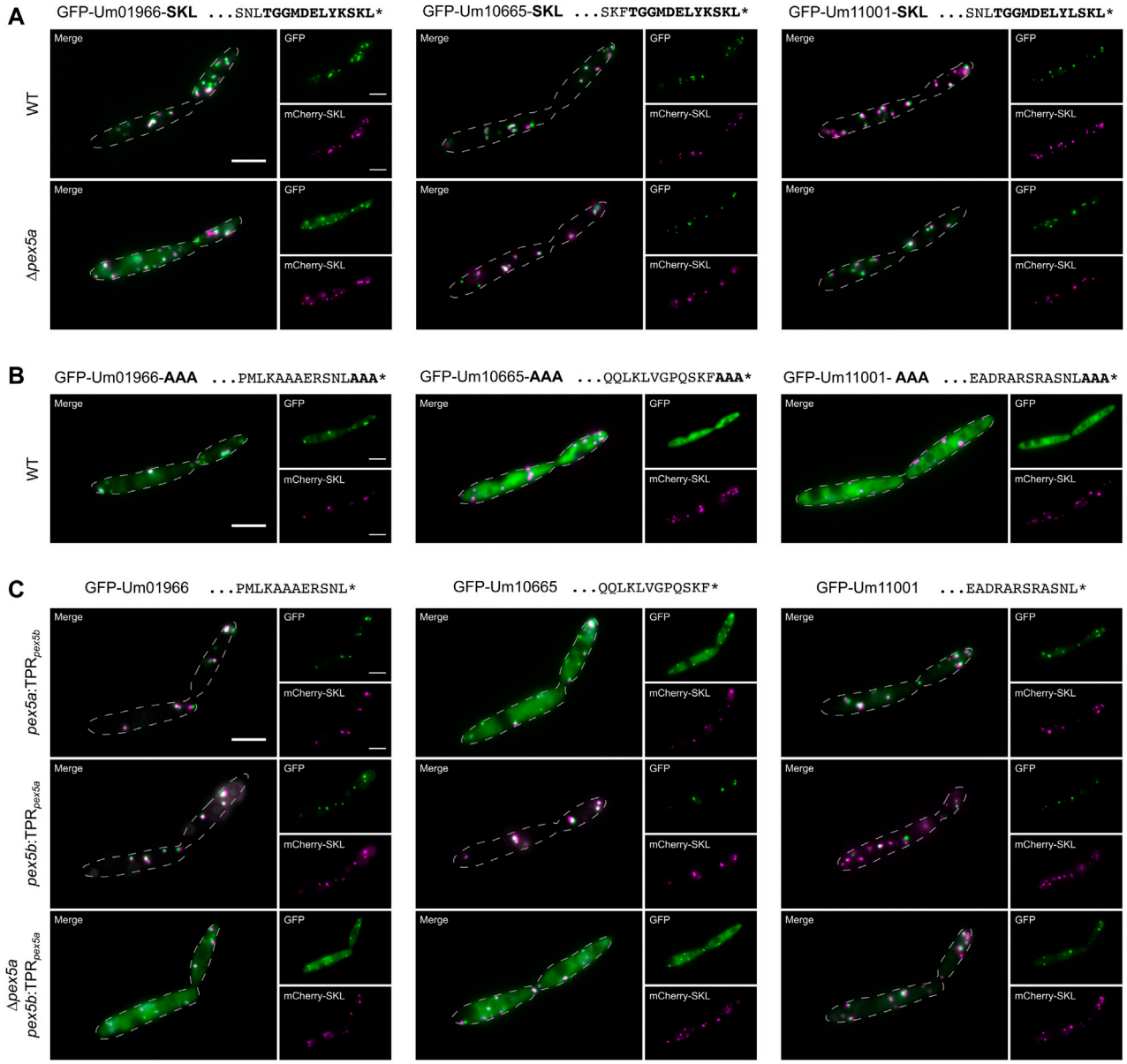

FIGURE 3 | The NTD of Pex5a acts as targeting factor for Um01966. Fluorescence microscopic images of indicated strains expressing the peroxisomal marker protein mCherry-SKL (magenta) together with GFP-tagged full-length proteins (green) with their usual PTS1 masked by SKL **(A)** or AAA **(B)** in Δ*pex5a* and Δ*pex5b* cells. **(C)** Representative images of GFP-tagged full-length proteins expressed in mutants containing chimeric receptor proteins. These data reveal that both the NTD and the CTD contribute to cargo import.

and Um11001 a putative enoyl-CoA hydratase (**Table 1**; Camões et al., 2015). *N*-terminally GFP-tagged full-length versions of all three proteins co-localized with mCherry-SKL in the presence of Pex5a, but showed pronounced cytosolic localization in Δ*pex5a* cells (**Figure 2B**). Cytosolic accumulation of GFP-tagged full-length proteins was even enhanced compared to the *C*-terminal dodecamers fused to GFP. Both experiments show that the three identified proteins are cargo with a preference for Pex5a.

Combinatorial Interaction With the NTD and the TPR Domain of Pex5a Determines Import Specificity

To discriminate between the function of the *C*-terminal TPR domain and the NTD of Pex5a for peroxisomal import of Um01966, Um10665 and Um11001 we added canonical SKL containing motifs at the *C*-terminus of each. Targeting to peroxisomes in Δ*pex5a* cells was drastically improved for GFP-Um10665-SKL and GFP-Um11001-SKL. Um01966-SKL

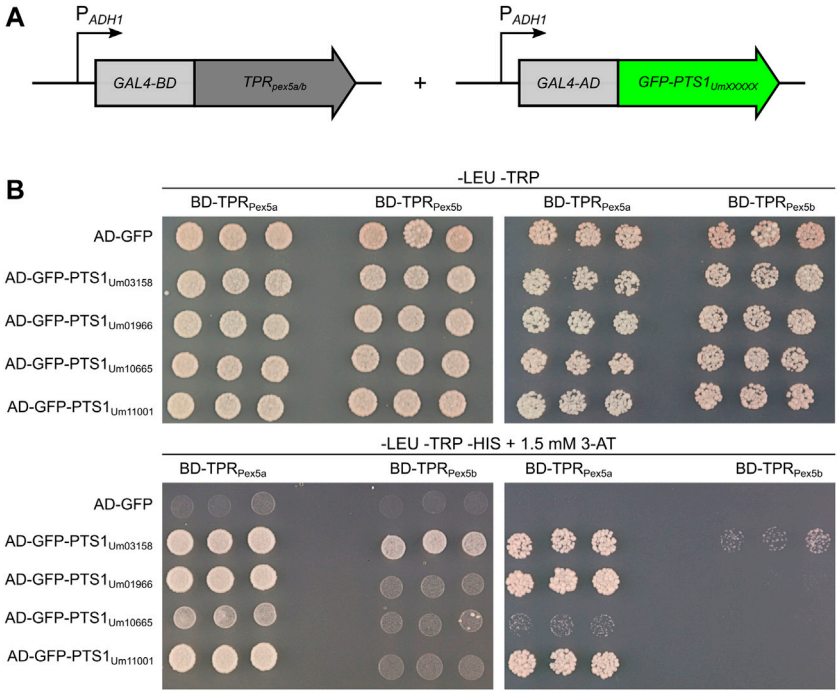

FIGURE 4 | PTS1 motifs with higher affinity to Pex5a. **(A)** Schematic drawing of constructs used for the yeast two-hybrid assay. Constructs were expressed in a strain derived from AH109 deleted for *PEX5* (Stehlik et al., 2020). TPR domains of either Pex5a or Pex5b were fused to the GAL4 DNA-binding domain (GAL4-BD), while *C*-terminal dodecamers of candidate proteins were fused to the GAL4 activation domain (GAL4-AD). **(B)** Fivefold and fiftyfold dilutions (OD_{600} = 0.2 and 0.02, respectively) of three independent transformants co-expressing indicated constructs were spotted on -LEU -TRP media and -LEU -TRP -HIS media and incubated for 3 days at 30°C. The selection medium (-LEU -TRP -HIS) contained 1.5 mM 3-Amino-1,2,4-triazole. This assay demonstrates that Um01966, Um10665 and Um11001 are substrates of the Pex5a TPRs and show only a very weak interaction with the Pex5b TPRs.

predominantly co-localized with mCherry-SKL positive foci in wild type cells but substantial cytosolic mistargeting was observed in a strain deleted for *pex5a* (**Figure 3A**). This suggests a critical function of Pex5a for import of the acyl-CoA oxidase Um01966, which cannot be entirely bypassed by addition of a *C*-terminal canonical targeting signal.

Upon masking the PTS1 by *C*-terminal addition of three alanine residues (AAA), GFP-Um10665-AAA and GFP-Um11001-AAA remained largely cytosolic, while GFP-Um01966-AAA partially co-localized with mCherry-SKL (**Figure 3B**). A GFP-tagged and AAA-masked *C*-terminal dodecamer of Um01966 remained cytosolic revealing an additional targeting signal within the full-length protein (**Supplementary Figure S5**). Microscopic analysis of strains expressing chimeric variants of Pex5a and Pex5b demonstrated that the Pex5a TPRs are not required for efficient targeting of GFP-Um01966 to peroxisomes (**Figure 3C**). However, in the absence of the NTD of Pex5a (Δ*pex5a pex5b:TPR*$_{pex5a}$) residual peroxisomal targeting of GFP-Um01966 was observed (**Figure 3C**), while GFP-Um01966 localized almost entirely in the cytosol upon depletion of *pex5a* (**Figure 2B**). This is probably due to the presence of the Pex5a TPRs, which might partially compensate for the absence of the Pex5a NTD in Δ*pex5a pex5b:TPR*$_{pex5a}$ cells (**Figure 3C**). These results are in accordance with our initial observation that the isolated PTS1 containing sequence requires Pex5a for efficient import (**Figure 2A**). Targeting of GFP-Um10665 and to a minor extent GFP-Um11001 was reduced in the absence of each part of Pex5a (**Figure 3C**). Together, these experiments suggest that it is the combination of affinities to the NTD and the CTD of Pex5a, which facilitates recognition and import of Pex5a specific cargo. The impact of each of the two domains can be different depending on individual substrates.

PTS1 Motifs With Higher Affinity to the TPR Domains of Pex5a

To test the binding affinities of TPR domains of Pex5a and Pex5b (**Figure 2**), we set up a yeast two-hybrid experiment (Chien et al., 1991). We attached the TPR domains of either protein to the Gal4-DNA-binding domain (BD), and GFP with *C*-terminal dodecamers of different candidate proteins to the Gal4-activation domain (AD) (**Figure 4A**). As a control we used a *C*-terminal dodecamer, which efficiently mediates import of GFP into peroxisomes in the absence of Pex5a (**Supplementary Figure S3**; Um03158). Constructs were transformed in respective combinations into AH109Δ*pex5* (Stehlik et al., 2020). Interactions were monitored for three independent transformants per combination by growth assays on high

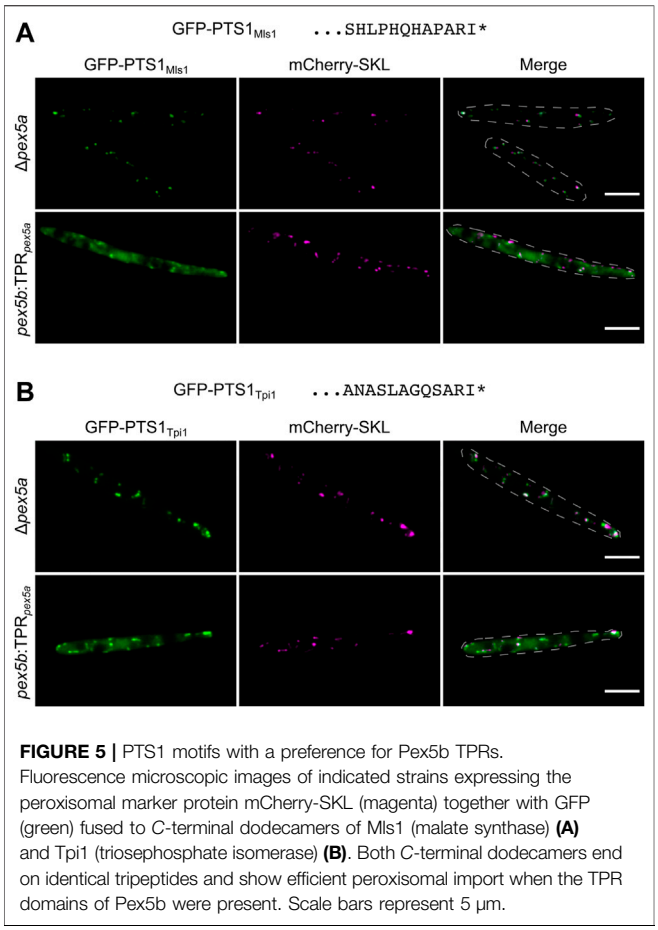

FIGURE 5 | PTS1 motifs with a preference for Pex5b TPRs. Fluorescence microscopic images of indicated strains expressing the peroxisomal marker protein mCherry-SKL (magenta) together with GFP (green) fused to *C*-terminal dodecamers of Mls1 (malate synthase) **(A)** and Tpi1 (triosephosphate isomerase) **(B)**. Both *C*-terminal dodecamers end on identical tripeptides and show efficient peroxisomal import when the TPR domains of Pex5b were present. Scale bars represent 5 µm.

stringency medium (**Figure 4B**). The assay revealed a stronger interaction of PTS1 motifs of Um01966, Um10665 and Um11001 with the TPR domain of Pex5a compared to the TPR domain of Pex5b. Among the tested candidates the PTS1 motif of Um03158 had the highest affinity to the TPRs of Pex5b and may thus be efficiently imported *via* both Pex5 proteins (**Figure 4B**). Interaction data from the two-hybrid experiment are in agreement with the data on import efficiency obtained by fluorescence microscopy (**Figure 2**). The weak interaction of the Um10665 PTS1 with the Pex5a TPRs may explain why efficient import of GFP-Um10665 is only observed when a native Pex5a protein containing the original NTD and CTD is expressed (**Figure 3C**). The strong interaction of the PTS1 of Um01966 with the Pex5a TPRs explains residual peroxisomal import of GFP-Um01966 in Δ*pex5a pex5b:TPR*$_{pex5a}$ cells (**Figure 3C**). Together, the results of the two-hybrid assay confirm that TPR domains of Pex5a and Pex5b show distinct preferences for variations of the *C*-terminal targeting signal and indicate that both cargo receptors have specific as well as shared substrates.

PTS1 Motifs With a Preference for Pex5b

Import of the putative Pox1 ortholog Um01966 shows similarity to Pox1 in *S. cerevisiae* since both can be imported *via* the NTD of a Pex5 protein (Klein et al., 2002). We wondered whether more similarities exist and tested import specificity of the glyoxylate cycle enzyme Mls1 – a Pex9 substrate in *S. cerevisiae* (Effelsberg et al., 2016; Yifrach et al., 2016) – in cells containing Pex5 derivatives with only one type of TPRs. To this end we fused the *C*-terminal dodecamers of the *U. maydis* malate synthase ortholog Mls1 (Um15004) to GFP. Indeed, we detected efficient peroxisomal import in the presence of the TPR domain of Pex5b but pronounced cytosolic localization when only the TPR domain of Pex5a was present (**Figure 5A**). mCherry-SKL predominantly localized in peroxisomes of both strains (**Figure 5A**). Mls1 from *U. maydis* contains the *C*-terminal tripeptide ARI. Remarkably, also a stop codon readthrough derived isoform of the glycolytic/gluconeogenetic enzyme triosephosphate isomerase (Tpi1; Um03299) harbors this *C*-terminal tripeptide (Freitag et al., 2012) and efficient import into peroxisomes also depends on the TPRs of Pex5b (**Figure 5B**). Thus, the highly similar PTS1 motifs of both enzymes are preferentially recognized by Pex5b.

Pex5b as Key Player for Matrix Protein Import in *U. maydis*

Of the cytosolic receptors, only Pex5b can mediate peroxisomal import as a single protein, while Pex5a requires the NTD of Pex5b (**Figure 1**). Pex5b might act as a co-receptor for Pex5a similar to Pex5-large for Pex7 in mammals or Pex18 and Pex21 for Pex7 in *S. cerevisiae* (Braverman et al., 1998; Otera et al., 1998; Purdue et al., 1998; Woodward and Bartel, 2005). Alternatively, Pex5b could be independently required for the activity of the peroxisomal import machinery.

In *U. maydis* PTS2-dependent transport may also involve Pex5b as a co-receptor, since the NTD of Pex5b contains a putative binding site for Pex7 (**Figure 1**; Kiel et al., 2006). In addition, the *U. maydis* genome lacks any ortholog of the yeast co-receptors Pex18 and Pex21 (Kämper et al., 2006). To test Pex5b for targeting of PTS2 proteins, we engineered a reporter protein by fusing an *N*-terminal fragment of the PTS2 protein Um01090 to GFP (PTS2-GFP; **Figure 5A**). The *N*-terminus of this predicted 3-keto-acyl-CoA thiolase related to yeast Pot1 contains a sequence matching the PTS2 consensus [R/K]-[L/V/I]-[X]5-[H/Q]-[L/A] (Lazarow, 2006; Camões et al., 2015; Kunze, 2020). We observed co-localization of PTS2-GFP with mCherry-SKL in peroxisomes and found that PTS2-GFP was retained in the cytosol upon deletion of the *pex7* ortholog (*um03596*) (**Figure 6A**). To address whether Pex5b acts as co-receptor for Pex7, we expressed PTS2-GFP in *pex5a* and in *pex5b* deletion mutants. While peroxisomal localization was not affected in Δ*pex5a* cells, absence of *pex5b* completely abolished peroxisomal import of PTS2-GFP (**Figure 6B**). Reintroduction of the NTD of Pex5b into Δ*pex5b* mutants partially restored targeting of PTS2-GFP to peroxisomes suggesting that the NTD of Pex5b acts as co-receptor for Pex7 in *U. maydis* (**Figure 6B**).

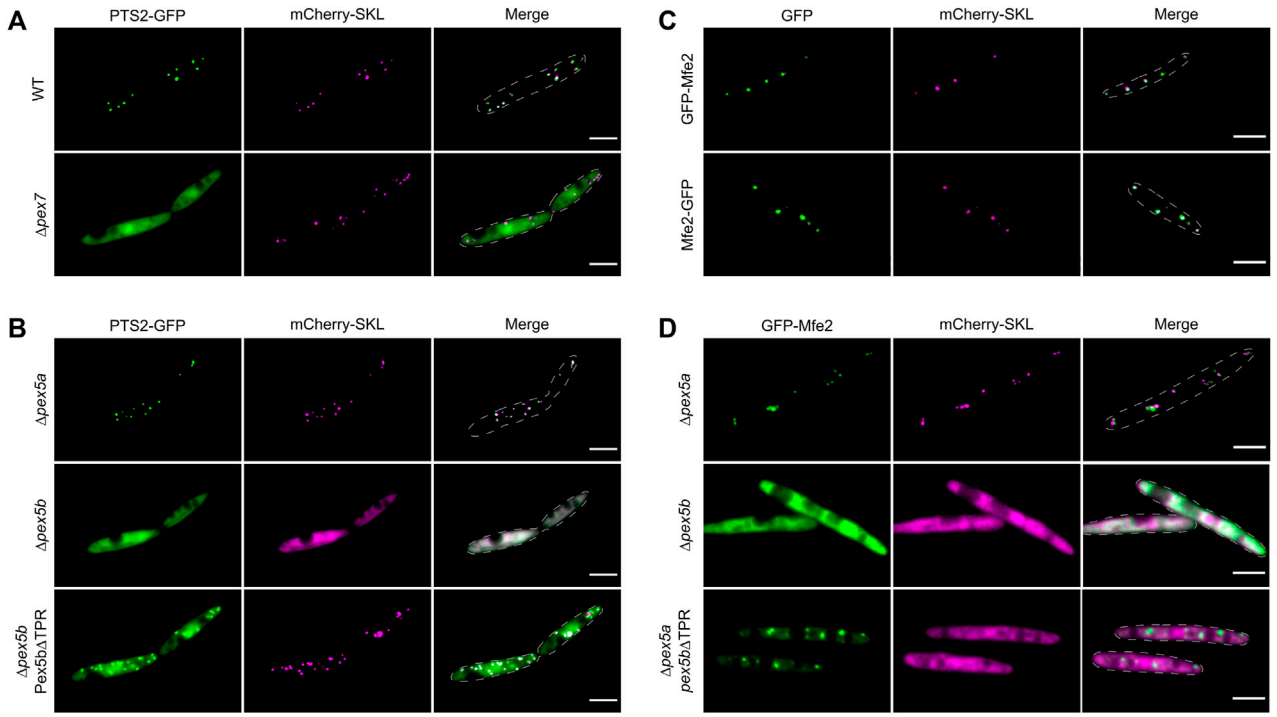

FIGURE 6 | The NTD of Pex5b is a crucial factor for matrix protein import in *U. maydis*. Fluorescence microscopic images of indicated strains expressing mCherry-SKL (magenta) together with PTS2-GFP (green) **(A,B)** or with GFP-tagged Mfe2 (green) **(C,D)**. The data show that the NTD of Pex5b is involved in peroxisomal targeting of PTS2 proteins and more unusual cargo such as the multifunctional enzymes (Mfe2). Scale bars represent 5 µm.

Pex5b-Dependent Import of a Matrix Protein Without a Canonical PTS

Finally, we focused on peroxisomal matrix proteins without a canonical peroxisomal targeting signal. Several proteins have been described that neither contain a PTS1 nor a PTS2 but, nevertheless, localize inside of peroxisomes (van der Klei and Veenhuis, 2006). In *U. maydis*, the multifunctional enzyme involved in peroxisomal fatty acid oxidation (Mfe2; Um10038) was characterized earlier (Klose and Kronstad, 2006). Although we could not detect any PTS motif in Mfe2, both *N*-terminally and *C*-terminally tagged GFP fusion proteins co-localized with mCherry-SKL suggesting that Mfe2 is imported into peroxisomes independently of recognition by Pex7 or the Pex5 TPRs (**Figure 6C**). We probed the mode of transport of Mfe2 by localization studies in a set of *U. maydis* mutants and found that peroxisomal targeting of Mfe2 requires Pex5b. The NTD of Pex5b was sufficient for partial peroxisomal localization of GFP-Mfe2 but import of Mfe2 was more efficient when the full-length protein was expressed (**Figures 6C,D**). This shows that the NTD of Pex5b also can act as receptor for peroxisomal matrix proteins in *U. maydis*.

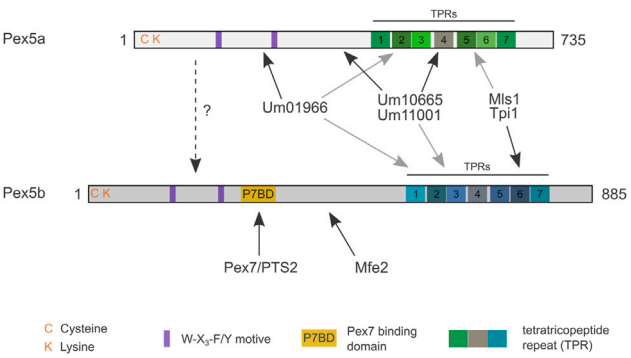

FIGURE 7 | Model highlighting preferential cargo of the different domains of Pex5a and Pex5b. Cargo proteins of different domains are shown. Black arrows point to preferred binding domains. Gray arrows point to secondary binding sites. Please note that the cargo affinities of the TPRs are overlapping, while PTS2 import *via* Pex7 seems to be a specific function of Pex5b. For Mls1 and Tpi1 only specificity of the *C*-terminal dodecamer was determined. If an interaction between Pex5a and Pex5b can occur during import (dashed arrow) or if other functions of Pex5b determine its critical role for Pex5a-dependent import remains to be established.

DISCUSSION

Our work uncovered a network of import modules for peroxisomal matrix proteins in *U. maydis* (**Figure 7**). We have identified five modules: Pex5b can transport substrates destined for the peroxisomal matrix either *via* its NTD (as coreceptor for Pex7 bound to PTS2-GFP, and Mfe2) or *via* its TPR domain (direct recognition of PTS1-containing proteins). The TPR domains of Pex5a and Pex5b bind to PTS1 motifs with

overlapping but not identical specificity (**Figures 2–5**). The NTD of Pex5a also contributes to targeting but does not facilitate peroxisomal import in the absence of Pex5b (**Figures 1–3**, **7**). Although the NTD of Pex5a is shorter in comparison to Pex5b, it contains the evolutionary conserved di-aromatic motifs for interaction with Pex14 (**Figure 1**). It is currently unclear why Pex5a alone is not sufficient to mediate cargo import. Recently, a role of Pex5 for insertion of membrane proteins was observed in *S. cerevisiae* (Martenson et al., 2020). A similar function of the Pex5b NTD may indirectly contribute to the critical importance of Pex5b for matrix protein import in *U. maydis* e.g., by targeting membrane proteins of the importomer.

Our genetic analyses demonstrate that two paralogs of Pex5 are necessary for optimal growth on oleic acid medium. Interestingly, key enzymes of the β-oxidation pathway seem to be preferentially targeted to peroxisomes *via* different factors. Pex5a is responsible for targeting of the acyl-CoA oxidase Um01966 related to *S. cerevisiae* Pox1, the multifunctional enzyme Mfe2 is imported into peroxisomes in the absence of Pex5a while the thiolase Um01090 depends on Pex7 for peroxisomal import (**Figures 2**, **6**). Three different import routes may ensure the correct stoichiometry of enzymes inside of each peroxisome in particular when peroxisomes proliferate. Of interest, the *S. cerevisiae* ortholog Pox1 can bind to the NTD of Pex5 to target peroxisomes (Skoneczny and Lazarow, 1998; Klein et al., 2002). Malate synthase belongs to the cargo recognized by the Pex5 paralog Pex9 in *S. cerevisae* (Effelsberg et al., 2016; Yifrach et al., 2016; Yifrach et al., 2022). In *U. maydis* Mls1 is a preferred substrate of Pex5b. Thus, an evolutionary conservation of targeting mechanisms for particular peroxisomal proteins may exist indicating biological relevance of specific routes for specific enzymes.

In addition, we observed a growth defect on glucose medium for several of the *pex5* mutants. A similar phenotype was already detected for *U. maydis* Δ*pex3* and Δ*pex6* cells as well as in other fungi (Idnurm et al., 2007; Freitag et al., 2012; Camões et al., 2015). Previously, we identified a metabolic network of carbohydrate metabolizing enzymes that are dually targeted to peroxisomes and the cytosol in a number of fungi (Freitag et al., 2012; Stiebler et al., 2014; Freitag et al., 2018; Kremp et al., 2020). A function of peroxisomes in regulating gluconeogenesis was recently described for *S. cerevisiae* and a number of novel, often dually localized peroxisomal proteins was discovered (Yifrach et al., 2021). Many metabolic and regulatory functions of peroxisomes still await elucidation and may contribute to reduced fitness observed for peroxisome-deficient mutants in glucose-containing medium. It is yet obscure, why growth of a mutant expressing only the NTD of Pex5b was more affected than any of the other strains (**Figure 1**). A possible explanation might be that import of only a subset of proteins e.g. Mfe2 or Pot1 is more detrimental for cells than retention of all peroxisomal matrix proteins in the cytosol.

Several peroxisomal proteins without a canonical PTS such as Mfe2 are known to bind to the NTD of Pex5 in *S. cerevisiae* (Skoneczny and Lazarow, 1998; Klein et al., 2002; Rymer et al., 2018; Kempiński et al., 2020). Aox1, Cta1, Fox2, Pox1 and Pox4 from different yeast species (Small et al., 1988; Kragler et al., 1993; Skoneczny and Lazarow, 1998; Gunkel et al., 2004; Rymer et al., 2018) resemble Um01966 and can be imported into peroxisomes if the PTS1 motifs are removed pointing to additional targeting signals. More such proteins likely exist, but two targeting signals may appear redundant and are therefore hard to detect. Specificity for a Pex5 protein seems to result from the combination of affinities towards the NTD and the CTD – for different cargo interaction with one or the other domain is more relevant or may even be sufficient (**Figures 2–6**). A very recent study focusing on TPR domains of the paralogs Pex5 and Pex9 from *S. cerevisiae* revealed that substrates can be discriminated by amino acids in vicinity of the *C*-terminal tripeptide (Yifrach et al., 2022). If this also applies to *U. maydis* or if other features of the motif determine specificity is an exciting question for future research. The *C*-terminal tripeptide could be important as well, as two of the three identified Pex5a substrates end on SNL, while two identified cargoes of Pex5b contain the tripeptide ARI at the *C*-terminus (**Figures 2**, **5**).

Pex7-mediated import in *U. maydis* differs from several yeast species since specific co- receptors for PTS2 import are not present (Purdue et al., 1998; Schäfer et al., 2004; Kiel et al., 2006). We could show that in *U. maydis* PTS2 import depends on the NTD of Pex5b and this pathway shows more similarity to plants and mammals (Braverman et al., 1998; Otera et al., 1998; Woodward and Bartel, 2005; Kunze et al., 2015).

Allosteric interactions upon cargo binding are important for turning Pex5 and Pex7 into import-competent receptors attaching to the docking complex followed by translocation and cargo release (Kunze et al., 2015; Bürgi et al., 2021). The Pex5 CTD inhibits docking of the NTD in the absence of cargo; the NTD can translocate into the peroxisomal membrane when the CTD is deleted (Klein et al., 2002; Gouveia et al., 2003; Gunkel et al., 2004; Dias et al., 2017). In agreement with these data we found that overexpression of Pex5a lacking the TPRs can rescue the growth defect of Δ*pex5a* cells (**Figure 1**). Furthermore, we detected targeting of GFP-Mfe2 and PTS2-GFP to peroxisomes upon expression of the Pex5b NTD in the absence of the full-length protein (**Figure 5**). The capability of the peroxisomal import machinery to translocate large oligomeric cargo has been described (Walton et al., 1995; Yang et al., 2018). It will be interesting to establish how interactions at different sites of Pex5 proteins influence import of bigger complexes and import kinetics. In addition, the exact mechanistic function of both Pex5 proteins might be worth to evaluate.

Taken together, our study reveals the impact of different domains of Pex5 paralogs on cargo recognition and on peroxisome function in different growth conditions and contributes to a better understanding of peroxisomal protein import. Versatile import routes for matrix proteins seem to be widespread and may be critical for the formation of functional peroxisomes in many species.

METHODS

Generation of Strains and Nucleic Acid Procedures

Constructs were generated using standard cloning procedures (Sambrook et al., 1989) or Gibson assembly (Gibson et al., 2009).

All plasmids were verified by sequencing. *Escherichia coli* strain Top Ten (Invitrogen) was used for transformation according to a standard protocol (Hanahan et al., 1991) and propagation of plasmid DNA. Transformation of *U. maydis* cells was achieved as described previously (Schulz et al., 1990). Deletion strains and chimeric variants were created using an *Sfi1* based cloning system (Brachmann et al., 2004; Kämper, 2004; **Supplementary Figure S3**). Genomic DNA was extracted according to an established protocol (Hoffman and Winston, 1987). Mutant strains were verified by Southern blot analysis (Sambrook et al., 1989). Proteins were expressed under control of the constitutive *otef*-promoter either integrated into the *cbx*-locus (Broomfield and Hargreaves, 1992; Spellig et al., 1996) or randomly integrated into the genome of *U. maydis* (mCherry-SKL). Similar expression levels were confirmed by measuring fluorescence using Synergy Mx multimode microplate reader (BioTek). All plasmids, strains and oligonucleotides used or generated during this study are listed in **Supplementary Table S1**. Progenitor plasmids used for this study were described (Spellig et al., 1996; Brachmann et al., 2004; Sandrock et al., 2006; Freitag et al., 2012; Stehlik et al., 2020). Genes can be accessed on NCBI.

Growth Conditions

U. maydis strains were grown at 28°C in liquid YEPSL (1% yeast extract, 0.4% peptone, 0.4% sucrose) or on solid potato dextrose broth containing 1.5% Bacto agar at 28°C. For selection solid media were supplemented with antibiotics (Brachmann et al., 2004). For growth assays 4 µl of serial tenfold dilutions of logarithmically growing cells starting with an OD_{600} of 1 (**Figure 1B** and **Supplementary Figure S2**) or 0.1 (**Figure 1D**) were spotted on solid minimal yeast nitrogen based media (Difco) with a pH of 5.7 supplemented with 0.5% ammonium sulfate. The plates contained 1.5% Bacto agar and either 2% glucose or a mixture of 0.2% oleic acid and 0.05% Tween-40. Plates were incubated for two (**Figure 1B** and **Supplementary Figure S2**) to 3 days (**Figure 1D**) at 23°C. All assays were at least repeated three times with similar results.

Growth Assays in Liquid Media

Cells of an OD_{600} of 1 were diluted to a starting OD_{600} of 0.1 and inoculated into fresh yeast nitrogen based media (Difco) with a pH of 5.7 supplemented with 0.5% ammonium sulfate and 2% glucose in a volume of 100 µl in flat bottom 96 well plates. Growth assays were performed in a Synergy Mx multimode microplate reader (BioTek) at 23°C with high shaking setting. OD_{600} was determined in 30 min intervals. Each strain was measured in five technical replicates and in three independent experiments. Mean values were plotted and original data and standard deviations are accessible in **Supplementary Table S2**.

Microscopy

A total of 200 µl of hot 1.5% agarose melted in water was used to create a thin agarose cushion on a 76 × 26 mm microscope slide (Roth). Cells from logarithmic growth phase incubated in yeast nitrogen based media (Difco) with a pH of 5.7 supplemented with 0.5% ammonium sulfate and 2% glucose were washed with water, concentrated fivefold, and 3 µl were spotted onto the middle of the agarose pad and covered with an 18 × 18 mm coverslip (Roth). Microscopy was performed on an Axiovert 200 M inverse microscope (Zeiss) equipped with a 1394 ORCA-ERA-CCD camera (Hamamatsu Photonics), filter sets for enhanced GFP (EGFP) and rhodamine (Chroma Technology), and a Zeiss 63×Plan Apochromat oil lens (NA 1.4). Single-plane bright field or phase contrast images and z-stacks of the cells (0.5 µm z-spacing) in the appropriate fluorescence channels were recorded, using the image acquisition software Volocity 5.3 (Perkin-Elmer). Images were processed and evaluated in ImageJ (Schneider et al., 2012). For protein localization analysis, single plain images or *z*-projections of deconvolved image stacks were used. Deconvolution was performed on the *z*-stacks by the ImageJ plugin DeconvolutionLab with 25 iterations of the Richardson – Lucy algorithm (Sage et al., 2017).

Yeast Two-Hybrid Assay

Sequences encoding the TPR domains of Pex5a and Pex5b were inserted into pGBKT7 (Matchmaker GAL4 Two-Hybrid System 3; Clontech) between the EcoRI and BamHI restriction sites *via* Gibson assembly. The ORFs for GFP or GFP modified with *C*-terminal dodecamers of Um01966, Um10665, Um11001, and Um03158 including PTS1 motifs were cloned into pGADT7 (Matchmaker GAL4 Two-Hybrid System 3; Clontech) between the EcoRI and BamHI restriction sites. Either pGBKT7-Pex5aTPR or pGBKT7-Pex5bTPR were co-transformed with one of the pGADT7 plasmids into YTS398, a derivative AH109 of deleted for *pex5* (Stehlik et al., 2020). Three independent transformants of each of the 10 combinations were grown in liquid synthetic defined (SD) medium lacking leucine and tryptophan to an OD_{600} of approx. 1. Cells were washed once with sterile water and 4 µl of fivefold or fiftyfold dilutions (OD_{600} = 0.2 or 0.02) were spotted on solid SD medium lacking leucine and tryptophan as growth control, and on SD medium lacking leucine, tryptophan and histidine, and containing 1.5 mM 3-amino-1,2,4-triazole to test for protein – protein interaction. Plates were incubated for 3 days at 30°C.

DATA AVAILABILITY STATEMENT

The original contributions presented in the study are included in the article/**Supplementary Material**, further inquiries can be directed to the corresponding author.

AUTHOR CONTRIBUTIONS

JA, MB, and JF designed the study. JA, NB, EB, DM, and HA performed the experiments. All authors contributed to data analysis. JA, NB, and EB created the figures. JF wrote the manuscript with input from all authors.

ACKNOWLEDGMENTS

We acknowledge Marisa Piscator for excellent technical assistance and Regine Kahmann from the MPI for Terrestrial Microbiology for sharing facilities. JA was supported by a fellowship from the Marburg Research Academy. MB acknowledges funding from DFG (BO2094-5). JF was supported by the DFG (grant ID FR-3586/2-1). We thank Thorsten Stehlik for many discussions and Björn Sandrock for critical reading of the manuscript. We are grateful to Michael Feldbrügge and Jörg Kämper for sharing plasmids. Open Access funding was provided by the Open Acess Publication Fund of Philipps-Universität Marburg with support of the DFG.

SUPPLEMENTARY MATERIAL

The Supplementary Material for this article can be found online at: https://www.frontiersin.org/articles/10.3389/fcell.2022.858084/full#supplementary-material

REFERENCES

Amery, L., Sano, H., Mannaerts, G. P., Snider, J., van Looy, J., Fransen, M., et al. (2001). Identification of PEX5p-Related Novel Peroxisome-Targeting Signal 1 (PTS1)-Binding Proteins in Mammals. *Biochem. J.* 357, 635–646. doi:10.1042/bj3570635

Brachmann, A., König, J., Julius, C., and Feldbrügge, M. (2004). A Reverse Genetic Approach for Generating Gene Replacement Mutants in *Ustilago maydis*. *Mol. Genet. Genomics* 272, 216–226. doi:10.1007/s00438-004-1047-z

Braverman, N., Dodt, G., Gould, S. J., and Valle, D. (1998). An Isoform of Pex5p, the Human PTS1 Receptor, Is Required for the Import of PTS2 Proteins into Peroxisomes. *Hum. Mol. Genet.* 7, 1195–1205. doi:10.1093/hmg/7.8.1195

Braverman, N., Steel, G., Obie, C., Moser, A., Moser, H., Gould, S. J., et al. (1997). Human PEX7 Encodes the Peroxisomal PTS2 Receptor and Is Responsible for Rhizomelic Chondrodysplasia Punctata. *Nat. Genet.* 15, 369–376. doi:10.1038/ng0497-369

Brocard, C., and Hartig, A. (2006). Peroxisome Targeting Signal 1: Is it Really a Simple Tripeptide? *Biochim. Biophys. Acta (Bba) - Mol. Cel. Res.* 1763, 1565–1573. doi:10.1016/j.bbamcr.2006.08.022

Brocard, C., Kragler, F., Simon, M. M., Schuster, T., and Hartig, A. (1994). The Tetratricopeptide Repeat Domain of the PAS10 Protein of Saccharomyces Cerevisiae Is Essential for Binding the Peroxisomal Targeting Signal-SKL. *Biochem. Biophysical Res. Commun.* 204, 1016–1022. doi:10.1006/bbrc.1994.2564

Broomfield, P. L. E., and Hargreaves, J. A. (1992). A Single Amino-Acid Change in the Iron-Sulphur Protein Subunit of Succinate Dehydrogenase Confers Resistance to Carboxin in *Ustilago maydis*. *Curr. Genet.* 22, 117–121. doi:10.1007/bf00351470

Bürgi, J., Ekal, L., and Wilmanns, M. (2021). Versatile Allosteric Properties in Pex5-Like Tetratricopeptide Repeat Proteins to Induce Diverse Downstream Function. *Traffic* 22, 140–152. doi:10.1111/tra.12785

Camões, F., Islinger, M., Guimarães, S. C., Kilaru, S., Schuster, M., Godinho, L. F., et al. (2015). New Insights into the Peroxisomal Protein Inventory: Acyl-CoA Oxidases And-Dehydrogenases Are an Ancient Feature of Peroxisomes. *Biochim. Biophys. Acta (Bba)-Molecular Cel. Res.* 1853, 111–125. doi:10.1016/j.bbamcr.2014.10.005

Carvalho, A. F., Costa-Rodrigues, J., Correia, I., Costa Pessoa, J., Faria, T. Q., Martins, C. L., et al. (2006). The N-Terminal Half of the Peroxisomal Cycling Receptor Pex5p Is a Natively Unfolded Domain. *J. Mol. Biol.* 356, 864–875. doi:10.1016/j.jmb.2005.12.002

Chien, C. T., Bartel, P. L., Sternglanz, R., and Fields, S. (1991). The Two-Hybrid System: a Method to Identify and Clone Genes for Proteins that Interact with a Protein of Interest. *Proc. Natl. Acad. Sci. U.S.A.* 88, 9578–9582. doi:10.1073/pnas.88.21.9578

Dias, A. F., Rodrigues, T. A., Pedrosa, A. G., Barros-Barbosa, A., Francisco, T., and Azevedo, J. E. (2017). The Peroxisomal Matrix Protein Translocon Is a Large Cavity-Forming Protein Assembly into Which PEX5 Protein Enters to Release its Cargo. *J. Biol. Chem.* 292, 15287–15300. doi:10.1074/jbc.m117.805044

Edward Purdue, P., Yang, X., and Lazarow, P. B. (1998). Pex18p and Pex21p, a Novel Pair of Related Peroxins Essential for Peroxisomal Targeting by the PTS2 Pathway. *J. Cel. Biol.* 143, 1859–1869. doi:10.1083/jcb.143.7.1859

Effelsberg, D., Cruz-Zaragoza, L. D., Schliebs, W., and Erdmann, R. (2016). Pex9p Is a New Yeast Peroxisomal Import Receptor for PTS1-Containing Proteins. *J. Cel. Sci.* 129, 4057–4066. doi:10.1242/jcs.195271

Effelsberg, D., Cruz-Zaragoza, L. D., Tonillo, J., Schliebs, W., and Erdmann, R. (2015). Role of Pex21p for Piggyback Import of Gpd1p and Pnc1p into Peroxisomes of *Saccharomyces cerevisiae*. *J. Biol. Chem.* 290, 25333–25342. doi:10.1074/jbc.m115.653451

El Magraoui, F., Brinkmeier, R., Mastalski, T., Hupperich, A., Strehl, C., Schwerter, D., et al. (2019). The Deubiquitination of the PTS1-Import Receptor Pex5p Is Required for Peroxisomal Matrix Protein Import. *Biochim. Biophys. Acta (Bba) - Mol. Cel. Res.* 1866, 199–213. doi:10.1016/j.bbamcr.2018.11.002

Francisco, T., Rodrigues, T. A., Dias, A. F., Barros-Barbosa, A., Bicho, D., and Azevedo, J. E. (2017). Protein Transport into Peroxisomes: Knowns and Unknowns. *BioEssays* 39, 1700047. doi:10.1002/bies.201700047

Freitag, J., Ast, J., and Bölker, M. (2012). Cryptic Peroxisomal Targeting via Alternative Splicing and Stop Codon Read-Through in Fungi. *Nature* 485, 522–525. doi:10.1038/nature11051

Freitag, J., Stehlik, T., Stiebler, A. C., and Bölker, M. (2018). "The Obvious and the Hidden: Prediction and Function of Fungal Peroxisomal Matrix Proteins," in *Proteomics of Peroxisomes*. Springer, 139–155.

Gabaldón, T. (2010). Peroxisome Diversity and Evolution. *Philos. Trans. R. Soc. Lond. B. Biol. Sci.* 365, 765–773. doi:10.1098/rstb.2009.0240

Gabay-Maskit, S., Cruz-Zaragoza, L. D., Shai, N., Eisenstein, M., Bibi, C., Cohen, N., et al. (2020). A Piggybacking Mechanism Enables Peroxisomal Localization of the Glyoxylate Cycle Enzyme Mdh2 in Yeast. *J. Cell Sci.* 133, jcs244376. doi:10.1242/jcs.244376

Gardner, B. M., Castanzo, D. T., Chowdhury, S., Stjepanovic, G., Stefely, M. S., Hurley, J. H., et al. (2018). The Peroxisomal AAA-ATPase Pex1/Pex6 Unfolds Substrates by Processive Threading. *Nat. Commun.* 9, 135. doi:10.1038/s41467-017-02474-4

Gatto, G. J., Geisbrecht, B. V., Gould, S. J., and Berg, J. M. (2000). Peroxisomal Targeting Signal-1 Recognition by the TPR Domains of Human PEX5. *Nat. Struct. Biol.* 7, 1091–1095. doi:10.1038/81930

Gibson, D. G., Young, L., Chuang, R.-Y., Venter, J. C., Hutchison, C. A., III, and Smith, H. O. (2009). Enzymatic Assembly of DNA Molecules up to Several Hundred Kilobases. *Nat. Methods* 6, 343–345. doi:10.1038/nmeth.1318

Glover, J. R., Andrews, D. W., and Rachubinski, R. A. (1994). Saccharomyces Cerevisiae Peroxisomal Thiolase is Imported as a Dimer. *Proc. Natl. Acad. Sci.* 91, 10541–10545.

Gould, S. J., Kalish, J. E., Morrell, J. C., Bjorkman, J., Urquhart, A. J., and Crane, D. I. (1996). Pex13p Is an SH3 Protein of the Peroxisome Membrane and a Docking Factor for the Predominantly Cytoplasmic PTs1 Receptor. *J. Cel. Biol.* 135, 85–95. doi:10.1083/jcb.135.1.85

Gould, S. J., Keller, G. A., Hosken, N., Wilkinson, J., and Subramani, S. (1989). A Conserved Tripeptide Sorts Proteins to Peroxisomes. *J. Cel. Biol.* 108, 1657–1664. doi:10.1083/jcb.108.5.1657

Gouveia, A. M., Guimarães, C. P., Oliveira, M. E., Sá-Miranda, C., and Azevedo, J. E. (2003). Insertion of Pex5p into the Peroxisomal Membrane Is Cargo Protein-Dependent. *J. Biol. Chem.* 278, 4389–4392. doi:10.1074/jbc.c200650200

Gunkel, K., van Dijk, R., Veenhuis, M., and van der Klei, I. J. (2004). Routing of *Hansenula polymorpha* Alcohol Oxidase: An Alternative Peroxisomal Protein-Sorting Machinery. *MBoC* 15, 1347–1355. doi:10.1091/mbc.e03-04-0258

Hanahan, D., Jessee, J., and Bloom, F. R. (1991). [4] Plasmid Transformation of *Escherichia coli* and Other Bacteria. *Methods Enzymol.* 204, 63–113. doi:10.1016/0076-6879(91)04006-a

Hoffman, C. S., and Winston, F. (1987). A Ten-Minute DNA Preparation from Yeast Efficiently Releases Autonomous Plasmids for Transformaion of *Escherichia coli*. *Gene* 57, 267–272. doi:10.1016/0378-1119(87)90131-4

Idnurm, A., Giles, S. S., Perfect, J. R., and Heitman, J. (2007). Peroxisome Function Regulates Growth on Glucose in the Basidiomycete Fungus Cryptococcus Neoformans. *Eukaryot. Cel.* 6, 60–72. doi:10.1128/ec.00214-06

Islinger, M., Li, K. W., Seitz, J., Völkl, A., and Lüers, G. H. (2009). Hitchhiking of Cu/Zn Superoxide Dismutase to Peroxisomes - Evidence for a Natural Piggyback Import Mechanism in Mammals. *Traffic* 10, 1711–1721. doi:10.1111/j.1600-0854.2009.00966.x

Kämper, J. (2004). A PCR-Based System for Highly Efficient Generation of Gene Replacement Mutants in *Ustilago maydis*. *Mol. Genet. Genomics* 271, 103–110. doi:10.1007/s00438-003-0962-8

Kämper, J., Kahmann, R., Bölker, M., Ma, L. J., Brefort, T., Saville, B. J., et al. (2006). Insights from the Genome of the Biotrophic Fungal Plant Pathogen *Ustilago maydis*. *Nature* 444, 97–101. doi:10.1038/nature05248

Kempiński, B., Chełstowska, A., Poznański, J., Król, K., Rymer, Ł., Frydzińska, Z., et al. (2020). The Peroxisomal Targeting Signal 3 (PTS3) of the Budding Yeast Acyl-CoA Oxidase Is a Signal Patch. *Front. Cel. Dev. Biol.* 8, 198. doi:10.3389/fcell.2020.00198

Kiel, J. A. K. W., Veenhuis, M., and Van Der Klei, I. J. (2006). PEX Genes in Fungal Genomes: Common, Rare or Redundant. *Traffic* 7, 1291–1303. doi:10.1111/j.1600-0854.2006.00479.x

Kim, P. K., and Hettema, E. H. (2015). Multiple Pathways for Protein Transport to Peroxisomes. *J. Mol. Biol.* 427, 1176–1190. doi:10.1016/j.jmb.2015.02.005

Klein, A. T. J., van den Berg, M., Bottger, G., Tabak, H. F., and Distel, B. (2002). *Saccharomyces cerevisiae* Acyl-CoA Oxidase Follows a Novel, Non-PTS1, Import Pathway into Peroxisomes that Is Dependent on Pex5p. *J. Biol. Chem.* 277, 25011–25019. doi:10.1074/jbc.m203254200

Klose, J., and Kronstad, J. W. (2006). The Multifunctional β-Oxidation Enzyme Is Required for Full Symptom Development by the Biotrophic Maize Pathogen *Ustilago maydis*. *Eukaryot. Cel.* 5, 2047–2061. doi:10.1128/ec.00231-06

Kragler, F., Langeder, A., Raupachova, J., Binder, M., and Hartig, A. (1993). Two Independent Peroxisomal Targeting Signals in Catalase A of *Saccharomyces cerevisiae*. *J. Cel. Biol.* 120, 665–673. doi:10.1083/jcb.120.3.665

Kremp, M., Bittner, E., Martorana, D., Klingenberger, A., Stehlik, T., Bölker, M., et al. (2020). Non-AUG Translation Initiation Generates Peroxisomal Isoforms of 6-Phosphogluconate Dehydrogenase in Fungi. *Front. Cel. Dev. Biol.* 8, 251. doi:10.3389/fcell.2020.00251

Kunze, M., Malkani, N., Maurer-Stroh, S., Wiesinger, C., Schmid, J. A., and Berger, J. (2015). Mechanistic Insights into PTS2-Mediated Peroxisomal Protein Import. *J. Biol. Chem.* 290, 4928–4940. doi:10.1074/jbc.m114.601575

Kunze, M., Neuberger, G., Maurer-Stroh, S., Ma, J., Eck, T., Braverman, N., et al. (2011). Structural Requirements for Interaction of Peroxisomal Targeting Signal 2 and its Receptor PEX7. *J. Biol. Chem.* 286, 45048–45062. doi:10.1074/jbc.m111.301853

Kunze, M. (2020). The Type-2 Peroxisomal Targeting Signal. *Biochim. Biophys. Acta (Bba) - Mol. Cel. Res.* 1867, 118609. doi:10.1016/j.bbamcr.2019.118609

Lanver, D., Tollot, M., Schweizer, G., Lo, P. L., Reissmann, S., Ma, L.-S., et al. (2017). Ustilago Maydis Effectors and Their Impact on Virulence. *Nat. Rev. Microbiol.* 15, 409.

Lazarow, P. B. (2006). Chapter 3.1.7. The Import Receptor Pex7p and the PTS2 Targeting Sequence. *Biochim. Biophys. Acta (Bba) - Mol. Cel. Res.* 1763, 1599–1604. doi:10.1016/j.bbamcr.2006.08.011

Lill, P., Hansen, T., Wendscheck, D., Klink, B. U., Jeziorek, T., Vismpas, D., et al. (2020). Towards the Molecular Architecture of the Peroxisomal Receptor Docking Complex. *Proc. Natl. Acad. Sci. U.S.A.* 117, 33216–33224. doi:10.1073/pnas.2009502117

Lingner, T., Kataya, A. R., Antonicelli, G. E., Benichou, A., Nilssen, K., Chen, X.-Y., et al. (2011). Identification of Novel Plant Peroxisomal Targeting Signals by a Combination of Machine Learning Methods and In Vivo Subcellular Targeting Analyses. *Plant Cell* 23, 1556–1572. doi:10.1105/tpc.111.084095

Lodish, H., Berk, A., Zipursky, S. L., Matsudaira, P., Baltimore, D., and Darnell, J. (2000). "Organelles of the Eukaryotic Cell," in *Molecular Cell Biology*. 4th edition. New York: W.H. Freeman.

Martenson, J. S., Tam, H., McQuown, A. J., Reif, D., Zhou, J., and Denic, V. (2020). The Importomer Is a Peroxisomal Membrane Protein Translocase. *bioRxiv*.

McNew, J. A., and Goodman, J. M. (1994). An Oligomeric Protein is Imported into Peroxisomes *in vivo*. *J. Cell Biol.* 127, 1245–1257.

Meinecke, M., Cizmowski, C., Schliebs, W., Krüger, V., Beck, S., Wagner, R., et al. (2010). The Peroxisomal Importomer Constitutes a Large and Highly Dynamic Pore. *Nat. Cel. Biol.* 12, 273–277. doi:10.1038/ncb2027

Miyata, N., and Fujiki, Y. (2005). Shuttling Mechanism of Peroxisome Targeting Signal Type 1 Receptor Pex5: ATP-Independent Import and ATP-Dependent Export. *Mol. Cel. Biol.* 25, 10822–10832. doi:10.1128/mcb.25.24.10822-10832.2005

Nötzel, C., Lingner, T., Klingenberg, H., and Thoms, S. (2016). Identification of New Fungal Peroxisomal Matrix Proteins and Revision of the PTS1 Consensus. *Traffic* 17, 1110–1124. doi:10.1111/tra.12426

Otera, H., Okumoto, K., Tateishi, K., Ikoma, Y., Matsuda, E., Nishimura, M., et al. (1998). Peroxisome Targeting Signal Type 1 (PTS1) Receptor Is Involved in Import of Both PTS1 and PTS2: Studies with PEX5-Defective CHO Cell Mutants. *Mol. Cel. Biol.* 18, 388–399. doi:10.1128/mcb.18.1.388

Otera, H., Setoguchi, K., Hamasaki, M., Kumashiro, T., Shimizu, N., and Fujiki, Y. (2002). Peroxisomal Targeting Signal Receptor Pex5p Interacts with Cargoes and Import Machinery Components in a Spatiotemporally Differentiated Manner: Conserved Pex5p WXXXF/Y Motifs Are Critical for Matrix Protein Import. *Mol. Cel. Biol.* 22, 1639–1655. doi:10.1128/mcb.22.6.1639-1655.2002

Pedrosa, A. G., Francisco, T., Bicho, D., Dias, A. F., Barros-Barbosa, A., Hagmann, V., et al. (2018). Peroxisomal Monoubiquitinated PEX5 Interacts with the AAA ATPases PEX1 and PEX6 and Is Unfolded During its Dislocation into the Cytosol. *J. Biol. Chem.* 293, 11553–11563. doi:10.1074/jbc.ra118.003669

Platta, H. W., Grunau, S., Rosenkranz, K., Girzalsky, W., and Erdmann, R. (2005). Functional Role of the AAA Peroxins in Dislocation of the Cycling PTS1 Receptor Back to the Cytosol. *Nat. Cel. Biol.* 7, 817–822. doi:10.1038/ncb1281

Platta, H. W., Magraoui, F. E., Schlee, D., Grunau, S., Girzalsky, W., and Erdmann, R. (2007). Ubiquitination of the Peroxisomal Import Receptor Pex5p Is Required for its Recycling. *J. Cel. Biol.* 177, 197–204. doi:10.1083/jcb.200611012

Rosenthal, M., Metzl-Raz, E., Bürgi, J., Yifrach, E., Drwesh, L., Fadel, A., et al. (2020). Uncovering Targeting Priority to Yeast Peroxisomes Using an In-Cell Competition Assay. *Proc. Natl. Acad. Sci. U.S.A.* 117, 21432–21440. doi:10.1073/pnas.1920078117

Rymer, Ł., Kempiński, B., Chełstowska, A., and Skoneczny, M. (2018). The Budding Yeast Pex5p Receptor Directs Fox2p and Cta1p into Peroxisomes via its N-Terminal Region Near the FxxxW Domain. *J. Cel. Sci.* 131, jcs216986. doi:10.1242/jcs.216986

Sage, D., Donati, L., Soulez, F., Fortun, D., Schmit, G., Seitz, A., et al. (2017). DeconvolutionLab2: An Open-Source Software for Deconvolution Microscopy. *Methods* 115, 28–41. doi:10.1016/j.ymeth.2016.12.015

Saidowsky, J., Dodt, G., Kirchberg, K., Wegner, A., Nastainczyk, W., Kunau, W.-H., et al. (2001). The Di-Aromatic Pentapeptide Repeats of the Human Peroxisome Import Receptor PEX5 Are Separate High Affinity Binding Sites for the Peroxisomal Membrane Protein PEX14. *J. Biol. Chem.* 276, 34524–34529. doi:10.1074/jbc.m104647200

Sambrook, J., Fritsch, E. F., and Maniatis, T. (1989). in *Molecular Cloning: A Laboratory Manual*. Editor J. Argentine. (Cold Spring Harbor, NY: Cold Spring Harbor Laboratory Press).

Sandrock, B., Böhmer, C., and Bölker, M. (2006). Dual Function of the Germinal Centre Kinase Don3 During Mitosis and Cytokinesis in *Ustilago maydis*. *Mol. Microbiol.* 62, 655–666. doi:10.1111/j.1365-2958.2006.05405.x

Santoro, B., Hu, L., Liu, H., Saponaro, A., Pian, P., Piskorowski, R. A., et al. (2011). TRIP8b Regulates HCN1 Channel Trafficking and Gating Through Two Distinct C-Terminal Interaction Sites. *J. Neurosci.* 31, 4074–4086. doi:10.1523/jneurosci.5707-10.2011

Santoro, B., Wainger, B. J., and Siegelbaum, S. A. (2004). Regulation of HCN Channel Surface Expression by a Novel C-Terminal Protein-Protein Interaction. *J. Neurosci.* 24, 10750–10762. doi:10.1523/jneurosci.3300-04.2004

Saryi, N. A. A., Hutchinson, J. D., Al-hejjaj, M. Y., Sedelnikova, S., Baker, P., and Hettema, E. H. (2017). Pnc1 Piggy-Back Import into Peroxisomes Relies on Gpd1 Homodimerisation. *Sci. Rep.* 7, 42579. doi:10.1038/srep42579

Schäfer, A., Kerssen, D., Veenhuis, M., Kunau, W. H., and Schliebs, W. (2004). Functional Similarity Between the Peroxisomal PTS2 Receptor Binding Protein Pex18p and the N-Terminal Half of the PTS1 Receptor Pex5p. *Mol. Cel. Biol.* 24, 8895–8906. doi:10.1128/MCB.24.20.8895-8906.2004

Schneider, C. A., Rasband, W. S., and Eliceiri, K. W. (2012). NIH Image to ImageJ: 25 Years of Image Analysis. *Nat. Methods* 9, 671–675. doi:10.1038/nmeth.2089

Schueren, F., Lingner, T., George, R., Hofhuis, J., Dickel, C., Gärtner, J., et al. (2014). Peroxisomal Lactate Dehydrogenase Is Generated by Translational Readthrough in Mammals. *Elife* 3, e03640. doi:10.7554/eLife.03640

Schulz, B., Banuett, F., Dahl, M., Schlesinger, R., Schäfer, W., Martin, T., et al. (1990). The B Alleles of *U. Maydis*, Whose Combinations Program Pathogenic Development, Code for Polypeptides Containing a Homeodomain-Related Motif. *Cell* 60, 295–306. doi:10.1016/0092-8674(90)90744-y

Skoneczny, M., and Lazarow, P. B. (1998). A Novel, Non-PTS1, Peroxisomal Import Route Dependent on the PTS1 Receptor Pex5p. *Mol. Biol. Cel.* 348A.

Small, G. M., Szabo, L. J., and Lazarow, P. B. (1988). Acyl-CoA Oxidase Contains Two Targeting Sequences Each of Which Can Mediate Protein Import into Peroxisomes. *EMBO J.* 7, 1167–1173. doi:10.1002/j.1460-2075.1988.tb02927.x

Smith, J. J., and Aitchison, J. D. (2013). Peroxisomes Take Shape. *Nat. Rev. Mol. Cel. Biol.* 14, 803–817. doi:10.1038/nrm3700

Spellig, T., Bottin, A., and Kahmann, R. (1996). Green Fluorescent Protein (GFP) as a New Vital Marker in the Phytopathogenic Fungus *Ustilago maydis*. *Mol. Gen. Genet.* 252, 503–509. doi:10.1007/s004380050257

Stiebler, A. C., Freitag, J., Schink, K. O., Tillmann, B. A. M., Ast, J., and Bölker, M. (2014). Ribosomal Readthrough at a Short UGA Stop Codon Context Triggers Dual Localization of Metabolic Enzymes in Fungi and Animals. *PLOS Genet.* 10, e1004685.

Stehlik, T., Kremp, M., Kahnt, J., Bölker, M., and Freitag, J. (2020). Peroxisomal Targeting of a Protein Phosphatase Type 2C via Mitochondrial Transit. *Nat. Commun.* 11, 2355. doi:10.1038/s41467-020-16146-3

Su, J.-R., Takeda, K., Tamura, S., Fujiki, Y., and Miki, K. (2009). Crystal Structure of the Conserved N-Terminal Domain of the Peroxisomal Matrix Protein Import Receptor, Pex14p. *Proc. Natl. Acad. Sci. U.S.A.* 106, 417–421. doi:10.1073/pnas.0808681106

Urquhart, A. J., Kennedy, D., Gould, S. J., and Crane, D. I. (2000). Interaction of Pex5p, the Type 1 Peroxisome Targeting Signal Receptor, with the Peroxisomal Membrane Proteins Pex14p and Pex13p. *J. Biol. Chem.* 275, 4127–4136. doi:10.1074/jbc.275.6.4127

van der Klei, I. J., and Veenhuis, M. (2006). PTS1-Independent Sorting of Peroxisomal Matrix Proteins by Pex5p. *Biochim. Biophys. Acta (Bba) - Mol. Cel. Res.* 1763, 1794–1800. doi:10.1016/j.bbamcr.2006.08.013

Walter, T., and Erdmann, R. (2019). Current Advances in Protein Import into Peroxisomes. *Protein J.* 38, 351–362. doi:10.1007/s10930-019-09835-6

Walton, P. A., Hill, P. E., and Subramani, S. (1995). Import of Stably Folded Proteins into Peroxisomes. *Mol. Biol. Cel.* 6, 675–683. doi:10.1091/mbc.6.6.675

Wanders, R. J. A. (2014). Metabolic Functions of Peroxisomes in Health and Disease. *Biochimie* 98, 36–44. doi:10.1016/j.biochi.2013.08.022

Woodward, A. W., and Bartel, B. (2005). The *Arabidopsis* Peroxisomal Targeting Signal Type 2 Receptor PEX7 Is Necessary for Peroxisome Function and Dependent on PEX5. *MBoC* 16, 573–583. doi:10.1091/mbc.e04-05-0422

Yang, J., Pieuchot, L., and Jedd, G. (2018). Artificial Import Substrates Reveal an Omnivorous Peroxisomal Importomer. *Traffic* 19, 786–797. doi:10.1111/tra.12607

Yifrach, E., Chuartzman, S. G., Dahan, N., Maskit, S., Zada, L., Weill, U., et al. (2016). Characterization of Proteome Dynamics During Growth in Oleate Reveals a New Peroxisome-Targeting Receptor. *J. Cel. Sci.* 129, 4067–4075. doi:10.1242/jcs.195255

Yifrach, E., Holbrook-Smith, D., Bürgi, J., Othman, A., Eisenstein, M., Van Roermund, C. W. T., et al. (2021). Systematic Multi-Level Analysis of an Organelle Proteome Reveals New Peroxisomal Functions. *bioRxiv*. doi:10.1101/2021.12.08.471723

Yifrach, E., Rudowitz, M., Cruz-Zaragoza, L. D., Tirosh, A., Gazi, Z., Peleg, Y., et al. (2022). Determining the Targeting Specificity of the Selective Peroxisomal Targeting Factor Pex9. *bioRxiv*. doi:10.1101/2022.02.02.478779

Conflict of Interest: The authors declare that the research was conducted in the absence of any commercial or financial relationships that could be construed as a potential conflict of interest.

Publisher's Note: All claims expressed in this article are solely those of the authors and do not necessarily represent those of their affiliated organizations, or those of the publisher, the editors and the reviewers. Any product that may be evaluated in this article, or claim that may be made by its manufacturer, is not guaranteed or endorsed by the publisher.

frontiers | Frontiers in Cell and Developmental Biology

BRIEF RESEARCH REPORT
published: 13 May 2022
doi: 10.3389/fcell.2022.856243

Peroxisomes Regulate Cellular Free Fatty Acids to Modulate Mast Cell TLR2, TLR4, and IgE-Mediated Activation

Dihia Meghnem[1,2,3], *Edwin Leong*[4], *Marinella Pinelli*[2,3], *Jean S. Marshall*[1,4,3*†] and *Francesca Di Cara*[2,3*†]

[1]Dalhousie Human Immunology and Inflammation Group, Department of Microbiology and Immunology, Dalhousie University, Halifax, NS, Canada, [2]Department of Pediatrics, Nova Scotia Health Authority IWK, Halifax, NS, Canada, [3]Department of Microbiology and Immunology, Dalhousie University, Halifax, NS, Canada, [4]Department of Pathology, Dalhousie University, Halifax, NS, Canada

OPEN ACCESS

Edited by:
Marek Skoneczny,
Institute of Biochemistry and Biophysics (PAN), Poland

Reviewed by:
Ronald Wanders,
University of Amsterdam, Netherlands
John Aitchison,
Seattle Children's Research Institute, United States

***Correspondence:**
Jean S. Marshall
Jean.marshall@dal.ca
Francesca Di Cara
dicara@dal.ca

[†]These authors have contributed equally to this work

Specialty section:
This article was submitted to Membrane Traffic, a section of the journal Frontiers in Cell and Developmental Biology

Received: 16 January 2022
Accepted: 12 April 2022
Published: 13 May 2022

Citation:
Meghnem D, Leong E, Pinelli M, Marshall JS and Di Cara F (2022) Peroxisomes Regulate Cellular Free Fatty Acids to Modulate Mast Cell TLR2, TLR4, and IgE-Mediated Activation. Front. Cell Dev. Biol. 10:856243. doi: 10.3389/fcell.2022.856243

Mast cells are specialized, tissue resident, immune effector cells able to respond to a wide range of stimuli. MCs are involved in the regulation of a variety of physiological functions, including vasodilation, angiogenesis and pathogen elimination. In addition, MCs recruit and regulate the functions of many immune cells such as dendritic cells, macrophages, T cells, B cells and eosinophils through their selective production of multiple cytokines and chemokines. MCs generate and release multi-potent molecules, such as histamine, proteases, prostanoids, leukotrienes, heparin, and many cytokines, chemokines, and growth factors through both degranulation dependent and independent pathways. Recent studies suggested that metabolic shifts dictate the activation and granule content secretion by MCs, however the metabolic signaling promoting these events is at its infancy. Lipid metabolism is recognized as a pivotal immunometabolic regulator during immune cell activation. Peroxisomes are organelles found across all eukaryotes, with a pivotal role in lipid metabolism and the detoxification of reactive oxygen species. Peroxisomes are one of the emerging axes in immunometabolism. Here we identified the peroxisome as an essential player in MCs activation. We determined that lack of functional peroxisomes in murine MCs causes a significant reduction of interleukin-6, Tumor necrosis factor and InterleukinL-13 following immunoglobulin IgE-mediated and Toll like receptor 2 and 4 activation compared to the Wild type (WT) BMMCs. We linked these defects in cytokine release to defects in free fatty acids homeostasis. In conclusion, our study identified the importance of peroxisomal fatty acids homeostasis in regulating mast cell-mediated immune functions.

Keywords: peroxisome, mast cell, IgE, TLR, free fatty acids

INTRODUCTION

Mast cells (MCs) are highly specialized cells able to respond to a large panel of stimuli (Theoharides et al., 2019). MCs are characterized by highly metachromatic granules with potential for different routes of release (Wernersson and Pejler, 2014; Jain et al., 2019). MCs can respond rapidly to stimuli by releasing granules containing antimicrobial cytotoxic mediators such as serine protease,

histamines, proteoglycans and lysosomal enzymes or performing *de novo* synthesis independent of degranulation of reactive oxygen species (RO) and cytokines (Moon et al., 2014). MCs are also endowed with complex lipid droplets (Dichlberger et al., 2013) making them an important source of various lipid mediators (eicosanoids) such as leukotrienes and prostaglandins which are important players in immune cell activation and recruitment (Boyce, 2005). In addition to lipid production, MCs have been shown to respond to lipid mediator stimulation (Abdel-Majid and Marshall, 2004; Wang and Kulka, 2015; Hagemann et al., 2019).

Changes in metabolism have recently been identified as a mechanism that supports MCs activation such as IgE mediated degranulation (Mendoza et al., 2021). Several studies have shown the importance of lipid metabolism in MCs that goes beyond the production of lipid mediators. In fact, high-fat diet or chronic insulin exposure led to a lipid accumulation and altered degranulation in MCs (Greineisen et al., 2015; Aldan et al., 2019). However, how lipid metabolism supports MCs activation and regulates their distinct activities such as degranulation and/or cytokine release is largely unexplored and represents an important area of investigation to unravel how these essential innate immune cells are regulated.

Peroxisomes are specialised organelles for metabolism found across all eukaryotes. Peroxisomes have a pivotal role in lipid metabolism and in detoxification of ROS and reactive nitrogen species. They also contribute to the metabolism of polyamines, carbohydrates and amino acids (Wanders and Waterham, 2006; Fransen et al., 2012; Smith and Aitchison, 2013; Liu et al., 2019). There is substantial evidence that peroxisomes actively contribute to cell signaling and that their function is required for human health (Beach et al., 2012; Braverman et al., 2013; Braverman et al., 2013; Fransen et al., 2013; Trompier et al., 2014; Colasante et al., 2015). Recent evidence corroborated a role for peroxisomes in modulating immune responses (Dixit et al., 2010; Di Cara et al., 2017; Di Cara, 2020). Indeed, peroxisomes were first described to have an important role during viral infections serving as signal platforms for mitochondrial antiviral signaling (MAVS) proteins and induction of interferon responses (Sychev et al., 2017; Xu et al., 2017; Cook et al., 2019; Merkling et al., 2019). In recent years, substantial evidence has shown the importance of peroxisome metabolism in macrophage activation and phagocytosis (Boncompain et al., 2014; Di Cara et al., 2017; Eguchi et al., 1979; Vijayan et al., 2017). Further studies showed the importance of peroxisome-derived ether lipids in natural killer T (NKT) cell thymic development (Brutkiewicz and Dent, 2012; Facciotti et al., 2012). Thus, peroxisomes contribute to drive signaling pathways in innate and adaptive immune responses through metabolites such as ROS and lipids such as fatty acids. The metabolism of fatty acids (FAs) is a major source of biological lipids that form cell membranes and regulate inflammatory processes (Puertollano et al., 2001; Sadik and Luster, 2012; Dowds et al., 2014; Hubler and Kennedy, 2016). FAs are precursors to phospholipids (PLs), sphingolipids (SLs), triglycerides (TAGs) and eicosanoids, which have critical roles in the activation and function of macrophages, invariant NKT cells (Lim et al., 2003; Miao et al., 2014; Bettencourt and Powell, 2017). Likewise, the PL precursor, phosphatidic acid (PA), regulates the mammalian target of rapamycin (TORC1)-dependent production of pro-inflammatory cytokines in macrophages (Lim et al., 2003).

MCs are essential innate immune cells. Beyond their activities in allergic disease, MCs play a crucial role in host defense (Marshall, 2004; Abraham and St John, 2010) and cancer immunity (Oldford et al., 2010; Komi and Redegeld, 2020; Hanes et al., 2021). Mast cell degranulation mechanisms are well studied but much less is known about how lipid metabolism regulates MCs functions. Here we determined the requirement for peroxisomes in regulating distinct immune functions in MCs. We probed the need for functional peroxisomes in mounting Toll like receptor(TLR)2 and 4, IgE-mediated activation of Bone marrow-derived mast cells (BMMCs) extracted from wildtype (WT) mice and mice carrying a global mutation for *Peroxin2*, a gene that encodes for an ubiquitin ligase essential for the biogenesis of peroxisomes in cells and therefore its mutation leads to cells with not functional peroxisomes (Faust and Hatten, 1997; Smith and Aitchison, 2013). Our work demonstrated a role for peroxisomes in modulating cellular free fatty acids (FFAs) to regulate TLR and IgE-dependent secretion of cytokines in MCs. In stimulated WT MCs, peroxisome number increases, contributes to cellular FFAs homeostasis and support cytokines release. Of note, peroxisomes appeared dispensable for IgE-mediated degranulation. Taken together our report provides evidence of a requirement for peroxisome to control cellular lipid metabolism for distinct MC immune functions. Defining the role of peroxisomal metabolism in MCs may uncover new avenues of treatment for immune disorders and requires greater insight into the function of specific metabolic pathways involved in immune responses.

METHODS

Pex2 Mutant Mice

The *Pex2* Mutant Mouse Strain used was 129S6.129-*Pex2*^{tm1Plf}/Mmmh(Null allele) (Faust and Hatten, 1997) and was obtained from the Mutant Mouse Resource and Research Centre (MMRRC) supported by the NIH. The mice used for this experiment were *Pex2*$^{+/+}$, *Pex2*$^{-/-}$, *Pex2*$^{+/-}$. Homozygous null mutant strains showed no *Pex2* transcript and protein. Homozygous mutants in this congenic strain show variable embryonic lethality, starting at ~E11. Approximately 20% of homozygotes survive to birth but are hypotonic, do not feed and die on the day of birth. Homozygous mutants that survive in the postnatal period are obtained by mating congenic 129S6.129-*Pex2*^{tm1Plf} +/- mice with wild-type Swiss Webster strain mice. F1-*Pxmp3*^{tm1Plf}+/- hybrids (designated Sw129) are then intercrossed to obtain Sw129-*Pxmp3*^{tm1Plf}–/– (indicated in the text as *Pex2*$^{-/-}$) mice.

Colonies were maintained as stable inbred lines in the Swiss Webster and 129SVEV background under approved animal protocol 21-023, abiding by the standards of the Canadian Council on Animal Care.

Mast Cell Culture

BMMCs were generated from SWR/J and *Pex2*$^{-/-}$ mice according to the method of (Tertian et al., 1981). After at least 4 weeks of culture, the purity of mast cells was evaluated based on the expression of the high-affinity IgE receptor, also known as FcεRI and tyrosine-protein kinase cKIT (Cluster of differentiation, CD117). Cells were used at >98% of purity and consistently contained metachromatic granules.

Polymerase Chain Reaction

Total RNA was extracted using the RNeasy Plus Mini Kit (Qiagen, Mississauga, Canada). Genomic DNA was depleted, and complementary DNA was amplified using the Platinum Taq Reverse Transcription Kit (Wisent). *Pex2* gene was amplified using HiFi Platinum Taq DNA kit (Thermofisher) and the following primers forward (5′-TGAAGGAACCAC TTAGAAATTACAGA) and reverse (5′-CCAGGGCCTTAT TCAGTTCA). Samples were loaded onto a 2.5% agarose gel (with ethidium bromide) in TAE and imaged using chemiDoc imaging system (Biorad).

Toluidine Blue Staining

Cytospins of mast cells were briefly fixed in Carnoy's fixative then rinsed in water and 0.033N HCl. Cells were then stained with Toluidine blue (pH 0.3) overnight then rinsed before drying and mounting in DPX (Sigma) for imaging with Mantra 2TM at ×40 magnification.

Degranulation Assessment

BMMCs (2×10^6/ml) in modified HEPES-Tyrode's buffer were treated for 15 min with increasing doses of TNP-BSA (Trinitrophenyated-Bovine serum albumin) (Bioresearch Technologies) or calcium ionophore A23187 (Sigma) as a positive control. The level of degranulation was assessed *via* β-hexosaminidase release according to the method of Schwartz et al. (Schwartz et al., 1979). The percentage of β-hexosaminidase release was calculated as follow:

$$\begin{aligned} \%\, of\ release\ = \{ &(O.D\ supernatant - O.D\ control) \div [\\ &\times (O.D\ supernatant - O.D\ control) \\ &+ (O.D\ pellet - O.D\ control)]\} X100 \end{aligned}$$

Mast Cell TLR and IgE Activation

Prior to all activations, BMMC were "rested" overnight in modified mast cell growth medium, with 3 ng/ml mIL-3 (Peprotech) or without PGE_2 (Tocris). For analysis of cytokine production, cells were washed twice and resuspended in medium consisting of RPMI 1640 with 1% FBS, 15 mM HEPES and 3 ng/ml rmIL-3 and 100 μg/ml of soybean trypsin inhibitor. For all activations, cells at 1×10^6/ml were incubated with Pam3-CSK4-KKKK (L2000, EMC microcollection) at 50 μg/ml or LPS (Sigma) at 50 μg/ml and A23187 (Sigma) at 0.5 μM for 24 h at 37°C. For IgE activation, BMMCs were sensitized with anti-TNP (Trinitrophenol phosphate) IgE overnight. Cells were then rinsed and treated with 10 ng/ml of TNP-BSA for 30 min, then supernatants were removed, and cells were cultured for a further 24 h. For mechanistic studies, cells were treated with 100 μg/ml of niacin (Sigma Aldrich) for 48 h or with 2.5 uM thioridazine for 1 h prior to IgE activation. Supernatants were removed, and cells were cultured for a further 24 h. Cell-free supernatants were collected and assayed for IL-6 (Peprotech), IL-13 (Peprotech) and TNF (Invitrogen) by ELISA from sources indicated.

Free Fatty Acid Assessment

One million BMMCs per genotype and under each condition was sensitized with anti-TNP as described above and treated with 10 ng/ml of TNP-BSA for 24 h. Supernatants were removed, and cells were analyzed for fatty acid accumulation using free fatty acid quantification kit (Sigma) according to manufacturer's recommendations.

ELISA: Levels of IL-6 (Peprotech), IL-13 (Peprotech) and TNF (Invitrogen) in supernatants were assessed according to the manufacturer recommendations.

Fluorescence Microscopy

Cells were fixed in 4% paraformaldehyde in PBS for 30 min and then incubated for 1 h at room temperature in 5% normal goat serum (Sigma) and for 16 h at 4°C with primary antibody at 1:100 dilution in 5% normal goat serum. Appropriate Alexa Fluor secondary antibodies (anti-rabbit secondary antibodies, were from Abcam) were then used at 1:1000 dilution in 5% normal goat serum. After 4 washes in PBST (PBS +0.1% (v/v) Triton X-100), cells were mounted in DAPI Pro-Gold Antifade Reagent (Thermo Fisher) and imaged using a ×100 oil immersion objective (NA = 1.4) mounted on an Zeiss800 confocal microscope (Zeiss) or using a Zeiss AxioObserver LSM 880, 100 × 1.4 oil plan-Apochromat lens. Primary antibody was rabbit anti-SKL antibody was previously described (Szilard et al., 1995).

Flow cytometry: Maturation of *Pex2*$^{-/-}$ and WT BMMC were assessed by flow cytometry. Antibodies to CD117 (Clone 2B8, Biolegend), FceR1(Clone MAR-1, Invitrogen) were used to assess the maturation of BMMC cells. Fc receptors were first blocked with anti CD16/CD32 (Clone 93, eBisocience) for 10 min. Combinations of the two anti-CD117 and anti-FceR1 fluorescently tagged antibodies (at manufacturers recommended dilutions) were added to each sample for 30 min at 4°C. For assessment of IgE binding, BMMCs were sensitized with anti-TNP (Trinitrophenol phosphate) IgE overnight. Cells were then rinsed then stained with fluorescently tagged anti-IgE antibody (ClonePME-1, Biolegend) or with isotype control rat IgG2b (Clone G0114F7, Biolegend) for 30 min at 4°C.

After stainings, cells were washed twice with PBS supplemented with 2% Fetal Calf Serum (FCS) (Gibco) then fixed with PBS containing 1% paraformaldehyde for 30 min 4°C before analysis on BD FACSCelesta™ (BD). Data were analyzed using FlowJo Version 10 software (BD).

Viability Assay

BMMCs were resuspended at a density of 1 million cells per mL in activating media and seeded into a 24-well plate. BMMCs were

stimulated in duplicates with either activation media, LPS (50 μg/ml), Pam3CSK4 (50 μg/ml), or thiorizi dine (2.5 uM) for 24 h. BMMCs were then washed in PBS prior to staining with fixable viability dye Efluor 450 for 20 min at 4°C then rinsed before fixation in 1% paraformaldehyde, and acquired on the FACS Canto II flow cytometer. Data were analyzed using FlowJo Version 10 software (BD).

Quantification and Statistical Analysis

Statistical analyses were performed using a non-parametric *t*-test comparing between *Pex2*$^{-/-}$ and WT BMMCs. *$p < 0.05$, **$p < 0.001$, ***$p < 0.0001$ ns: not significant. All results are represented as the mean of at least 3 independent experiment ± Standard error of the mean.

Quantification of SKL-Puncta

Average number of puncta per cell were calculated using ImageJ software, applying the following steps to each image:

1—We opened stacks image.

File -> Open. . .

2—We filtered to remove noise.

Process -> Filters -> Gaussian Blur. . .

3—We subtracted background.

Process -> Subtract Background. . .
(the box marked "Light Background" was unticked).

4—We clicked on "Image"

Color -> Split the channels . . .
In this step, brightness and contrast were adjusted, and setting were applied to all stacks.

5—We performed threshold image.

Image -> Adjust -> Threshold. . .
(We selected: Apply it to all stacks).
Box labeled "Dark Background" was ticked. We adjusted the sliders so that features were red colored, but the rest of the image was not. Then we clicked "Apply" button. This replaced grayscale image with an "8-bit binary image." All "red" pixels were converted to a value of "255," while all non-red pixels were given a value of "0."

6—We filled in any holes in the nuclei.

Process -> Binary -> Fill Holes

7—We separated "Touching" puncta.

Process -> Binary -> Watershed.
Process -> Find Edges.

8—We performed the analysis.

Analyze -> Analyze Particles. . .
In this dialog box the algorithm started to include or exclude puncta based on their attributes. "Size" smaller than 0.1 mm and larger than 1 mm "Circularity" set range: 200-1.

RESULTS

Lack of Functional Peroxisomes Does Not Alter Mast Cell Morphology or Degranulation But Reduces Cytokine Release

To study the requirement of peroxisomes for MCs function, we assayed BMMCs from wildtype and *Peroxin2* null mutant mice (*Pex2*$^{-/-}$) (**Supplementray Figure S1A**) (Faust and Hatten, 1997). We confirmed the presence of peroxisomes by performing indirect immunofluorescence (IF) using an antibody against the C-terminal Peroxisome Targeting Sequence Type 1 Ser-Lys-Leu (SKL), the canonical marker for peroxisomal matrix proteins (Szilard et al., 1995).

WT MCs showed SKL-positive puncta while intense diffuse staining was observed in *Pex2*$^{-/-}$ MCs confirming that the MCs from *Pex2* mutant mouse do not form functional peroxisomes due to defects in peroxisomal protein import into the matrix (Smith and Aitchison, 2013) (**Figures 1A,B**, **Supplementary Figure S1A**; **Supplementary Data Sheet S1, S2**). Assessment of maturation based on the expression of FceR1 and CD117 by flow cytometry showed no differences between the two cell types (**Supplementary Figure S1B**). *Pex2*$^{-/-}$ BMMCs exhibited a similar morphology and granularity compared to the WT BMMCs (**Supplementary Figure S1C**). All together these observations indicated that absence of peroxisomes did not alter maturation, morphology, or granule content of MCs.

Through IgE-mediated degranulation, MCs hold a key role in allergic disease and host defence against several parasites. Peroxisomes are known to proliferate and increase during responses to viral infection (Cook et al., 2019; Knoblach et al., 2021). To assess the role of IgE-mediated activation and peroxisomes we measured peroxisome numbers in WT BMMCs when stimulated with IgE. Indirect IF followed by automated quantification showed an increase in SKL-positive puncta in stimulated MCs (**Figures 1C,D**, **Supplementary Data Sheet S3, S4**) indicating that an increase in cellular peroxisomes occurs during the IgE mediated MC response. We next assessed whether an absence of peroxisomes altered IgE/antigen-induced degranulation, assessed via a β-hexosaminidase release. Peroxisome biogenesis defects caused by mutations in *Pex2* have been linked to lipid metabolic defects (Faust and Hatten, 1997; Faust, 2003) thus, affecting the lipid milieu of the cell membrane (Schrader et al., 2020). In fact, an altered membrane lipids environment was reported to compromise signaling (Lodhi et al., 2015) in multiple cell types including immune cells (Lodhi et al., 2015; Di Cara et al., 2019). Thus, we first assessed the ability

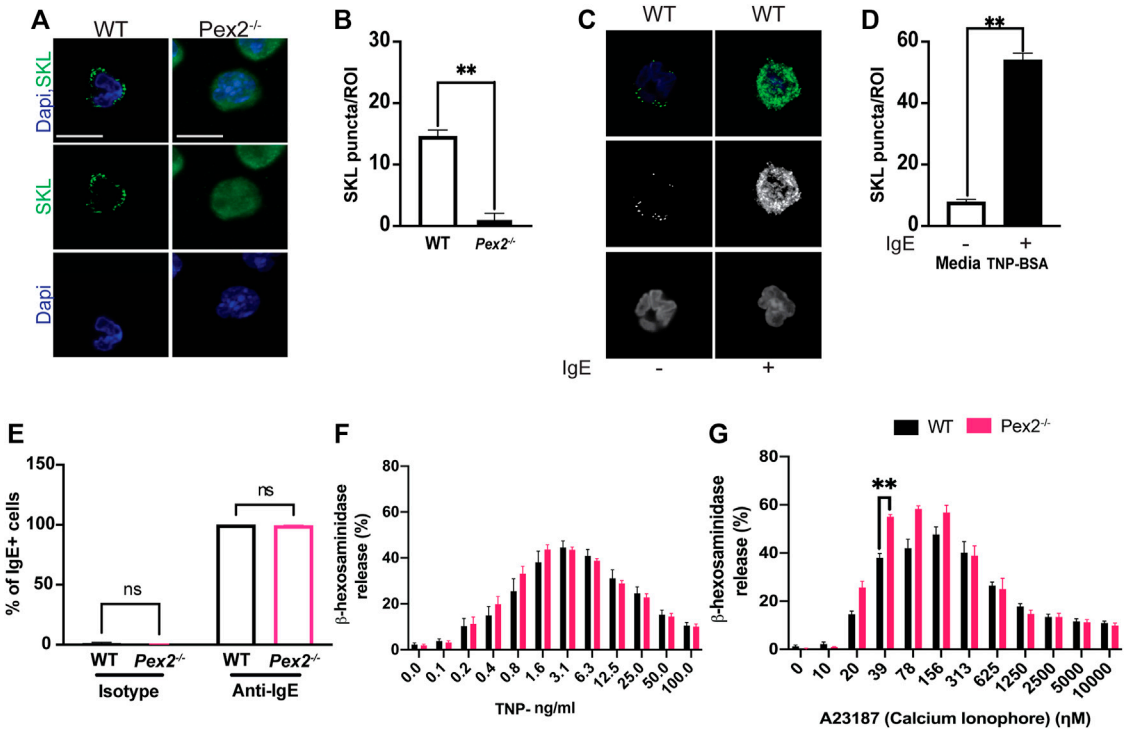

FIGURE 1 | Peroxisome do not alter MCs granularity and degranulation: **(A)** WT and *Pex2*$^{-/-}$ BMMCs were stained for peroxisome (SKL, Green) and nuclei (Dapi, Blue). Scale bar, 10 μm. **(B)** Peroxisomes number was defined by automated counting of SKL-positive puncta per region of interest (ROI). The graph bars represent the number of SKL-positive puncta in stack z = 3. N = 25 cells. For each cell 22 stacks were acquired. **(C)** Indirect immunofluorescence of WT and *Pex2*$^{-/-}$ BMMCs were stained for peroxisome (SKL, Green) and nuclei (Dapi, Blue). Scale bar, 10 μm. **(D)** Peroxisomes number was defined by automated counting of SKL-positive puncta. The graph bars represent the number of SKL-positive puncta in stack z = 3. The graph bars represent the number of SKL-positive puncta in stack z = 3. N = 25 cells. For each cell 22 stacks were acquired. **(E)** WT and *Pex2*$^{-/-}$ BMMCs were tested for their ability to bind to the anti-TNP specific IgE by flow cytometry. **(F)** Percentage of beta -h exosaminidase degranulation was assessed upon 15 min of TNP-BSA IgE-mediated degranulation and **(G)** A23187 calcium ionophore-mediated degranulation. Graphs represent the average of three independent experiments ±SEM. Statistical analyses were performed using a non-parametric *t*-test comparing between *Pex2*$^{-/-}$ and WT BMMCs. ***p* < 0.01, ns: not significant.

of WT and *Pex2*$^{-/-}$ BMMCs to bind IgE by flow cytometry. WT and *Pex2*$^{-/-}$ BMMCs demonstrated equivalent IgE binding (**Figure 1E** and **Supplementary Figure S1D**). Next, BMMCs were loaded with Anti-TNP IgE overnight then crosslinked with a dose range of TNP-BSA antigen or treated with calcium ionophore A23187 allowing degranulation for 15 min. *Pex2*$^{-/-}$ BMMCs displayed similar degranulation potential compared to their WT counterparts (**Figure 1F**). When treated with calcium ionophore A23187, *Pex2*$^{-/-}$ BMMCs demonstrated a higher percent degranulation at lower A23187 doses (**Figure 1G**). Overall, lack of functional peroxisomes did not adversely affect mast cell degranulation.

Peroxisome Supports Cytokine Release Upon TLRs and IgE Activation in Mast Cells

It is well established that MCs have degranulation-independent pathways which allow the production of cytokines and chemokines independent of classical degranulation (Leal-Berumen et al., 1994; Moon et al., 2014). Beyond their role in allergy, MCs are key player in responses to pathogens (Marshall, 2004; Abraham and St John, 2010). MCs express and respond via Toll like receptors (TLRs) to several bacterial or viral products (McCurdy et al., 2003; Agier et al., 2018). We thus asked whether peroxisome function is necessary for cytokine release upon TLR2 or TLR4 stimulation induced by Pam3CSK4 (Pam3) and *E.coli* lipopolysaccharide (LPS) respectively. We assessed whether the lack of functional peroxisomes affected TLR and IgE-mediated interleukin 6 (IL-6), interleukin 13 (IL-13) and Tumor Necrosis Factor (TNF) production after 24 h stimulation. Our data showed that IL-6 (**Figure 2A**) and IL-13 (**Figure 2B**) were produced in response to TLR2 and TLR4 stimulation in WT BMMCs but production of both cytokines was significantly reduced in *Pex2*$^{-/-}$ cells. On the other hand, TNF production was significantly reduced only upon LPS treatment in *Pex2*$^{-/-}$ compared to WT MCs (**Figure 2C**). Interestingly, while IgE-mediated degranulation was not affected by the absence of functional peroxisomes, cytokine production was markedly reduced in *Pex2*$^{-/-}$ BMMCs upon IgE stimulation followed by TNP-BSA treatment (**Figures 2D–F**). Additionally, IL-13 secretion was lower in *Pex2*$^{-/-}$ BMMCs after IgE stimulation followed by treatment with both TNP-BSA or with the calcium ionophore A231287

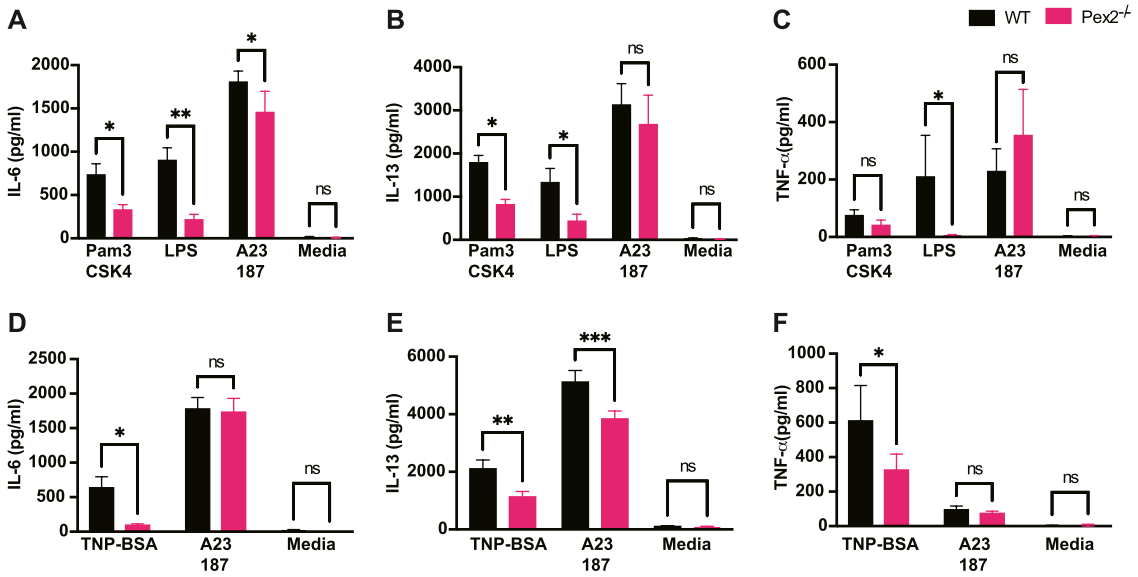

FIGURE 2 | Absence of peroxisome leads to decreased MCs cytokine release upon TLRs and IgE-mediated activation: WT and Pex2–/– BMMCs were treated with TLRs agonist or TNP-BSA for 24 h and cytokines amounts were measured by ELISA. **(A)** IL-6, **(B)** IL-13 and **(C)** TNF-α production after TLR2 agonist Pam3CSK4, TLR4 agonist LPS and calcium ionophore A23187 treatments. **(D–F)** Same readouts were measured after IgE crosslinking with TNP-BSA treatment for 24 h. The media columns in each graph represent the baseline level detected for each cytokine. The graphs represent the average of three independent experiments ±SEM. Statistical analyses were performed using a non-parametric t-test comparing between $Pex2^{-/-}$ and WT BMMCs. $^{*}p < 0.05$, $^{**}p < 0.001$, ns: not significant.

(**Figure 2E**). We tested the secretion of other cytokines such as interleukin 5 (IL-5), Granulocyte-macrophage colony-stimulating factor (GM-CSF) and Chemokine (C-C motif) ligand 3 (CCL3) (**Supplementary Figure S2A–C**). A23187 selectively induced CCL3 production which was significantly decreased in *Pex2*$^{-/-}$ compared to the WT BMMCs (**Supplementary Figure S2C**). All together these results indicated a requirement for peroxisomes in MCs activation in response to IgE-mediated, TLR2 or TLR4 stimulation.

Peroxisome Regulates Free Fatty Acid Metabolism During MCs Activation

Peroxisomes are highly conserved organelles and play a pivotal role in lipid metabolism and ROS such as hydrogen peroxide (H_2O_2) catabolism (Liu et al., 2019). Both ROS and lipids are important mediators in cellular signaling in immune cells (Di Cara, 2020; Di Cara et al., 2017; 2019). H_2O_2 is a permeable and diffusible molecule involved in inter- and intracellular signaling during host defense (Bedard and Krause, 2007; Blander and Sander, 2012). We measured the cellular amount of H_2O_2 in *Pex2*$^{-/-}$ and WT BMMCs. At rest, BMMCs lacking peroxisome function exhibited similar amounts of H_2O_2 (**Figure 3A**) as WT BMMCs.

Different studies have shown that the metabolism of fatty acids (FAs) is a major source of biological lipids that form cell membranes and regulate inflammatory functions (Dowds et al., 2014; Hubler and Kennedy, 2016; Nath et al., 2022; O'Neill et al., 2016; Puertollano et al., 2001; Sadik and Luster, 2012). Peroxisomes contribute to the homeostasis of FAs in the cell (Wanders and Waterham, 2006; Lodhi and Semenkovich, 2014) and we probed whether free fatty acids (FFAs) are altered in MCs in absence of peroxisomes, affecting cytokine release. We measured cellular FFAs and observed a significant accumulation of FFAs in *Pex2*$^{-/-}$ BMMCs compared to WT BMMCs, at rest (**Figure 3B**). Interestingly, we observed that IgE stimulation triggers a significant increase of FFAs in WT BMMCs while the level remained unchanged in IgE stimulated *Pex2*$^{-/-}$ (**Figure 3B**). These results indicated that IgE-mediated stimulation triggers an increase in cellular FFAs in MCs while lack of functional peroxisomes affects FFA metabolism and turnover at rest and during IgE-mediated activation.

To explore the link between FFAs and MCs activation, we used Niacin a vitamin B3 shown to reduce FFAs in plasma, macrophages and adipocytes by inducing anti-lipolytic effects (Tunaru et al., 2003; Nath et al., 2022). Human MCs have been shown to respond to niacin treatment by prostaglandin D2 (PGD_2) production (Papaliodis et al., 2008). We hypothesised that the accumulation of FFAs in WT BMMCs was hindering cytokine release under IgE-mediated stimulation conditions. To test this hypothesis, we treated *Pex2*$^{-/-}$ BMMCs with niacin for 48 h to reduce FFAs (**Figure 3B**) and then we stimulated the cells. Treatments with niacin reduced FFAs in *Pex2*$^{-/-}$ BMMCs at rest to the amount observed in WT. Moreover, after IgE stimulation, niacin treatment recapitulated the increase FFAs observed in IgE stimulated WT BMMC (**Figure 3B**). Intriguingly, the amounts of released IL-6 and IL-13 after IgE-mediated activation was rescued to WT levels in *Pex2*$^{-/-}$ BMMCs upon 48 h treatment with niacin (**Figures 3C,D**). This result provides a link between the cellular FFAs milieu, regulated by peroxisomes, and cytokine release by MCs.

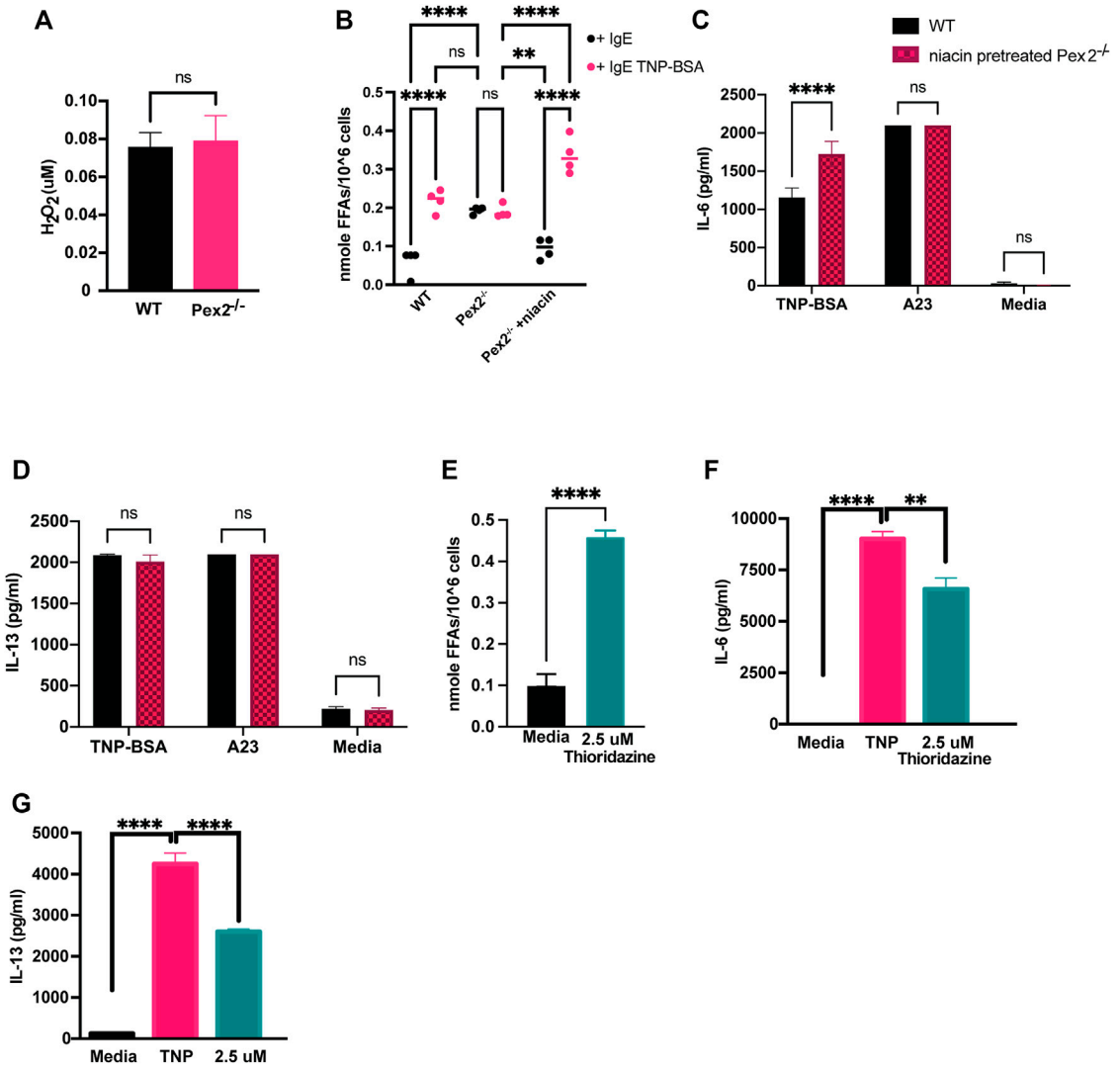

FIGURE 3 | Defects in peroxisomal fatty acid metabolism affects cytokines release in MCs: **(A)** WT and Pex2$^{-/-}$ BMMCs pellets were assessed for the level of H2O2 and **(B)** free fatty acids at baseline and after 24 h IgE mediated activation with TNP-BSA in WT, Pex2$^{-/-}$ and niacin-treated Pex2–/– BMMCs. **(C,D)** Concentrations of IL-6 and IL-13 were assessed after 48 h of niacin treatment followed by 24 h IgE or A23 activation. **(E)** Free fatty acids amounts measured in WT BMMC at baseline and after 24 h of treatment with thioridazine. **(F–G)** Effect of free fatty acid metabolism inhibition on IgE-mediated IL-6 and IL-13 release was assessed in C57BL/6 BMMCs. The media column in graphs C-G represent the baseline level detected for each cytokine. The graphs represent the average of three independent experiments ±SEM. Statistical analysis was performed using a non-parametric *t*-test comparing between Pex2$^{-/-}$ and WT BMMCs. $^{**}p < 0.001$, $^{***}p < 0.0001$, $^{****}p < 0.00001$, ns: not significant.

We affected cellular FFAs by treatment with thioridazine, a small molecule that causes accumulation of FFAs (Van den Branden and Roels, 1985; Shi et al., 2012). Similar to *Pex2*$^{-/-}$ BMMCs, thioridazine-treated WT BMMCs present high amount of cellular FFAs. Upon IgE stimulation, thioridazine-treated WT BMMCs secreted lower amount of IL-6 (**Figure 3E**) and IL-13 (**Figure 3F**) compared to untreated WT BMMCs. Of note, all the treatments used to stimulate MCs and/or to manipulate cellular FFAs did not affect cell viability (**Supplementary Figure S2D**).

These results indicated that peroxisomal control of cellular FFAs is required in MCs to respond to and participate in inflammatory signaling cascades (**Figure 4**).

DISCUSSION

Peroxisomes are ubiquitous organelles with a central role in lipid metabolism and ROS production and scavenging (Schrader and Fahimi, 2006). Peroxisomes have been recognized as organelles of immunity with central immunometabolic and signaling functions to regulate immune response to pathogens (Sychev et al., 2017; Xu et al., 2017; Cook et al., 2019; Merkling et al., 2019). We have previously shown the central role of peroxisome in macrophage-mediated host defense (Di Cara et al., 2017; Nath et al., 2022). The present study aimed to define the role of peroxisome metabolism in the context of TLR and IgE-mediated activation of MCs. In the

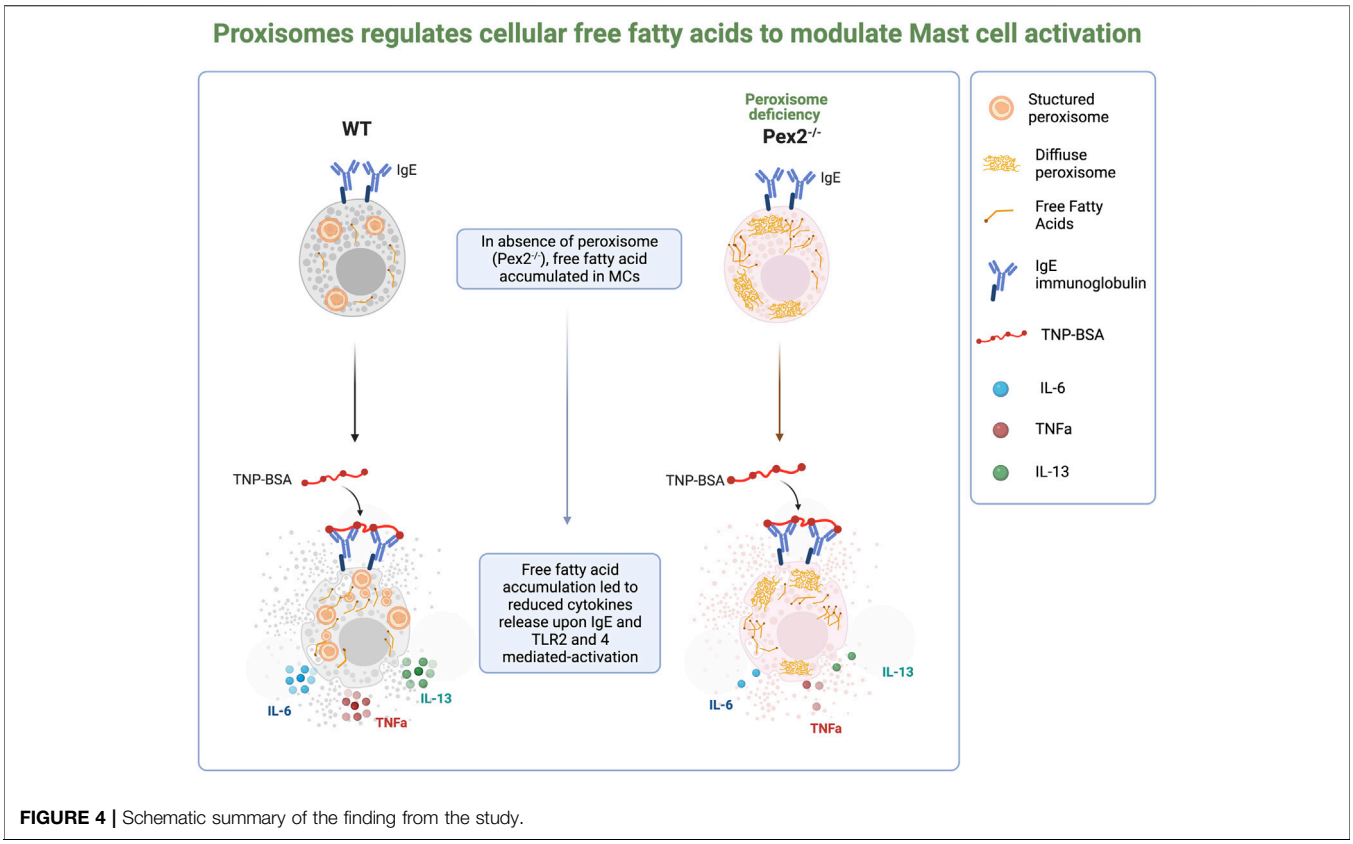

FIGURE 4 | Schematic summary of the finding from the study.

immune compartment, peroxisome-derived lipids have been shown to be involved in the development, survival and functions of multiple innate and adaptive immune effector cells (Brutkiewicz and Dent, 2012; Facciotti et al., 2012; Di Cara, 2020).

Lipids are important mediators of mast cell immune functions (Nakamura et al., 1991; Austen, 2005; Dichlberger et al., 2013). However, the role of peroxisomes in regulating MCs development and activation is unknown. Here we determined that lack of functional peroxisomes in MCs did not alter their maturation, morphology, or granulation. We report that an increase in peroxisome number occurs in MCs upon IgE-mediated activation, indicating the involvement of peroxisomes or peroxisome metabolism in mast cell responses. Peroxisomes have been shown to mobilize and to metabolically support activation during viral infection (Cook et al., 2019) as well as phagocytosis by macrophages (Eguchi et al., 1979; Di Cara et al., 2017). While the number of peroxisomes are increased during IgE-mediated activation, MC degranulation remained unchanged in absence of peroxisomes, suggesting that peroxisomes might support other mast cell-specific responses to IgE stimulation but not the degranulation.

Interestingly, in our study, an absence of functional peroxisomes in MCs led to a significant decrease in TLR2 and TLR4-mediated IL-6, IL-13 and TNF cytokine production compared to WT MCs. In potential contrast, Vijayan et al. showed that peroxisome induction with 4-phenyl butyric acid in macrophages dampened their IL-6, IL-12 and TNF production in response to TLR4-mediated activation, suggesting an anti-inflammatory role for peroxisomes in these cells (Vijayan et al., 2017). On the other hand, Nath et al., reported a deficiency in IL-6, IL-1β, and TNF secretion in response to TLR1/2 and TLR4-mediated activation in *Pex2*$^{-/-}$ macrophages. When stimulated with IgE/antigen MCs exhibited a decrease in IL-6, IL-13, and TNF release supporting the hypothesis that peroxisomes might have pro or anti-inflammatory functions in different myeloid cells. Of note, peroxisome dysfunction also impacted cytokine release following calcium ionophore stimulation but to a lesser extent. All together our results indicated a stimuli-dependent role of peroxisomes in MC activation.

Peroxisomes main metabolic functions include β-oxidation of very long chain fatty acids and metabolism of ROS. We previously showed that lack of functional peroxisomes affects cellular H_2O_2-mediated signaling that controls uptake of pathogens by phagocytosis and activation of NF-κB (Di Cara et al., 2017). While ROS catabolism was unaffected in MCs which lacked functional peroxisomes, as H_2O_2 amounts were unchanged, cellular amounts of FFAs were altered in the absence of peroxisomes under both unstimulated and stimulated conditions. Upon activation, changes in lipid composition are expected in immune cells (Sadik and Luster, 2012; Lodhi et al., 2015) as lipids are crucial mediators for cell signaling as well as regulation of inflammation (Sadik and Luster, 2012). Wild-type MCs exhibited an increased FFAs level after IgE-mediated activation while this increase was not observed in the absence of peroxisomes, highlighting the importance of peroxisomes in

lipid dynamics in MCs. These observations indicate an excess of lipids in the absence of functional peroxisomes in MCs. Remarkably, when peroxisome deficient MCs were treated, prior to activation, with niacin, a FFAs scavenger (Papaliodis et al., 2008), their cytokine release function was restored, indicating a restored FFAs turnover with the treatment. Furthermore, we demonstrated that peroxisome metabolism has a role in regulating FFAs cellular amounts observed during IgE activation of MCs. This FFAs regulation appeared a key mechanism of peroxisome activity in MCs. In fact, treatment of mast cells with thioridazine, a small molecule that triggers accumulation of cellular FFAs, recapitulated the phenotype observed in *Pex2*$^{-/-}$ cells. The roles of peroxisomal FFAs homeostasis have not been extensively studied in immune cells, nevertheless, a few studies showed that thioridazine treatment decreased TLR mediated activation in macrophages (Baig et al., 2018; Ganguli et al., 2019) and in T cells reducing *in vitro* murine Treg cell polarization while no effects were found on Th1 or Th17 cells (Moreno-Fernandez et al., 2018).

MCs are critical, tissue-resident sentinel cells with a wide range of impacts on innate immunity and the mobilisation of effective acquired immune responses to infection, as well as impacts on cancer development and anti-cancer immunity. They are rich at sites that interface with the external environment such as skin and mucosae and also elevated around many types of solid tumours. They have been implicated in effective local mobilisation of immune responses to a number of parasitic, bacterial, viral and fungal challenges, in some cases, these include the generation of ROS, as well as degranulation or selective cytokine and chemokine production. These studies suggest that many aspects of such sentinel functions against infection, such as the production of pro-inflammatory cytokines might be modulated by peroxisomal activity. Mast cell responses are known to be modulated by lipid mediators, endocannabinoids and FFAs (Abdel-Majid and Marshall, 2004; Hagemann et al., 2019). The current study showed the importance of peroxisome-mediated lipid metabolism in MCs and indicates that proper regulation of FFAs modulates MCs activation and cytokine production. Our work and recent studies (Eguchi et al., 1979; Singh et al., 2004; Di Cara et al., 2017, 2019; Vijayan et al., 2017; Nath et al., 2022) revealing peroxisome involvement in immune processes, provide a new avenue for therapeutic targeting. Such interventions, focused on MCs, may allow local modulation of immune and inflammatory events in specific mast cell-rich tissues such as the skin, airways or tumour microenvironment. The selective nature of the impact of peroxisomes on mast cell function may suggest new pharmacological approaches to modify cytokine production, such as that observed in chronic inflammatory sites without limiting the acute degranulation events necessary for rapid recruitment of immune effector cells and dendritic cell mobilisation at the very earliest stages of infection. The role of peroxisomes in MCs in regulating allergic disease remains unclear, however the impact of peroxisome defects on IL-13 production may also suggest that such organelle function could be targeted in the context of chronic allergic inflammation.

DATA AVAILABILITY STATEMENT

The original contributions presented in the study are included in the article/**Supplementary Material**, further inquiries can be directed to the corresponding authors.

ETHICS STATEMENT

The animal study was reviewed and approved by Dalhousie University, University Committee on Laboratory Animals protocol number: 21-023 Investigator: FD category/level: B–(experiments which cause little or no discomfort or stress) title of study: (21-023) Defining the peroxisome-lipid signaling network in innate immunity.

AUTHOR CONTRIBUTIONS

DM designed the study, performed experiments, analyzed, and interpreted the data, and wrote the manuscript with support from JM and FD. MP and FD assayed Fatty acids and analyzed the data. EL performed and analysed experiments, JM and FD conceptualised the study helped DM to design the study, interpret the data and edit the manuscript.

FUNDING

This work was funded by a Discovery Grant from Natural Sciences and Engineering Research Council of Canada (NSERC) to FD, a Canada Foundation for Innovation (CFI) JELF equipment grant to FD, a Dalhousie Medical Research Foundation start-up fund to FD a Canadian Institute of Health Research project grant to JM. DM is supported by Dr. David H. Hubel Postdoctoral Fellowship funded by the Dalhousie Medical Research Foundation.

ACKNOWLEDGMENTS

Flow cytometry was performed at Dalhousie University, Faculty of Medicine Flow Cytometry Core Facility. Microscopy was performed at Dalhousie University, Faculty of Medicine Cellular and Molecular Digital Imaging. We thank Stephen Whitefield and Brianne Lindsay for help with microscopy and Derek Rowter for training and for technical help in flow cytometry.

SUPPLEMENTARY MATERIAL

The Supplementary Material for this article can be found online at: https://www.frontiersin.org/articles/10.3389/fcell.2022.856243/full#supplementary-material

REFERENCES

Abdel-Majid, R. M., and Marshall, J. S. (2004). Prostaglandin E2Induces Degranulation-independent Production of Vascular Endothelial Growth Factor by Human Mast Cells. *J. Immunol.* 172, 1227–1236. doi:10.4049/jimmunol.172.2.1227

Abraham, S. N., and St. John, A. L. (2010). Mast Cell-Orchestrated Immunity to Pathogens. *Nat. Rev. Immunol.* 10, 440–452. doi:10.1038/nri2782

Agier, J., Pastwińska, J., and Brzezińska-Błaszczyk, E. (2018). An Overview of Mast Cell Pattern Recognition Receptors. *Inflamm. Res.* 67, 737–746. doi:10.1007/s00011-018-1164-5

Aldan, J. T., Jansen, C., Speck, M., Maaetoft-Udsen, K., Cordasco, E. A., Faiai, M. U., et al. (2019). Insulin-induced Lipid Body Accumulation Is Accompanied by Lipid Remodelling in Model Mast Cells. *Adipocyte* 8, 265–279. doi:10.1080/21623945.2019.1636624

Baig, M. S., Saqib, U., Rajpoot, S., Srivastava, M., Naim, A., Liu, D., et al. (2018). Repurposing Thioridazine (TDZ) as an Anti-inflammatory Agent. *Sci. Rep.* 8, 12471. doi:10.1038/s41598-018-30763-5

Beach, A., Burstein, M. T., Richard, V. R., Leonov, A., Levy, S., and Titorenko, V. I. (2012). Integration of Peroxisomes into an Endomembrane System that Governs Cellular Aging. *Front. Physio.* 3, 283. doi:10.3389/fphys.2012.00283

Bedard, K., and Krause, K.-H. (2007). The NOX Family of ROS-Generating NADPH Oxidases: Physiology and Pathophysiology. *Physiol. Rev.* 87, 245–313. doi:10.1152/physrev.00044.2005

Bettencourt, I. A., and Powell, J. D. (2017). Targeting Metabolism as a Novel Therapeutic Approach to Autoimmunity, Inflammation, and Transplantation. *J. Immunol.* 198, 999–1005. doi:10.4049/jimmunol.1601318

Blander, J. M., and Sander, L. E. (2012). Beyond Pattern Recognition: Five Immune Checkpoints for Scaling the Microbial Threat. *Nat. Rev. Immunol.* 12, 215–225. doi:10.1038/nri3167

Boncompain, G., Muller, C., Meas-Yedid, V., Schmitt-Kopplin, P., Lazarow, P. B., and Subtil, A. (2014). The Intracellular Bacteria Chlamydia Hijack Peroxisomes and Utilize Their Enzymatic Capacity to Produce Bacteria-Specific Phospholipids. *PLoS One* 9, e86196

Boyce, J. A. (2005). Eicosanoid Mediators of Mast Cells: Receptors, Regulation of Synthesis, and Pathobiologic Implications. *Chem. Immunol. Allergy* 87, 59–79. doi:10.1159/000087571

Braverman, N. E., D'Agostino, M. D., and Maclean, G. E. (2013). Peroxisome Biogenesis Disorders: Biological, Clinical and Pathophysiological Perspectives. *Dev. Disabil. Res. Rev.* 17, 187–196. doi:10.1002/ddrr.1113

Brutkiewicz, R. R., and Dent, A. L. (2012). Lipids-Я-Us: Peroxisome Generation of iNKT Ligands. *Nat. Immunol.* 13, 435–436. doi:10.1038/ni.2288

Colasante, C., Chen, J., Ahlemeyer, B., and Baumgart-Vogt, E. (2015). Peroxisomes in Cardiomyocytes and the Peroxisome/Peroxisome Proliferator-Activated Receptor-Loop. *Thromb. Haemost.* 113, 452–463. doi:10.1160/TH14-06-0497

Cook, K. C., Moreno, J. A., Jean Beltran, P. M., and Cristea, I. M. (2019). Peroxisome Plasticity at the Virus-Host Interface. *Trends Microbiol.* 27, 906–914. doi:10.1016/j.tim.2019.06.006

Di Cara, F., Andreoletti, P., Trompier, D., Vejux, A., Bülow, M. H., Sellin, J., et al. (2019). Peroxisomes in Immune Response and Inflammation. *Int. J. Mol. Sci.* 20, 3877. doi:10.3390/ijms20163877

Di Cara, F. (2020). Peroxisomes in Host Defense. *Plos Pathog.* 16, e1008636. doi:10.1371/journal.ppat.1008636

Di Cara, F., Sheshachalam, A., Braverman, N. E., Rachubinski, R. A., and Simmonds, A. J. (2017). Peroxisome-Mediated Metabolism Is Required for Immune Response to Microbial Infection. *Immunity* 47, 93–106. doi:10.1016/j.immuni.2017.06.016

Dichlberger, A., Kovanen, P. T., and Schneider, W. J. (2013). Mast Cells: from Lipid Droplets to Lipid Mediators. *Clin. Sci. (Lond)* 125, 121–130. doi:10.1042/CS20120602

Dixit, E., Boulant, S., Zhang, Y., Lee, A. S. Y., Odendall, C., Shum, B., et al. (2010). Peroxisomes Are Signaling Platforms for Antiviral Innate Immunity. *Cell* 141, 668–681. doi:10.1016/j.cell.2010.04.018

Dowds, C. M., Kornell, S.-C., Blumberg, R. S., and Zeissig, S. (2014). Lipid Antigens in Immunity. *Biol. Chem.* 395, 61–81. doi:10.1515/hsz-2013-0220

Eguchi, M., Sannes, P. L., and Spicer, S. S. (1979). Peroxisomes of Rat Peritoneal Macrophages during Phagocytosis. *Am. J. Pathol.* 95, 281

Facciotti, F., Ramanjaneyulu, G. S., Lepore, M., Sansano, S., Cavallari, M., Kistowska, M., et al. (2012). Peroxisome-derived Lipids Are Self Antigens that Stimulate Invariant Natural Killer T Cells in the Thymus. *Nat. Immunol.* 13, 474–480. doi:10.1038/ni.2245

Faust, P. L. (2003). Abnormal Cerebellar Histogenesis inPEX2 Zellweger Mice Reflects Multiple Neuronal Defects Induced by Peroxisome Deficiency. *J. Comp. Neurol.* 461, 394–413. doi:10.1002/cne.10699

Faust, P. L., and Hatten, M. E. (1997). Targeted Deletion of the PEX2 Peroxisome Assembly Gene in Mice Provides a Model for Zellweger Syndrome, a Human Neuronal Migration Disorder. *J. Cell Biol* 139, 1293–1305. doi:10.1083/jcb.139.5.1293

Frank Austen, K. (2005). The Mast Cell and the Cysteinyl Leukotrienes. *Novartis Found Symp.* 271, 166–178. doi:10.1002/9780470033449.ch13

Fransen, M., Nordgren, M., Wang, B., and Apanasets, O. (2012). Role of Peroxisomes in ROS/RNS-metabolism: Implications for Human Disease. *Biochim. Biophys. Acta (Bba) - Mol. Basis Dis.* 1822, 1363–1373. doi:10.1016/j.bbadis.2011.12.001

Fransen, M., Nordgren, M., Wang, B., Apanasets, O., and Van Veldhoven, P. P. (2013). Aging, Age-Related Diseases and Peroxisomes. *Subcell Biochem.* 69, 45–65. doi:10.1007/978-94-007-6889-5_3

Ganguli, G., Mukherjee, U., and Sonawane, A. (2019). Peroxisomes and Oxidative Stress: Their Implications in the Modulation of Cellular Immunity during Mycobacterial Infection. *Front. Microbiol.* 10, 1121. doi:10.3389/fmicb.2019.01121

Germain, V., Rylott, E. L., Larson, T. R., Sherson, S. M., Bechtold, N., Carde, J.-P., et al. (2001). Requirement for 3-Ketoacyl-CoA Thiolase-2 in Peroxisome Development, Fatty Acid β-oxidation and Breakdown of Triacylglycerol in Lipid Bodies of Arabidopsis Seedlings. *Plant J.* 28, 1–12. doi:10.1046/j.1365-313x.2001.01095.x

Greineisen, W. E., Maaetoft-Udsen, K., Speck, M., Balajadia, J., Shimoda, L. M. N., Sung, C., et al. (2015). Chronic Insulin Exposure Induces ER Stress and Lipid Body Accumulation in Mast Cells at the Expense of Their Secretory Degranulation Response. *PLoS One* 10, e0130198. doi:10.1371/journal.pone.0130198

Hagemann, P. M., Nsiah-Dosu, S., Hundt, J. E., Hartmann, K., and Orinska, Z. (2019). Modulation of Mast Cell Reactivity by Lipids: The Neglected Side of Allergic Diseases. *Front. Immunol.* 10, 1174. doi:10.3389/fimmu.2019.01174

Hanes, M. R., Giacomantonio, C. A., and Marshall, J. S. (2021). Mast Cells and Skin and Breast Cancers: A Complicated and Microenvironment-dependent Role. *Cells* 10, 986. doi:10.3390/cells10050986

Hubler, M. J., and Kennedy, A. J. (2016). Role of Lipids in the Metabolism and Activation of Immune Cells. *J. Nutr. Biochem.* 34, 1–7. doi:10.1016/j.jnutbio.2015.11.002

Jain, R., Tikoo, S., and Weninger, W. (2019). Mast Cell Granules: Modulating Adaptive Immune Response Remotely. *J. Allergy Clin. Immunol.* 143, 1731–1733. doi:10.1016/j.jaci.2018.11.029

Knoblach, B., Ishida, R., Hobman, T. C., and Rachubinski, R. A. (2021). Peroxisomes Exhibit Compromised Structure and Matrix Protein Content in SARS-CoV-2-Infected Cells. *MBoC* 32, 1273–1282. doi:10.1091/mbc.E21-02-0074

Komi, D. E. A., and Redegeld, F. A. (2020). Role of Mast Cells in Shaping the Tumor Microenvironment. *Clinic Rev. Allerg Immunol.* 58, 313–325. doi:10.1007/s12016-019-08753-w

Leal-Berumen, I., Conlon, P., and Marshall, J. S. (1994). IL-6 Production by Rat Peritoneal Mast Cells Is Not Necessarily Preceded by Histamine Release and Can Be Induced by Bacterial Lipopolysaccharide. *J. Immunol.* 152, 5468

Lim, H.-K., Choi, Y.-A., Park, W., Lee, T., Ryu, S. H., Kim, S.-Y., et al. (2003). Phosphatidic Acid Regulates Systemic Inflammatory Responses by Modulating the Akt-Mammalian Target of Rapamycin-P70 S6 Kinase 1 Pathway. *J. Biol. Chem.* 278, 45117–45127. doi:10.1074/jbc.M303789200

Liu, J., Lu, W., Shi, B., Klein, S., and Su, X. (2019). Peroxisomal Regulation of Redox Homeostasis and Adipocyte Metabolism. *Redox Biol.* 24, 101167. doi:10.1016/j.redox.2019.101167

Lodhi, I. J., and Semenkovich, C. F. (2014). Peroxisomes: a Nexus for Lipid Metabolism and Cellular Signaling. *Cell Metab.* 19, 380–392. doi:10.1016/j.cmet.2014.01.002

Lodhi, I. J., Wei, X., Yin, L., Feng, C., Adak, S., Abou-Ezzi, G., et al. (2015). Peroxisomal Lipid Synthesis Regulates Inflammation by Sustaining Neutrophil Membrane Phospholipid Composition and Viability. *Cell Metab.* 21, 51–64. doi:10.1016/j.cmet.2014.12.002

Marshall, J. S. (2004). Mast-cell Responses to Pathogens. *Nat. Rev. Immunol.* 4, 787–799. doi:10.1038/nri1460

McCurdy, J. D., Olynych, T. J., Maher, L. H., and Marshall, J. S. (2003). Cutting Edge: Distinct Toll-like Receptor 2 Activators Selectively Induce Different Classes of Mediator Production from Human Mast Cells. *J. Immunol.* 170, 1625–1629. doi:10.4049/jimmunol.170.4.1625

Mendoza, R. P., Anderson, C. C., Fudge, D. H., Roede, J. R., and Brown, J. M. (2021). Metabolic Consequences of IgE- and Non-IgE-mediated Mast Cell Degranulation. *J. Immunol.* 207, 2637–2648.

Merkling, S. H., Riahi, H., Overheul, G. J., Schenck, A., and van Rij, R. P. (2019). Peroxisome-associated Sgroppino Links Fat Metabolism with Survival after RNA Virus Infection in Drosophila. *Sci. Rep.* 9, 2065–2112. doi:10.1038/s41598-019-38559-x

Miao, H., Ou, J., Ma, Y., Guo, F., Yang, Z., Wiggins, M., et al. (2014). Macrophage CGI-58 Deficiency Activates ROS-Inflammasome Pathway to Promote Insulin Resistance in Mice. *Cell Rep.* 7, 223–235. doi:10.1016/j.celrep.2014.02.047

Moon, T. C., Befus, A. D., and Kulka, M. (2014). Mast Cell Mediators: Their Differential Release and the Secretory Pathways Involved. *Front. Immunol.* 5, 569. doi:10.3389/fimmu.2014.00569

Moreno-Fernandez, M. E., Giles, D. A., Stankiewicz, T. E., Sheridan, R., Karns, R., Cappelletti, M., et al. (2018). Peroxisomal β-oxidation Regulates Whole Body Metabolism, Inflammatory Vigor, and Pathogenesis of Nonalcoholic Fatty Liver Disease. *JCI Insight* 3, e93626. doi:10.1172/jci.insight.93626

Nakamura, T., Fonteh, A. N., Hubbard, W. C., Triggiani, M., Inagaki, N., Ishizaka, T., et al. (1991). Arachidonic Acid Metabolism during Antigen and Ionophore Activation of the Mouse Bone Marrow Derived Mast Cell. *Biochim. Biophys. Acta.* 1085, 191–200. doi:10.1016/0005-2760(91)90094-x

Nath, A. S., Parsons, B. D., Makdissi, S., Chilvers, R. L., Mu, Y., Weaver, C. M., et al. (2022). Modulation of the Cell Membrane Lipid Milieu by Peroxisomal β-oxidation Induces Rho1 Signaling to Trigger Inflammatory Responses. *Cell Rep.* 38, 110433. doi:10.1016/j.celrep.2022.110433

O'Neill, L. A. J., Kishton, R. J., and Rathmell, J. (2016). A Guide to Immunometabolism for Immunologists. *Nat. Rev. Immunol.* 16, 553–565. doi:10.1038/nri.2016.70

Oldford, S. A., Haidl, I. D., Howatt, M. A., Leiva, C. A., Johnston, B., and Marshall, J. S. (2010). A Critical Role for Mast Cells and Mast Cell-Derived IL-6 in TLR2-Mediated Inhibition of Tumor Growth. *J. Immunol.* 185, 7067–7076. doi:10.4049/jimmunol.1001137

Papaliodis, D., Boucher, W., Kempuraj, D., Michaelian, M., Wolfberg, A., House, M., et al. (2008). Niacin-induced "Flush" Involves Release of Prostaglandin D2from Mast Cells and Serotonin from Platelets: Evidence from Human Cells *In Vitro* and an Animal Model. *J. Pharmacol. Exp. Ther.* 327, 665–672. doi:10.1124/jpet.108.141333

Puertollano, M. A., Pablo, M. A., and Ã lvarez de Cienfuegos, G. (2001). Immunomodulatory Effects of Dietary Lipids Alter Host Natural Resistance of Mice toListeria Monocytogenesinfection. *FEMS Immunol. Med. Microbiol.* 32, 47–52. doi:10.1111/j.1574-695X.2001.tb00533.x

Sadik, C. D., and Luster, A. D. (2012). Lipid-cytokine-chemokine Cascades Orchestrate Leukocyte Recruitment in Inflammation. *J. Leukoc. Biol.* 91, 207–215. doi:10.1189/jlb.0811402

Schrader, M., and Fahimi, H. D. (2006). Peroxisomes and Oxidative Stress. *Biochim. Biophys. Acta.* 1763, 1755–1766. doi:10.1016/j.bbamcr.2006.09.006

Schrader, M., Kamoshita, M., and Islinger, M. (2020). Organelle Interplay-Peroxisome Interactions in Health and Disease. *J. Inherit. Metab. Dis.* 43, 71–89. doi:10.1002/jimd.12083

Schwartz, L. B., Austen, K. F., and Wasserman, S. I. (1979). Immunologic Release of Beta-Hexosaminidase and Beta-Glucuronidase from Purified Rat Serosal Mast Cells. *J. Immunol.* 123, 1445

Shi, R., Zhang, Y., Shi, Y., Shi, S., and Jiang, L. (2012). Inhibition of Peroxisomal β-oxidation by Thioridazine Increases the Amount of VLCFAs and Aβ Generation in the Rat Brain. *Neurosci. Lett.* 528, 6–10. doi:10.1016/j.neulet.2012.08.086

Singh, I., Paintlia, A. S., Khan, M., Stanislaus, R., Paintlia, M. K., Haq, E., et al. (2004). Impaired Peroxisomal Function in the central Nervous System with Inflammatory Disease of Experimental Autoimmune Encephalomyelitis Animals and protection by Lovastatin Treatment. *Brain Res.* 1022, 1–11. doi:10.1016/j.brainres.2004.06.059

Smith, J. J., and Aitchison, J. D. (2013). Peroxisomes Take Shape. *Nat. Rev. Mol. Cell Biol* 14, 803–817. doi:10.1038/nrm3700

Sychev, Z. E., Hu, A., DiMaio, T. A., Gitter, A., Camp, N. D., Noble, W. S., et al. (2017). Integrated Systems Biology Analysis of KSHV Latent Infection Reveals Viral Induction and reliance on Peroxisome Mediated Lipid Metabolism. *Plos Pathog.* 13, e1006256. doi:10.1371/journal.ppat.1006256

Szilard, R. K., Titorenko, V. I., Veenhuis, M., and Rachubinski, R. A. (1995). Pay32p of the Yeast Yarrowia Lipolytica Is an Intraperoxisomal Component of the Matrix Protein Translocation Machinery. *J. Cell Biol* 131, 1453–1469. doi:10.1083/jcb.131.6.1453

Tertian, G., Yung, Y. P., Guy-Grand, D., and Moore, M. A. (1981). Long-term *In Vitro* Culture of Murine Mast Cells. I Description of a Growth Factor-dependent Culture Technique. *J. Immunol.* 127, 788

Theoharides, T. C., Tsilioni, I., and Ren, H. (2019). Recent Advances in Our Understanding of Mast Cell Activation - or Should it Be Mast Cell Mediator Disorders? *Expert Rev. Clin. Immunol.* 15, 639–656. doi:10.1080/1744666X.2019.1596800

Trompier, D., Vejux, A., Zarrouk, A., Gondcaille, C., Geillon, F., Nury, T., Savary, S., and Lizard, G. (2014). Brain peroxisomes. *Biochimie* 98, 102–110. doi:10.1016/j.biochi.2013.09.009

Tunaru, S., Kero, J., Schaub, A., Wufka, C., Blaukat, A., Pfeffer, K., et al. (2003). PUMA-G and HM_{74} Are Receptors for Nicotinic Acid and Mediate its Anti-lipolytic Effect. *Nat. Med.* 9, 352–355. doi:10.1038/nm824

Van den Branden, C., and Roels, F. (1985). Thioridazine: a Selective Inhibitor of Peroxisomal β-oxidation *In Vivo*. *FEBS Lett.* 187, 331–333. doi:10.1016/0014-5793(85)81270-9

Vijayan, V., Srinu, T., Karnati, S., Garikapati, V., Linke, M., Kamalyan, L., et al. (2017). A New Immunomodulatory Role for Peroxisomes in Macrophages Activated by the TLR4 Ligand Lipopolysaccharide. *J. Immunol.* 198, 2414–2425. doi:10.4049/jimmunol.1601596

Wanders, R. J. A., and Waterham, H. R. (2006). Biochemistry of Mammalian Peroxisomes Revisited. *Annu. Rev. Biochem.* 75, 295–332. doi:10.1146/annurev.biochem.74.082803.133329

Wang, X., and Kulka, M. (2015). n-3 Polyunsaturated Fatty Acids and Mast Cell Activation. *J. Leukoc. Biol.* 97, 859–871. doi:10.1189/jlb.2RU0814-388R

Wernersson, S., and Pejler, G. (2014). Mast Cell Secretory Granules: Armed for Battle. *Nat. Rev. Immunol.* 14, 478–494. doi:10.1038/nri3690

Xu, Z., Asahchop, E. L., Branton, W. G., Gelman, B. B., Power, C., and Hobman, T. C. (2017). MicroRNAs Upregulated during HIV Infection Target Peroxisome Biogenesis Factors: Implications for Virus Biology, Disease Mechanisms and Neuropathology. *Plos Pathog.* 13, e1006360. doi:10.1371/journal.ppat.1006360

Conflict of Interest: The authors declare that the research was conducted in the absence of any commercial or financial relationships that could be construed as a potential conflict of interest.

Publisher's Note: All claims expressed in this article are solely those of the authors and do not necessarily represent those of their affiliated organizations, or those of the publisher, the editors and the reviewers. Any product that may be evaluated in this article, or claim that may be made by its manufacturer, is not guaranteed or endorsed by the publisher.

frontiers | Frontiers in Cell and Developmental Biology

TYPE Hypothesis and Theory
PUBLISHED 12 September 2022
DOI 10.3389/fcell.2022.979269

OPEN ACCESS

EDITED BY
Marek Skoneczny,
Institute of Biochemistry and Biophysics (PAN), Poland

REVIEWED BY
Richard Rachubinski,
University of Alberta, Canada
Antonio Uttaro,
CONICET Instituto de Biología Molecular y Celular de Rosario (IBR), Argentina
Marc Fransen,
KU Leuven, Belgium

*CORRESPONDENCE
Paul A. M. Michels,
paul.michels@ed.ac.uk

†PRESENT ADDRESS
Alejandro D. Bonive-Boscan,
Max Planck Institute for Evolutionary Biology, Plön, Germany

SPECIALTY SECTION
This article was submitted to Membrane Traffic,
a section of the journal
Frontiers in Cell and Developmental Biology

RECEIVED 27 June 2022
ACCEPTED 17 August 2022
PUBLISHED 12 September 2022

CITATION
Andrade-Alviárez D, Bonive-Boscan AD, Cáceres AJ, Quiñones W, Gualdrón-López M, Ginger ML and Michels PAM (2022), Delineating transitions during the evolution of specialised peroxisomes: Glycosome formation in kinetoplastid and diplonemid protists.
Front. Cell Dev. Biol. 10:979269.
doi: 10.3389/fcell.2022.979269

Delineating transitions during the evolution of specialised peroxisomes: Glycosome formation in kinetoplastid and diplonemid protists

Diego Andrade-Alviárez[1], Alejandro D. Bonive-Boscan[1†], Ana J. Cáceres[1], Wilfredo Quiñones[1], Melisa Gualdrón-López[2], Michael L. Ginger[3] and Paul A. M. Michels[4]*

[1]Laboratorio de Enzimología de Parásitos, Departamento de Biología, Facultad de Ciencias, Universidad de Los Andes, Mérida, Venezuela, [2]School of Public Health, University of Alberta, Edmonton, AB, Canada, [3]School of Applied Sciences, University of Huddersfield, Huddersfield, United Kingdom, [4]Centre for Immunity, Infection and Evolution and Centre for Translational and Chemical Biology, School of Biological Sciences, The University of Edinburgh, Edinburgh, United Kingdom

One peculiarity of protists belonging to classes Kinetoplastea and Diplonemea within the phylum Euglenozoa is compartmentalisation of most glycolytic enzymes within peroxisomes that are hence called glycosomes. This pathway is not sequestered in peroxisomes of the third Euglenozoan class, Euglenida. Previous analysis of well-studied kinetoplastids, the 'TriTryps' parasites *Trypanosoma brucei*, *Trypanosoma cruzi* and *Leishmania* spp., identified within glycosomes other metabolic processes usually not present in peroxisomes. In addition, trypanosomatid peroxins, *i.e.* proteins involved in biogenesis of these organelles, are divergent from human and yeast orthologues. In recent years, genomes, transcriptomes and proteomes for a variety of euglenozoans have become available. Here, we track the possible evolution of glycosomes by querying these databases, as well as the genome *of Naegleria gruberi*, a non-euglenozoan, which belongs to the same protist supergroup Discoba. We searched for orthologues of TriTryps proteins involved in glycosomal metabolism and biogenesis. Predicted cellular location(s) of each metabolic enzyme identified was inferred from presence or absence of peroxisomal-targeting signals. Combined with a survey of relevant literature, we refine extensively our previously postulated hypothesis about glycosome evolution. The data agree glycolysis was compartmentalised in a common ancestor of the kinetoplastids and diplonemids, yet additionally indicates most other processes found in glycosomes of extant trypanosomatids, but not in peroxisomes of other eukaryotes were either sequestered in this ancestor or shortly after separation of the two lineages. In contrast, peroxin divergence is evident in all euglenozoans. Following their gain of pathway complexity, subsequent evolution of peroxisome/glycosome function is complex. We hypothesize compartmentalisation in glycosomes of glycolytic enzymes, their cofactors and subsequently other metabolic enzymes provided selective advantage to kinetoplastids and diplonemids during their

evolution in changing marine environments. We contend two specific properties derived from the ancestral peroxisomes were key: existence of nonselective pores for small solutes and the possibility of high turnover by pexophagy. Critically, such pores and pexophagy are characterised in extant trypanosomatids. Increasing amenability of free-living kinetoplastids and recently isolated diplonemids to experimental study means our hypothesis and interpretation of bioinformatic data are suited to experimental interrogation.

KEYWORDS

Euglenozoa, peroxisome, phylogenomics, metabolic compartmentalisation, biogenesis, pexophagy, glycosome, glycolysis

Introduction

Glycosomes are peroxisomes that compartmentalise glycolytic enzymes. These organelles were initially detected in the African sleeping sickness parasite *Trypanosoma brucei* as single-membrane bounded microbodies containing glycolytic enzymes, hence called glycosomes (Opperdoes and Borst, 1977). Glycosomes were subsequently observed in other members of the parasitic taxonomic order Trypanosomatida, class Kinetoplastea, including *Trypanosoma cruzi* and *Leishmania* spp, and then found in bodonid representatives of the Kinetoplastea (Figure 1) (Taylor et al., 1980; Hart and Opperdoes, 1984; Opperdoes et al., 1988; Ardelli et al., 2000). The range of enzymes detected in glycosomes also broadened; notably, from the perspective of carbohydrate metabolism key enzymes of gluconeogenesis, phosphoenolpyruvate carboxykinase (PEPCK) and fructose-1,6-bisphosphatase (FBPase), were found to be glycosomal (Parsons and Smith, 1989; Hannaert et al., 2003a).

Trypanosomatid protists are relatively well known as some species are aetiological agents of serious neglected tropical diseases in people, veterinary diseases, or are plant pathogens (Jaskowska et al., 2015; Giordani et al., 2016; Field et al., 2017). With rare exception, these parasites are transmitted between

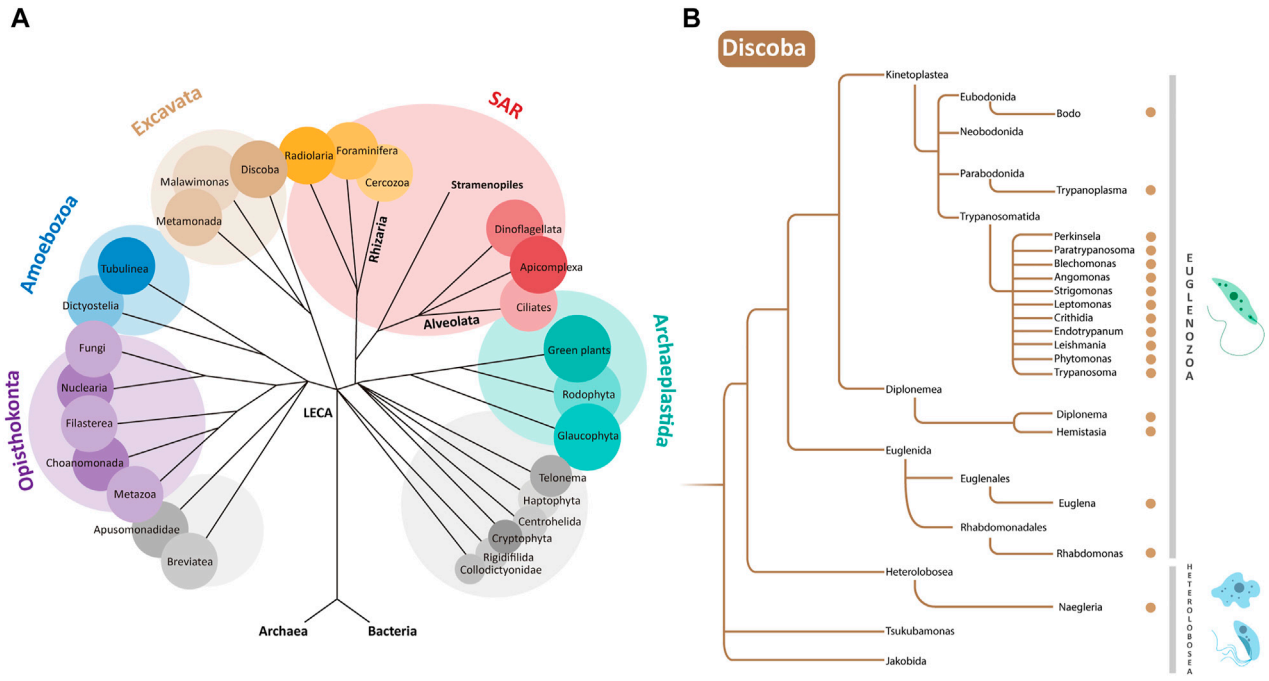

FIGURE 1
(A) Phylogenetic relationships of eukaryotes. LECA is the "Last Eukaryotic Common Ancestor" from which different supergroups evolved. Euglenozoa are a phylum within the supergroup Discoba belonging to the Excavata (Adl et al., 2019). **(B)** Zoom of a simplified representation of the Discoba clade. Genera containing organisms discussed in this paper are indicated by brown dots. Examples of organisms from the Euglenozoa and Heterolobosea phyla are depicted at the right.

hosts by an insect vector. Indeed, the vast majority of trypanosomatids are simply monoxenous parasites of insects. Yet, irrespective of whether trypanosomatids are monoxenous or dixenous in lifestyle, their life cycles are invariably complex requiring differentiation through different morphological forms, and often adaptation of their metabolic network to different nutritional conditions (*e.g.* Wheeler et al., 2013; Atwood et al., 2005; Urbaniak et al., 2012). Such adaptation includes enzyme content of the glycosomes, with important changes in the expression of glycolytic enzymes. *T. brucei* provides a prime example. Here, parasites residing in the mammalian bloodstream require glycolysis for ATP generation and glycolytic enzymes comprise 90–95% of the glycosomal protein content. In contrast, in the digestive tract of the tsetse fly vector sugar availability is typically low and pathways other than glycolysis are preferred for ATP production (Michels et al., 2021); although glycosomes are now used for gluconeogenesis (Wargnies et al., 2018), levels of glycosomal glycolytic enzymes are 40–50% that of bloodstream trypanosomes (Hart et al., 1984; Misset et al., 1986).

Enzymes from other ubiquitous metabolic systems that are generally not present or found rarely in peroxisomes of mammals, plants, or yeasts have also been fully or partially localised to trypanosomatid glycosomes. The diverse list includes some enzymes of pyrimidine synthesis, purine salvage and squalene biosynthesis, many of the enzymes participating in nucleotide-sugar biosynthesis, some additional enzymes of carbohydrate metabolism such as those involved in the pentose-phosphate pathway (PPP), succinic fermentation and gluconeogenesis (Haanstra et al., 2016; Allmann and Bringaud, 2017; Quiñones et al., 2020; Michels et al., 2021). Initially, these enzymes were reported as glycosomal based on cell fractionation and enzyme assays in one or several different trypanosomatids (e.g., Hammond et al., 1981; Hammond and Gutteridge, 1982; Concepción et al., 1998; Heise and Opperdoes, 1999; Hannaert et al., 2003a; Coustou et al., 2006; Sampaio Guther et al., 2021). Latterly, these reports were confirmed or extended by mass spectrometry-based proteomics studies (Colascante et al., 2006; Vertommen et al., 2008; Colasante et al., 2013; Güther et al., 2014; Acosta et al., 2019).

Despite presence of a single boundary membrane, high protein content and no nucleic acids, unusual enzyme content coupled to an absence of catalase led initially to scepticism about assignment of glycosomes to the peroxisome family. However, indication of the evolutionary relationship of glycosomes with peroxisomes came first from detection of 'classic' peroxisome enzymes, such as those involved in ether-lipid biosynthesis (Opperdoes, 1984) or fatty-acid β-oxidation (Hart and Opperdoes, 1984; Wiemer et al., 1996), in trypanosome glycosomes. Subsequently, identification of protein targeting to glycosomes using typical peroxisomal-targeting signals (PTS) – a C-terminal tripeptide (PTS1) or a nonapeptide near the N-terminus (PTS2) – and the requirement of peroxin proteins for organelle biogenesis showed unequivocally that glycosomes are specialized peroxisomes, unique for their sequestration of many enzymes required for glycolysis or the extended metabolism of glycolytic intermediates (reviewed in Gualdrón-López et al., 2012a; Gabaldón et al., 2016). Quite why and how a kinetoplastid ancestor remodelled peroxisome function so dramatically remain open questions in evolutionary biology. Here, we address these questions through analysis of recently available genomes and transcriptomes from across the Euglenozoa, the phylum to which kinetoplastids belong, and survey of the wider literature. From the data, we provide a fresh view of the cumulative gain of glycosomal metabolic complexity during euglenozoan evolution and offer an original posit that divergence evident in trypanosomatid peroxins occurred early during euglenozoan evolution.

Identification of candidate glycosomal proteins in Euglenozoa

The classes Kinetoplastea, Diplonemea, and Euglenida provide the three major lineages of the Euglenozoa (Kostygov et al., 2021). There is also an enigmatic fourth lineage, Symbiontida (Yubuki and Leander, 2018) but in the absence of genome or transcriptome data, these little-studied euglenozoans are not considered further here. Instead, to trace the origin of glycosomes from peroxisomes and their subsequent evolution within **Euglenozoa**, taxa were selected as listed below. From **Kinetoplastea**: *Trypanosoma brucei, Trypanosoma vivax, Trypanosoma cruzi, Leishmania major, Endotrypanum monterogeii* (all dixenous–*i.e.*, having two hosts–parasites of mammals, transmitted by insect vectors), *Leishmania tarentolae* (a reptile parasite), *Crithidia fasciculata, Blechomonas ayalai, Leptomonas pyrrhocoris, Leptomonas seymouri, Paratrypanosoma confusum, Angomonas deanei, Strigomonas culicis* (all monoxenous insect parasites), *Phytomonas* (a dixenous plant parasite), *Perkinsela* sp. (an endosymbiont of the amoeba *Paramoeba*), *Trypanoplasma borreli* (a fish parasite) and *Bodo saltans* (a free-living flagellate). From **Diplonemea**: *Diplonema papillatum*[1], *Diplonema japonicum, Diplonema ambulator, and Hemistasia phaeocysticola* (all free-living organisms). From **Euglenida**: *Euglena gracilis, Euglena longa* and *Rhabdomonas costata* (all free-living organisms).

Euglenozoa belong to the protist supergroup **Discoba** (Adl et al., 2019; Burki et al., 2020), which also contains the phylum **Heterolobosea.** For use as a not-distant outgroup in our analysis,

1 Note: Diplonemid diversity has only begun to be truly recognised during the last 12–15 years. Consequently, taxonomic reassignment should see reclassification of *Diplonema papillatum* to *Paradiplonema papillatum*, separate from other species in the genus *Diplonema* (Tahyreva et al., 2022). Here, we use nomenclature still in use.

we selected from Heterolobosea species of *Naegleria* known to contain peroxisomes (González-Robles et al., 2020): *N. gruberi* (a free-living soil and freshwater amoeboflagellate), *N. fowleri* (a free-living, but deadly opportunistic pathogen) and *N. lovaniensis* (a free-living thermophile). Phylogenetic relationships between all organisms listed are summarised in Figure 1B.

In searches, amino-acid sequences of known glycosomal proteins from different organisms provided queries to retrieve orthologues and paralogues from the following databases: TriTrypDB (https://tritrypdb.org/tritrypdb/app), AmoebaDB (https://amoebadb.org/amoeba/app), OrthoMCL DB (https://orthomcl.org/orthomcl/app), NCBI (National Center for Biotechnology Information, https://www.ncbi.nlm.nih.gov/) and DiscobaDB (https://zenodo.org/record/5563074) (Wheeler, 2021). Query sequences were adopted on a basis of glycosomal localisation from proteomic and genomic studies (Colasante et al., 2006, 2013; Güther et al., 2014; Morales et al., 2016; Acosta et al., 2019; Durrani et al., 2020; González-Robles et al., 2020; Quiñones et al., 2020; Jansen et al., 2021; Wheeler, 2021; Škodová-Sveráková et al., 2021) or the many biochemical and cell biological studies published previously. Sequence screening in DiscobaDB (Wheeler, 2021) was done using Geneious Prime® 2022.0.1 and BLASTp with default parameters. OrthoMCL DB was used to verify the number of orthologues or target genes during data collection in TriTrypDB and AmoebaDB.

Amino-acid sequences retrieved were analysed considering specific criteria: the presence of PTS2 and/or PTS1 motifs, and possible experimental evidence of their localisation in glycosomes or peroxisomes. PTS signatures were identified using the ScanProsite Tool (https://prosite.expasy.org/scanprosite/; option 3: "Submit PROTEIN sequences and MOTIFS to scan them against each other") with the following motifs for **PTS1** (**A**) [ASCGPNYTV]-[KNRHQDS]-[LMVAIF]> (Acosta et al., 2019) (**B**) [STAGCN]-[RKH]-[LIVMAFY]> (**C**) S-S-[LIF]> (Opperdoes and Skizora, 2006) (**D**) [ACGHNPT]-[HMNQRS]-[IMY]> (Sommer et al., 1992); and for **PTS2** (**E**) [RKHQ]-[VLIWFY]-X (5)-[HKQR]-[ILVYAF] (Acosta et al., 2019) (**F**) <M-X(0,20)-[RK]-[LVI]-X(5)-[HQ]-[ILAF] (Opperdoes and Skizora, 2006) (**G**) R-[LVIQ]-X(2)-[LVIH]-[LSGA]-X-[HQ]-[LA] (**H**) [RK]-[LVIQ]-X(2)-[LVIHQ]-[LSGAK]-X-[HQ]-[LAF] (Petriv et al., 2004) and (**I**) R-[LI]-X(2)-[LI]-X (2)-[HQ]-L (Kunze, 2020). This analysis was applied for all orthologues or paralogues of metabolic enzymes considered to be possibly present inside glycosomes/peroxisomes, except for candidate biogenesis proteins (peroxins). For the latter, the screening for specific domains was applied using the web server HMMER (https://www.ebi.ac.uk/Tools/hmmer/search/phmmer) and InterProScan (https://www.ebi.ac.uk/interpro/result/InterProScan/). Peroxin sequence alignments were made using MAFFT (https://www.ebi.ac.uk/Tools/msa/mafft/) and MUSCLE (https://www.ebi.ac.uk/Tools/msa/muscle/) and visualized in BioEdit Sequence Alignment Editor, v7.2.5.

Under what condition(s) did glycosomes originate?

Long-standing questions about glycosomes are when, in an ancestral organism, peroxisomes acquired novel functions to become glycosomes; when did they lose some typical peroxisomal functions such as part of the H_2O_2-dependent metabolism; how did it happen and what could have been the selective advantage(s) (Borst, 1986; Opperdoes, 1987; Borst, 1989; Michels and Opperdoes, 1991; Michels and Hannaert, 1994; Hannaert et al., 2003b; Gualdrón-López et al., 2012a; Gabaldón et al., 2016)? A possible evolutionary scenario was described in Gualdrón-López et al. (2012a). However, this scenario was based on limited knowledge then available: the analysis of the 'TriTryp' (*T. brucei*, *T. cruzi* and *L. major*) genomes (El-Sayed et al., 2005); from the biochemical characterisation of glycosomes from several trypanosomatids and the parasitic bodonid *T. borreli* (Opperdoes et al., 1988); and discovery of a PTS2 motif in the glycolytic enzyme aldolase from the diplonemid *D. papillatum* coupled to its localisation in cell compartments reminiscent of glycosomes (Makuichi et al., 2011). The presence of glycosomes was subsequently confirmed in *D. papillatum* (Morales et al., 2016), indicating glycosome origin predated divergence of a last common kinetoplastid ancestor. However, biochemical analyses of carbohydrate metabolism suggests *D. papillatum* glycosomes principally function in the direction of gluconeogenesis, rather than glycolysis (Morales et al., 2016; Škodová-Sveráková et al., 2021). In *D. papillatum*, a marine flagellate, amino acids are considered to provide the predominant carbon source for central energy metabolism. Detection of organellar FBPase activity but no phosphofructokinase (PFK) supported an idea that ancestrally gluconeogenesis provided a selective driver for glycosome evolution (Morales et al., 2016). From transcriptome data it is now known that *D. papillatum* expresses a PFK that has homology to pyrophosphate (PPi)-dependent PFKs from other organisms and contains a PTS1 motif (Škodová-Sveráková et al., 2021).

Critically, realisation that the appearance of glycosomes predates a last common ancestor of diplonemids and kinetoplastids argues we need to look widely across the Euglenozoa for when the metabolic functionality of their peroxisomes began to diversify. *Euglena gracilis*, in which peroxisomes lack glycolytic enzyme activities (Opperdoes et al., 1988) provides a poor proxy for understanding peroxisome diversity among euglenids. There are ~1,000 euglenid species known and photosynthetic euglenids represent only one subclade within the group (Lax et al., 2021). Most euglenids are free-living heterotrophic phagotrophs; some are non-photosynthetic osmotrophs. With availability of a *R. costata* genome sequence it becomes possible to begin to look more widely among euglenids at peroxisome diversity.

Euglenids, diplonemids, and kinetoplastids are all cosmopolitan with respect to their geographic distributions. Euglenids and free-living kinetoplastids are ubiquitous in moist soils and species from all three lineages are readily found in both freshwater and marine environments. Indeed, ribosomal DNA sequencing of planktonic samples recently and unexpectedly revealed Diplonemea as an extremely diverse, abundant class of flagellates throughout temperate and tropical oceans. They appear particularly abundant in the nutrient-poor, colder mesopelagic zone of the oceans (*i.e.*, approximately 200 – 1,000 m below the ocean surface) and are also present at abyssal and hadal depths. Kinetoplastids are also found in a similarly diverse array of oceanic niches (Salani et al., 2012; Flegontova et al., 2020; Kostygov et al., 2021; Schoenle et al., 2021).

If it was in a common ancestor of Diplonemea and Kinetoplastea in which glycolysis became uniquely compartmentalised within peroxisomes, then it is reasonable to estimate that this ancestor lived >600 million years ago, most likely in the oceans, at a point in Earth's history when only the uppermost regions of the oceans were considered oxygenated (Holland, 2006; Mills et al., 2022). Diplonemid life cycles turn to be surprisingly complex (Tahyreva et al., 2022). Environmental change is likely a cue for cellular differentiation, as it is in many microbial eukaryotes. Most spectacularly in methylotrophic yeasts a shift in nutrient availability is the cue for metabolic reprogramming that triggers biogenesis of peroxisomes with their own atypical metabolic profile, while redundant ones are turned over en mass through a specific form of autophagy called pexophagy (reviewed in (Manjithaya et al., 2010; Yoshimoto et al., 2010) and discussed in (Hannaert et al., 2003b; Michels et al., 2005; Gualdrón-López et al., 2012a)). Pexophagy occurs in trypanosomatids (Herman et al., 2008; Cull et al., 2014); we contend any hypothesis about the origin of glycosomes should be compatible with the conserved phenomenon of pexophagy. Thus, the wide variety of environments in which extant euglenozoans are found, with inherent variation of nutrient or oxygen availability evident, coupled to complex life cycles, suggests an euglenozoan ancestor would also have lived amid dynamic environmental conditions that could have favoured development of atypical peroxisomes or glycosomes. In response to specific cues, evolution of such atypical peroxisomes might also have been favoured by their ability to be subject to rapid, efficient turnover. Taking note of the availability of numerous euglenozoan genomes and transcriptomes, we have used bioinformatics to attempt to chronologise how the metabolic complexity seen in extant trypanosomatid glycosomes arose.

Bioinformatic chronology of glycosomal metabolism I: Carbohydrate and energy metabolism

The hallmark feature of glycosomes is the presence of most enzymes of the glycolytic pathway in its matrix. In addition, these organelles may contain other enzymes of carbohydrate metabolism, such as those in gluconeogenesis, the PPP as well as in glycerol metabolism. Figure 2 summarizes the glycosomal carbon metabolic network that is representative of most trypanosomatids studied experimentally to date. Most of the enzymes involved contain a consensus PTS. We find this situation is largely conserved in all kinetoplastids and diplonemids analysed (Supplementary Table S1), but not in euglenids or *Naegleria* spp., although the latter possess respectively one or two glycolytic isoenzymes with a predicted PTS. The PTS sequences of kinetoplastid and diplonemid enzymes may differ between orthologues, and in some species no typical PTS can be detected in an orthologue, suggesting that glycosomal targeting is then achieved differently, although an extraglycosomal localisation cannot be excluded. Overall, the data indicate glycolysis from hexokinase (HK) to phosphoglycerate kinase (PGK) must have been compartmentalised in a common ancestor of kinetoplastids and diplonemids and has been retained thereafter.

We note several other interesting evolutionary aspects about glycosomal glycolytic enzymes. First, most kinetoplastids and diplonemids contain both a glycosomal HK with a PTS2 and a glucokinase (GlcK) with a PTS1. However, in some trypanosomatid species and the bodonids a HK without PTS was detected (although in the case of *B. saltans* this could be due to an incomplete sequence (Opperdoes et al., 2016)), while the GlcK has been lost from African trypanosomes (Cáceres et al., 2007). In all species analysed, at least one of the two hexose-phosphorylating enzymes with a PTS is present. HK and GlcK have different anomer preferences: HK for α-glucose, GlcK for the β anomer (Cordeiro et al., 2007). Since enzymes using the product glucose 6-phosphate as substrate, glucose-6-phosphate isomerase in glycolysis and glucose-6-phosphate dehydrogenase in the PPP, have a specificity for the β anomer, a glucose-6-phosphate 1-epimerase is required for interconversion of the anomers. This enzyme with a PTS1 is detected in the databases for all kinetoplastids analysed except *P. confusum*, but not in those of diplonemids and euglenids. Interestingly, it is also found with a PTS1 in *Naegleria* species. Glycosomes of an ancestral kinetoplastid probably acquired the enzyme shortly after divergence from diplonemids, whereas compartmentalisation in peroxisomes of *Naegleria* may have been an independent event. Second, trypanosomatids may contain different isoenzymes for PGK, in glycosomes and the cytosol caused by gene duplications (Rojas-Pirela et al., 2020). Previously we identified a PGK with an N-terminally fused PAS domain associated with *T. cruzi* glycosomes (Rojas-Pirela et al., 2018). PAS domains are involved in signalling, acting as sensors binding small molecules or proteins, but the function of such domain linked to an active PGK is unknown. This PAS-PGK appears to be present in all kinetoplastids, except African trypanosomes that have lost it, and seems to have arisen shortly after the divergence of kinetoplastids and

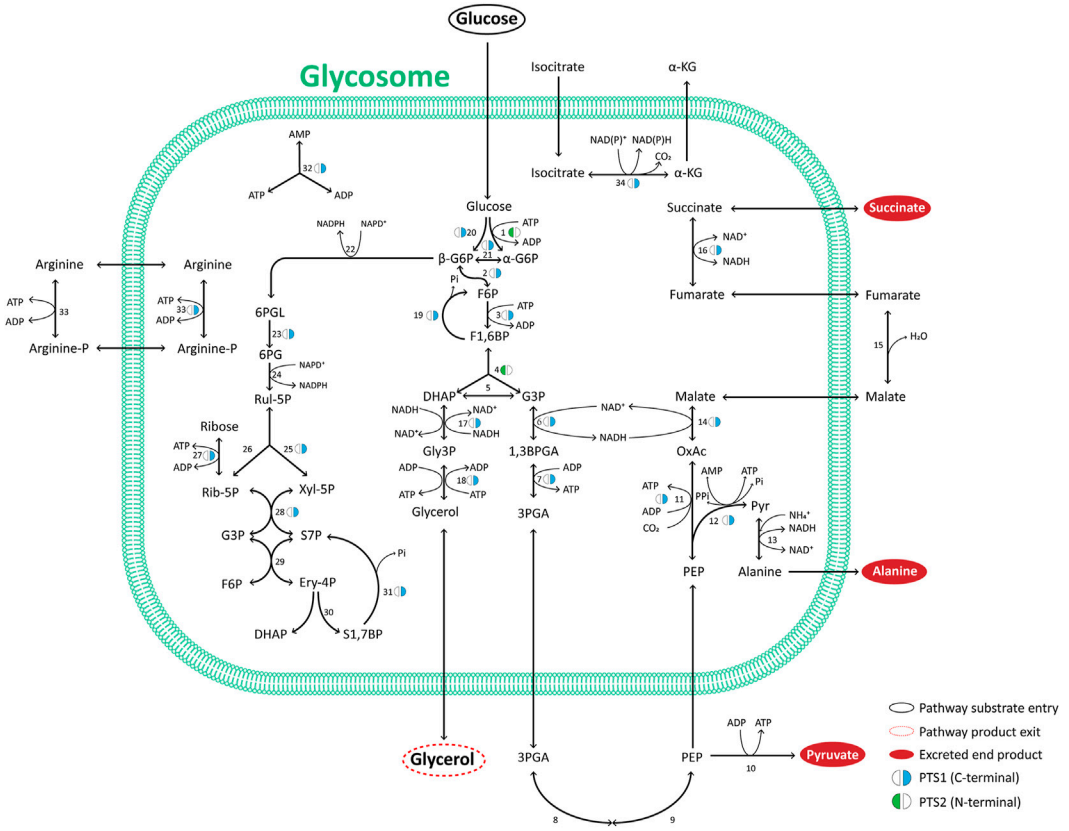

FIGURE 2
Major pathways of glycosomal carbon metabolism in TriTryps species. Indicated are enzymes of glycolysis, its auxiliary branches, gluconeogenesis, glycerol metabolism and the pentose-phosphate pathway. Note that not all enzymes indicated are present in each of the TriTryps species or expressed in each of their life-cycle stages. Enzymes: **1**. Hexokinase; **2**. Glucose-6-phosphate isomerase; **3**. Phosphofructokinase; **4**. Aldolase; **5**. Triose-phosphate isomerase; **6**. Glyceraldehyde-3-phosphate dehydrogenase; **7**. Phosphoglycerate kinase; **8**. Phosphoglycerate mutase; **9**. Enolase; **10**. Pyruvate kinase; **11**. Phosphoenolpyruvate carboxykinase; **12**. Pyruvate phosphate dikinase; **13**. Alanine dehydrogenase; **14**. Malate dehydrogenase; **15**. Fumarate hydratase; **16**. NADH-dependent fumarate reductase; **17**. Glycerol-3-phosphate dehydrogenase; **18**. Glycerol kinase; **19**. Fructose-1,6-bisphosphatase; **20**. Glucokinase; **21**. D-Hexose-6-Phosphate-1-epimerase; **22**. Glucose-6-phosphate dehydrogenase; **23**. 6-Phosphogluconolactonase; **24**; 6-Phosphogluconate dehydrogenase; **25**. Ribulose-5-phosphate epimerase; **26**. Ribulose-5-phosphate isomerase; **27**. Ribokinase; **28**. Transketolase; **29**. Transaldolase; **30.** Sedoheptulose-1,7-phosphate transaldolase; **31**. Sedoheptulose-1,7-bisphosphatase; **32**. Adenylate kinase; **33**. Arginine kinase; **34**. Isocitrate dehydrogenase. The presence of a PTS1 or 2, the carbon sources used, and the excreted end products are indicated.

diplonemids. Third, PFK has undergone a peculiar evolution that we consider separately.

Like glycolytic enzymes, a glycosomal gluconeogenic FBPase appears likely in all kinetoplastids and diplonemids as inferred from the presence of a PTS1. The same is true for two enzymes of glycerol metabolism, glycerol kinase and glycerol-3-phosphate dehydrogenase, although the latter was not detected with a PTS in bodonid databases. These enzymes are functionally closely linked with both glycolysis and gluconeogenesis. Furthermore, in the TriTryps, phosphoenolpyruvate produced in glycolysis can be further metabolised in three ways: to pyruvate by either cytosolic pyruvate kinase or glycosomal pyruvate phosphate dikinase (PPDK), or to succinate via the so-called succinic branch comprising glycosomal PEPCK, malate dehydrogenase (MDH) and fumarate reductase (FRD). The fumarate hydratase (FH) of the TriTryps is located in the cytosol, implying a cytosolic loop in the glycosomal succinic branch (Figure 2). Whereas a PTS1 is present in the PPDK in all kinetoplastids and diplonemids analysed, the situation seems more complex for the enzymes of the succinic branch. PEPCK with a PTS1 is present in most representatives of the kinetoplastids, but not diplonemids. MDH with a PTS1 is present only in trypanosomatids, not bodonids and diplonemids, and FRD with a PTS1 is detected in all. It suggests fumarate reduction inside glycosomes is important for kinetoplastids and diplonemids and may already have been rerouted in their common ancestor. But unless current information in the databases is incomplete or alternative targeting signals are present in orthologues, the cytosolic fumarase loop is expanded with one or two neighbouring enzymes in different species. We anticipate the carbon

metabolism network would not be substantially affected by rerouting these enzymes because of the existence of pores in membranes of peroxisomes, including glycosomes, considered to allow passage of solutes (inorganic ions and metabolites) with a molecular mass up to approximately 400 Da (Antonenkov and Hiltunen, 2012; Gualdrón-López et al., 2012b; Quiñones et al., 2020; Chornyi et al., 2021; Michels and Gualdrón-López, 2022. The permissiveness of solute passage through peroxisomal membranes is a second key criterion with which any hypothesis about the origin of glycosomes should be compatible. Since the enzymes of the succinic branch use ATP, ADP and NAD(H) as cofactors, which will not pass through the pores, the selective force for their re-routing may be sought in the specific manner by which the different species maintain their intraglycosomal ATP/ADP and redox homeostasis.

The PPP and several of its enzymes have been studied in detail in the TriTryps species (reviewed by Kovářová and Barrett, 2016). It has a dual localisation, with the largest fraction of each enzyme in the cytosol and a smaller part in the glycosomes. Moreover, the size of the glycosomal fraction can differ considerably between the enzymes. Activities and the extent of compartmentalisation of the enzymes vary also with environmental conditions and during the life cycle of the parasites. However, only some of the many PPP enzymes possess a PTS. Transketolase contains a PTS1 in almost all trypanosomatid sequences analysed, but not in those of the bodonids and diplonemids. Regarding 6-phosphogluconolactonase, only the *T. brucei*, *B. saltans* and *D. papillatum* enzymes have a detectable PTS1, while for ribokinase potential PTS1 motifs were detected only in the enzymes from *T. cruzi*, *T. borreli* and *D. japonicum*. Previously, a ribulose-5-phosphate epimerase (RPE) isoenzyme with a PTS1 was detected in *T. cruzi* glycosomes (Gonzalez et al., 2017) and a gene coding for a RPE with a PTS1 found in *D. papillatum* (Škodová-Sveráková et al., 2021). We identified PTS1-containing sequences also in the databases of several other trypanosomatids and *B. saltans*. Together, the data suggest the PPP must have acquired its dual localization early in the evolution of the kinetoplastids/diplonemids, but details of the evolutionary scenario are difficult to trace due to the paucity of consensus glycosomal targeting motifs among PPP enzymes. Major roles of the glycosomal PPP may be to provide NADPH within the organelles for anabolic processes and oxidative defence.

In *T. brucei*, a gene encoding a sedoheptulose-1,7-bisphosphatase (SBPase) with a PTS1 was detected previously (Hannaert et al., 2003a). SBPase is classically an enzyme of the Calvin cycle, not present in trypanosomes, but it has been hypothesised that the enzyme could function in a non-conventional form of the non-oxidative branch of the parasite's PPP (Hannaert et al., 2003b). It is currently not known if trypanosome SBPase has a dual localisation similar to the PPP enzymes. Our bioinformatics analysis did not identify a SBPase in diplonemids or kinetoplastids, aside from different *Trypanosoma* species, *P. confusum* and *B. saltans*. When present, it always possesses a PTS1. Phototrophic *E. gracilis* contains a SBPase for the Calvin cycle in its plastid; its two 75% identical subunits are encoded as biprotein precursor that must have originated from a gene duplication. The protein is very different from that found in kinetoplastids (Teich et al., 2007). No orthologue of the kinetoplastid SBPase was detected in *N. gruberi* (Opperdoes et al., 2011). These results suggest kinetoplastids gained SBPase through lateral gene transfer.

Isocitrate dehydrogenase (IDH) with a PTS1 has been detected in *T. brucei* and *T. cruzi*. The enzyme could possibly function as an extra mechanism for providing intraglycosomal NAD(P)H. Euglenozoans, like other eukaryotes, possess multiple IDH isoenzymes but in this protist group the gene family has gone through a puzzling evolution. As with euglenozoan PFK, we consider IDH evolution in a subsequent section.

Nucleotide-sugar biosynthesis has been identified as a glycosomal process in the TriTryps. In *T. brucei*, glucose is converted into five essential nucleotide sugars, required for the synthesis of glycoconjugates: UDP-Glc, UDP-Gal, UDP-GlcNAc, GDP-man and GDP-Fuc by 13 enzymes, most of them present in glycosomes, five of them having a predicted PTS (Sampaio-Guther et al., 2021). The process occurs also within glycosomes of *T. cruzi* and *Leishmania* spp., as inferred from the presence of PTS motifs in several of its enzymes (Sampaio-Guther et al., 2021) (Supplementary Figure S1 and Supplementary Table S1). In these latter parasites, galactose can also serve as substrate for the synthesis of nucleotide sugars, because of the presence in their glycosomes of both a galactokinase (phosphorylating the sugar at its C1 position) and an UDP-pyrophosphatase; these enzymes are absent from *T. brucei* (Lobo-Rojas et al., 2016; Michels et al., 2021). Orthologues of several enzymes of nucleotide-sugar biosynthetic enzymes with a PTS can be detected in each trypanosomatid, bodonid and diplonemid analysed, but not in euglenids or *Naegleria* spp. The process was thus probably compartmentalised already in the common ancestor, simultaneously with or shortly after the routing of glycolytic/gluconeogenic enzymes to the organelles. No galactokinase orthologue was found in diplonemids, suggesting that the possibility to use this sugar was only acquired by kinetoplastids. Yet, absence of this kinase from African trypanosomes, plus the fact it was not found in the databases of some other kinetoplastids–*P. confusum* and *B. ayalai*–suggests either acquisition or loss on multiple occasions.

Euglenozoan PFKs–surprisingly complex evolutionary histories

The evolution of PFK in Euglenozoa is intriguing. Homology exists between the majority of PFKs in nature, but eight different clades can be distinguished, some comprising mainly enzymes that use ATP as phospho donor, while in other groups most PFKs

FIGURE 3
Relationships between phosphofructokinase (PFK) sequences. The evolutionary history of PFK sequences was inferred by from their amino-acid sequences by using the Maximum Likelihood method and JTT matrix-based model (Jones et al., 1992). For each enzyme analysed, a bootstrap consensus tree inferred from 500 replicates (Felsenstein, 1985) (*Continued*)

act with PPi (Mertens et al., 1998; Bapteste et al., 2003). Previously, the enzyme in *T. brucei* and the other TriTryps was phylogenetically shown to belong to a group consisting predominantly of PPi-PFKs, although it is catalytically strictly dependent on ATP. During its evolution, the enzyme must have undergone mutations that changed its phospho-donor specificity (Michels et al., 1997; McNae et al., 2009). Such changes have also been reported for other lineages of microorganisms (Bapteste et al., 2003). This can occur easily, as was experimentally demonstrated; substitution of only two specific active-site residues of the *Entamoeba histolytica* PPi-PFK were sufficient to change a 10^6-fold preference for PPi over ATP (calculated as the ratio of k_{cat}/K_m) into a 10^2-fold preference for ATP (Chi and Kemp, 2000). An essential difference between ATP and PPi catalysed PFK reactions is that the former is virtually irreversible under physiological conditions, whereas the latter readily carries out both forward and reverse reactions, and thus can also replace the FBPase in the gluconeogenic pathway. In glycosomes, where under certain conditions a low ATP/ADP ratio can occur independently of the ratio in the cytosol, it may be possible to also reverse the ATP-PFK reaction (Fernandes et al., 2019; Michels et al., 2021).

Each TriTryp PFK contains a PTS1 and is found in glycosomes. Our bioinformatic analysis revealed homologous PFKs with a PTS1 can be detected in all other kinetoplastids analysed, except in *Leptomonas* species where the enzyme does not contain a consensus PTS motif (Supplementary Table S1). Furthermore, we detected in the transcriptomes of the euglenids *E. gracilis* and *E. longa* three sequences encoding related (appr. 50 – 65% identity) PFKs, each without PTS. They share 47–48% identity with different kinetoplastid PFKs and phylogenetically clustered with them in a clade previously called X (Bapteste et al., 2003) containing mostly PPi-PFKs as well as some ATP-dependent enzymes (Figure 3). These *Euglena* PFKs are predicted to have ATP-dependent activity as we conclude from the

FIGURE 3 (Continued)
was taken to represent the evolutionary history (Felsenstein, 1985). Branches corresponding to partitions reproduced in less than 50% bootstrap replicates were collapsed. The percentage of replicate trees in which the associated taxa clustered together in the bootstrap test (50 replicates) are shown next to the branches of the trees (Felsenstein, 1985). Initial tree(s) for the heuristic search were obtained automatically by applying the Maximum Parsimony method. All positions with less than 95% site coverage were eliminated, *i.e.*, fewer than 5% alignment gaps, missing data, and ambiguous bases were allowed at any position (partial deletion option). Evolutionary analyses were conducted in MEGA X (Kumar et al., 2018). The analysis involved 75 amino-acid sequences, with a total of 242 positions in the final dataset. The stars indicate sequences with a PTS1. Sequences used for the construction of the tree were retrieved from the following databases: NCBI, TriTrypDB and AmoebaDB and uploaded in FASTA format. The sequences were aligned with Clustal and the alignment was manually refined with the program MEGA X. The nomenclature of the clades was taken from Bapteste et al., 2003.

conservation of residues known to be involved in the binding of this phospho donor in trypanosomes (McNae et al., 2009). In addition, a very different PFK was found in the euglenid databases, annotated as β-PFK. Plants and algae including *E. gracilis* contain three PFKs: ATP-PFK and PPi-PFK in the cytosol, and another ATP-PFK in the chloroplast (Mertens, 1991). The PPi-PFK is usually a heterotetramer consisting of large homologous catalytic (β) and regulatory (α) subunits, which are often about 35% identical. A homologous heteromeric PPi-PFK is present in some protists and prokaryotes. Indeed, this *Euglena* β-PFK is phylogenetically found with these PPi-PFKs in a clade called 'Long' (Mertens et al., 1998; Bapteste et al., 2003) (Figure 3).

In contrast, we did not detect an orthologue of the kinetoplastid/euglenid PFK for diplonemids in the databases, in agreement with previous reports by Morales et al. (2016) and Škodová-Sveráková et al., 2021. The *D. papillatum* genome database contains three PFKs, one called DpPFK2, that shows most identity (about 36%) with the PFK of the algal haptophyte *Emiliana huxleyi* and belongs to 'clade B' alongside principally algal and plant PFKs. Identity with kinetoplastid PFKs is less than 30%, and there is no consensus PTS motif (Morales et al., 2016). We assume it was acquired by horizontal gene transfer (Škodová-Sveráková et al., 2021). The two other *D. papillatum* sequences, one originally identified (Morales et al., 2016) and called DpPFK1 (classically also denoted as PFP for PPi-fructose 6-phosphate 1-phosphotransferase) and a related one, identified later (Škodová-Sveráková et al., 2021) are similar to each other (35% identity) and each contains a PTS1 (-PKL). They show most, but still relatively low identity, with α and β subunits of plant/algal/prokaryote PPi-PFKs, including euglenid β-PPi-PFK (30 and 27%), with which they display only a distant relationship by phylogeny. Therefore, it seems unlikely that *Diplonema* inherited a heteromeric PPi-PFK from the common Euglenozoa ancestor. More plausible is a bacterial origin, as also proposed previously (Škodová-Sveráková et al., 2021), for example by acquisition of a DNA segment containing (part of) an operon with the genes of the two subunits, followed by creation of topogenic signals to route the gene products into glycosomes. Inspection of the sequences using information from the crystal structure of *Borrelia burgdorferi* PPi-PFK (Moore et al., 2002) indicated one of these *D. papillatum* proteins contains all essential residues for PPi-dependent PFK activity, thus probably is the β-subunit, whereas the other lacks many residues required for activity and is thus a likely α-subunit candidate.

A comparable although more complicated situation is found in the distantly related diplonemid *H. phaeocysticola* (Tashyreva et al., 2022) where we identified six putative PFK sequences in its transcriptome database (not shown). Two belong to the 'Long' clade, with one possessing a PTS1 (-AHL) and being mostly similar to the *D. papillatum* β-PFK1 and less to *E. gracilis* β-PFK (51 and 31% identity, respectively). The other sequence is very different, sharing 34% identity with the putative β-HpPFK and less than 20% with both α- and β-DpPFK1 and β-EgPFK. The other four Hp sequences are smaller: two have a PTS1 (-PKL and -SRM), contrary to the corresponding DpPFK2. Three of the sequences are 57–61% identical to each other and all are more similar to DpPFK2 and *E. huxley* PFK than to kinetoplastid PFKs. Together, the data about *H. phaeocysticola* PFK corroborate the evolutionary scenario depicted for *Diplonema* spp.

In summary, kinetoplastids undoubtedly inherited the cytosolic 'clade X' PFK from a common ancestor with *Euglena* and compartmentalised it, together with other glycolytic enzymes, into their peroxisomes that so became glycosomes. In contrast, they lost the 'clade Long' PPi-PFK that was probably present in the ancestor. PFK 'clade X' of the common Euglenozoa ancestor was almost certainly ATP dependent, indicating phospho-donor specificity had already changed from PPi to ATP at an earlier evolutionary stage. Diplonemids seem to have lost the PFKs of both clades but acquired others by horizontal gene transfer, retaining the PPi-dependent activity of the enzyme that became sequestered in the glycosomes.

Intriguing questions raised by the proposed evolutionary scenario are why an ancestral diplonemid acquired different PFKs by horizontal gene transfer while having lost its ancestral ones, and why are both new PFKs retained in different progeny lineages. What has been the evolutionary driver to maintain a PPi-PFK together with a (probable) ATP-PFK and FBPase? Perhaps adaptation to possible anoxic conditions played a role with a somewhat higher glycolytic ATP yield with a PPi-PFK compared to ATP-PFK (Mertens 1993; Saavedra et al., 2019). Alternatively, there is conceivably a large requirement for gluconeogenesis when these diplomemids rely on amino acids as nutrients and need to synthesize purines, pyrimidines and ribose-phosphates for their massive kinetoplast DNA networks (Lukeš et al., 2018). Answers to the questions posed will require more information about the kinetic and activity-regulated properties of the ATP-PFK, FBPase and PPi-PFK, and their expression levels under different conditions.

Intriguingly, the eubodonid *B. saltans* contains, in addition to a PTS1 (-SKL) containing PFK related to the glycosomal PFK of all other kinetoplastids, a very different PFK (25% identity). It also has a PTS1 (-SRL) (Opperdoes et al., 2016). No similar sequence was detected in any other kinetoplastid, including the parabodonid *T. borreli* and the early-branching intracellular kinetoplastid *Perkinsela* sp. It was presumably acquired by horizontal gene transfer. However, it is doubtful this protein has PFK activity because several typical substrate (ATP/PPi and fructose 6-phosphate) binding residues have been substituted. The possible function of this PTS1-containing protein is unknown.

Euglenozoan isocitrate dehydrogenase families—Diverse evolutionary trajectories

Three different types of IDHs are generally distinguished in eukaryotes: an $NADP^+$-dependent IDH1 in the cytosol and/or

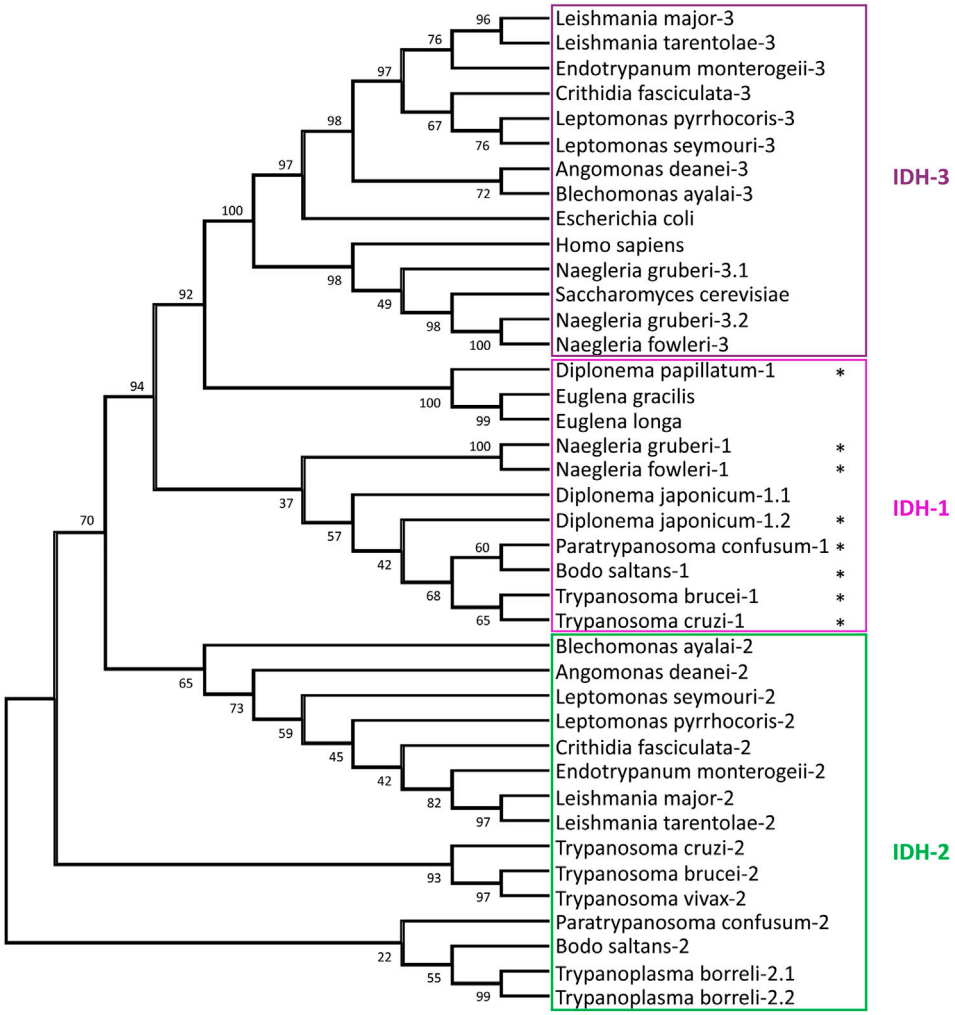

FIGURE 4
Relationships between isocitrate dehydrogenase (IDH) sequences. The evolutionary history of IDH sequences was inferred by methods described in the legend of Figure 3. The analysis involved 40 amino-acid sequences, with a total of 319 positions in the final dataset. The stars indicate sequences with a PTS1. The following IDH sequences were retrieved from the NCBI: *H. sapiens*, *S. cerevisiae*, *E. coli*, *T. borreli*, *D. papillatum*, *D. japonicum*, *E. longa*, and *E. gracilis*, whereas for *Naegleria* spp. the sequences were retrieved from AmoebaDB. The other euglenozoan sequences were taken from TriTrypDB.

peroxisomes and $NADP^+$- and NAD^+-dependent IDH2 and IDH3, respectively, in mitochondria. IDH1 and IDH2 show considerable similarity, whereas IDH3, which functions in the tricarboxylic acid (TCA) cycle, is very different and most related to prokaryotic $NADP^+/NAD^+$ IDHs. The *T. brucei* genome contains two genes, coding for IDH1 and IDH2, enzymes which are 62% identical. Its IDH1 has a PTS1 (-SKV) and the IDH2 a predicted N-terminal mitochondrial-targeting signal (MTS). Only the IDH1 has been experimentally characterised (Wang et al., 2017) and, surprisingly, showed activity with both $NADP^+$ and NAD^+, even higher with the latter cofactor. The orthologues in *T. cruzi*, which were both shown to be strictly $NADP^+$-dependent, have also a PTS1 and MTS, respectively. Whereas the IDH2 was indeed located in the mitochondrion, essentially all IDH1 was, in epimastigotes, in the cytosol (Leroux et al., 2011). No evidence was found for the typical TCA cycle-related NAD^+-dependent IDH3 in the *Trypanosoma* species. In *L. mexicana* two IDH isoenzymes are also found: one, with an MTS and high $NADP^+$ specificity is most related to IDH2 of trypanosomes, whereas the other exclusively uses NAD^+, and is very different (Giordana and Nowicki, 2020). This isoform contains no strong targeting motif, and appears most related to the TCA-cycle IDH3 enzyme of bacteria and other eukaryotes. Both *Leishmania* IDHs exhibit dual localisation in the mitochondrion and cytosol. Orthologues of both *Leishmania* IDHs were reported for *Leptomonas* and *Crithidia*. Our

bioinformatic analysis did also not identify IDH1 orthologues in this *Leishmania*/*Leptomonas*/*Crithidia* group, nor in *Endotrypanum*, *Angomonas* or *Blechomonas*. However, IDH1 with a PTS1 was, additionally to *Trypanosoma* species, also detected in the kinetoplastids *P. confusum* and *B. saltans,* in diplonemids and in *Naegleria*, but not in *Euglena* (Supplementary Table S2). Figure 4 shows a phylogenetic analysis of all IDHs detected in the genome databases of all these Discoba protists. Data about *Euglena* and *Diplonema* species are probably still incomplete. The clustering of the IDH1s of *Naegleria*, *Diplonema* and kinetoplastids reveals glycosomes retained this isoform with its characteristic partial organellar localisation when they evolved from peroxisomes, but a common ancestor of the *Leishmania*/*Leptomonas*/*Crithidia*/*Angomonas*/*Blechomonas* group must have lost it. In contrast, these kinetoplastids possess a mitochondrial NAD^+-IDH3. Apparent absence of an IDH3 in the other kinetoplastids and diplonemids, as well as the large difference (about 30% identity) with the *Naegleria* IDH3 indicates IDH3 was obtained by lateral gene transfer from a bacterium. Intriguingly, two very different *N. gruberi* IDH3s, both with an MTS, were detected by in genome and transcriptome databases. We were also surprised to observe two very similar IDH1s (83% identity) but no IDH2 in *D. japonicum*. One sequence contains a PTS1, whereas the other has a potential MTS. We suggest this diplonemid has lost an IDH2 gene but compensated by duplication of the IDH1 gene with adaptation of the required targeting motifs of the encoded proteins. In contrast, in *T. borreli* genes encoding two very similar IDH2s (81% identity) were detected, both with an MTS, but no IDH1 was found.

The finding that, in several kinetoplastids such as trypanosomes, the mitochondrion lacks the NAD-dependent IDH3 in several kinetoplastids, but has a NADP-dependent IDH2, suggests the absence of a fully functional TCA cycle in these organisms, with the other cycle enzymes functioning in metabolising products of fatty acid and amino acid oxidation. IDH2 serves to maintain the mitochondrial $NADP^+$/NADPH ratio (Opperdoes et al., 2016).

The function of an IDH within glycosomes remains to be established. It may contribute to the maintenance of the $NAD(P)^+$/NAD(P)H balance, with the substrate and product of the reaction, isocitrate and α-ketoglutarate, exchanging across the membrane (Figure 2). The level of expression of this redox shuttle may vary during life-cycle stages and/or environmental conditions, while in some kinetoplastids presence of a glycosomal IDH may have become redundant and lost. Whether there is a functional link between this loss and the acquisition of a mitochondrial IDH3 by lateral gene transfer is not clear. A shuttle involving isocitrate and α-ketoglutarate has also been identified for peroxisomes of yeast and proposed for those of mammalian cells (reviewed by Chornyi et al., 2021).

Finally, an α-ketoglutarate decarboxylase (α-KDE1), the E1 subunit of the TCA-cycle α-ketoglutarate complex, was located in the mitochondrion and glycosomes of *T. brucei* (Sykes et al., 2015). The E2 and E3 subunits are not glycosomal. Here, glycosomal targeting is via an unusual PTS2 motif partially overlapping with the N-terminal MTS (MMRRLSPVNGSV-). Whether this glycosomal α-KDE1 acts on the IDH1 product or if it has an unknown moonlighting function awaits discovery. In addition, variations in the unusual PTS in the α-KDE1 homologue of other euglenids preclude making predictions of conservation of the glycosomal localisation.

Bioinformatic chronology of glycosomal metabolism II: ATP/ADP/AMP homeostasis

Two other enzymes related to energy metabolism are found in glycosomes: adenylate kinase (ADK) and arginine kinase (AK). ADKs contribute to homeostasis of the adenine nucleotide pool by reversible phosphoryl transfer resulting in the interconversion of two ADP molecules and ATP plus AMP (Figure 2). Trypanosomes contain multiple ADKs, including one in glycosomes (Ginger et al., 2005). In all kinetoplastids analysed an ADK with a PTS1 was detected (Supplementary Table S1). Morales et al. (2016) concluded from phylogenetic analysis that kinetoplastids had acquired the glycosomal isoform by lateral gene transfer from a bacterium. However, we detected an ADK with a PTS1 in *Diplonema* spp., but not in *Euglena* and *Naegleria*, suggesting that the acquisition occurred earlier.

AKs catalyse the reversible phosphorylation of arginine by ATP. Phosphoarginine provides an energy reserve in many invertebrates and in some unicellular eukaryotes. *T. brucei* contains three highly similar AK isoforms located in the flagellum, cytosol and glycosomes, the latter has a PTS1 (Voncken et al., 2013). A PTS1 containing AK was also found in *T. vivax*. Only glycosomes of African trypanosomes acquired an AK, possibly creating a relay system between cytosol and glycosomes allowing the maintenance of the intraglycosomal ATP/ADP balance when required without the need for transfer of adenine nucleotides across the organellar membrane. *T. cruzi* has two AK isoforms, each without a PTS and not detected in the organelles (Miranda et al., 2009). Genes encoding AK orthologues were found only in genomes of a few other kinetoplastids (*Blechomonas ayalai* and *Bodo saltans,* in each case without PTS). Sequences annotated as arginine or creatine kinases were also detected in diplonemid databases, with an enzyme in *D. ambulator* (27–29% identity with *Trypanosoma* AKs) containing a PTS1.

It has been proposed that absence of AK in several species is linked to the presence of the arginine-consuming enzyme arginase (ARG); simultaneous activity of AK and ARG within a cell should be incompatible (Canepa et al., 2011). Indeed, *Trypanosoma* and other trypanosomatids such as *Phytomonas*

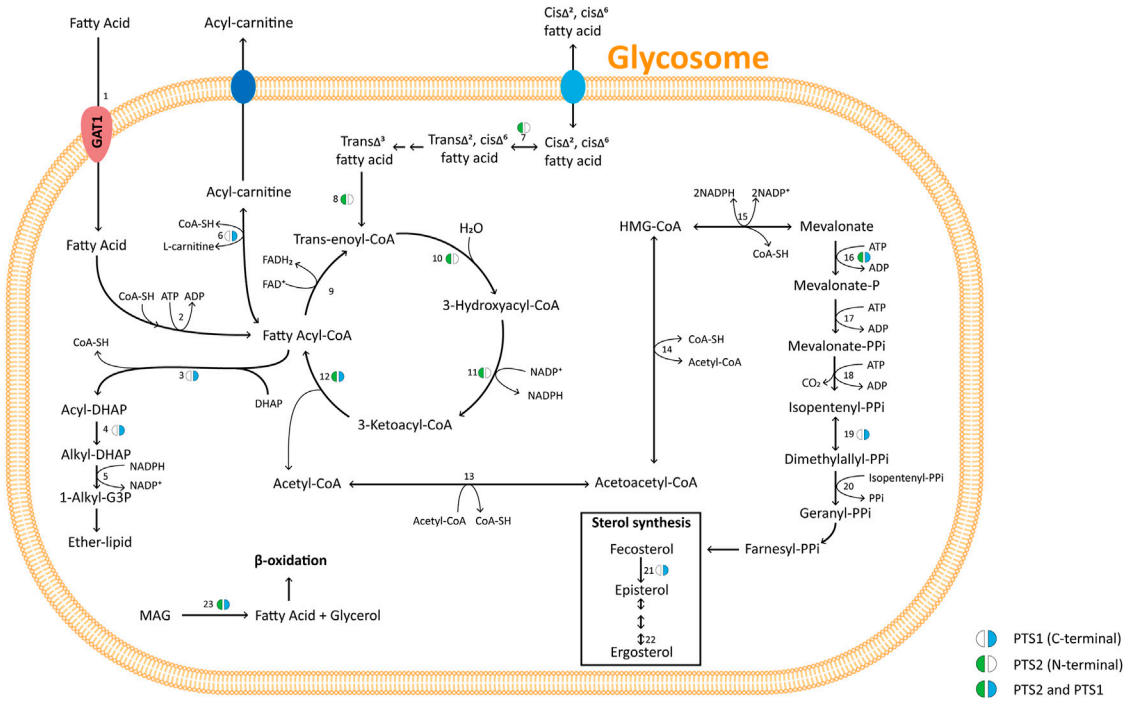

FIGURE 5
Pathways of glycosomal lipid metabolism in TriTryps species. Pathways of ether-lipid synthesis (enzymes 3 – 5), fatty-acid β-oxidation (9 – 12), and sterol synthesis (16 – 23) are represented. Note that not all enzymes indicated are present in each of the TriTryps species or expressed in each of their life-cycle stages, and for simplicity not all reactions are represented. Enzymes/transporter: **1.** Glycosomal ABC transporter (GAT1); **2.** Fatty-acyl CoA synthetase; **3**. DHAP acyltransferase; **4**. Alkyl-dihydroxyacetone phosphate synthase; **5**: 1-Alkyl G3P:NADP⁺ oxidoreductase; **6**. Carnitine O-palmitoyltransferase; **7.** 3,2-Trans-enoyl-CoA isomerase; **8.** Enoyl-CoA isomerase; **9**. Acyl-CoA dehydrogenase; **10, 11, 12.** Enoyl-CoA hydratase/3-hydroxyacyl-CoA dehydrogenase/3-ketoacyl-CoA thiolase (trifunctional enzyme); **13**. Acetyl-CoA acetyltransferase **14**. 3-Hydroxy-3-methylglutaryl CoA synthase; **15**. 3-Hydroxy-3-methylglutaryl-CoA reductase; **16**. Mevalonate kinase; **17**. Phosphomevalonate kinase **18**. Mevalonate diphosphate decarboxylase **19.** Isopentenyl-diphosphate δ-isomerase; **20**. Farnesyl diphosphate synthase **21**. C-8 sterol isomerase; **22**. Sterol C-24 reductase; **23.** Monoacylglyceride lipase. **MAG**: monoacylglycerol. Enzymes **13, 14, 15, 17, 18** and **20** have been detected experimentally with a PTS motif in mammalian peroxisomes (references cited in Acosta et al., 2019).

that possess an AK lack a functional ARG, whereas the opposite situation is found in Leishmaniinae (*Leishmania*, *Crithidia*, *Endotrypanum*, *Leptomonas*) and *Angomonas*. However, *B. saltans* contains, in addition to a predicted AK gene, a potential ARG with a PTS1 (Opperdoes et al., 2016). Confirmation of whether this protein has arginase activity is required. Preventing incompatibility of the ARG and AK by differential regulation at gene expression and/or activity level can also not be excluded. The *B. saltans* ARG is not orthologous to the Leishmaniinae ARG (Opperdoes and Michels 2008; Opperdoes et al., 2016) that is glycosomal with a PTS1 in all species analysed (Roberts et al., 2004). Phylogenetic analysis suggested that the Leishmaniinae gene was acquired by lateral transfer from fungi. Arginases convert arginine to ornithine, a precursor for polyamine biosynthesis. Kinetoplastids without this enzyme, like *Trypanosoma* species, rely on the uptake of ornithine (Marchese et al., 2018). The evolution of AK and ARG in Euglenozoa probably involved multiple acquisition and losses of genes. Likelihood of independent acquisition of glycosomal targeting requires further study.

Bioinformatic chronology of glycosomal metabolism III: Lipid metabolism

Peroxisomes play a major role in the lipid metabolism of many eukaryotes. This is also true for trypanosomatid glycosomes as previously shown in several functional and proteomic studies (reviewed by Allmann and Bringaud, 2017) and other euglenozoans as demonstrated in this work (Figure 5 and Supplementary Table S2). Different enzymes of sterol metabolism (C-8 sterol isomerase, isopentenyl-diphosphate δ-isomerase, mevalonate kinase) are detected throughout the kinetoplastid lineage with either a type 1 or 2 PTS, while some of these enzymes containing a PTS are found in databases of *Diplonema* spp., *Euglena* spp. and *Naegleria* spp.

Enzymes involved in the formation of fatty acids from phospholipids and their oxidation have also been detected in *Trypanosoma* and *Leishmania* glycosomes. Several are found with a PTS in many euglenozoans and in *Naegleria* spp. monoglyceride lipase, acyl-CoA binding protein, carnitine O-palmitoyltransferase, and each of the β-oxidation enzymes. This indicates all were peroxisomal ancestrally in the kinetoplastid/diplonemid progenitor before glycolysis became sequestered in the organelles.

Similar to mammals, β-oxidation in kinetoplastids occurs in both peroxisomes/glycosomes and mitochondria. In plants and yeast, β-oxidation occurs only in peroxisomes. There is a major difference between mitochondrial and peroxisomal β-oxidation: the first oxidative step of the mitochondrial pathway is catalysed by an acyl-CoA dehydrogenase (ACAD) in which electrons are transferred to the respiratory chain, but in peroxisomes this step typically involves an acyl-CoA oxidase (ACOX) that reduces O_2 to H_2O_2. However, often organisms contain different isoenzyme families for both ACADs and ACOXs, and ACADs containing a PTS are functional within peroxisomes in mammals and fungi (Camões et al., 2015). ACADs and ACOXs are related, FAD-containing enzymes (Kim and Miura, 2004). In the *N. gruberi* genome, a putative ACAD with a PTS1 was detected, but no ACOX gene (Opperdoes et al., 2011) and recent analysis of *D. papillatum* revealed four very different transcripts encoding putative ACADs (including one with a PTS1) plus three strikingly different mRNAs for predicted ACOXs (also including one with a PTS1) (Škodová-Sveráková et al., 2021). Candidate ACADs and ACOXs with PTS1 motifs were detected in other diplonemids, euglenids and *Naegleria*, but not in any kinetoplastid (Supplementary Table S2). According to TriTrypDB, kinetoplastids contain different predicted ACADs and ACOXs, but a PTS was only detected in candidate ACOXs of *B. saltans* (Opperdoes et al., 2016) and *P. confusum* with no apparent homologues in the other species. It should be noted that different online informatics resources provided different outcomes for ACAD vs. ACOX prediction. Thus, future use of more bespoke software and/or experimental approaches will be required to reach definite conclusions.

While, to our knowledge, no activity of the first step of glycosomal β-oxidation in trypanosomes has been reported, activities have been demonstrated for the other three reactions (Wiemer et al., 1996; Mazet et al., 2011). The second and third enzymes, enoyl-CoA hydratase and 3-hydroxyacyl-CoA dehydrogenase, together with enoyl-CoA isomerase, are present as a trifunctional enzyme, while the last enzyme, 3-ketoacyl-CoA thiolase, is separate.

Thiolases exist in different isoforms with different substrate specificity and metabolic functions. The SCP2-isoform was detected in each TriTryps parasite and was the only isoform detected in *T. brucei*; *T. cruzi* and *Leishmania* spp. contain one and two other isoforms, respectively (Mazet et al., 2011). Trypanosomatid SCP2 isoform contains a candidate PTS1 and at its N-terminus both a predicted MTS and PTS2. The *T. brucei* protein, when expressed as recombinant protein, was shown to be active in both directions, and would thus be able to participate in β-oxidation when required. However, in procyclic trypanosomes it was located in the mitochondrion and shown to be involved in lipid biosynthesis (Harijan et al., 2016). Although glycosomal β-oxidation is potentially possible, it is not yet experimentally demonstrated. The predicted glycosomal targeting situation for the trifunctional enzyme and SCP2 thiolase in Euglenozoa is very similar, with a potential PTS2 in most kinetoplastids, and a PTS1 in diplonemids, euglenids and *N. gruberi*. Moreover, some thiolases, like that of *T. cruzi* and *C. fasciculata* also possess a candidate PTS1.

Enzymes of ether-lipid biosynthesis (dihydroxyacetone-phosphate acyltransferase, alkyl-dihydroxyacetone-phosphate synthase, fatty acyl-CoA reductase) are well-known peroxisomal markers (Opperdoes, 1984) and contain a PTS1 or PTS2 in all Euglenozoa analysed, as well as in *Naegleria*.

Finally, the presence of a novel phospholipase dually localised in the cytosol and glycosomes of *T. brucei* was recently reported (Monic et al., 2022). The enzyme has a non-canonical PTS1 (-SKS) required for glycosomal import, although this motif showed very poor efficiency in previous comparative glycosomal-targeting experiments (Sommer et al., 1992). Moreover, the novel lipase appeared to be excreted by bloodstream-form (BSF) trypanosomes. The possible function of the lipase within glycosomes is unknown. Orthologues with a potential PTS1 were only detected in databases of *T. cruzi* (-SKA) and *D. japonicum* (-SNM).

Bioinformatic chronology of glycosomal metabolism IV: Antioxidant metabolism

Glycosomal antoxidant metabolism is depicted in Supplementary Figure S2. Strikingly, the hallmark peroxisomal enzyme catalase, responsible for the dismutation of the reactive H_2O_2, could never be detected in glycosomes or elsewhere in the cells of TriTryps parasites. It was thought this was due to a reduced peroxide metabolism. Activity of ACOXs and other H_2O_2-producing enzymes such as D-amino acid oxidase and 2-hydroxy acid oxidase could not be detected in *T. brucei*, nor have these enzymes been detected in any of the more recent glycosomal proteome analyses. However, the latter two oxidases and catalase have been reported for other trypanosomatids like *C. fasciculata*, but not in association with the organelles (Opperdoes et al., 1977; Gutteridge et al., 1982; Opperdoes, 1987). We detected in TriTrypDB an *A. deanei* oxidase with a FAD-binding domain and PTS1, annotated as having a predicted 2-hydroxy acid oxidase function (Supplementary Table S2). It has homologues with a PTS in most kinetoplastids but was absent from *Trypanosoma* species. A possible D-amino acid oxidase with PTS1 was detected in the database of *B. saltans*, but no obvious

homologues of it was detected in other Euglenozoa. These data, together with the predicted presence of ACOXs mentioned in the preceding section, suggest H_2O_2 metabolism in glycosomes may be more prominent than appreciated so far.

Catalase, not detected in the TriTryps parasites, appears present in diverse euglenozoans. Many years previously, it was detected in glycosomes of *T. borreli* (Opperdoes et al., 1988). Recently, however, detailed genomic analysis provided evidence for independent catalase gene acquisitions by several Euglenozoa through horizontal transfers to execute specific molecular tasks (Škodová-Sveráková et al., 2020). Genes encoding a catalase with a PTS motif (-SQA) were only reported for two diplonemids–*D. papillatum* and *D. japonicum*–but not in other diplonemids or kinetoplastids.

In the absence of catalase, detoxification of glycosomal H_2O_2 may be performed by the trypanothione-based peroxide detoxification system. Although this system is primarily present in the cytosol of trypanosomatids, small amounts of some of its proteins have been found associated with glycosomes (Irigoín et al., 2008; Güther et al., 2014). Moreover, several of these proteins contain a PTS (Opperdoes and Szikora, 2006), conserved in all kinetoplastids and diplonemids. Other enzymes of antioxidant metabolism detected in *Trypanosoma* glycosomes are a PTS1 containing L-galactonolactone oxidase involved in ascorbate synthesis and two iron-containing superoxide dismutase (Fe-SOD) isoenzymes, one of them having a PTS1 (Wilkinson et al., 2005; Dufernez et al., 2006; Wilkinson et al., 2006). Among the Euglenozoa a PTS-containing L-galactonolactone oxidase was only detected in *B. ayalai*, whereas Fe-SODs with a PTS1 are present throughout the phylum.

Bioinformatic chronology of glycosomal metabolism V: Pyrimidine synthesis, purine salvage

Trypanosomatids perform *de novo* pyrimidine synthesis (Supplementary Figure S3). Most of the six enzymes involved occur in the cytosol. However, the last step of UMP biosynthesis involves two enzymatic activities, orotidine-5′-monophosphate decarboxylase and orotate phosphoribosyltransferase, that in trypanosomatids are carried out by a glycosomal bifunctional enzyme (OMPDC/OPRT) with a PTS1 encoded by a single, fused gene (Gao et al., 1999). Interestingly, a bifunctional enzyme is also present in many other eukaryotes including *Euglena* and *Naegleria*, but with enzymatic domains fused in the reverse order (OPRT/OMPDC) (Makiuchi et al., 2007). Orthologues of the bifunctional enzyme with a PTS1 were detected in all kinetoplastids analysed in this study, but not in diplonemids, euglenids or *Naegleria* spp. (Supplementary Table S2). Butenko et al. (2020) detected separate OMPDC and OPRT transcripts in diplonemids and euglenids, as well as a transcript encoding the fused protein in some euglenids and the diplonemid *Hemistasia phaeocysticola* but not in other diplonemid species studied. However, each of the proteins encoded by these transcripts lacks a PTS. The authors thus concluded that the common ancestor of Euglenozoa had separate genes for OPRT and OMPDC that underwent duplications and fusions in different orders in the different progeny lineages, with targeting of the encoded bifunctional enzyme to glycosomes only in kinetoplastids.

Trypanosomatids, like many other protists including *Naegleria gruberi* are not capable of purine synthesis *de novo*, but rely on salvage from nucleotides (Supplementary Figure S3). The parasites have different isoforms for some enzymes of the purine-nucleotide cycle and the interconversion of purine bases and nucleotides. Previously, it was found that most but not all trypanosomatid enzymes involved in purine salvage, or in some cases one of the isoforms, possess a PTS1 and/or have been experimentally located in glycosomes: adenine phosphoribosyltransferase (APRT), hypoxanthine-guanine phosphoribosyl transferase (HGPRT), xanthine phosphoribosyl transferase (XPRT), inosine-5′-monophosphate dehydrogenase (IMPDH), guanosine monophosphate reductase, AMP deaminase and guanylate kinase (for *Leishmania* reviewed by Boitz et al., 2012). We detected orthologues of these enzymes with a PTS in the databases of most kinetoplastids, including the bodonids, and the diplonemids, but not in *Euglena* and *Naegleria* species (Supplementary Table S2), suggesting the pathway was compartmentalised at a very early stage of glycosome evolution. However, the compartmentalisation is partial, with variations evident in different species.

The two very different (22% identity) APRT isoforms in *T. brucei* have been studied in detail; APRT1 has no PTS and is cytosolic, whereas APRT2, with a PTS2, is glycosomal (Lüscher et al., 2013). However, only APRT1 displayed activity; no function could yet be attributed to APRT2 (Glockzin et al., 2022). It is not known whether APRT2 has activity in other euglenids. APRT2 possesses a PTS1 in other *Trypanosoma* species and in *P. confusum*, but it has no characteristic PTS in any other species analysed. Curiously, there is a specific XPRT not found in mammals and many other organisms present in Euglenozoa. In other protists, XPRT activity is often associated with HGPRT. Jardim et al. (1999) showed that, in *L. donovani*, the XPRT amino acid sequence is 33% identical to that of HGPRT with the HGPRT and XPRT genes arranged in tandem, pointing to gene duplication followed by evolution of one paralogue to a XPRT. The duplication possibly happened early in the evolution of the kinetoplastid lineage, because database analysis shows syntenic orthologues in all kinetoplastids. Only a single gene was detected in diplonemids and euglenids. The ancestral HGPRT may already have been glycosomal: a PTS was identified in most kinetoplastid HGPRTs,

and also in diplonemids. XPRT has a PTS1 in all kinetoplastids studied.

Several of the glycosomal enzymes of pyrimidine biosynthesis and purine salvage use 5-phosphoribosyl-1-pyrophosphate (PRPP) as a substrate. Since this is a rather large molecule (390 Da), that may not easily traverse the glycosomal membrane, we looked for a glycosomal PRPP synthase. Proteomic analyses of *T. brucei* glycosomes suggested the presence of two isoenzymes, although both without a PTS (Güther et al., 2014). The two proteins, encoded by non-linked genes, are 54% identical and share significant similarity with an active PRPP synthase of *Leishmania donovani* of unspecified subcellular localization (Hendrickson et al., 1993). Orthologues of the two *T. brucei* candidate PRPP synthases can be detected in databases of all organisms analysed, but with a PTS in only a few kinetoplastid species (Supplementary Table S2).

Bioinformatic chronology of glycosomal metabolism VI: Phosphatases

Although glycosomal proteins can be phosphorylated (Zhang et al., 2020), no protein kinases have been detected in trypanosomatid glycosomes. However, several phosphatases have been identified in *T. brucei* glycosomes (Szöőr et al., 2010; Güther et al., 2014). Phosphorylation of glycosomal proteins potentially occurs in the cytosol, prior to their import and, when appropriate, they are dephosphorylated by organellar phosphatases. Such a mechanism would probably imply metabolic regulation at a longer time span than usually is the case for enzyme activity modification by phosphorylation/dephosphorylation. It would link the phosphorylation/dephosphorylation process to the biogenesis of the organelles. Such mechanism is reminiscent of observations by Szöőr et al. (2019) made for the serine/threonine phosphatase PIP39 that possesses a PTS1. This phosphatase is itself phosphorylated outside the glycosomes by an as yet unidentified tyrosine kinase resulting in PIP39 activation and relocation to glycosomes. This occurs during the second stage of the process, triggered by a quorum-sensing mechanism, by which proliferating slender BSF trypanosomes first differentiate to quiescent stumpy BSF forms, which then develop further to procyclic-form (PCF) trypanosomes after ingestion by the tsetse fly. Intraglycosomal targets of PIP39 remain to be identified.

Since glycosomes are massively degraded by pexophagy during differentiation to PCFs and a new population of organelles is formed (Herman et al., 2008), it is feasible that the sequestering of PIP39 is meant to neutralise it after having exerted its activity in the cytosol upon the trigger for the second differentiation step. Yet, PIP39 with a PTS1 is also found in other kinetoplastids including the bodonids *T. borreli* and *B. saltans* which are parasitic and free living, respectively (Supplementary Table S2). Whether the protein is involved in performing a similar role in differentiation in all these other organisms when they must adapt to different environmental conditions remains to be studied.

Among the different types of protein phosphatases present in trypanosomatids are representatives of the 'non-conventional' ApaH-like phosphatases (Alphs) (Brenchley et al., 2007). One Alph has a PTS1 in *Trypanosoma* species, but no Alphs with a PTS were detected in any other trypanosomatid analysed. An Alph with a potential PTS2 was detected in the bodonid *T. borreli*, while different species of *Diplonema* possess an Alph with either a PTS2 or PTS1. The function of this glycosomal phosphatase is unknown, but it seems most likely that early in *Trypanosoma* evolution one Alph became rerouted to glycosomes.

A third glycosomal enzyme exhibiting phosphatase activity is one of the Nudix hydrolase isoforms found in *T. brucei*. *T. brucei* and *T. cruzi* contain inorganic polyphosphate (polyP) in different cell compartments including acidocalcisomes, nucleus, cytosol and glycosomes (Negreiros et al., 2018). The role of polyP in glycosomes is not yet clear: it is not known how it arrives in glycosomes or whether it is synthesized inside glycosomes. It could be a storage product of Pi or PPi, or have a structural function.

The glycosomal Nudix hydrolase shows exo- and endophosphatase activity towards polyP (Cordeiro et al., 2019). The enzyme has a PTS1, and genes encoding orthologues with a PTS1 are also found in various other trypanosomatids but were not found in other euglenozoans. It remains to be determined if glycosomes in other species also contain polyP and if the polyP hydrolysis is the only or main activity of the enzyme.

Bioinformatic chronology of glycosomal metabolism VII: Glycosomal ABC transporters (GATs).

Peroxisomal membranes usually contain multiple ABC transporters of the D-subfamily-type. These are half-size transporters with typically one transmembrane domain (TMD) comprising six transmembrane-spanning segments and one cytosol-facing C-terminal nucleotide-binding domain (NBD) with canonical Walker A and B motifs for ATP binding (Chornyi et al., 2021). They form functional transporters with a dimeric NBD by homo- or heterodimerisation. Human and *S. cerevisiae* peroxisomal ABC transporters import fatty acids and/or acyl-CoAs. Three half-size ABC transporters with glycosomal localisation occur in *T. brucei*, called GAT1-3 (for glycosomal ABC transporter) (Yernaux et al., 2006). GAT1 and GAT2 are ~30% identical and display ~25% identity with human, yeast and plant homologues. GAT3 is very different. GAT1 mediates

uptake of oleoyl-CoA into *T. brucei* glycosomes (Igoillo-Esteve et al., 2011). Specificities of GAT2 and GAT3 require determination.

Sequences homologous with each *T. brucei* GAT were detected in all euglenozoans and *N. gruberi* (Supplementary Figures S4A–C). Between different kinetoplastid genera, pairwise identities vary between 50 and 60% for each of the GATs from *T. brucei* and *T. cruzi*, between 50 and 85% between the GATs from different Leishmaniinae genera and values down to 10–30% when comparing the corresponding proteins from more distantly related euglenozoans or these with three different predicted *Naegleria* peroxisomal transporters. Supplementary Figure S4D shows a multiple alignment of GAT1, two and three from each TriTryps species plus two well-characterised half-size *S. cerevisiae* ABC transporters, Pxa1p and Pxa2p. The six transmembrane segments that together form the TMD in the N-terminal half are readily identifiable in all sequences, as well as the C-terminal NBD domain, including the Walker A and B motifs and the conserved linker that forms the so-called ABC signature. Together, the data indicate three different half-size ABC transporters were present in the common euglenozoan ancestor.

Bioinformatic consideration of glycosome assembly: Peroxin evolution in Euglenozoa

Glycosome biogenesis occurs by a process similar to that of peroxisomes in mammalian, plant and yeast cells, involving conserved proteins called peroxins or PEX proteins. *T. brucei* peroxins acting in various aspects of biogenesis have been identified–and orthologues also in other trypanosomatids (Supplementary Figures S5) (reviewed by Galland and Michels, 2010; Bauer and Morris, 2017; Kalel and Erdmann, 2018; Michels and Gualdrón-López, 2022).

In general, trypanosomatid peroxins are noticeably divergent from their peroxisomal counterparts in mammals, plants and yeasts; in some cases, homology is barely recognisable. Key questions are therefore whether this divergence is a characteristic of all euglenozoans; whether divergence is evident in only some euglenozoan lineages, perhaps coincident with the shift from typical peroxisome to glycosome; or whether peroxin divergence is seen in other Discoba, e.g. *Naegleria* spp. Using bioinformatics, we addressed these questions for different peroxins, such as PEX5 and PEX7, and others which in previous *T. brucei* research showed particularly unique features compared to counterparts in peroxisomes of mammals, yeasts and plants (i.e., PEX3, PEX13, PEX19, PEX11/GIM5A and GIM5B). The general structural organisation of these peroxins is presented in Figure 6.

PEX5 is a cytosolic protein composed of two domains: an N-terminal domain responsible for association with the docking complex in the peroxisomal/glycosomal membrane and a C-terminal PTS1-protein binding domain. The N-terminal domain contains several WxxxF/Y pentapeptide motifs with the propensity to form amphiphilic helices that mediate binding of PEX5 to PEX14. A species-dependent variable number of pentapeptide motifs has been observed, from two in *S. cerevisiae* to eleven in some plants; three were identified in *T. brucei*, with boxes 1 and 3 showing high binding affinity for PEX14 (Choe et al., 2003). In mammals and plants, PTS2-protein import has been shown to converge with a PTS1-protein import route by interaction of PEX7 with an approximately 35-residues long region in the N-terminal half of PEX5 called PEX7-binding box (Braverman et al., 1998; Otera et al., 1998). In contrast, in *S. cerevisiae* PTS1- and PTS2-protein import occurs via separate routes (Montilla-Martinez et al., 2015). A sequence similar to the PEX7-binding box of mammalian PEX5 has been found in PEX7-binding proteins of yeasts and fungi (Dodt et al., 2001; Einwachter et al., 2001) as well as in PEX5 of the TriTryps species with experimental data supporting an interaction (Galland et al., 2007). The C-terminal half of PEX5 is a tetratricopeptide repeat (TPR) domain, consisting of seven degenerate TPR motifs. The crystal structure of the PEX5 TPR domain has been solved for human and *T. brucei* (Gatto et al., 2000; Sampathkumar et al., 2008). The repeats form two subdomains, made up of TPR1-3 and TPR5-7 respectively, connected by TPR4, thus forming a cavity in which the C-terminal peptide of a PTS1 protein binds. The seven TPR motifs of the C-terminal domain are found in all euglenozoans. The positions of the three pentapeptide motifs in the N-terminal domain are also well conserved, although *B. ayalai* has lost the first and in *P. confusum* the second appears absent (Supplementary Figure S6). The putative PEX7-binding box is found in all kinetoplastids, but its presence in diplonemids, *E. gracilis* and *N. fowleri* is less certain.

PEX7 is a cytosolic protein containing six WD repeats that make up almost the entire length of the protein. Each repeat has about 40–60 residues with a characteristic central tryptophan-aspartate (WD) pair. The protein forms a ring structure with a seven-bladed β-propeller fold. Six blades are formed by each of the WD repeats and most of the seventh by the N-terminal region (although it has low similarity to WD motifs) that unites with the C-terminal end to close the ring (Pan et al., 2013; Kunze, 2020). The PTS2 nonapeptide forms an amphipathic α-helix that binds in a horizontal, large cleft on top of PEX7.

The WD repeats that form six of the seven blades of the PEX7 propeller structure are recognisable in a multiple sequence alignment of all euglenozoan PEX7s, although the primary structure is highly variable (Supplementary Figure S7).

PEX3 is a central component of the machinery for insertion of proteins into the peroxisomal membrane and considered a master regulator of peroxisome biogenesis. It is an integral membrane protein with a single transmembrane segment close to its N-terminus and three PEX19 binding sites. Its presence in glycosomal membranes of trypanosomes remained

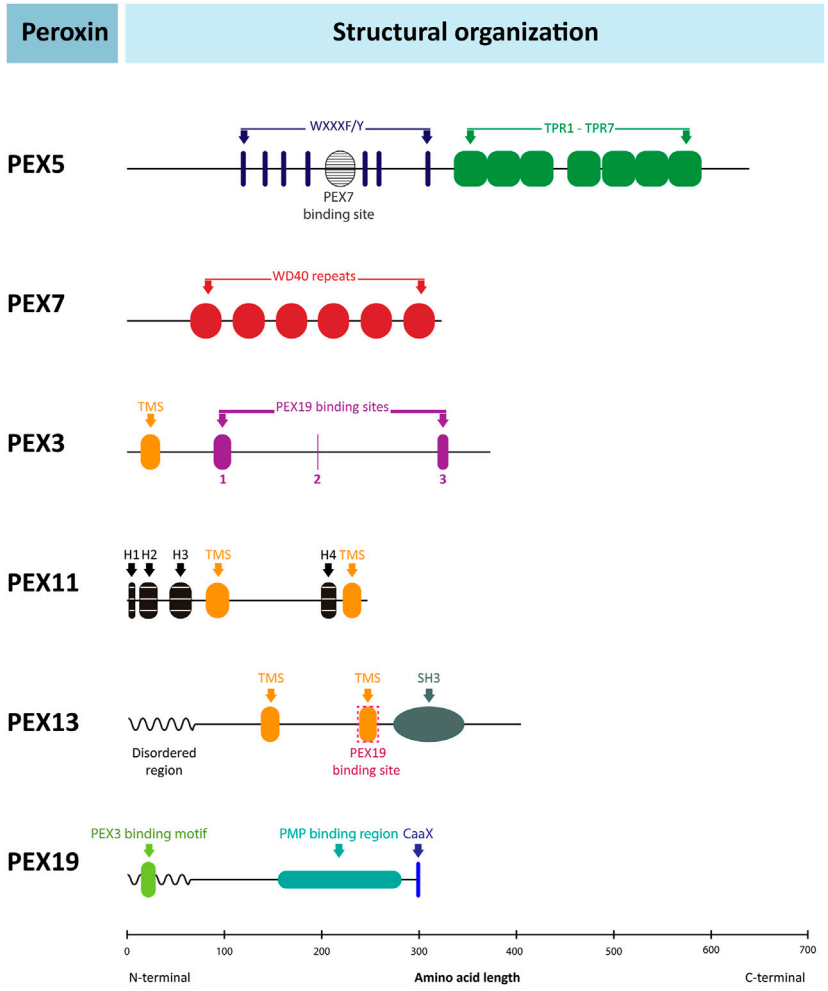

FIGURE 6
Structural organisation of peroxins. Schematic representation of the structure of several human peroxins with the relative position of their functional motifs indicated by coloured boxes and identities specified. The organisation of the corresponding peroxins from yeasts and plants is very similar, but many important differences are found in the peroxins of Euglenozoa as discussed in the text and shown in detail in the sequence alignments in Figure 7 and Supplementary Figures S6–S12. The human peroxins IDs are: PEX5 (P50542); PEX7 (O00628); PEX3 (P56589); PEX11α (O75192); PEX13 (Q92968); PEX19 (P40855). TPR: tetratricopeptide repeats; TMS: transmembrane segment; H1-3: amphiphilic helices.

enigmatic for a long time. Only recently, two groups independently identified the *T. brucei* peroxin using different bespoke methods. Banerjee et al. (2019) found a candidate PEX3 using the HHpred protein comparative tool for remote protein homology detection and structure prediction, while Kalel et al. (2019) used a combinatory approach involving identifying PEX19-interacting proteins and secondary structure homology. The teams subsequently confirmed PEX3 candidature through functional studies. They reported very low overall sequence identity between the *T. brucei* protein and known peroxisomal PEX3s (<7%, or 11% if large trypanosome-sequence specific insertions are omitted), but higher (>30%) for the known PEX19 binding sites. The very high diversity of PEX3s complicated their identification in the Euglenozoa, even with knowledge of the *T. brucei* peroxin, but a multiple alignment of selected putative PEX3 sequences is presented in Figure 7. It shows that also amongst most of these protists the degree of its conservation is very low, although 65–80% identity is found between the PEX3s of the Leishmaniinae genera; for *T. cruzi*, only an unlikely PEX3 candidate with an estimated 12% identity to the *T. brucei* PEX3 was found. For the residues involved in PEX19 binding, as reported for *T. brucei* PEX3 (Kalel et al., 2019), some conservation is generally found.

The PEX11 family, which in most eukaryotes where peroxisome biogenesis has been studied is a multigene family arising as consequences of lineage-specific duplications and paralogue divergence (Schrader et al., 2012; Schrader et al., 2016; Jansen et al., 2021). PEX11 isoforms are integral

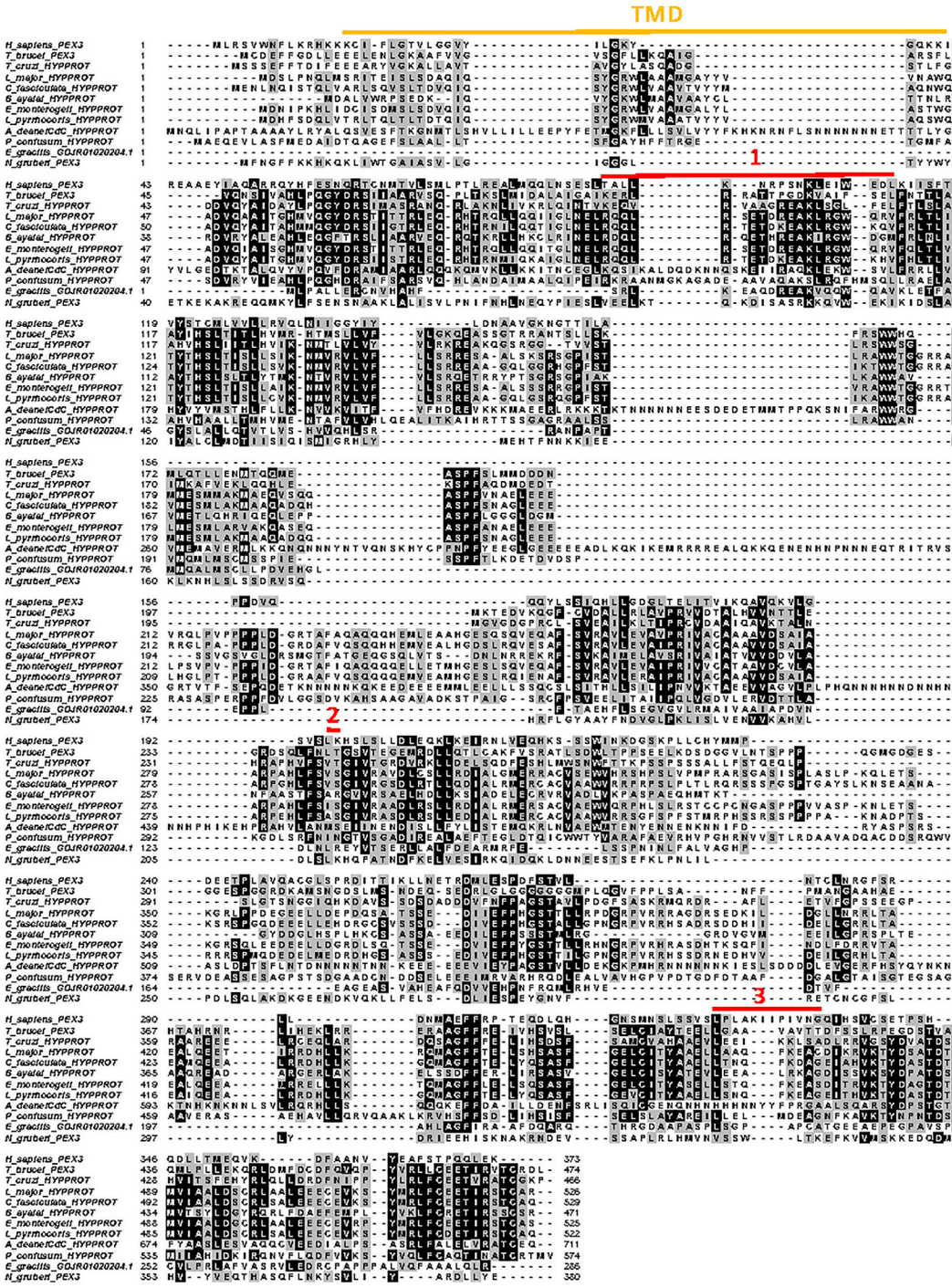

FIGURE 7
Alignment of PEX3 amino-acid sequences from selected Euglenozoa, *Naegleria* and human. Sequence IDs: *H. sapiens*: P56589; *T. brucei*: Tb927.11.10260; *T. cruzi*: TcCLB.510,719.280; *L. major*: LmjF.36.4010; *C. fasciculata*: CFAC1_280044800; *B. ayalai*: Baya_134_0190; *E. monterogeii*: EMOLV88_360046900; *L. pyrrhocoris*: LpyrH10_06_1720; *P. confusum*: PCON_0042250; *E. gracilis*: GDJR01020204.1; *N. gruberi*: NAEGRDRAFT_68465. The transmembrane region is highlighted by the yellow line above the alignment, and the amino acids involved in PEX19 binding are indicated by red lines numbered 1 to 3 (Kalel et al., 2019). The alignment was made in MUSCLE.

membrane proteins, although for *S. cerevisiae* peripheral association with the membrane was reported. The N- and C-termini are present in the cytosol, but detailed information about the topology is limited. Usually two or four transmembrane-spanning segments are predicted from the sequences, two for *T. brucei* PEX11 (Lorenz et al., 1998).

PEX11s are involved in regulating peroxisome size and number. In mammals, PEX11β functions in peroxisome elongation and recruiting proteins necessary for constriction and fission of the organelles. The specific molecular roles of PEX11α and γ in this process are less known; they don't complement loss of PEX11β. Additionally, PEX11 of yeast has been shown to also possess the capacity to form pores in the peroxisomal membrane allowing passage of solutes with molecular mass up to 300–400 Da (Minthoff et al., 2016). Trypanosomes also contain three family members, called PEX11, GIM5A and GIM5B. Their PEX11 seems to exert a role most similar to that of mammalian PEX11β, since overexpression in *T. brucei* resulted in changing normally spherical glycosomes into clusters of long tubules, whereas knockdown led to fewer but larger organelles (Lorenz et al., 1998). The roles of GIM5A and GIM5B are less clear. The genes are tandemly arranged, and the encoded proteins are 88% identical, but very different (21% identity) from PEX11 of which the gene is present on a different chromosome. GIM5A/B depletion resulted in a pleiomorphic phenotype, demonstrating the two proteins have non-redundant but overlapping functions. Changes included decreased glycosome numbers and alterations in their morphology, as well as increased cellular fragility and several metabolic effects, some suggestive that like PEX11 in yeast these proteins may also be involved in metabolite transport (Voncken et al., 2003).

PEX11 sequences were identified from different Euglenozoa (Supplementary Figure S1). Despite the high diversity, the positions of two predicted transmembrane segments appear conserved in the different PEX11 candidates. Conserved are three peptide sequences in the N-terminal region with propensity to form amphipathic helices that, in *Penicillium chrysogenum*, are essential for the membrane remodelling capacity of PEX11 (Opalinski et al., 2011; Schrader et al., 2012). An amphipathic helix near the C-terminus is also conserved, but its function is still unknown (Zientara-Rytter et al., 2022).

Sequences highly related to *T. brucei* GIM5A/B were detected in all kinetoplastids and diplonemids analysed (a selection is aligned in Supplementary Figure S9), but not in euglenids (although a possible GIM5-related fragment was found for *Rhabdomonas*) or *Naegleria*. Analogous to *T. brucei*, in several other kinetoplastids two linked, related GIM5 genes were detected, indicating the gene duplication characterised by Voncken et al. (2003) was most likely not a recent event.

PEX13 is present in all members of the organelle family of peroxisomes, including glycosomes. This protein is part of the docking complex for the cytosolic receptor charged with a matrix protein to be imported. It is an integral membrane protein with N- and C-terminus exposed to the cytosol. Characteristic for PEX13 is an N-terminal part containing a proline-rich region, often with a KWPE motif, followed by a glycine-rich segment with many Tyr-Gly motifs. The C-terminal half contains two membrane-spanning helices, followed by a SH3 domain in the peroxin of yeasts and animal; this domain is absent from plant PEX13. Curiously, in trypanosomatid glycosomes two PEX13 isoforms, PEX13.1 and PEX13.2, are present; strikingly, both share very low sequence identity with the single PEX13 identified in peroxisomes of other taxa (7–18% identity). They also differ markedly between each other (11–16% identity) (Verplaetse et al., 2009; Brennand et al., 2012; Verplaetse et al., 2012). PEX13.1 contains the Tyr-Gly motifs and SH3 domain, but is unusual because it lacks the proline-rich region near the N-terminus and has a typical PTS1-like motif (-TKL, conserved in the TriTryps parasites) at its cytosolically exposed C-terminus, not found in any other PEX13. In contrast, PEX13.2 possesses a proline-rich region with a RPWE motif and a Tyr-Gly motif containing glycine-rich segment, but no SH3 domain. Both PEX13 proteins were located in the *T. brucei* docking complex, where they interact with each other and with PEX14 (Verplaetse et al., 2012; Crowe et al., 2020).

PEX13.1 sequences were detected in the databases for representatives of all kinetoplastid groups, but not for diplonemids and euglenids (Supplementary Figure S10). The unique features detected in the *T. brucei* peroxin are generally present, despite high sequence diversity. In contrast, potential PEX13.2 sequences were found for kinetoplastids and euglenids (*E. gracilis*, *E. longa* and *R. costata*) (Supplementary Figure S11). Like PEX13.1, characteristic features identified previously for the *T. brucei* peroxin are conserved despite high sequence variation. Together, the data indicate this peroxin was realistically already present in the common ancestor of the Euglenozoa. It remains to be determined when this protein originated. We did not detect a homologue in the databases of *Naegleria* species.

PEX19 is a cytosolic peroxin that functions as receptor and chaperone of peroxisomal membrane proteins (PMPs). PEX19, complexed with a PMP synthesised in the cytosol, docks at the peroxisomal membrane at PEX3, followed by membrane insertion. The N-terminal part of PEX19 contains binding sites for PEX3 and/or PEX14, whereas PMP binding occurs at the C-terminal domain. Furthermore, PEX19 proteins previously studied contain a CaaX motif for farnesylation near the C-terminus. Farnesylation is required for PEX19 structural integrity and its recognition of PMPs (Rucktäschel et al., 2009; Emmanouilidis et al., 2017). Curiously, trypanosomatid PEX19 lacks the motif for posttranslational modification that plays such an important role in peroxisome biogenesis in other organisms (Banerjee et al., 2005; Yernaux et al., 2006).

Putative PEX19 sequences were detected in most kinetoplastids and some euglenids and *Naegleria* species, but not in diplonemids (Supplementary Figure S12). These PEX19 candidates show considerable sequence variation. Importantly, the C-terminal CaaX farnesylation motif is absent in all euglenozoans, but is present in PEX19 from *Naegleria*. How euglenozoan PEX19 functions without apparent farnesylation remains to be determined.

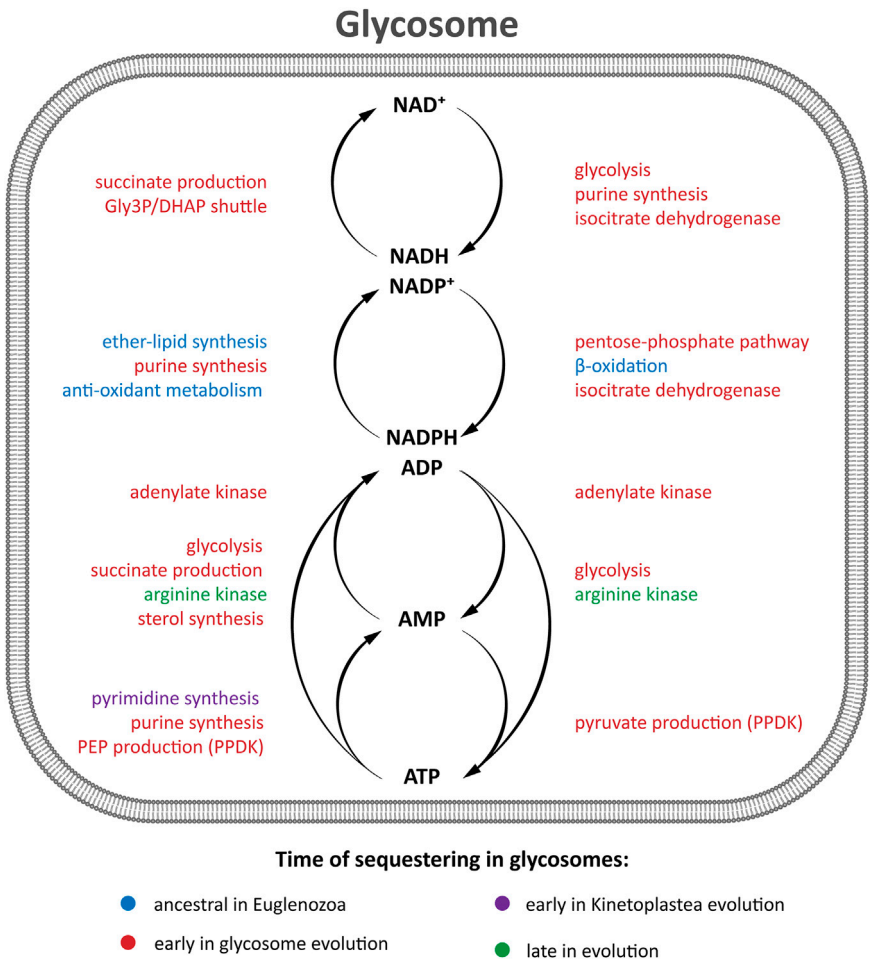

FIGURE 8
Glycosomal homeostasis of cofactors. Glycosomes harbour a pool of adenine nucleotides and nicotinamide-adenine nucleotides, separate from the cytosolic pool, that is involved in various branches of glycosomal catabolism and anabolism. The presence or absence of PTS motifs suggests that enzymes of the metabolic processes listed in the figure were sequestered at different stages in the evolution of glycosomes: already present in peroxisomes of ancestral organisms (blue); sequestered within glycosomes during or shortly after the origin of these organelles from peroxisomes (red); sequestered only in kinetoplastids at an early stage (mauve); sequestered late in glycosomes of some taxa (green). However, it should be noted that specific enzymes of some processes mentioned in the figure were not compartmentalised or even lost from all or certain taxa, as described in the text.

Discussion: Reconciling bioinformatics observations with a 'how' and 'why' of glycosome evolution

Combining literature survey with bioinformatic predictions of presence or absence of PTS motifs, we refine a timeline for how metabolically complex glycosomes evolved in Euglenozoa. Availability of much sequence data for diverse discoban protists allows us to add considerable depth to a timeline offered by Gualdrón-López et al. (2012a). Recently, Durrani et al. (2020) reported a similar global bioinformatics approach. Caveats associated with estimating peroxisome localisation on a basis of detecting PTS motifs must be acknowledged: many peroxisomal and glycosomal proteins do not possess consensus PTS motifs; proteins with a PTS are often not detected in these organelles but elsewhere in a cell; and Güther et al. (2014), analysing the high-confidence proteome of epitope-tagged enriched glycosomes of PCF *T. brucei*, concluded use of PTS sequence searches in *T. brucei* has a sensitivity of <40% and a specificity of <50%.

In part, the efficiency with which PTS1 motifs are recognised as determinants for peroxisome targeting is influenced by the identity of amino acid residues immediately adjacent to a PTS motif (Brocard and Hartig, 2006). Yet, the frequency of dual protein localisation within peroxisomes and cytosol in many eukaryotes together with the wide range of PTS motifs known to confer organelle targeting (Sommer et al., 1992; Freitag et al., 2018; Kunze, 2020), often in

TABLE 1 Outstanding questions about glycosome evolution.

- Do free-living kinetoplastids and diplonemids alter their glycosomal enzyme content when they encounter environmental changes? If so, then does pexophagy play a role?
- Why is PFK evolution so complex in Euglenozoa? What was (were) the evolutionary driver(s) for acquisition and losses of glycosomal PFKs with different phospho donor specificity (i.e. ATP versus PPi)?
- What explains the isoform complexity of PFK families in different diplonemids?
- Is an acyl-CoA oxidase or acyl-CoA dehydrogenase involved in glycosomal fatty-acid β-oxidation? Has use of these enzymes swapped around during glycosome evolution?
- Looking beyond proposed ecological advantages, did peroxin divergence or another biochemical trait influence large-scale re-compartmentalisation of carbohydrate metabolism in diplonemids and kinetoplastids?
- Why did the very divergent PEX13.2 paralogue evolve?
- Why is absence of PEX19 farnesylation not a problem for glycosome biogenesis or integrity?
- What evolutionary and functional advantages are provided by two highly divergent members of the PEX11 family, GIM5A and GIM5B?
- Does glycosomal master regulator PIP39 play a role in the developmental differentiation of other euglenozoans? How did its role in trypanosome differentiation evolve?
- Are peroxisomes or glycosomes present in Symbiotida, the enigmatic, fourth lineage of Euglenozoa?

heterologous systems, argue strongly for the value inherent in estimating peroxisome localisation from PTS motif conservation in related eukaryotes. Indeed, minimal simplicity of C-terminal tripeptide or N-terminal nonapeptide motifs, often without absolute requirement for amino acid specificity in order to confer some degree of organelle targeting, is readily compatible with Martin's view that metabolic pathways could easily be rerouted in organisms whenever inevitable minor mis-targeting of proteins provides a small selective advantage; protein mis-targeting happens often in eukaryotic cells (Martin, 2010). Conversely, free passage of metabolites <400 Da across glycosomal membranes (Quiñones et al., 2020; Michels and Gualdrón-López, 2022) suggests 'hard-wiring' organelle re-routed cytosolic pathways is not necessarily readily achieved, thereby explaining a sometimes patchwork conservation of PTS motifs observed in some euglenozoan enzymes, as indicated in Supplementary Tables S1 and S2. In this work, we also dated divergence of trypanosomatid peroxins to an early point in euglenozoan evolution. Provocatively, divergence of a broadly conserved peroxisome biogenesis machinery may have helped cement transitions from 'mis-targeting' to 're-compartmentalisation' for enzymes and processes that with rare exception are cytosolic in other eukaryotes.

Possible selective advantage(s) obtained by sequestering glycolytic enzymes within peroxisomes has often been addressed since the serendipitous discovery of glycosomes in experimentally tractable tropical disease parasites during the 1970s. Initially, compartmentalisation was considered to sustain high glycolytic flux (Borst, 1986; Opperdoes, 1987; Borst, 1989; Michels and Opperdoes, 1991) or physically separate opposing pathways as an alternative to activity regulation, thereby avoiding futile cycling (Michels and Hannaert, 1994). Such hypotheses have been discarded (reviewed by Gualdrón-López et al., 2012a), but a role for pexophagy–the turnover 'en masse' of whole peroxisomes enabling rapid, extensive metabolic reprogramming–remains highly relevant to theorizing about glycosome origin and evolution. We argued earlier in this work that free-living ancestral euglenozoans plausibly lived in dynamic conditions where ability to turnover a major part of carbohydrate metabolic network quickly conceivably provided key selective advantage. Moreover, massive glycosome turnover involving pexophagy occurs during differentiation of extant trypanosomatids and is potentially key to their success as parasites (Herman et al., 2008; Cull et al., 2014).

Besides endowing cells efficient adaptation to changing conditions, development of glycosomes may have provided other or additional selective advantage. They contain enzymes to catalyse reactions involving ATP, NADH, and NADPH (Figure 8). Strikingly, use and production of each of these cofactors seems in balance within glycosomes (Opperdoes and Borst, 1977; Bakker et al., 1997); the membrane is not permeable for these bulky molecules and there are no indications for their transport across the membrane at a rate commensurate with the metabolic fluxes through the organelles. Glycosomes thus create separate compartments with their own redox state (ratios of $NADH/NAD^+$ and $NADPH/NADP^+$) and ATP/ADP ratio different from that in cytosol and mitochondrion, thus providing the cell more metabolic flexibility. Similar reasoning has been offered to explain the unexpected dual localisation in peroxisome and cytosol of enzymes from the central part of glycolysis in several fungi; here, iso-enzyme targeting is achieved through cryptic PTS motifs made available from alternative splicing or translation stop-codon read-through of RNA encoding cytosolic triose-phosphate isomerase, GAPDH, and/or PGK (Freitag et al., 2012). Of course, crosstalk occurs between different compartments by the exchange of metabolites–including substrates and products of enzymes using the cofactors, but the redox state and ATP/ADP ratios will differ as demonstrated *in silico* for *T. brucei* using realistic kinetic models (Bakker et al., 1997; Bakker et al., 2000).

A major revelation from the *in silico* analysis we report here is that much of the metabolic complexity evident in trypanosomatid glycosomes was already established prior to the divergence of a last common ancestor of diplonemids and kinetoplastids. During subsequent evolution of both lineages only relatively minor embellishments and alterations to this complexity occurred (Figure 8). Strikingly, H_2O_2 metabolism in glycosomes also appears more prominent than previously

thought. Atypical localisation of ubiquitous cytosolic enzymes to peroxisomes is not evident in either euglenids or the closest distant relations of the Euglenozoa for which relevant genome data is available (*Naegleria* spp.).

Looking forwards, gene and candidate PTS motif inventories archived in Supplementary Tables S1 and S2 provide foundations for experimental interrogation of evolutionary scenarios we have discussed. Critically, our interpretation of the data is compatible with two phenomena we consider key in glycosome evolution: turnover of organelles by pexophagy and permeability of peroxisome and glycosome membranes to metabolites <400 Da. Finally, parallels and divergence between glycosome evolution and the establishment of different atypical peroxisomes in other eukaryotes–*e.g.* peroxisomes in methylotrophic yeasts, woronin bodies in filamentous fungi, glyoxysomes in plants, recently discovered anaerobic peroxisomes in anaerobic amoebae (Le et al., 2020; Verner et al., 2021) – provide other avenues for further discussion and experimentation. Many outstanding questions about glycosomes have recently been discussed by Michels and Gualdrón-López (2022). Additional questions that speak to the evolution of these organelles and could be addressed experimentally are listed in Table 1.

Data availability statement

The original contributions presented in the study are included in the article/Supplementary Material, further inquiries can be directed to the corresponding author.

Author contributions

DA-A, AB B, AC, and WQ conducted all bioinformatics studies and AC performed the phylogenetic analyses. PM analysed the results. AC, WQ, MG-L, MG and PM have previously been involved in experimental research that provided many published data used in the current analysis. All authors discussed frequently results, ideas and progress of the project, and made contributions to the preparation of the manuscript for which DA-A prepared the figures. PM conceived the project and, together with MG prepared the final version of the manuscript that was approved by all authors.

Conflict of interest

The authors declare that the research was conducted in the absence of any commercial or financial relationships that could be construed as a potential conflict of interest.

The reviewer RR declared a shared affiliation with the author MG-L to the handling editor at the time of review.

Publisher's note

All claims expressed in this article are solely those of the authors and do not necessarily represent those of their affiliated organizations, or those of the publisher, the editors and the reviewers. Any product that may be evaluated in this article, or claim that may be made by its manufacturer, is not guaranteed or endorsed by the publisher.

Supplementary Material

The Supplementary Material for this article can be found online at: https://www.frontiersin.org/articles/10.3389/fcell.2022.979269/full#supplementary-material

References

Acosta, H., Burchmore, R., Naula, C., Gualdrón-López, M., Quintero-Troconis, E., Cáceres, A. J., et al. (2019). Proteomic analysis of glycosomes from Trypanosoma cruzi epimastigotes. *Mol. Biochem. Parasitol.* 229, 62–74. doi:10.1016/j.molbiopara.2019.02.008

Adl, S. M., Bass, D., Lane, C. E., Lukeš, J., Schoch, C. L., Smirnov, A., et al. (2019). Revisions to the classification, nomenclature, and diversity of eukaryotes. *J. Eukaryot. Microbiol.* 66 (1), 4–119. doi:10.1111/jeu.12691

Allmann, S., and Bringaud, F. (2017). Glycosomes: A comprehensive view of their metabolic roles in T. brucei. *Int. J. Biochem. Cell Biol.* 85, 85–90. doi:10.1016/j.biocel.2017.01.015

Antonenkov, V. D., and Hiltunen, J. K. (2012). Transfer of metabolites across the peroxisomal membrane. *Biochim. Biophys. Acta* 1822 (9), 1374–1386. doi:10.1016/j.bbadis.2011.12.011

Ardelli, B. F., Witt, J. D., and Woo, P. T. (2000). Identification of glycosomes and metabolic end products in pathogenic and nonpathogenic strains of Cryptobia salmositica (Kinetoplastida: Bodonidae). *Dis. Aquat. Organ.* 42 (1), 41–51. doi:10.3354/dao042041

Atwood, J. A., 3rd, Weatherly, D. B., Minning, T. A., Bundy, B., Cavola, C., Opperdoes, F. R., et al. (2005). The Trypanosoma cruzi proteome. *Science* 309 (5733), 473–476. doi:10.1126/science.1110289

Bakker, B. M., Mensonides, F. I., Teusink, B., Van Hoek, P., Michels, P. A. M., and Westerhoff, H. V. (2000). Compartmentation protects trypanosomes from the dangerous design of glycolysis. *Proc. Natl. Acad. Sci. U. S. A.* 97 (5), 2087–2092. doi:10.1073/pnas.030539197

Bakker, B. M., Michels, P. A. M., Opperdoes, F. R., and Westerhoff, H. V. (1997). Glycolysis in bloodstream form Trypanosoma brucei can be understood in terms of the kinetics of the glycolytic enzymes. *J. Biol. Chem.* 272 (6), 3207–3215. doi:10.1074/jbc.272.6.3207

Banerjee, H., Knoblach, B., and Rachubinski, R. A. (2019). The early-acting glycosome biogenic protein Pex3 is essential for trypanosome viability. *Life Sci. Alliance* 2 (4), e201900421. doi:10.26508/lsa.201900421

Banerjee, S. K., Kessler, P. S., Saveria, T., and Parsons, M. (2005). Identification of trypanosomatid PEX19: Functional characterization reveals impact on cell growth and glycosome size and number. *Mol. Biochem. Parasitol.* 142 (1), 47–55. doi:10.1016/j.molbiopara.2005.03.008

Bapteste, E., Moreira, D., and Philippe, H. (2003). Rampant horizontal gene transfer and phospho-donor change in the evolution of the phosphofructokinase. *Gene* 18, 185–191. doi:10.1016/s0378-1119(03)00797-2

Bauer, S., and Morris, M. T. (2017). Glycosome biogenesis in trypanosomes and the de novo dilemma. *PLoS Negl. Trop. Dis.* 11 (4), e0005333. doi:10.1371/journal.pntd.0005333

Boitz, J. M., Ullman, B., Jardim, A., and Carter, N. S. (2012). Purine salvage in Leishmania: Complex or simple by design? *Trends Parasitol.* 28 (8), 345–352. doi:10.1016/j.pt.2012.05.005

Borst, P. (1986). How proteins get into microbodies (peroxisomes, glyoxysomes, glycosomes). *Biochim. Biophys. Acta* 866 (4), 179–203. doi:10.1016/0167-4781(86)90044-8

Borst, P. (1989). Peroxisome biogenesis revisited. *Biochim. Biophys. Acta* 1008 (1), 1–13. doi:10.1016/0167-4781(89)90163-2

Braverman, N., Dodt, G., Gould, S. J., and Valle, D. (1998). An isoform of pex5p, the human PTS1 receptor, is required for the import of PTS2 proteins into peroxisomes. *Hum. Mol. Genet.* 7 (8), 1195–1205. doi:10.1093/hmg/7.8.1195

Brenchley, R., Tariq, H., McElhinney, H., Szöőr, B., Huxley-Jones, J., Stevens, R., et al. (2007). The TriTryp phosphatome: Analysis of the protein phosphatase catalytic domains. *BMC Genomics* 8, 434. doi:10.1186/1471-2164-8-434

Brennand, A., Rigden, D. J., and Michels, P. A. M. (2012). Trypanosomes contain two highly different isoforms of peroxin PEX13 involved in glycosome biogenesis. *FEBS Lett.* 586 (13), 1765–1771. doi:10.1016/j.febslet.2012.05.019

Brocard, C., and Hartig, A. (2006). Peroxisome targeting signal 1: Is it really a simple tripeptide? *Biochim. Biophys. Acta* 1763 (12), 1565–1573. doi:10.1016/j.bbamcr.2006.08.022

Burki, F., Roger, A. J., Brown, M. W., and Simpson, A. G. B. (2020). The new tree of eukaryotes. *Trends Ecol. Evol.* 35 (1), 43–55. doi:10.1016/j.tree.2019.08.008

Butenko, A., Opperdoes, F. R., Flegontova, O., Horák, A., Hampl, V., Keeling, P., et al. (2020). Evolution of metabolic capabilities and molecular features of diplonemids, kinetoplastids, and euglenids. *BMC Biol.* 18 (1), 23. doi:10.1186/s12915-020-0754-1

Cáceres, A. J., Quiñones, W., Gualdrón, M., Cordeiro, A., Avilán, L., Michels, P. A. M., et al. (2007). Molecular and biochemical characterization of novel glucokinases from Trypanosoma cruzi and Leishmania spp. *Mol. Biochem. Parasitol.* 156 (2), 235–245. doi:10.1016/j.molbiopara.2007.08.007

Camões, F., Islinger, M., Guimarães, S. C., Kilaru, S., Schuster, M., Godinho, L. F., et al. (2015). New insights into the peroxisomal protein inventory: Acyl-CoA oxidases and -dehydrogenases are an ancient feature of peroxisomes. *Biochim. Biophys. Acta* 1853 (1), 111–125. doi:10.1016/j.bbamcr.2014.10.005

Canepa, G. E., Carrillo, C., Miranda, M. R., Sayé, M., and Pereira, C. A. (2011). Arginine kinase in Phytomonas, a trypanosomatid parasite of plants. *Comp. Biochem. Physiol. B Biochem. Mol. Biol.* 160 (1), 40–43. doi:10.1016/j.cbpb.2011.05.006

Chi, A., and Kemp, R. G. (2000). The primordial high energy compound: ATP or inorganic pyrophosphate? *J. Biol. Chem.* 275 (46), 35677–35679. doi:10.1074/jbc.C000581200

Choe, J., Moyersoen, J., Roach, C., Carter, T. L., Fan, E., Michels, P. A. M., et al. (2003). Analysis of the sequence motifs responsible for the interactions of peroxins 14 and 5, which are involved in glycosome biogenesis in Trypanosoma brucei. *Biochemistry* 42 (37), 10915–10922. doi:10.1021/bi034248n

Chornyi, S., IJlst, L., Van Roermund, C. W. T., Wanders, R. J. A., and Waterham, H. R. (2021). Peroxisomal metabolite and cofactor transport in humans. *Front. Cell Dev. Biol.* 8, 613892. doi:10.3389/fcell.2020.613892

Colasante, C., Ellis, M., Ruppert, T., and Voncken, F. (2006). Comparative proteomics of glycosomes from bloodstream form and procyclic culture form Trypanosoma brucei brucei. *Proteomics* 6 (11), 3275–3293. doi:10.1002/pmic.200500668

Colasante, C., Voncken, F., Manful, T., Ruppert, T., Tielens, A. G. M., Van Hellemond, J. J., et al. (2013F1000). Proteins and lipids of glycosomal membranes from Leishmania tarentolae and Trypanosoma brucei. *F1000Res.* 2, 27. doi:10.12688/f1000research.2-27.v1

Concepción, J. L., Gonzalez-Pacanowska, D., and Urbina, J. A. (1998). 3-Hydroxy-3-methyl-glutaryl-CoA reductase in trypanosoma (schizotrypanum) cruzi: Subcellular localization and kinetic properties. *Arch. Biochem. Biophys.* 352 (1), 114–120. doi:10.1006/abbi.1998.0577

Cordeiro, A. T., Cáceres, A. J., Vertommen, D., Concepción, J. L., Michels, P. A. M., and Versées, W. (2007). The crystal structure of Trypanosoma cruzi glucokinase reveals features determining oligomerization and anomer specificity of hexose-phosphorylating enzymes. *J. Mol. Biol.* 372 (5), 1215–1226. doi:10.1016/j.jmb.2007.07.021

Cordeiro, C. D., Ahmed, M. A., Windle, B., and Docampo, R. (2019). NUDIX hydrolases with inorganic polyphosphate exo- and endopolyphosphatase activities in the glycosome, cytosol and nucleus of Trypanosoma brucei. *Biosci. Rep.* 39 (5), BSR20190894. doi:10.1042/BSR20190894

Coustou, V., Biran, M., Besteiro, S., Rivière, L., Baltz, T., Franconi, J. M., et al. (2006). Fumarate is an essential intermediary metabolite produced by the procyclic Trypanosoma brucei. *J. Biol. Chem.* 281 (37), 26832–26846. doi:10.1074/jbc.M601377200

Crowe, L. P., Wilkinson, C. L., Nicholson, K. R., and Morris, M. T. (2020). Trypanosoma brucei Pex13.2 is an accessory peroxin that functions in the import of peroxisome targeting sequence type 2 proteins and localizes to subdomains of the glycosome. *mSphere* 5 (1), e00744–19. doi:10.1128/mSphere.00744-19

Cull, B., Prado Godinho, J. L., Fernandes Rodrigues, J. C., Frank, B., Schurigt, U., Williams, R. A., et al. (2014). Glycosome turnover in Leishmania major is mediated by autophagy. *Autophagy* 10 (12), 2143–2157. doi:10.4161/auto.36438

Dodt, G., Warren, D., Becker, E., Rehling, P., and Gould, S. J. (2001). Domain mapping of human PEX5 reveals functional and structural similarities to Saccharomyces cerevisiae Pex18p and Pex21p. *J. Biol. Chem.* 276 (45), 41769–41781. doi:10.1074/jbc.M106932200

Dufernez, F., Yernaux, C., Gerbod, D., Noël, C., Chauvenet, M., Wintjens, R., et al. (2006). The presence of four iron-containing superoxide dismutase isozymes in trypanosomatidae: Characterization, subcellular localization, and phylogenetic origin in trypanosoma brucei. *Free Radic. Biol. Med.* 40 (2), 210–225. doi:10.1016/j.freeradbiomed.2005.06.021

Durrani, H., Hampton, M., Rumbley, J. N., and Zimmer, S. L. (2020). A global analysis of enzyme compartmentalization to glycosomes. *Pathogens* 9 (4), 281. doi:10.3390/pathogens9040281

Einwächter, H., Sowinski, S., Kunau, W. H., and Schliebs, W. (2001). Yarrowia lipolytica Pex20p, Saccharomyces cerevisiae Pex18p/Pex21p and mammalian Pex5pL fulfil a common function in the early steps of the peroxisomal PTS2 import pathway. *EMBO Rep.* 2 (11), 1035–1039. doi:10.1093/embo-reports/kve228

El-Sayed, N. M., Myler, P. J., Blandin, G., Berriman, M., Crabtree, J., Aggarwal, G., et al. (2005). Comparative genomics of trypanosomatid parasitic protozoa. *Science* 309 (5733), 404–409. doi:10.1126/science.1112181

Emmanouilidis, L., Schütz, U., Tripsianes, K., Madl, T., Radke, J., Rucktäschel, R., et al. (2017). Allosteric modulation of peroxisomal membrane protein recognition by farnesylation of the peroxisomal import receptor PEX19. *Nat. Commun.* 8, 14635. doi:10.1038/ncomms14635

Felsenstein, J. (1985). Confidence limits on phylogenies: An approach using the bootstrap. *Evolution* 39 (4), 783–791. doi:10.1111/j.1558-5646.1985.tb00420.x

Fernandes, P. M., Kinkead, J., McNae, I. W., Bringaud, F., Michels, P. A. M., and Walkinshaw, M. D. (2019). The kinetic characteristics of human and trypanosomatid phosphofructokinases for the reverse reaction. *Biochem. J.* 476 (2), 179–191. doi:10.1042/BCJ20180635

Field, M. C., Horn, D., Fairlamb, A. H., Ferguson, M. A., Gray, D. W., Read, K. D., et al. (2017). Anti-trypanosomatid drug discovery: An ongoing challenge and a continuing need. *Nat. Rev. Microbiol.* 15 (4), 217–231. doi:10.1038/nrmicro.2016.193

Flegontova, O., Flegontov, P., Londoño, P. A. C., Walczowski, W., ŠantiŮ, D., Edgcomb, V. P., et al. (2020). Environmental determinants of the distribution of planktonic diplonemids and kinetoplastids in the oceans. *Environ. Microbiol.* 22 (9), 4014–4031. doi:10.1111/1462-2920.15190

Freitag, J., Ast, J., and Bölker, M. (2012). Cryptic peroxisomal targeting via alternative splicing and stop codon read-through in fungi. *Nature* 485, 522–525. doi:10.1038/nature11051

Freitag, J., Stehlik, T., Stiebler, A. C., and Bölker, M. (2018). The obvious and the hidden: Prediction and function of fungal peroxisomal matrix proteins. *Subcell. Biochem.* 89, 139–155. doi:10.1007/978-981-13-2233-4_6

Gabaldón, T., Ginger, M. L., and Michels, P. A. M. (2016). Peroxisomes in parasitic protists. *Mol. Biochem. Parasitol.* 209 (1-2), 35–45. doi:10.1016/j.molbiopara.2016.02.005

Galland, N., Demeure, F., Hannaert, V., Verplaetse, E., Vertommen, D., Van der Smissen, P., et al. (2007). Characterization of the role of the receptors PEX5 and PEX7 in the import of proteins into glycosomes of Trypanosoma brucei. *Biochim. Biophys. Acta* 1773, 521–535. doi:10.1016/j.bbamcr.2007.01.006

Galland, N., and Michels, P. A. M. (2010). Comparison of the peroxisomal matrix protein import system of different organisms. Exploration of possibilities for developing inhibitors of the import system of trypanosomatids for anti-parasite chemotherapy. *Eur. J. Cell Biol.* 89, 621–637. doi:10.1016/j.ejcb.2010.04.001

Gao, G., Nara, T., Nakajima-Shimada, J., and Aoki, T. (1999). Novel organization and sequences of five genes encoding all six enzymes for de novo pyrimidine biosynthesis in Trypanosoma cruzi. *J. Mol. Biol.* 285 (1), 149–161. doi:10.1006/jmbi.1998.2293

Gatto, G. J., Jr., Geisbrecht, B. V., Gould, S. J., and Berg, J. M. (2000). Peroxisomal targeting signal-1 recognition by the TPR domains of human PEX5. *Nat. Struct. Biol.* 7 (12), 1091–1095. doi:10.1038/81930

Ginger, M. L., Ngazoa, E. S., Pereira, C. A., Pullen, T. J., Kabiri, M., Becker, K., et al. (2005). Intracellular positioning of isoforms explains an unusually large adenylatekinase gene family in the parasite Trypanosoma brucei. *J. Biol. Chem.* 280 (12), 11781–11789. doi:10.1074/jbc.M413821200

Giordana, L., and Nowicki, C. (2020). Two phylogenetically divergent isocitrate dehydrogenases are encoded in Leishmania parasites. Molecular and functional characterization of Leishmania mexicana isoenzymes with specificity towards NAD+ and NADP. *Mol. Biochem. Parasitol.* 240, 111320. doi:10.1016/j.molbiopara.2020.111320

Giordani, F., Morrison, L. J., Rowan, T. G., De Koning, H. P., and Barrett, M. P. (2016). The animal trypanosomiases and their chemotherapy: A review. *Parasitology* 143 (14), 1862–1889. doi:10.1017/S0031182016001268

Glockzin, K., Meek, T. D., and Katzfuss, A. (2022). Characterization of adenine phosphoribosyltransferase (APRT) activity in Trypanosoma brucei brucei: Only one of the two isoforms is kinetically active. *PLoS Negl. Trop. Dis.* 16 (2), e0009926. doi:10.1371/journal.pntd.0009926

Gonzalez, S. N., Valsecchi, W. M., Maugeri, D., Delfino, J. M., and Cazzulo, J. J. (2017). Structure, kinetic characterization and subcellular localization of the two ribulose 5-phosphate epimerase isoenzymes from Trypanosoma cruzi. *PLoS One* 12 (2), e0172405. doi:10.1371/journal.pone.0172405

González-Robles, A., González-Lázaro, M., Lagunes-Guillén, A. E., Omaña-Molina, M., Lares-Jiménez, L. F., Lares-Villa, F., et al. (2020). Ultrastructural, cytochemical, and comparative genomic evidence of peroxisomes in three genera of pathogenic free-living amoebae, including the first morphological data for the presence of this organelle in heteroloboseans. *Genome Biol. Evol.* 12 (10), 1734–1750. doi:10.1093/gbe/evaa129

Gualdrón-López, M., Brennand, A., Hannaert, V., Quiñones, W., Cáceres, A. J., Bringaud, F., et al. (2012a). When, how and why glycolysis became compartmentalised in the Kinetoplastea. A new look at an ancient organelle. *Int. J. Parasitol.* 42 (1), 1–20. doi:10.1016/j.ijpara.2011.10.007

Gualdrón-López, M., Vapola, M. H., Miinalainen, I. J., Hiltunen, J. K., Michels, P. A. M., and Antonenkov, V. D. (2012b). Channel-forming activities in the glycosomal fraction from the bloodstream form of Trypanosoma brucei. *PLoS One* 7 (4), e34530. doi:10.1371/journal.pone.0034530

Güther, M. L., Urbaniak, M. D., Tavendale, A., Prescott, A., and Ferguson, M. A. (2014). High-confidence glycosome proteome for procyclic form Trypanosoma brucei by epitope-tag organelle enrichment and SILAC proteomics. *J. Proteome Res.* 13 (6), 2796–2806. doi:10.1021/pr401209w

Gutteridge, W. E., Ross, J., Hargadon, M. R., and Hudson, J. E. (1982). Crithidia fasciculata: A catalase-containing trypanosomatid sensitive to nitroheterocyclic drugs. *Trans. R. Soc. Trop. Med. Hyg.* 76 (4), 493–496. doi:10.1016/0035-9203(82)90146-8

Haanstra, J. R., González-Marcano, E. B., Gualdrón-López, M., and Michels, P. A. M. (2016). Biogenesis, maintenance and dynamics of glycosomes in trypanosomatid parasites. *Biochim. Biophys. Acta* 1863 (5), 1038–1048. doi:10.1016/j.bbamcr.2015.09.015

Hammond, D. J., Gutteridge, W. E., and Opperdoes, F. R. (1981). A novel location for two enzymes of de novo pyrimidine biosynthesis in trypanosomes and Leishmania. *FEBS Lett.* 128 (1), 27–29. doi:10.1016/0014-5793(81)81070-8

Hammond, D. J., and Gutteridge, W. E. (1982). UMP synthesis in the Kinetoplastida. *Biochim. Biophys. Acta* 718 (1), 1–10. doi:10.1016/0304-4165(82)90002-2

Hannaert, V., Bringaud, F., Opperdoes, F. R., and Michels, P. A. M. (2003b). Evolution of energy metabolism and its compartmentation in Kinetoplastida. *Kinetoplastid Biol. Dis.* 2 (1), 11. doi:10.1186/1475-9292-2-11

Hannaert, V., Saavedra, E., Duffieux, F., Szikora, J. P., Rigden, D. J., Michels, P. A. M., et al. (2003a). Plant-like traits associated with metabolism of Trypanosoma parasites. *Proc. Natl. Acad. Sci. U. S. A.* 100 (3), 1067–1071. doi:10.1073/pnas.0335769100

Harijan, R. K., Mazet, M., Kiema, T. R., Bouyssou, G., Alexson, S. E., Bergmann, U., et al. (2016). The SCP2-thiolase-like protein (SLP) of Trypanosoma brucei is an enzyme involved in lipid metabolism. *Proteins* 84 (8), 1075–1096. doi:10.1002/prot.25054

Hart, D. T., Misset, O., Edwards, S. W., and Opperdoes, F. R. (1984). A comparison of the glycosomes (microbodies) isolated from Trypanosoma brucei bloodstream form and cultured procyclic trypomastigotes. *Mol. Biochem. Parasitol.* 12 (1), 25–35. doi:10.1016/0166-6851(84)90041-0

Hart, D. T., and Opperdoes, F. R. (1984). The occurrence of glycosomes (microbodies) in the promastigote stage of four major Leishmania species. *Mol. Biochem. Parasitol.* 13 (2), 159–172. doi:10.1016/0166-6851(84)90110-5

Heise, N., and Opperdoes, F. R. (1999). Purification, localisation and characterisation of glucose-6-phosphate dehydrogenase of Trypanosoma brucei. *Mol. Biochem. Parasitol.* 99 (1), 21–32. doi:10.1016/s0166-6851(98)00176-5

Hendrickson, N., Allen, T., and Ullman, B. (1993). Molecular characterization of phosphoribosylpyrophosphate synthetase from Leishmania donovani. *Mol. Biochem. Parasitol.* 59 (1), 15–27. doi:10.1016/0166-6851(93)90003-g

Herman, M., Pérez-Morga, D., Schtickzelle, N., and Michels, P. A. M. (2008). Turnover of glycosomes during life-cycle differentiation of Trypanosoma brucei. *Autophagy* 4 (3), 294–308. doi:10.4161/auto.5443

Holland, H. D. (2006). The oxygenation of the atmosphere and oceans. *Philos. Trans. R. Soc. Lond. B Biol. Sci.* 361 (1470), 903–915. doi:10.1098/rstb.2006.1838

Igoillo-Esteve, M., Mazet, M., Deumer, G., Wallemacq, P., and Michels, P. A. M. (2011). Glycosomal ABC transporters of trypanosoma brucei: Characterisation of their expression, topology and substrate specificity. *Int. J. Parasitol.* 41 (3-4), 429–438. doi:10.1016/j.ijpara.2010.11.002

Irigoín, F., Cibils, L., Comini, M. A., Wilkinson, S. R., Flohé, L., and Radi, R. (2008). Insights into the redox biology of Trypanosoma cruzi: Trypanothione metabolism and oxidant detoxification. *Free Radic. Biol. Med.* 45 (6), 733–742. doi:10.1016/j.freeradbiomed.2008.05.028

Jansen, R. L. M., Santana-Molina, C., Van den Noort, M., Devos, D. P., and Van der Klei, I. J. (2021). Comparative genomics of peroxisome biogenesis proteins: Making sense of the PEX proteins. *Front. Cell Dev. Biol.* 9, 654163. doi:10.3389/fcell.2021.654163

Jardim, A., Bergeson, S. E., Shih, S., Carter, N., Lucas, R. W., Merlin, G., et al. (1999). Xanthine phosphoribosyltransferase from Leishmania donovani. Molecular cloning, biochemical characterization, and genetic analysis. *J. Biol. Chem.* 274 (48), 34403–34410. doi:10.1074/jbc.274.48.34403

Jaskowska, E., Butler, C., Preston, G., and Kelly, S. (2015). Phytomonas: Trypanosomatids adapted to plant environments. *PLoS Pathog.* 11 (1), e1004484. doi:10.1371/journal.ppat.1004484

Jones, D. T., Taylor, W. R., and Thornton, J. M. (1992). The rapid generation of mutation data matrices from protein sequences. *Comput. Appl. Biosci.* 8 (3), 275–282. doi:10.1093/bioinformatics/8.3.275

Kalel, V. C., and Erdmann, R. (2018). Unraveling of the structure and function of peroxisomal protein import machineries. *Subcell. Biochem.* 89, 299–321. doi:10.1007/978-981-13-2233-4_13

Kalel, V. C., Li, M., Gaussmann, S., Delhommel, F., Schäfer, A. B., Tippler, B., et al. (2019). Evolutionary divergent PEX3 is essential for glycosome biogenesis and survival of trypanosomatid parasites. *Biochim. Biophys. Acta. Mol. Cell Res.* 1866 (12), 118520. doi:10.1016/j.bbamcr.2019.07.015

Kim, J. J., and Miura, R. (2004). Acyl-CoA dehydrogenases and acyl-CoA oxidases. Structural basis for mechanistic similarities and differences. *Eur. J. Biochem.* 271 (3), 483–493. doi:10.1046/j.1432-1033.2003.03948.x

Kostygov, A. Y., Karnkowska, A., Votýpka, J., Tashyreva, D., Maciszewski, K., Yurchenko, V., et al. (2021). Euglenozoa: Taxonomy, diversity and ecology, symbioses and viruses. *Open Biol.* 11 (3), 200407. doi:10.1098/rsob.200407

Kovářová, J., and Barrett, M. P. (2016). The pentose phosphate pathway in parasitic trypanosomatids. *Trends Parasitol.* 32 (8), 622–634. doi:10.1016/j.pt.2016.04.010

Kumar, S., Stecher, G., Li, M., Knyaz, C., and Tamura, K. (2018). Mega X: Molecular evolutionary genetics analysis across computing platforms. *Mol. Biol. Evol.* 35 (6), 1547–1549. doi:10.1093/molbev/msy096

Kunze, M. (2020). The type-2 peroxisomal targeting signal. *Biochim. Biophys. Acta. Mol. Cell Res.* 1867 (2), 118609. doi:10.1016/j.bbamcr.2019.118609

Lax, G., Kolisko, M., Eglit, Y., Lee, W. J., Yubuki, N., Karnkowska, A., et al. (2021). Multigene phylogenetics of euglenids based on single-cell transcriptomics of diverse phagotrophs. *Mol. Phylogenet. Evol.* 159, 107088. doi:10.1016/j.ympev.2021.107088

Le, T., Žárský, V., Nývltová, E., Rada, P., Harant, K., Vancová, M., et al. (2020). Anaerobic peroxisomes in Mastigamoeba balamuthi. *Proc. Natl. Acad. Sci. U. S. A.* 117 (4), 2065–2075. doi:10.1073/pnas.1909755117

Leroux, A. E., Maugeri, D. A., Cazzulo, J. J., and Nowicki, C. (2011). Functional characterization of NADP-dependent isocitrate dehydrogenase isozymes from Trypanosoma cruzi. *Mol. Biochem. Parasitol.* 177 (1), 61–64. doi:10.1016/j.molbiopara.2011.01.010

Lobo-Rojas, Á. E., González-Marcano, E. B., Valera-Vera, E. A., Acosta, H. R., Quiñones, W. A., Burchmore, R. J., et al. (2016). Trypanosoma cruzi contains two galactokinases; molecular and biochemical characterization. *Parasitol. Int.* 65 (5), 472–482. doi:10.1016/j.parint.2016.06.008

Lorenz, P., Maier, A. G., Baumgart, E., Erdmann, R., and Clayton, C. (1998). Elongation and clustering of glycosomes in Trypanosoma brucei overexpressing the glycosomal Pex11p. *EMBO J.* 17, 3542–3555. doi:10.1093/emboj/17.13.3542

Lukeš, J., Wheeler, R., Jirsová, D., David, V., and Archibald, J. M. (2018). Massive mitochondrial DNA content in diplonemid and kinetoplastid protists. *IUBMB Life* 70 (12), 1267–1274. doi:10.1002/iub.1894

Lüscher, A., Lamprea-Burgunder, E., Graf, F. E., De Koning, H. P., and Mäser, P. (2013). Trypanosoma brucei adenine-phosphoribosyltransferases mediate adenine salvage and aminopurinol susceptibility but not adenine toxicity. *Int. J. Parasitol. Drugs Drug Resist.* 4 (1), 55–63. doi:10.1016/j.ijpddr.2013.12.001

Makiuchi, T., Annoura, T., Hashimoto, M., Hashimoto, T., Aoki, T., and Nara, T. (2011). Compartmentalization of a glycolytic enzyme in Diplonema, a non-kinetoplastid euglenozoan. *Protist* 162 (3), 482–489. doi:10.1016/j.protis.2010.11.003

Makiuchi, T., Nara, T., Annoura, T., Hashimoto, T., and Aoki, T. (2007). Occurrence of multiple, independent gene fusion events for the fifth and sixth enzymes of pyrimidine biosynthesis in different eukaryotic groups. *Gene* 394 (1-2), 78–86. doi:10.1016/j.gene.2007.02.009

Manjithaya, R., Nazarko, T. Y., Farré, J. C., and Subramani, S. (2010). Molecular mechanism and physiological role of pexophagy. *FEBS Lett.* 584 (7), 1367–1373. doi:10.1016/j.febslet.2010.01.019

Marchese, L., Nascimento, J. F., Damasceno, F. S., Bringaud, F., Michels, P. A. M., and Silber, A. M. (2018). The uptake and metabolism of amino acids, and their unique role in the biology of pathogenic trypanosomatids. *Pathogens* 7 (2), 36. doi:10.3390/pathogens7020036

Martin, W. (2010). Evolutionary origins of metabolic compartmentalization in eukaryotes. *Philos. Trans. R. Soc. Lond. B Biol. Sci.* 365 (1541), 847–855. doi:10.1098/rstb.2009.0252

Mazet, M., Harijan, R. K., Kiema, T. R., Haapalainen, A. M., Morand, P., Morales, J., et al. (2011). The characterization and evolutionary relationships of a trypanosomal thiolase. *Int. J. Parasitol.* 41 (12), 1273–1283. doi:10.1016/j.ijpara.2011.07.009

McNae, I. W., Martinez-Oyanedel, J., Keillor, J. W., Michels, P. A. M., Fothergill-Gilmore, L. A., and Walkinshaw, M. D. (2009). The crystal structure of ATP-bound phosphofructokinase from Trypanosoma brucei reveals conformational transitions different from those of other phosphofructokinases. *J. Mol. Biol.* 385 (5), 1519–1533. doi:10.1016/j.jmb.2008.11.047

Mertens, E. (1993). ATP versus pyrophosphate: Glycolysis revisited in parasitic protists. *Parasitol. Today* 9 (4), 122–126. doi:10.1016/0169-4758(93)90169-g

Mertens, E., Ladror, U. S., Lee, J. A., Miretsky, A., Morris, A., Rozario, C., et al. (1998). The pyrophosphate-dependent phosphofructokinase of the protist, Trichomonas vaginalis, and the evolutionary relationships of protist phosphofructokinases. *J. Mol. Evol.* 47 (6), 739–750. doi:10.1007/pl00006433

Mertens, E. (1991). Pyrophosphate-dependent phosphofructokinase, an anaerobic glycolytic enzyme? *FEBS Lett.* 85 (1), 1–5. doi:10.1016/0014-5793(91)80711-b

Michels, P. A. M., Chevalier, N., Opperdoes, F. R., Rider, M. H., and Rigden, D. J. (1997). The glycosomal ATP-dependent phosphofructokinase of Trypanosoma brucei must have evolved from an ancestral pyrophosphate-dependent enzyme. *Eur. J. Biochem.* 250 (3), 698–704. doi:10.1111/j.1432-1033.1997.00698.x

Michels, P. A. M., and Gualdrón-López, M. (2022). Biogenesis and metabolic homeostasis of trypanosomatid glycosomes: New insights and new questions. *J. Eukaryot. Microbiol.*, e12897. doi:10.1111/jeu.12897

Michels, P. A. M., and Hannaert, V. (1994). The evolution of kinetoplastid glycosomes. *J. Bioenerg. Biomembr.* 26 (2), 213–219. doi:10.1007/BF00763070

Michels, P. A. M., Moyersoen, J., Krazy, H., Galland, N., Herman, M., and Hannaert, V. (2005). Peroxisomes, glyoxysomes and glycosomes (review). *Mol. Membr. Biol.* 22 (1-2), 133–145. doi:10.1080/09687860400024186

Michels, P. A. M., and Opperdoes, F. R. (1991). The evolutionary origin of glycosomes. *Parasitol. Today* 7 (5), 105–109. doi:10.1016/0169-4758(91)90167-m

Michels, P. A. M., Villafraz, O., Pineda, E., Alencar, M. B., Cáceres, A. J., Silber, A. M., et al. (2021). Carbohydrate metabolism in trypanosomatids: New insights revealing novel complexity, diversity and species-unique features. *Exp. Parasitol.* 224, 108102. doi:10.1016/j.exppara.2021.108102

Mills, D. B., Boyle, R. A., Daines, S. J., Sperling, E. A., Pisani, D., Donoghue, P. C. J., et al. (2022). Eukaryogenesis and oxygen in Earth history. *Nat. Ecol. Evol.* 6 (5), 520–532. doi:10.1038/s41559-022-01733-y

Mindthoff, S., Grunau, S., Steinfort, L. L., Girzalsky, W., Hiltunen, J. K., Erdmann, R., et al. (2016). Peroxisomal Pex11 is a pore-forming protein homologous to TRPM channels. *Biochim. Biophys. Acta* 1863, 271–283. doi:10.1016/j.bbamcr.2015.11.013

Miranda, M. R., Bouvier, L. A., Canepa, G. E., and Pereira, C. A. (2009). Subcellular localization of Trypanosoma cruzi arginine kinase. *Parasitology* 136 (10), 1201–1207. doi:10.1017/S0031182009990448

Misset, O., Bos, O. J., and Opperdoes, F. R. (1986). Glycolytic enzymes of Trypanosoma brucei. Simultaneous purification, intraglycosomal concentrations and physical properties. *Eur. J. Biochem.* 157 (2), 441–453. doi:10.1111/j.1432-1033.1986.tb09687.x

Monic, S. G., Lamy, A., Thonnus, M., Bizarra-Rebelo, T., Bringaud, F., Smith, T. K., et al. (2022). A novel lipase with dual localisation in Trypanosoma brucei. *Sci. Rep.* 12 (1), 4766. doi:10.1038/s41598-022-08546-w

Montilla-Martinez, M., Beck, S., Klümper, J., Meinecke, M., Schliebs, W., Wagner, R., et al. (2015). Distinct pores for peroxisomal import of PTS1 and PTS2 proteins. *Cell Rep.* 13, 2126–2134. doi:10.1016/j.celrep.2015.11.016

Moore, S. A., Ronimus, R. S., Roberson, R. S., and Morgan, H. W. (2002). The structure of a pyrophosphate-dependent phosphofructokinase from the Lyme disease spirochete Borrelia burgdorferi. *Structure* 10 (5), 659–671. doi:10.1016/s0969-2126(02)00760-8

Morales, J., Hashimoto, M., Williams, T. A., Hirawake-Mogi, H., Makiuchi, T., Tsubouchi, A., et al. (2016). Differential remodelling of peroxisome function underpins the environmental and metabolic adaptability of diplonemids and kinetoplastids. *Proc. Biol. Sci.* 283 (1830), 20160520. doi:10.1098/rspb.2016.0520

Negreiros, R. S., Lander, N., Huang, G., Cordeiro, C. D., Smith, S. A., Morrissey, J. H., et al. (2018). Inorganic polyphosphate interacts with nucleolar and glycosomal proteins in trypanosomatids. *Mol. Microbiol.* 110 (6), 973–994. doi:10.1111/mmi.14131

Opaliński, Ł., Kiel, J. A., Williams, C., Veenhuis, M., and Van der Klei, I. J. (2011). Membrane curvature during peroxisome fission requires Pex11. *EMBO J.* 30 (1), 5–16. doi:10.1038/emboj.2010.299

Opperdoes, F. R., and Borst, P. (1977). Localization of nine glycolytic enzymes in a microbody-like organelle in trypanosoma brucei: The glycosome. *FEBS Lett.* 80 (2), 360–364. doi:10.1016/0014-5793(77)80476-6

Opperdoes, F. R., Borst, P., and Spits, H. (1977). Particle-bound enzymes in the bloodstream form of Trypanosoma brucei. *Eur. J. Biochem.* 176 (1), 21–28. doi:10.1111/j.1432-1033.1977.tb11566.x

Opperdoes, F. R., Butenko, A., Flegontov, P., Yurchenko, V., and Lukeš, J. (2016). Comparative metabolism of free-living Bodo saltans and parasitic trypanosomatids. *J. Eukaryot. Microbiol.* 63 (5), 657–678. doi:10.1111/jeu.12315

Opperdoes, F. R. (1987). Compartmentation of carbohydrate metabolism in trypanosomes. *Annu. Rev. Microbiol.* 41, 127–151. doi:10.1146/annurev.mi.41.100187.001015

Opperdoes, F. R., De Jonckheere, J. F., and Tielens, A. G. M. (2011). Naegleria gruberi metabolism. *Int. J. Parasitol.* 41 (9), 915–924. doi:10.1016/j.ijpara.2011.04.004

Opperdoes, F. R. (1984). Localization of the initial steps in alkoxyphospholipid biosynthesis in glycosomes (microbodies) of Trypanosoma brucei. *FEBS Lett.* 169 (1), 35–39. doi:10.1016/0014-5793(84)80284-7

Opperdoes, F. R., and Michels, P. A. M. (2008). in *The metabolic repertoire of Leishmania and implications for drug discovery" in Leishmania: After the genome*. Editors P. J. Myler and N. Fasel (U.K.: Caister Academic Press), 123–158. 978-1-904455-28-8.

Opperdoes, F. R., Nohynkova, E., Van Schaftingen, E., Lambeir, A. M., Veenhuis, M., and Van Roy, J. (1988). Demonstration of glycosomes (microbodies) in the Bodonid flagellate Trypanoplasma borelli (Protozoa, Kinetoplastida). *Mol. Biochem. Parasitol.* 30 (2), 155–163. doi:10.1016/0166-6851(88)90108-9

Opperdoes, F. R., and Szikora, J. P. (2006). *In silico* prediction of the glycosomal enzymes of Leishmania major and trypanosomes. *Mol. Biochem. Parasitol.* 147 (2), 193–206. doi:10.1016/j.molbiopara.2006.02.010

Otera, H., Okumoto, K., Tateishi, K., Ikoma, Y., Matsuda, E., Nishimura, M., et al. (1998). Peroxisome targeting signal type 1 (PTS1) receptor is involved in import of both PTS1 and PTS2: Studies with PEX5-defective CHO cell mutants. *Mol. Cell. Biol.* 18 (1), 388–399. doi:10.1128/MCB.18.1.388

Pan, D., Nakatsu, T., and Kato, H. (2013). Crystal structure of peroxisomal targeting signal-2 bound to its receptor complex Pex7p-Pex21p. *Nat. Struct. Mol. Biol.* 20 (8), 987–993. doi:10.1038/nsmb.2618

Parsons, M., and Smith, J. M. (1989). Trypanosome glycosomal protein P60 is homologous to phosphoenolpyruvate carboxykinase (ATP). *Nucleic Acids Res.* 17 (15), 6411. doi:10.1093/nar/17.15.6411

Petriv, O. I., Tang, L., Titorenko, V. I., and Rachubinski, R. A. (2004). A new definition for the consensus sequence of the peroxisome targeting signal type 2. *J. Mol. Biol.* 341 (1), 119–134. doi:10.1016/j.jmb.2004.05.064

Quiñones, W., Acosta, H., Gonçalves, C. S., Motta, M. C. M., Gualdrón-López, M., and Michels, P. A. M. (2020). Structure, properties, and function of glycosomes in trypanosoma cruzi. *Front. Cell. Infect. Microbiol.* 10, 25. doi:10.3389/fcimb.2020.00025

Roberts, S. C., Tancer, M. J., Polinsky, M. R., Gibson, K. M., Heby, O., and Ullman, B. (2004). Arginase plays a pivotal role in polyamine precursor metabolism in Leishmania. Characterization of gene deletion mutants. *J. Biol. Chem.* 279 (22), 23668–23678. doi:10.1074/jbc.M402042200

Rojas-Pirela, M., Andrade-Alviárez, D., Rojas, V., Kemmerling, U., Cáceres, A. J., Michels, P. A. M., et al. (2020). Phosphoglycerate kinase: Structural aspects and

functions, with special emphasis on the enzyme from Kinetoplastea. *Open Biol.* 10 (11), 200302. doi:10.1098/rsob.200302

Rojas-Pirela, M., Rigden, D. J., Michels, P. A. M., Cáceres, A. J., Concepción, J. L., and Quiñones, W. (2018). Structure and function of Per-ARNT-Sim domains and their possible role in the life-cycle biology of Trypanosoma cruzi. *Mol. Biochem. Parasitol.* 219, 52–66. doi:10.1016/j.molbiopara.2017.11.002

Rucktäschel, R., Thoms, S., Sidorovitch, V., Halbach, A., Pechlivanis, M., Volkmer, R., et al. (2009). Farnesylation of pex19p is required for its structural integrity and function in peroxisome biogenesis. *J. Biol. Chem.* 284, 20885–20896. doi:10.1074/jbc.M109.016584

Saavedra, E., Encalada, R., Vázquez, C., Olivos-García, A., Michels, P. A. M., and Moreno-Sánchez, R. (2019). Control and regulation of the pyrophosphate-dependent glucose metabolism in Entamoeba histolytica. *Mol. Biochem. Parasitol.* 229, 75–87. doi:10.1016/j.molbiopara.2019.02.002

Salani, F. S., Arndt, H., Hausmann, K., Nitsche, F., and Scheckenbach, F. (2012). Analysis of the community structure of abyssal kinetoplastids revealed similar communities at larger spatial scales. *ISME J.* 6 (4), 713–723. doi:10.1038/ismej.2011.138

Sampaio Guther, M. L., Prescott, A. R., Kuettel, S., Tinti, M., and Ferguson, M. A. J. (2021). Nucleotide sugar biosynthesis occurs in the glycosomes of procyclic and bloodstream form Trypanosoma brucei. *PLoS Negl. Trop. Dis.* 15 (2), e0009132. doi:10.1371/journal.pntd.0009132

Sampathkumar, P., Roach, C., Michels, P. A. M., and Hol, W. G. J. (2008). Structural insights into the recognition of peroxisomal targeting signal 1 by Trypanosoma brucei peroxin 5. *J. Mol. Biol.* 381 (4), 867–880. doi:10.1016/j.jmb.2008.05.089

Schoenle, A., Hohlfeld, M., Hermanns, K., Mahé, F., de Vargas, C., Nitsche, F., et al. (2021). High and specific diversity of protists in the deep-sea basins dominated by diplonemids, kinetoplastids, ciliates and foraminiferans. *Commun. Biol.* 4 (1), 501. doi:10.1038/s42003-021-02012-5

Schrader, M., Bonekamp, N. A., and Islinger, M. (2012). Fission and proliferation of peroxisomes. *Biochim. Biophys. Acta* 1822 (9), 1343–1357. doi:10.1016/j.bbadis.2011.12.014

Schrader, M., Costello, J. L., Godinho, L. F., Azadi, A. S., and Islinger, M. (2016). Proliferation and fission of peroxisomes - an update. *Biochim. Biophys. Acta* 1863, 971–983. doi:10.1016/j.bbamcr.2015.09.024

Škodová-Sveráková, I., Záhonová, K., Bučková, B., Füssy, Z., Yurchenko, V., and Lukeš, J. (2020). Catalase and ascorbate peroxidase in euglenozoan protists. *Pathogens* 9 (4), 317. doi:10.3390/pathogens9040317

Škodová-Sveráková, I., Záhonová, K., Juricová, V., Danchenko, M., Moos, M., Baráth, P., et al. (2021). Highly flexible metabolism of the marine euglenozoan protist Diplonema papillatum. *BMC Biol.* 19 (1), 251. doi:10.1186/s12915-021-01186-y

Sommer, J. M., Cheng, Q. L., Keller, G. A., and Wang, C. C. (1992). *In vivo* import of firefly luciferase into the glycosomes of Trypanosoma brucei and mutational analysis of the C-terminal targeting signal. *Mol. Biol. Cell* 3 (7), 749–759. doi:10.1091/mbc.3.7.749

Sykes, S., Szempruch, A., and Hajduk, S. (2015). The krebs cycle enzyme α-ketoglutarate decarboxylase is an essential glycosomal protein in bloodstream African trypanosomes. *Eukaryot. Cell* 14 (3), 206–215. doi:10.1128/EC.00214-14

Szöőr, B., Ruberto, I., Burchmore, R., and Matthews, K. R. (2010). A novel phosphatase cascade regulates differentiation in Trypanosoma brucei via a glycosomal signaling pathway. *Genes Dev.* 24 (12), 1306–1316. doi:10.1101/gad.570310

Szöőr, B., Simon, D. V., Rojas, F., Young, J., Robinson, D. R., Krüger, T., et al. (2019). Positional dynamics and glycosomal recruitment of developmental regulators during trypanosome differentiation. *mBio* 10 (4), e00875–19. doi:10.1128/mBio.00875-19

Tashyreva, D., Simpson, A. G. B., Prokopchuk, G., Škodová-Sveráková, I., Butenko, A., Hammond, M., et al. (2022). Diplonemids - a review on "new" flagellates on the oceanic block. *Protist* 173 (2), 125868. doi:10.1016/j.protis.2022.125868

Taylor, M. B., Berghausen, H., Heyworth, P., Messenger, N., Rees, L. J., and Gutteridge, W. E. (1980). Subcellular localization of some glycolytic enzymes in parasitic flagellated protozoa. *Int. J. Biochem.* 11 (2), 117–120. doi:10.1016/0020-711x(80)90243-8

Teich, R., Zauner, S., Baurain, D., Brinkmann, H., and Petersen, J. (2007). Origin and distribution of Calvin cycle fructose and sedoheptulose bisphosphatases in plantae and complex algae: A single secondary origin of complex red plastids and subsequent propagation via tertiary endosymbioses. *Protist* 158 (3), 263–276. doi:10.1016/j.protis.2006.12.004

Urbaniak, M. D., Güther, M. L., and Ferguson, M. A. (2012). Comparative SILAC proteomic analysis of Trypanosoma brucei bloodstream and procyclic lifecycle stages. *PLoS One* 7 (5), e36619. doi:10.1371/journal.pone.0036619

Verner, Z., Žárský, V., Le, T., Narayanasamy, R. K., Rada, P., Rozbeský, D., et al. (2021). Anaerobic peroxisomes in Entamoeba histolytica metabolize myo-inositol. *PLoS Pathog.* 17 (11), e1010041. doi:10.1371/journal.ppat.1010041

Verplaetse, E., Gualdrón-López, M., Chevalier, N., and Michels, P. A. M. (2012). Studies on the organization of the docking complex involved in matrix protein import into glycosomes of Trypanosoma brucei. *Biochem. Biophys. Res. Commun.* 424 (4), 781–785. doi:10.1016/j.bbrc.2012.07.035

Verplaetse, E., Rigden, D. J., and Michels, P. A. M. (2009). Identification, characterization and essentiality of the unusual peroxin 13 from Trypanosoma brucei. *Biochim. Biophys. Acta* 1793 (3), 516–527. doi:10.1016/j.bbamcr.2008.12.020

Vertommen, D., Van Roy, J., Szikora, J. P., Rider, M. H., Michels, P. A. M., and Opperdoes, F. R. (2008). Differential expression of glycosomal and mitochondrial proteins in the two major life-cycle stages of Trypanosoma brucei. *Mol. Biochem. Parasitol.* 158 (2), 189–201. doi:10.1016/j.molbiopara.2007.12.008

Voncken, F., Gao, F., Wadforth, C., Harley, M., and Colasante, C. (2013). The phosphoarginine energy-buffering system of Trypanosoma brucei involves multiple arginine kinase isoforms with different subcellular locations. *PLoS One* 8 (6), e65908. doi:10.1371/journal.pone.0065908

Voncken, F., Van Hellemond, J. J., Pfisterer, I., Maier, A., Hillmer, S., and Clayton, C. (2003). Depletion of GIM5 causes cellular fragility, a decreased glycosome number, and reduced levels of ether-linked phospholipids in trypanosomes. *J. Biol. Chem.* 278, 35299–35310. doi:10.1074/jbc.M301811200

Wang, X., Inaoka, D. K., Shiba, T., Balogun, E. O., Allmann, S., Watanabe, Y. I., et al. (2017). Expression, purification, and crystallization of type 1 isocitrate dehydrogenase from Trypanosoma brucei brucei. *Protein Expr. Purif.* 138, 56–62. doi:10.1016/j.pep.2017.06.011

Wargnies, M., Bertiaux, E., Cahoreau, E., Ziebart, N., Crouzols, A., Morand, P., et al. (2018). Gluconeogenesis is essential for trypanosome development in the tsetse fly vector. *PLoS Pathog.* 14 (12), e1007502. doi:10.1371/journal.ppat.1007502

Wheeler, R. J. (2021). A resource for improved predictions of Trypanosoma and Leishmania protein three-dimensional structure. *PLoS One* 16 (11), e0259871. doi:10.1371/journal.pone.0259871

Wheeler, R. J., Gluenz, E., and Gull, K. (2013). The limits on trypanosomatid morphological diversity. *PLoS One* 8 (11), e79581. doi:10.1371/journal.pone.0079581

Wiemer, E. A., IJlst, L., Van Roy, J., Wanders, R. J., and Opperdoes, F. R. (1996). Identification of 2-enoyl coenzyme A hydratase and NADP+-dependent 3-hydroxyacyl-CoA dehydrogenase activity in glycosomes of procyclic Trypanosoma brucei. *Mol. Biochem. Parasitol.* 82 (1), 107–111. doi:10.1016/0166-6851(96)02710-7

Wilkinson, S. R., Prathalingam, S. R., Taylor, M. C., Ahmed, A., Horn, D., and Kelly, J. M. (2006). Functional characterisation of the iron superoxide dismutase gene repertoire in Trypanosoma brucei. *Free Radic. Biol. Med.* 40 (2), 198–209. doi:10.1016/j.freeradbiomed.2005.06.022

Wilkinson, S. R., Prathalingam, S. R., Taylor, M. C., Horn, D., and Kelly, J. M. (2005). Vitamin C biosynthesis in trypanosomes: A role for the glycosome. *Proc. Natl. Acad. Sci. U. S. A.* 102 (33), 11645–11650. doi:10.1073/pnas.0504251102

Yernaux, C., Fransen, M., Brees, C., Lorenzen, S., and Michels, P. A. M. (2006). Trypanosoma brucei glycosomal ABC transporters: Identification and membrane targeting. *Mol. Membr. Biol.* 23 (2), 157–172. doi:10.1080/09687860500460124

Yoshimoto, K., Takano, Y., and Sakai, Y. (2010). Autophagy in plants and phytopathogens. *FEBS Lett.* 584 (7), 1350–1358. doi:10.1016/j.febslet.2010.01.007

Yubuki, N., and Leander, B. S. (2018). Diversity and evolutionary history of the Symbiontida (Euglenozoa). *Front. Ecol. Evol.* 6, 100. doi:10.3389/fevo.2018.00100

Zhang, N., Jiang, N., Zhang, K., Zheng, L., Zhang, D., Sang, X., et al. (2020). Landscapes of protein posttranslational modifications of african trypanosoma parasites. *iScience* 23 (5), 101074. doi:10.1016/j.isci.2020.101074

Zientara-Rytter, K. M., Mahalingam, S. S., Farré, J. C., Carolino, K., and Subramani, S. (2022). Recognition and chaperoning by Pex19, followed by trafficking and membrane insertion of the peroxisome proliferation protein, Pex11. *Cells* 11 (1), 157. doi:10.3390/cells11010157

frontiers | Frontiers in Cell and Developmental Biology

TYPE Original Research
PUBLISHED 03 November 2022
DOI 10.3389/fcell.2022.1026388

OPEN ACCESS

EDITED BY
Christos Gatsogiannis,
University of Münster, Germany

REVIEWED BY
Johannes Freitag,
University of Marburg, Germany
Michael Ginger,
University of Huddersfield,
United Kingdom

*CORRESPONDENCE
Markus Kunze,
markus.kunze@meduniwien.ac.at

†These authors have contributed equally to this work

SPECIALTY SECTION
This article was submitted to Membrane Traffic,
a section of the journal
Frontiers in Cell and Developmental Biology

RECEIVED 23 August 2022
ACCEPTED 20 October 2022
PUBLISHED 03 November 2022

CITATION
Hochreiter B, Malagon-Vina H, Schmid JA, Berger J and Kunze M (2022), Studying the interaction between PEX5 and its full-length cargo proteins in living cells by a novel Förstes resonance energy transfer-based competition assay.
Front. Cell Dev. Biol. 10:1026388.
doi: 10.3389/fcell.2022.1026388

Studying the interaction between PEX5 and its full-length cargo proteins in living cells by a novel Förstes resonance energy transfer-based competition assay

Bernhard Hochreiter[1†], Hugo Malagon-Vina[2†], Johannes A. Schmid[1], Johannes Berger[3] and Markus Kunze[3*†]

[1]Institute for Vascular Biology and Thrombosis Research, Center for Physiology and Pharmacology, Medical University of Vienna, Vienna, Austria, [2]Department of Cognitive Neurobiology, Center for Brain Research, Medical University of Vienna, Vienna, Austria, [3]Department of Pathobiology of the Nervous System, Center for Brain Research, Medical University of Vienna, Vienna, Austria

The import of the majority of soluble peroxisomal proteins is initiated by the interaction between type-1 peroxisomal targeting signals (PTS1) and their receptor PEX5. PTS1 motifs reside at the extreme C-terminus of proteins and consist of a characteristic tripeptide and a modulatory upstream region. Various PTS1-PEX5 interactions have been studied by biophysical methods using isolated proteins or in heterologous systems such as two-hybrid assays, but a recently established approach based on Försters resonance energy transfer (FRET) allows a quantifying investigation in living cells. FRET is the radiation-free energy transfer between two fluorophores in close proximity and can be used to estimate the fraction of acceptor molecules bound to a donor molecule. For PTS1-PEX5 this method relies on the measurement of FRET-efficiency between the PTS1-binding TPR-domain of PEX5 tagged with mCherry and EGFP fused to a PTS1 peptide. However, this method is less suitable for binding partners with low affinity and protein complexes involving large proteins such as the interaction between full-length PTS1-carrying cargo proteins and PEX5. To overcome this limitation, we introduce a life-cell competition assay based on the same FRET approach but including a fusion protein of Cerulean with the protein of interest as a competitor. After implementing the mathematical description of competitive binding experiments into a fitting algorithm, we demonstrate the functionality of this approach using known interaction partners, its ability to circumvent previous limitations of FRET-measurements and its ability to study the interaction between PEX5 and its full-length cargo proteins. We find that some proteins (SCP2 and AGXT) bind PEX5 with higher affinity than their PTS1-peptides alone, but other proteins (ACOX3, DAO, PerCR-SRL) bind with lower but reasonable affinity, whereas GSTK1 binds with very low affinity. This binding strength was not increased upon elongating the PEX5 TPR-domain at its N-terminus, PEX5(N-TPR), although it interacts specifically with the N-terminal domain of PEX14. Finally, we demonstrate that the latter reduces the interaction strength

between PEX5(N-TPR) and PTS1 by a dose-dependent but apparently non-competitive mechanism. Altogether, this demonstrates the power of this novel FRET-based competition approach for studying cargo recognition by PEX5 and protein complexes including large proteins in general.

KEYWORDS

peroxisomes, PEX5, PTS1, PEX14, FRET, fitting algorithm, competition experiments

1 Introduction

Most protein transport processes are initiated by the specific interaction between a targeting signal within the proteins primary sequence and a corresponding receptor protein specifying one subcellular compartment (Kunze and Berger, 2015). Among these compartments, peroxisomes are characterized by a single membrane, the enzymatic equipment for various specific metabolic pathways including the degradation of various fatty acids or hydrogen peroxide (Waterham et al., 2016), and an import machinery for fully folded soluble proteins (Kim and Hettema, 2015). The importance of peroxisomes for human physiology is highlighted by a variety of inherited human diseases caused by a complete dysfunction of peroxisomes (ZSD, Zellweger syndrome disorder) or a defect of one of the peroxisomal enzymes (Waterham et al., 2016). Protein import of soluble proteins is induced by the interaction between peroxisomal targeting signals residing either at the extreme C-terminus (type-1 peroxisomal targeting signal, PTS1) or in close proximity to the N-terminus (type-2 peroxisomal targeting signal, PTS2) (Brocard and Hartig, 2006; Kunze, 2020). These targeting signals are recognized by the cognate soluble receptors PEX5 or PEX7 (Dahan et al., 2021), respectively, the latter acting together with a co-receptor (Kunze, 2020). These receptor proteins mediate the transport to and across the peroxisomal membrane and become recycled to the cytosol upon release of their cargo proteins into the peroxisomal lumen (Francisco et al., 2017). Most matrix proteins harbor a PTS1, which has been originally described as a C-terminal tripeptide consisting of serine-lysine-leucine (-SKL) or conserved variants thereof (Gould et al., 1989), but later-on a broader variety of tripeptides was shown to interact with the receptor and the preceding sequence also contributes to the interaction (Lametschwandtner et al., 1998; Brocard and Hartig, 2006; Ghosh and Berg, 2010; Hagen et al., 2015; Hochreiter et al., 2020). The PTS1-binding domain of PEX5 has the characteristic shape of tetratricopeptide (TPR)-proteins and interacts with the PTS1 *via* a deep cave into which PTS1 motifs are inserted (Gatto et al., 2000; Stanley et al., 2006; Burgi et al., 2021). The specificity of the interaction between PEX5 and its cargo has been initially attributed to the PTS1 motif alone (Gatto et al., 2000; Brocard and Hartig, 2006; Ghosh and Berg, 2010), but the resolution of the 3D-structure of PEX5 together with either sterol carrier protein 2 (SCP2) (Stanley et al., 2006) or alanine-glyoxylate aminotransferase (AGXT) (Fodor et al., 2012; Fodor et al., 2015) as bound cargo revealed that additional interphases exist. However, mutating individual PEX5 residues participating in this interphase had only moderate effects on the interaction strength with SCP2 (Williams et al., 2011), or import efficiency (Fodor et al., 2012; Fodor et al., 2015). The complexity of receptor-cargo interactions is further increased by the fact that many peroxisomal proteins act as dimers or oligomers, and for some of them, a piggy-back-like import mechanism of PTS1-free proteins has been demonstrated (Leon et al., 2006; Islinger et al., 2009). However, such piggy-back transport is not applicable for all peroxisomal proteins (Tanaka et al., 2008) and their general importance for peroxisomal import has been debated (Dias et al., 2016). Surprisingly, a PEX5 variant consisting of the TPR-domain together with a short N-terminal extension (N-TPR) was found to resolve human catalase tetramers in *in vitro* experiments (Freitas et al., 2011), resulting in the attribution of chaperone activity to the N-terminal part of PEX5 (Francisco et al., 2013), which might prevent proteins from complete cytosolic oligomerization. This effect was reduced by the N-terminal domain (NTD) of PEX14 bound to this N-terminal extension of PEX5 (Neufeld et al., 2009; Freitas et al., 2011; Neuhaus et al., 2014).

Various detailed studies investigated the binding strength between PEX5 from diverse species and different PTS1-peptides using isolated proteins (Gatto et al., 2003; Maynard et al., 2004; Maynard and Berg, 2007; Ghosh and Berg, 2010), yeast two-hybrid assay (Lametschwandtner et al., 1998) or more advanced techniques such as mass-spectrometry-based interaction tests (Skoulding et al., 2015; Cross et al., 2017; Rosenthal et al., 2020) and found different affinities ranging across several orders of magnitude. We recently introduced a novel application of FRET-efficiency measurements combined with a fitting algorithm to calculate numeric values for the apparent interaction strength between proteins (Hochreiter et al., 2019) and demonstrated its versatility to study the interaction between PEX5 and diverse PTS1 peptides in living cells (Chong et al., 2019; Hochreiter et al., 2020).

Försters resonance energy transfer (FRET) is a well-established method to investigate protein-protein interactions (PPI), which relies on the radiation-free energy transfer between a donor and an acceptor protein (Bunt and Wouters, 2017;

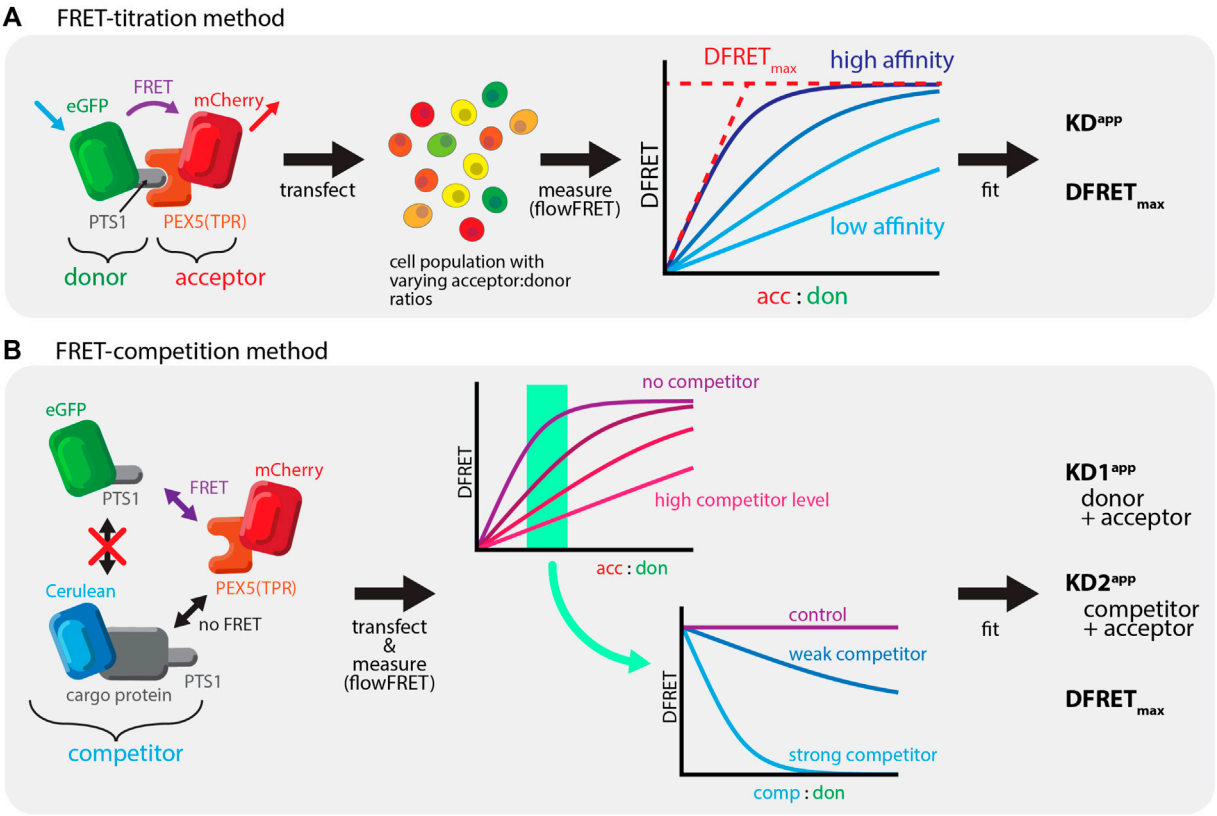

FIGURE 1
Studying PEX5-cargo interactions using FRET-measurements: **(A)** Bimolecular FRET measurements: *left*: FRET as radiation free energy transfer between fluorescent proteins in close proximity is used to measure the interaction between mCherry-extended by the TPR-domain of PEX5 (PEX5 (TPR)) and EGFP equipped with a PTS1; *middle*: a large number of cells expressing these proteins are systematically investigated using a flow-cytometer, *right*: saturation curves can be obtained by plotting the acc:don ratio against a measure of energy transfer efficiency (DFRET), in which the slope reflects the affinity and the saturation level the distance of the fluorogenic centers; **(B)** Competition based FRET experiments: *left*: when studying a defined FRET-pair (mCherry-PEX5(TPR) and EGFP-PTS1) the presence of a third protein also interacting with the acceptor (Cerulean-cargo-PTS1) exerts a competitive effect; *middle*: when plotting a saturation curve (acc:don) an increasing amount of competitor changes its shape to suggest a reduction of the interaction strength of the FRET-pair (minor slope) in a dose dependent manner; *right*: plotting DFRET against the competitor to donor ratio (comp:don) results in traditional decay curves, in which the slope of the decay reflects the relative affinity of the competitor (to the donor).

Okamoto and Sako, 2017). The effectivity of the transfer depends on the distance between the fluorophores but can also be used to estimate the fraction of donor and acceptor molecules engaged in a complex, which is determined by the affinity of the two proteins. Thus, the quantitative determination of a normalized measure of energy transfer (donor normalized FRET, DFRET) together with an estimation of the relative abundance of donor and acceptor molecules per cell allows the estimation of key parameters. These are a measure for the apparent interaction strength (KD^{app}) and the plateau level of the DFRET saturation curve (DFRETmax). However, in combination with high-throughput measurements such as flow cytometry (flowFRET) it can serve as a powerful tool to investigate PPI (Hochreiter et al., 2019) (Figure 1A). To study PTS1-PEX5 interactions, we investigated FRET-efficiency between the mCherry-tagged TPR-domain of PEX5 [mCherry-PEX5 (TPR)] and different PTS1 peptides fused to EGFP in murine embryonic fibroblasts obtained from a PEX5-deficient KO-mouse [$pex5^{-/-}$ (Baes et al., 1997)], in which the binding partners remain in the cytosol. Certainly, the gold-standard for PEX5-cargo recognition is its interaction with full-length proteins in living cells. However, as the sensitivity of FRET efficiency measurements is limited by the distance between donor and acceptor domains and thus often by the size of the interacting proteins, we had to adapt our flowFRET method to study full-length PTS1-carrying cargo proteins.

In this manuscript we describe a FRET-based quantifying competition method, which allows the first study of PPIs between PEX5 and diverse full-length PTS1-carrying cargo proteins in living cells. We recently described qualitatively the phenomenon of competition (Hochreiter et al., 2020), which reduces the average DFRET value of populations depending on the competitor level and its affinity (Figure 1B). Moreover, we

verify the interaction between PEX14(NTD) and PEX5 and demonstrate that this interaction modulates the interaction strength between PEX5 and PTS1-carrying proteins in a non-competitive manner.

2 Materials and methods

2.1 Cloning procedure

Restriction enzymes, Klenow polymerase were obtained from Fermentas/Thermo-Fisher (United States), the TA Cloning™ Kit (with pCR™2.1 Vector, without competent cells) from Thermo. PCR-reactions were performed with high-fidelity PCR (PrimeSTAR high-fidelity PCR) from Takara (JP); *in vitro* mutagenesis was performed using QuikChange® II XL Site-Directed Mutagenesis Kit from Stratagene/Agilent (US) and by independent PCR reactions using high fidelity polymerase (Pfu-I, Takara) a subsequent digestion with DpnI (Thermo-Fisher).

2.2 Plasmids (*cf.* Supplementary Table S3)

The EGFP-PTS1 expression plasmids were obtained by digesting EGFP-C3 (Clontech) with restriction enzymes HindIII and BglII and ligate it with the annealed oligonucleotides encoding the PTS1 of *Mm*SCP2, *Hs*AGT, *Hs*DAO, *Hs*GSTK1, *Hs*PECR, *Ss*PerCR-SRL, *Mm*ZADH2. The following expression plasmids were available [EGFP-*Mm*ZADH2 (Wiese et al., 2007), EGFP-*Hs*GSTK1 (Wang et al., 2013)] or kindly provided [EGFP-*Hs*DAO kindly provided by Loredano Pollegioni (Sacchi et al., 2011), EGFP-*Hs*AGT by Wolfgang Schliebs (Fodor et al., 2012)].

The ORF for pig PerCR-SRL was obtained by PCR using oligonucleotides Oli_2719 and Oli_2720 (*cf.* Supplementary Table S3) and the expression plasmid for PerCR-SRL (Tanaka et al., 2008) as template, the ORFs for murine SCPx was obtained by PCR using oligonucleotides Oli_901 and Oli_902 and mouse liver cDNA as template, the ORF for SCP2 was generated by PCR using oligonucleotides Oli_2615 and Oli_902 using EGFP-SCPx as template. PCR-fragments were treated with Taq-polymerase to add an additional A at the 3′-end and ligated to pCR2.1 according to manufacturer´s instructions and the correct sequence of the ORFs was confirmed by sequencing. The ORF of SCP2 or mutated variants thereof were cloned as NcoI/EcoRI-fragments and that of SCPx as XhoI/EcoRI-fragment into EGFP-C1 (Clontech) digested with the same restriction enzymes. The ORF of PerCR-SRL was cloned as BglII/SalI fragment into EGFP-C1 digested with the same restriction enzyme. The mutations in EGFP-SCP2 were either introduced by PCR using oligonucleotides (Oli_2736 and Oli_2737) including the point mutations for G139L and AKV, respectively, or by *in vitro* mutagenesis for and the double mutation E35K/K38E using oligonucleotides Oli_3002 and Oli_3003. Cerulean-tagged variants of full-length proteins were obtained by digesting the corresponding EGFP-plasmids by NheI/BsrGI and inserting the ORF of Cerulean obtained by digesting Cerulean-C1 with the same enzymes.

mCherry-PEX5(N-TPR) was obtained by cloning the SacII/BamHI fragment of full-length PEX5 into mCherry-C1 digested with the same restriction enzymes and subsequently inserting the TPR-domain of PEX5 obtained from plasmid mCherry-PEX5 (TPR) (Hochreiter et al., 2020) as BamHI/BamHI fragment.

2.2.1 PEX14(NTD)-EGFP

The N-terminal domain of PEX14 was obtained by PCR using oligonucleotides Oli_1529 and Oli_2799 and after subcloning into pCR2.1 the XhoI/BamHI fragment was inserted into EGFP-N2 (Clontech).

2.2.2 PEX14(NTD)-cerulean

The DNA-fragment encoding the PEX14(NTD) was cloned as XhoI/BamHI-fragment into Cerulean-N1 digested with the same enzymes. Subsequently, the reading frame was shifted by first digesting the plasmid with BamHI, the 5′-overhang ends were filled up Klenow-polymerase (Thermo) and the fragment was religated.

2.3 FlowFRET experiments

Experiments were performed as described before (Hochreiter et al., 2019; Hochreiter et al., 2020), but a general description is summarized here: Pex5$^{-/-}$ MEF cells were cultivated in DMEM (10%FBS). One day prior to transfection, cells were seeded in 48-well plates. The confluency of cells at the time of transfection must not exceed 70%. Cells were transfected with Turbofect™ (Thermo Scientific™ R0531). The amount of DNA used was optimized to be half the amount according to protocol (i.e., per 48-well: 0.25 µg DNA + 1 µl Turbofect in 50 µl serum free medium). To span a wide array of protein concentration ratios, multiple wells contained the same sample at different transfection ratios. The transfection mixture was incubated at room temperature for 15–20 min and pipetted onto the cells. Cells were centrifuged in a swing-out centrifuge at 300 g for 30 min and subsequently incubated overnight. Transfection efficiency was usually around 20–40% with virtually no cell death. Each experiment also contained necessary controls (i.e.,: untransfected cells; single fluorophores: EGFP, mCherry, Cerulean; fusion proteins: mCherry-EGFP, mCherry-Cerulean). 24 h past transfection, cells were washed with PBS and trypsinized in small batches of no more than eight samples at a time (multiple wells with the same DNA at different transfection ratios were often combined). Cells were immediately measured on the CytoFLEX (Beckman Coulter)

flow cytometer at "fast" speed (~1min per sample). Donor channel: ex: 488, em: 525/40; Acceptor channel: ex: 561, em: 610/20; FRET channel: ex: 488, em:610/20; Competitor channel: ex: 405, em: 450/45. Data was exported from CytExpert as fcs files and subsequently processed in R to obtain and the measured raw data and calculated values according to our previously published method (Hochreiter et al., 2019).

2.4 Fitting algorithm

Given the equations in (Wang, 1995), the theoretical DFRET (tDFRET) is calculated using [1–7]:

$$\text{tDFRET} = [\text{AB}]*\frac{DFRETmax}{[B]} \tag{1}$$

$$[\text{AB}] = \frac{[B]*\{2\sqrt{(a^2-3b)}\,\cos(\theta/3)-a\}}{3KD1+\{\{2\sqrt{(a^2-3b)}\,\cos(\theta/3)-a\}\}} \tag{2}$$

$$tDFRET = \frac{[B]*\{2\sqrt{(a^2-3b)}\,\cos(\theta/3)-a\}}{3KD1+\{\{2\sqrt{(a^2-3b)}\,\cos(\theta/3)-a\}\}}*\frac{DFRETmax}{[B]} \tag{3}$$

Where:

$$a = KD1 + KD2 + D + C - A \tag{4}$$

$$b = KD2\,(D-A) + KD1\,(C-A) + KD1{*}KD2 \tag{5}$$

$$c = -KD1{*}KD2{*}A \tag{6}$$

and

$$\theta = \cos^{-1}\left(\frac{-2a^3+9ab-27c}{2\sqrt{(a^2-3b)^3}}\right) \tag{7}$$

with

A = amount of acceptor
B = amount of donor
C = amount of competitor
KD1 = Donor affinity
KD2 = Competitor affinity
AB = amount of acc.don pair

A fitting algorithm was used to find the parameters: $KD1^{app}$, $KD2^{app}$ and DFRETmax, by minimizing the mean squared error (MSE) between the observed DFRET (oDFRET) and the tDFRET [3], given different parameter ranges

$$minimize:\ \frac{1}{n}\sum_{i=1}^{n}(oDFRET - tDFRET)^2 \tag{8}$$

Because of the complexity of the equations, and the fact that the KD1 and KD2 ranges are from one to >1e12, and DFRETmax ranges are from 0.01 to >0.5, the fitting algorithm used is a modified grid search, with a dynamic range selection to avoid local minima.

For any given data set, an initial fitting was obtained by averaging the resulting fitted parameters of 3 wide searches (covering the big range of the parameters (KD1, KD2 = 1 to 1e12 and DFRETmax = 0.01–0.5) performed in randomly selected subsamples of the original data set (80% of the data). This was to avoid local minima given by the entirety of the data. Then, those averaged parameters were used as the center of new ranges (given by expanding both sides by an area predefined by the user). This created a more localized grid than the initial one. The new fitted parameters that minimized the MSE were then again assumed to be the centers of new ranges, and in iteratively manner, approach the global minimum MSE. The search was stopped when the difference between a previous MSE and a new given MSE was less than 1e-6%.

2.5 Statistics

Unless stated different in the text, all statistics were non-parametric. To explore differences between multiple groups, the proper ANOVA was used (1-way, 2-way or 3-way) and Tukey-Kramer post-hoc test for multi-comparisons. An overview of all statistical tests is available in Supplementary Table S1.

2.5.1 Fitting results and their comparisons

An overview, the numerical results of individual fittings of the different data sets and a descriptive statistic (mean and SD) are available in Supplementary Table S2. To reflect the special combination of flowFRET measurements (primary data) and the computational extraction of key parameters of interest in each independent experiment (inference) we evaluated for complex experiments the reliability of the ranking of affinities between experiments using a bootstrapping method and for less complex experiments a direct comparison of pairs of proteins of interest defined by specific research questions using a paired t-test, but to avoid a confusion of comparing data and comparing prediction results the results of the latter are indicated only in Supplementary Table S2.

2.5.2 Bootstrapping method

The *p* values for ranking of the predicted affinities among the different experiments (Figures 4D,F, 5G, 6J) were compared by bootstrapping methods. We determined the consistency in the rankings over the days for different plasmids by calculating the total sum of the absolute differences between the rankings assigned to a plasmid over different days (e.g., if ACOX3 is ranked 1, 3, and 5 over the course of 3 days, the total sum of their differences is 16). We then sum all these values for all the plasmids in the experiments. Using bootstrap methods, we calculate the probabilities of obtaining the same values of

summarized differences by randomizing the original data into corresponding groups. Please note that it is not the probability of getting the same ranking orders for all the days but rather the probability of obtaining relatively similar distances between their rankings [it was done one million (1e6) times]. If over 3 days 2 plasmids have 1, 1, 1, and 2, 2, 2, their value sum is the same as 2,2,2 and 1,1,1, which means we are not testing the actual exact ranking but the probability of obtaining a similarly consistent ordination.

2.5.3 Paired t-tests

For the comparison of selected pairs of proteins a paired t-test was used ($p < 0,05$), the results of which can be found in Supplementary Table S2.

2.5.4 Plots and curve progressions

Axes values are depicted on each plot. Data was analysed within the ratios shown in the figures or stated in the figure legends. To plot the curve progressions (e.g., Figure 2D or Figure 4B), the median DFRET value for different ratios (acceptor to donor or competitor to donor, depending on the plot) was calculated. The ratios used were from 2^{-4} to 2^{8} in increments of $2^{0.5}$. The median DFRET values was then plotted in the place where the median ratio (for each interval) is located.

3 Results

3.1 Limits of the bimolecular försters resonance energy transfer-based method

FlowFRET proved to be a valuable tool for studying PEX5-PTS1 interactions, but it was unclear whether the approach was suitable for the study of full-length cargo proteins, because a large size reduces the DFRETmax (Figure 2A) and thus deteriorates the signal to noise ratio. Similarly, only low DFRET signal intensities are obtained for binding partners with weak interaction, because only a small fraction of donor is engaged with acceptor proteins limiting the power of the method as well (Figure 2A). Thus, we first studied the effect of protein size on the power of flowFRET taking advantage of two protein variants of the murine sterol-carrier protein (mSCP) sharing the C-terminal domain. These are the 143 amino acids (aa) long SCP2 protein consisting solely of the characteristic SCP-domain and the 547aa SCPx protein comprised of the SCP-domain and an additional N-terminal thiolase domain (Figure 2B). Using flowFRET experiments in pex5$^{-/-}$ MEF, we studied the interaction between mCherry-PEX5 (TPR) and EGFP-tagged variants of these two proteins (EGFP-SCP2, EGFP-SCPx) or EGFP-PTS1 encoding the C-terminal 12 amino acids of SCP2 (EGFP-PTS1(SCP2) as described before (Hochreiter et al., 2020). As the composition of data sets markedly affects the output (Hochreiter et al., 2019) we selected subsets of cells sharing acceptor to donor ratios (acc:don) within a very narrow range and compared DFRET values as proxies for the interaction strength at three different ratios (Figure 2C) (numerical results can be found in Supplementary Table S1). At equimolarity (1:1) the median DFRET value of EGFP-PTS1(SCP2) was slightly but significantly higher than that of EGFP-SCP2, whereas the median DFRET of EGFP-SCPx was markedly lower, reflecting the larger size of SCPx and thus a lower DFRETmax. This interpretation is supported at higher acc:don ratios and by plotting all cells to depict saturation curves and to visualize their slopes and plateau level (Figure 2D). Comparing results of three different experiments revealed consistent overall patterns (Figure 2E). However, neither of these depictions of primary data is able to disentangle the contributions of different affinities (KDs) and different protein sizes (DFRETmax), which are reflected by different slopes and plateau levels of the saturation curves, respectively. However, when applying the fitting algorithm (Hochreiter et al., 2020) to infer measures of interaction strength (apparent KD, KD^{app})[1] and DFRETmax (Figure 2F), we found that the predicted affinity of SCP2 was significantly higher than of the isolated PTS1 alone [numerical results can be found in Supplementary Table S2(overview)], whereas the affinity of SCPx appeared drastically lower. Moreover, the size of the donor molecules was reflected by the predicted DFRETmax values, as the PTS1 peptide has the highest and the large SCPx the lowest DFRETmax.

Next, we took advantage of this method to investigate the effect of two point mutations in the PTS1 of full-length SCP2 on its affinity to PEX5. On the one hand, the characteristic leucine at the ultimate position was substituted by the biophysically similar valine [AKL→AKV], which is hardly found in naturally occurring PTS1 and on the other hand the small residue glycine at position 139 directly involved in PEX5-binding (Stanley et al., 2006) was substituted by leucine (G139L, GNAKL). When flowFRET experiments were performed using SCP2, SCP2(AKL→AKV) and SCP2(G139L) we found that the median DFRET values of populations with equimolar acc:don ratio were markedly lower for AKV, but only slightly reduced for G139L (Figure 2G) and only the curve progression of SCP2(AKL→AKV) showed a clearly reduced slope in the ascending phase (Figure 2H). Comparing three different experiments showed a similar pattern (Figure 2I) and extracting KD1^{app}s by fitting showed a clear increase

1 Please note that in contrast to (Hochreiter, et al., 2020) we use here KD1^{app} as measure for interaction strength between donor and acceptor for which lower values indicate higher affinity.

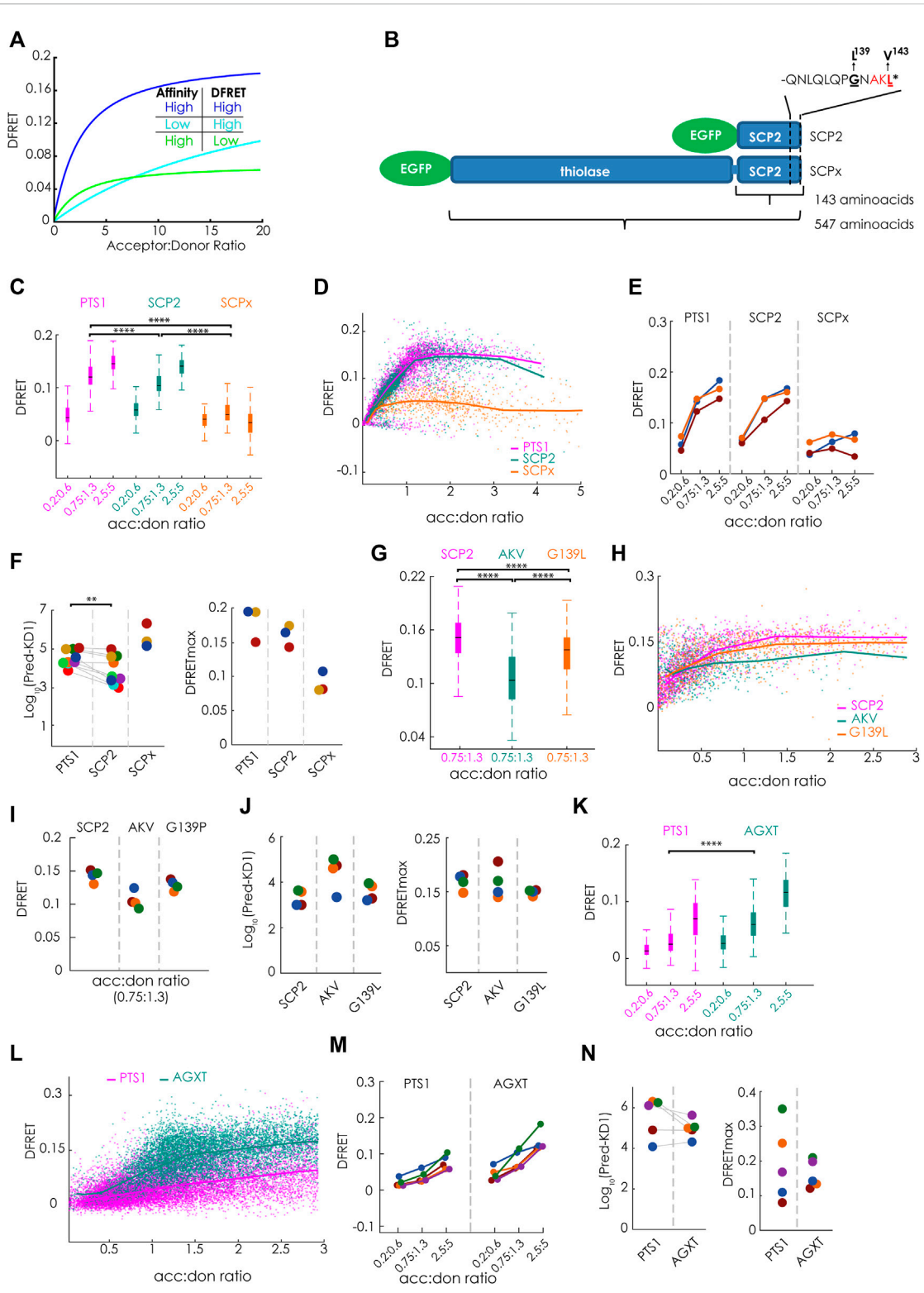

FIGURE 2
Bimolecular flowFRET analysis of protein complexes involving large proteins or low affinity binding partners: **(A)** Traditional limitations of FRET-measurements are protein complexes involving large proteins (low DFRETmax) (green) or low affinity binding partners (cyan) compared to complexes involving small proteins with high affinity (blue); **(B)** Schematic depiction of the PTS1-carrying murine proteins SCPx and SCP2 sharing the same C-terminal domain, but differing in protein size due to an additional thiolase domain in SCPx, the last 12 amino acids encoding the PTS1 (PTS1(SCP2)) are depicted separetely; **(C–N)** pex5$^{-/-}$ MEF expressing mCherry-PEX5(TPR) as acceptor and various EGFP-tagged donor molecules
(*Continued*)

FIGURE 2 (Continued)
were analyzed by flow cytometry to measure a large number of cells; **(C–F)** donors: EGFP-PTS1(SCP2) (12aa), EGFP-SCP2 (SCP2: 143aa) and EGFP-SCPx (SCPx: 547aa), **(C)** comparison of DFRET values of three subpopulations of cells each sharing the same acc:don ratio; **(D)** DFRET values of all cells to generate a saturation curves; **(E)** comparison of the median DFRET values of the groups described in **(C)** for three independent experiments; **(F)** results of computational extraction of the key parameter KD^{app} (left) and DFRETmax (right), each point represents one experiment, the same color indicate the same day; **(G–J)** donors: EGFP-SCP2, EGFP-SCP2(AKL→AKV) and EGFP-SCP2(G139L) data are depicted as in **(C–F)**; **(K–N)** donors: EGFP-PTS1(AGXT) and EGFP-AGXT, data are depicted are in **(C–F)**; Statistics: C,G,K: box blots with quartiles and ranges, multicomparison "Tukey-Kramer" for cells sharing acc:don 0,75 < x < 1,3 (C: PTS1 vs. SCP2 = 4.30e-14, PTS1 vs. SCPx < 1e-100, SCP2 vs. SCPx = < 1e-100; **(G)** SCP2 vs. AKV < 1e-100, SCP2 vs. G139P< = 1.445e-07, AKV vs. G139p = 2.0431e-15; **(I)** PTS1 vs. AGXT < 1e-100); **(F)** Wilcoxon signed rank test (p = 0.0039 for 9 pairs).

[AKL→AKV] reflecting a lower interaction strength, whereas [G139L] did not significantly change the KD^{app} (Figure 2J).

Moreover, we explored the reliability of flowFRET for low-affinity binding partners. For that purpose, we studied the interaction between PEX5 (TPR) and the low-affinity PTS1 of human alanine-glyoxylate aminotransferase (AGXT) (PTS1 (AGXT)) (Ghosh and Berg, 2010) using the interaction with the full-length AGXT protein as comparison. Due to the low affinity of PTS1 (AGXT) the median DFRET of subpopulations was lower than for PTS1(SCP2) (*cf.*Figure 1A) (Figure 2K) and the saturation curve steadily increased even at high acc:don ratios without reaching the plateau level (Figure 2L). The higher binding strength of full-length AGXT compared to PTS1 (AGXT) is reflected by a higher median DFRET value of subpopulations with equimolar acc:don ratio in spite of a lower expected saturation level (DFRETmax) (Figure 2K) and a steeper ascend of the saturation curve (Figure 2L). Multiple independent experiments showed similar patterns with consistently low median DFRET values (Figure 2M). Although the median DFRET values of subpopulations and the curve progression clearly indicate PEX5 binding for PTS1 (AGXT), extracting numerical values for KD^{app} and DFRETmax by the fitting algorithm shows highly variable results due to the low affinity of the peptide, which exceeds the detrimental effects of the comparably larger size of the full-length protein (Figure 2N). Altogether, these results confirmed the applicability of the method for small proteins, but also demonstrated its limitations for the study of larger proteins and binding partners with low affinity.

3.2 Life cell competition experiments to circumvent problems due to low affinity or large protein size

To circumvent these limitations, we took advantage of the observation that ectopically expressed PTS1-carrying proteins exert a competitive effect on the interaction between mCherry-PEX5 (TPR) and EGFP-PTS1, which is reflected by a reduction of the DFRET values obtained by flowFRET (Hochreiter et al., 2020). When acting as a competitor, neither a large protein size nor a low affinity to the acceptor should be detrimental for FRET-measurements as these competitor proteins do not directly participate in measuring FRET efficiency but only modify the DFRET value of a cell. Tagging competitor proteins with the fluorescent protein Cerulean allows the estimation of the cellular level of competitor protein, which is essential to establish a quantifying fitting algorithm for extracting critical parameters of the competition. For a computational analysis of data sets obtained by flowFRET competition experiments, we had to solve the mathematical problem of this three-component system and to generate a computational program to infer the key parameters of the competition, namely $KD1^{app}$ (donor-acceptor), DFRETmax, and $KD2^{app}$ (competitor-acceptor). For that purpose, we adapted the analytic solution of the theoretical competition problem (Wang, 1995) and implemented it into a novel fitting program (*cf.* materials and methods). For internal normalization of the values in the Cerulean channel and to estimate the amount of competitor in a cell, we took advantage of the fusion protein mCherry-Cerulean and calculated proper conversion factor estimates (Hochreiter et al., 2020).

To verify the mathematical approach, we took advantage of available large data sets originating from experiments, in which the apparent interaction strength between mCherry-PEX5 (TPR) and EGFP-PTS1, harboring the arbitrary PTS1-peptide Hs55 (EGFP-PTS1(Hs55) (Lametschwandtner et al., 1998)), was modulated by Cerulean-tagged PTS1 peptides, encoding either the same high affinity PTS1 Hs55 or the low affinity PTS1 Hs57, using Cerulean alone as a negative control, which should not affect the interaction strength [(Hochreiter et al., 2020), Figure 5]. To estimate the effect size of competition, we first preselected cells sharing an acc:don ration around one (0.75 < x < 1.3) and compared the changes in the median DFRET values of subpopulations each sharing narrow, but well-defined competitor to donor (comp:don) ranges. By this means, we were able to visualize differences between samples expressing a competitor or not, but also between competitors with high (Hs55) or low (Hs57) affinity (Figure 3A). The overall shape of the curve progression of the decay curve (increasing comp:don) also differed clearly between high and low affinity competitors (Figure 3B). Similarly, comparing subpopulations sharing a comp:don ratio of one, but differing in the acc:don ratio showed clear differences as well (Figure 3C) and also the

10.3389/fcell.2022.1026388

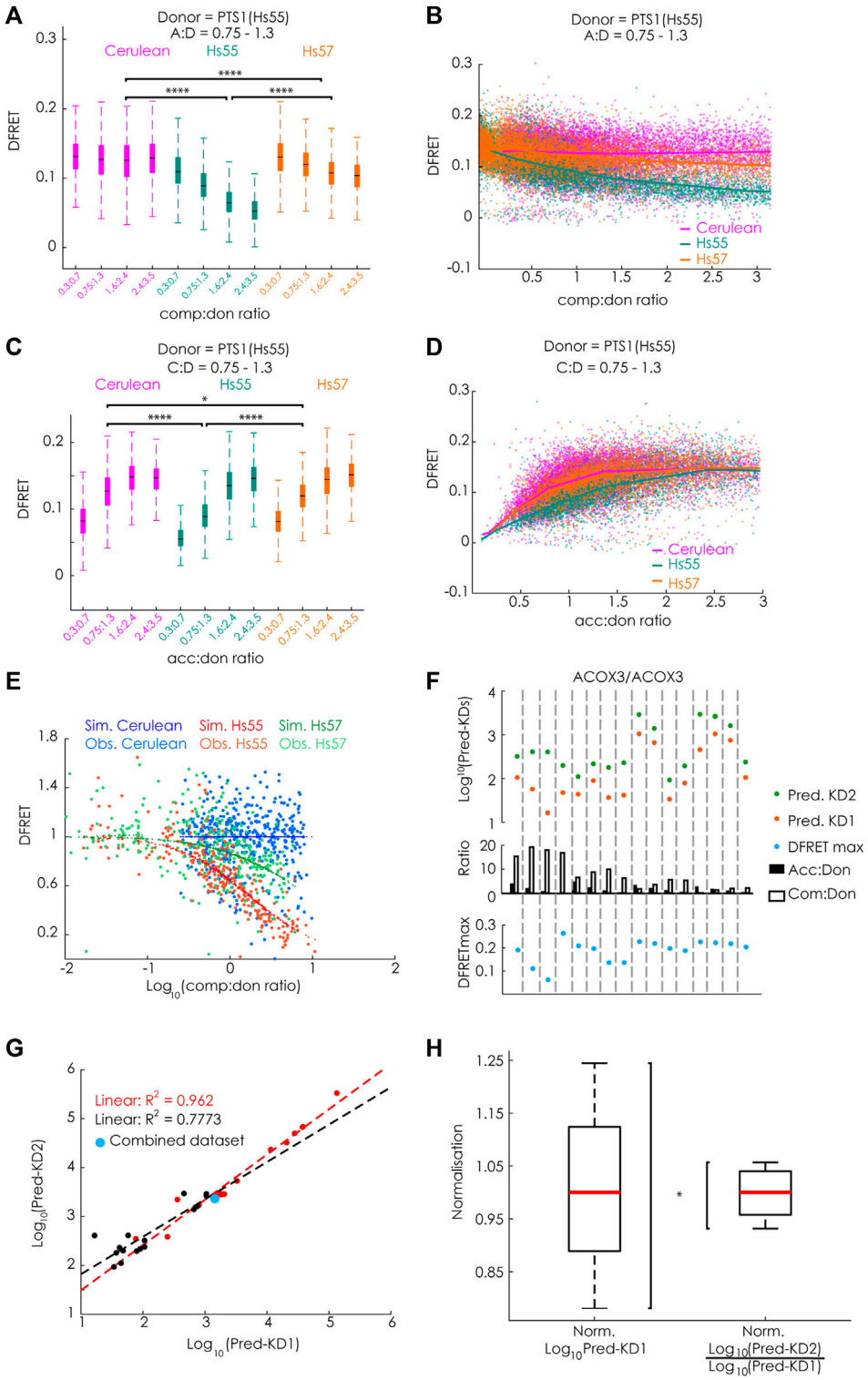

FIGURE 3
FlowFRET allows a competition assay in living cells: pex5$^{-/-}$ MEF expressing mCherry-PEX5(TPR) as acceptor and various donor and competitor molecules were analyzed by flow cytometry to measure a large number of cells; **(A–E)** donor: EGFP-PTS1(Hs55), competitor: Cerulean, Cerulean-PTS1(Hs55) or Cerulean-PTS1(Hs57); **(A)** comparison of DFRET values of subpopulations of cells sharing an acc:don ratio of 0,75 < x < 1,3 and different comp:don ratios, **(B)** DFRET decay curves (increasing comp:don) of all cells sharing an acc:don ratio of 0,75 < x < 1,3; **(C)** comparison of DFRET values of subpopulations of cells sharing an comp:don ratio of 0,75 < x < 1,3 and different acc:don ratios; **(D)** plotting DFRET values of all cells sharing
(*Continued*)

FIGURE 3 (Continued)
a comp:don ratio between 0,75 < x < 1,3 to generate saturation curves (increasing acc:don); **(E)** the results the fitting algorithm for Hs55 ($KD1^{app}$: 14076, $KD2^{app}$: 26258 and DFRETmax: 0.153) and Hs57 ($KD1^{app}$: 14400, $KD2^{app}$: 199636 and DFRETmax: 0.153) were used to calculate for each cell based on the values for the donor, acceptor and competitor level the expected values for DFRET in the presence or absence of competitor, the ration of the values as % were plotted against the Log_{10} of the comp:don ratio to obtain a traditional inhibition curve (blue, green and red) and the corresponding ration of the observed values are depicted as with the same colors; **(F–H)** donor: EGFP-PTS1(ACOX3), competitor: Cerulean-PTS1 (ACOX3): **(F)** cell populations obtained by independent transformations with different relative amouts of expression plasmids for donor and acceptor display different medians of acc:don (black) or comp:don (white) ratios (middle), when extracting by the fitting algorithm $KD1^{app}$ (Pred.$KD1^{app}$, orange), $KD2^{app}$ (Pred.$KD2^{app}$, green) and DFRETmax (blue) values for each of these different data we obtained results of marked variability; **(G)** however, when plotting the Log_{10}(Pred-$KD1^{app}$) against the Log_{10}(Pred-$KD2^{app}$) the values were highly correlated (black line), which became even stronger (orange line) when the fitting was performed with a predefined DFRETmax (0.226), which was obtained by predicting these values from a united data set composed of all 16 data sets (blue point); **(H)** compiling the results of fittings applied to all available data sets obtained either by bimolecular flowFRET (donor: PTS1(ACOX3)) or competitive flowFRET (donor and acceptor PTS1(ACOX3)) the normalized variability (s/median) was markedly smaller for the latter expressed as $Log_{10}(KD2^{app})/Log_{10}(KD1^{app})$ compared to the first expressed as $Log_{10}(KD1^{app})$. Statistics: A&C: box blots with quartils and ranges, multicomparison "Tukey-Kramer" for cells sharing comp:don ratios between 1,6 < x < 2,4 (A, Cerulean vs. Hs55 < 1e-100, Cerulean vs. Hs57 < 1e-100, Hs55 vs. Hs57 < 1e-100) or acc:don rations between 0,75 < x< 1,3 (C, Cerulean vs. Hs55 < 1e-100; Cerulean vs. Hs57 = 0.0305; Hs55 vs. Hs57 < 4.825e-07); **(H)** Two-sample F-test for equal variances (p = 0.0356).

saturation curve (increasing acc:don) showed clear differences (Figure 3D). When analyzing these data sets with our newly generated algorithm we obtained values for $KD1^{app}$, $KD2^{app}$ and DFRETmax, which were comparable to those obtained by bimolecular flowFRET. Next, we used these values to calculate the fraction of donor molecules engaged in acceptor-donor complexes (acc.don) in the presence or absence of competitor and estimated the expected reduction of DFRET due to competition for each data point. Plotting these values against the comp:don ratio depicted as Log_{10} showed a decay curve very similar to characteristic curves of biochemical competition experiments, which supported the validity of the mathematical solution (Figure 3E).

3.3 Computational exploration of the fitting algorithm

To further validate the power of this life-cell competition approach, we systematically investigated different aspects of this method to explore possible limitations. Although Cerulean-tagged proteins do not affect FRET efficiency measurements between EGFP and mCherry, the energy transfer from Cerulean-tagged cargo proteins to mCherry-PEX5(TPR) reduces the measured intensity in the Cerulean channel. To estimate the consequences of a comparably small underestimation of the Cerulean level, we calculated the effective changes for the results of competition experiments using EGFP-PTS1(Hs55) as donor and Cerulean-PTS1(Hs55) as competitor (Hs55/Hs55), because a competitor with a short, but high-affinity peptide should present with the largest deviations (for details see Supplementary File S1A). We found that the mean error size for Cerulean intensity values was around 5.87 ± 2.89% and when using corrected values for the Cerulean channel the changes in acc.don complexes, which directly relates to the error of the DFRET value, were about 1.27 ± 0.8%. Subjecting the corrected data set to the fitting protocol resulted in very similar values for $KD1^{app}$ (4% lower), $KD2^{app}$ (1.7% lower) values and the DFRETmax level (0.65% lower), which is negligible compared to the variation obtained between the results of different experiments. Moreover, we validated that the output of the fitting was robust against a slight misjudgment of the background value of the FRET-channel. When all data points of a given data set, either Hs55/Hs55 or Hs55/Hs57, were incrementally in- or decreased and these modified data sets were refitted (Supplementary File S1B), we found that the values of $KD1^{app}$ and $KD2^{app}$ expressed as Log_{10} often remained unchanged and only occasionally $KD1^{app}$ and $KD2^{app}$ changed, but then in a similar manner. In contrast, the extracted values for DFRETmax followed the incremental changes in the DFRET values demonstrating the robustness of the fitting algorithm to slight inconsistencies in the definition of the DFRET-background level, next to the expected changes in DFRETmax. Furthermore, we investigated in how far the reliability of the fitting procedure was affected by the sample size. For that purpose, we randomly drew subpopulations of different size from the data set Hs55/Hs55, and independently fitted ten subpopulations of the same size to compare the inferred values for $KD1^{app}$ and $KD2^{app}$ and to estimate their variance. We found that already at sample sizes of 250 data points the median of ten samples was close to the result obtained by fitting the entire data set, but a low variance among different subsets was observed only when at least 1,000 data points per subset were used (for details see Supplementary File S1C). Moreover, we investigate the interdependence of the three fitted parameters, $KD1^{app}$, $KD2^{app}$ and DFRETmax by analyzing the changes in the mean error size (mean square error, MSE) upon incrementally changing and predefining one of these values and resubmitting the data set to another fitting (Supplementary File S1D). When the two other parameters were predefined at the original values the MSE drastically increased in all cases, whereas only minor changes were observed when the values for the other parameters were free to readapt. Especially $KD1^{app}$ and $KD2^{app}$ very effectively compensated aberration of the other value, which corroborates the capability of the fitting procedure to recapitulate

the tight relation between the slope of the decay curve and the KD2/KD1 ratio. This suggested that the ratio of $KD2^{app}$ and $KD1^{app}$ is a more robust measure of the relative binding strength obtained by this fitting procedure. Next, we tested the effect of marked changes in the composition of a data set with regard to the relative amounts of acceptor, donor and competitor expressed in the cells. For that purpose, we repeated the fitting of the competition experiment using the data sets Hs55/Hs55 and Hs55/Hs57, but considered only cells within predefined ranges of acc:don and comp:don (Supplementary File S1E). We found that the results of fittings using subsamples that cover exclusively very low or very high acc:don ratios and subsamples enclosing only high comp:don ratios inferred markedly different values for $KD1^{app}$ and $KD2^{app}$ even when expressed as $Log_{10}(KD^{app})$. However, importantly, the two values consistently changed into the same direction supporting the hypothesis that the $Log_{10}(KD2^{app})/Log_{10}(KD1^{app})$ is more reliable. As these subdivisions were artificially generated by strict threshold, we independently confirmed this observation by using donor and competitor proteins equipped with the PTS1 of ACOX3 (PTS1(ACOX3)), ACOX3/ACOX3. Cells were transfected with expression plasmids encoding donor, acceptor and competitor in widely differing combinations and each of these transformations was used as an independent sample (Figures 3F,G). We found that overall high acc:don ratios were associated with high median DFRET values and high comp:don levels with low median DFRET values (Supplementary Figure S2A). Moreover, uniting all independently transformed cells (ACOX3/ACOX3_1–16) to one large data set, subdividing this data set according to the comp:don ratio and independently subjecting these subpopulations to the bimolecular fitting verified a direct correlation between the comp:don ratio and the inferred value for $KD1^{app}$ (Supplementary Figure S2B), which confirmed the internal coherence of the different subsets. Moreover, when fitting the original data sets independently the predicted values for $Log_{10}(KD1^{app})$ and $Log_{10}(KD2^{app})$ varied markedly between the samples (Figure 3F), but the difference between these values and thus the ratio of $KD2^{app}$ to $KD1^{app}$ was more similar. When plotting $Log_{10}(KD2^{app})$ against $Log_{10}(KD1^{app})$ we found a high correlation ($R^2 = 0.773$) (Figure 3G), which was further increased ($R^2 = 0.962$) when for the fitting identical DFRETmax values were predefined for all samples and thus compensatory effects related to the adjustment of the DFRETmax value were excluded. These results confirmed that a certain bias in the inference of $KD1^{app}$ and $KD2^{app}$ caused by a biased composition of the data set is compensated by the concomitant deviation of both values and importantly, the values for $KD1^{app}$ and $KD2^{app}$ inferred from the united large data set is located at the center of the two curves (blue point). Thus, the internal normalization renders this fitting approach more robust. To verify this hypothesis, we analyzed all available results of independent flowFRET experiments studying the interaction between PEX5(TPR) and the PTS1(ACOX3) either by traditional bimolecular measurements between mCherry-PEX5(TPR) and EGFP-PTS1(ACOX3) or competition experiments in which Cerulean-PTS1(ACOX3) was included (Figure 3H). We found that the normalized variance was significantly lower for the competition experiments, which confirmed that the $Log_{10}(KD2^{app})/Log_{10}(KD1^{app})$ ratio is a more robust and reliable measure for the apparent interaction strength.

3.4 Verifying the power of the live-cell flowFRET competition assay

Next, we evaluated, whether our new method can discriminate competitors with different binding strengths and measure the interaction strength of large binding proteins. For that purpose, we first systematically investigated the modulatory effect of different competitor proteins on the interaction between mCherry-PEX5(TPR) and EGFP-PTS1(ACOX3). We used Cerulean extended by the PTS1 of ACOX3 or two variants thereof with lower affinity (K-1E or LK/SE) or the PTS1 of Hs55 or Hs57 (Hochreiter et al., 2020). We analyzed these data sets by first selecting cells with an acc:comp ratio of about one and depicting the effect of increasing comp:don ratio on the median DFRET value either by comparing subpopulations with different comp:don ratio (Figure 4A) or by depicting decay curves (Figure 4B). Alternatively, we selected cells with a comp:don ratio around one and followed the ascending DFRET values with increasing acc:don ratios at the level of subpopulations (Figure 4C) or as saturation curves (Figure 4D). Depicting subpopulations revealed differences in the median DFRET with a comp:don ratio around two or an acc:don ratio of about one (Figure 4A&3C) and the decay and saturation curves displayed different slopes (Figures 4B,D). The relative fall of the decay curves differed among the competitors (Figure 4C) and their ranking reflected the affinity of the competitor peptides, with ACOX3 and Hs55 being high affinity, Hs57 and K-1E being intermediate affinity and LK/SE being a low-affinity binders [based on previous experiments (Hochreiter et al., 2020)]. Moreover, the pattern of DFRET decay of the selected populations was similar among different independent experiments (Figure 4E). Conversely, the apparent slope in the ascending phase of the saturation curve in the presence of a competitor decreased with the competitor´s increasing affinity (Figure 4D). When these data sets were subjected to the fitting algorithm and the extracted values were plotted as ratio $Log_{10}(KD2^{app})/Log_{10}(KD1^{app})$, we obtained consistent results (Figure 4F, left side) and the ranking of these values reflected the relative slope of the decay curves. In addition, by plotting the average of the $Log_{10}(KD2^{app})/Log_{10}(KD1^{app})$ values for the peptides against the values obtained by bimolecular measurements [(Hochreiter et al., 2020); inverse values as K_a^{app} had been used) we obtained a high correlation (Figure 4G). However, when inspecting the

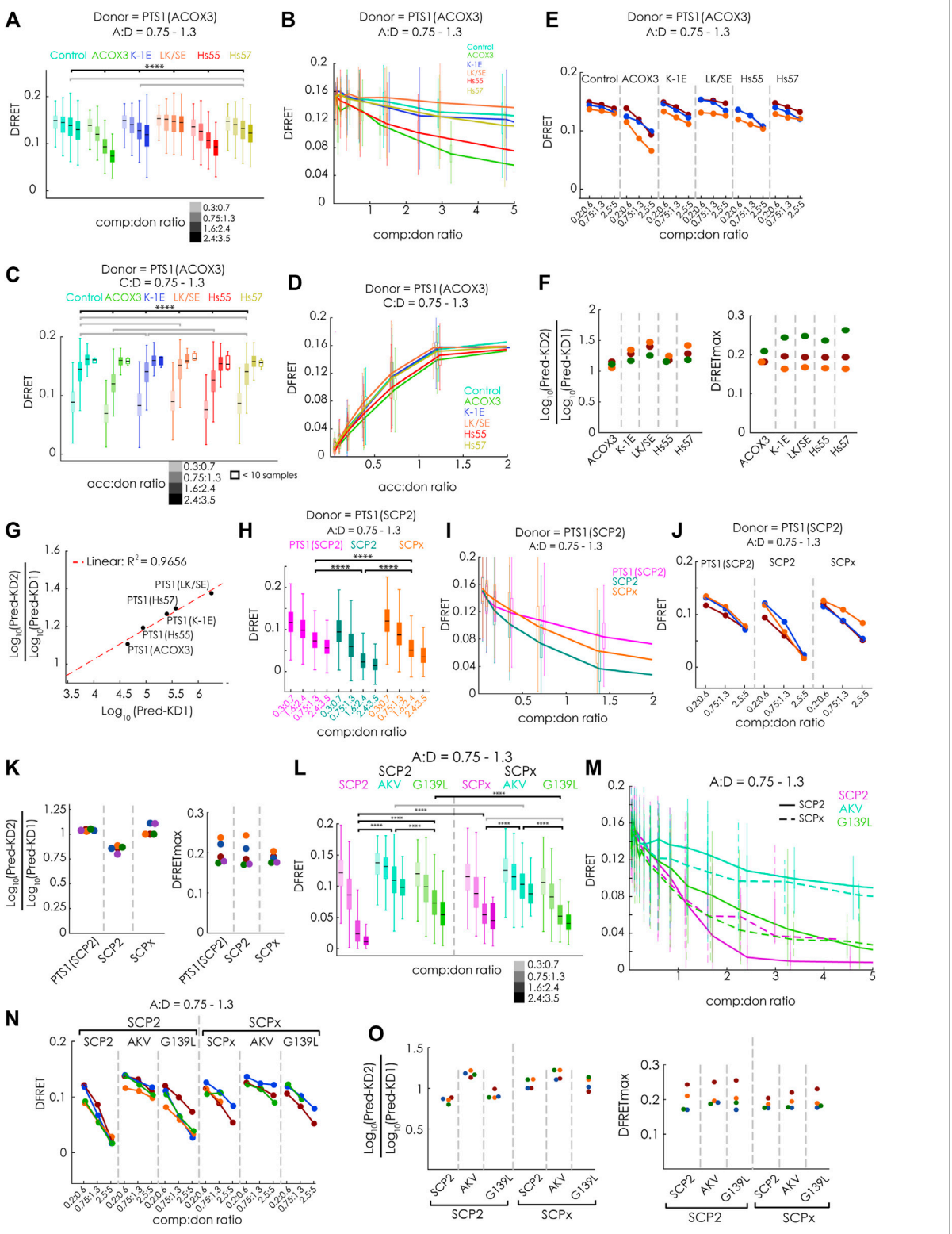

FIGURE 4
FlowFRET competition assays in living cells allow the discrimination of affinities and is applicable to large proteins: pex5$^{-/-}$ MEF expressing mCherry-PEX5(TPR) as acceptor and various donor and competitor molecules were analyzed by flow cytometry to obtain a large number of cells: **(A–G)** donor: EGFP-PTS1 (ACOX3), competitor: various Cerulean-PTS1 proteins harboring the PTS1 motifs of Hs55, Hs57, ACOX3, ACOX3_K-1E, ACOX3_LK/SE or Cerulean alone; **(H–K)** donor EGFP-PTS1(SCP2), competitor Cerulean-PTS1(SCP2), Cerulean-SCP2 or Cerulean-SCPx; **(L–O)**
(*Continued*)

FIGURE 4 (Continued)
donor EGFP-PTS1(SCP2), competitor Cerulean-SCP2, Cerulean-SCP2(AKL→AKV) or Cerulean-SCP2(G139L), Cerulean-SCPx, Cerulean-SCPx (AKL→AKV) or Cerulean-SCPx(G139L); to compare cells expressing different competitor proteins either **(A,H,L)** the median DFRET values of subpopulations sharing an acc:don ratio of 0,75 < x < 1,3 and different competitor to donor ratios or **(B,I,M)** the DFRET decay curves (increasing comp:don) of cells sharing an acc:don ratio of 0,75 < x < 1,3 are depicted; alternatively, **(C)** the median DFRET values of subpopulations sharing a comp:don ratio of 0,75 < x < 1,3 and different acc:don ratios or **(D)** the DFRET saturation curves (increasing acc:don) in the presence of a comp:donor ratio of 0,75 < x < 1,3 are depicted; **(E,J,N)** the pattern of a decay of median DFRET values with increasing median comp:don ratios is comparable between three different experiments and **(F,K,O)** the results of the fitting algorithm (Pred-KD1^{app}, Pred-KD2^{app} and DFRETmax) are plotted as ratio Log_{10}(Pred.-KD2)/Log_{10}(Pred.-KD1) (left side) and as DFRETmax (right side); **(G)** plotting the affinities of these peptides as Log_{10}(KD) from our previous study (Hochreiter et al., 2020) against the Log_{10}(Pred.-KD2)/Log_{10}(Pred.-KD1) from the competition method we obtained a high correlation. Statistics: A,C,H,L: box blots with quartiles and ranges, multicomparison "Tukey-Kramer" for cells sharing acc:don rations between 0,75 < x < 1,3 and comp:don ratios between 1,6 < x < 2,4 (A,H,L) or cells sharing comp:don rations between 0,75 < x < 1,3 and acc:don ratios between 0,75 < x < 1,3 **(C)**, predictions **(F)** were analyzed by a bootstrapping method (details of the statistics *cf.* Supplementary Table S2).

predicted DFRETmax of these data sets (Figure 4F, right side], these values were relatively similar for each experiment reflecting the use of the identical donor but differed more between the experiments. These results demonstrate that the competition assay can effectively discriminate the affinity of different PTS1 peptides and that for peptides the results are in good agreement with the results of bimolecular measurements.

To verify that the competition approach is also capable of improving the performance for large proteins less accessible by bimolecular measurements due to limitations by the low DFRETmax value (cf.Figure 1B), we performed flowFRET competition experiments using EGFP-PTS1(SCP2) as donor and Cerulean-PTS1(SPC2), Cerulean-SCP2 or Cerulean-SCPx as competitors (Figures 4H–K). Comparing subsets with acc:don ratios around one and different comp:don ratios, the median DFRET value of cells expressing SCP2 was lower than those with PTS1(SCP2), reflecting a higher affinity of SCP2, whereas SCPx caused an intermediate reduction (Figure 4H). However, in contrast to Figure 1, the median DFRET values at low comp:don levels were very similar between all samples and thus are not affected by the size of the competitor. The negative slopes of the decay curves were also steeper for Cerulean-SCP2 than for those caused by Cerulean-SCPx or Cerulean-PTS1(SCP2) (Figure 4I), and comparison of three different experiments showed similar overall shapes, although the decay curve due to SCPx appears more similar to that caused by PTS1(SCPx) (Figure 4J). Upon fitting these data sets, we found that PTS1(SCP2) presents with a Log_{10}(KD2^{app})/Log_{10}(KD1^{app}) value around one, which reflects the identity of the PTS1 in donor and competitor protein, whereas SCP2 shows a lower Log_{10}(KD2^{app})/Log_{10}(KD1^{app}) ratio and thus a higher affinity than the PTS1 of the donor (Figure 4K, left part). The Log_{10}(KD2^{app})/Log_{10}(KD1^{app}) ratio for SCPx was also around one and resembles the isolated PTS1. Again, the predicted values for DFRETmax were similar between different samples within the same experiment reflecting the identity of the donor molecules but displayed higher variability between the experiments (Figure 4K, right part).

Finally, we addressed the question, whether differences in the affinities can be reliably measured for such large proteins as well. For that purpose, we repeated the competition experiments but compared the effects of the mutations [AKL→AKV] and [G139L] (*cf.* Figure 1) on the affinity of SCP2 and SCPx (Figures 4L–O). We found, at the level of individual subpopulations, that the effectivity of competition was markedly reduced by the mutation [AKL→AKV], whereas that of [G139L] was clearly reduced for SCP2 but less so for SCPx (Figure 4L), which was also reflected in the early phase of the decay curve (Figure 4M). Comparing three repetitions of these experiments show very similar patterns (Figure 4N), and the results of extracting key parameter from these data sets by the fitting algorithm were consistent (Figure 4O). On the one hand, the Log_{10}(KD2^{app})/Log_{10}(KD1^{app}) ratios were larger for the mutation [–AKV], whereas no apparent differences were found for the mutation [G139L], but on the other hand, the results appear highly consistent between the different experiments, but also regarding the predicted DFRETmax for each experiment. These results verify that this competition-based method is well-suited to study complexes including large proteins.

3.5 Investigation of full-length cargo-binding by PEX5 (TPR)

After these confirmations, we investigated the interaction of PEX5(TPR) with several PTS1-carrying full-length proteins, namely human AGXT (Fodor et al., 2012), acyl-CoA oxidase 3 (ACOX3) (Van Veldhoven et al., 1994), D-amino acid oxidase (DAO) (Sacchi et al., 2011) and Glutathione-S-transferase kappa-1 (GSTK1) (Wang et al., 2013) as well as pig peroxisomal carbonyl-reductase (PerCR-SRL) (Tanaka et al., 2008). We used mCherry-PEX5(TPR) and EGFP-PTS1 (ACOX3) as FRET-pair and co-expressed the above-mentioned proteins as fusion proteins with Cerulean. We found that in individual experiments, the median DFRET values of subpopulations with very similar acc:don and comp:don ratios were consistently reduced in a dose-dependent manner (Figure 5A). This effect appeared smaller than for SCP2 (*cf.* Figure 3H), but in the latter case EGFP-PTS1(SCP2) with a lower affinity was used as donor. The curve progressions showed a clear decay for

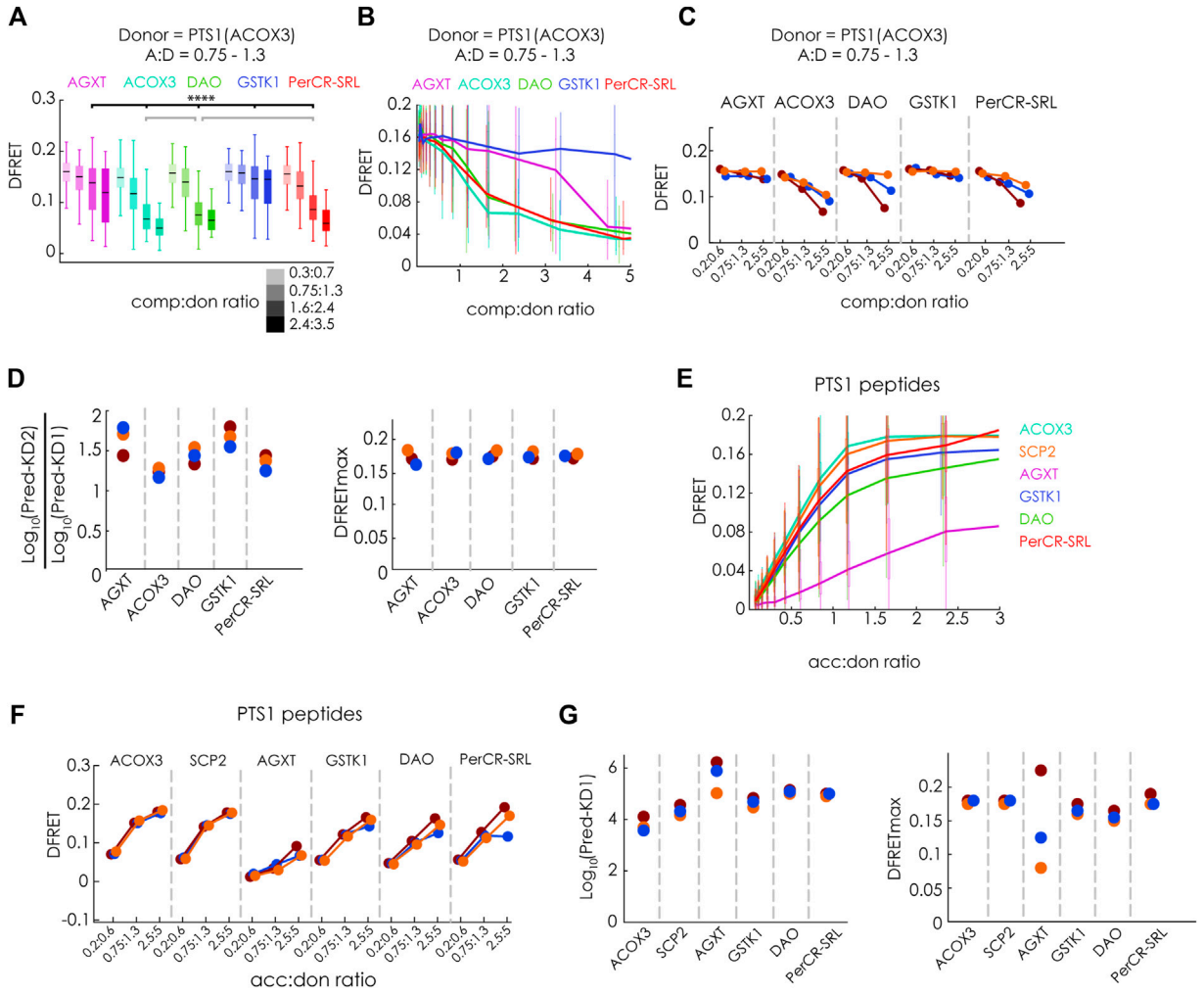

FIGURE 5
Studying the binding of full-length PTS1-carrying proteins to PEX5 by flowFRET competition experiments: pex5$^{-/-}$ MEF expressing mCherry-PEX5(TPR) as acceptor and various donor and competitor molecules were analyzed by flow cytometry to obtain a large number of cells **(A–D)** donor: EGFP-PTS1(ACOX3), competitor: Cerulean-tagged full length proteins of hAGXT, hACOX3, hDAO, hGSTK1, pig PerCR; **(A)** the median DFRET values of subpopulations sharing an acc:don ratio of 0,75 < x < 1,3 and different competitor to donor ratios or **(B)** the DFRET decay curves (increasing comp:don) of cells sharing an acc:don ratio of 0,75 < x < 1,3 are depicted (*cf.* Figures 3A,B); **(C)** the pattern of the decay curves is comparable between three different experiments and **(D)** the results of the fitting (Pred.-KD1, Pred.-KD2 and DFRETmax) are plotted as ratio of Log_{10} (Pred.-KD2)/Log_{10} (Pred.-KD1) or as DFRETmax; **(E–G)** donor: EGFP-PTS1 variants harboring the PTS1 of hAGXT, hACOX3, hDAO, hGSTK1, pig PerCR; **(E)** DFRET saturation curves (increasing acc:don); **(F)** when comparing subpopulations sharing the same acc:don ratio the pattern is comparable between three different experiments and **(G)** results of the fitting algorithm (Pred.-KD1, and DFRETmax) are plotted as Log_{10}(Pred.-KD1) (left side) and DFRETmax (right side). Statistics: **(A)** box blots with quartiles and ranges, multicomparison "Tukey-Kramer" for cells sharing acc:don rations between 0,75 < x < 1,3 and comp:don ratios between 1,6 < x < 2,4, predictions **(D)** and **(G)** were analyzed by a bootstrapping method (details of the statistics *cf.* Supplementary Table S2).

ACOX3, DAO and PerCR-SRL, whereas the slope was less pronounced for AGXT and minimal for GSTK1 (Figure 5B). These results were consistently found in three independent experiments (Figure 5C). When the data sets were subjected to the fitting algorithm, $Log_{10}(KD2^{app})/Log_{10}(KD1^{app})$ ratios were rather similar between the experiments as were the values for the predicted DFRETmax values (Figure 5D). Although clear differences in the competitive effectivity for the different full-length proteins were observed, the values for $Log_{10}(KD2^{app})/Log_{10}(KD1^{app})$ were markedly larger than one, suggesting a drastically lower affinity than the donor. However, again, a direct comparison with results obtained for SCP2 (*cf.*Figures 3G–N) is not possible, because in these experiments EGFP-PTS1(ACOX3) served as donor, whereas in the latter experiments PTS1(SCP2). Thus, we compared these results with competition experiments using EGFP-PTS1(SCP2) as

donor and found that the effectivity of competition was higher (Supplementary Figure S3A) and the $Log_{10}(KD2^{app})$/$Log_{10}(KD1^{app})$ ratio for the same full-length proteins was lower (Supplementary Figure S3B). Importantly, the relative binding strength was retained between these experiments as the results of both experiments showed good correlation (Supplementary Figure S3C), but nonetheless, the $Log_{10}(KD2^{app})/Log_{10}(KD1^{app})$ ratios were markedly larger than one suggesting that these full-length proteins did not bind as strong to PEX5 as did SCP2.

To better relate these results to the affinity of isolated PTS1 peptides within living cells, we independently investigated the affinity of different EGFP-PTS1 variants harboring the last 12 amino acids of the studied proteins and mCherry-PEX5(TPR) by bimolecular flowFRET experiments. We found saturation curves with clearly different slopes (Figure 5E). In three independent experiments we consistently found high DFRET signals in subfractions sharing the same acc:don ratio except for the PTS1 of AGXT (Figure 5F). When extracting $KD1^{app}$ and DFRETmax by the fitting algorithm (Figure 5G), we obtained different affinities ranging across more than an order of magnitude as described previously (Ghosh and Berg, 2010; Hochreiter et al., 2020), whereas the inferred DFRETmax values were similar except for the high variability of DFRETmax of PTS1 (AGXT), similar to our previous results (*cf.*Figure 1L).

Overall, the ranking of the affinities of these 12aa long peptides fused to EGFP was similar to that obtained by biophysical measurements of isolated PEX5 and 6aa peptides (Ghosh and Berg, 2010) and correlated with full-length proteins except for the peptide of GSTK1 (12aa), which appeared with intermediate affinity binding peptide in our assay but displayed comparably weak binding as 6aa peptide and very weak binding as full-length protein (*cf.* Figures 4C,D). However, although the relative affinities of full-length proteins and isolated PTS1 peptides was similar except for GSTK1 and consistent between experiments using different donors, the comparably low affinity of full-length proteins was surprising, because the PTS1 peptides of SCP2 and AGXT had a clearly lower affinity to PEX5 than the corresponding full-length proteins (*Cf.*Figure 1). In the latter cases the stronger binding can probably be retraced to additional interaction domains with PEX5 (Stanley et al., 2006; Fodor et al., 2012) although overall AGXT bound with markedly lower affinity than SCP2. We assumed that the oligomerization status of the investigated proteins might affect the binding strength, because in the case of human catalase tetramerization and PEX5 binding were found to compete (Freitas et al., 2011), whereas the previously studied SCP2 occurs exclusively as a monomeric protein and AGXT dimers can effectively bind to PEX5 (Fodor et al., 2012). Among the studied proteins DAO and GSTK1 have been described as dimers (Kawazoe et al., 2006; Wang et al., 2011), PerCR as tetramer (Tanaka et al., 2008) and ACOX3 even as octamer (Van Veldhoven et al., 1994). Provided that some fully folded proteins expose their C-terminus less effectively upon oligomerization, mCherry-PEX5(TPR) used in our study might not be able to effectively compete for the PTS1, because only a PEX5-variant in which the TPR-domain is extended at its N-terminus was able to disassemble catalase oligomers (Freitas et al., 2011).

3.6 Investigating PEX5(N-TPR)

To test the hypothesis that a PEX5-variant with an N-terminal elongation (N-TPR) has markedly higher affinities to these full-length PTS1-carrying proteins, because it is able to disassemble oligomeric protein complexes preventing PEX5 (TPR) from binding, this protein, PEX5(N-TPR), was studied in detail. We first performed a flowFRET experiment to study the interaction between EGFP-PTS1(SCP2) and either PEX5(TPR) or PEX5(N-TPR) and found that the slope of the saturation curves appeared very similar. However, in the presence of the N-terminal extension the DFRETmax level was reduced, which was expected and reflected the larger distance between EGFP and mCherry in the complex (Figure 6A). This pattern was also found when comparing median DFRET values at equimolar acc:don ratio of independent experiments and different PTS1(SCP2 and ACOX) as binding partners, although the difference was less clear for PTS1(ACOX3) (Figure 6B). Applying the fitting algorithm to these data sets allowed the extraction of KD^{app}, which appeared slightly higher for PEX5(N-TPR) for PTS1(SCP2), whereas no difference was found for PTS1 (ACOX3) (Figure 6C). Next, we investigated, whether PEX5(N-TPR) binds SCP2 with higher affinity than PTS1(SCP2) as well and studied the effect of inverting the charge of two positions in the N-terminal part of SCP2, namely glutamate 35 to lysine (E35K) and lysine 38 to glutamate (K38E), which are clearly separated from the PTS1 but in the 3D-structure were found to participate in an additional PEX5-binding domain (Stanley et al., 2006). When bimolecular flowFRET experiments were performed comparing EGFP-PTS1(SCP2), EGFP-SCP2 or EGFP-SCP2(E35K/K38E), we found that the slope of the saturation curve appears steeper for SCP2, whereas the plateau level was clearly higher for PTS1(SCP2) (Figure 6D). A similar pattern was observed in three independent experiments when plotting subpopulations with similar acc:don ratio (Figure 6E), but again the contribution of the affinity and the saturation level could not be disentangled (*cf.*Figure 1). However, when applying the fitting algorithm to the corresponding data sets independent values for $KD1^{app}$ and DFRETmax were extracted (Figure 6F). The affinity of full-length SCP2 was estimated to be higher than an isolated PTS1 but introducing the point mutations E35K and K38E ablated this difference, whereas the DFRETmax values still reflected differences in protein size. These results suggests that

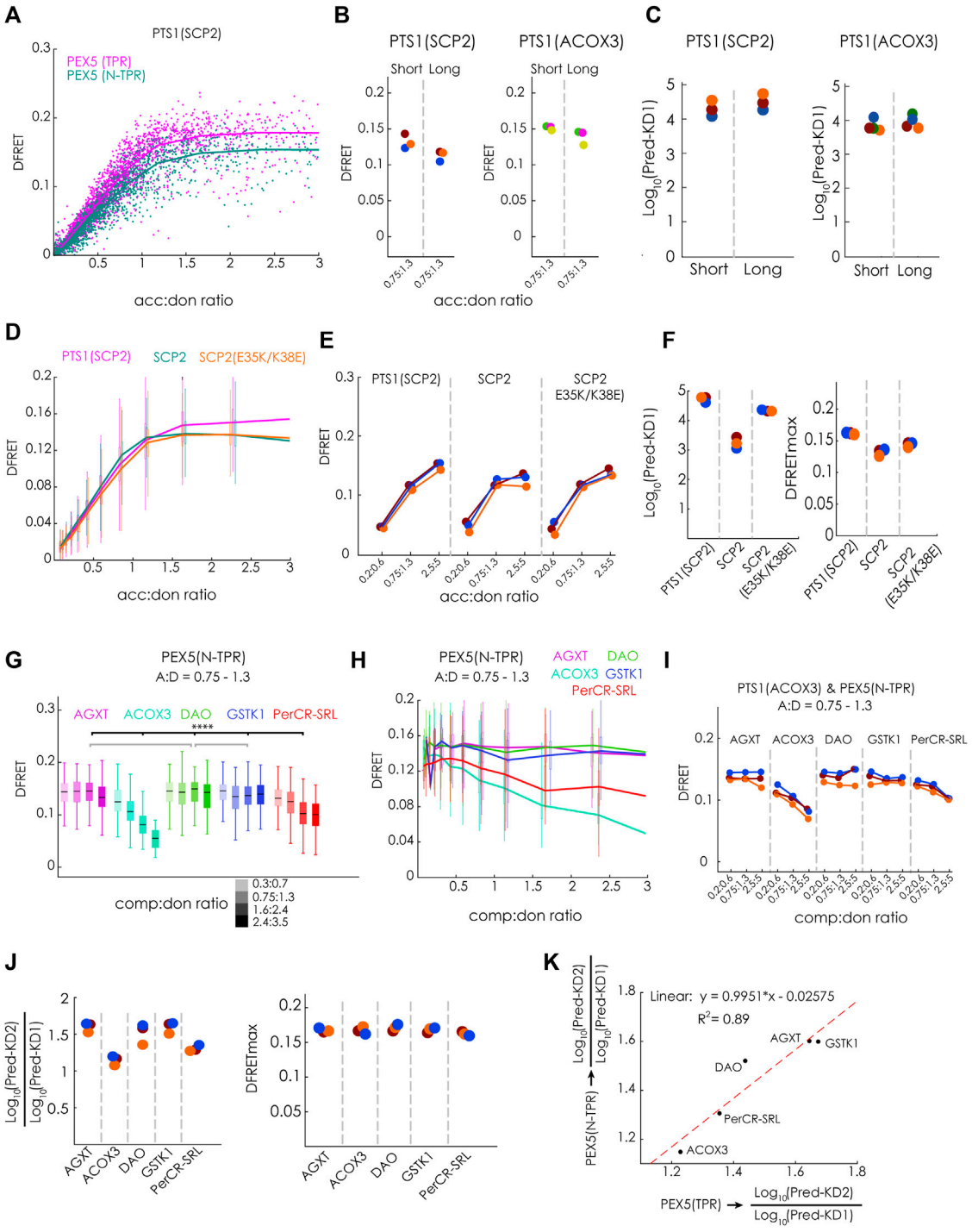

FIGURE 6
N-terminal extension of the PEX5-TPR domain (PEX5(N-TPR)) has a similar affinity to full-length PT1-carrying cargo proteins: **(A–F)** Bimolecular flowFRET experiments in pex5$^{-/-}$ MEF: **(A)** saturation curves of cells expression EGFP-PTS1(SCP2) as donor and either mCherry-PEX5(TPR) or mCherry-PEX5(N-TPR) as acceptor show different plateau levels; **(B)** the median DFRET value of populations sharing an acc:don ratio (0,75 < x < 1,3) is higher for mCherry-PEX5(TPR) than for mCherry-PEX5(N-TPR) when comparing repeated experiments and using either EGFP-PTS1(SCP2) or EGFP-PTS1(ACOX3) as binding partners, **(C)** the results of fitting these data sets (Pred-KD1^{app}) are plotted; **(D)** saturation curves for mCherry-PEX5(N-TPR) as donor and either EGFP-PTS1(SCP2), EGFP-SCP2 or EGFP-SCP2(E35K/K38E); **(E)** overall pattern of median DFRET values for different acc:don subpopulations is consistently observed in three different experiments of the one described in **(D)**; **(F)** the results of the fitting algorithm (Pred-KD1^{app} and DFRETmax) are plotted for the interactions in **(D)** and **(E)**; **(G–K)** flowFRET competition experiments: pex5$^{-/-}$ MEF expressing mCherry-PEX5(N-TPR) as acceptor, EGFP-PTS1(ACOX3) as donor and different Cerulean-tagged full-length proteins as competitor molecules were
(*Continued*)

FIGURE 6 (Continued)
analyzed by flow cytometry to obtain a large number of cells, **(G)** median DFRET values of subpopulations sharing an acc:don ratio of 0,75 < x < 1,3 and different competitor to donor ratios or **(H)** DFRET decay curves (increasing comp:don ratios) of cells sharing an acc:don ratio of 0,75 < x < 1,3 are depicted; **(I)** the pattern of progressive reduction in the median DFRET value of populations with increasing comp:don ratios is consistently observed in three different experiments; **(J)** the results of the fitting algorithm (Pred-KD1, Pred-KD2 and DFRETmax) are plotted as ratio Log_{10}(Pred.-KD2)/Log_{10}(Pred.-KD1) or as DFRETmax, **(K)** plotting the Log_{10}(Pred.-KD2)/Log_{10}(Pred.KD1) values for the interaction of the same competitor molecules with either PEX5(TPR) (x-axis) or PEX5(N-TPR) (y-axis) are highly correlated. Statistics: **(G)** box blots with quartiles and ranges, multicomparison "Tukey-Kramer" for cells sharing acc:don rations between 0,75 < x < 1,3 and comp:don ratios between 1,6 < x < 2,4, predictions **(J)** were analyzed by a bootstrapping method (details of the statistics *cf.* Supplementary Table S2).

the contribution of the additional interphase between SCP2 and PEX5 is abrogated in SCP2(E35K/K38E).

When we performed flowFRET competition experiments using mCherry-PEX5(N-TPR) together with the same PTS1-carrying full-length proteins as before (*cf.*Figure 4), we found that the median DFRET values of subpopulations sharing an acc:don ration around one and different comp:don ratios were markedly reduced in the presence of ACOX3 as competitor protein, intermediate effects were observed for PerCR-SRL, low effects for AGXT, and nearly no effect was found for DAO and GSTK1 (Figure 6G). This pattern was also supported by the decay curves (Figure 6H) and observed in three independent experiments (Figure 6I). Subjecting these data sets to the fitting algorithm allowed the extraction of very similar values for DFRETmax, whereas for the different competitor proteins different $Log_{10}(KD2^{app})/Log_{10}(KD1^{app})$ ratios were obtained (Figure 6J). The pattern of $Log_{10}(KD2^{app})/Log_{10}(KD1^{app})$ values for PEX5(N-TPR) resembled those for PEX5(TPR) (*cf.*Figure 4G), with a high correlation (R^2 = 0,89) and a slope very close to one (Figure 6K).

Altogether, these results demonstrate that the affinity of full-length PTS1-carrying proteins to PEX5(TPR) and PEX5(N-TPR) is comparable and that the extension of the TPR domain at the N-terminus does not increase the apparent affinity for these proteins in living cells.

3.7 Modulatory role of the N-terminal domain of PEX14

Finally, we investigated whether our method is capable of discriminating different modes of inhibiting protein-protein interaction, which are traditionally classified as competitive and non-competitive (or allosteric). For that purpose, we compared the inhibitory effects of the competitive inhibitor Cerulean-PTS1, with that of a putatively non-competitive modulator PEX14(NTD)-Cerulean, which has been shown to interfere with the ability of PEX5(N-TPR) to disassemble oligomeric catalase tetramers (Freitas et al., 2011) (Figure 7A). First, we confirmed that the tagged proteins, PEX14(NTD)-EGFP and mCherry-PEX5(N-TPR), actually interact in living cells, and used mCherry-PEX5(TPR) as negative control (Figure 7B). The apparent interaction strength $KD1^{app}$ obtained by bimolecular fitting was in the same range as PTS1 motifs (~5.0E4 a. u.). Moreover, we demonstrated that overexpression of Cerulean-PTS1 (ACOX3) did not change the apparent interaction strength between PEX14(NTD) and PEX5(N-TPR), as overexpression of Cerulean-PTS1(ACOX1) did not affect the shape of the saturation curve (Figure 7C) and the comp:don dose response curve was flat (Figure 7D), a pattern, which was consistently found in three independent experiments (Figures 7E,F). This suggests that cargo-binding of PEX5(N-TPR) is not prerequisite for the interaction between PEX5(N-TPR) and PEX14(NTD).

Finally, we compared the modulatory effects of Cerulean-PTS1 (ACOX3) and PEX14(NTD)-Cerulean on the interaction between EGFP-PTS1 (ACOX3) and mCherry-PEX5(N-TPR) (Figures 7G–N). As expected, we found that increasing comp:don ratios of Cerulean-PTS1(ACOX3) progressively reduced the median DFRET values of subpopulations sharing the same acc:don ratios for mCherry-PEX5(N-TPR) as well as for mCherry-PEX5 (TPR) (Figure 7G, green). In contrast, the median DFRET values of mCherry-PEX5(N-TPR) were clearly reduced by PEX14(NTD)-Cerulean in a dose dependent, but not for mCherry-PEX5(TPR) although a comparison of the populations at a comp:don ratio between 1,6 and 2,4 showed a significant different due to the large number of cells although the effect size was very small (~3.5%) (Figure 7G, blue). The decay curves due to Cerulean-PTS1 had similar shapes for PEX5(TPR) and PEX5(N-TPR) (Figure 7H, green), whereas PEX14(NTD) only caused a dose dependent decay in DFRET for mCherry-PEX5(N-TPR) (Figure 7H, blue). Interestingly, the decay curve caused by PEX14(NTD) seemed to have a different shape and appeared to reach a plateau above background level, which could reflect an allosteric inhibition, and was even clearer for higher acc:don ratios (Figure 7I), whereas no such pattern appeared when comparing the curve progression upon inhibition by Cerulean-PTS1 (Figure 7J). Similarly, the ascending phase of the saturation curve showed characteristic reductions in the slope upon overexpressing Cerulean-PTS1 for PEX5(TPR) and PEX5(N-TPR) (Figure 7K, green), whereas PEX14-Cerulean only reduced those of PEX5(N-TPR) (Figure 7K, blue). Importantly, the latter

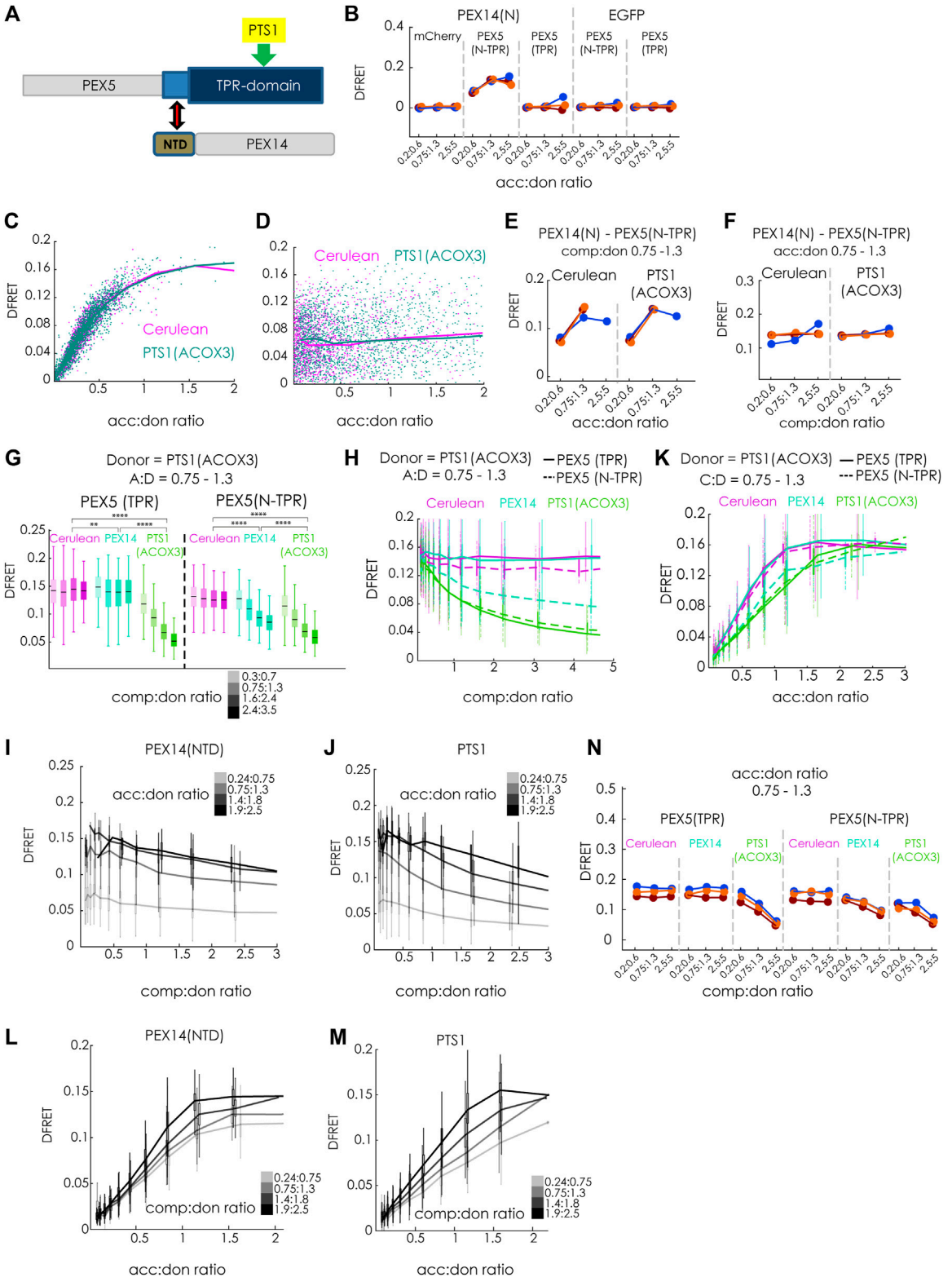

FIGURE 7
The N-terminal domain of PEX14 modulates the affinity of PEX5 and its cargo by a non-competitive mechanism: (A) Scheme: the interaction between the TPR-domain of PEX5 (blue) and the PTS1 (yellow) is modulated by the N-terminal domain (NTD, brown) of PEX14, binding to an N-terminal extension of the TPR-domain (bright blue); grey: parts of PEX5 and PEX14 not encoded in the test proteins; **(B)** bimolecular flowFRET
(*Continued*)

FIGURE 7 (Continued)
experiments in pex5$^{-/-}$ MEF verifying the interaction between PEX14(NTD)-EGFP and mCherry-PEX5(N-TPR), but not mCherry-PEX5(TPR) in living cells; **(C–F)** flowFRET experiments in pex5$^{-/-}$ MEF: the interaction between PEX14(NTD)-EGFP and mCherry-PEX5(N-TPR) is not affected by the expression Cerulean-PTS1 compared to Cerulean alone, when depicted as saturation curve **(C)** or as dose-response curve with respect to Cerulean-PTS1 **(D)**; these results are consistently observed in three independent experiments; (**G–M**) flowFRET competition experiments: pex5$^{-/-}$ MEF were transfected mCherry-PEX5(N-TPR) as acceptor and EGFP-PTS1 (ACOX3) as donor together with either PEX14(NTD)-Cerulean, Cerulean-PTS1 or Cerulean alone **(G)** the median DFRET values of subpopulations sharing an acc:don ratio of 0,75 < x < 1,3 and different competitor to donor ratios or **(H)** the DFRET decay curves (increasing comp:don) of all cells sharing an acc:don ratio of 0,75 < x < 1,3 are depicted; **(I)** and **(J)** comparison of decay curves due to PEX14(NTD)-Cerulean **(J)** or Cerulean-PTS1 **(K)** of cells sharing different acc:don ratios; **(K)** DFRET saturation curves (increasing acc:don) in the presence of a comp to donor ratio of 0,75 < x < 1,3 are depicted; **(L,M)** comparison of changes in the saturation curves due to PEX14(NTD)-Cerulean **(L)** or Cerulean-PTS1 **(M)** are depicted for different comp:don ratios; **(N)** the pattern of DFRET values of subpopulations sharing an acc:don ratio of 0,75 < x < 1,3 and different competitor to donor ratios is similar between three independent experiments. Statistics: **(G)** box blots with quartiles and ranges, multicomparison "Tukey-Kramer" for cells sharing acc:don rations between 0,75 < x < 1,3 and comp:don ratios between 1,6 < x < 2,4 (details of the statistics *cf.* Supplementary Table S2).

curve seemed to reach a lower DFRETmax plateau level, which is supported when inspecting curves based on a higher comp:don ratio (Figure 7L) but not for an inhibition by Cerulean-PTS1 (Figure 7M). Thus, overall, the curve progressions caused by PEX14(NTD) were obviously different from those caused by PTS1 as competitor and their shape resembled that of a non-competitive inhibition. These signs of another type of inhibition exerted by PEX14(NTD) on PEX5(N-TPR) were consistently found in three independent experiments (Figure 7N). However, as the presumable mode of inhibition is different for PEX14(NTD) the application of the fitting algorithm is not suitable and this allows only a qualitative description of the inhibitory effect. Altogether, these results not only verified the interaction between PEX5 and PEX14(NTD) in living cells, but also demonstrated that this interaction was not modulated by cargo proteins. On the contrary, PEX14(NTD) negatively modulated the interaction between PEX5(N-TPR) and its cargo, but the results provide evidence that the mode of inhibition is not a competitive one.

4 Discussion

The identification of PTS1 motifs, their ranking according to the affinity and the mode of recognition by the receptor PEX5 are long-standing research questions. However, investigating the interaction between full-length PTS1-carrying proteins and PEX5 has been a demanding task because this requires isolation and purification of proteins and the measurement of binding strengths by physical methods such as isothermal titration (Williams et al., 2011). In this manuscript, we describe a further development of our recently developed FRET-based method to study PEX5-PTS1 interactions in living cells (Hochreiter et al., 2020), which allows the measurement of the interaction strength between PEX5 and different full-length PTS1-containing cargo proteins. Although the coupling of FRET efficiency measurements and flow cytometry is a well-established method (Lim et al., 2022), our flowFRET approach unites an internal normalization procedure and mathematical analyses to estimate numerical values for apparent interaction strength and for the distance between donor and acceptor molecule. Here, we demonstrate that the overexpression of tagged competitor proteins, together with a suitable fitting algorithm, allows an efficient estimation of a measure for the interaction strength between the proteins. Using this approach, two traditional limitations of FRET measurements, namely the investigation of large proteins and low-affinity interactions can be effectively circumvented.

To verify the functionality of this approach, we demonstrate that the results of the prediction can depict characteristic properties of decay curves traditionally studied by binding assays, and the results of the fitting algorithms are in very good agreement with those obtained by bimolecular flowFRET measurements studying the same peptides directly. This method benefits from the internal normalization by concomitant measurement of the affinity of the acceptor to the donor (KD1) and the competitor (KD2), respectively. Thus, $Log_{10}(KD2^{app})/Log_{10}(KD1^{app})$ are highly correlated under different conditions, such as differences in the composition of data sets with respect to the acc:don or comp:don ratio. This renders the results of the fitting algorithm more robust, especially when using the ratio $Log_{10}(KD2^{app})/Log_{10}(KD1^{app})$ as output, and the results of experiments using the competition approach show lower normalized variability than bimolecular approaches. This competition method is especially well-suited to study the binding of low-affinity competitors such as the PTS1 of ACOX3-LK/SE or SCP2[AKL→AKV], which are difficult to study by bimolecular flowFRET experiments due to the low DFRET values of the entire sample. Moreover, we demonstrate that by this competition method, large proteins such as SCPx can be effectively studied with comparable variability to much smaller proteins such as SCP2. Finally, we provide the first evidence that this method might even be able to distinguish competitive modes of inhibition, for which the fitting

10.3389/fcell.2022.1026388

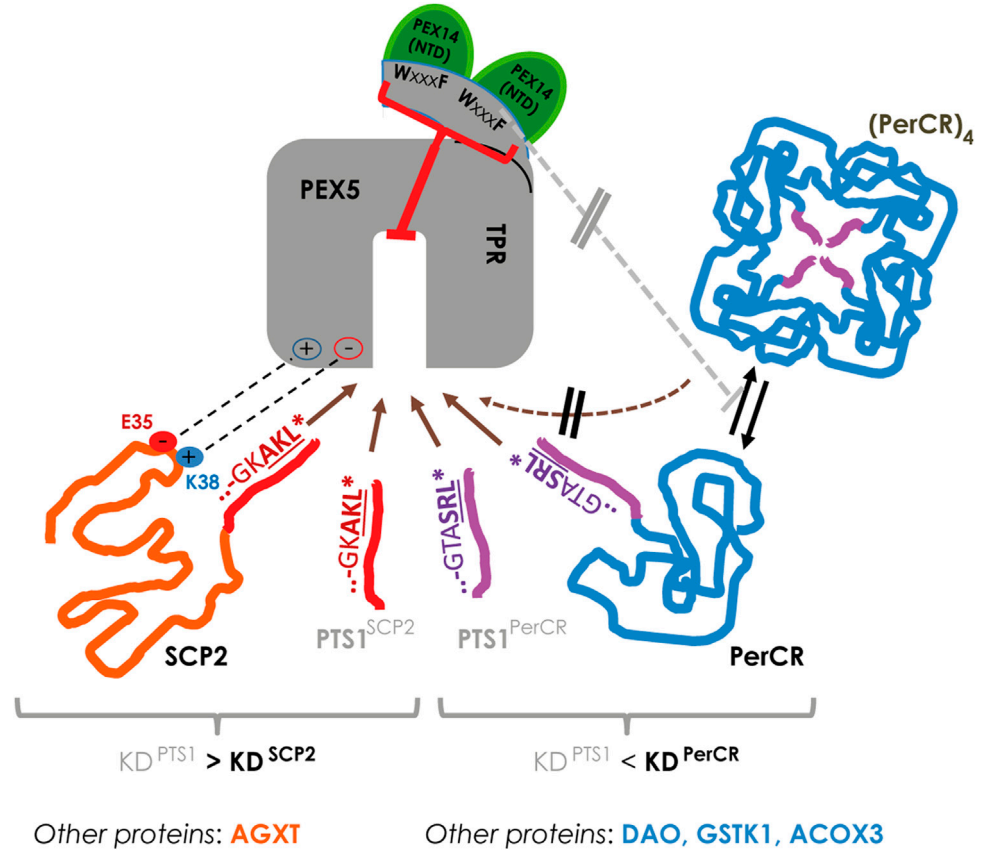

FIGURE 8
In living cells the interaction strength between PEX5 and its cargo proteins is modulated at various levels: *left*: in SCP2 the PTS1 binds PEX5 with lower affinity than the full-length protein due to an additional interaction domain (involving E35 and K38 of SCP2), which may also apply for the AGXT; *right*: in other proteins such as PerCR the interaction strength appears lower than the isolated PTS1, which is also observed for DAO, GSTK1 and ACOX3; in PerCR the PTS1 is inside the tetramer and thus not accessible to PEX5; thus, PerCR tetramers ($(PerCR)_4$) cannot bind PEX5 (hatched brown arrow) reducing the apparent interaction strength, but this effect is not modulated by elongating the TPR domain of PEX5 (PEX5(N-TPR)) (grey line).

algorithm has been developed, from other modes such as non-competitive or allosteric inhibition. Saturation (acc:don) and the decay (comp:don) curves caused by competitive inhibitors converge to the same plateau level or background level, whereas curves shaped by non-competitive mechanisms apparently present with different plateau levels. These differences simulate the curve progression for competitive and non-competitive inhibition of enzymes, but more detailed studies are needed and a mathematical solution for the fitting problem has to be developed.

Applying flowFRET based competition to study the interaction between PEX5 and its cargo proteins, we were able to verify the surprisingly low affinity of the PTS1 of AGXT (about 13,5 μM (Ghosh and Berg, 2010)), which nonetheless mediates PEX5 binding and the import of full-length AGXT (Motley et al., 1995; Huber et al., 2005). Similar to AGXT, the affinity of the 12 amino acid long PTS1(SCP2) was markedly lower than that of SCP2 (summarized in Figure 8, left side), which agrees with previous results using the last 6 amino acids (Williams et al., 2011). Here, we retrace the higher affinity of SCP2 to the contribution of two charged residues in the N-terminus of SCP2 participating in the additional interphase between SCP2 and PEX5 and required to lift the affinity above that of the isolated PTS1(SCP2) peptide. However, we find that SCPx binds PEX5 with lower affinity than monomeric SCP2 and the apparent interaction strength of SCPx is more similar to that of isolated PTS1. As the C-terminal domain of SCP2 and SCPx is identical this difference is presumably caused by a shielding effect mediated by the N-terminal thiolase domain, which affects either directly the PTS1 or the additional N-terminal PEX5-binding domain of SCP2. Interestingly, the thiolase domain of

the fish orthologoue (*D.rerio*) can occur as dimer (Kiema et al., 2019), which adds another level of complexity, because this dimerization also induces a conformational change in the thiolase domain. A similar difference between SCP2 and SCPx was observed when studying the effect of mutations directly in the PTS1, because we found that substituting a glycine of the PTS1 directly involved in PEX5-binding (Stanley et al., 2006) with the voluminous leucine (G139L) hardly affects the binding strength of SCPx to PEX5 but reduced that of SCP2 slightly. In contrast, substituting the C-terminal leucine by the equally bulky and hydrophobic valine (AKL→AKV) drastically reduced the affinity of SCP2 for PEX5, which can serve as explanation for the high abundance of leucine at the last position of naturally occurring tripeptides whereas valine is hardly found. This surprising result verifies in living cells for human PEX5 and a full-length protein a similar observation made by biophysical competition experiments using isolated plant PEX5 and PTS1-peptides (Skoulding et al., 2015). Surprisingly, the other full-length proteins investigated, such as *Hs*DAO, *Ss*PerCR, *Hs*ACOX3, and *Hs*GSTK1, presented with comparably low affinities compared to the PTS1 in isolation. However, only for SCP2 and AGXT a complex of cargo loaded PEX5 has been demonstrated by 3D-structures, whereas protein oligomerization and PEX5 binding might act competitively as has been described experimentally for human catalase (Freitas et al., 2011) or has been suggested based on steric restrictions in PerCR (Tanaka et al., 2008) (summarized in Figure 8, right side). Such competitive effects might contribute to our results, because in this system cargo proteins remain in the cytosol for a long time and thus might be prone to oligomerization. We exclude that an N-terminally extended variant of the PEX5 TPR-domain, which is able to bind PEX14 and was reported to disassemble catalase tetramers by a chaperone-like activity (Freitas et al., 2011) is sufficient to alleviate such competition effect, because the relative affinity of PEX5(TPR) and PEX5(N-TPR) to the investigated cargo proteins is similar. However, we cannot exclude the possibility that endogenous PEX14 might dissolve some of the cytosolic PEX5(N-TPR)-cargo complexes and thus hide a possible increase in affinity, although the high overexpression of donor and acceptor proteins is not favor of such model.

Finally, we provide evidence that the trimeric complex consisting of PEX5(N-TPR, aa268-602), PEX14(aa16–80) and SCP2, which has been reconstituted from isolated proteins (Shiozawa et al., 2009), also occurs in our system, because the interaction between PEX5(N-TPR) and PEX14(NTD) was well detectable, but not modulated by the presence of cargo proteins. Moreover, we also demonstrate that PEX14(NTD) reduces the affinity of human PEX5 (N-TPR) to a cargo protein, which had previously been shown for rat PEX14(NTD) in the context of inhibiting catalase tetramerization (Freitas et al., 2011). However, our results allow a quantifying description of the inhibitory effect, although the shape of the decay curve suggests a non-competitive mode of inhibition. Thus, these results further corroborate a PEX14-induced intraperoxisomal cargo release from PEX5 (Freitas et al., 2011), as a non-competitive mode of affinity modulation appears well suited for such mechanism (Figure 8).

Altogether, we introduce a novel method to study PPI in complexes involving large proteins by flowFRET and, by this means enlarged the toolbox for the peroxisome community to study the interaction between PEX5 and its full-length cargo proteins in more detail. Our experiments not only verified in living murine cells results obtained with isolated proteins but also provide the first description of a comparisons of different full-length PTS1-carrying proteins to PEX5.

Data availability statement

The raw data supporting the conclusions of this article will be made available by the authors, without undue reservation.

Author contributions

BH and MK performed experiments. HM and MK developed the program. BH and MK conceived the project. JS and JB helped with discussion. MK and HM wrote the paper, BH, HM, JB and JS edited the paper.

Funding

This research was funded by the Austrian Science Fund (FWF) project P34723-B to JB and the Austrian Science Fund (FWF) projects P-27842 und SFB-F54 to JS. For the purpose of open access, the authors JB and JS have applied a CC BY public copyright license to any author accepted manuscript version arising from this submission.

Acknowledgments

The authors are grateful for support by providing plasmids: EGFP-*Hs*DAO was kindly provided by Loredano (Sacchi et al., 2011) was kindly provided by (Tanaka et al., 2008) was kindly provided by Nobutada Tanaka (Showa University, Tokyo, JAP), EGFP-*Hs*AGXT (Fodor et al., 2012) was kindly provided by Wolfgang Schliebs (Univ.Bochum, Bochum, GER).

Conflict of interest

The authors declare that the research was conducted in the absence of any commercial or financial relationships that could be construed as a potential conflict of interest.

Publisher's note

All claims expressed in this article are solely those of the authors and do not necessarily represent those of their affiliated organizations, or those of the publisher, the editors and the reviewers. Any product that may be evaluated in this article, or claim that may be made by its manufacturer, is not guaranteed or endorsed by the publisher.

Supplementary material

The Supplementary Material for this article can be found online at: https://www.frontiersin.org/articles/10.3389/fcell.2022.1026388/full#supplementary-material

References

Baes, M., Gressens, P., Baumgart, E., Carmeliet, P., Casteels, M., Fransen, M., et al. (1997). A mouse model for Zellweger syndrome. *Nat. Genet.* 17, 49–57. doi:10.1038/ng0997-49

Brocard, C., and Hartig, A. (2006). Peroxisome targeting signal 1: Is it really a simple tripeptide? *Biochim. Biophys. Acta* 1763, 1565–1573. doi:10.1016/j.bbamcr.2006.08.022

Bunt, G., and Wouters, F. S. (2017). FRET from single to multiplexed signaling events. *Biophys. Rev.* 9, 119–129. doi:10.1007/s12551-017-0252-z

Burgi, J., Ekal, L., and Wilmanns, M. (2021). Versatile allosteric properties in Pex5-like tetratricopeptide repeat proteins to induce diverse downstream function. *Traffic* 22, 140–152. doi:10.1111/tra.12785

Chong, C. S., Kunze, M., Hochreiter, B., Krenn, M., Berger, J., and Maurer-Stroh, S. (2019). Rare human missense variants can affect the function of disease-relevant proteins by loss and gain of peroxisomal targeting motifs. *Int. J. Mol. Sci.* 20, E4609. doi:10.3390/ijms20184609

Cross, L. L., Paudyal, R., Kamisugi, Y., Berry, A., Cuming, A. C., Baker, A., et al. (2017). Towards designer organelles by subverting the peroxisomal import pathway. *Nat. Commun.* 8, 454. doi:10.1038/s41467-017-00487-7

Dahan, N., Francisco, T., Falter, C., Rodrigues, T., Kalel, V., Kunze, M., et al. (2021). Current advances in the function and biogenesis of peroxisomes and their roles in health and disease. *Histochem. Cell Biol.* 155, 513–524. doi:10.1007/s00418-021-01982-1

Dias, A. F., Francisco, T., Rodrigues, T. A., Grou, C. P., and Azevedo, J. E. (2016). The first minutes in the life of a peroxisomal matrix protein. *Biochim. Biophys. Acta* 1863, 814–820. doi:10.1016/j.bbamcr.2015.09.025

Fodor, K., Wolf, J., Erdmann, R., Schliebs, W., and Wilmanns, M. (2012). Molecular requirements for peroxisomal targeting of alanine-glyoxylate aminotransferase as an essential determinant in primary hyperoxaluria type 1. *PLoS Biol.* 10, e1001309. doi:10.1371/journal.pbio.1001309

Fodor, K., Wolf, J., Reglinski, K., Passon, D. M., Lou, Y., Schliebs, W., et al. (2015). Ligand-induced compaction of the PEX5 receptor-binding cavity impacts protein import efficiency into peroxisomes. *Traffic* 16, 85–98. doi:10.1111/tra.12238

Francisco, T., Rodrigues, T. A., Dias, A. F., Barros-Barbosa, A., Bicho, D., and Azevedo, J. E. (2017). Protein transport into peroxisomes: Knowns and unknowns. *BioEssays* 39, 1700047. doi:10.1002/bies.201700047

Francisco, T., Rodrigues, T. A., Freitas, M. O., Grou, C. P., Carvalho, A. F., Sa-Miranda, C., et al. (2013). A cargo-centered perspective on the PEX5 receptor-mediated peroxisomal protein import pathway. *J. Biol. Chem.* 288, 29151–29159. doi:10.1074/jbc.M113.487140

Freitas, M. O., Francisco, T., Rodrigues, T. A., Alencastre, I. S., Pinto, M. P., Grou, C. P., et al. (2011). PEX5 protein binds monomeric catalase blocking its tetramerization and releases it upon binding the N-terminal domain of PEX14. *J. Biol. Chem.* 286, 40509–40519. doi:10.1074/jbc.M111.287201

Gatto, G. J., Jr., Geisbrecht, B. V., Gould, S. J., and Berg, J. M. (2000). Peroxisomal targeting signal-1 recognition by the TPR domains of human PEX5. *Nat. Struct. Biol.* 7, 1091–1095. doi:10.1038/81930

Gatto, G. J., Jr., Maynard, E. L., Guerrerio, A. L., Geisbrecht, B. V., Gould, S. J., and Berg, J. M. (2003). Correlating structure and affinity for PEX5:PTS1 complexes. *Biochemistry* 42, 1660–1666. doi:10.1021/bi027034z

Ghosh, D., and Berg, J. M. (2010). A proteome-wide perspective on peroxisome targeting signal 1(PTS1)-Pex5p affinities. *J. Am. Chem. Soc.* 132, 3973–3979. doi:10.1021/ja9109049

Gould, S. J., Keller, G. A., Hosken, N., Wilkinson, J., and Subramani, S. (1989). A conserved tripeptide sorts proteins to peroxisomes. *J. Cell Biol.* 108, 1657–1664. doi:10.1083/jcb.108.5.1657

Hagen, S., Drepper, F., Fischer, S., Fodor, K., Passon, D., Platta, H. W., et al. (2015). Structural insights into cargo recognition by the yeast PTS1 receptor. *J. Biol. Chem.* 290, 26610–26626. doi:10.1074/jbc.M115.657973

Hochreiter, B., Chong, C. S., Hartig, A., Maurer-Stroh, S., Berger, J., Schmid, J. A., et al. (2020). A novel FRET approach quantifies the interaction strength of peroxisomal targeting signals and their receptor in living cells. *Cells* 9, 2381. doi:10.3390/cells9112381

Hochreiter, B., Kunze, M., Moser, B., and Schmid, J. A. (2019). Advanced FRET normalization allows quantitative analysis of protein interactions including stoichiometries and relative affinities in living cells. *Sci. Rep.* 9, 8233. doi:10.1038/s41598-019-44650-0

Huber, P. A., Birdsey, G. M., Lumb, M. J., Prowse, D. T., Perkins, T. J., Knight, D. R., et al. (2005). Peroxisomal import of human alanine:glyoxylate aminotransferase requires ancillary targeting information remote from its C terminus. *J. Biol. Chem.* 280, 27111–27120. doi:10.1074/jbc.M502719200

Islinger, M., Li, K. W., Seitz, J., Volkl, A., and Luers, G. H. (2009). Hitchhiking of Cu/Zn superoxide dismutase to peroxisomes--evidence for a natural piggyback import mechanism in mammals. *Traffic* 10, 1711–1721. doi:10.1111/j.1600-0854.2009.00966.x

Kawazoe, T., Tsuge, H., Pilone, M. S., and Fukui, K. (2006). Crystal structure of human D-amino acid oxidase: Context-dependent variability of the backbone conformation of the VAAGL hydrophobic stretch located at the si-face of the flavin ring. *Protein Sci.* 15, 2708–2717. doi:10.1110/ps.062421606

Kiema, T. R., Thapa, C. J., Laitaoja, M., Schmitz, W., Maksimainen, M. M., Fukao, T., et al. (2019). The peroxisomal zebrafish SCP2-thiolase (type-1) is a weak transient dimer as revealed by crystal structures and native mass spectrometry. *Biochem. J.* 476, 307–332. doi:10.1042/BCJ20180788

Kim, P. K., and Hettema, E. H. (2015). Multiple pathways for protein transport to peroxisomes. *J. Mol. Biol.* 427, 1176–1190. doi:10.1016/j.jmb.2015.02.005

Kunze, M., and Berger, J. (2015). The similarity between N-terminal targeting signals for protein import into different organelles and its evolutionary relevance. *Front. Physiol.* 6, 259. doi:10.3389/fphys.2015.00259

Kunze, M. (2020). The type-2 peroxisomal targeting signal. *Biochim. Biophys. Acta. Mol. Cell Res.* 1867, 118609. doi:10.1016/j.bbamcr.2019.118609

Lametschwandtner, G., Brocard, C., Fransen, M., Van Veldhoven, P., Berger, J., and Hartig, A. (1998). The difference in recognition of terminal tripeptides as peroxisomal targeting signal 1 between yeast and human is due to different affinities of their receptor Pex5p to the cognate signal and to residues adjacent to it. *J. Biol. Chem.* 273, 33635–33643. doi:10.1074/jbc.273.50.33635

Leon, S., Goodman, J. M., and Subramani, S. (2006). Uniqueness of the mechanism of protein import into the peroxisome matrix: Transport of folded, co-factor-bound and oligomeric proteins by shuttling receptors. *Biochim. Biophys. Acta* 1763, 1552–1564. doi:10.1016/j.bbamcr.2006.08.037

Lim, J., Petersen, M., Bunz, M., Simon, C., and Schindler, M. (2022). Flow cytometry based-FRET: Basics, novel developments and future perspectives. *Cell. Mol. Life Sci.* 79, 217. doi:10.1007/s00018-022-04232-2

Maynard, E. L., and Berg, J. M. (2007). Quantitative analysis of peroxisomal targeting signal type-1 binding to wild-type and pathogenic mutants of Pex5p

supports an affinity threshold for peroxisomal protein targeting. *J. Mol. Biol.* 368, 1259–1266. doi:10.1016/j.jmb.2007.03.005

Maynard, E. L., Gatto, G. J., Jr., and Berg, J. M. (2004). Pex5p binding affinities for canonical and noncanonical PTS1 peptides. *Proteins* 55, 856–861. doi:10.1002/prot.20112

Motley, A., Lumb, M. J., Oatey, P. B., Jennings, P. R., De Zoysa, P. A., Wanders, R. J., et al. (1995). Mammalian alanine/glyoxylate aminotransferase 1 is imported into peroxisomes via the PTS1 translocation pathway. Increased degeneracy and context specificity of the mammalian PTS1 motif and implications for the peroxisome-to-mitochondrion mistargeting of AGT in primary hyperoxaluria type 1. *J. Cell Biol.* 131, 95–109. doi:10.1083/jcb.131.1.95

Neufeld, C., Filipp, F. V., Simon, B., Neuhaus, A., Schuller, N., David, C., et al. (2009). Structural basis for competitive interactions of Pex14 with the import receptors Pex5 and Pex19. *EMBO J.* 28, 745–754. doi:10.1038/emboj.2009.7

Neuhaus, A., Kooshapur, H., Wolf, J., Meyer, N. H., Madl, T., Saidowsky, J., et al. (2014). A novel Pex14 protein-interacting site of human Pex5 is critical for matrix protein import into peroxisomes. *J. Biol. Chem.* 289, 437–448. doi:10.1074/jbc.M113.499707

Okamoto, K., and Sako, Y. (2017). Recent advances in FRET for the study of protein interactions and dynamics. *Curr. Opin. Struct. Biol.* 46, 16–23. doi:10.1016/j.sbi.2017.03.010

Rosenthal, M., Metzl-Raz, E., Burgi, J., Yifrach, E., Drwesh, L., Fadel, A., et al. (2020). Uncovering targeting priority to yeast peroxisomes using an in-cell competition assay. *Proc. Natl. Acad. Sci. U. S. A.* 117, 21432–21440. doi:10.1073/pnas.1920078117

Sacchi, S., Cappelletti, P., Giovannardi, S., and Pollegioni, L. (2011). Evidence for the interaction of D-amino acid oxidase with pLG72 in a glial cell line. *Mol. Cell. Neurosci.* 48, 20–28. doi:10.1016/j.mcn.2011.06.001

Shiozawa, K., Konarev, P. V., Neufeld, C., Wilmanns, M., and Svergun, D. I. (2009). Solution structure of human Pex5.Pex14.PTS1 protein complexes obtained by small angle X-ray scattering. *J. Biol. Chem.* 284, 25334–25342. doi:10.1074/jbc.M109.002311

Skoulding, N. S., Chowdhary, G., Deus, M. J., Baker, A., Reumann, S., and Warriner, S. L. (2015). Experimental validation of plant peroxisomal targeting prediction algorithms by systematic comparison of *in vivo* import efficiency and *in vitro* PTS1 binding affinity. *J. Mol. Biol.* 427, 1085–1101. doi:10.1016/j.jmb.2014.12.003

Stanley, W. A., Filipp, F. V., Kursula, P., Schuller, N., Erdmann, R., Schliebs, W., et al. (2006). Recognition of a functional peroxisome type 1 target by the dynamic import receptor pex5p. *Mol. Cell* 24, 653–663. doi:10.1016/j.molcel.2006.10.024

Tanaka, N., Aoki, K., Ishikura, S., Nagano, M., Imamura, Y., Hara, A., et al. (2008). Molecular basis for peroxisomal localization of tetrameric carbonyl reductase. *Structure* 16, 388–397. doi:10.1016/j.str.2007.12.022

Van Veldhoven, P. P., Van Rompuy, P., Fransen, M., De Bethune, B., and Mannaerts, G. P. (1994). Large-scale purification and further characterization of rat pristanoyl-CoA oxidase. *Eur. J. Biochem.* 222, 795–801. doi:10.1111/j.1432-1033.1994.tb18926.x

Wang, B., Peng, Y., Zhang, T., and Ding, J. (2011). Crystal structures and kinetic studies of human Kappa class glutathione transferase provide insights into the catalytic mechanism. *Biochem. J.* 439, 215–225. doi:10.1042/BJ20110753

Wang, B., Van Veldhoven, P. P., Brees, C., Rubio, N., Nordgren, M., Apanasets, O., et al. (2013). Mitochondria are targets for peroxisome-derived oxidative stress in cultured mammalian cells. *Free Radic. Biol. Med.* 65, 882–894. doi:10.1016/j.freeradbiomed.2013.08.173

Wang, Z. X. (1995). An exact mathematical expression for describing competitive binding of two different ligands to a protein molecule. *FEBS Lett.* 360, 111–114. doi:10.1016/0014-5793(95)00062-e

Waterham, H. R., Ferdinandusse, S., and Wanders, R. J. (2016). Human disorders of peroxisome metabolism and biogenesis. *Biochim. Biophys. Acta* 1863, 922–933. doi:10.1016/j.bbamcr.2015.11.015

Wiese, S., Gronemeyer, T., Ofman, R., Kunze, M., Grou, C. P., Almeida, J. A., et al. (2007). Proteomics characterization of mouse kidney peroxisomes by tandem mass spectrometry and protein correlation profiling. *Mol. Cell. Proteomics* 6, 2045–2057. doi:10.1074/mcp.M700169-MCP200

Williams, C. P., Schueller, N., Thompson, C. A., Van Den Berg, M., Van Haren, S. D., Erdmann, R., et al. (2011). The Peroxisomal Targeting Signal 1 in sterol carrier protein 2 is autonomous and essential for receptor recognition. *BMC Biochem.* 12, 12. doi:10.1186/1471-2091-12-12

Frontiers in
Cell and Developmental Biology

Explores the fundamental biological processes of life, covering intracellular and extracellular dynamics.

The world's most cited developmental biology journal, advancing our understanding of the fundamental processes of life. It explores a wide spectrum of cell and developmental biology, covering intracellular and extracellular dynamics.

Discover the latest Research Topics

See more →

Frontiers

Avenue du Tribunal-Fédéral 34
1005 Lausanne, Switzerland
frontiersin.org

Contact us

+41 (0)21 510 17 00
frontiersin.org/about/contact